Krishan K. Chawla

Composite Materials

Science and Engineering

Fourth Edition

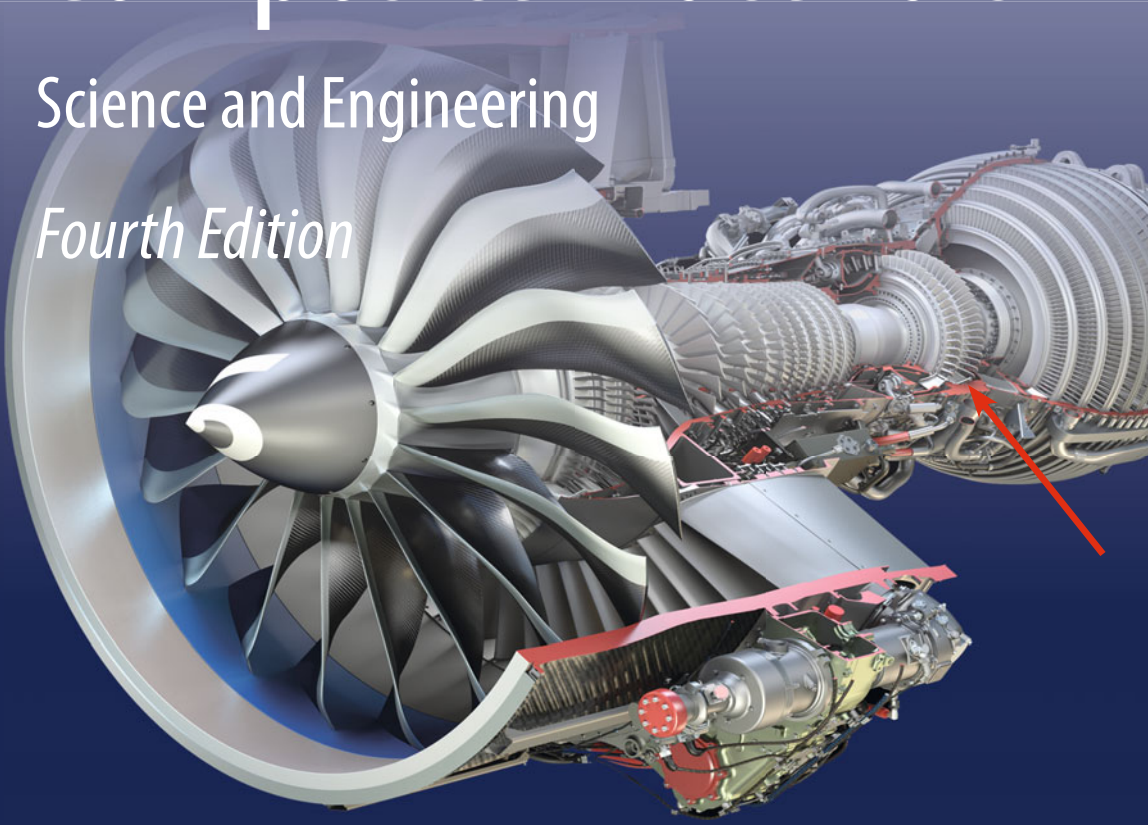

Springer

Composite Materials

Krishan K. Chawla

Composite Materials

Science and Engineering

Fourth Edition

Springer

Krishan K. Chawla
Department of Materials Science
and Engineering
The University of Alabama at Birmingham
Birmingham, AL, USA

ISBN 978-3-030-28982-9 ISBN 978-3-030-28983-6 (eBook)
https://doi.org/10.1007/978-3-030-28983-6

Cover illustration: Leap aircraft engine that uses shrouds made of ceramic matrix composites (silicon carbide fiber/silicon carbide matrix). [*Courtesy*: General Electric Co.] Arrow indicates the high pressure turbine region where CMC shrouds are used.

This Springer imprint is published by the registered company Springer Nature Switzerland AG
The registered company address is: Gewerbestrasse 11, 6330 Cham, Switzerland

आ नो भद्राः क्रतवो यन्तु विश्वतः

Ā no bhadrāḥ kratavo yantu viśvataḥ
Let noble thoughts come to us from every side

Rigveda 1-89-i

Dedicated affectionately to
A^2, D, K^3, and N^3

Preface to the Fourth Edition

It is with great pleasure that I offer this fourth edition of Composite Materials: Science and Engineering to the readers. The book has been thoroughly updated, new material been been added in all chapters, plus a new chapter, Repair and Recycling of Composites, has been added.

The third edition of this book saw the light of the day in 2012. Boeing 787 and Airbus 350 XWB entered into service in 2012 and 2015, respectively. Those two marked a major shift in the large-scale use of composites. Since then, GE and Safran have made tremendous inroads into the use of ceramic matrix composites in aircraft engines. The cover picture of this edition shows the LEAP engine, which uses shrouds made of silicon carbide fiber/silicon carbide matrix composites. Those developments are deservedly highlighted in this fourth edition. These developments have also brought home our attention to repair and recycling of composites, because nothing lasts forever. Inevitably there will be damage to components made of composites, which will require repair. Additionally, there is the question of the end of life of any component, which makes one think of recycling of composites. I have added a new chapter covering these two areas.

I would like to make an interesting observation about the cover of this book. The first edition of the book had no cover picture. The second edtion had the picture of a silicon carbide reinforced titanium alloy composite. The third edition had the picture of aircraft engine, GE90, which highlighted the fan blades made of carbon fiber reinforced epoxy. The present, fourth edition, shows Leap aircraft engine that uses components made of ceramic matrix composites. It has been a remarkable journey.

I am grateful to various institutions that funded my research work over the years; this book would not have come about without that research work. Of course, this kind of book is never produced as strictly the job of a single person. There are many people who made this journey bearable, even enjoyable. Among the people with whom I have had the privilege of collaborating over the years and who have enriched my life, professional and otherwise, I should mention, in alphabetical order, C.H. Barham, A.R. Boccaccini, K. Carlisle, K. Chawla, N. Chawla, X. Deng, Z. Fang, the late M.E. Fine, S.G. Fishman, G. Gladysz, A. Goel, the late B. Ilschner, M. Koopman, R.R. Kulkarni, A. Mortensen, B. Patel, B.R. Patterson,

P.D. Portella, the late J.M. Rigsbee, P. Rohatgi, H. Schneider, Y.-L Shen, Z.R. Xu, R. Vaidya, U. Vaidya, and A.K. Vasudevan. I am grateful to Prof. O. Weichold for help with Appendix B (Fiber Packing). Thanks are due to Kanika Chawla and Micah Armstrong for help with the figures in this edition. I owe a special debt of gratitude to my wife, Nivi, with whom I celebrated 50 years of married life in 2019. Last but not least, I will always be in debt to my parents, the late Manohar L. and Sumitra Chawla for all they did for me.

Birmingham, AL, USA Krishan K. Chawla
May 2019

Preface to the Third Edition

Since the publication of the second edition of this book, there has been a spate of activity in the field of composites, in the academia as well as in the industry. The industrial activity, in particular, has been led by the large scale use of composites by aerospace companies, mainly Boeing and Airbus. It would not be far off the mark to say that the extensive use of carbon fiber/epoxy resin composites in Boeing 787 aircraft and a fairly large use of composites in Airbus's A 380 aircraft represents a paradigm shift. Boeing 787 has composites in the fuselage, windows, wings, tails, stabilizers, etc. resulting in 50 percent in composites by weight. Nevertheless, it should be pointed out that in reality, the extensive use of composites in aircraft is a culmination of series of earlier steps over the decades since mid-1960s. Besides, the large scale applications in the aerospace industry, there have been impressive developments in other other fields such as automotive, sporting goods, superconductivity, etc.

All of this activity has led to a substantial addition of new material in this edition. Among these are: Carbon/carbon brakes, nanocomposites, biocomposites, self-healing composites, self-reinforced composites, fiber/metal laminate composites, composites for civilian aircraft, composites for aircraft jet engine, second generation high temperature superconducting composites, WC/metal particulate composites, new solved examples, and new problems, etc. In addition, I have added a new chapter, called non-conventional composites. This chapter deals with some non-conventional composites: Nanocomposites (polymer, metal, and ceramic matrix), self healing composites, self reinforced composites, biocomposites, and laminates made of bidimensional layers.

Once again, I plead guilty to the charge that the material contained in this edition is more than can be covered in a normal, semester-long course. The instructor of course can cut the content to his/her requirements. I have always had the broader aim of providing a text that is suitable as a source of reference for the practicing researcher, scientist, and engineer.

Finally, there is the pleasant task of acknowledgments. I am grateful to National Science Foundation, Office of Naval Research, Federal Transit Administration, Los Alamos National Laboratory Sandia national Laboratory, Oak Ridge National Laboratory, Smith International Inc., and Trelleborg, Inc. for supporting my research work over the years, some of which is included in this text. Among the people with whom I have had the privilege of collaborating over the years and who have enriched my life, professional and otherwise, I would like to mention, in alphabetical order, C.H. Barham, A.R. Boccaccini, K. Carlisle, K. Chawla, N. Chawla, X. Deng, Z. Fang, M.E. Fine, S.G. Fishman, G. Gladysz, A. Goel, N. Gupta, the late B. Ilschner, M. Koopman, R.R. Kulkarni, B.A. MacDonald, A. Mortensen, B. Patel, B.R. Patterson, P.D. Portella, J.M. Rigsbee, P. Rohatgi, H. Schneider, N.S. Stoloff, Y.-L Shen, S. Suresh, Z.R. Xu, U. Vaidya, and A.K. Vasudevan. Thanks are due to Kanika Chawla and Satyam Patel for help with the figures in this edition. I owe a special debt of gratitude to my wife, Nivi, for being there all the time. Last but not least, I am ever grateful to my parents, the late Manohar L. and Sumitra Chawla for their guidance and support.

Birmingham, AL, USA Krishan K. Chawla
March 2011

Preface to the Second Edition

The first edition of this book came out in 1987, offering an integrated coverage of the field of composite materials. I am gratified at the reception it received at the hands of the students and faculty. The second edition follows the same format as the first one, namely, a well-balanced treatment of materials and mechanics aspects of composites, with due recognition of the importance of the processing. The second edition is a fully revised, updated, and enlarged edition of this widely used text. There are some new chapters, and others have been brought up-to-date in light of the extensive work done in the decade since publication of the first edition. Many people who used the first edition as a classroom text urged me to include some solved examples. In deference to their wishes I have done so. I am sorry that it took me such a long time to prepare the second edition. Things are happening at a very fast pace in the field of composites, and there is no question that a lot of very interesting and important work has been done in the past decade or so. Out of necessity, one must limit the amount of material to be included in a textbook. In spite of this view, it took me much more time than I anticipated. In this second edition, I have resisted the temptation to cover the whole waterfront. So the reader will find here an up-to-date treatment of the fundamental aspects. Even so, I do recognize that the material contained in this second edition is more than what can be covered in the classroom in a semester. I consider that to be a positive aspect of the book. The reader (student, researcher, practicing scientist/engineer) can profitably use this as a reference text. For the person interested in digging deeper into a particular aspect, I provide an extensive and updated list of references and suggested reading.

There remains the pleasant task of thanking people who have been very helpful and a constant source of encouragement to me over the years: M.E. Fine, S.G. Fishman, J.C. Hurt, B. Ilschner, B.A. MacDonald, A. Mortensen, J.M. Rigsbee, P. Rohatgi, S. Suresh, H. Schneider, N.S. Stoloff, and A.K. Vasudevan. Among my students and post-docs, I would like to acknowledge G. Gladysz, H. Liu, and Z.R. Xu. I am immensely grateful to my family members, Nivi, Nikhil, and Kanika. They were patient and understanding throughout.

Without Kanika's help in word processing and fixing things, this work would still be unfinished. Once again I wish to record my gratitude to my parents, Manohar L. Chawla and the late Sumitra Chawla for all they have done for me!

Birmingham, AL, USA Krishan K. Chawla
February 1998

Preface to the First Edition

The subject of composite materials is truly an inter- and multidisciplinary one. People working in fields such as metallurgy and materials science and engineering, chemistry and chemical engineering, solid mechanics, and fracture mechanics have made important contributions to the field of composite materials. It would be an impossible task to cover the subject from all these viewpoints. Instead, we shall restrict ourselves in this book to the objective of obtaining an understanding of composite properties (e.g., mechanical, physical, and thermal) as controlled by their structure at micro- and macro-levels. This involves a knowledge of the properties of the individual constituents that form the composite system, the role of interface between the components, the consequences of joining together, say, a fiber and matrix material to form a unit composite ply, and the consequences of joining together these unit composites or plies to form a macrocomposite, a macroscopic engineering component as per some optimum engineering specifications. Time and again, we shall be emphasizing this main theme, that is structure–property correlations at various levels that help us to understand the behavior of composites.

In Part I, after an introduction (Chap. 1), fabrication and properties of the various types of reinforcement are described with a special emphasis on microstructure–property correlations (Chap. 2). This is followed by a chapter (Chap. 3) on the three main types of matrix materials, namely, polymers, metals, and ceramics. It is becoming increasingly evident that the role of the matrix is not just that of a binding medium for the fibers but it can contribute decisively toward the composite performance. This is followed by a general description of the interface in composites (Chap. 4). In Part II a detailed description is given of some of the important types of composites (Chap. 5), metal matrix composites (Chap. 6), ceramic composites (Chap. 7), carbon fiber composites (Chap. 8), and multifilamentary superconducting composites (Chap. 9). The last two are described separately because they are the most advanced fiber composite systems of the 1960s and 1970s. Specific characteristics and applications of these composite systems are brought out in these chapters. Finally, in Part III, the micromechanics (Chap. 10) and macromechanics (Chap. 11) of composites are described in detail, again emphasizing the theme of how structure (micro and macro) controls the properties. This is followed by a

description of strength and fracture modes in composites (Chap. 12). This chapter also describes some salient points of difference, in regard to design, between conventional and fiber composite materials. This is indeed of fundamental importance in view of the fact that composite materials are not just any other new material. They represent a total departure from the way we are used to handling conventional monolithic materials, and, consequently, they require unconventional approaches to designing with them.

Throughout this book examples are given from practical applications of composites in various fields. There has been a tremendous increase in applications of composites in sophisticated engineering items. Modern aircraft industry readily comes to mind as an ideal example. Boeing Company, for example, has made widespread use of structural components made of "advanced" composites in 757 and 767 planes. Yet another striking example is that of the Beechcraft Company's Starship 1 aircraft. This small aircraft (8–10 passengers plus crew) is primarily made of carbon and other high-performance fibers in epoxy matrix. The use of composite materials results in 19% weight reduction compared to an identical aluminum airframe. Besides this weight reduction, the use of composites made a new wing design configuration possible, namely, a variable-geometry forward wing that sweeps forward during takeoff and landing to give stability and sweeps back 30° in level flight to reduce drag. As a bonus, the smooth structure of composite wings helps to maintain laminar air flow. Readers will get an idea of the tremendous advances made in the composites field if they would just remind themselves that until about 1975 these materials were being produced mostly on a laboratory scale. Besides the aerospace industry, chemical, electrical, automobile, and sports industries are the other big users, in one form or another, of composite materials.

This book has grown out of lectures given over a period of more than a decade to audiences comprised of senior year undergraduate and graduate students, as well as practicing engineers from industry. The idea of this book was conceived at Instituto Militar de Engenharia, Rio de Janeiro. I am grateful to my former colleagues there, in particular, J.R.C. Guimarães, W.P. Longo, J.C.M. Suarez, and A.J.P. Haiad, for their stimulating companionship. The book's major gestation period was at the University of Illinois at Urbana-Champaign, where C.A. Wert and J.M. Rigsbee helped me to complete the manuscript. The book is now seeing the light of the day at the New Mexico Institute of Mining and Technology. I would like to thank my colleagues there, in particular, O.T. Inal, P. Lessing, M.A. Meyers, A. Miller, C.J. Popp, and G.R. Purcell, for their cooperation in many ways, tangible and intangible. An immense debt of gratitude is owed to N.J. Grant of MIT, a true gentleman and scholar, for his encouragement, corrections, and suggestions as he read the manuscript. Thanks are also due to R. Signorelli, J. Cornie, and P.K. Rohatgi for reading portions of the manuscript and for their very constructive suggestions. I would be remiss in not mentioning the students who took my courses on composite materials at New Mexico Tech and gave very constructive feedback. A special mention should be made of C.K. Chang, C.S. Lee, and N. Pehlivanturk for their relentless queries and discussions. Thanks are also due to my wife, Nivedita Chawla, and Elizabeth Fraissinet for their diligent word processing; my

son, Nikhilesh Chawla, helped in the index preparation. I would like to express my gratitude to my parents, Manohar L. and Sumitra Chawla, for their ever-constant encouragement and inspiration.

Socorro, NM, USA Krishan K. Chawla
June 1987

Other Books by Krishan K. Chawla

Fibrous Materials, 2nd ed., Cambridge University Press, Cambridge, 2016.
Voids in Materials (*coauthor*), Elsevier, Boston, 2015.
Mechanical Behavior of Materials (*coauthor*), 2nd ed., Cambridge University Press, Cambridge, 2009.
Metal Matrix Composites (*coauthor*), 2nd ed., Springer, New York, 2006.
Ceramic Matrix Composites, 2nd ed., Kluwer Acad. Press, Boston, 2003.
Mechanical Metallurgy (*coauthor*), Prentice–Hall, Englewood Cliffs, NJ, 1984.
Metalurgia Mecânica (*coauthor*), Edgard Blucher, Sâo Paulo, 1982.

Contents

About the Author

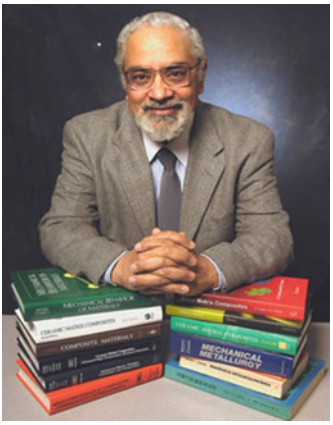

Prof. Krishan K. Chawla obtained his B.S. from Banaras Hindu University and his M.S. and Ph.D. degrees from the University of Illinois *at* Urbana-Champaign. He has taught and/or done research at (in alphabetical order) Arizona State University, Tempe, AZ; Ecole Polytechnique Federale de Lausanne (Switzerland); Federal Institute for Materials Research and Testing (BAM), Berlin (Germany); German Aerospace Research Institute (DLR), Cologne (Germany); Instituto Militar de Engenharia (Brazil); Laval University (Canada); Los Alamos National Lab, (USA); New Mexico Tech (USA); Northwestern University (USA); University of Alabama at Birmingham (USA), and University of Illinois *at* Urbana-Champaign (USA).

He has published extensively in the areas of processing, microstructure, and mechanical behavior of materials, in general, and composite materials and fibers in particular. Besides being a member of various professional societies, Professor Chawla is Editor of **International Materials Review** (published by Taylor and Francis for ASM International, USA and the Institute of Materials, Minerals and Mining, UK) and a member of the Editorial Board of various journals. During 1989–1990, Professor Chawla served as a Program Director for metals and ceramics in the Division of Materials Research, National Science Foundation, Washington, DC. Professor Chawla serves as a consultant to the industry, US

national laboratories, and various US federal government and international agencies. In 1990, he was selected an **ASM International–Indian Institute of Metals lecturer**. In 1992, he was the recipient of the **Eshbach Society Distinguished Visiting Scholar Award** from Northwestern University. During the period of June, 1994 through June, 1995 he held the **US Department of Energy Faculty Fellowship** at Oak Ridge National Lab. In 1996 he was given the **Distinguished Researcher Award** by the New Mexico Tech. In 1997, he was made a **Fellow of ASM international**. In 2000 he was awarded the **Distinguished Alumnus** award by Banaras Hindu University. He received the **President's Award for Excellence in Teaching**, University of Alabama at Birmingham in 2006. He received the **Educator Award** by The Minerals, Metals and Materials Society (TMS) in 2011. In 2018, he received the Albert Nelson Marquis **Lifetime Achievement Award**.

Part I

Chapter 1
Introduction

It is a truism that technological development depends on advances in the field of materials. One does not have to be an expert to realize that the most advanced turbine or aircraft design is of no use if adequate materials to bear the service loads and conditions are not available. Whatever the field may be, the final limitation on advancement depends on materials. Composite materials in this regard represent nothing but a giant step in the ever-constant endeavor of optimization in materials.

Strictly speaking, the idea of composite materials is not a new or recent one. Nature is full of examples wherein the idea of composite materials is used. The coconut palm leaf, for example, is essentially a cantilever using the concept of fiber reinforcement. Wood is a fibrous composite: cellulose fibers in a lignin matrix. The cellulose fibers have high tensile strength but are very flexible (because of low stiffness), while the lignin matrix joins the fibers and furnishes the stiffness. Bone is yet another example of a natural composite that supports the weight of various members of the body. It consists of short and soft collagen fibers embedded in a mineral matrix called apatite. Weiner and Wagner (1998) give a good description of structure and properties of bone. For descriptions of the structure–function relationships in the plant and animal kingdoms, the reader is referred to Elices (2000) and Wainwright et al. (1982). In addition to these naturally occurring composites, there are many other engineering materials that are composites in a very general way and that have been in use for a very long time. Evidence of the use of straw to reinforce clay can be traced to prehistoric times. Figure 1.1 shows straw reinforced adobe wall in Taos pueblo in New Mexico, USA. The carbon black in rubber, Portland cement or asphalt mixed with sand, and glass fibers in resin are other common examples. Thus, we see that the idea of composite materials is not that recent. Nevertheless, one can safely mark the origin of the distinct discipline of composite materials as the beginning of the 1960s. It would not be too much off the mark to say that a concerted research and development effort in composite materials began in 1965. Since the early 1960s, there has been an increasing demand for materials that are stiffer and stronger yet lighter in fields as diverse as aerospace,

K. K. Chawla, *Composite Materials*,
https://doi.org/10.1007/978-3-030-28983-6_1

energy, and civil construction. The demands made on materials for better overall performance are so great and diverse that no one material can satisfy them. This naturally led to a resurgence of the ancient concept of combining different materials in an integral-composite material to satisfy the user requirements. Such composite material systems result in a performance unattainable by the individual constituents, and they offer the great advantage of a flexible design, that is, one can, in principle, tailor-make the material as per specifications of an optimum design. This is a much more powerful statement than it might appear at first sight. It implies that, given the most efficient design of, say, an aerospace structure, an automobile, a boat, or an electric motor, we can make a composite material that meets the need. Schier and Juergens (1983) surveyed the design impact of composites on fighter aircraft. According to these authors, "composites have introduced an extraordinary fluidity to design engineering, in effect forcing the designer-analyst to create a different material for each application as he pursues savings in weight and cost."

Yet another conspicuous development has been the integration of the materials science and engineering input with the manufacturing and design inputs at all levels, from conception to commissioning of an item, through the inspection during the lifetime, as well as failure analysis. More down-to-earth, however, is the fact that our society has become very energy conscious. This has led to an increasing demand for lightweight yet strong and stiff structures in all walks of life. And composite materials are increasingly providing the answers. Figure 1.2 makes a comparison, admittedly for illustrative purposes, between conventional monolithic materials, such as aluminum and steel, and composite materials (Deutsch 1978). This figure indicates the possibilities of improvements that one can obtain over conventional materials by the use of composite materials. As such, it describes vividly the driving force behind the large effort in the field of composite materials. Glass fiber reinforced resins have been in use since the early twentieth century. Glass fiber reinforced resins are very light and strong materials, although their stiffness (modulus) is not very high, mainly because the glass fiber itself is not very stiff. The third quarter of the twentieth century saw the emergence of the so-called advanced fibers of extremely high modulus, for example, boron, carbon, silicon carbide, and alumina (Chawla 2005, 2016). These fibers have been used for reinforcement of resin, metal, and ceramic matrices. Fiber reinforced composites have been more prominent than other types of composites for the simple reason that most materials are stronger and stiffer in the fibrous form than in any other form. By the same token, it must be recognized that a fibrous form results in reinforcement mainly in fiber direction. Transverse to the fiber direction, there is little or no reinforcement. Of course, one can arrange fibers in two-dimensional or even three-dimensional arrays, but this still does not gainsay the fact that one is not getting the full reinforcement effect in directions other than the fiber axis. Thus, if a less anisotropic behavior is the objective, then perhaps laminate or sandwich composites made of, say, two different materials would be more effective. A particle reinforced composite will also be reasonably isotropic. There may also be specific nonmechanical objectives for making a fibrous composite. For example, an abrasion or corrosion-resistant surface would require the use of a laminate (sandwich)

Fig. 1.1 Straw reinforced adobe wall in Taos pueblo in New Mexico, USA

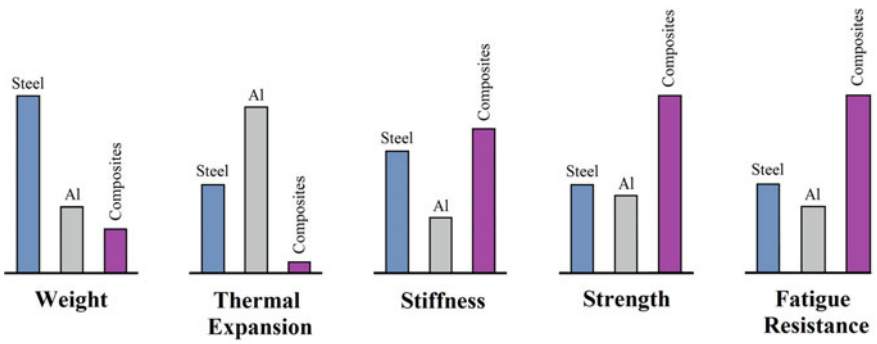

Fig. 1.2 Comparison between conventional monolithic materials and composite materials (From Deutsch (1978), used with permission.)

form, while in superconductors the problem of flux pinning requires the use of extremely fine filaments embedded in a conductive matrix. In what follows, we discuss the various aspects of composites, mostly fiber composites, in greater detail, but first let us agree on an acceptable definition of a composite material. Practically, everything in this world is a composite material. Thus, a common piece of metal is a composite (polycrystal) of many grains (or single crystals). Such a definition would make things quite unwieldy. Therefore, we must agree on an operational definition of *composite material* for our purposes in this text. We shall call a material that satisfies the following conditions a composite material:

1. It is manufactured (i.e., naturally occurring composites, such as wood, are excluded).
2. It consists of two or more physically and/or chemically distinct, suitably arranged or distributed phases with an interface separating them.
3. It has characteristics that are not depicted by any of the components in isolation.

Problems

1.1 Describe the structure and properties of some fiber reinforced composites that occur in nature.
1.2 Many ceramic-based composite materials are used in electronics industry. Describe some of these electroceramic composites.
1.3 Voyager airplane circled the globe for the first time without refueling in flight. Describe the use of composite materials in this plane.
1.4 Nail is a natural fibrous composite. Describe its components, microstructure, and properties.
1.5 Discuss the use of composite materials in civilian aircraft, with special attention to Boeing 787 and Airbus 350 and 380 aircrafts.

References

K.K. Chawla, J. Miner. Metals Mater. Soc. **57**, 46 (Feb., 2005)
K.K. Chawla, *Fibrous Materials*, 2nd edn. (Cambridge University Press, Cambridge, England, 2016)
S. Deutsch, in *23rd National SAMPE Symposium* (1978), p 34
M. Elices (ed.), *Structural Biological Materials* (Pergamon Press, Amsterdam, 2000)
J.F. Schier, R.J. Juergens, Astronaut. Aeronaut. **21**, 44 (1983)
S.A. Wainwright, W.D. Biggs, J.D. Currey, J.M. Gosline, *Mechanical Design in Organisms* (Princeton University Press, Princeton, NJ, 1982)
S. Weiner, H.D. Wagner, Ann. Rev. Mater. **28**, 271 (1998)

Chapter 2
Reinforcements

2.1 Introduction

Reinforcements can be in the form of particles, flakes, whiskers, short fibers, continuous fibers, or sheets. It turns out that most reinforcements used in composites have a fibrous form because materials are stronger and stiffer in the fibrous form than in any other form and the matter in a fibrous form can be very flexible (Chawla 2016). Specifically, in the category of fibrous reinforcements, we are most interested in the so-called advanced fibers, which possess very high strength and very high stiffness coupled with a very low density. The reader should realize that many naturally occurring fibers can be and are used in situations involving not very high stresses (Chawla 1976; Chawla and Bastos 1979). The great advantage in this case, of course, is its low cost. The vegetable kingdom is, in fact, the largest source of fibrous materials. Cellulosic fibers in the form of cotton, flax, jute, hemp, sisal, and ramie, for example, have been used in the textile industry, while wood and straw have been used in the paper industry. Other natural fibers, such as hair, wool, and silk, consist of different forms of protein. Silk fibers produced by a variety of spiders, in particular, appear to be very attractive because of their high work of fracture. Any discussion of such fibers is beyond the scope of this book. The interested reader is directed to some books that cover the vast field of fibers used as reinforcements (Chawla 2016; Warner 1995). In this chapter, we confine ourselves to a variety of man-made reinforcements. Glass fiber, in its various forms, has been the most common reinforcement for polymeric matrices. Aramid fiber, launched in the 1960s, is much stiffer and lighter than glass fiber. It should be pointed out that Kevlar is DuPont's trade name for aramid fiber while Twaron is the trade name of aramid fiber made by Teijin Aramid. Gel-spun polyethylene fiber, which has a stiffness comparable to that of aramid fiber, was commercialized in the 1980s. Other high-performance fibers that combine high strength with high stiffness are boron, silicon carbide, carbon, and alumina. These were all developed in the second part of the twentieth century. In particular, some ceramic fibers were developed in the last

K. K. Chawla, *Composite Materials*,
https://doi.org/10.1007/978-3-030-28983-6_2

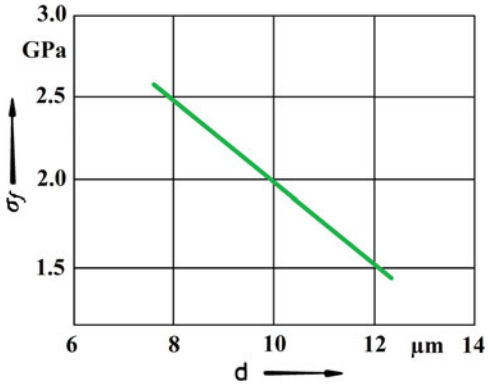

Fig. 2.1 Decrease in strength (σ_f) of a carbon fiber with increase in diameter. (From de Lamotte and Perry 1970, used with permission)

quarter of the twentieth century by some very novel processing techniques, namely, sol–gel processing and controlled pyrolysis of organic precursors. We will highlight some of these processes later in this chapter.

The use of fibers as high-performance engineering materials is based on three important characteristics (Dresher 1969):

1. A small diameter with respect to its grain size or other microstructural unit. This allows a higher fraction of the theoretical strength to be attained than is possible in a bulk form. This is a direct result of the so-called *size effect*; the smaller the size, the lower the probability of having imperfections in the material. Figure 2.1 shows that the strength of a carbon fiber decreases as its diameter increases (de Lamotte and Perry 1970). Although this figure shows a linear drop in strength with increasing fiber diameter, a nonlinear relationship is not uncommon. Figure 2.1 should be taken only as a general trend indicator.
2. A high aspect ratio (length/diameter, *l*/*d*), which allows a very large fraction of the applied load to be transferred via the matrix to the stiff and strong fiber (see Chap. 10).
3. A very high degree of flexibility, which is really a characteristic of a material that has a low modulus or stiffness and a small diameter. This flexibility permits the use of a variety of techniques for making composites with these fibers.

Next, we consider the concept of flexibility, and then we describe the general fiber spinning processes.

2.1.1 Flexibility

Flexibility of a given material, as pointed out in the attributes above, is a function of its elastic stiffness and dimensions of the cross section. Intuitively, one can easily visualize that the higher the stiffness of material, the less flexible it will be. But

when we think of flexibility of a fiber or thread, we wish to know to what arbitrary radius we can bend it to before it fails. We can treat our single fiber to be an elongated elastic beam. Let us subject this fiber of Young's modulus, E and diameter, d to a bending moment, M, which will bend it to a radius, R. For such an elastic bending of a beam, we define *flexural rigidity* as the product, MR. From elementary strength of materials, we have the following relationship for a beam bent to a radius R:

$$\frac{M}{I} = \frac{E}{R}$$

or

$$MR = EI,$$

where E is the Young's modulus of the material and I is the second moment of area or moment of inertia of its cross section. For a beam or a fiber of diameter, d, the second moment of area about an axis through the centroid of the beam is given by $I = \pi d^4/64$. Now, we can define flexibility of the fiber (i.e., the elastic beam under consideration) as the inverse of flexural rigidity. In other words, flexibility of a fiber is an inverse function of its elastic modulus, E, and the second moment of area or moment of inertia of its cross section, I. The elastic modulus of a material is independent of its form or size and is generally a material constant for a given chemical composition (assuming a fully dense material). Thus, for a given composition and density, the flexibility of a material is determined by its shape, or more precisely by its diameter. Substituting for $I = \pi d^4/64$ in the above expression, we get

$$MR = EI = \frac{E\pi d^4}{64}.$$

Or, the flexibility, being equal to $1/MR$, is

$$\text{Flexibility} = \frac{1}{MR} = \frac{64}{E\pi d^4}, \tag{2.1}$$

where d is the equivalent diameter and I is the moment of inertia of the beam (fiber). Equation (2.1) tells us that flexibility, $1/MR$, is a very sensitive function of diameter, d. We can summarize the important implications of Eq. (2.1) as follows:

- Flexibility of a fiber is a very sensitive inverse function of its diameter, d.
- Given a sufficiently small diameter, it is possible to produce, in principle, a fiber as flexible as any from any material, a polymer, a metal, or a ceramic.
- One can make very flexible fibers out of inherently brittle materials such as glass, silicon carbide, alumina, etc. provided one can shape these brittle materials into a fine-diameter fiber. Producing a fine-diameter ceramic fiber, however, is a daunting problem in processing.

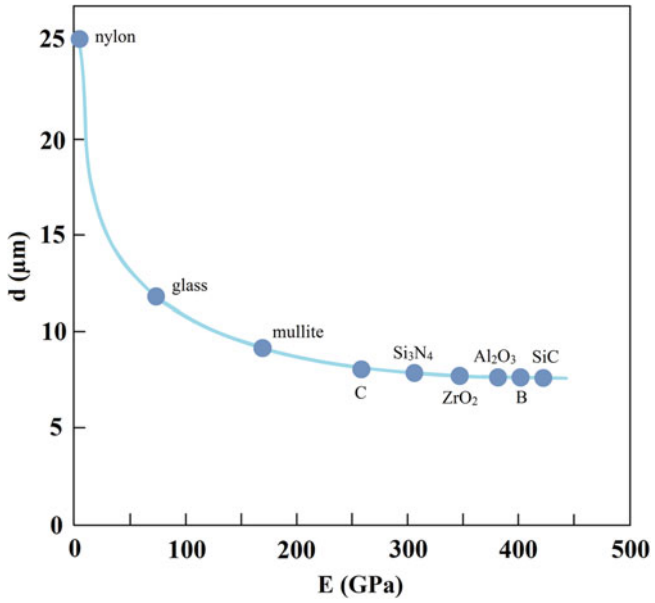

Fig. 2.2 Fiber diameter of different materials with flexibility equal to that of a nylon (polyamide) fiber of diameter equal to 25 μm. Note that one can make very flexible fibers out of brittle materials such as glass, silicon carbide, alumina, etc. provided one can process them into a small diameter

To illustrate this concept of flexibility, we plot the diameter of various materials in fibrous form with flexibility ($1/MR$) equal to that of highly flexible filament, namely, a 25 μm diameter nylon (polyamide) fiber as function of the elastic modulus, E, Fig. 2.2. Note that given a sufficiently small diameter, it is possible for a metal or ceramic material to have the same degree of flexibility as that of a 25 μm diameter nylon fiber; it is, however, another matter that obtaining such a small diameter in practice can be prohibitively expensive.

2.1.2 Fiber Spinning Processes

Fiber spinning is the process of extruding a liquid through small holes in a spinneret to form solid filaments. In nature, silkworms and spiders produce continuous filaments by this process. There exists a variety of different fiber spinning techniques; some of the important ones are as follows:

Wet spinning: A solution is extruded into a coagulating bath. The jets of liquid freeze or harden in the coagulating bath as a result of chemical or physical changes.
Dry spinning: A solution consisting of a fiber-forming material and a solvent is extruded through a spinneret. A stream of hot air impinges on the jets of solution

emerging from the spinneret, the solvent evaporates, and solid filaments are left behind.
Melt spinning: The fiber-forming material is heated above its melting point and the molten material is extruded through a spinneret. The liquid jets harden into solid filaments in air on emerging from the spinneret holes.
Dry-jet wet spinning: This is a special process devised for spinning of aramid fibers. In this process, an appropriate polymer liquid crystal solution is extruded through spinneret holes, passes through an air gap before entering a coagulation bath, and then goes onto a spool for winding. We describe this process in detail in Sect. 2.6.2.

2.1.3 Stretching and Orientation

The process of extrusion through a spinneret results in some chain orientation in a polymeric fiber. Generally, the molecules in the surface region undergo more orientation than the ones in the interior because the edges of the spinneret hole affect the near-surface molecules more than those in the interior. This is known as the *skin effect*, and it can affect many other properties of the fiber, such as the adhesion with a polymeric matrix or the ability to be dyed. Generally, the as-spun fiber is subjected to some stretching, causing further chain orientation along the fiber axis and consequently better tensile properties, such as stiffness and strength, along the fiber axis. The amount of stretch is generally described in terms of a draw ratio, which is the ratio of the initial diameter to the final diameter. For example, nylon (polyamide) fibers are typically subjected to a draw ratio of 5 after spinning. A high draw ratio results in a high elastic modulus. Increased alignment of chains means a higher degree of crystallinity in a fiber. This also affects the ability of a fiber to absorb moisture. The higher the degree of crystallinity, the lower the moisture absorption. In general, the higher degree of crystallinity translates into a higher resistance to penetration by foreign molecules, i.e., a greater chemical stability. The stretching treatment serves to orient the molecular structure along the fiber axis. It does not, generally, result in complete elimination of molecular branching, that is, one gets molecular orientation but not molecular extension. Such stretching treatments do result in somewhat more efficient packing than in the unstretched polymer, but there is a limit to the amount of stretch that can be given to a polymer because the necking of fiber can intervene and cause rupture of the fiber.

2.2 Glass Fibers

Glass fiber is a generic name like carbon fiber or steel or aluminum. Just as different compositions of steel or aluminum alloys are available, there are many different chemical compositions of glass fibers that are commercially available. Common

Table 2.1 Approximate chemical composition of some glass fibers (*wt%*)

Composition	E glass	C glass	S glass
SiO_2	55.2	65.0	65.0
Al_2O_3	8.0	4.0	25.0
CaO	18.7	14.0	–
MgO	4.6	3.0	10.0
Na_2O	0.3	8.5	0.3
K_2O	0.2	–	–
B_2O_3	7.3	5.0	–

glass fibers are silica based ($\sim$50–60% SiO_2) and contain a host of other oxides—of calcium, boron, sodium, aluminum, and iron, for example. Table 2.1 gives the composition of some commonly used glass fibers. The designation *E* stands for electrical because *E* glass is a good electrical insulator in addition to having good strength and a reasonable Young's modulus; *C* stands for corrosion and C glass has a better resistance to chemical corrosion than other glasses; and *S* stands for the high silica content that makes S glass withstand higher temperatures than other glasses. It should be pointed out that most of the continuous glass fiber produced is of the E glass type but, notwithstanding the designation E, electrical uses of E glass fiber are only a small fraction of the total market.

2.2.1 Fabrication

Figure 2.3 shows schematically the conventional fabrication procedure for glass fibers (specifically, the *E* glass fiber that constitutes the workhorse of the resin

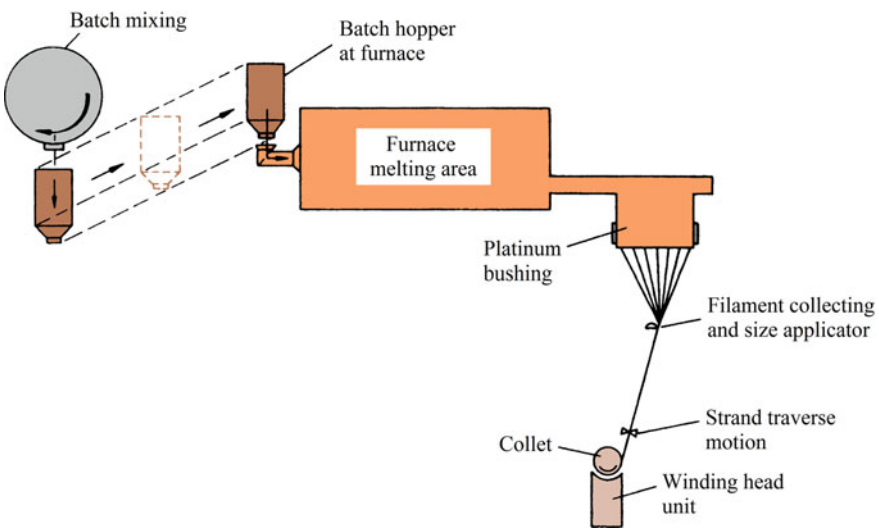

Fig. 2.3 Schematic of glass fiber manufacture

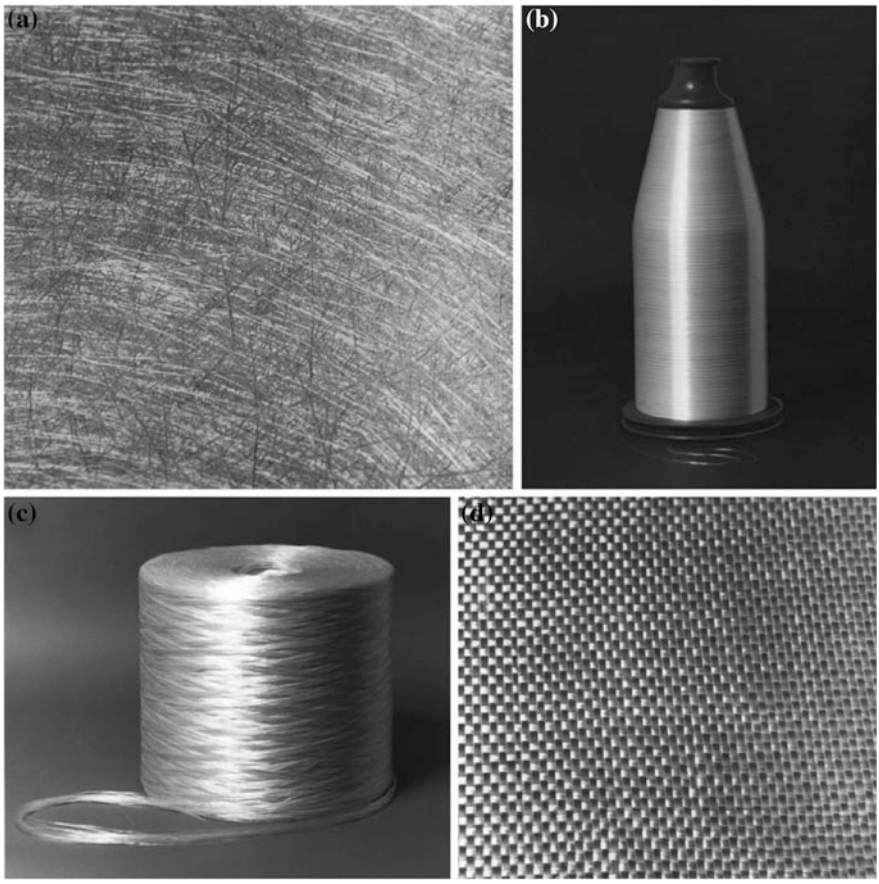

Fig. 2.4 Glass fiber is available in a variety of forms: **a** chopped strand, **b** continuous yarn, **c** roving, **d** fabric. (Courtesy of Morrison Molded Fiber Glass Company)

reinforcement industry) (Loewenstein 1983; Parkyn 1970; Lowrie 1967). The raw materials are melted in a hopper and the molten glass is fed into the electrically heated platinum bushings or crucibles; each bushing contains about 200 holes at its base. The molten glass flows by gravity through these holes, forming fine continuous filaments; these are gathered together into a strand and a *size* is applied before it is wound on a drum. The final fiber diameter is a function of the bushing orifice diameter; viscosity, which is a function of composition and temperature; and the head of glass in the hopper. In many old industrial plants, the glass fibers are not produced directly from fresh molten glass. Instead, molten glass is first turned into marbles, which after inspection are melted in the bushings. Modern plants do produce glass fibers by direct drawing. Figure 2.4 shows some forms in which glass fiber is commercially available.

The conventional methods of making glass or ceramic fibers involve drawing from high-temperature melts of appropriate compositions. This route has many practical difficulties such as the need to process at high temperatures, the immiscibility of components in the liquid state, and the easy crystallization during cooling. Several techniques have been developed for preparing glass and ceramic fibers (Chawla 2016). An important technique is called the sol–gel technique (Brinker and Scherer 1990; Jones 1989). We shall come back to this sol–gel technique at various places in this book. Here we will just provide a brief description. A *sol* is a colloidal suspension in which the individual particles are so small (generally in the *nm* range) that they show no sedimentation. A *gel*, on the other hand, is a suspension in which the liquid medium has become viscous enough to behave more or less like a solid. The sol–gel process of making a fiber involves a conversion of fibrous gels, drawn from a solution at a low temperature, into glass or ceramic fibers at several hundred degrees Celsius. The maximum heating temperature in this process is much lower than that in conventional glass fiber manufacture. The sol–gel method uses metal alkoxides as precursors. The process consists of preparing an appropriate homogeneous solution, changing the solution to a sol, gelling the sol, and converting the gel to glass or ceramic by heating. The sol–gel technique is a very powerful technique for making glass and ceramic fibers. The 3M Company produces a series of alumina and silica-alumina fibers, called the Nextel fibers, from metal alkoxide solutions (see Sect. 2.7). Figure 2.5 shows an example of silica fibers (cut from a continuous fiber spool) obtained by the sol–gel technique (Sakka 1985).

Glass filaments are easily damaged by the introduction of surface defects. To minimize this and to make handling of these fibers easy, a sizing treatment is given. The size, or coating, protects and binds the filaments into a strand.

Fig. 2.5 Continuous glass fibers (cut from a spool) obtained by the sol–gel technique. (From Sakka 1985, used with permission)

2.2.2 Structure

Inorganic, silica-based glasses are analogous to organic glassy polymers in that they are amorphous, i.e., devoid of any long-range order that is characteristic of a crystalline material. Pure, crystalline silica melts at 1800 °C. However, by adding some metal oxides, we can break the Si–O bonds and obtain a series of amorphous glasses with rather low glass transition temperatures. Figure 2.6a shows a two-dimensional network of silica glass. Each polyhedron consists of oxygen atoms bonded covalently to silicon. What happens to this structure when Na_2O is added to the glass is shown in Fig. 2.6b. Sodium ions are linked ionically with oxygen but they do not join the network directly. Too much Na_2O will impair the tendency for glassy structure formation. The addition of other metal oxide types (Table 2.1) serves to alter the network structure and the bonding and, consequently, the properties. Note the isotropic, three-dimensional network structure of glass (Fig. 2.6); this leads to the more or less isotropic properties of glass fibers. That is, for the glass fiber, Young's modulus and thermal expansion coefficient are the same along the fiber axis and perpendicular to it. This is unlike many other fibers, such as aramid and carbon, which are highly anisotropic.

2.2.3 Properties and Applications

Typical mechanical properties of E glass fibers are summarized in Table 2.2. Note that the density is quite low and the strength is quite high; Young's modulus, however, is not very high. Thus, while the strength-to-weight ratio of glass fibers is quite high, the modulus-to-weight ratio is only moderate. It is this latter characteristic that led the aerospace industry to other so-called advanced fibers (e.g., boron, carbon, Al_2O_3, and SiC). Glass fibers continue to be used for reinforcement of polyester, epoxy, and phenolic resins. It is quite cheap, and it is

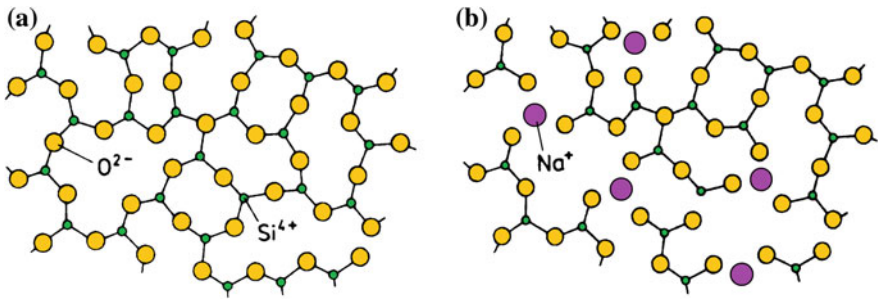

Fig. 2.6 Amorphous structure of glass: **a** a two-dimensional representation of silica glass network and **b** a modified network that results when Na_2O is added to **a**. Note that Na^+ is ionically linked with O^{2-} but does not join the network directly

Table 2.2 Typical properties of E glass fibers

Density ($g\ cm^{-3}$)	Tensile strength (MPa)	Young's modulus (GPa)	Coefficient of thermal expansion ($10^{-6}\ K^{-1}$)
2.55	1750	70	4.7

available in a variety of forms (see Fig. 2.4). Continuous strand is a group of individual fibers; roving is a group of parallel strands; and chopped fibers consist of strand or roving chopped to lengths between 5 and 50 *mm*. Glass fibers are also available in the form of woven fabrics or nonwoven mats.

Moisture decreases glass fiber strength. Glass fibers are also susceptible to what is called static fatigue, that is, when subjected to a constant load for an extended time period, glass fibers can undergo subcritical crack growth. This leads to failure over time at loads that might be safe when considering instantaneous loading.

Glass fiber reinforced resins are used widely in the building and construction industry. Commonly, these are called glass fiber reinforced plastics, or *GFRP*. They are used in the form of a cladding for other structural materials or as an integral part of a structural or non-load-bearing wall panel; window frames, tanks, bathroom units, pipes, and ducts are common examples. Boat hulls, since the mid-1960s, have primarily been made of *GFRP*. Use of *GFRP* in the chemical industry (e.g., as storage tanks, pipelines, and process vessels) is fairly routine. The rail and road transportation industry and the aerospace industry are other big users of *GFRP*.

2.3 Basalt Fibers

Basalt is an igneous rock found in North America, Eastern Europe, Russia, etc. Basalt fibers can be obtained from this rock by a process similar to that of glass fiber manufacture. In many ways, basalt fiber is very similar to glass fiber; hence, its inclusion at this point.

An approximate chemical composition of basalt (in *wt%*) is given in Table 2.3. The exact composition depends on the native basalt rock from which the fibers are obtained.

Typical properties of basalt fiber are summarized in Table 2.4. Note that the density and Young's modulus of basalt are similar to those of glass fiber but the tensile strength is much higher than that of glass fiber.

Figure 2.7 shows a woven fabric made of basalt fiber.

Table 2.3 Chemical composition of basalt fiber[a]

Compound	Weight %
SiO_2	50–55
Al_2O_3	15
Fe_2O_3	10–13
MgO	5
Na_2O	3
TiO_2	1–3
K_2O	1

[a]Indicative values

Table 2.4 Typical properties of basalt fibers

Density ($g\ cm^{-3}$)	Tensile strength (MPa)	Young's modulus (GPa)	Coefficient of thermal expansion ($10^{-6}\ K^{-1}$)
2.67	3000	85	1.4

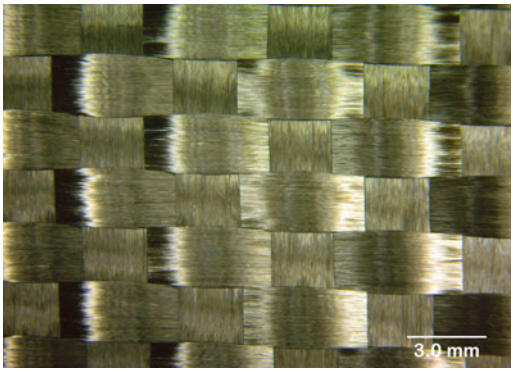

Fig. 2.7 A woven fabric made of basalt fiber

2.4 Boron Fibers

Boron is an inherently brittle material. It is commercially made by chemical vapor deposition of boron on a substrate, that is, boron fiber as produced is itself a composite fiber.

In view of the fact that rather high temperatures are required for the vapor deposition process, the choice of substrate material that goes to form the core of the finished boron fiber is limited. Generally, a fine-diameter tungsten wire is used for this purpose. A carbon fiber substrate can also be used. The first boron fibers were obtained by Weintraub (1911) by means of reduction of a boron halide with

hydrogen on a hot wire substrate. The real impulse in boron fiber fabrication, however, came in 1959, when Talley (Talley 1959; Talley et al. 1960) used the process of halide reduction to obtain amorphous boron fibers of high strength. Since then, interest in the use of strong but light boron fibers as a possible structural component in aerospace and other structures has increased, although it must be admitted that this interest has periodically waxed and waned in the face of rather stiff competition from other so-called advanced fibers, in particular, carbon fibers.

2.4.1 Fabrication

Boron fibers are obtained by chemical vapor deposition (CVD) on a substrate. There are two processes:

1. *Thermal decomposition of a boron hydride*. This method involves low temperatures, and, thus, carbon-coated glass fibers can be used as a substrate. The boron fibers produced by this method, however, are weak because of a lack of adherence between the boron and the core. These fibers are much less dense owing to the trapped gases.
2. *Reduction of boron halide*. Hydrogen gas is used to reduce boron trihalide:

$$2BX_3 + 3H_2 \rightarrow 2B + 6HX, \tag{2.2}$$

where X denotes a halogen: Cl, Br, or I.

In this process of halide reduction, the temperatures involved are very high, and, thus, one needs a refractory material, for example, a high-melting-point metal such as tungsten, as a substrate. It turns out that such metals are also very heavy. This process, however, has won over the thermal reduction process despite the disadvantage of a rather high-density substrate (the density of tungsten is 19.3 $g\ cm^{-3}$) mainly because this process gives boron fibers of a very high and uniform quality. Figure 2.8a shows a schematic of boron filament production by the CVD technique, and Fig. 2.8b shows a commercial boron filament production facility; each vertical reactor shown in this picture produces continuous boron monofilament.

In the process of BCl_3 reduction, a very fine tungsten wire (10–12 μm diameter) is pulled into a reaction chamber at one end through a mercury seal and out at the other end through another mercury seal. The mercury seals act as electrical contacts for resistance heating of the substrate wire when gases (BCl_3+H_2) pass through the reaction chamber, where they react on the incandescent wire substrate. The reactor can be vertical or horizontal, Fig. 2.9 shows a vertical one. BCl_3 is an expensive chemical, and only about 10% of it is converted into boron in this reaction. Thus, an efficient recovery of the unused BCl_3 can result in a considerable lowering of the boron filament cost.

There is a critical temperature for obtaining a boron fiber with optimum properties and structure (van Maaren et al. 1975). The desirable amorphous form of

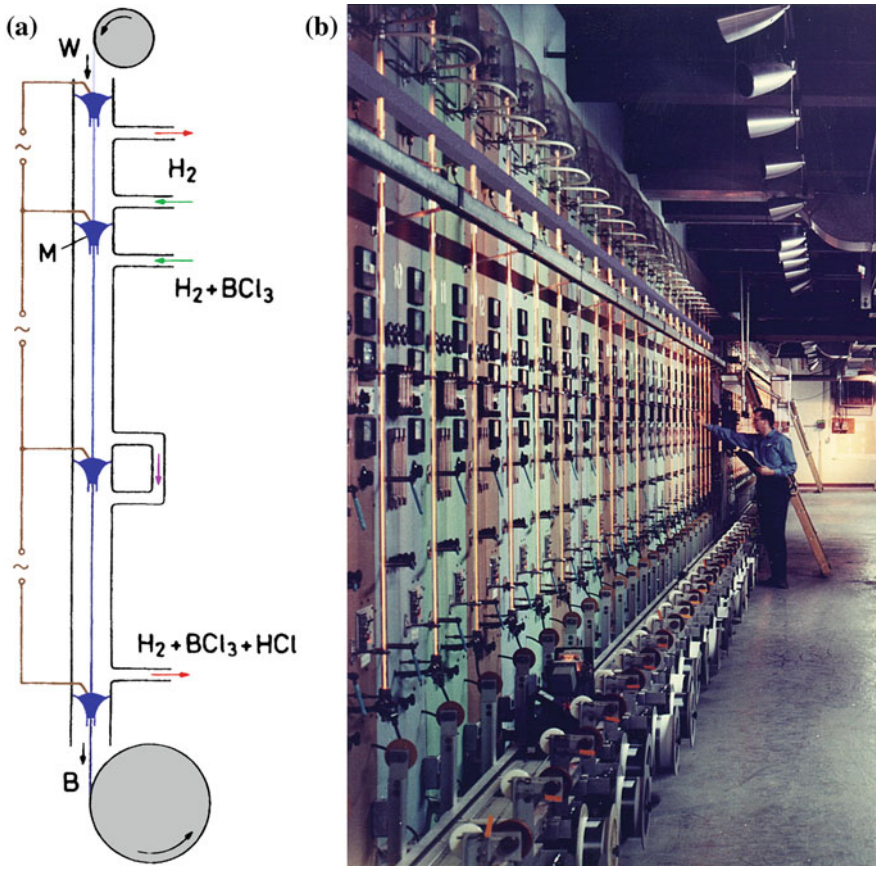

Fig. 2.8 **a** Schematic of boron (*B*) fiber production by halide decomposition on a tungsten (*W*) substrate. [From van Maaren et al. (1975), used with permission.] **b** A boron filament production facility. (Courtesy of AVCO Specialty Materials Co.)

boron occurs below this critical temperature while above this temperature crystalline forms of boron also occur that are undesirable from a mechanical properties viewpoint, as we shall see in Sect. 2.4.2. With the substrate wire stationary in the reactor, this critical temperature is about 1000 °*C*. In a system where the wire is moving, this critical temperature is higher, and it increases with the speed of the wire. One can use a diagram of the type shown in Fig. 2.9, which shows the various combinations of wire temperature and wire drawing speed to produce a certain diameter of boron fiber. Fibers formed in the region above the dashed line are relatively weak because they contain undesirable forms of boron because of recrystallization. The explanation for this relationship between critical temperature and wire speed is that boron is deposited in an amorphous state and the more rapidly the wire is drawn out from the reactor, the higher the allowed temperature

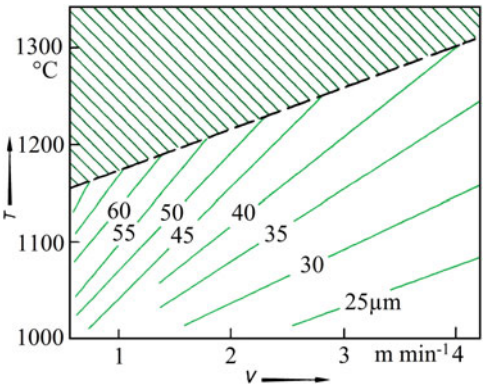

Fig. 2.9 Temperature (T) versus wire speed (V) for a series of boron filament diameters. Filaments formed in the gray region (above the dashed line) contain crystalline regions and are undesirable. (From van Maaren et al. 1975, used with permission)

is. Of course, higher wire drawing speed also results in an increase in production rate and lower costs.

Boron deposition on a carbon monofilament ($\sim 35\ \mu m$ diameter) substrate involves precoating the carbon substrate with a layer of pyrolytic graphite. This coating accommodates the growth strains that result during boron deposition (Krukonis 1977). The reactor assembly is slightly different from that for boron on tungsten substrate, because pyrolytic graphite is applied online.

2.4.2 Structure and Morphology

The structure and morphology of boron fibers depend on the conditions of deposition: temperature, composition of gases, gas dynamics, and so on. While theoretically the mechanical properties are limited only by the strength of the atomic bond, in practice, there are always structural defects and morphological irregularities present that lower the mechanical properties. Temperature gradients and trace concentrations of impurity elements inevitably cause process irregularities. Even greater irregularities are caused by fluctuations in electric power, instability in gas flow, and any other operator-induced variables.

2.4.2.1 Structure

Depending on the conditions of deposition, the elemental boron can exist in various crystalline polymorphs. The form produced by crystallization from the melt or chemical vapor deposition above 1300 °C is β-rhombohedral. At temperatures lower than this, if crystalline boron is produced, the most commonly observed structure is α-rhombohedral.

Boron fibers produced by the CVD method described earlier have a microcrystalline structure that is generally called *amorphous*. This designation is based on the characteristic X-ray diffraction pattern produced by the filament in the Debye–Scherrer method, that is, large and diffuse halos with *d* spacings of 0.44, 0.25, 0.17, 1.4, 1.1, and 0.091 *nm*, typical of amorphous material (Vega-Boggio and Vingsbo 1978). Electron diffraction studies, however, lead one to conclude that this "amorphous" boron is really a nanocrystalline phase with a grain diameter of the order of 2 *nm* (Krukonis 1977).

Based on X-ray and electron diffraction studies, one can conclude that amorphous boron is really nanocrystalline β-rhombohedral. In practice, the presence of microcrystalline phases (crystals or groups of crystals observable in the electron microscope) constitutes an imperfection in the fiber that should be avoided. Larger and more serious imperfections generally result from surpassing the critical temperature of deposition (see Sect. 2.4.1) or the presence of impurities in the gases.

When boron fiber is made by deposition on a tungsten substrate, then depending on the temperature conditions during deposition, the core may consist of, in addition to tungsten, a series of compounds, such as W_2B, WB, W_2B_5, and WB_4 (Galasso et al. 1967). A boron fiber cross section (100 μm diameter) is shown in Fig. 2.10a, while Fig. 2.10b shows schematically the various subparts of the cross section. The various tungsten boride phases are formed by diffusion of boron into tungsten. Generally, the fiber core consists only of WB_4 and W_2B_5. On prolonged heating, the core may be completely converted into WB_4. As boron diffuses into the tungsten substrate to form borides, the core expands from its original 12.5 μm (original tungsten wire diameter) to 17.5 μm. The SiC coating shown in Fig. 2.10b is a barrier coating used to prevent any adverse reaction between B and the matrix, such as Al, at high temperatures. The SiC barrier layer is vapor deposited onto boron using a mixture of hydrogen and methyltrichlorosilane.

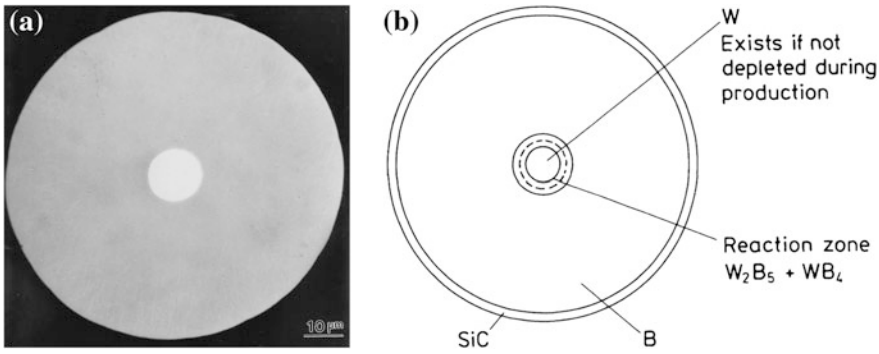

Fig. 2.10 **a** Cross section of a 100-μm-diameter boron fiber. **b** Schematic of the cross section of a boron fiber with SiC barrier layer

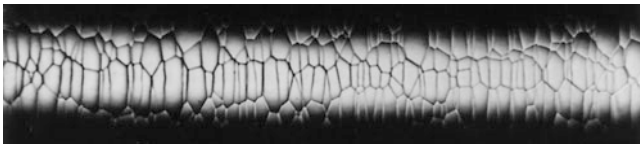

Fig. 2.11 Characteristic corncob structure of boron fiber. (From van Maaren et al. 1975, used with permission)

2.4.2.2 Morphology

The boron fiber surface shows a "corncob" structure consisting of nodules separated by boundaries (Fig. 2.11). The nodule size varies during the course of fabrication. In a very general way, the nodules start as individual nuclei on the substrate and then grow outward in a conical form until a filament diameter of 80–90 μm is reached, above which the nodules seem to decrease in size. Occasionally, new cones may nucleate in the material, but they always originate at an interface with a foreign particle or inclusion.

2.4.3 Residual Stresses

Boron fibers have inherent residual stresses that have their origin in the process of chemical vapor deposition. Growth stresses in the nodules of boron, stresses induced by the diffusion of boron into the tungsten core, and stresses generated by the difference in the coefficient of expansion of deposited boron and tungsten boride core, all contribute to the residual stresses and thus can have a considerable influence on the mechanical properties of the fiber. The residual stress pattern across the transverse section of a boron fiber is shown in Fig. 2.12 (Vega-Boggio and Vingsbo 1978). The compressive stresses on the fiber surface are due to the quenching action involved in pulling the fiber out from the chamber (Vega-Boggio and Vingsbo 1978). Morphologically, the most conspicuous aspect of these internal stresses is the frequently observed radial crack in the transverse section of these fibers. The crack runs from within the core to just inside the external surface. Some workers, however, doubt the preexistence of this radial crack (Krukonis 1977). They think that the crack appears during the process of boron fiber fracture.

2.4.4 Fracture Characteristics

It is well known that brittle materials show a distribution of strengths rather than a single value. Imperfections in these materials lead to stress concentrations much higher than the applied stress levels. Because the brittle material is not capable of

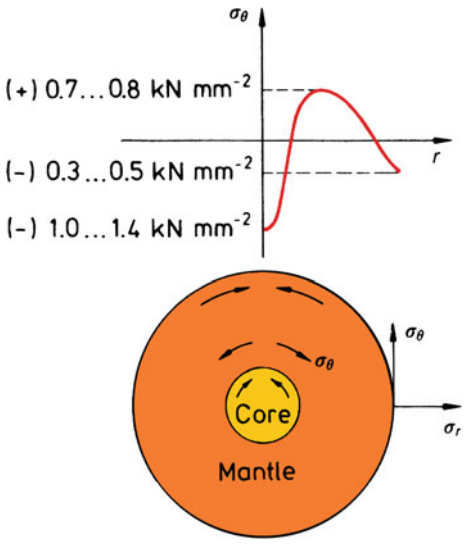

Fig. 2.12 Schematic of residual stress pattern across the transverse section of a boron fiber. (From Vega-Boggio and Vingsbo 1978, used with permission)

deforming plastically in response to these stress concentrations, fracture ensues at one or more such sites. Boron fiber is indeed a very brittle material, and cracks originate at preexisting defects located at either the boron–core interface or the surface. Figure 2.14 shows the characteristic brittle fracture of a boron fiber; note the radical crack. It is worth pointing out here that the radial crack does not extend all the way to the surface of the fiber. This is because the surface layer of boron fiber is in compression; see Fig. 2.12. The surface defects in boron fiber stem from the nodular surface that results from the growth of boron cones. In particular, when a nodule coarsens due to an exaggerated growth around a contaminating particle, a crack can result from this large nodule and weaken the fiber.

2.4.5 Properties and Applications of Boron Fibers

Many researchers have investigated the mechanical properties of boron fibers (Krukonis 1977; Vega-Boggio and Vingsbo 1978; Galasso et al. 1967; Galasso and Paton 1966; DeBolt 1982; Wawner 1967; DiCarlo 1985). Due to the composite nature of the boron fiber, complex internal stresses are present and defects such as voids and structural discontinuities result because of the presence of a core and sheath. Thus, one would not expect boron fiber to show the intrinsic strength of boron. The average tensile strength of boron fiber is 3–4 *GPa*, while its Young's modulus is between 380 and 400 *GPa*.

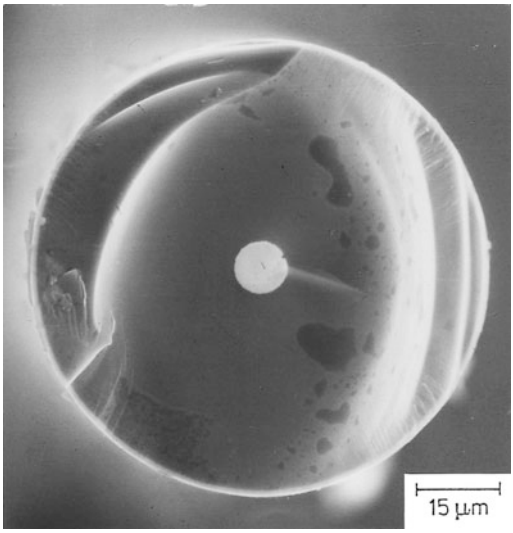

Fig. 2.13 Fracture surface of a boron fiber showing a characteristically brittle fracture and a radial crack

An idea of the intrinsic strength of boron can be obtained in a flexure test (Wawner 1967). In flexure, assuming the core/sheath interface to be near the neutral axis, critical tensile stresses would not develop at the interface. Flexure tests on boron fibers lightly etched to remove any surface defects gave a strength of 14 *GPa*. Without etching, the strength was half this value. Table 2.5 provides a summary of the characteristics of boron fiber (DiCarlo 1985). Commercially produced 142 μm-diameter boron fiber shows average tensile strength of 3.8 *GPa*. The tensile strength and fracture energy values of the as-received and some limited-production-run larger diameter fibers showed improvement after chemical polishing, as shown in Table 2.5. Fibers showing strengths greater than 4 *GPa* had their fracture controlled by a tungsten boride core, while fibers with strengths of 4 *GPa* or less were controlled by fiber surface flaws. The high-temperature

Table 2.5 Strength properties of improved large diameter boron fibers

		Strength		Relative fracture energy
Diameter (μm)	Treatment	Average[a] (*GPa*)	COV[b] (%)	
142	As-produced	3.8	10	1.0
406	As-produced	2.1	14	0.3
382	Chemical polish	4.6	4	1.4
382	Heat treatment plus polish	5.7	4	2.2

[a]Gage length = 25 *mm*

[b]Coefficient of variation = standard deviation/average value

Source Reprinted with permission from *Journal of Metals*, **37**, No. 6, 1985, a publication of The Metallurgical Society, Warrendale, PA

treatment, indicated in Table 2.5, improved the fiber properties by putting a permanent axial compressive strain in the sheath.

Boron has a density of 2.34 $g\ cm^{-3}$ (about 15% less than that of aluminum). Boron fiber with a tungsten core has a density of 2.6 $g\ cm^{-3}$ for a fiber with 100 μm diameter. Its melting point is 2040 $°C$, and it has a thermal expansion coefficient of $8.3 \times 10^{-6}\ °C^{-1}$ up to 315 $°C$.

Boron fiber composites are in use in a number of U.S. military aircraft, notably the F-14 and F-15, and in the U.S. space shuttle. They are also used for stiffening golf shafts, tennis rackets, bicycle frames, and in making repair patches for polymer matrix composites (PMCs). A big advantage of boron fiber over other high-performance fibers is their relatively better properties in compression. This stems from their larger diameter. A commercial product called Hy-Bor composite uses a mix of carbon and boron fibers in an epoxy matrix, which has improved properties in compression because of the boron fibers. One big obstacle to the widespread use of boron fiber is its high cost compared to that of other fibers.

2.5 Carbon Fibers

Carbon is a very light element with a density equal to 2.268 $g\ cm^{-3}$. Carbon can exist in a variety of crystalline forms. Our interest here is in the so-called graphitic structure of carbon wherein the carbon atoms are arranged in the form of hexagonal layers. Among the other well-known forms of carbon is the covalent diamond structure wherein the carbon atoms are arranged in a three-dimensional configuration with little structural flexibility. Another form of carbon is Buckminsterfullerene (or buckyball), with a molecular composition of C_{60} or C_{70}. One can also have carbon nanotubes, which are nothing but drawn out version of buckyballs.

Carbon in the graphitic form is highly anisotropic, with a theoretical Young's modulus in the layer plane being equal to about 1000 GPa, while that along the c-axis is equal to about 35 GPa. The graphitic structure (Fig. 2.14a) has a very dense packing in the layer planes. The lattice structure is shown more clearly with only lattice planes in Fig. 2.14b. As we know, the bond strength determines the modulus of a material. Thus, the high strength bond between carbon atoms in the layer plane results in an extremely high modulus while the weak van der Waals-type bond between the neighboring layers results in a lower modulus in the c-direction. Consequently, almost all processing techniques of carbon fiber have the goal of obtaining a very high degree of preferred orientation of hexagonal planes along the fiber axis.

Carbon fibers of extremely high modulus can be made by carbonization of organic precursor fibers followed by graphitization at high temperatures. The organic precursor fiber, that is, the raw material for carbon fiber, is generally a special textile polymeric fiber that can be carbonized without melting. The precursor fiber, like any polymeric fiber, consists of long-chain molecules (0.1–1 μm

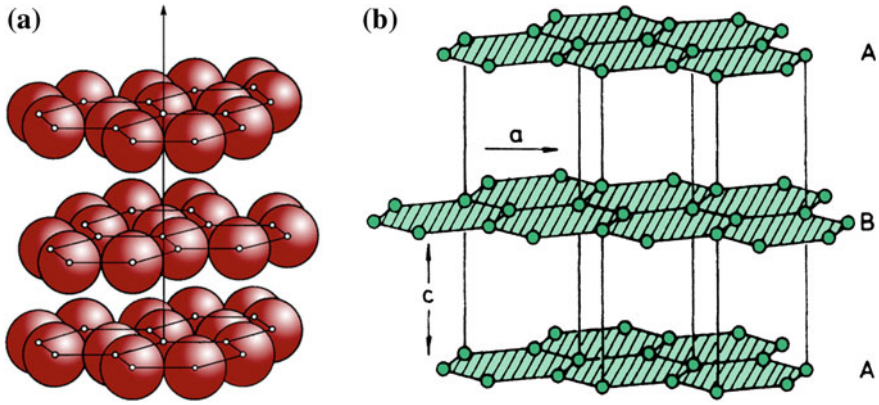

Fig. 2.14 **a** Graphitic layer structure. The layers are shown not in contact for visual ease. **b** The hexagonal lattice structure of graphite

when fully stretched) arranged in a random manner. Such polymeric fibers generally have poor mechanical properties and typically show rather large deformations at low stresses mainly because the polymeric chains are not ordered. A commonly used precursor fiber is polyacrylonitrile (PAN). Other precursor fibers include rayon and the ones obtained from pitches, polyvinyl alcohol, polyimides, and phenolics. There is work involving the use of lignin as a precursor fiber.

Carbon fiber is a generic term representing a family of fibers (Chawla 1981). As pointed out earlier, unlike the rigid diamond structure, graphitic carbon has a lamellar structure. Thus, depending on the size of the lamellar packets, their stacking heights, and the resulting crystalline orientations, one can obtain a range of properties. Most of the carbon fiber fabrication processes involve the following essential steps:

1. A *fiberization* procedure to make a precursor fiber. This generally involves wet, dry, or melt spinning followed by some drawing or stretching.
2. A *stabilization* treatment that prevents the fiber from melting in the subsequent high-temperature treatments.
3. A thermal treatment called *carbonization* that removes most noncarbon elements.
4. An optional thermal treatment called *graphitization* that improves the properties of carbon fiber obtained in step 3.

It should be clear to the reader by now that in order to make a high modulus fiber, one must improve the orientation of graphitic crystals or lamellas. This is achieved by various kinds of thermal and stretching treatments involving rather rigorous controls.

2.5.1 Processing

Back in late nineteenth century, Thomas Edison converted cellulose in the form of cotton fiber to carbon fiber. He was interested in using carbon fibers in incandescent lamps. In modern times, the field of high modulus carbon fibers for use in composites is said to have started when Shindo (1961) in Japan prepared high modulus carbon fiber starting from polyacrylonitrile (PAN). He obtained a Young's modulus of about 170 *GPa*. In 1963, British researchers at Rolls Royce discovered that carbon fiber with an elastic modulus much higher than that obtained by Shindo could be obtained by incorporating a stretching treatment during the oxidation stage of processing. They obtained, starting from PAN, a carbon fiber with an elastic modulus of about 600 *GPa*. Since then, developments in the technology of carbon fibers have occurred in rapid strides. The minute details of the conversion processes from precursor fiber to a high modulus carbon fiber continue to be proprietary secrets. All the methods, however, exploit the phenomenon of thermal decomposition of an organic precursor fiber under well-controlled conditions of rate and time of heating, environment, and so on. Also, in all processes, the precursor is stretched at some stage of pyrolysis to obtain the high degree of alignment of graphitic basal planes.

2.5.1.1 Ex-PAN Carbon Fibers

Carbon fibers made from PAN (polyacrylonitrile) are called *ex-PAN carbon fibers*. The polyacrylonitrile fibers are stabilized in air (a few hours at 250 °*C*) to prevent melting during the subsequent higher temperature treatment. The fibers are kept under tension, i.e., they are prevented from contracting during this oxidation treatment. The white PAN fibers become black after oxidation. The black fibers obtained after this treatment are heated slowly in an inert atmosphere to a temperature between 1000 and 1500 °*C*. Slow heating allows the high degree of order in the fiber to be maintained. The rate of temperature increase should be low so as not to destroy the molecular order in the fibers. The final optional heat treatment consists of holding the fibers for very short duration at temperatures up to 3000 °*C*. This improves the fiber texture, i.e., the orientation of the basal planes and thus increases the elastic modulus of the fiber in the axial direction. Figure 2.15 shows, schematically, this PAN-based carbon fiber production process (Baker 1983). Typically, the carbon fiber yield is about 50%.

Figure 2.16a shows the flexible PAN molecular structure. Note the all-carbon backbone. This structure is essentially that of polyethylene with a nitrile (CN) group on every alternate carbon atom. The structural changes occurring during the conversion of PAN to carbon fiber are as follows. The initial stretching treatment of PAN improves the axial alignment of the polymer molecules. During this oxidation treatment, the fibers are maintained under tension to keep the alignment of PAN while it transforms into rigid ladder polymer (Fig. 2.16b). In the absence of tensile

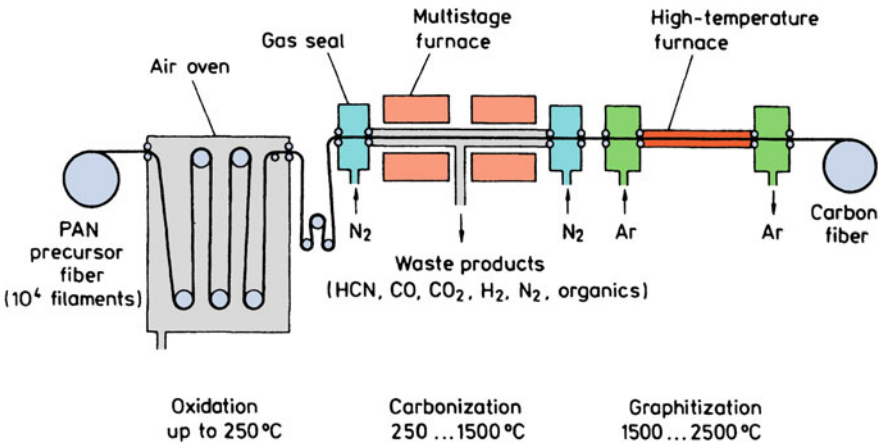

Fig. 2.15 Schematic of PAN-based carbon fiber production. (Reprinted with permission from Baker 1983)

stress in this step, a relaxation will occur, and the ladder polymer structure will become disoriented with respect to the fiber axis. After the stabilizing treatment, the resulting ladder-type structure (also called *oriented cyclic structure*) has a high glass transition temperature so that there is no need to stretch the fiber during the next stage, which is carbonization. There are still considerable quantities of nitrogen and hydrogen present, which are eliminated as gaseous waste products during carbonization, that is, heating to 1000–1500 °*C* (Fig. 2.15). The carbon atoms remaining after this treatment are mainly in the form of a network of extended hexagonal ribbons, which has been called *turbostratic* graphite structure in the

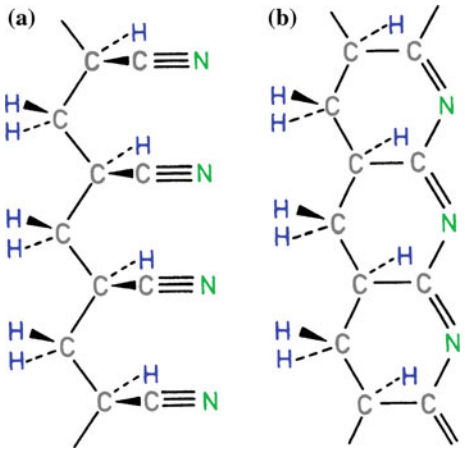

Fig. 2.16 **a** Flexible polyacrylonitrile molecule. **b** Rigid ladder (or oriented cyclic) molecule

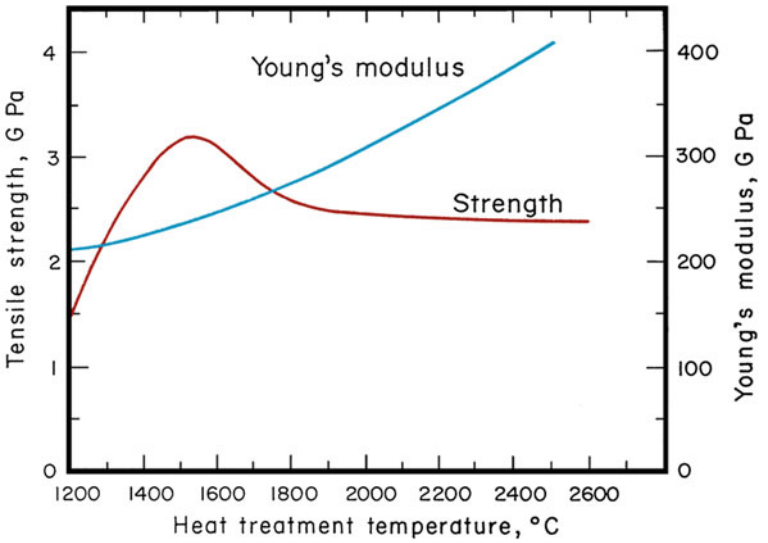

Fig. 2.17 Strength and elastic modulus of carbon fiber as a function of final heat treatment temperature. (After Watt 1970, used with permission)

literature. Although these strips tend to align parallel to the fiber axis, the degree of order of one ribbon with respect to another is relatively low. This can be improved further by heat treatment at still higher temperatures (up to 3000 °*C*). This is the graphitization treatment (Fig. 2.15). The mechanical properties of the resultant carbon fiber may vary over a large range depending mainly on the temperature of the final heat treatment (Fig. 2.17) (Watt 1970). The graphitization treatment involving hot stretching above 2000 °*C* results in plastic deformation of carbon fibers, leading to an improvement in elastic modulus.

2.5.1.2 Ex-Cellulose Carbon Fibers

Cellulose is a natural polymer that is frequently found in a fibrous form. In fact, cotton fiber, which is cellulosic, was one of the first to be carbonized. As mentioned above, Thomas Edison did that to obtain carbon filament for incandescent lamp. Cotton has the desirable property of decomposing before melting. It is not very suitable, however, for high modulus carbon fiber manufacture because it has a rather low degree of orientation along the fiber axis, although it is highly crystalline. It is also not available as a tow of continuous filaments and is quite expensive. These difficulties have been overcome in the case of rayon fiber, which is made from wood pulp, a cheap source. The cellulose is extracted from wood pulp, and continuous filament tows are produced by wet spinning.

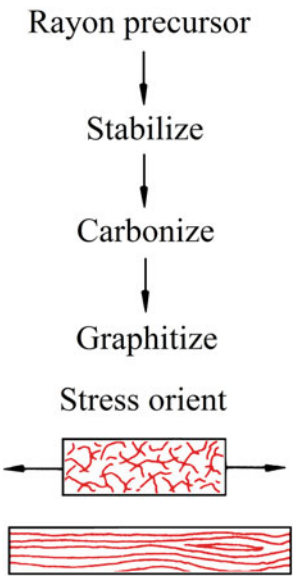

Fig. 2.18 Schematic of rayon-based carbon fiber production. (After Diefendorf and Tokarsky 1975, used with permission)

Rayon is a thermosetting polymer. The process used for the conversion of rayon into carbon fiber involves the same stages: fiberization, stabilization in a reactive atmosphere (air or oxygen, <400 °*C*), carbonization (<1500 °*C*), and graphitization (>2500 °*C*). Various reactions occur during the first stage, causing extensive decomposition and evolution of H_2O, CO, CO_2, and tar. The stabilization is carried out in a reactive atmosphere to inhibit tar formation and improve yield (Bacon 1973). Chain fragmentation or depolymerization occurs in this stage. Because of this depolymerization, stabilizing under tension, as in the case of PAN precursor, does not work (Bacon 1973). The carbonization treatment involves heating to about 1000 °*C* in nitrogen. Graphitization is carried out at 2800 °*C* under stress. This orienting stress at high temperature results in plastic deformation via operation of slp on multiple systems and diffusion. Figure 2.18 shows the process schematically. The carbon fiber yield from rayon is between 15 and 30% by weight, compared to a yield of about 50% in the case of PAN precursors.

2.5.1.3 Ex-Pitch Carbon Fibers

Commercial pitches are mixtures of various organic compounds with an average molecular weight between 400 and 600. There are various sources of pitch, but the three commonly used sources are polyvinyl chloride (PVC), petroleum asphalt, and coal tar. Pitch-based carbon fibers are attractive because of the cheap raw material, high yield of carbon fiber, and a highly oriented carbon fiber that can be obtained from mesophase pitch precursor fiber.

The same sequence of oxidation, carbonization, and graphitization is required for making carbon fibers from a pitch precursor. Orientation in this case is obtained by spinning. An isotropic but aromatic pitch is subjected to melt spinning at very high strain rates and quenched to give a highly oriented, pitch precursor fiber. This thermoplastic fiber is then oxidized to form a crosslinked structure that makes the fiber nonmelting. This is followed by carbonization and graphitization.

Prolonged heating of pitch above 350 °*C* results in the formation of a highly oriented, optically anisotropic liquid crystalline phase (also called *mesophase*, Greek for intermediate phase). When observed under polarized light, anisotropic mesophase pitch appears as microspheres floating in an isotropic pitch. The liquid crystalline mesophase pitch can be melt spun into a precursor for carbon fiber. The melt spinning process involves shear and elongation in the direction of fiber axis, and thus a high degree of preferred orientation is achieved. This orientation can be further developed during conversion to carbon fiber. The pitch molecules (aromatics of low molecular weight) are stripped of hydrogen, and the aromatic molecules coalesce to form larger bidimensional molecules. Very high values of Young's modulus can be obtained. It should be appreciated that one must have the pitch in a state amenable to spinning in order to produce the precursor fiber, which is made infusible to allow carbonization to occur without melting. Thus, the pitches obtained from petroleum asphalt and coal tar need pretreatments. This pretreatment can be avoided in the case of PVC by means of a carefully controlled thermal degradation of PVC.

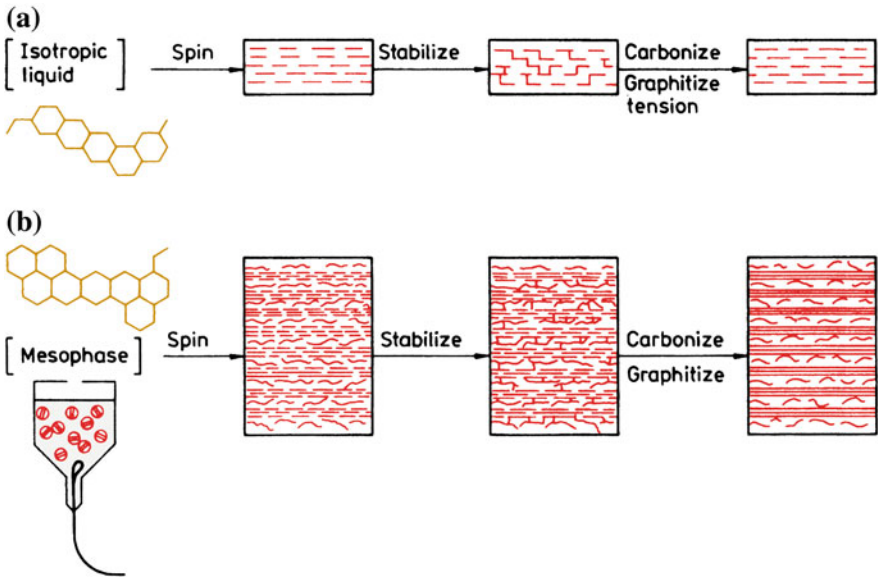

Fig. 2.19 Schematic of pitch-based carbon fiber production: **a** isotropic pitch process, **b** mesophase pitch process. (With permission from Diefendorf and Tokarsky 1975)

Pitches are polydispersoid systems, and thus they show a wide distribution of molecular weights, which can be adjusted by solvent extraction or distillation. The molecular weight controls the viscosity of the polymer melt and the melting range. Thus, it also controls the temperature and the spinning speed. Figure 2.19 shows the process of pitch-based carbon fiber manufacture starting from an isotropic pitch and a mesophase pitch (Diefendorf and Tokarsky 1975).

2.5.2 *Structural Changes Occurring During Processing*

The thermal treatments for all precursor fibers serve to remove noncarbon elements in the form of gases. For this, the precursor fibers are stabilized to ensure that they decompose rather than melt. Generally, they become black after this treatment. Carbon fibers obtained after carbonization contain many *grown-in* defects because the thermal energy supplied at these low temperatures is not enough to break the already formed carbon–carbon bonds. That is why these carbon fibers are very stable up to 2500–3000 $^{\circ}C$ when they change to graphite. The decomposition of the precursor fiber invariably results in a weight loss and a decrease in fiber diameter. The weight loss can be considerable—from 40 to 90%, depending on the precursor and treatment (Ezekiel and Spain 1967). The external morphology of the fiber, however, is generally maintained. Thus, precursor fibers with transverse sections in the form of a kidney bean, dog bone, or circle maintain their form after conversion to carbon fiber. Figure 2.20 shows a scanning electron micrograph of a PAN-based carbon fiber. Note the surface markings that appear during the fiber drawing process.

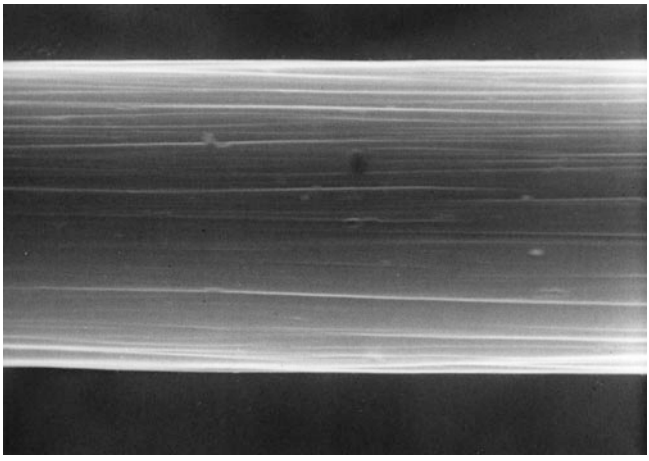

Fig. 2.20 Scanning electron micrograph of PAN-based carbon fiber (fiber diameter is 8 μm). Note the surface markings that stem from the fiber drawing process

At the microscopic level, carbon fibers possess a rather heterogeneous microstructure. Not surprisingly, many workers (Diefendorf and Tokarsky 1975; Watt and Johnson 1969; Johnson and Tyson 1969; Perret and Ruland 1970; Bennett and Johnson 1978, 1979; Inal et al. 1980) have attempted to characterize the structure of carbon fibers, and one can find a number of models in the literature. There is a better understanding of the structure of PAN-based carbon fibers. Essentially, a carbon fiber consists of many graphitic lamellar ribbons oriented roughly parallel to the fiber axis with a complex interlinking of layer planes both longitudinally and laterally. Based on high-resolution lattice fringe images of longitudinal and transverse sections in TEM, a schematic two-dimensional representation is given in Fig. 2.21 (Bennett and Johnson 1979), while a three-dimensional model is shown in Fig. 2.22 (Bennett and Johnson 1978). The structure is typically defined in terms of crystallite dimensions, L_a and L_c in directions a and c, respectively, as shown in Fig. 2.23. The degree of alignment and the magnitude of parameters L_a and L_c vary with the graphitization temperature. Both L_a and L_c increase with increasing heat treatment temperature.

2.5.3 *Properties and Applications*

The density of the carbon fiber varies with the precursor and the thermal treatment given. It is generally in the range of 1.6–2.0 $g\ cm^{-3}$. Note that the density of the carbon fiber is more than that of the precursor fiber; the density of the precursor is generally between 1.14 and 1.19 $g\ cm^{-3}$ (Bennett et al. 1983). There are always

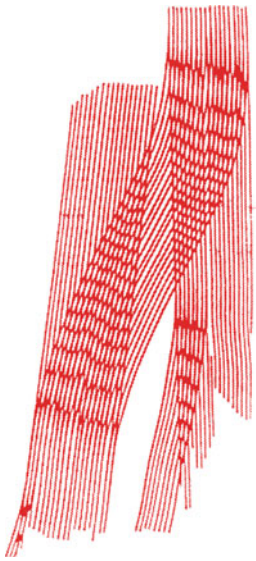

Fig. 2.21 Two-dimensional representation of PAN-based carbon fiber. (After Bennett and Johnson (1979), used with permission)

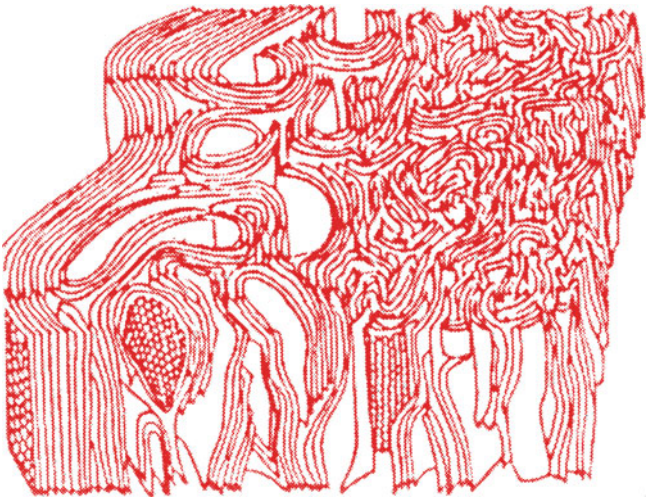

Fig. 2.22 Three-dimensional representation of PAN-based carbon fiber. (From Bennett and Johnson 1978, used with permission)

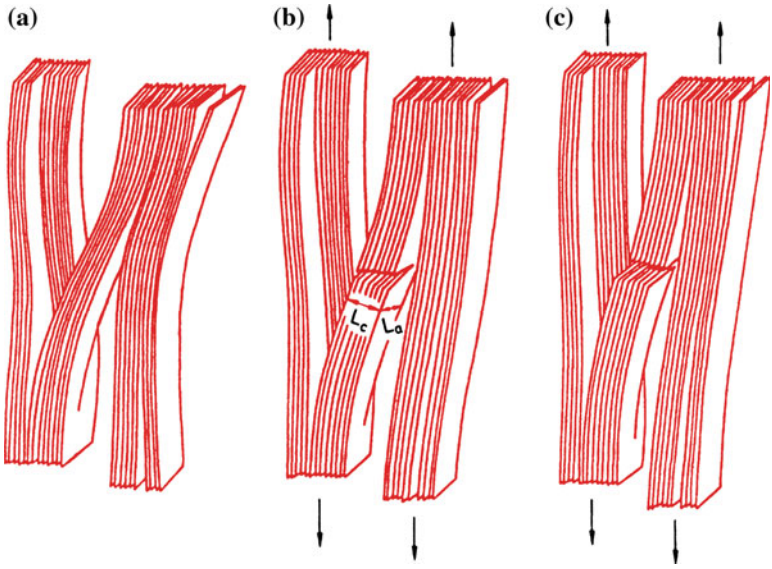

Fig. 2.23 Model for tensile failure of carbon fiber: **a** a misoriented crystallite linking two crystallites parallel to the fiber axis, **b** basal plane rupture under the action of applied stress, **c** complete failure of the misoriented crystallite. (From Bennett et al. 1983, used with permission)

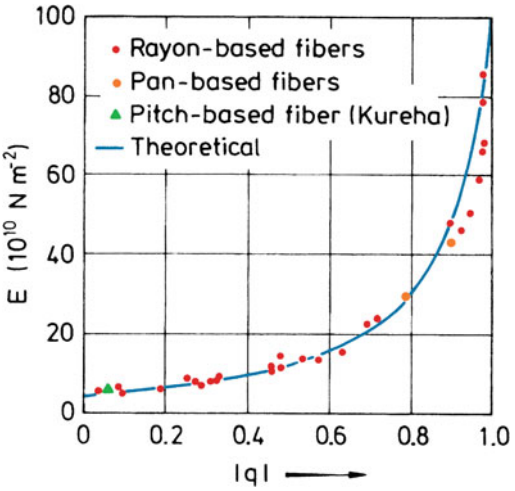

Fig. 2.24 Variation of longitudinal Young's modulus for various carbon fibers with the degree of preferred orientation. The value of the orientation parameter, q, is 1 for perfect orientation and zero for the isotropic case. (From Fourdeux et al. 1971, used with permission)

flaws of various kinds present, which may arise from impurities in the precursors or may simply be the misoriented layer planes. A mechanism of tensile failure of carbon fiber based on the presence of misoriented crystallites is shown in Fig. 2.23 (Bennett et al. 1983). Figure 2.23a shows a misoriented crystallite linking two crystallites parallel to the fiber axis. Under the action of applied stress, basal plane rupture occurs in the misoriented crystallite in the L_c direction, followed by crack development along L_a and L_c (Fig. 2.23b). Continued stressing causes complete failure of the misoriented crystallite (Fig. 2.23c). If the crack size is greater than the critical size in the L_a and L_c directions, catastrophic failure results.

As mentioned earlier, the degree of order, and consequently the modulus in the fiber axial direction, increases with increasing graphitization temperature. Fourdeux et al. (1971) measured the preferred orientation of various carbon fibers and plotted the Young's modulus of the carbon fibers obtained by different precursors against an orientation parameter, q (Fig. 2.24). The absolute value of this parameter, $|q|$ has a value of 1 for perfect orientation and zero for the isotropic case. In Fig. 2.24, we have plotted the absolute value of q. Note also that the modulus has been corrected for porosity. The theoretical curve fits the experimental data very well.

Even among the ex-PAN carbon fibers, we can have a series of carbon fibers, for example, high tensile strength but medium Young's modulus (HT) fiber (200–300 *GPa*), high Young's modulus (HM) fiber (400 *GPa*), extra- or superhigh tensile strength (SHT), and superhigh modulus-type (SHM) carbon fibers. The mesophase pitch-based carbon fibers show rather high modulus but low strength levels (2 *GPa*). Not unexpectedly, the HT-type carbon fibers show a much higher strain-to-failure value than the HM type. The mesophase pitch-based carbon fibers are used for reinforcement, while the isotropic pitch-based carbon fibers (very low modulus) are more frequently used as insulation and fillers. Table 2.6 compares the properties of some common carbon fibers and graphite monocrystal (Singer 1979).

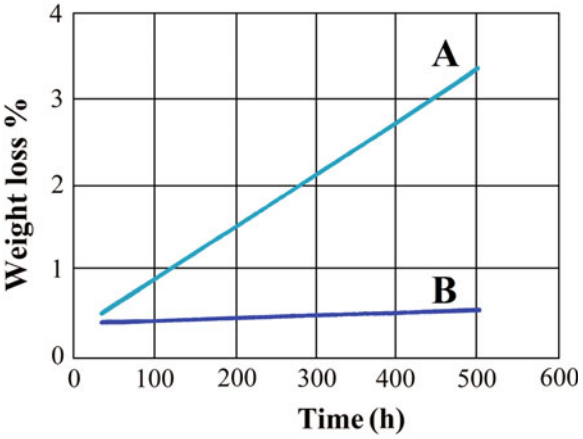

Fig. 2.25 Oxidation resistance, measured as weight loss in air at 350 °*C*, of carbon fibers having different moduli: (A) Low modulus Celion 3000 (240 *GPa*) and (B) High modulus Celion G-50 (345 *GPa*). (After J.P. Riggs, *Encyclopedia of Polymer Science and Engineering*, 2nd ed, Vol. 2, 1985, John Wiley and Sons, New York, reprinted with permission)

For high-temperature applications involving carbon fibers, it is important to take into account the variation of inherent oxidation resistance of carbon fibers with modulus. Figure 2.25 shows that the oxidation resistance of carbon fiber increases with the modulus value (Riggs 1985). The modulus, as we know, increases with the final heat treatment temperature during processing.

Table 2.6 Comparison of properties of different carbon fibers

Precursor	Density ($g\ cm{-}3$)	Young's modulus (*GPa*)	Electrical resistivity ($10^{-4}\ \Omega\ cm$)
Rayon[a]	1.66	390	10
Polyacrylonitrile[b] (PAN)	1.74	230	18
Pitch (Kureha)			
LT[c]	1.6	41	100
HT[d]	1.6	41	50
Mesophase pitch[e]			
LT	2.1	340	9
HT	2.2	690	1.8
Single crystal graphite[f]	2.25	1000	0.40

[a]Union Carbide, Thornel 50
[b]Union Carbide, Thornel 300
[c]LT, low-temperature heat-treated
[d]HT, high-temperature heat-treated
[e]Union Carbide-type P fibers
[f]Modulus and resistivity are in-plane values
Source Adapted with permission from Singer (1979)

We note from Table 2.6 that the carbon fibers produced from various precursor materials are fairly good electrical conductors along the fiber axial direction. Although this led to some work toward a potential use of carbon fibers as current carriers for electrical power transmission (Murday et al. 1984), it also caused extreme concern in many quarters. The reason for this concern is that if the extremely fine carbon fibers accidentally become airborne (during manufacture or service) they can settle on electrical equipment and cause short circuit.

An interesting characteristic of ex-mesophase pitch carbon fiber is the extremely high thermal conductivity it can have. Ex-pitch carbon fibers with a suitably oriented microstructure can have thermal conductivity as high as 1100 *W/mK*. The figure for an ex-PAN carbon fiber is generally less than 50 *W/mK*.

Anisotropic as the carbon fibers are, they have two principal coefficients of thermal expansion, namely, longitudinal or parallel to the fiber axis, α_l and transverse or perpendicular to the fiber axis, α_t. Typical values of the expansion coefficients are

$$\alpha_l \approx 5.5 \text{ to } 8.4 \times 10^{-6} K^{-1}$$

$$\alpha_t \approx -0.5 \text{ to } -1.3 \times 10^{-6} K^{-1}.$$

Compressive strength of carbon fibers is about half their tensile strength (Chawla 2018; Kumar et al. 2013)! Still, they are an order of magnitude better than aramid-type fibers (see Sect. 2.6).

Carbon fibers are used in a variety of applications in the aerospace and sporting goods industries. Cargo bay doors and booster rocket casings in the U.S. space shuttle are made of carbon fiber reinforced epoxy composites. Modern commercial aircraft such as Boeing 787 (Dreamliner) has fuselage and wings made of carbon fiber/epoxy composites. With the ever decreasing price of carbon fibers, applications of carbon fibers in other areas have also increased, for example, various machinery items such as turbine, compressor, and windmill blades and flywheels; in the field of medicine, the applications include both equipment and implant materials (e.g., ligament replacement in knees and hip joint replacement). We discuss these in more detail in Chap. 5.

2.6 Organic Fibers

In general, polymeric chains assume a random coil configuration, i.e., they have the so-called cooked spaghetti structure (see Chap. 3). In this random coil structure, the macromolecular chains are neither aligned in one direction nor stretched out. Thus, they have predominantly weak van der Waals interactions rather than strong covalent interactions, resulting in a low strength and stiffness. Because the covalent carbon–carbon bond is very strong, one would expect that linear chain polymers, such as polyethylene, would be potentially very strong and stiff. Conventional

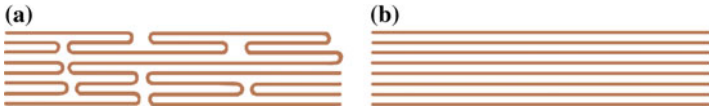

Fig. 2.26 Two types of molecular orientation: **a** oriented *without* high molecular extension and **b** oriented *with* high molecular extension. (From Barham and Keller 1985, used with permission)

polymers show a Young's modulus, *E*, of about 10 *GPa* or less. Highly drawn polymers with a Young's modulus of about 70 *GPa* can be obtained easily. However, if one wants strong and stiff organic fibers, one must obtain not only oriented molecular chains but also oriented *and* fully extended chains. Thus, in order to obtain high stiffness and high strength polymers, we must extend these polymer chains and pack them in a parallel array. The orientation of these polymer chains with respect to the fiber axis and the manner in which they fit together (i.e., order or crystallinity) are controlled by their chemical nature and the processing route. The case of molecular chain orientation without high molecular extension is shown in Fig. 2.26a while chain orientation with high molecular extension is depicted in Fig. 2.26b. It is the chain structure shown in Fig. 2.26b, i.e., molecular chain orientation coupled with molecular chain extension, which is needed for high stiffness and high strength. To get a Young's modulus value greater than 70 *GPa*, one needs rather high draw ratios, i.e., a very high degree of elongation must be carried out under such conditions that macroscopic elongation results in a corresponding elongation at a molecular level. It turns out that the Young's modulus, *E*, of a polymeric fiber increases linearly with the deformation ratio (draw ratio in tensile drawing or die drawing and extrusion ratio in hydrostatic extrusion). The drawing behavior of a polymer is a sensitive function of (i) its molecular weight and molecular weight distribution and (ii) deformation conditions (temperature and strain rate). Too low a drawing temperature produces voids, while too high a drawing temperature results in flow drawing, i.e., the macroscopic elongation of the material does not result in a molecular alignment, and consequently no stiffness enhancement results. An oriented and extended macromolecular chain structure, however, is not easy to achieve in practice.

Nevertheless, considerable progress in this area was made during the last quarter of the twentieth century. Organic fibers, such as aramid and polyethylene, possessing high strength and modulus are the fruits of this realization. Two very different approaches have been taken to make high modulus organic fibers. These are as follows:

1. Process the conventional flexible chain polymers in such a way that the internal structure takes a highly oriented and extended chain arrangement. Structural modification of "conventional" polymers such as high modulus polyethylene was developed by choosing appropriate molecular weight distributions, followed by drawing at suitable temperatures to convert the original folded chain structure into an oriented, extended chain structure.

2. The second, radically different, approach involves synthesis, followed by extrusion of a new class of polymers, called liquid crystal polymers. These have a rigid rod molecular chain structure. The liquid crystalline state, as we shall see, has played a very significant role in providing highly ordered, extended chain fibers.

These two approaches have resulted in two commercialized high strength and high stiffness fibers, polyethylene and aramid. Next, we will describe the processing, structure, and properties of these two fibers.

2.6.1 Oriented Polyethylene Fibers

The ultrahigh molecular weight polyethylene (UHMWPE) fiber is a highly crystalline fiber with very high stiffness and strength. This results from some innovative processing and control of the structure of polyethylene as explained below.

2.6.1.1 Processing of Polyethylene Fibers

Drawing of melt crystallized polyethylene (molecular weight between 10^4 and 10^5) to very high draw ratios can result in elastic moduli of up to 70 *GPa*. Tensile drawing, die drawing, or hydrostatic extrusion can be used to obtain the high permanent or plastic strains required to obtain a high elastic modulus. It turns out that modulus is dependent on the draw ratio but independent of how the draw ratio is obtained (Capaccio et al. 1979). In all these drawing processes, the polymer chains become merely oriented without undergoing molecular extension, and we obtain the kind of structure shown in Fig. 2.26a. Later developments led to solution and gel spinning of very high molecular weight polyethylene ($>10^6$) with moduli as high as 200 *GPa*. The gel spinning method of making polyethylene fibers has become technologically and commercially most successful. Pennings and coworkers (Kalb and Pennings 1980; Smook and Pennings 1984) made high modulus polyethylene fiber by solution spinning. Their work was followed by Smith and Lemstra (1976, 1980), who made polyethylene fiber by gel spinning. The gel spinning process of making polyethylene was industrialized in the 1980s. *Gels* are swollen networks in which crystalline regions form the network junctions. An appropriate polymer solution is converted into gel, which is drawn to give the fiber. At least three commercial firms produce oriented polyethylene fiber using similar techniques; *Dyneema*, *Spectra*, *Tekmilon* are the trade names of these ultrahigh molecular weight polyethylene (UHMWPE) fibers. Next, we will describe the gel spinning process of making the high stiffness polyethylene fiber.

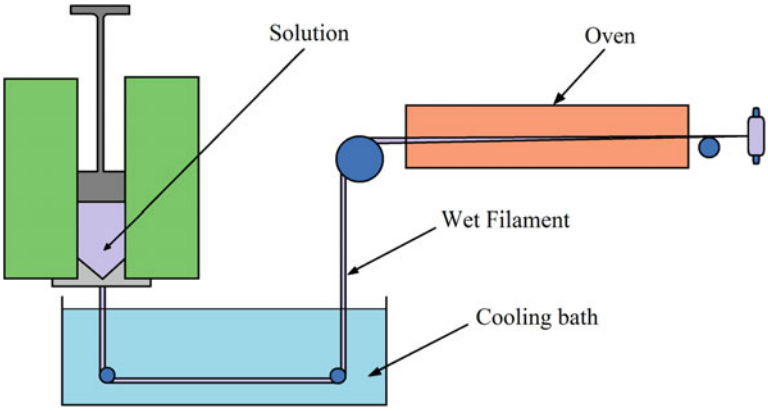

Fig. 2.27 Gel spinning process for making the high modulus polyethylene fiber concentration

2.6.1.2 Gel Spinning of Polyethylene Fiber

Polyethylene (PE) is a particularly simple, linear macromolecule, with the following chemical formula:

$$[-CH_2 - CH_2 - CH_2 - CH_2 - CH_2 - CH_2 - CH_2 - CH_2-]_n.$$

Thus, compared to other polymers, it is easier to obtain an extended and oriented chain structure in polyethylene. High density polyethylene (HDPE) is preferred to other types of polyethylene because HDPE has fewer branch points along its backbone and a high degree of crystallinity. The characteristics of linearity and crystallinity are important from the point of getting a high degree of orientational order and obtaining an extended chain structure in the final fiber. Figure 2.27 provides a flow diagram of the gel spinning process for making the high modulus polyethylene fiber. Different companies use different solvents, such as decalin, paraffin oil, and paraffin wax, to make a dilute (5–10%) solution of polymer in the appropriate solvent at about 150 °*C*. A dilute solution is important in that it allows for a lesser chain entanglement, which makes it easier for the final fiber to be highly oriented. A polyethylene gel is produced when the solution coming out of the spinneret is quenched by air. The as-spun gelled fiber enters a cooling bath. At this stage, the fiber is thought to have a structure consisting of folded chain lamellae with solvent between them and a swollen network of entanglements. These entanglements allow the as-spun fiber to be drawn to very high draw ratios, which can be as high as 200. The maximum draw ratio is related to the average distance between the entanglements, i.e., the solution concentration. The gelled fibers are drawn at 120 °*C*. One problem with this gel route is the rather low spinning rates of 1.5 $m\ min^{-1}$. At higher rates, the properties obtained are not very good (Kalb and Pennings 1980; Smook and Pennings 1984).

2.6.1.3 Structure and Properties of Polyethylene Fiber

The unit cell of a single crystal (orthorhombic) of polyethylene has the dimensions of 0.741, 0.494, and 0.255 *nm*. There are four carbon and eight hydrogen atoms per unit cell. One can compute the theoretical density of polyethylene, assuming a 100% single crystal polyethylene. If one does that, the theoretical density of polyethylene comes out to be 0.9979 $g\ cm^{-3}$; of course, in practice, one can only tend toward this theoretical value. As it turns out, the highly crystalline, oriented, and extended chain UHMWPE fiber has a density of 0.97 $g\ cm^{-3}$, which is very near the theoretical value. Thus, polyethylene fiber is very light; in fact, it is lighter than water and thus floats on water. Properties of some commercially available polyethylene fibers are summarized in Table 2.7.

Its strength and modulus are slightly lower than those of aramid fibers but on a per-unit-weight basis, i.e., specific property values are about 30% to 40% higher than those of aramid. As is true of most organic fibers, both polyethylene and aramid fibers must be limited to low-temperature (less than 150 °*C*) applications.

Another effect of the high degree of chain alignment in these fibers is their super smooth surface. This is manifested when these fibers are put in a polymeric matrix to form a fiber reinforced composite. High modulus polyethylene fibers, such as Spectra or Dyneema, are hard to bond with any polymeric matrix. Some kind of surface treatment must be given to the polyethylene fiber to bond with resins such as epoxy and PMMA. By far, the most successful surface treatment involves a cold gas (such as air, ammonia, or argon) plasma (Kaplan et al. 1988). Recall that a plasma consists of gas molecules in an excited state, i.e., highly reactive, dissociated molecules. When the polyethylene, or any other fiber, is treated with a plasma, surface modification occurs by removal of any surface contaminants and highly oriented surface layers, addition of polar and functional groups on the surface, and introduction of surface roughness; all these factors contribute to an enhanced fiber/matrix interfacial strength (Biro et al. 1992; Brown et al. 1992; Hild and Schwartz 1992a, b; Kaplan et al. 1988; Li et al. 1992). Exposure to the plasma for just a few minutes is enough.

Polyethylene fiber (the gel-spun UHMWPE variety) is 90–95% crystalline and has a density of 0.97 $g\ cm^{-3}$. There is a linear relationship between density and crystallinity for polyethylene. A 100% crystalline polyethylene will have a theoretical density, based on an orthorhombic unit cell, of about 1 $g\ cm^{-3}$. A totally

Table 2.7 Properties of polyethylene fibers[a]

Property	Spectra 900	Spectra 1000
Density ($g\ cm^{-3}$)	0.97	0.97
Diameter (μm)	38	27
Tensile strength (*GPa*)	2.7	3.0
Tensile modulus (*GPa*)	119	175
Tensile strain-to-fracture (%)	3.5	2.7

[a]Manufacturer's data; indicative values

amorphous polyethylene (0% crystallinity) will have a density of about 0.85 $g\ cm^{-3}$. Raman spectroscopy has been used to study the deformation behavior of polyethylene fiber. Creep properties of these fibers are not very good, Spectra 1000 has better creep properties than Spectra 900. It should be mentioned that although plasma treatment, in general, improves the interfacial adhesion between the fiber and the matrix, it does result in some deterioration of the mechanical properties of the fiber.

2.6.2 Aramid Fibers

Aramid fiber is a generic term for a class of synthetic organic fibers called aromatic polyamide fibers. The U.S. Federal Trade Commission gives a good definition of an aramid fiber as "a manufactured fiber in which the fiber forming substance is a long-chain synthetic polyamide in which at least 85% of the amide linkages are attached directly to two aromatic rings." Well-known commercial names of aramid fibers include Kevlar and Nomex (DuPont) and Twaron (Teijin Aramid). Teijinconex and Technora are two other commercially available fibers from Teijin. *Nylon* is a generic name for any long-chain polyamide. Aramid fibers such as Nomex or Kevlar or Twaron, however, are ring compounds based on the structure of benzene as opposed to the linear compounds used to make nylon. The basic difference between Kevlar and Nomex is that Kevlar has *para*-oriented aromatic rings, i.e., its basic unit is a symmetric molecule, with bonds from each aromatic ring being parallel, while Nomex is *meta*-oriented, with bonds at 120° angles to each other. Teijinconex is similar to Nomex while Twaron is similar to Kevlar. Technora is a copolyamide. The basic chemical structure of aramid fibers consists of oriented para-substituted aromatic units, which makes them rigid rodlike polymers. The rigid rodlike structure results in a high glass transition temperature and poor solubility, which makes fabrication of these polymers, by conventional drawing techniques, difficult. Instead, they are spun from liquid crystalline polymer solutions by dry-jet wet spinning, as described in the next section.

2.6.2.1 Processing of Aramid Fibers

Processing of aramid fibers involves solution polycondensation of diamines and diacid halides at low temperatures. Hodd and Turley (1978), Morgan (1979), and Magat (1980) have given simplified accounts of the theory involved in the fabrication of aramid fibers.

The most important point is that the starting spinnable solutions that give high strength and high modulus fibers have liquid crystalline order. Figure 2.28 shows schematically various states of a polymer in solution. Figure 2.28a shows two-dimensional, linear, flexible chain polymers in solution. These are called *random coils*, as the figure suggests. If the polymer chains can be made of rigid

units, that is, rodlike, we can represent them as a random array of rods (Fig. 2.28b). Any associated solvent may contribute to the rigidity and to the volume occupied by each polymer molecule. It is easy to see that with increasing concentration of rodlike molecules, one can dissolve more polymer by forming regions of partial order, that is, regions in which the chains form a parallel array. This partially ordered state is called a *liquid crystalline state* (Fig. 2.28c). When the rodlike chains become approximately arranged parallel to their long axes, but their centers remain unorganized or randomly distributed, we have what is called a *nematic* liquid crystal (Fig. 2.28d). It is this kind of order that is found in the extended chain polyamides.

Liquid crystal solutions, because of the presence of the ordered domains, are optically anisotropic, that is, they show the phenomenon of *birefringence*. Birefringence, also known as, double refraction, is the phenomenon of splitting of a ray of light into two rays when it passes through certain types of material, depending on the polarization of the light. Figure 2.29 shows the anisotropic solution of Kevlar aramid and sulfuric acid at rest between crossed polarizers. Note the parallel arrays of ordered polymer chains in the liquid crystalline state, which become even more ordered when these solutions are subjected to shear as, for example, in extruding through a spinneret hole. It is this inherent property of liquid crystal solutions that is exploited in the manufacture of aramid fibers. This alignment of polymer crystallites along the fiber axis results in the characteristic fibrillar structure of aramid fibers. Para-oriented aromatic polyamides form liquid crystal solutions under certain conditions of concentration, temperature, solvent, and molecular weight. This can be represented in the form of a phase diagram. As an example, Fig. 2.30a shows a phase diagram of the system poly-*p*-benzamide in tetramethylurea-LiCl solutions (Magat 1980). The region marked anisotropic represents the liquid crystalline state. Only under certain conditions do we get this desirable anisotropic state. There also occurs an anomalous relationship between viscosity and polymer concentration in liquid crystal solutions. Initially, an increase in viscosity occurs as the concentration of polymer in solution increases, as it would in any ordinary polymer solution. At a critical point where it starts assuming an

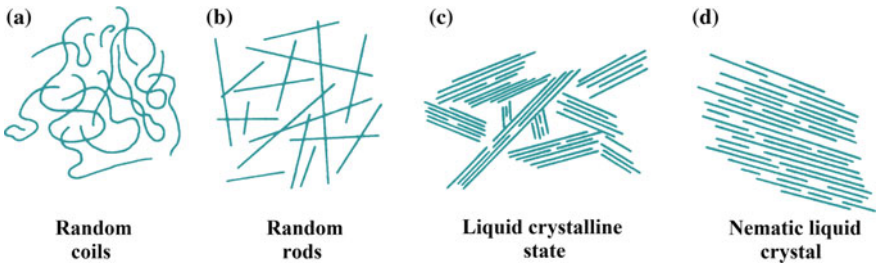

Fig. 2.28 Various states of polymer in solution: **a** two-dimensional, linear, flexible chains (random coils), **b** random array of rods, **c** partially ordered liquid crystalline state, and **d** nematic liquid crystal (randomly distributed parallel rods)

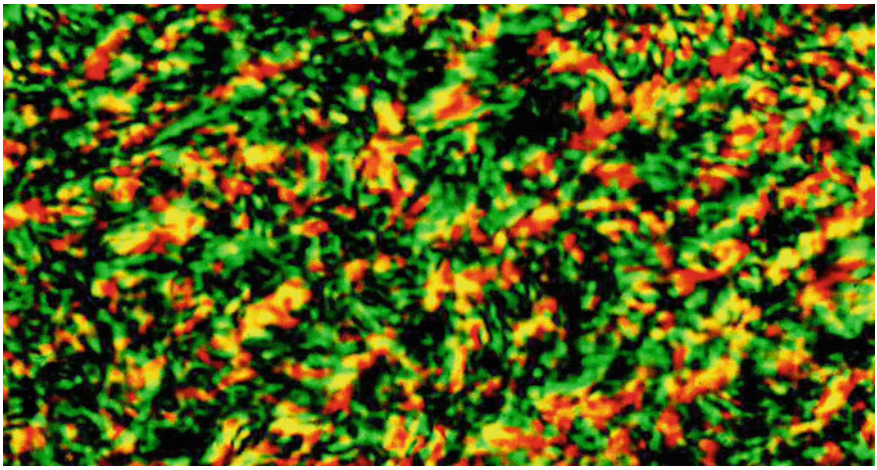

Fig. 2.29 Anisotropic Kevlar aramid and sulfuric acid solution at rest between crossed polarizers. (Courtesy of Du Pont Co.)

anisotropic liquid crystalline shape, a sharp drop in the viscosity occurs; see Fig. 2.30b. This drop in viscosity of liquid crystal polymers at a critical concentration was predicted by Flory (1956). The drop in viscosity occurs due to the formation of a lyotropic nematic structure. The liquid crystalline regions act like dispersed particles and contribute very little to viscosity of the solution. With increasing polymer concentration, the amount of liquid crystalline phase increases up to a point after which the viscosity tends to rise again. There are other requirements for forming a liquid crystalline solution from aromatic polyamides. The molecular weight must be greater than some minimum value and the solubility must exceed the critical concentration required for liquid crystallinity. Thus, starting from liquid crystalline spinning solutions containing highly ordered arrays of extended polymer chains, we can spin fibers directly into an extremely oriented, chain-extended form. These as-spun fibers are quite strong and, because the chains are highly extended and oriented, the use of conventional drawing techniques becomes optional.

Para-oriented rigid diamines and dibasic acids give polyamides that yield, under appropriate conditions of solvent, polymer concentration, and polymer molecular weight, the desired nematic liquid crystal structure. One would like to have, for any solution spinning process, a high molecular weight in order to have improved mechanical properties, a low viscosity to easily spin the fiber, and a high polymer concentration for high yield. For para-aramid, poly-*p*-phenylene terephthalamide (PPTA), the nematic liquid crystalline state is obtained in 100% sulfuric acid solvent at a polymer concentration of about 20%. That is, to dissolve PPTA we need concentrated sulfuric acid as the solvent. In industry, this solution is often referred to as the *dope*.

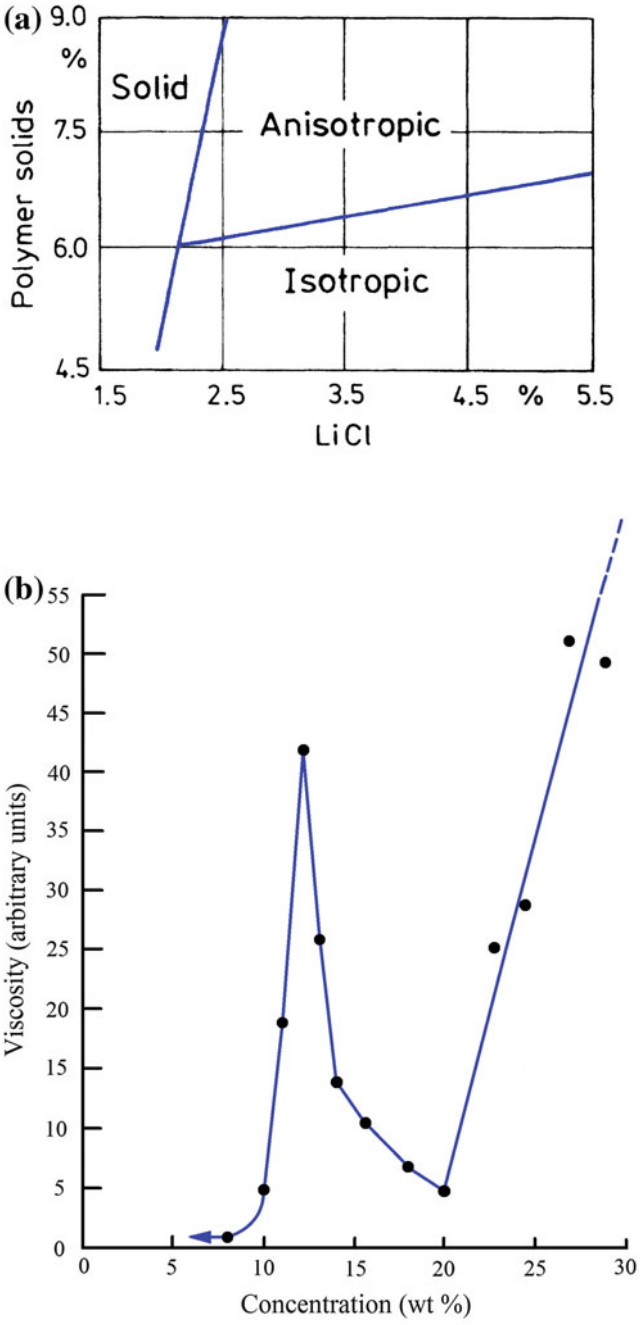

◂**Fig. 2.30** **a** Phase diagram of poly-*p*-benzamide in tetramethylurea–LiCl solutions. Note that the anisotropic state is obtained under certain conditions. (With permission from Magat 1980). **b** Viscosity versus polymer concentration in solution. A sharp drop in viscosity occurs when the solution starts becoming anisotropic liquid crystal. (After Kwolek and Yang 1993)

For aramid fibers, the dry-jet wet spinning method is used. The process is illustrated in Fig. 2.31. Solution polycondensation of diamines and diacid halides at low temperatures (near 0 °*C*) gives the aramid forming polyamides. Low temperatures are used to inhibit any by-product generation and promote linear polyamide formation. The resulting polymer is pulverized, washed, and dried; mixed with concentrated H_2SO_4; and extruded through a spinneret at about 100 °*C*. The jets from the orifices pass through about 1 *cm* of air layer before entering a cold water (0–4 °*C*) bath. The fiber solidifies in the air gap, and the acid is removed in the coagulation bath. The spinneret capillary and air gap cause rotation and alignment of the domains, resulting in highly crystalline and oriented as-spun fibers. The air gap also allows the dope to be at a higher temperature than is possible without the air gap. The higher temperature allows a more concentrated spinning solution to be used, and higher spinning rates are possible. Spinning rates of several hundred meters per minute are not unusual. Figure 2.32 compares the dry-jet wet spinning method used with nematic liquid crystals and the spinning of a conventional polymer. The oriented chain structure, together with molecular extension, is achieved with dry-jet wet spinning. The conventional wet or dry spinning gives precursors that need further processing for a marked improvement in properties (Jaffe and Jones 1985). The as-spun aramid fibers are washed in water, wound on a

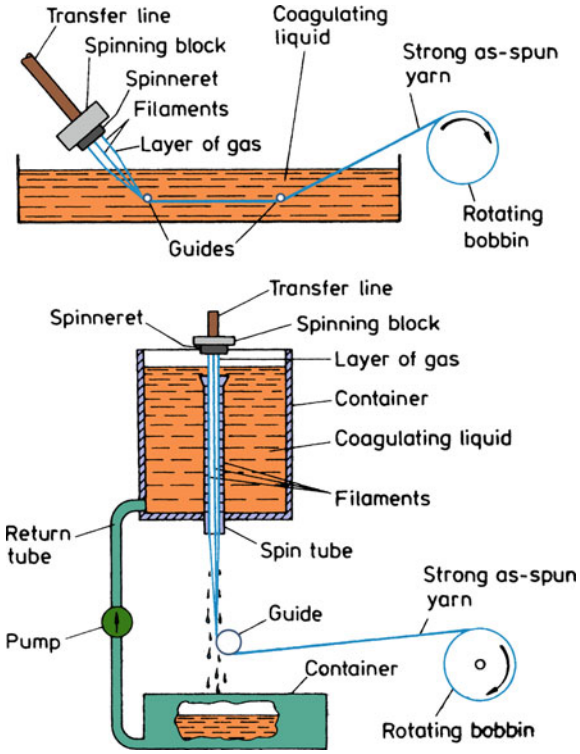

Fig. 2.31 The dry-jet wet spinning process of producing aramid fibers

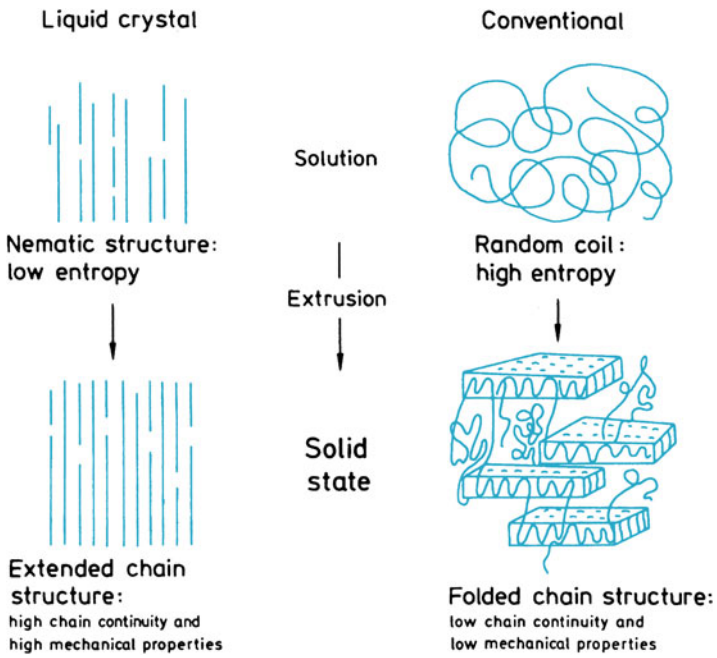

Fig. 2.32 Comparison of dry-jet wet spinning of nematic liquid crystalline solution and conventional spinning of a polymer. (Reprinted from Jaffe and Jones 1985, p. 349, courtesy of Marcel Dekker, Inc.)

bobbin, and dried. Fiber properties are modified by the use of appropriate solvent additives, by changing the spinning conditions, and by means of some post-spinning heat treatments, if necessary.

The aramid fiber known as Technora (formerly HM-50) is made slightly differently from the liquid crystal route just described. Three monomers—terephthalic acid, *p*-phenylenediamine (PDA), and 3,4-diamino diphenyl ether—are used. The ether monomer provides more flexibility to the backbone chain, which results in a fiber that has slightly better compressive properties than PPTA aramid fiber made via the liquid crystal route. An amide solvent with a small amount of salt (calcium chloride or lithium chloride) is used as a solvent (Ozawa et al. 1978). The polymerization is done at 0–80 °*C* in 1–5 h and with a polymer concentration of 6–12%. The reaction mixture is spun from a spinneret into a coagulation bath 35–50% $CaCl_2$. Draw ratios between 6 and 10 are used.

2.6.2.2 Structure of Aramid Fibers

Kevlar aramid fiber is the most studied of all aramid fibers. Thus, our description of structure will mostly be from the work done on Kevlar, but it applies to Twaron as

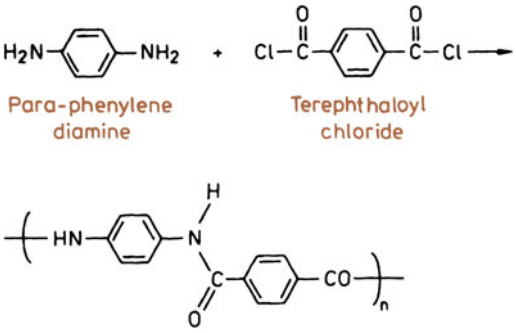

Fig. 2.33 Chemical structure of aramid fiber

well. The chemical formula of aramid is given in Fig. 2.33. Chemically, the Kevlar- or Twaron-type aramid fiber is poly (*p*-phenyleneterephthalamide), which is a polycondensation product of terephthaloyl chloride and *p*-phenylene diamine. The aromatic rings impart the rigid rodlike chain structure of aramid. These chains are highly oriented and extended along the fiber axis, with the resultant high modulus. Aramid fiber has a highly crystalline structure and the para orientation of the aromatic rings in the polymer chains results in a high packing efficiency. Strong covalent bonding in the fiber direction and weak hydrogen bonding in the transverse direction (see Fig. 2.34) result in highly anisotropic properties, i.e., high tensile properties along the fiber axis but poor compressive properties along the fiber axis. Properties are also poor in the radial direction.

The structure of Kevlar aramid fiber has been investigated by electron microscopy and diffraction. A schematic representation of the supramolecular structure of Kevlar 49 is shown in Fig. 2.35 (Dobb et al. 1980). It shows radially arranged, axially pleated crystalline supramolecular sheets. The molecules form a planar array with interchain hydrogen bonding. The stacking sheets form a crystalline array, but between the sheets the bonding is rather weak. Each pleat is about 500 *nm* long, and the pleats are separated by transitional bands. The adjacent components of a pleat make an angle of 170°. Such a structure is consistent with the experimentally observed rather low longitudinal shear modulus and poor properties in compression and transverse to the Kevlar fiber axis. A correlation between good compressive characteristics and a high glass transition temperature (or melting point) has been suggested (Northolt 1981). Thus, since the glass transition temperature of organic fibers is lower than that of inorganic fibers, the former would be expected to show poorer properties in compression. For aramid- and polyethylene-type high stiffness fibers, compression results in the formation of kink bands leading to an eventual ductile failure. Yielding is observed at about 0.5% strain; this is thought to correspond to a molecular rotation of the amide carbon–nitrogen bond shown in Fig. 2.33 from the normal, extended, *trans* configuration to a kinked, *cis* configuration (Tanner et al. 1986). In the chemical literature, this is referred to as *cis–trans* isomerism. It describes the orientation of functional groups in a molecule. In

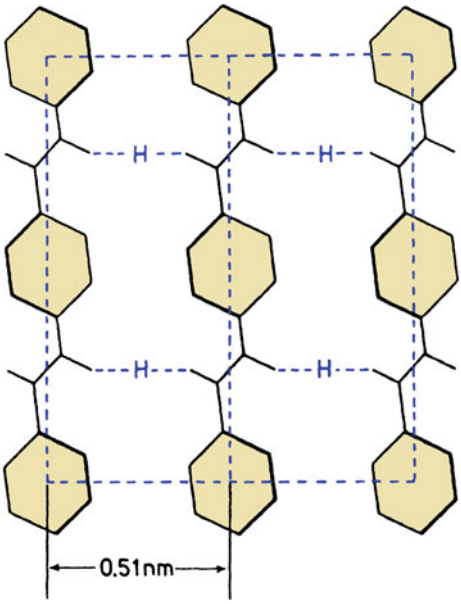

Fig. 2.34 Strong covalent bonding in the fiber direction and weak hydrogen bonding (indicated by *H*) in the transverse direction

aromatic structures, the rotation of bonds is greatly restricted. *Cis* in Latin means "on the same side" while *trans* means "on the other side" or "across". This *trans* to *cis* rotation in the aramid fiber causes a 45° bend in the chain. This bend propagates across the unit cell, the microfibrils, and a kink band results in the fiber. This anisotropic behavior of aramid fiber is revealed in a vivid manner in the SEM micrograph of knotted fiber shown in Fig. 2.36. Note the buckling or kink marks on the compressive side of a knotted Kevlar aramid fiber. Note also the absence of

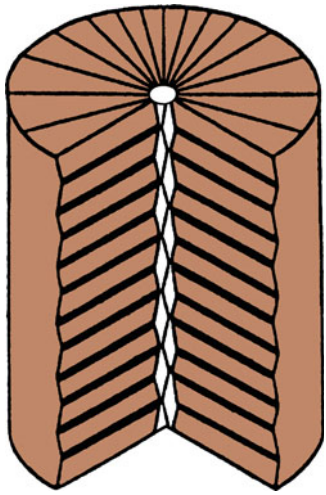

Fig. 2.35 Schematic representation of the supramolecular structure of aramid fiber, Kevlar 49. The structure consists of radially arranged, axially pleated crystalline sheets. (From Dobb et al. 1980, used with permission)

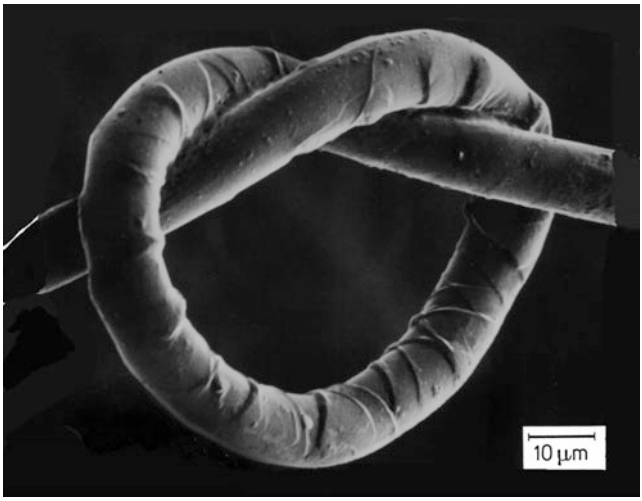

Fig. 2.36 Knotted Kevlar aramid fiber showing buckling marks on the compressive side. The tensile side is smooth. (Courtesy of Fabric Research Corp.)

such markings on the tensile side. Such markings on the aramid fiber surface have also been reported by, among others, DeTeresa et al. (1984) when the aramid fiber is subjected to uniform compression or torsion.

2.6.2.3 Properties and Applications of Aramid Fibers

Some of the important properties of Kevlar aramid fibers are summarized in Table 2.8. As can be seen from this table, the aramid fiber is very light and has very high stiffness and strength in tension. The two well-known varieties are Kevlar 49 and Kevlar 29. Kevlar 29 has about half the modulus but double the strain-to-failure of Kevlar 49. It is this high strain-to-failure of Kevlar 29 that makes it useful for making vests that are used for protection against small arms. It should be emphasized that aramid fiber, like most other high-performance organic fibers, has rather poor characteristics in compression, its compressive strength being only about 1/8 of its tensile strength. This follows from the anisotropic nature of the fiber as previously discussed. In tensile loading, the load is carried by the strong covalent bonds while in compressive loading, weak hydrogen bonding and van der Waals bonds come into play, which lead to rather easy local yielding, buckling, and kinking of the fiber. Thus, aramid type high-performance fibers are not suitable for applications involving compressive forces.

Aramid fiber has good vibration damping characteristics. Dynamic (commonly sinusoidal) perturbations are used to study the damping behavior of a material. The material is subjected to an oscillatory strain. We can characterize the damping behavior in terms of a quantity called the logarithmic decrement, Δ, which is

Table 2.8 Properties of Kevlar aramid fiber yarns[a]

Property	K 29	K 49	K 119	K 129	K 149
Density ($g\ cm^{-3}$)	1.44	1.45	1.44	1.45	1.47
Diameter (μm)	12	12	12	12	12
Tensile strength (GPa)	2.8	2.8	3.0	3.4	2.4
Tensile strain-to-fracture (%)	3.5–4.0	2.8	4.4	3.3	1.5–1.9
Tensile modulus (GPa)	65	125	55	100	147
Moisture regain (%) at 25 °C, 65% RH	6	4.3	–	–	1.5
Coefficient of expansion ($10^{-6}\ K^{-1}$)	−4.0	−4.9	–	–	–

[a]All data from DuPont brochures. Indicative values only. 25-cm yarn length was used in tests (ASTM D-885). *K* stands for Kevlar, a trademark of DuPont

defined as the natural logarithm of the ratio of amplitudes of successive vibrations, i.e.,

$$\Delta = \ln \frac{\theta_n}{\theta_{n+1}},$$

where θ_n and θ_{n+1} are the two successive amplitudes. The logarithmic decrement is proportional to the ratio of maximum energy dissipated per cycle/maximum energy stored in the cycle. Composites of aramid fiber/epoxy matrix show a logarithmic decrement about 5 times that of glass fiber/epoxy.

Like other polymers, aramid fibers are sensitive to ultraviolet (UV) light. When exposed to ultraviolet light, aramid fibers discolor from yellow to brown and lose mechanical properties. Radiation of a particular wavelength can cause degradation because of absorption by the polymer and breakage of chemical bonds. Near-UV and part of the visible spectrum should be avoided for outdoor applications involving use of unprotected aramid fibers. A small amount of such light emanates from incandescent and fluorescent lamps or sunlight filtered by window glass. DuPont Co. recommends that Kevlar aramid yarn should not be stored within one foot (0.3 m) of fluorescent lamps or near windows.

The Technora fiber of Teijin shows properties that are a compromise between conventional fibers and rigidrod fibers; Table 2.9 provides a summary of these. In terms of its stress–strain behavior, it can be said that Technora fiber lies between Kevlar 49 and Kevlar 29.

Table 2.9 Properties of Technora fiber[a]

Density ($g\ cm^{-3}$)	Diameter (μm)	Tensile strength (GPa)	Tensile modulus (GPa)	Tensile strain-to-fracture (%)
1.39	12	3.1	71	4.4

[a]Manufacturer's data; indicative values only

Different types of Kevlar aramid fibers provide an impressive set of properties, see Table 2.8. The three important types of Kevlar aramid fibers are used for specific applications (Magat 1980):

1. *Kevlar*. This is meant mainly for use as rubber reinforcement for tires (belts or radial tires for cars and carcasses of radial tires for trucks) and, in general, for mechanical rubber goods.
2. *Kevlar 29*. This is used for ropes, cables, coated fabrics for inflatables, architectural fabrics, and ballistic protection fabrics. Vests made of Kevlar 29 have been used by law enforcement agencies in many countries.
3. *Kevlar 49*. This is meant for reinforcement of epoxy, polyester, and other resins for use in the aerospace, marine, automotive, and sports industries.

2.7 Ceramic Fibers

Continuous ceramic fibers present an attractive package of properties. They combine high strength and elastic modulus with high-temperature capability and a general freedom from environmental attack. These characteristics make them attractive as reinforcements in high-temperature structural materials.

There are three methods to fabricate ceramic fibers: chemical vapor deposition, polymer pyrolysis, and sol–gel techniques. The latter two involve rather novel techniques of obtaining ceramics from organometallic polymers. The sol–gel technique was mentioned in Sect. 2.2 in regard to the manufacture of silica-based glass fibers. The sol–gel technique is also used to produce a variety of alumina-based oxide fibers commercially. Another breakthrough in the ceramic fiber area is the concept of pyrolyzing, under controlled conditions, polymers containing silicon and carbon or nitrogen to produce high-temperature ceramic fibers. This idea is nothing but an extension of the polymer pyrolysis route to produce a variety of carbon fibers wherein a suitable carbon-based polymer (e.g., PAN or pitch) is subjected to controlled heating to produce carbon fibers (see Sect. 2.5). The pyrolysis route of producing ceramic fibers has been used with polymers containing silicon, carbon, nitrogen, and boron, with the end products being SiC, Si_3N_4, B_4C, and BN in fiber form, foam, or coating. We describe below some important ceramic fibers.

2.7.1 Oxide Fibers

Many alumina-type oxide fibers are available commercially. Alumina has many allotropic forms: γ, δ, η, and α. Of these, α-alumina is the most stable form. A variety of alumina-based continuous fibers made by sol–gel processing are

available commercially. The sol–gel process of making fibers involves the following steps, common to all fibers:

1. Formulate sol.
2. Concentrate to form a viscous gel.
3. Spin the precursor fiber.
4. Calcine to obtain the oxide fiber.

3M Co. produces a series of ceramic fibers called the Nextel fibers. They are mainly Al_2O_3+SiO_2 and some B_2O_3. The compositions and properties of some Nextel fibers are given in Table 2.10. Nextel is the trademark of 3M Co. Figure 2.37 shows an optical micrograph of Nextel 312 fibers. The sol–gel manufacturing process used by 3M Co. has metal alkoxides as the starting materials. The reader will recall that metal alkoxides are $M(OR)_n$-type compounds, where *M* is the metal, *n* is the metal valence, and *R* is an organic compound. Selection of an appropriate organic group is very important. It should provide sufficient stability and volatility to the alkoxide so that M–OR bonds are broken and MO–R is obtained to give the desired oxide ceramics. Hydrolysis of metal alkoxides results in sols that are spun and gelled. The gelled fiber is then densified at relatively low temperatures. The high surface free energy available in the pores of the gelled fiber allows for densification at relatively low temperatures. The sol–gel process provides close control over solution composition and rheology of fiber diameter. The

Table 2.10 Composition and properties of some oxide fibers[a]

Fiber type	Composition, wt. %	Diameter (μm)	Density ($g\ cm^{-3}$)	Tensile strength (*GPa*)	Young's modulus (*GPa*)
Nextel 312	Al_2O_3–62.5, SiO_2–24.5, B_2O_3–13	10–12	2.70	1.7	150
Nextel 440	Al_2O_3–70, SiO_2–28, B_2O_3–2	10–12	3.05	2.0	190
Nextel 550	Al_2O_3–73, SiO_2–27	10–12	3.03	2.0	193
Nextel 610	Al_2O_3–99+	10–12	3.9	3.1	370
Nextel 650	Al_2O_3–89, ZrO_2–10, Y_2O_3–1	10–12	4.10	2.5	358
Nextel 720	Al_2O_3–85, SiO_2–15	10–12	3.40	2.1	260
Saffil	Al_2O_3–96, SiO_2–4	3	2.3	1.0	100
Saphikon	Single Crystal Al_2O_3	75–250	3.8	3.1	380
Sumitomo	Al_2O_3–85, SiO_2–15	9	3.2	2.6	250

[a]Manufacturer's data

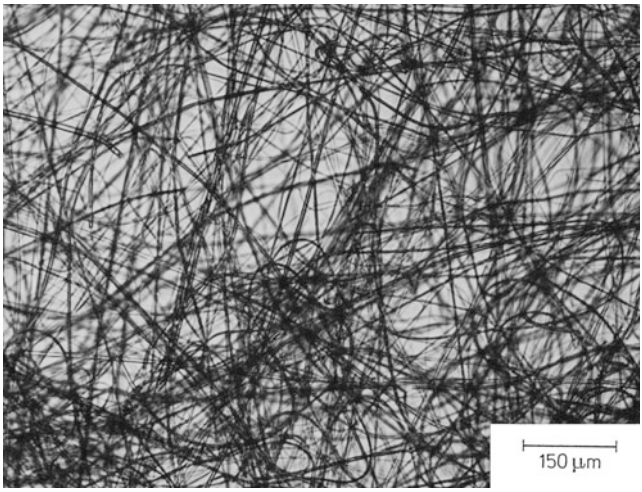

Fig. 2.37 Optical micrograph of Nextel 312 (Al_2O_3 + B_2O_3 + SiO_2) fiber

disadvantage is that rather large dimensional changes must be accommodated and fiber integrity preserved.

Sowman (1988) has provided details of the process used by 3M Co. for making the Nextel oxide fibers. Aluminum acetate [$Al(OH)_2(OOCCH_3) \cdot 1/3H_3BO_3$], e.g., "Niaproof," from Niacet Corp., is the starting material. Aluminum acetate with an Al_2O_3/B_2O_3 ratio of 3 to 1 becomes spinnable after water removal from an aqueous solution. In the fabrication of 3M continuous fibers, a 37.5% solution of basic aluminum acetate in water is concentrated in a rotating flask partially immersed in a water bath at 32–36 °*C*. After concentration to an equivalent Al_2O_3 content of 28.5%, a viscous solution with viscosity, η, between 100 and 150 *Pas* is obtained. This is extruded through a spinneret under a pressure of 800–1000 *kPa*. Shiny, colorless fibers are obtained on firing to 1000 °*C*. The microstructure shows cube- and lath-shaped crystals. The boria addition lowers the temperature required for mullite formation and retards the transformation of alumina to α-Al_2O_3. One needs boria in an amount equivalent to or greater than a 9 Al_2O_3:2 B_2O_3 ratio in Al_2O_3–B_2O_3–SiO_2 compositions to prevent the formation of crystalline alumina.

Crystaline alumina fibers are also made via sol–gel. Boric salts of aluminum decompose into transition aluminum oxide spinels such as η-Al_2O_3 above 400 °*C*. These transition cubic spinels convert to hexagonal α-Al_2O_3 on heating to between 1000 and 1200 °*C*. The problem is that the nucleation rate of pure α-Al_2O_3 is too low and results in rather large grains. Also, during the transformation to α phase, a large shrinkage results in a rather large porosity. The α-Al_2O_3 fiber, 3M Co.'s tradename Nextel 610, is obtained by seeding the high-temperature α-alumina with a very fine hydrous colloidal iron oxide. The fine iron oxide improves the nucleation rate of α-Al_2O_3, resulting in a high-density, ultrafine grain, homogeneous α-Al_2O_3 fiber (Wilson 1990). α-Fe_2O_3 is isostructural with α-Al_2O_3 (5.5% lattice

mismatch). 3M's hydrous colloidal iron oxide sol appears to be an efficient nucleating agent. Without the seeding with iron oxide, the η-alumina-to-α-alumina transformation occurred at about 1100 °*C*. With 1% Fe_2O_3, the transformation temperature was decreased to 1010 °*C*, while with 4% Fe_2O_3, the transformation temperature came down to 977 °*C*. Concomitantly, the grain size was refined. In addition to Fe_2O_3, about 0.5 *wt%* SiO_2 is added to reduce the final grain size of Nextel 610 fiber, although SiO_2 inhibits the transformation to the α phase. The SiO_2 addition also reduces grain growth during soaking at 1400 °*C*.

Many other alumina- or alumina-silica-type fibers are available. Most of these are also made by the sol–gel process. Sumitomo Chemical Co. produces a fiber that is a mixture of alumina and silica. The flow diagram of this process is shown in Fig. 2.38. Starting from an organoaluminum (polyaluminoxanes or a mixture of polyaluminoxanes and one or more kinds of Si-containing compounds), a precursor fiber is obtained by dry spinning. This precursor fiber is calcined to produce the final fiber. The fiber structure consists of fine crystallites of spinel. SiO_2 serves to stabilize the spinel structure and prevents it from transforming to α-Al_2O_3 (Saitow 1992). Yet another variety of alumina fiber available commercially is a δ-Al_2O_3, a staple fiber (tradename *Saffil*). This fiber has about 4% SiO_2 and a very fine diameter (3 μm). The starting material for Saffil is an aqueous phase containing an oxide sol and an organic polymer: Aluminum oxychloride [$Al_2(OH)_5Cl$] is mixed with a medium-molecular-weight polymer such as 2 *wt%* polyvinyl alcohol. The sol is extruded as filaments into a coagulating (or precipitating) bath in which the extruded shape gels. The gelled fiber is then dried and calcined to produce the final oxide fiber. This solution is slowly evaporated in a rotary evaporator until a viscosity of about 80 *Pas* (800 *P*) is attained. The starting solution is extruded through a spinneret; the fibers are wound on a drum, and fired to about 800 °*C*. The organic material is burned away, and a fine-grained alumina fiber with 5–10% porosity and a diameter of 3–5 μm is obtained. The fibers as produced at this stage are suitable for filtering purposes because of their high porosity. By heating them to 1400–1500 °*C*, which causes 3–4% of linear shrinkage, one obtains a refractory alumina fiber suitable for reinforcement purposes. Care is taken to produce fibers with diameter greater than 1 μm (to avoid biological hazards) but less than 6 μm (to avoid skin irritation).

A technique called *edge-defined film-fed growth* (EFG) has been used to make continuous, monocrystalline sapphire (Al_2O_3) fiber (LaBelle and Mlavsky 1967; LaBelle 1971; Pollack 1972; Hurley and Pollack 1972). LaBelle and Mlavsky (1967) grew sapphire (Al_2O_3) single crystal fibers using a modified Czochralski puller and radio-frequency heating. The process is called the edge-defined film-fed growth method because the external edge of the die defines the shape of the fiber and the liquid is fed in the form of a film. Fiber growth rates as high as 200 mm/min have been attained. The die material must be stable at the melting point of alumina; a molybdenum die is commonly used. A capillary supplies a constant liquid level at the crystal interface. A sapphire seed crystal is used to control the orientation of the single crystal fiber. Molten alumina wets both molybdenum and alumina. The crystal grows from a molten film between the growing crystal and the die. The

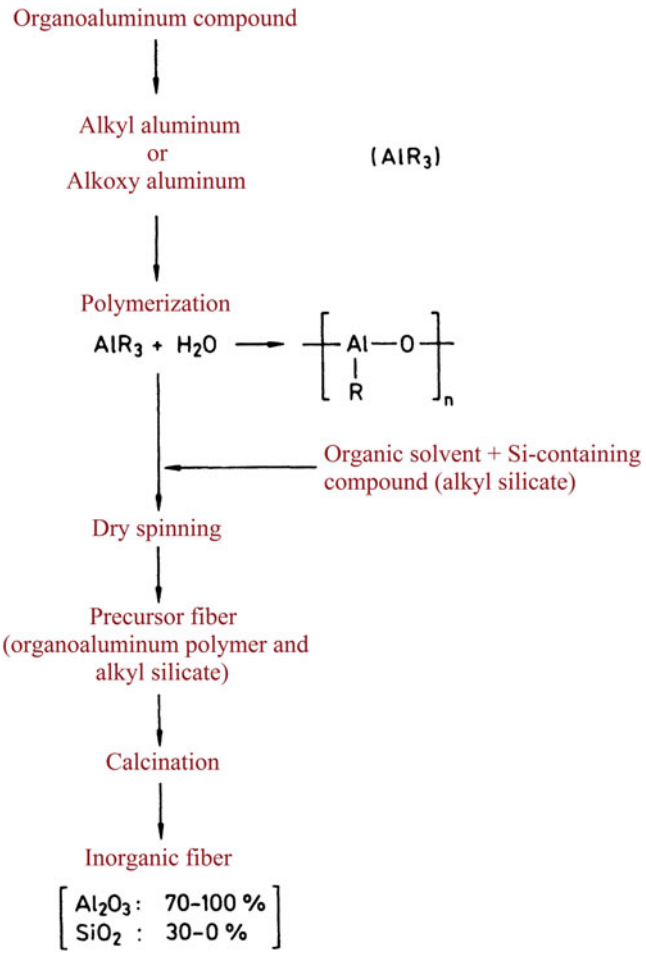

Fig. 2.38 Flow diagram of an alumina + silica fiber production

crystal shape is defined by the external shape of the die rather than the internal shape. A commercial fiber produced by this method, called *Saphikon*, has a hexagonal structure with its *c*-axis parallel to the fiber axis. The diameter (actually it has rounded triangular cross section) is rather large, between 125 and 250 μm.

A *laser-heated floating zone method* has been devised to make a variety of ceramic fibers. Gasson and Cockayne (1970) used laser heating for crystal growth of Al_2O_3, Y_2O_3, $MgAl_2O_4$, and Na_2O_3. Haggerty (1972) used a four-beam laser-heated float zone method to grow single crystal fibers of Al_2O_3, Y_2O_3, TiC, and TiB_2. A CO_2 laser is focused on the molten zone. A source rod is brought into the focused laser beam. A seed crystal, dipped into the molten zone, is used to control the orientation. Crystal growth starts by moving the source and seed rods

simultaneously. Mass conservation dictates that the diameter is reduced as the square root of the feed rate/pull rate ratio. It is easy to see that, in this process, the fiber purity is determined by the purity of the starting material.

2.7.2 Nonoxide Fibers

Nonoxides such as silicon carbide and silicon nitride have very attractive properties. Silicon carbide, in particular, is commercially available in a fibrous form. In this section, we describe some of these nonoxide fibers.

2.7.2.1 Silicon Carbide Fibers

Silicon carbide fiber must be regarded as a major development in the field of ceramic reinforcements during the last quarter of the twentieth century. In particular, a process developed by Professor Yajima in Japan, involving controlled pyrolysis of a polycarbosilane precursor to yield a small diameter, flexible fiber, must be considered to be the harbinger of the manufacture of ceramic fibers from polymeric precursors. In this section, we describe the processing, microstructure, and properties of the silicon carbide fibers in some detail.

We can easily classify the fabrication methods for SiC as conventional or nonconventional. The conventional category would include chemical vapor deposition (CVD) while the nonconventional would include controlled pyrolysis of polymeric precursors. There is yet another important type of SiC available for reinforcement purposes: SiC whiskers.

2.7.2.2 Silicon Carbide Fibers by CVD

Silicon carbide fiber can be made by chemical vapor deposition on a substrate heated to approximately 1300 $^{\circ}C$. The substrate can be tungsten or carbon. The reactive gaseous mixture contains hydrogen and alkyl silanes. Typically, a gaseous mixture consisting of 70% hydrogen and 30% silanes is introduced at the reactor top (Fig. 2.39), where the tungsten substrate ($\sim$13 μm diameter) also enters the reactor. Mercury seals are used at both ends as contact electrodes for the filament. The substrate is heated by combined direct current (250 mA) and very high frequency (VHF $\sim$ 60 MHz) to obtain an optimum temperature profile. To obtain a 100 μm diameter SiC monofilament, it generally takes about 20 s in the reactor. The filament is wound on a spool at the bottom of the reactor. The exhaust gases (95% of the original mixture + HCl) are passed around a condenser to recover the unused silanes. Efficient reclamation of the unused silanes is very important for a cost-effective production process. This CVD process of making SiC fiber is very similar to that of B fiber manufacture. The nodules on the surface of SiC are smaller

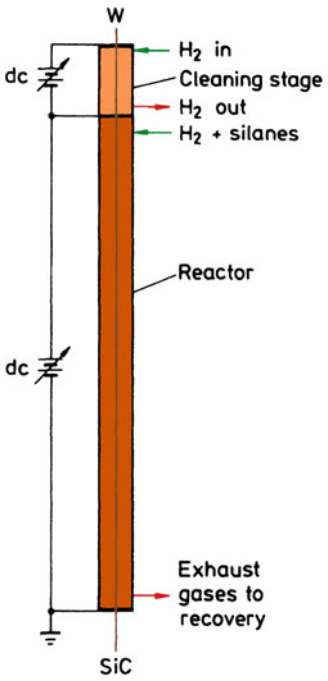

Fig. 2.39 CVD process for SiC monofilament fabrication. (From Milewski et al. 1974, reproduced with permission)

than those seen on B fibers. Such CVD processes result in composite monofilaments that have built-in residual stresses. The process is, of course, very expensive. Methyltrichlorosilane is an ideal raw material for SiC, as it contains one silicon and one carbon atom, i.e., one would expect a stoichiometric SiC to be deposited. The chemical reaction is

$$CH_3SiCl_3(g) \xrightarrow{H_2} SiC(s) + 3HCl(g).$$

An optimum amount of hydrogen is required. If the hydrogen is less than sufficient, chlorosilanes will not be reduced to Si and free carbon will be present in the mixture. If too much hydrogen is present, the excess Si will form in the end product. Generally, solid (free) carbon and solid or liquid silicon are mixed with SiC. The final monofilament (100–150 μm) consists of a sheath of mainly β-SiC with some α-SiC on the tungsten core. The {111} planes in SiC deposit are parallel to the fiber axis. The cross section of SiC monofilament resembles closely that of a boron fiber. Properties of a CVD SiC monofilament are given in Table 2.11.

Commercially, a series of surface-modified silicon carbide fibers, called SCS fibers, is available. These special fibers have a complex through the thickness gradient structure. SCS-6, for example, is a thick fiber (diameter = 142 μm) that is produced by chemical vapor deposition of silicon- and carbon-containing compounds onto a pyrolytic graphite-coated carbon fiber core. The pyrolytic graphite

coating is applied to a carbon monofilament to give a substrate of 37 μm. This is then coated with SiC by CVD to give a final monofilament of 142 μm diameter. The surface modification of the SCS-6 fibers consists of the following. Figure 2.40 shows schematically the SCS-6 silicon carbide fiber and its characteristic surface compositional gradient. The bulk of the 1-μm-thick surface coating consists of C-doped Si. Zone I at and near the surface is a carbon-rich zone. In zone II, Si content decreases. This is followed by zone III in which the Si content increases back to the stoichiometric SiC composition. Thus, the SCS-6 silicon carbide fiber has a carbon-rich surface and back to stoichiometric SiC a few μm from the surface.

Another CVD-type silicon carbide fiber is called *sigma fiber*. Sigma fiber is a continuous silicon carbide monofilament by CVD on a tungsten substrate.

2.7.2.3 Nonoxide Fibers Via Polymers

As pointed out earlier, the SiC fiber obtained via CVD is very thick and not very flexible. Work on alternate routes of obtaining fine, continuous, and flexible fiber had been ongoing, when in the mid-1970s Yajima et al. (1976), Yajima (1980) in Japan developed a process of making such a fiber by controlled pyrolysis of a polymeric precursor. This method of using silicon-based polymers to produce a

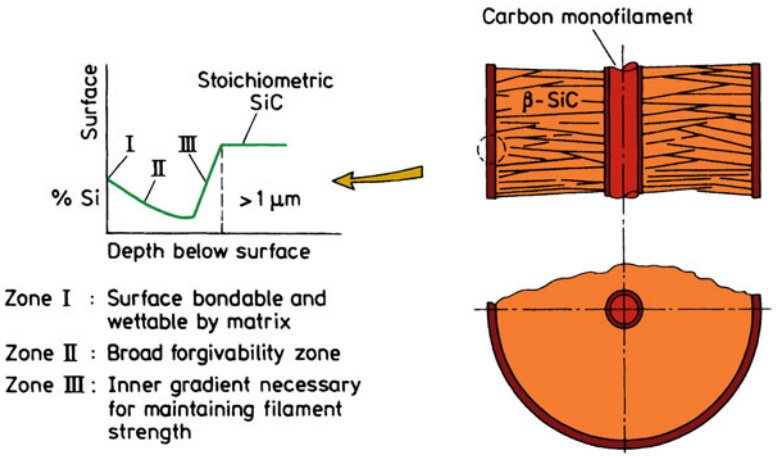

Fig. 2.40 Schematic of SCS-6 silicon carbide fiber and its surface compositional gradient. (Courtesy of Textron Specialty Materials Co.)

Table 2.11 Properties of CVD SiC monofilament

Composition	Diameter (μm)	Density ($g\ cm{-}3$)	Tensile strength (MPa)	Young's modulus (GPa)
β-SiC	140	3.3	3500	430

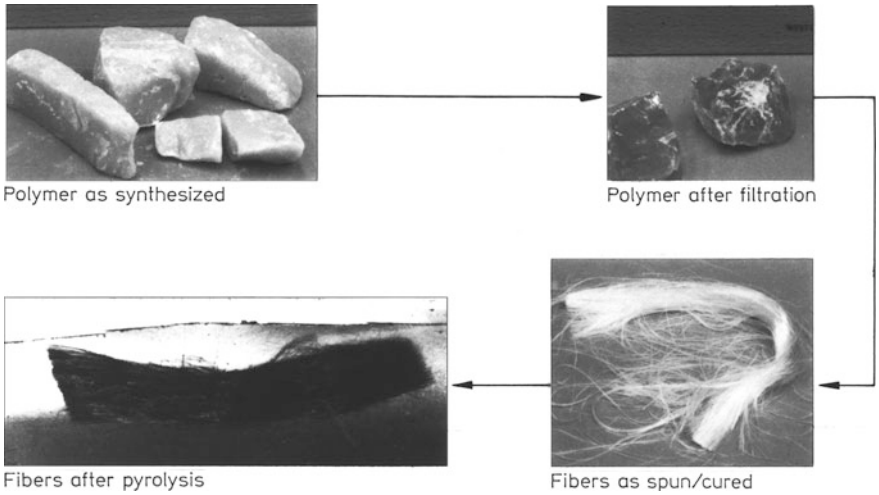

Fig. 2.41 Schematic of ceramic fiber production starting from silicon-based polymers. (Adapted from Wax 1985, used with permission)

family of ceramic fibers with good mechanical properties, good thermal stability, and oxidation resistance has become quite successful. The various steps involved in this polymer route, shown in Fig. 2.41 (Wax 1985), are as follows:

1. Synthesis and characterization of polymer (yield, molecular weight, purity, and so on).
2. Melt spin polymer into a precursor fiber.
3. Cure the precursor fiber to crosslink the molecular chains, making it infusible during the final stage of pyrolysis.

Specifically, the Yajima process of making fine-diameter SiC fiber involves the following steps and is shown schematically in Fig. 2.42. Polycarbosilane, a high molecular weight polymer containing Si and C, is synthesized. The starting material is commercially available dimethylchlorosilane. Solid polydimethylsilane is obtained by dechlorination of dimethylchlorosilane by reacting it with sodium. Polycarbosilane is obtained by polymerization and thermal decomposition of polydimethylsilane. This is carried out under high pressure in an autoclave at 470 $^{\circ}C$ in an argon atmosphere for 8–14 h. A vacuum distillation treatment at up to 280 $^{\circ}C$ follows. The average molecular weight of the resulting polymer is about 1500. This is melt spun from a 500-hole spinneret at about 350 $^{\circ}C$ in nitrogenous atmosphere to obtain the preceramic continuous, precursor fiber. The precursor fiber is quite weak (tensile strength ~ 10 MPa). This is converted to inorganic SiC by curing in air, heating to about 1000 $^{\circ}C$ in N_2 gas, followed by heating to 1300 $^{\circ}C$ in N_2 under stretch. This is basically the Nippon Carbon Co. manufacturing process for Nicalon (the commercial name of fine-diameter silicon carbide fiber) fibers

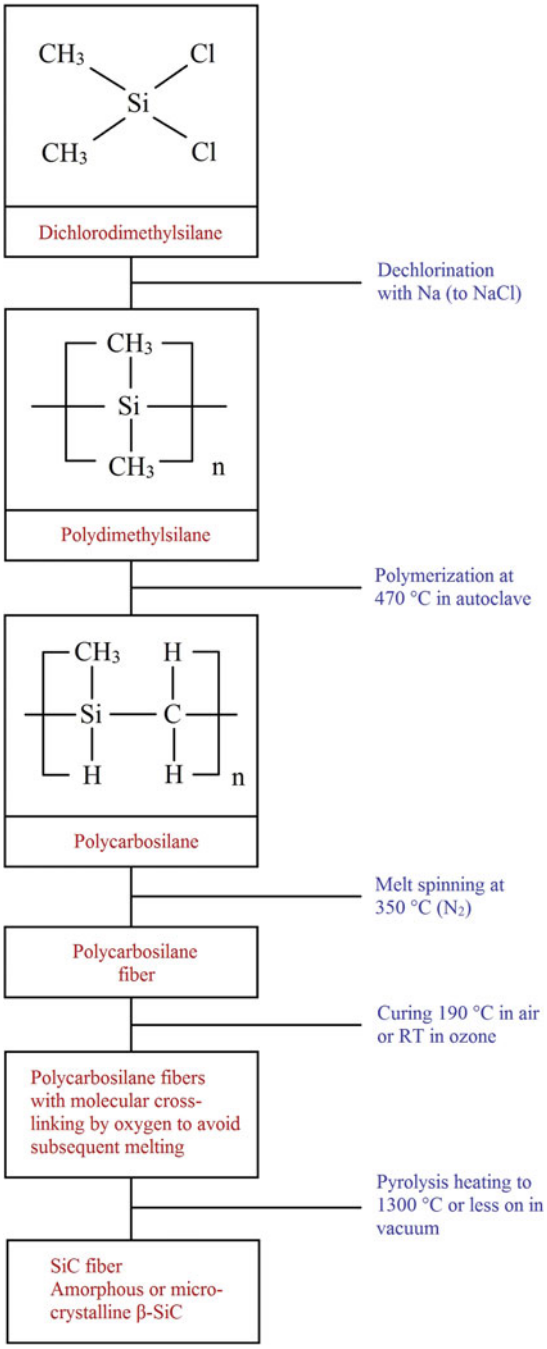

Fig. 2.42 Schematic of SiC (Nicalon) production. (Adapted from Andersson and Warren 1984, used with permission)

(Andersson and Warren 1984, Simon and Bunsell 1984). During the pyrolysis, the first stage of conversion occurs at approximately 550 °*C* when crosslinking of polymer chains occurs. Above this temperature, the side chains containing hydrogen and methyl groups decompose. Fiber density and mechanical properties improve sharply. The conversion to SiC takes place above about 850 °*C*.

There are different grades of Nicalon (nominally SiC) available commercially. The properties of the first generation of Nicalon fiber were less than desirable, they would start degrading above about 600 °*C* because of the thermodynamic instability of composition and microstructure. A ceramic-grade Nicalon fiber, called NLP-202, having low oxygen content is also available and shows better high-temperature properties. Yet another version of multifilament silicon carbide fiber is Tyranno. Tyranno fiber has been commercialized by Ube industries. Its processing involves the grafting of titanium alkoxide $Ti(OR)_4$ on the PCS chain, which is used to make polytitanocarbosilane (PTC), which is used to produce SiC fibers. This fiber contains between 1.5 and 4 *wt%* titanium.

Fine-diameter, polymer-derived silicon carbide fibers, such as Nicalon, generally have high oxygen content. This results from the curing of the precursor fibers in an oxidizing atmosphere to introduce crosslinking. Crosslinking is required to make the precursor fiber infusible during the subsequent pyrolysis step. One way around this is to use electron beam curing. Other techniques involve dry spinning of high-molecular-weight polycarbosilane polymers (Sacks et al. 1995). In this case, the as-spun fiber does not require a curing step because of the high-molecular-weight polycarbosilane polymer used, i.e., it does not melt during pyrolysis without requiring curing. Sacks et al. (1995) used dopants to produce low-oxygen, near-stoichiometric, small-diameter (10–15 μm) SiC fibers. They reported an average tensile strength for these fibers of about 2.8 *GPa*. Their fiber had a C-rich and near- stoichiometric SiC and low oxygen content (Sacks et al. 1995; Toreki et al. 1994). They started with polydimethylsilane (PDMS), which has a Si–Si backbone. This was subjected to pressure pyrolysis to obtain polycarbosilane (PCS), which has a Si–C backbone. The key point in their process is to have a molecular weight of PCS between 5000 and 20,000. This is a high molecular weight compared to that used in other processes. The spinning dope was obtained by adding suitable spinning aids and a solvent. This dope was dry spun to produce *green fibers*, which were heated under controlled conditions to produce SiC fiber.

Laine et al. (1993, 1995) and Zhang et al. (1994) have used a polyemethylsilane (PMS) ($[CH_3SiH]_x$) as the precursor polymer for making a fine-diameter, silicon carbide fiber. Spinning aids were used to stabilize the polymer solution and the precursor fiber was extruded from a 140 μm orifice extruder into an argon atmosphere. The precursor fiber was pyrolyzed at 1800 °*C* in Ar. Boron, added as a sintering aid, helped to obtain a dense product.

Another silicon carbide multifilament fiber made via a polymeric precursor and available commercially is called *Sylramic*. According to the manufacturer, this textile-grade silicon carbide fiber (about 10 μm in diameter) is a nanocrystalline,

stoichiometric silicon carbide (crystallite size of 0.5 μm). Its density is 3.0 $g\ cm^{-3}$, and it has average tensile strength and modulus of 3.15 *GPa* and 405 *GPa*, respectively. Boron was used as sintering aid in the earlier processing of this fiber which resulted in poor creep properties. Later a heat treatment was used that made boron to diffuse out to the surface of the fiber. This fiber, called *Sylramic-iBN*, showed better creep properties.

2.7.2.4 Structure and Properties

The structure of Nicalon fiber has been studied by a number of researchers. Figure 2.43 shows a high-resolution transmission electron micrograph of Nicalon-type SiC produced in laboratory, indicating the amorphous nature of the SiC produced by the Yajima process. The commercial variety of Nicalon has an amorphous structure while another, noncommercial variety, showed a microcrystalline structure (SiC grain radius of 1.7 *nm*) (Laffon et al. 1989). The microstructural analysis shows that both fibers contain SiO_2 and free carbon in addition to SiC. The density of the fiber is about 2.6 $g\ cm^{-3}$, which is low compared to that of pure β–SiC, which is not surprising because the composition of Nicalon fiber is a mixture of SiC, SiO_2, and C.

The properties of various fine-diameter, polymer-derived SiC-type fibers are summarized in Table 2.12. One would expect CVD SiC fiber to show superior creep properties vis à vis Nicalon fiber, mainly because CVD SiC fiber has mostly β-SiC while the Nicalon fiber is a mixture of SiC, SiO_2, and free carbon. This is shown in Fig. 2.44 where we make a log–log plot of creep strain as a function of

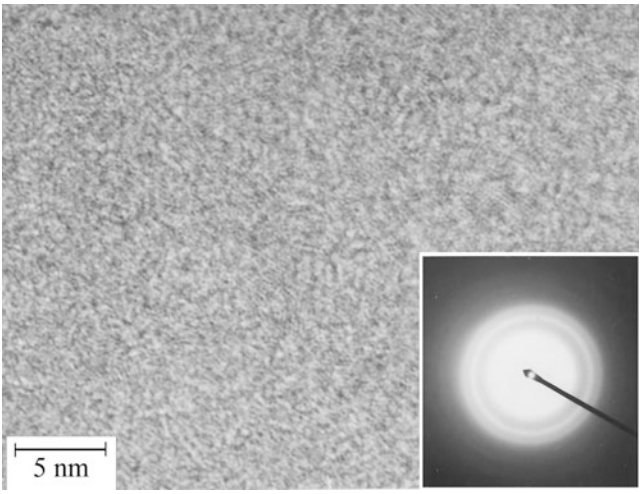

Fig. 2.43 High-resolution transmission electron micrograph of Nicalon fiber showing its amorphous structure. (Courtesy of K. Okamura)

Table 2.12 Properties of some fine-diameter SiC-type fibers[a]

Fiber	Tensile strength (*GPa*)	Young's of thermal modulus (*GPa*)	Coefficient expansion, $10^{-6}\ K^{-1}$
Nicalon 200	2	200	3.2
Hi-Nicalon	2.8	270	3.5
Hi-Nicalon S	2.5	400	–
Sylramic-iBN	3.5	400	5.4
Tyranno SA3	2.9	375	–

[a]After Bunsell and Piant (2006)

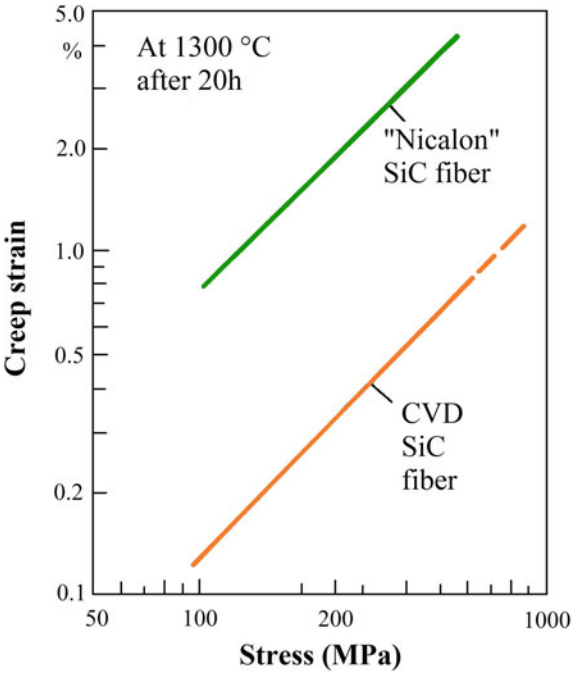

Fig. 2.44 Comparison of creep strain in CVD SiC and Nicalon fibers. (Reprinted with permission from *Journal of Metals*, **37**, No. 6, 1985, a publication of the Metallurgical Society, Warrendale, PA)

stress for Nicalon and CVD SiC fibers. Notice the superior performance of the CVD SiC fiber. Recall that the CVD SiC fiber has a large diameter, and thus is not flexible.

2.8 Whiskers

Whiskers are monocrystalline, short fibers with extremely high strength. This high strength, approaching the theoretical strength, comes about because of the absence of crystalline imperfections such as dislocations. Being monocrystalline, there are

no grain boundaries either. Typically, whiskers have a diameter of a few μm and a length of a few mm. Thus, their aspect ratio (length/diameter) can vary from 50 to 10,000. Whiskers do not have uniform dimensions or properties. This is perhaps their greatest disadvantage, i.e., the spread in properties is extremely large. Handling and alignment of whiskers in a matrix to produce a composite are other problems.

Whiskers are normally obtained by vapor phase growth. Back in the 1970s, a new process was developed that used rice hulls as the starting material to produce SiC particles and whiskers (Lee and Cutler 1975; Milewski et al. 1974). The SiC particles produced by this process are of a finer size. Rice hulls are a waste by-product of rice milling. For each 100 kg of rice milled, about 20 kg of rice hull is produced. Rice hulls contain cellulose, silica, and other organic and inorganic materials. Silica from soil is dissolved and transported in the plant as monosilicic acid. This is deposited in the cellulosic structure by liquid evaporation. It turns out that most of the silica ends up in hull. It is the intimate mixture of silica within the cellulose that gives the near-ideal amounts of silica and carbon for silicon carbide production. Raw rice hulls are heated in the absence of oxygen at about 700 $^{\circ}C$ to drive out the volatile compounds. This process is called *coking*. Coked rice hulls, containing about equal amounts of SiO_2 and free C, are heated in inert or reducing atmosphere (flowing N_2 or NH_3 gas) at a temperature between 1500 and 1600 $^{\circ}C$ for about 1 h to form silicon carbide as per the following reaction:

$$3C + SiO_2 \rightarrow SiC + 2CO.$$

Figure 2.45 shows the schematic of the process. When the reaction is over, the residue is heated to 800 $^{\circ}C$ to remove any free C. Generally, both particles and whiskers are produced, together with some excess free carbon. A wet process is used to separate the particles and the whiskers. Typically, the average aspect ratio of the as-produced whiskers is 75.

Exceptionally strong and stiff silicon carbide whiskers have been grown using the so-called VLS process (Milewski et al. 1985; Petrovic et al. 1985). The average tensile strength and modulus were 8.4 GPa and 581 GPa, respectively. The acronym *VLS* stands for *vapor* feed gases, *liquid* catalyst, and *solid* crystalline whiskers. In this process, the catalyst forms a liquid solution interface with the growing crystalline phase, while elements are fed from the vapor phase through the liquid/vapor interface. Whisker growth takes place by precipitation from the supersaturated liquid at the solid/liquid interface. The catalyst must take in solution the atomic species of the whisker to be grown. For SiC whiskers, transition metals and iron alloys meet this requirement. Figure 2.46 illustrates the process for SiC whisker growth. Steel particles (~ 30 μm) are used as the catalyst. At 1400 $^{\circ}C$, the solid steel catalyst particle melts and forms a liquid catalyst ball. From the vapor feed of SiC, H_2, and CH_4, the liquid catalyst extracts C and Si atoms and forms a supersaturated solution. The gaseous silicon monoxide is generated as per the following reaction:

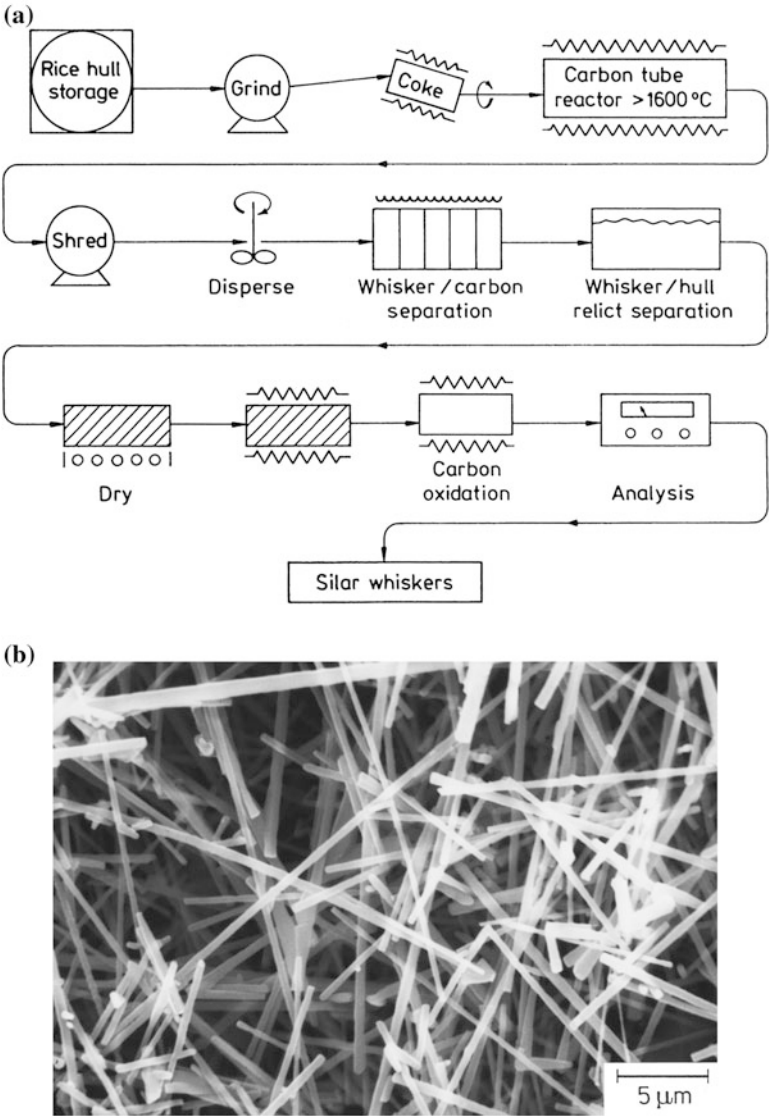

Fig. 2.45 **a** Schematic of SiC whisker production process starting from rice hulls. **b** Scanning electron micrograph of SiC whiskers obtained from rice hulls. [Courtesy of Advanced Composite Materials Corporation (formerly Arco)]

$$SiO_2(g) + C(s) \rightarrow SiO(g) + CO(g).$$

The supersaturated solution of C and Si in the liquid catalyst precipitates out solid SiC whisker on the substrate. As the precipitation continues, the whisker grows (Fig. 2.46). Generally, the process results in a range of whisker morphologies. The tensile strength values vary a lot, they ranged from 1.7 to 23.7 *GPa* in 40 tests. Whisker lengths were about 10 *mm* and the equivalent circular diameter averaged 5.9 μm.

2.8.1 Other Nonoxide Fibers

In addition to silicon carbide-based ceramic fibers, there are other promising ceramic fibers, e.g., silicon nitride, boron carbide, and boron nitride.

Silicon nitride (Si_3N_4) fibers can be prepared by reactive chemical vapor deposition (CVD) using volatile silicon compounds. The reactants are generally $SiCl_4$ and NH_3. Si_3N_4 is deposited on a carbon or tungsten substrate. Again, as in other CVD processes, the resultant fiber has good properties, but the diameter is very large and it is expensive. In the polymer route, organosilazane polymers with methyl groups on Si and N have been used as silicon nitride precursors. Such carbon-containing, silicon-nitrogen precursors, on pyrolysis, give silicon carbide as well as silicon nitride, i.e., the resulting fiber is not a SiC-free silicon nitride fiber. Wills et al. (1983) have discussed the mechanisms involved in the conversion of various organometallic compounds into ceramics.

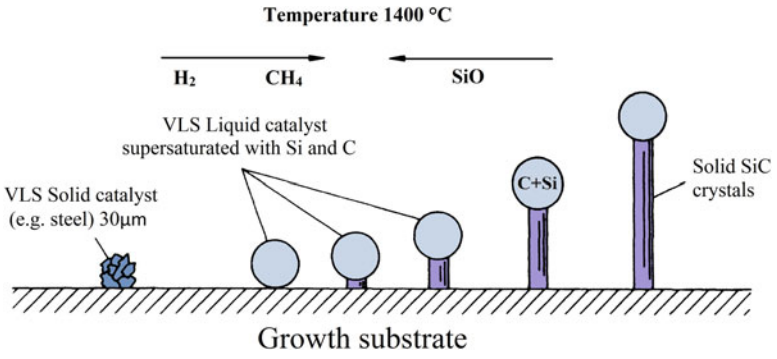

Fig. 2.46 The VLS process for SiC whisker growth. [After Milewski et al. (1985), used with permission.]

2.8.2 Silicon Carbide in a Particulate Form

SiC in particulate form has been available quite cheaply and abundantly for abrasive, refractories, and chemical uses. In this conventional process, silica in the form of sand and carbon in the form of coke are made to react at 2400 °*C* in an electric furnace. The SiC produced in the form of large granules is subsequently comminuted to the desired size.

2.8.2.1 Tungsten Carbide Particles

Tungsten carbide is made by carburization of tungsten metal, which, in turn, is prepared by hydrogen reduction of tungsten oxide. A mixture of tungsten powder and carbon black in the appropriate particle size and distribution is obtained by ball milling. The addition of carbon black helps control particle size and size distribution. The objective is to produce stoichiometric tungsten carbide (WC) with a small excess of free carbon, which prevents the formation of the highly undesirable *eta*-phase. Carburization is done in the presence of hydrogen at temperatures between 1400 and 2650 °*C*. The hydrogen reacts with the carbon black to form gaseous hydrocarbons, which react with tungsten to form tungsten carbide as per the following reaction:

$$W + CH_4 \rightarrow WC + 2H_2$$

Commonly, after carburization, WC particles are deagglomerated by milling. The final particle size can range from 0.5 to 30 μm. The particles are generally quite angular.

2.9 Effect of High Temperature Exposure on the Strength of Ceramic Fibers

Carbon fiber is excellent at high temperatures in an inert atmosphere. In air, at temperatures above 400–450 °*C*, it starts oxidizing. SiC and Si_xN_y show reasonable oxidation resistance for controlled composition fibers. SiC starts oxidizing above 1300–1400 °*C* in air. The high temperature strength of the SiC-type fibers is limited by oxidation and internal void formation, while in the case of oxide fibers any intergranular glassy phase leads to softening. Mah et al. (1984) studied the degradation of Nicalon fiber after heat treatment in different environments. The strength degradation of this fiber at temperatures greater than 1200 °*C* was because of CO evaporation from the fiber as well as β-SiC grain growth. Ceramic fibers made via pyrolysis of polymeric precursors, especially with compositions Si–C–O

and Si–N–C–O, have lower densities than the theoretical values (Lipowitz et al. 1990). The theoretical density, ρ_t, can be calculated using the relationship

$$\rho_t = \rho_i V_i,$$

where ρ is the density, V is the volume fraction, the subscript i indicates the ith phase, and summation over all the phases present is implied (see also Chap. 10). X-ray scattering techniques were used to show that porosity present in such fibers was in the form of globular pores of *nm* size and that the pore fractions ranged from 5 to 25% (Lipowitz et al. 1990). Channels of *nm* size diameter form during the early states of pyrolysis, when rather large volumes of gases are given out. In the later stages of pyrolysis, smaller volumes of gases are given out. In the later stages of pyrolysis, i.e., during densification, these nanochannels suffer a viscous collapse and nanopores are formed. The volume fraction of nanopores decreases with increasing pyrolysis temperature. The reader should note that a higher density and the consequent lower void fraction will result in higher elastic modulus and strength of these ceramic fibers.

2.10 Comparison of Fibers

A comparison of some important characteristics of reinforcements discussed individually in Sects. 2.2–2.7 is made in Table 2.13, and a plot of strength versus modulus is shown in Fig. 2.47. We compare and contrast some salient points of these fibers.

First of all, we note that all these high performance fibers have low density values. If we take the general low density of these fibers as a given, the best of these fibers group together in the top right hand corner of Fig. 2.46. The reader will also recognize that the elements comprising these fibers pertain to the first two rows of the periodic table. Also to be noted is the fact that, irrespective of whether in

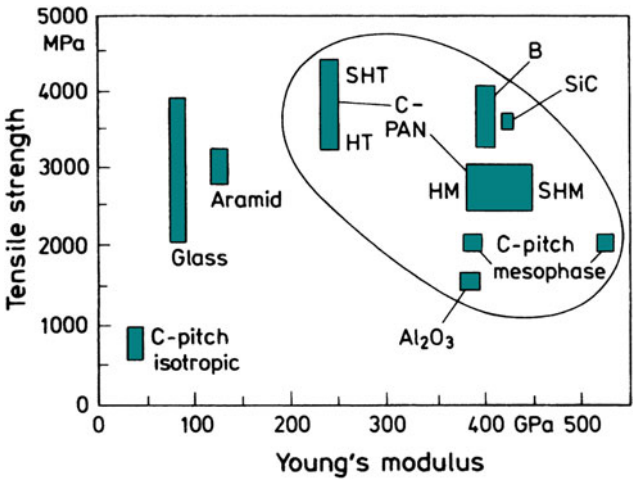

Fig. 2.47 Comparison of different fibers

Table 2.13 Properties of reinforcement fibers

Characteristic	PAN-based carbon		Kevlar		SiC			
	HM	HS	49	E glass	CVD	Nicalon	Al_2O_3	Boron (*W*)
Diameter (μm)	7–10	7.6–8.6	12	8–14	100–200	10–20	20	100–200
Density ($g\ cm^{-3}$)	1.95	1.75	1.45	2.55	3.3	2.6	3.95	2.6
Young's modulus (*GPa*)								
parallel to fiber axis	390	250	125	70	430	80	379	385
perpendicular to fiber axis	12	20	–	70	–	–	–	–
Tensile strength (*GPa*)	2.2	2.7	2.8–3.5	1.5–2.5	3.5	2	1.4	3.8
Strain-to-fracture (%)	0.5	1.0	2.2–2.8	1.8–3.2	–	–	–	–
Coefficient of thermal expansion ($10^{-6}\ K^{-1}$)								
parallel to fiber axis	−0.5–0.1	0.1–0.5	−2–5	4.7	5.7	–	7.5	8.3
perpendicular to fiber axis	7–12	7–12	59	4.7	–	–	–	–

compound or elemental form, they are mostly covalently bonded, which is the strongest bond. Generally, such light, strong, and stiff materials are very desirable in most applications, but particularly in aerospace, land transportation, energy-related industry, housing and civil construction, and so on.

Fiber flexibility is associated with the Young's modulus and the diameter (see Sect. 2.1). In the general area of high modulus (i.e., high E) fibers, the diameter becomes the dominant parameter controlling the flexibility. For a given *E*, the smaller the diameter the more flexible it is. Fiber flexibility is a very desirable characteristic if one wants to bend, wind, and weave a fiber in order to make a complex-shaped final product.

Some of these fibers have quite anisotropic characteristics. Consider the situation in regard to thermal properties; in particular, the thermal expansion coefficient of carbon is quite different in the radial and longitudinal directions. This would also be true of any single crystal fiber or whisker, e.g., alumina single crystal fiber, which has a hexagonal structure. Polycrystalline fibers such as SiC or Al_2O_3 are isotropic. Carbon, aramid, and polyethylene are anisotropic because of the high degree of alignment of their microstructural units along the axis. Ceramic matrix composites can go to very high temperatures, indeed. An important problem that comes up at these very high temperatures (>1500 °*C*) is that of fiber (and matrix) oxidation. Carbon fiber, for example, does not have good oxidation resistance at high temperatures. SiC- or Si_3N_4-type ceramic fibers are the only suitable candidates for reinforcement at very high temperatures (>1200–1300 °*C*) and in air. It would appear that oxide fibers would be the likely candidates, because of their inherent

stability in air, for applications at temperatures higher than 1300 °*C* in air. The problem with oxide fibers is their poor creep properties.

Another important characteristic of these high-performance fibers is their rather low values of strain-to-fracture, generally less than 2–3%. This means that in a CMC, the reinforcement and the matrix may not be much different in terms of strain-to-fracture. Also, in CMCs the modulus ratio of the reinforcement and the matrix may be 2–3 or as low as 1. This is a very different situation from that encountered in PMCs and MMCs.

Problems

2.1. Nonwoven fibrous mats can be formed through entanglement and/or by bonding fibers in the form of webs or yarns by chemical or mechanical means. What are the advantages and disadvantages of such nonwovens over similar woven mats?
2.2. Glass fibers are complex mixtures of silicates and borosilicates containing mixed sodium, potassium, calcium, magnesium, and other oxides. Such a glass fiber can be regarded as an inorganic polymeric fiber. Do you think you can provide the chemical structure of such an inorganic polymer chain?
2.3. A special kind of glass fiber is used as a medium for the transmission of light signals. Discuss the specific requirements for such an optical fiber.
2.4. The compressive strength of aramid fiber is about one-eighth of its tensile stress. Estimate the smallest diameter of a rod on which the aramid fiber can be wound without causing kinks, etc. on its compression side.
2.5. Several types of Kevlar aramid fibers are available commercially. Draw schematically the stress–strain curves of Kevlar 49 and Kevlar 29. Describe how much of the strain is elastic (linear or nonlinear). What microstructural processes occur during their deformation?
2.6. Aramid fiber, when fractured in tension, shows very characteristic longitudinal splitting, i.e., microfibrillation is observed. Explain why.
2.7. Describe the structural differences between Kevlar and Nomex (both aramids) that are responsible for their different mechanical characteristics.
2.8. What is asbestos fiber and why is it considered to be a health hazard?
2.9. Describe the problems involved in mechanical testing of short fibers such as whiskers.

References

C.-H. Andersson, R. Warren, Composites **15**, 16 (1984)
R. Bacon, *Chemistry and Physics of Carbon*, vol. 9 (Marcel Dekker, New York, 1973), p. 1
A.A. Baker, Metals Forum. **6**, 81 (1983)
P.J. Barham, A. Keller, J. Mater. Sci. **20**, 2281 (1985)

S.C. Bennett, D.J. Johnson, *Fifth International Carbon and Graphite Conference* (Society of the Chemical Industry, London, 1978), p. 377
S.C. Bennett, D.J. Johnson, Carbon **17**, 25 (1979)
S.C. Bennett, D.J. Johnson, W. Johnson, J. Mater. Sci. **18**, 3337 (1983)
D.A. Biro, G. Pleizier, Y. Deslandes, J. Mater. Sci. Lett. **11**, 698 (1992)
C.J. Brinker, G. Scherer, *The Sol-Gel Science* (Academic Press, New York, 1990)
Brown JR, Chappell PJC, Mathys Z, J. Mater. Sci. **27**, 3167 (1992)
A.R. Bunsell, A. Piant, J. Mater. Sci. **40**, 823 (2006)
G. Capaccio, A.G. Gibson, I.M. Ward, *Ultra-High Modulus Polymers* (Applied Science Publishers, London, 1979), p. 1
K.K. Chawla, *Proceedings of the International Conference on the Mechanical Behavior of Materials II* (ASM, Metals Park, Ohio, 1976), p. 1920
K.K. Chawla, Mater. Sci. Eng. **48**, 137 (1981)
K.K. Chawla, *Fibrous Materials*, 2nd ed. (Cambridge University Press, Cambridge, 2016)
K.K. Chawla, *Handbook of Mechanics of Materials*, ed. by C.-H. Hsueh et al. (Springer Nature, Singapore, 2018)
K.K. Chawla, A.C. Bastos, *Proceedings of the International Conference on the Mechanical Behavior of Materials III* (Pergamon Press, Oxford, 1979), p. 191
E. de Lamotte, A.J. Perry, Fibre Sci. Tech. **3**, 157 (1970)
H.E. DeBolt, *Handbook of Composites* (Van Nostrand Reinhold, New York, 1982), p. 171
S.J. DeTeresa, S.R. Allen, R.J. Farris, R.S. Porter, J. Mater. Sd. **19**, 57 (1984)
J.A. DiCarlo, J. Met. **37**, 44 (1985)
R.J. Diefendorf, E. Tokarsky, Polym. Eng. Sci. **15**, 150 (1975)
M.G. Dobb, D.J. Johnson, B.P. Saville, Philos. Trans. R. Soc. Lond. **A294**, 483 (1980)
W.H. Dresher, J. Metals **21**, 17 (1969)
H.N. Ezekiel, R.G. Spain, J. Polym. Sci. C **19**, 271 (1967)
P.J. Flory, Proc. R. Soc. (London) **234A**, 73 (1956)
A. Fourdeux, R. Perret, W. Ruland, *Carbon Fibres: Their Composites and Applications* (The Plastics Institute, London, 1971), p. 57
F. Galasso, A. Paton, Trans. Met. Soc. AIME **236**, 1751 (1966)
F. Galasso, D. Knebl, W. Tice, J. Appl. Phys. **38**, 414 (1967)
D.G. Gasson, B. Cockayne, J. Mater. Sci. **5**, 100 (1970)
J.S. Haggerty (1972). *NASA-CR-120948*, NASA Lewis Res. Center, Cleveland, OH
D.N. Hild, P. Schwartz, J. Adhes. Sci. Technol. **6**, 879 (1992a)
D.N. Hild, P. Schwartz, J. Adhes. Sci. Technol. **6**, 897 (1992b)
K.A. Hodd, D.C. Turley, Chem. Br. **14**, 545 (1978)
G.F. Hurley, J.T.A. Pollack, Met Trans **7**, 397 (1972)
O.T. Inal, N. Leca, L. Keller, Phys. Status Solidi. **62**, 681 (1980)
M. Jaffe, R.S. Jones, *Handbook of Fiber Science & Technology*, vol. 111, *High Technology Fibers* (Part A, Marcel Dekker, New York, 1985), p. 349
J. Johnson, C.N. Tyson, Br. J. Appl. Phys. **2**, 787 (1969)
R.W. Jones, *Fundamental Principles of Sol-Gel Technology* (The Institute of Metals, London, 1989)
B. Kalb, A.J. Pennings, J. Mater. Sci. **15**, 2584 (1980)
S.L. Kaplan, P.W. Rose, H.X. Nguyen, H.W. Chang, SAMPE Q. **19**, 55 (1988)
V. Krukonis, *Boron and Refractory Borides* (Springer, Berlin, 1977), p. 517
S.L. Kwolek, H.H. Yang, *Manmade Fibers: Their Origin and Development* (Elsevier Applied Science London, 1993), p. 315
I.P. Kumar, P.M. Mohite, S. Kamle, Arch. Mech. Warszawa **65**, 27 (2013)
H.E. LaBelle, Mater. Res. Bull. **6**, 581 (1971)
H.E. LaBelle, A.I. Mlavsky, Nature **216**, 574–575 (1967)
C. Laffon, A.M. Flank, P. Lagarde, M. Laridjani, R. Hagege, P. Olry, J. Cotteret, J. Dixmier, J.L. Niquel, H. Hommel, A.P. Legrand, J. Mater. Sci. **24**, 1503 (1989)
R.M. Laine, F. Babonneau, Chem Mater **5**, 260 (1993)

R.M. Laine, Z-F. Zhang, K.W. Chew, M. Kannisto, C. Scotto, *Ceramic Processing Science and Technology*. J. Am. Ceram. Soc., (Westerville, OH, 1995), p. 179
J.-G. Lee, I.B. Cutler, Am. Ceram. Soc. Bull. **54**, 195 (1975)
Z.F. Li, A.N. Netravali, W. Sachse, J. Mater. Sci. **27**, 4625 (1992)
J. Lipowitz, J.A. Rabe, L.K. Frevel, J. Mater. Sci. **25**, 2118 (1990)
K.L. Loewenstein, *The Manufacturing Technology of Continuous Glass Fibers*, 2nd edn. (Elsevier, New York, 1983)
R.E. Lowrie, *Modern Composite Materials* (Reading, MA, Addison-Wesley, 1967), p. 270
E.E. Magat, Philos. Trans. R. Soc. London **A296**, 463 (1980)
T. Mah, N.L. Hecht, D.E. McCullum, J.R. Hoenigman, H.M. Kim, A.P. Katz, H.A. Lipsitt, J. Mater. Sci. **19**, 1191 (1984)
J.V. Milcwski, J.L. Sandstrom, W.S. Brown, *Silicon Carbide 1973* (University of South Carolina Press, Columbia, 1974), p. 634
J.V. Milewski, F.D. Gac, J.J. Petrovic, S.R. Skaggs, J. Mater. Sci. **20**, 1160 (1985)
P.W. Morgan, Plast. Rubber: Mater. Appl. **4**, 1 (1979)
J.S. Murday, D.D. Dominguez, L.A. Moran, W.D. Lee, R. Eaton, Synth. Met. **9**, 397 (1984)
M.G. Northolt, J. Mater. Sci. **16**, 2025 (1981)
S. Ozawa, Y. Nakagawa, K. Matsuda, T. Nishihara, H. Yunoki (1978) US patent 4,075,172
B. Parkyn (ed.), *Glass Reinforced Plastics* (Butterworth, London, 1970)
R. Perret, W. Ruland, J. AppI. Crystallogr. **3**, 525 (1970)
J.J. Petrovic. J.V. Milewski. D.L. Rohr, F.D. Gac (1985). J. Mater. Sd. **20**, 1167
J.T.A. Pollack, J. Mater. Sci. **7**, 787 (1972)
J.P. Riggs, *Encyclopedia of Polymer Science & Engineering*, 2nd ed., vol. 2. (Wiley, New York, 1985), p. 640
M.D. Sacks, G.W. Scheiffele, M. Saleem, G.A. Staab, A.A. Morrone, T.J. Williams, *Ceramic Matrix Composites: Advanced High-Temperature Structural Materials* (Pittsburgh, PA, MRS, 1995), p. 3
S. Sakka, Am. Ceram. Soc. Bull. **64**, 1463 (1985)
G. Simon, A.R. Bunsell, J. Mater. Sci. **19**, 3649 (1984)
L.S. Singer, *Ultra-High Modulus Polymers* (Applied Science Publishers, Essex, England, 1979), p. 251
Shindo A, Rep. Osaka Ind. Res. Inst. No. 317 (1961)
P. Smith, P.J. Lemstra, Colloid Polymer Sci. **15**, 258 (1976)
P. Smith, P.J. Lemstra, J. Mater. Sci. **15**, 505 (1980)
J. Smook, A.J. Pennings, J. Mater. Sci. **19**, 31 (1984)
H.G. Sowman, *Sol-Gel Technology*, ed. by L.J. Klein (Noyes Pub., Park Ridge, NJ, 1988), p. 162
C.P. Talley, J. Appl. Phys. **30**, 1114 (1959)
C.P. Talley, L. Line, O. Overman, *Boron: Synthesis, Structure, and Properties* (Plenum Press, New York, 1960), p. 94
D. Tanner, A.K. Dhingra, J.J. Pigliacampi, J. Met. **38**, 21 (1986)
W. Toreki, C.D. Batich, M.D. Sacks, M. Saleem, G.J. Choi, A.A. Morrone, Compos. Sci. Technol. **51**, 145 (1994)
A.C. van Maaren, O. Schob, W. Westerveld, Philips Tech. Rev. **35**, 125 (1975)
J. Vega-Boggio, O. Vingsbo, *1978 International Conference on Composite Materials, ICCM/2* (TMS-AIME, New York, 1978), p. 909
S.B. Warner, *Fiber Science* (Prentice Hall, Englewood Cliffs, NJ, 1995)
R. Warren, C.-H. Andersson, Composites **15**, 101 (1984)
W. Watt, Proc. R. Soc. **A319**, 5 (1970)
W. Watt, W. Johnson, Appl. Polym. Symp. **9**, 215 (1969)
F.W. Wawner, *Modern Composite Materials* (Reading, MA, Addison-Wesley, 1967), p. 244
S.G. Wax, Am. Ceram. Soc. Bull. **64**, 1096 (1985)
E. Weintraub, J. Ind. Eng. Chem. **3**, 299 (1911)
R.R. Wills, R.A. Mankle, S.P. Mukherjee, Am. Ceram. Soc. Bull. **62**, 904 (1983)

D.M. Wilson, *Proceedings of the 14th Conference on Metal Matrix, Carbon, and Ceramic Matrix Composites, Cocoa Beach, FL, Jan. 17–19, 1990*, NASA Conference Publication 3097, Part 1 (1990), p. 105
S. Yajima, Philos. Trans. R. Soc. Lond. **A294**, 419 (1980)
S. Yajima, K. Okamura, J. Hayashi, M. Omori, J. Am. Ceram. Soc. **59**, 324 (1976)
Z.-F. Zhang, S. Scotto, R.M. Laine, Ceram. Eng. Sci. Proc. **15**, 152 (1994)

Suggested Reading

A.R. Bunsell (ed.), *Fibre Reinforcements for Composite Materials* (Elsevier, Amsterdam, 1988)
A.R. Bunsell, M. Berger (eds.), *Fine Ceramic Fibers* (Marcel Dekker, New York, 1999)
K.K. Chawla, *Fibrous Materials*, 2nd ed. (Cambridge University Press, Cambridge, 2016)
J.-B. Donnet, T.K. Wang, J.C.M. Peng, S. Rebouillat (eds.), *Carbon Fibers*, 3rd edn. (Marcel Dekker, New York, 1998)
E. Fitzer, *Carbon Fibres and Their Composites* (Springer, Berlin, 1985)
L.H. Peebles, *Carbon Fibers* (CRC Press, Boca Raton, FL, 1995)
W. Watt, B.V. Perov (Eds.), *Strong Fibres*, Handbook of Composites Series, vol. 1 (North-Holland, Amsterdam, 1985)
H.H. Yang, *Kevlar Aramid Fiber* (Wiley, Chichester, UK, 1993)

Chapter 3
Matrix Materials

A brief description of the various matrix materials, polymers, metals, and ceramics is given in this chapter. We emphasize the characteristics that are relevant for the mechanical properties of composites. The reader should consult the references listed under Suggested Reading for greater details regarding any particular aspect of these materials.

3.1 Polymers

Polymers are structurally much more complex than metals or ceramics. They are cheap and can be easily processed. On the other hand, polymers have lower strength and modulus and lower temperature use limits. Prolonged exposure to ultraviolet light and some solvents can cause degradation of polymer properties. Because of predominantly covalent bonding, polymers are generally poor conductors of heat and electricity. Polymers, however, are generally more resistant to chemicals than are metals. Structurally, polymers are giant chain-like molecules (hence the name *macromolecules*) with covalently bonded carbon atoms forming the backbone of the chain. The process of forming large molecules from small ones is called *polymerization*, that is, polymerization is the process of joining many monomers, the basic building blocks, together to form polymers. There are two important classes of polymerization:

1. *Condensation polymerization*: In this process, a stepwise reaction of molecules occurs and in each step a molecule of a simple compound, generally water, is formed as a by-product.
2. *Addition polymerization*: In this process, monomers join to form a polymer without producing any by-product. Addition polymerization is generally carried out in the presence of catalysts. The linear addition of ethylene molecules (CH_2)

K. K. Chawla, *Composite Materials*,
https://doi.org/10.1007/978-3-030-28983-6_3

results in polyethylene (a chain of ethylene molecules), with the final mass of polymer being the sum of monomer masses.

Based on their behavior, there are two major classes of polymers, produced by either condensation or addition polymerization, i.e., thermosetting and thermoplastic polymers. Thermosets undergo a curing reaction that involves crosslinking of polymeric chains. They harden on curing, and hence the term *thermoset*. The curing reaction can be initiated by appropriate chemical agents or by application of heat and pressure, or by exposing the monomer to an electron beam. Thermoplastics are polymers that flow under the application of heat and pressure, i.e., they soften or become plastic on heating. Cooling to room temperature hardens thermoplastics. Their different behavior, however, stems from their molecular structure and shape, molecular size or mass, and the amount and type of bond (covalent or van der Waals). We first describe the basic molecular structure in terms of the configurations of chain molecules. Figure 3.1 shows the different chain configuration types.

1. *Linear polymers*. As the name suggests, this type of polymer consists of a long chain of atoms with attached side groups. Examples include polyethylene, polyvinyl chloride, and polymethyl methacrylate. Figure 3.1a shows the configuration of linear polymers; note the coiling and bending of chains.
2. *Branched polymers*. Polymer branching can occur with linear, crosslinked, or any other type of polymer; see Fig. 3.1b.
3. *Crosslinked polymers*. In this case, molecules of one chain are bonded with those of another; see Fig. 3.1c. Crosslinking of molecular chains results in a three-dimensional network. Crosslinking makes sliding of molecules past one another difficult, thus such polymers are strong and rigid.
4. *Ladder polymers*. If we have two linear polymers linked in a regular manner, i.e., at regular distances (see Fig. 3.1d) we get a ladder polymer. A well-known example is DNA molecule, which consists of double-stranded chains linked by hydrogen bonds at regular intervals. DNA molecule forms a twisted ladder.

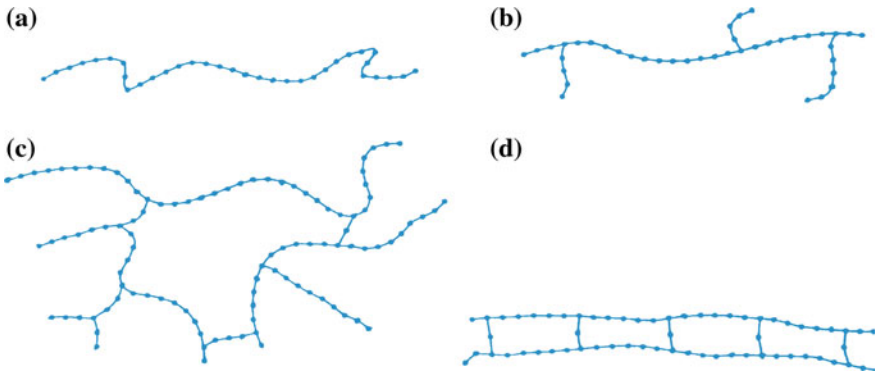

Fig. 3.1 Different molecular chain configurations: **a** linear, **b** branched, **c** crosslinked, **d** ladder

Aromatic polyamides or aramids are other examples. Not unexpectedly, ladder polymers are more rigid and thermally more stable than linear polymers.

3.1.1 Glass Transition Temperature

Pure crystalline materials (generally, metals and ceramics) have well-defined melting temperatures. The melting point is the temperature at which crystalline order is completely destroyed on heating. Polymers, however, show a different behavior. Figure 3.2 shows specific volume (volume/unit mass) versus temperature curves for amorphous and semicrystalline polymers. When a polymer liquid is cooled, it contracts. The contraction occurs because of a decrease in the thermal vibration of molecules and a reduction in the free space, that is, the molecules occupy the space less loosely. At a fixed temperature, called the melting point, T_m, there occurs a thermodynamic phase transformation and the material assumes an orderly crystalline structure. In the case of a semicrystalline polymer that consists of a crystalline and an amorphous phase, the crystalline part undergoes this transformation. In the case of amorphous polymers, there is no fixed melting point, T_m. The polymer liquid continues to contract, below what would be the melting point for the crystalline phase. It does so down to a less well defined temperature called the glass transition temperature, T_g. Below T_g, it becomes a supercooled liquid polymer that is quite rigid and solidlike because of very high viscosity. Unlike the crystalline phase, the structure of a glassy or amorphous material below T_g is essentially that of a liquid (highly disordered), albeit a very viscous one. Such a phenomenon is also observed in silica-based inorganic glasses. In the case of amorphous polymers, we are dealing with a glassy structure made of organic molecules. The glass transition temperature T_g, although it does not represent a thermodynamic phase transformation, is in many ways akin to the melting point for the crystalline solids. Many physical properties (e.g., viscosity, heat capacity, elastic modulus, and thermal expansion coefficient) change quite rapidly at T_g. Polystyrene, for example, has a T_g of about 100 $°C$ and is therefore rigid at room temperature. Rubber, on the other hand, has a T_g of about -75 $°C$ and therefore is flexible at room temperature. T_g is a function of the chemical structure of the polymer. For example, if a polymer has a rigid backbone structure and/or bulky branch groups, then its T_g will be quite high.

Although both amorphous polymers and inorganic silica-based glasses have a glass transition temperature T_g, generally, the T_g of inorganic glasses is several hundred degrees Celsius higher than that of polymers. The reason for this is the different types of bonding and the amount of crosslinking in the polymers and glasses. Inorganic glasses have mixed covalent and ionic bonding and are highly crosslinked. This gives them a higher thermal stability than polymers, which have covalent and van der Waals bonding and a lesser amount of crosslinking than found in inorganic glasses.

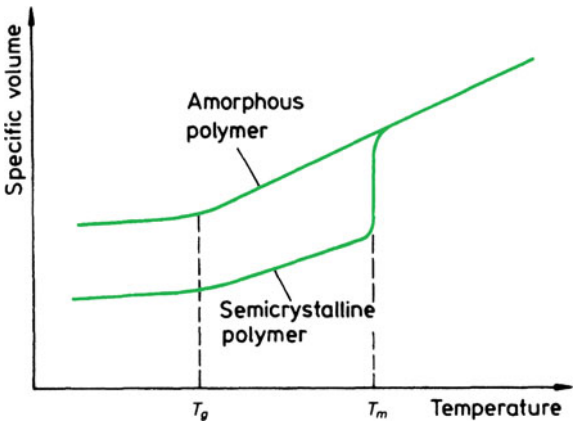

Fig. 3.2 Specific volume versus temperature for an amorphous and a semicrystalline polymer

3.1.2 Thermoplastics and Thermosets

Polymers that soften or melt on heating are called thermoplastic polymers and are suitable for liquid flow forming. Examples include low- and high-density polyethylene, polystyrene, and polymethyl methacrylate (PMMA). When the structure is amorphous, there is no apparent order among the molecules and the chains are arranged randomly; see Fig. 3.3a. Small, plate-like single crystalline regions called *lamellae* or *crystallites* can be obtained by precipitation of the polymer from a dilute solution. In the lamellae, long molecular chains are folded in a regular manner; see Fig. 3.3b. Many crystallites group together and form spherulites, much like grains in metals.

When the molecules in a polymer are crosslinked in the form of a network, they do not soften on heating. We call such crosslinked polymers *thermosetting polymers*. Thermosetting polymers decompose on heating. Crosslinking makes sliding

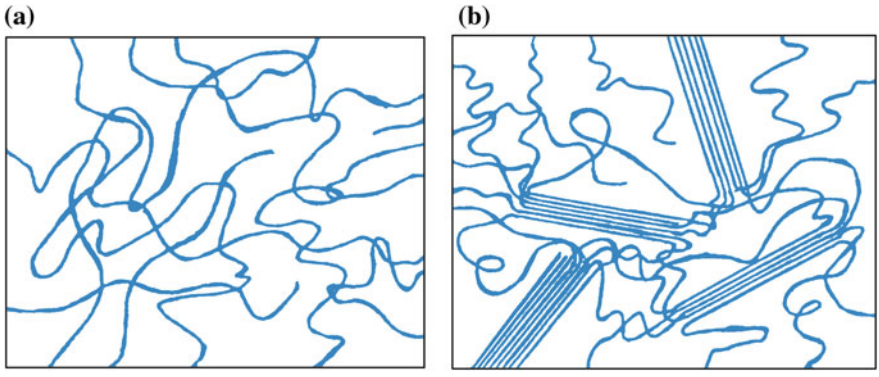

Fig. 3.3 Possible arrangements of polymer molecules: **a** amorphous, **b** semicrystalline

of molecules past one another difficult, making the polymer strong and rigid. A typical example is that of rubber crosslinked with sulfur, that is, vulcanized rubber. Vulcanized rubber has ten times the strength of natural rubber. Common examples of thermosetting polymers include epoxy, phenolic, unsaturated polyester, and vinyl ester.

3.1.3 Copolymers

There is another type of classification of polymers based on the type of repeating unit. When we have one type of repeating unit forming the polymer chain, we call it a *homopolymer. Copolymers*, on the other hand, are polymer chains with two different monomers. If the two different monomers are distributed randomly along the chain, we have a *regular*, or *random, copolymer*. If, however, a long sequence of one monomer is followed by a long sequence of another monomer, we have a *block copolymer*. If we have a chain of one type of monomer and branches of another type, we have a *graft copolymer*. Figure 3.4 shows schematically the different types of copolymers.

3.1.4 Molecular Weight

Molecular weight (MW) is a very important parameter for characterization of polymers. Generally, strength increases but strain-to-failure decreases with increasing molecular weight. Of course, concomitant with increasing molecular weight, the processing of polymers becomes more difficult. The degree of polymerization (DP) indicates the number of basic units (mers) in a polymer. These two parameters are related as follows:

$$\mathrm{MW} = \mathrm{DP} \times (\mathrm{MW})_u,$$

where $(MW)_u$ is the molecular weight of the repeating unit. In general, polymers do not have exactly identical molecular chains but may consist of a mixture of different

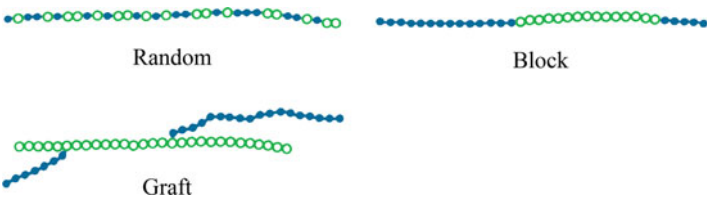

Fig. 3.4 Different types of copolymers

species, each of which has a different molecular weight or DP. Thus, the molecular weight of the polymer is characterized by a distribution function. Clearly, the narrower this distribution function, the more homogeneous the polymer. That is why one speaks of an average molecular weight or degree of polymerization.

It is instructive to compare the molecular weights of some common polymeric materials vis à vis monomeric materials. A molecule of water, H_2O, has a molecular weight of 18. Benzene, C_6H_6, a low-molecular-weight organic solvent, has a molecular weight of 78. Compared to these, natural rubber can have a molecular weight of about 10^6. Polyethylene, a common synthetic polymer, can have molecular weights greater than 10^5. The molecular size of these high-molecular-weight solids is also very large. The molecular diameter of water, for example, is 40 *nm*, while that of polyethylene can be as large as 6400 *nm* (Mandelkern 1983).

3.1.5 Degree of Crystallinity

Polymers can be amorphous or partially crystalline; see Fig. 3.3. A 100% crystalline polymer is difficult to obtain. In practice, depending on the polymer type, molecular weight, and crystallization temperature, the amount of crystallinity in a polymer can vary from 30 to 90%. The inability to attain a fully crystalline structure is mainly due to the long-chain structure of polymers. Some twisted and entangled segments of chains that get trapped between crystalline regions never undergo the conformational reorganization necessary to achieve a fully crystalline state. Molecular architecture also has an important bearing on the polymer crystallization behavior. Linear molecules with small or no side groups crystallize easily. Branched chain molecules with bulky side groups do not crystallize as easily. For example, linear high-density polyethylene can be crystallized to 90%, while branched polyethylene can be crystallized to only about 65%. Generally, the stiffness and strength of a polymer increase with the degree of crystallinity. It should be mentioned that deformation processes such as slip and twinning, as well as phase transformations that take place in monomeric crystalline solids, can also occur in polymeric crystals.

3.1.6 Stress–Strain Behavior

Characteristic stress–strain curves of an amorphous polymer and of an elastomer (a rubbery polymer) are shown in Fig. 3.5a and b, respectively. Note that the elastomer does not show a Hookean (linear elastic) behavior; its behavior is characterized as nonlinear elastic. The characteristically large elastic range shown by elastomers results from an easy reorganization of the tangled chains under the action of an applied stress.

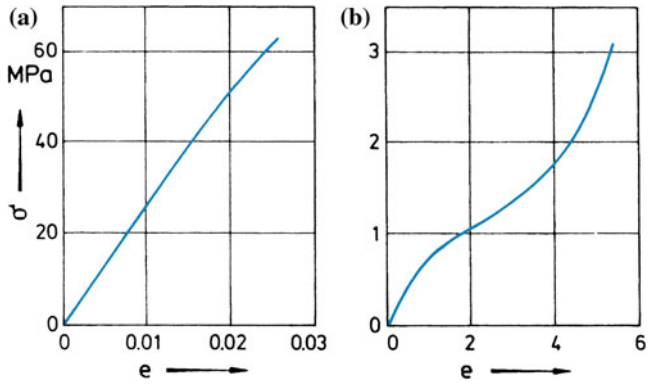

Fig. 3.5 **a** Hookean elastic behavior of a glassy polymer. **b** Nonlinear elastic behavior of an elastomer

Yet another point in which polymers differ from metals and ceramics is the extreme temperature dependence of their elastic moduli. Figure 3.6 shows schematically the variation of the elastic modulus of an amorphous polymer with temperature. In the temperature range below T_g, the polymer is hard and a typical value of elastic modulus would be about 5 *GPa*. Above T_g, the modulus value drops significantly and the polymer shows a rubbery behavior. Above T_f (the temperature at which the polymer becomes fluid), the modulus drops abruptly. It is in this region of temperatures above T_f that polymers are subjected to various processing operations.

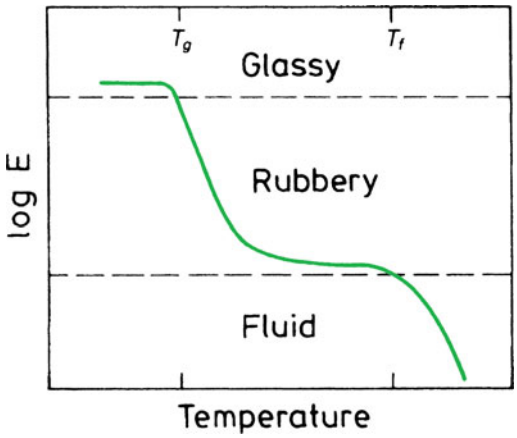

Fig. 3.6 Variation of elastic modulus of an amorphous polymer with temperature (schematic)

3.1.7 Thermal Expansion

Polymers generally have higher thermal expansivities than metals and ceramics. Furthermore, their thermal expansion coefficients are not truly constants, that is, the polymers expand markedly in a nonlinear way with temperature. Epoxy resins have coefficient of linear expansion values between 50×10^{-6} and 100×10^{-6} K^{-1} while unsaturated polyesters show values between 100×10^{-6} and 200×10^{-6} K^{-1}. Small compositional changes can have a marked influence on the polymer expansion characteristics.

3.1.8 Fire Resistance or Flammability

Fire performance of a polymer depends on a number of variables, such as surface spreading of flame, fuel penetration, and limiting oxygen index. The limiting oxygen index (LOI) is defined as the minimum amount of oxygen that will support combustion.

The degree of flammability of a polymer or a polymer matrix composite (PMC) is a function of the following parameters:

- Matrix type and amount (dominant!).
- Quantity of fire-retardant additives.
- Type and amount of reinforcement (if any).

The order of increasing fire resistance of common polymer matrix materials is: unsaturated polyester, vinyl ester, epoxy, and phenolic. Phenolic has very low smoke emission and gives out no toxic by-products. An added advantage of phenolic is that when it burns, it leaves behind char, which is a good thermal insulator. In the case of thermosets, such as unsaturated polyester, it is a common practice to add fire-retardant additives. Addition of large amount of glass fiber also helps.

3.1.9 Common Polymeric Matrix Materials

Thermosets and thermoplastic polymers are common matrix materials. A brief description of important polymer matrix materials is provided here.

3.1.9.1 Common Thermoset Matrix Materials

Among the common polymer matrix materials used with continuous fibers are epoxy and unsaturated polyester resins. We provide a summary of thermosetting resins commonly used as matrix materials.

Epoxy

This is one of the major thermoset matrix materials. An epoxy is a polymer that contains an epoxide group (one oxygen atom and two carbon atoms) in its chemical structure; see Fig. 3.7. Diglycidyl ether of bisphenol-A (DGEBA) is an example. DGEBA, containing two epoxide groups, is a low-molecular-weight organic liquid. Frequently, one uses various additives to modify the characteristics of epoxies. For example, diluents are used to reduce the viscosity. Flexibilizing agents are used to make the epoxy flexible. Other agents are used for protection against ultraviolet radiation. Curing agents are organic amino or acid compounds, and crosslinking is obtained by introducing chemicals that react with the epoxy and hydroxy groups between adjacent chains. A common curing agent for DGEBA epoxy is diethylenetriamine (DETA). The extent of crosslinking is a function of the amount of curing agent added. Generally, 10–15% by weight of amines or acid anhydrides is added, and they become part of the epoxy structure. An accelerator, if added, can speed up the curing process. In general, characteristics such as stiffness, strength, and glass transition temperature increase with increased crosslinking, but toughness decreases.

Epoxy resins are more expensive than unsaturated polyesters, but they have better moisture resistance, lower shrinkage on curing (about 3%), a higher maximum use temperature, and good adhesion with glass fibers. Many proprietary formulations of epoxies are available, and a very large fraction of high-performance polymer matrix composites has thermosetting epoxies as matrices.

The curing reaction of an epoxy can be slowed by lowering the reaction temperature. An epoxy before it is fully crosslinked is said to be in stage B. In stage B, an epoxy has a characteristic *tackiness*. This B-stage resin is used to make a fiber prepreg, which is shipped to the manufacturer where it can be fully cured into a hard solid. The type and extent of curing agent addition will control the total curing time (also called the *shelf life* or *pot life*). In order to increase the shelf life, such B-stage cured epoxy matrix prepregs are transported in refrigerated trucks and stored in refrigerated storage. Table 3.1 gives some important characteristics of epoxy at room temperature. Epoxy matrix composites were originally formulated to withstand prolonged service at 180 °*C* (∼350 °*F*). In the 1970s, it came to be recognized that they are prone to hygrothermal effects and their service temperature limitation is 120 °*C* (250 °*F*). A detailed account of structure–property relationships of epoxies used as composite matrices is provided by Morgan (1985).

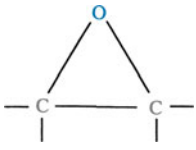

Fig. 3.7 Chemical structure of the epoxide group

Table 3.1 Some important characteristics of epoxy

Density, ρ ($g\ cm^{-3}$)	Strength, σ (MPa)	Modulus, E (GPa)	Poisson's ratio, v	CTE α ($10^{-6}\ K^{-1}$)	Cure shrinkage (%)	Service temp. (°C)
1.2–1.3	50–125	2.5–4	0.2–0.33	50–100	1–5	120

Unsaturated Polyester

An unsaturated polyester resin contains a number of C=C double bonds. A condensation reaction between a glycol (ethylene, propylene, or diethylene glycol) and an unsaturated dibasic acid (maleic or fumaric) results in a linear polyester that contains double bonds between certain carbon atoms. The term *unsaturated* means that there are reactive sites in the molecule. Diluents such as styrene are used to reduce the viscosity of polyester. Styrene contains C=C double bonds and crosslinks the adjacent polyester molecules at the unsaturation points. Hardening and curing agents and ultraviolet absorbents are usually added. Frequently, a catalyst such as organic peroxide is added to initiate the curing action. One can hasten the curing process by raising the temperature and this increases the decomposition rate of the catalyst. This can also be accomplished by using an accelerator such as cobalt naphthalate. Unsaturated polyester has adequate resistance to water and a variety of chemicals, weathering, aging, and, last but not least, it is very cheap. It can withstand temperatures up to about 80 °C and combines easily with glass fibers. Polyester resins shrink between 4 and 8% on curing. Table 3.2 gives some important room temperature properties of polyester.

There is an unfortunate confusion about the term polyester. The same term is used for two very different polymers. Unsaturated polyester is a thermoset resin commonly used as a matrix material in polymer composites. Commonly referred to just as polyester, it is very different from the thermoplastic polyester (see below). As pointed out above, unsaturated polyester resin is amorphous in structure and is obtained by condensation of an unsaturated dibasic acid and a glycol (commonly polypropylene glycol). For use in composites, one starts with a very viscous liquid unsaturated polyester resin. Styrene is used to control the viscosity of the resin. The resin undergoes a curing reaction involving crosslinking of chains that leads to hardening. A catalyst (commonly, methyl ethyl ketone peroxide, MEKP) is used to start the curing reaction. The cured thermoset is amorphous in structure. This thermoset polymer finds extensive uses in products such as glass fiber reinforced boats, pipes, shower stalls, etc.

Table 3.2 Some important characteristics of polyester

Density, ρ ($g\ cm^{-3}$)	Strength, σ (MPa)	Modulus, E (GPa)	Poisson's ratio, v	CTE α ($10^{-6}\ K^{-1}$)	Cure shrinkage (%)	Service temp. (°C)
1.1–1.4	30–100	2–4	0.2–0.33	50–100	5–12	80

We digress here to clarify a nomenclature problem. There is another resin which is also commonly referred to as polyester, but it is very different from the unsaturated polyester described above. The full name of this thermoplastic polyester is polyethylene terephthalate or PET (sometimes PETE). It is one of the three major commodity thermoplastics—PE, PP, and PET. PET is made by an esterification reaction between terephthalic acid and ethylene glycol to produce the monomer PET, with water as a by-product. The PET monomer is subjected to polymerization via a polycondensation reaction of monomers. Interestingly, ethylene glycol is a by-product of this reaction, which is of course recycled. PET, or polyester as it is commonly called, is used extensively to make fibers, films, and bottles for water and soda pop. The bottle variety has a higher molecular weight. PET is a semicrystalline material. PET-based fibers form about 60% of the market while bottles make up 30%. Common trade names of PET-based fibers include Tergal, Terylene, and Dacron fibers.

Other Thermosets

As pointed out above, epoxy materials have a prolonged service temperature of about 120 °*C*, which serves the airline industry. There is a considerable interest in developing polymeric materials that can withstand high temperatures. The design goals for space vehicles, new commercial aircraft, and defense aircraft require sustained service temperatures in the range of 300–500 °*C*. Polyimides are thermosetting polymers that have a relatively high service temperature range, 250–300 °*C*. However, like other thermosetting resins, they are brittle. Their fracture energies are in the 15–70 $J\ m^{-2}$ range. A major problem with polyimides is the elimination of water of condensation and solvents during processing. Polyimides represent a class of resins that can have a higher service temperature than epoxies. The acronym PMR stands for polymerized monomeric reactant. PMR resins are based on aromatic dianhydride ester acid and aromatic diamine.

They are polymerized via solvent addition. PMR-15 and PMR-II-50 are two trade names for these. Their service temperature can be around 250 °*C*. Their use has been limited, mainly because PMR resins contain a toxic compound, methylenedianiline (MDA), and emit volatile organic compounds (VOCs) during processing.

A polyimide developed by NASA is called DMBZ-15, wherein MDA is replaced with a noncoplanar diamine, 2,2′-dimethylbenzidine (DMBZ). The DMBZ-15 composition has a glass transition temperature of 414 °*C*, an increase in use temperature of 55 °*C* over PMR-15 composites. Carbon fibers reinforced DMBZ-15 have an operational temperature range up to 335 °*C* and good thermo-oxidative stability in aircraft engine or missile environments.

Some other resins can extend the use temperature range to 300 °*C*. An example is PETI—phenylethynyl-terminated imide (PETI) oligomers. PETI-298, PETI-330, and PETI-365 are the designations with the numbers indicating the glass transition temperature in °*C*. In particular, PETI-330 is a high-temperature resin (PETI resins were developed at NASA) that is suitable for infusion and resin transfer molding (RTM) processes. This resin has high-temperature mechanical properties coupled

with low melt viscosity (<10 *Pas* at 288 °*C*) and melt stability which allow it to be processed by relatively cheap RTM. The resin has a high glass transition temperature of 330 °*C*, it can be processed without use of solvents, i.e., no VOCs are generated during processing.

Bismaleimides (BMI), thermosetting polymers, can have service temperatures between 180 and 200 °*C*. They have good resistance to hygrothermal effects. Because they are thermosets, they are quite brittle and must be cured at higher temperatures than conventional epoxies.

Curing

Figure 3.8 shows schematically the variation of viscosity of a thermoset as a function of time for two different temperatures ($T_1 > T_2$). There occurs a slight decrease in viscosity in the beginning because of the heat generated by the exothermic curing reaction. As the crosslinking progresses, the molecular mass of the thermoset increases, viscosity increases at first slowly and then very rapidly. At the time corresponding to a perceptible change in viscosity, t_{gel}, a gel-like lump appears. At times greater than t_{gel}, viscosity tends to infinity and the thermoset can be treated as a solid. Figure 3.9 shows the variation of mechanical properties as a function of curing time. After a time marked t_{cure}, the mechanical properties of a thermoset essentially do not change with time.

Electron Beam Curing

An electron beam (1–10 *MeV*) is a good source of ionizing radiation that can be used to initiate polymerization or the curing reaction in a polymer. Parts up to 25 *mm* thick can be cured. Higher energy beams are required for parts thicker than 25 *mm*. It turns out that one needs to modify the resin formulation for electron beam

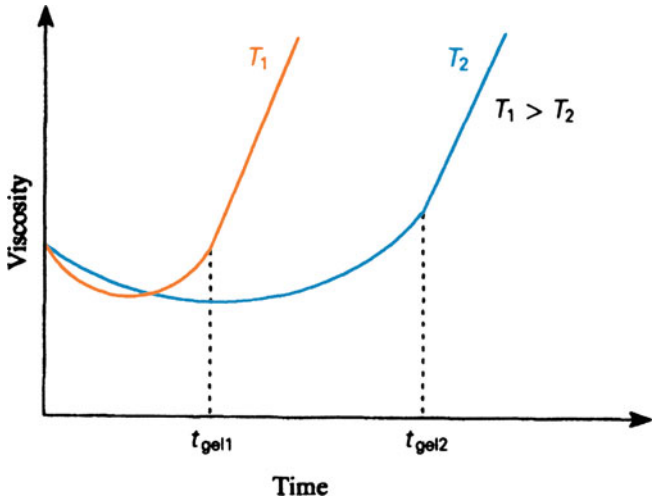

Fig. 3.8 Viscosity (η) versus time (t) for a thermoset for two different temperatures, $T_1 > T_2$

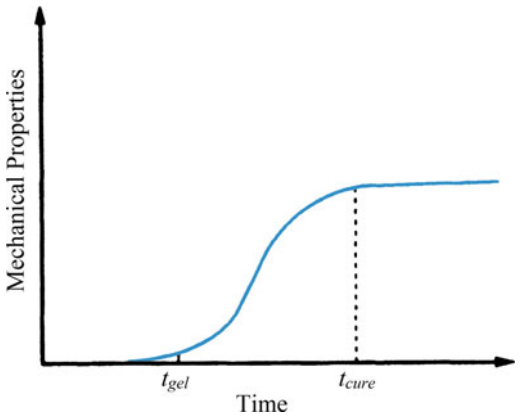

Fig. 3.9 Variation of mechanical properties with curing time

curing. Addition of 1–3 parts per hundred of a cationic photo-initiator can do the job. No hardener is required. However, other conventional additives, such as toughening agents or diluents, can be used to improve the processability of the resin. Among the advantages of electron beam curing, one may list

- Shorter cure times (minutes rather than the hours required by conventional thermal processes).
- Curing can be accomplished at a selected temperature (room temperature or near the service temperature).
- Lower energy consumption than in thermal curing.
- Removal of hardener means elimination of the undesirable volatile organic compounds. It also allows the use of thermoset resins with unlimited shelf life.

Among the limitations, one may list the following:

- Only a few electron beam curing facilities are available, especially for large and complex structures. This is especially so in the 5–15 *MeV* range.
- Shipping parts to outside accelerator facilities can be problematic.
- Long-term testing and experience in the field are missing, that is, customer confidence needs to be built.

3.1.9.2 Common Thermoplastic Matrix Materials

Thermoplastics are characterized by linear chain molecules and can be repeatedly melted or reprocessed. It is important to note that in this regard the cool-down time affects the degree of crystallinity of the thermoplastic. This is because the polymer chains need time to get organized in the orderly pattern of the crystalline state; too quick a cooling rate will not allow crystallization to occur. Although repeated melting and processing are possible with thermoplastics, it should be recognized

that thermal exposure (too high a temperature or too long a dwell time at a given temperature) can degrade the polymer properties, especially impact properties.

Linear molecules in a thermoplastic result in higher strain-to-failure values compared to those of thermosets, i.e., thermoplastics are tougher than the cross-linked thermosets. Thermoplastic matrix materials can have failure strains ranging from 30 to 100%, while the thermosets typically range from 1 to 3%. The large range of failure strains in thermoplastics stems from the rather large variations in the amount of crystallinity.

Common thermoplastic resins used as matrix materials in composites include some conventional thermoplastics such as polypropylene (PP), polyamide (PA) or nylon, thermoplastic polyesters (PET, PBT), and polycarbonates. Some of the new thermoplastic matrix materials include polyamide imide, polyphenylene sulfide (PPS), polyarylsulfone, and polyetherether ketone (PEEK). Figure 3.10 shows the chemical structure of some of these thermoplastics. PEEK is an attractive matrix material because of its toughness and impact properties, which are a function of its crystalline content and morphology. It should be pointed out that crystallization kinetics of a thermoplastic matrix can vary substantially because of the presence of fibers (Waddon et al. 1987). In order to make a thermoplastic matrix flow, heating must be done to a temperature above the melting point of the matrix. In the case of PEEK, the melting point of the crystalline component is 343 °*C*. In general, most thermoplastics are harder to flow vis à vis thermosets such as epoxy! The viscosity of thermoplastics decreases with increasing temperature, but at higher temperatures there is the danger of decomposition of resin.

Polyphenylene sulfide (PPS) is a linear polymer of "modest" molecular weight ($\sim$150) and low mold shrinkage (0.1–0.5% range). It can be injection molded, and the scrap can be ground and reused without much effect on processability and performance of the part. Polyethersulfone (PES) belongs to the polysulfone group of thermoplastics. Its chemical structure has an aromatic sulfone unit, which imparts

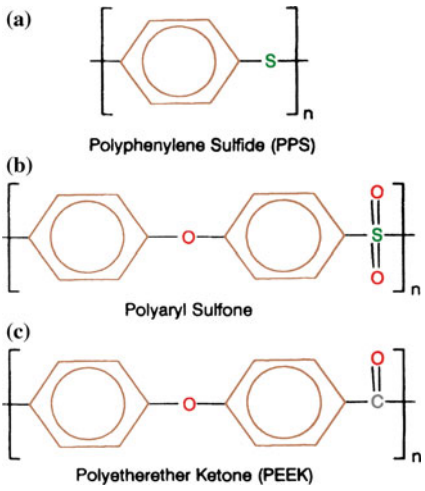

Fig. 3.10 Chemical structure of **a** Polyphenylene sulfide (PPS), **b** Polyaryl sulfone, and **c** Polyetherether ketone (PEEK)

high thermal stability and mechanical strength. It is completely amorphous and can withstand loads for long periods up to 190 °*C*. Both PEEK and PES are wholly aromatic polymers suitable for high temperatures, and both can be processed as conventional thermoplastics. PEEK, however, is partially crystalline, while PES is amorphous. The crystalline component of PEEK has a high melting point (343 °*C*) and good oxidative stability. PEEK has a long-term use temperature of 250 °*C* and a short use temperature of 300 °*C*.

Polyimides are among the most temperature-resistant engineering polymers. They can be linear or crosslinked, aromatic polymers. Processing problems and high cost have limited their use. Avimid K is a trade name of an amorphous, linear, thermoplastic polyimide resin that can be used to make fibrous prepregs. These prepregs are processed by a vacuum bag layup technique in an autoclave. Avimid K resin is made by condensation. An aromatic diethyl ester diacid is reacted with an aromatic diamine in *n*-methyl pyrrolidone (NMP) solvent. The by-products of the reaction are water, ethanol, and the solvent.

Thermoplastic resins have the advantage that they can be recycled. Heat and pressure are applied to form and shape them. More often than not, short fibers are used with thermoplastic resins but in the late 1970s continuous fiber reinforced thermoplastics began to be produced. The disadvantages of thermoplastics include their rather large expansion and low viscosity characteristics.

An important problem with polymer matrices is associated with environmental effects. Polymers can degrade at moderately high temperatures and through moisture absorption. Absorption of moisture from the environment causes swelling in the polymer as well as a reduction in its T_g. In the presence of fibers bonded to the matrix, these hygrothermal effects can lead to severe internal stresses in the composite. The presence of thermal stresses resulting from thermal mismatch between matrix and fiber is, of course, a general problem in all kinds of composite materials; it is much more so in polymer matrix composites because polymers have high thermal expansivities.

Typical properties of some common polymeric matrix materials are summarized in Table 3.3 (English 1985).

Matrix Toughness

Thermosetting resins (e.g., unsaturated polyesters, epoxies, and polyimides) are highly crosslinked and provide adequate modulus, strength, and creep resistance, but the same crosslinking of molecular chains causes extreme brittleness, that is, very low fracture toughness. By *fracture toughness*, we mean resistance to crack propagation. It came to be realized in the 1970s that matrix fracture characteristics (strain-to-failure, work of fracture, or fracture toughness) are as important as lightness, stiffness, and strength properties. Figure 3.11 compares some common materials in terms of their fracture toughness (note the log scale) as measured by the fracture energy in J/m^2 (Ting 1983). Note that thermosetting resins have values that are only slightly higher than those of inorganic glasses. Thermoplastic resins such as PMMA have fracture energies of about 1 kJ/m^2, while polysulfone thermoplastics have fracture energies of several kJ/m^2, almost

Table 3.3 Representative properties of some polymeric matrix materials

Property	Epoxy	Polyimide	PEEK	Polyamideimide	Polyetherimide	Polysulfone	Polyphenylene sulfide	Phenolics
Tensile strength (*MPa*)	35–85	120	92	95	105	75	70	50–55
Flexural modulus (*GPa*)	15–35	35	40	50	35	28	40	–
Density ($g\ cm^{-3}$)	1.38	1.46	1.30	1.38	–	1.25	1.32	1.30
Continuous-service temperature (°*C*)	25–85	260–425	310	–	170	175–190	260	150–175
Coefficient of thermal expansion ($10^{-6}\ K^{-1}$)	80–110	90	–	63	56	94–100	99	45–110
Water absorption (24 h %)	0.1	0.3	0.1	0.3	0.25	0.2	0.2	0.1–0.2

Source Adapted with permission from English (1985)

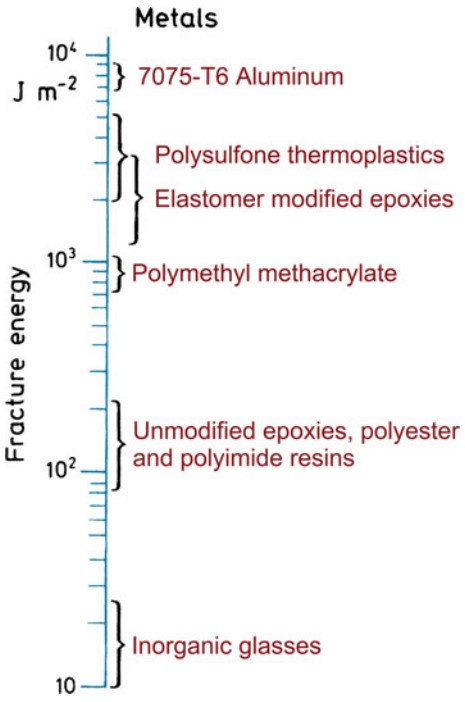

Fig. 3.11 Fracture energy for some common materials. (Adapted from Ting 1983, used with permission)

approaching those of the 7075-T6 aluminum alloy (Al alloy containing Zn and Mg, T6 is the aging heat treatment). Amorphous thermoplastic polymers show higher fracture energy values because they have a large free volume available that absorbs the energy associated with crack propagation. Among the well-known modified thermoplastics are the acrylonitrile-butadiene-styrene (ABS) copolymer and high impact polystyrene (HIPS). One class of thermosetting resins that comes close to polysulfones is the elastomer-modified epoxies. Elastomer-modified or rubber-modified thermosetting epoxies form multiphase systems, a kind of composite in their own right. Small (a few micrometers or less), soft, rubbery inclusions distributed in a hard, brittle epoxy matrix enhance its toughness by several orders of magnitude (Sultan and McGarry 1973; Riew et al. 1976; Bascom and Cottington 1976; St. Clair and St. Clair, 1981; Scott and Phillips 1975).

Epoxy and unsaturated polyester resins are commonly modified by introducing carboxyl-terminated butadiene-acrylonitrile copolymers (CTBN). The methods of manufacture can be simple mechanical blending of the soft, rubbery particles and the resin or copolymerization of a mixture of the two. Figure 3.12 shows the increase in fracture surface energy of an epoxy as a function of weight % of CTBN elastomer (Scott and Phillips 1975).

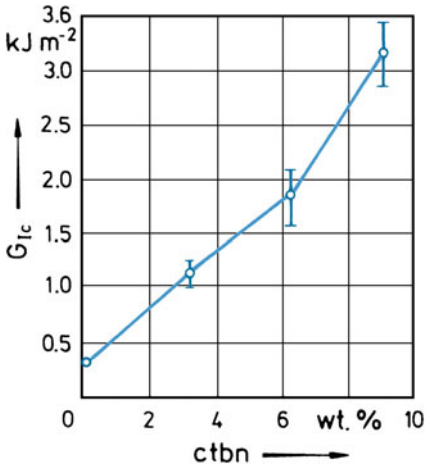

Fig. 3.12 Fracture surface energy of an epoxy as a function of weight % of carboxyl-terminated butadiene-acrylonitrile (CTBN). (Adapted from Scott and Phillips 1975, used with permission)

Toughening of glassy polymers by elastomeric additions involves different mechanisms for different polymers. Among the mechanisms proposed for explaining this enhanced toughness are triaxial dilation of rubber particles at the crack tip, particle elongation, and plastic flow of the epoxy. Ting (1983) studied such a rubber-modified epoxy containing glass or carbon fibers. He observed that the mechanical properties of rubber-modified composite improved more in flexure than in tension. Scott and Phillips (1975) obtained a large increase in matrix toughness by adding CTBN in unreinforced epoxy. But this large increase in toughness could be translated into only a modest increase in carbon fiber reinforced modified epoxy matrix composite. Introduction of a tough elastomeric phase, for example, a silicone rubber with good thermal resistance in a polyimide resin, produced a tough matrix material: a three-to-fivefold gain in toughness, G_{Ic} without a reduction in T_g (St. Clair and St. Clair 1981).

Continuous fiber reinforced thermoplastics show superior toughness values owing to superior matrix toughness. PEEK is a semicrystalline aromatic thermoplastic (Hartness 1983; Cogswell 1983; Blundell et al. 1985) that is quite tough. PEEK can have 20–40% crystalline phase. At 35% crystallinity, the spherulite size is about 2 μm (Cogswell 1983). Its glass transition temperature T_g is about 150 $°C$, and the crystalline phase melts at about 350 $°C$. It has an elastic modulus of about 4 GPa, a yield stress of 100 MPa, and a relatively high fracture energy of about 500 J/m^2. In addition to PEEK, other tough thermoplastic resins are available, for example, thermoplastic polyimides and polyphenylene sulfide (PPS), which is a semicrystalline aromatic sulfide. PPS is the simplest member of a family of polyarylene sulfides (O'Connor et al. 1986). PPS (trade name Ryton), a semicrystalline polymer, has been reinforced by chopped carbon fibers and prepregged with continuous carbon fibers (O'Connor et al. 1986).

3.2 Metals

Metals are very versatile engineering materials. They are strong and tough. They can be plastically deformed, and they can be strengthened by a wide variety of methods, mostly involving obstruction of movement of lineal defects called *dislocations*.

3.2.1 Structure

Metals, with the exception of metallic glasses, are crystalline materials. Most metals exist in one of the following three crystalline forms:

- Face-centered cubic (fcc),
- Body-centered cubic (bcc), and
- Hexagonal close packed (hcp).

Figure 3.13 shows these three structures. The black dots mark the centers of the atomic positions, and some of the atomic planes are shown shaded. In real metals, the atoms touch each other and all the space is filled up. Some important metals with their respective crystalline structures are listed in Table 3.4. Metals are crystalline materials; however, the crystalline structure is never perfect. Metals contain a variety of crystal imperfections. We can classify these as follows:

1. Point defects (zero dimensional),
2. Line defects (unidimensional),
3. Planar or interfacial defects (bidimensional), and
4. Volume defects (tridimensional).

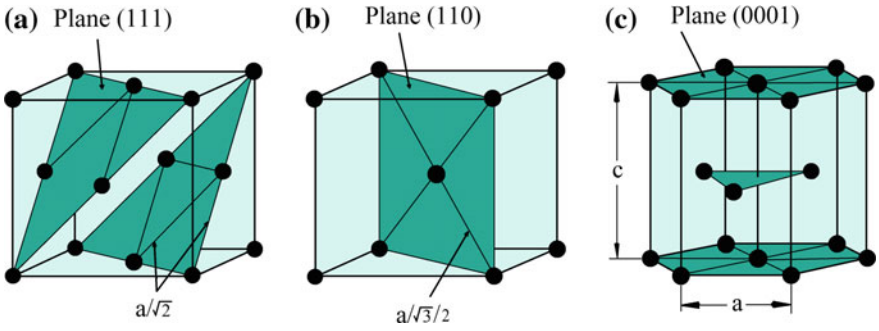

Fig. 3.13 **a**–**c** Three crystalline forms of metals: **a** Face-centered cubic, **b** body-centered cubic, **c** hexagonal close packed. a is the side of the cube in **a** and **b**, while it is the side of the hexagon base in **c**

Table 3.4 Crystal structure of some important metals

fcc	bcc	hcp
Iron (910–1390 °C)	Iron ($T < 910$ °C and $T > 1390$ °C)	Titanium[a]
Nickel	Beryllium ($T > 1250$ °C)	Beryllium ($T < 1250$ °C)
Copper	Cobalt ($T > 427$ °C)	Cobalt ($T < 427$ °C)
Aluminum	Tungsten	Cerium (-150 °C $< T < -10$ °C)
Gold	Molybdenum	Zinc
Lead	Chromium	Magnesium
Platinum	Vanadium	Zirconium[a]
Silver	Niobium	Hafnium[a] ($T < 1950$ °C)

[a]Undergoes a bcc ↔ hcp transformation at different temperatures

Point defects can be of three types. A *vacancy* is created when an atomic position in the crystal lattice is vacant. An *interstitial* is produced when an atom of material or a foreign atom occupies an interstitial or nonlattice position. A *substitutional point defect* comes into being when a regular atomic position is occupied by a foreign atom. *Intrinsic point defects* (vacancies and self-interstitials) in metals exist at a given temperature in equilibrium concentrations. Increased concentrations of these defects can be produced by quenching from high temperatures, bombarding with energetic particles such as neutrons, and plastic deformation. Point defects can have a marked effect on the mechanical properties.

Line imperfections, called dislocations, represent a critically important structural imperfection that plays a very important role in the area of physical and mechanical metallurgy, diffusion, and corrosion. A dislocation is defined by two vectors: a dislocation line vector, t (tangent to the dislocation line) and its Burgers vector, b, which gives the magnitude and direction of atomic displacement associated with the dislocation. There are two types of dislocations: in an edge dislocation b and t vectors are perpendicular to each other, while in a screw dislocation, b and t are parallel. The dislocation has a kind of lever effect because its movement allows one part of metal to be sheared over the other without the need for simultaneous movement of atoms across the whole plane. It is the presence of these line imperfections that makes it easy to deform metals plastically. Under normal circumstances then, the plastic deformation of metals is accomplished by the movement of these dislocations. Figure 3.14a shows an edge dislocation. The two vectors, defining the dislocation line and the Burgers vector, are designated as t (not shown) and b, respectively (see Fig. 3.14a). The dislocation permits shear in metals at stresses much below those required for simultaneous shear across a plane. Figure 3.14b shows this in an analogy. A carpet, of course, can be moved by pushing or pulling. However, a much lower force is required to move the carpet by a distance b if a defect (a bump in the carpet) is introduced into it and made to move the whole extension of the carpet. Figure 3.15 shows dislocations as seen by

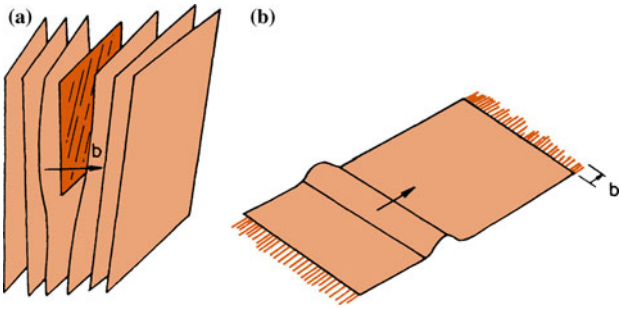

Fig. 3.14 aEdge dislocation, **b** dislocation in a carpet

transmission electron microscopy in a thin foil of steel. This is a dark field electron micrograph; dislocation lines appear as white lines. Dislocations become visible in the transmission electron microscope because of the distortion of the atomic planes owing to the presence of dislocations. Also visible in this micrograph are equiaxial precipitate particles pinning the dislocations at various points.

The interfacial or planar defects occupy an area or surface of the crystal, for example, grain boundaries, twin boundaries, domain, or antiphase boundaries. Grain boundaries are, by far, the most important of these planar defects from the mechanical behavior point of view. Among the volumetric or tridimensional defects, we can include large inclusions and porosity and preexisting cracks.

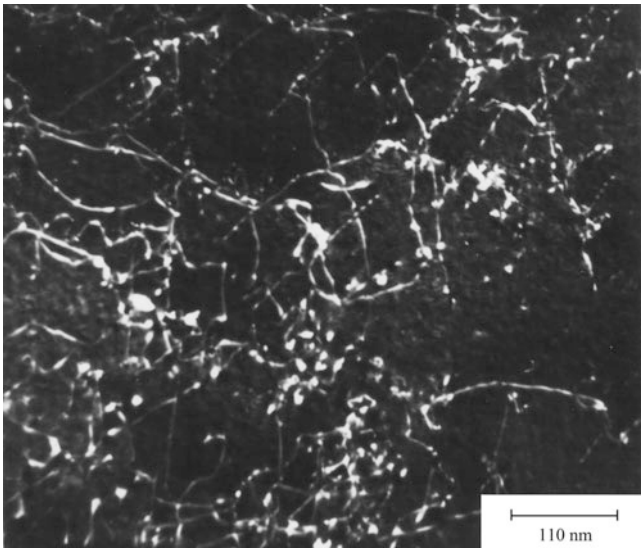

Fig. 3.15 Dislocations (*white lines*) in a steel sample: dark field transmission electron micrograph. Also visible are equiaxial precipitate particles

3.2.2 Conventional Strengthening Methods

Experimental results show that work hardening (or strain hardening), which is the ability of a metal to become more resistant to deformation as it is deformed, is related in a singular way to the dislocation density (ρ) after deformation. There exists a linear relationship between the flow stress in shear, τ and $\sqrt{\rho}$ (Meyers and Chawla 2009):

$$\tau = \tau_0 + \alpha G b \sqrt{\rho}, \tag{3.1}$$

where G is the shear modulus, b is the Burgers vector, α is an adjustable parameter, and τ_0 is the shear stress required to move a dislocation in the absence of any other dislocations. Basically, work hardening results from the interactions among dislocations moving on different slip planes. A tangled dislocation network results after a small plastic deformation, which impedes the motion of other dislocations. This, in turn, requires higher loads for further plastic deformation. Various theories (Seeger 1957; Kuhlmann-Wilsdorf 1977) explain the interactions of dislocations with different kinds of barriers (e.g., dislocations, grain boundaries, solute atoms, and precipitates) that result in characteristic strain hardening of metals. All these theories arrive at the relationship between τ and ρ given in Eq. (3.1), indicating that a particular dislocation distribution is not crucial and that strain hardening in practice remains the same for various dislocation distributions and configurations. Cold working of metals, which leads to the strengthening of metals as a result of increase in dislocation density and work hardening, is a routinely used strengthening technique.

A similar relationship exists between the flow stress, τ and the mean grain size (or dislocation cell size) to an undetermined level

$$\tau = \tau_0 + \frac{\alpha' G b}{D^{1/2}}, \tag{3.2}$$

where D is the mean grain diameter. This relationship is known as the *Hall–Petch relationship* after the two researchers who first postulated it (Hall 1951; Petch 1953). Again, various models have been proposed to explain this inverse square root dependence of strength of the metal on grain size. Earlier explanations involved a dislocation pileup bursting through the boundary owing to stress concentrations at the pileup tip and activation of dislocation sources in adjacent grains (Cottrell 1958). Later theories involved the activation of grain boundaries as sources of dislocations (Li 1963). An important aspect of strengthening by grain refinement is that, unlike other strengthening mechanisms, it results in an improvement in toughness concurrent with that in strength (again to an undefined lower grain size). Another easy way of strengthening metals by impeding

dislocation motion is that of introducing heterogeneities such as solute atoms or precipitates or hard particles in a ductile matrix. When we introduce solute atoms (e.g., carbon, nitrogen, or manganese in iron) we obtain solid solution hardening. Interstitial solutes such as carbon and nitrogen are much more efficient strengthening agents than substitutional solutes such as manganese and silicon. This is because the interstitials cause a tetragonal distortion in the lattice and thus interact with both screw and edge dislocations, while the substitutional atoms cause a spherical distortion that interacts only with edge dislocations, because the screw dislocations have a pure shear stress field and no hydrostatic component. Precipitation hardening of a metal is obtained by decomposing a supersaturated solid solution to form a finely distributed second phase. Classical examples of precipitation strengthening alloys are Al-Cu and Al-Zn-Mg alloys, which are used in the aircraft industry (Fine 1964). Oxide dispersion strengthening involves artificially dispersing rather small volume fractions (0.5–3 *vol %*) of strong and inert oxide particles (e.g., Al_2O_3, Y_2O_3, and ThO_2) in a ductile matrix by internal oxidation or powder metallurgy blending techniques (Ansell 1968). Both the second phase precipitates and dispersoids act as barriers to dislocation motion in the ductile matrix, thus making the matrix more deformation-resistant. Dispersion hardened systems (e.g., Al + Al_2O_3) show high strength levels at elevated temperatures while precipitates (say, $CuAl_2$ in aluminum) tend to dissolve at those temperatures. Precipitation hardening systems, however, have the advantage of enabling one to process the alloy in a soft condition, followed by giving the precipitation treatment to the finished part. The precipitation process carried out for long periods of time can also lead to overaging and solution, that is, a weakening of the alloy can result.

Quenching a steel to produce a martensitic phase has been a time honored strengthening mechanism for steels. The strength of the martensite phase in steel depends on a variety of factors, the most important being the amount of carbon. The chemical composition of martensite is the same as that of the parent austenite phase from which it formed, but it is supersaturated with carbon (Roberts and Owen 1968). Carbon saturation and the lattice distortion that accompanies the transformation lead to the high hardness and strength of martensite.

Another approach to obtaining enhanced mechanical performance is rapid solidification processing (Grant 1985). By cooling metals at rates in the 10^4–10^9 Ks^{-1} range, it is possible to produce unique microstructures. Very fine powders or ribbons of rapidly solidified materials are processed into bulk materials by hot pressing, hot isostatic pressing, or hot extrusion. The rapidly solidified materials can be amorphous (noncrystalline), nanocrystalline (grain size in the *nm* range), or microdendritic solid solutions containing solute concentrations vastly superior to those of conventionally processed materials. Effectively, massive second phase particles are eliminated. These unique microstructures lead to very favorable mechanical properties.

3.2.3 Properties of Metals

Typical values of elastic modulus, yield strength, and ultimate strength in tension and fracture toughness of some common metals and their alloys are listed in Table 3.5, while typical engineering stress–strain curves in tension are shown in Fig. 3.16. Note the large plastic strain range.

3.2.4 Why Fiber Reinforcement of Metals?

Precipitation or dispersion hardening of a metal can result in a dramatic increase in the yield stress and/or the work hardening rate. The influence of these obstacles on the elastic modulus is negligible. This is because the intrinsic properties of the strong particles (e.g., the high elastic modulus) are not used. Their only function is to impede dislocation motion in the metal. The improvement in stiffness can be profitably obtained by incorporating high modulus fibers in a metal matrix. It turns out that most of these high modulus fibers are also lighter than the metallic matrix materials, the only exception being tungsten, which has a high modulus and is very heavy. Table 3.6 lists some common metals and their densities, ρ. The densities of various fibers were given in Chap. 2.

Although one generally thinks of a high Young's modulus, E as something very desirable from a structural point of view, it turns out that for structural applications involving compression or flexural loading of beams (for example, in an airplane, rocket, or truck), it is the E/ρ^2 value, ρ being the density, that should be maximized. Consider a simple square section cantilever beam of length l and thickness t under an applied force P. The elastic deflection of this beam, ignoring self-weight, is given by (Fitzgerald 1982)

$$\delta = \frac{Pl^3}{3EI},$$

Table 3.5 Mechanical properties of some common metals and alloys

Property	E (*GPa*)	σ_y (*MPa*)	σ_{max} (*MPa*)	K_{Ic} ($MPam^{1/2}$)
Pure (ductile) metals				
Aluminum	70	40	200	100
Copper	120	60	400	–
Nickel	210	70	400	350
Ti-6Al-4V	110	900	1000	120
Aluminum alloys (Low strength–high strength)	70	100–380	250–480	40–23
Plain carbon steel	210	250	420	140
Stainless steel (304)	195	240	365	200

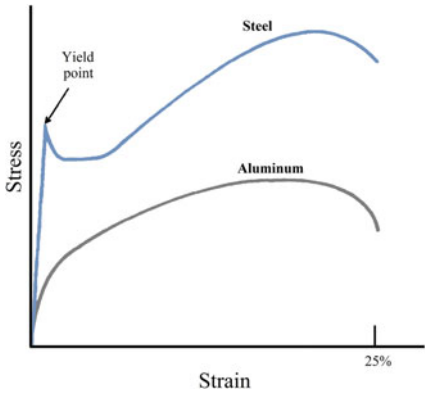

Fig. 3.16 Stress–strain curves of two common metals. Note the large plastic strain range

Table 3.6 Density of some common metals

Metal	Density ($g\ cm^{-3}$)	Metal	Density ($g\ cm^{-3}$)
Aluminum	2.7	Lead	11.0
Beryllium	1.8	Nickel	8.9
Copper	8.9	Silver	10.5
Gold	19.3	Titanium	4.5
Iron	7.9	Tungsten	19.3

where I is the moment of inertia or the second moment of area; in this case, it is equal to $t^4/12$.

Therefore,

$$\delta = \frac{4l^3P}{Et^4}. \tag{3.3}$$

The mass of this beam is

$$M = \text{volume} \times \text{density} = lt^2\rho$$

or

$$t = \left(\frac{M}{l\rho}\right)^{1/2}. \tag{3.4}$$

From Eqs. (3.3) and (3.4), we have

$$\delta = \left(\frac{4l^3P}{E}\right)\left(\frac{l^2\rho^2}{M^2}\right)$$

or

$$M = \left(\frac{4l^5P}{\delta}\right)\left(\frac{\rho^2}{E}\right)^{1/2}.$$

Thus, for a given rigidity or stiffness P/δ, we have a minimum of mass when the parameter E/ρ^2 is a maximum. What this simple analysis shows is that it makes good sense to use high modulus fibers to reinforce metals in a structural application and it makes eminently more sense to use fibers that are not only stiffer than metallic matrices but also lighter. Continuous ceramic fibers such as SiC, Al_2O_3, and B (see Chap. 2) would meet these requirements.

3.3 Ceramic Matrix Materials

Ceramic materials are very hard and brittle. Generally, they consist of one or more metals combined with a nonmetal such as oxygen, carbon, or nitrogen. They have strong covalent and ionic bonds and very few slip systems available compared to metals. Thus, characteristically, ceramics have low failure strains and low toughness or fracture energies. In addition to being brittle, they lack uniformity in properties, have low thermal and mechanical shock resistance, and have low tensile strength. On the other hand, ceramic materials have very high elastic moduli, low densities, and can withstand very high temperatures. The last item is very important and is the real driving force behind the effort to produce tough ceramics. Consider the fact that metallic superalloys, used in jet engines, can easily withstand temperatures up to 800 °*C* and can go up to 1100 °*C* with oxidation-resistant coatings. Beyond this temperature, one must use ceramic materials if they are available with the requisite toughness.

By far, the major disadvantage of ceramics is their extreme brittleness. Even the minutest of surface flaws (scratches or nicks) or internal flaws (inclusions, pores, or microcracks) can have disastrous results. One important approach to toughen ceramics involves fiber reinforcement of brittle ceramics. We shall describe the ceramic matrix composites in Chap. 7. Here we make a brief survey of ceramic materials, emphasizing the ones that are commonly used as matrices.

3.3.1 Bonding and Structure

Ceramic materials, with the exception of glasses, are crystalline, as are metals. Unlike metals, however, ceramic materials have mostly ionic bonding and some covalent bonding. Ionic bonding involves electron transfer between atomic species constituting the ceramic compound, that is, one atom gives up electron(s) while

another accepts electron(s). Electrical neutrality is maintained, that is, positively charged ions (*cations*) balance the negatively charged ions (*anions*). Generally, ceramic compounds are stoichiometric, that is, there exists a fixed ratio of cations to anions. Examples are alumina (Al_2O_3), beryllia (BeO), spinels ($MgAl_2O_4$), silicon carbide (SiC), and silicon nitride (Si_3N_4). It is not uncommon, however, to have nonstoichiometric ceramic compounds, for example, $Fe_{0.96}O$. The oxygen ion (anion) is generally very large compared to the metal ion (cation). Thus, cations occupy interstitial positions in a crystalline array of anions.

Crystalline ceramics generally exhibit cubic close packed and hexagonal close packed structures. The simple cubic structure is also called the cesium chloride structure. It is, however, not very common. CsCl, CsBr, and CsI show this structure. The two species form an interpenetrating cubic array, with anions occupying the cube corner positions while cations go to the interstitial sites. Cubic close packed is really a variation of the fcc structure described in Sect. 3.2. Oxygen ions (anions) make the proper fcc structure with metal ions (cations) in the interstices. Many ceramic materials show this structure, also called the NaCl or rock salt-type structure. Examples include MgO, CaO, FeO, NiO, MnO, and BaO. There are other variations of fcc close packed structures, for example, zinc blende types (ZnS) and fluorite types (CaF). The hexagonal close packed structure is also observed in ceramics. ZnS, for example, also crystallizes in the hcp form. Other examples are nickel arsenide (NiAs) and corundum (Al_2O_3). Figure 3.17 shows the hcp crystal structure of α-Al_2O_3. A and B layers consist of oxygen atoms while C_1, C_2, and C_3 layers contain aluminum atoms. The C layers are only two-thirds full.

Glass–ceramic materials form yet another important category of ceramics. They form a sort of composite material because they consist of 95–98% by volume of crystalline phase and the rest is glassy phase. The crystalline phase is very fine (grain size less than 1 μm in diameter). Such a fine grain size is obtained by adding

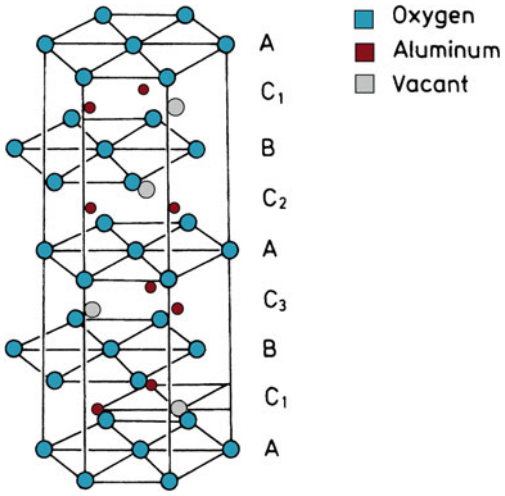

Fig. 3.17 Hexagonal close packed structure of α-alumina. A and B layers contain oxygen atoms. C_1, C_2, and C_3 contain aluminum atoms. The C layers are only two-thirds full

nucleating agents (commonly TiO_2 and ZrO_2) during the melting operation, followed by controlled crystallization. Important examples of glass–ceramic systems include the following:

1. Li_2O-Al_2O_3-SiO_2: This has a very low thermal expansion and is therefore very resistant to thermal shock. Corningware is a well-known trade name of this class of glass–ceramic.
2. MgO-Al_2O_3-SiO_2: This has high electrical resistance coupled with high mechanical strength.

Ceramic materials can also form solid solutions. Unlike metals, however, interstitial solid solutions are less likely in ceramics because the normal interstitial sites are already filled. Introduction of solute ions disrupts the charge neutrality. Vacancies accommodate the unbalanced charge. For example, FeO has a NaCl-type structure with an equal number of Fe^{2+} and O^{2-} ions. If, however, two Fe^{3+} ions were to replace three Fe^{2+} ions we would have a vacancy where an iron ion would form.

Glasses, the traditional silicate ceramic materials, are inorganic solidlike materials that do not crystallize when cooled from the liquid state. Their structure (see Fig. 2.5) is not crystalline but that of a supercooled liquid. In this case, we have a specific volume versus temperature curve similar to the one for polymers (see Fig. 3.2) and a characteristic glass transition temperature, T_g. Under certain conditions, crystallization of glass can occur with an accompanying abrupt decrease in volume because the atoms take up ordered positions.

3.3.2 *Effect of Flaws on Strength*

As in metals, imperfections in crystal packing of ceramics do exist and reduce their strength. The difference is that important defects in ceramic materials are surface flaws and vacancies. Dislocations do exist but are relatively immobile. Grain boundaries and free surfaces are important planar defects. As in metals, small grain size improves the mechanical properties of ceramics at low-to-medium temperatures.

Surface flaws and internal pores (Griffith flaws) are particularly dangerous for strength and fracture toughness of ceramics. Fracture stress, σ_f, for an elastic material having an internal crack of length $2a$ is given by the Griffith relationship:

$$\sigma_f = \left(\frac{2E\gamma}{a}\right)^{1/2},$$

where E is the Young's modulus, γ is the surface energy, and a is the half crack length. Linear elastic fracture mechanics treats this problem of brittle behavior in

terms of a parameter called the *stress intensity factor, K*. The stresses at the crack tip are given by

$$\sigma_{ij} = \left[\frac{K}{(2\pi r)^{1/2}}\right] f_{ij}(\theta),$$

where $f_{ij}(\theta)$ is a function of the angle θ. Fracture occurs when K attains a critical value, K_{Ic}. Yet another approach is based on the energy viewpoint, a modification of the Griffith idea. Fracture occurs, according to this approach, when the crack extension force G reaches a critical value G_{Ic}. For ceramic materials, $G_{Ic} = 2\gamma$. It can also be shown that $K^2 = EG$ for the opening failure mode and plane stress, that is, the stress intensity factor and the energy approaches are equivalent.

3.3.3 Common Ceramic Matrix Materials

Silicon carbide has excellent high temperature resistance. The major problem is that it is quite brittle up to very high temperatures and in all environments. Silicon nitride is also an important nonoxide ceramic matrix material. Among the oxide ceramics, alumina and mullite are quite promising. Silica-based glasses and glass–ceramics are other ceramic matrices. With glass–ceramics, one can densify the matrix in a glassy state with fibers, followed by crystallization of the matrix to obtain high temperature stability.

Ceramic matrices are used to make fiber reinforced composites to achieve gains in fracture toughness. Gains in strength and stiffness are less important except in glass matrix composites. Table 3.7 summarizes some of the important characteristics of common ceramic matrix materials (Phillips 1983).

Problems

3.1. Ductility, the ability to deform plastically in response to stresses, is more of a characteristic of metals than it is of ceramics or polymers. Why?

3.2. Ceramic materials generally have some residual porosity. How does the presence of porosity affect the elastic constants of ceramic materials? How does it affect the fracture energy of ceramics?

3.3. Explain why it is difficult to compare the stress–strain behavior of polymers (particularly thermoplastics) with that of metals.

3.4. The mechanical behavior of a polymer can be represented by an elastic spring and a dashpot in parallel (Voigt model). For such a model, we can take the total stress that consists of an elastic part (σ_{el}) and a viscous part (σ_{visc}). Thus,

$$\sigma = \sigma_{el} + \sigma_{visc} = E\varepsilon + \eta d\varepsilon/dt$$

Table 3.7 Properties of some ceramic matrix materials

Material	Young's modulus (*GPa*)	Tensile strength (*MPa*)	Coefficient of thermal expansion ($10^{-6}\ K^{-1}$)	Density ($g\ cm^{-3}$)
Borosilicate glass	60	100	3.5	2.3
Soda glass	60	100	8.9	2.5
Lithium aluminosilicate glass–ceramic	100	100–150	1.5	2.0
Magnesium aluminosilicate glass–ceramic	120	110–170	2.5–5.5	2.6–2.8
Mullite	143	83	5.3	
MgO	210–300	97–130	13.8	3.6
Si_3N_4	310	410	2.25–2.87	3.2
Al_2O_3	360–400	250–300	8.5	3.9–4.0
SiC	400–440	310	4.8	3.2

Source Adapted with permission from Phillips (1983)

where E is the Young's modulus, ε is the strain, η is the viscosity, and t is the time. Show that

$$\varepsilon = \sigma/E[1 - \exp(-E/\eta)t].$$

3.5. What is the effect of the degree of crystallinity on fatigue resistance of polymers?
3.6. Discuss the importance of thermal effects (hysteretic heating) on fatigue of polymers.
3.7. Glass–ceramics combine the generally superior mechanical properties of crystalline ceramics with the processing ease of glasses. Give a typical thermal cycle involving the various stages for producing a glass–ceramic.
3.8. Silica-based glasses and many polymers have amorphous structure. An amorphous structure is characterized by a glass transition temperature. Explain why silica-based glasses have a much higher glass transition temperature than polymers.

References

G.S. Ansell (ed.), *Oxide Dispersion Strengthening* (Gordon & Breach, New York, 1968)
W.D. Bascom, R.L. Cottington, J. Adhes. **7**, 333 (1976)
D.J. Blundell, J.M. Chalmers, M.W. Mackenzie, W.F. Gaskin, Sampe Q. **16**, 22 (1985)
F.N. Cogswell, Sampe Q. **14**, 33(1983)
A.H. Cottrell, Trans. TMS-AIME **212**, 192 (1958)
L.K. English, Mater. Eng. **102**, 32 (1985)
M.E. Fine, *Phase Transformations in Condensed Systems* (Macmillan, New York, 1964)
R.W. Fitzgerald, *Mechanics of Materials*, 2nd edn. (Addison-Wesley, Reading, MA, 1982), p. 205

N.J. Grant, *Frontiers in Materials Technologies* (Elsevier, New York, 1985), p. 125
E.O. Hall, Proc. R. Soc. Lond. **B64**, 474 (1951)
J.T. Hartness, Sampe Q **14**, 33 (1983)
D. Kuhlmann-Wilsdorf, *Work Hardening in Tension and Fatigue* (TMS-AIME, New York, 1977), p. 1
J.C.M. Li, Trans. TMS-AIME **227**, 239 (1963)
L. Mandelkern, *An Introduction to Macromolecules*, 2nd edn. (Springer, New York, 1983a), p. 1
M.A. Meyers, K.K. Chawla, *Mechanical Behavior of Materials*, 2nd edn. (Cambridge University Press, Cambridge, UK, 2009a)
R.J. Morgan, *Epoxy Resins and Composites* (Springer, Berlin, 1985), p. 1
J.E. O'Connor, W.R. Beever, J.F. Geibel, Proc. Sampe Mater. Symp. **31**, 1313 (1986)
N.J. Petch, J. Iron Steel Inst. **174**, 25 (1953)
D.C. Phillips, *Fabrication of Composites* (North-Holland, Amsterdam, 1983), p. 373
C.K. Riew, E.H. Rowe, A.R. Siehert, *Toughness and Brittleness of Plastics*. Advances in Chemistry Series, vol. 154 (American Chemical Society, 1976), p. 326
M.J. Roberts, W.S. Owen, J. Iron Steel Inst. **206**, 375 (1968)
J.M. Scott, D.C. Phillips, J. Mater. Sci. **10**, 551 (1975)
A. Seeger, *Dislocations and Mechanical Properties of Crystals* (Wiley, New York, 1957), p. 23
A.K. St. Clair, T.L. St. Clair, J. Adhes. Adhes. **1**, 249 (1981)
J.N. Sultan, F.J. McGarry, Polym. Eng. Sci. **13**, 29 (1973)
R.Y. Ting, *The Role of Polymeric Matrix in the Processing and Structural Properties of Composite Materials* (Plenum Press, New York, 1983), p. 171
A.J. Waddon, M.J. Hill, A. Keller, D.J. Blundell, J. Mater. Sci. **22**, 1773 (1987)

Suggested Reading

C.S. Barrett, T.B. Massalski, *Structure of Metals*, 3rd edn. (Pergamon Press, Oxford, 1980)
K. Dusek (ed.), *Epoxy Resins and Composites I*. Advances in Polymer Science, vol. 72. (Springer, Berlin, 1985)
W.D. Kingery, H.K. Bowen, D.R. Uhlmann, *Introduction to Ceramics*, 2nd edn. (Wiley, New York, 1976)
J. Roesler, H. Harders, M. Baeker, *Mechanical Behaviour of Engineering Materials* (Springer, Berlin, 2007)
L. Mandelkern, *An Introduction to Macromolecules*, 2nd edn. (Springer, New York, 1983b)
M.A. Meyers, K.K. Chawla, *Mechanical Metallurgy: Principles and Applications* (Prentice-Hall, Englewood Cliffs, NJ, 1984)
M.A. Meyers, K.K. Chawla, *Mechanical Behavior of Materials*, 2nd edn. (Cambridge University Press, Cambridge, UK, 2009b)
J.B. Wachtman, *Mechanical Properties of Ceramics* (Wiley, New York, 1996)

Chapter 4
Interfaces

We can define an interface between a reinforcement and a matrix as the bounding surface between the two across which a discontinuity in some parameter occurs. The discontinuity across the interface may be sharp or gradual. Mathematically, interface is a bidimensional region. In practice, we have an interfacial region with a finite thickness. In any event, an interface is the region through which material parameters, such as concentration of an element, crystal structure, atomic registry, elastic modulus, density, coefficient of thermal expansion, etc., change from one side to another. Clearly, a given interface may involve one or more of these items.

The behavior of a composite material is a result of the combined behavior of the following three entities:

- Fiber or the reinforcing element,
- Matrix, and
- Reinforcement/matrix interface.

The reason the interface in a composite is of great importance is that the internal surface area occupied by the interface is quite extensive. It can easily go as high as 3000 cm^2/cm^3 in a composite containing a reasonable fiber volume fraction. We can demonstrate this very easily for a cylindrical fiber in a matrix. The fiber surface area is essentially the same as the interfacial area. Ignoring the fiber ends, one can write the surface-to-volume ratio (S/V) of the fiber as

$$S/V = 2\pi rl/\pi r^2 l = 2/r, \tag{4.1}$$

where r and l are the fiber radius and length of the fiber, respectively. Thus, the surface area of a fiber or the interfacial area per unit volume increases as r decreases. Clearly, it is important that the fibers not be weakened by flaws because of an adverse interfacial reaction. Also, the applied load should be effectively transferred from the matrix to the fibers via the interface. Thus, it becomes extremely important to understand the nature of the interface region of any given composite system under a given set of conditions. Specifically, in the case of a fiber reinforced

K. K. Chawla, *Composite Materials*,
https://doi.org/10.1007/978-3-030-28983-6_4

composite material, the interface, or more precisely the interfacial zone, consists of near-surface layers of fiber and matrix and any layer(s) of material existing between these surfaces. Wettability of the fiber or any other reinforcement by the matrix and the type of bonding between the two components constitute the primary considerations. Additionally, one should determine the characteristics of the interface and how they are affected by temperature, diffusion, residual stresses, and so on. It is important to appreciate the distinction between wettability and bonding. One can have good wettability but weak bonding between two components. On the other hand, one can also have strong bonding but poor wettability, which in effect will mean weak interface because we will have gaps or voids at the interface because of the poor wettability. In what follows, we discuss some of the interfacial characteristics and the associated problems in composites in a general way. The details regarding interfaces in polymer matrix, metal matrix, and ceramic matrix composites will be provided in specific chapters devoted to those composite types.

4.1 Wettability

Various mechanisms can assist or impede adhesion (Baier et al. 1968). A key concept in this regard is that of wettability. Wettability tells us about the ability of a liquid to spread on a solid surface. We can measure the wettability of a given solid by a liquid by considering the equilibrium of forces in a system consisting of a drop of liquid resting on a plane, solid surface in the appropriate atmosphere. Figure 4.1a shows the situation schematically. The liquid drop will spread and wet the surface only if this results in a net reduction of free energy of the system. The spreading of the liquid drop on the solid results in a portion of the solid/vapor interface to be substituted by the solid/liquid interface. Contact angle, θ, of a liquid on the solid surface fiber is a convenient and important parameter to characterize wettability. Commonly, the contact angle is measured by putting a sessile drop of the liquid on the flat surface of a solid substrate. The contact angle is obtained from the tangents along three interfaces: solid/liquid, liquid/vapor, and solid/vapor. The contact angle, θ can be measured directly by a goniometer or calculated by using simple trigonometric relationships involving drop dimensions. An example of contact angle measurement in practice is shown in Fig. 4.1b (Chawla et al. 2009). This example shows the contact angle between a drop of water and a polydimethylsiloxane (PDMS) substrate. The top picture shows a contact angle of 109° while the bottom picture shows almost full wetting with a contact angle of less than 15° of the modified PDMS substrate with water.

One uses the following expression, called Young's equation:

$$\gamma_{SV} = \gamma_{LS} + \gamma_{LV} \cos\theta, \tag{4.2}$$

where γ is the specific surface energy and the subscripts *SV, LS*, and *LV* represent solid/vapor, liquid/solid, and liquid/vapor interfaces, respectively, to characterize

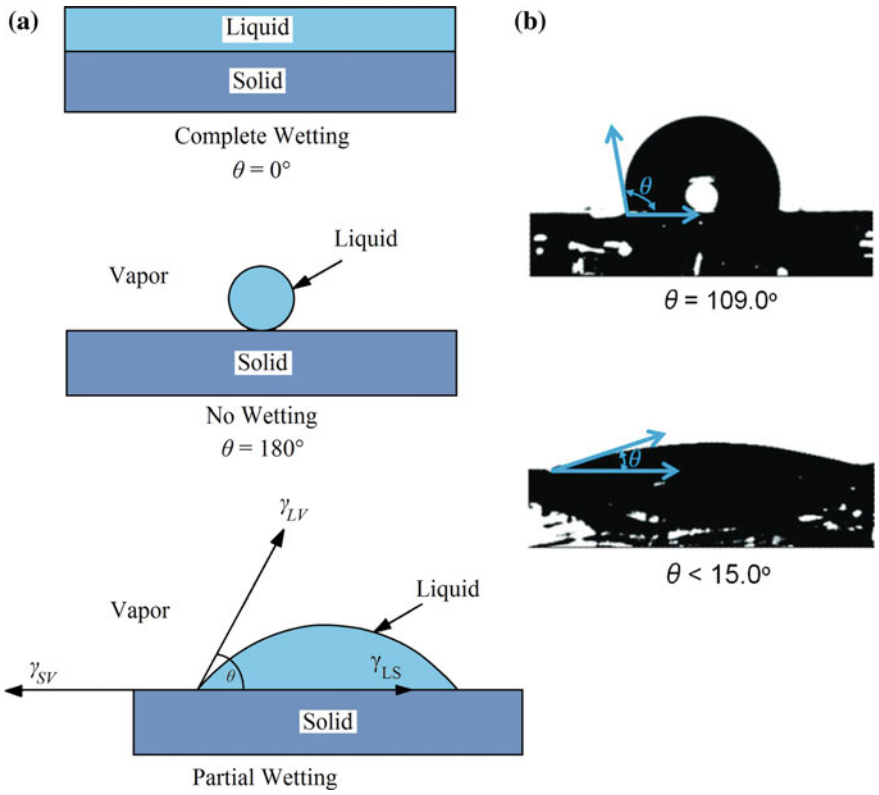

Fig. 4.1 **a** Three different conditions of wetting: complete wetting, no wetting, and partial wetting. **b** An example of contact angle measured between the surface of polydimethylsiloxane (PDMS) and a drop of liquid water, top figure. The bottom figure shows almost full wettability between modified PDMS surface and water (Chawla et al. 2009, Used with permission)

the wetting of a solid by a liquid. If this process of substitution of the solid/vapor interface involves an increase in the free energy of the system, then complete spontaneous wetting will not result. In a general situation, the liquid will spread until a balance of forces acting on the surface is attained, that is, we shall have partial wetting. A small θ implies good wetting. Two extreme cases are $\theta = 0°$, corresponding to perfect wetting and $\theta = 180°$, corresponding to no wetting. In practice, it is rarely possible to obtain a unique equilibrium value of θ. Also, there exists a range of contact angles between the maximum or advancing angle, θ_a, and the minimum or receding angle, θ_r. This phenomenon, called the *contact-angle hysteresis*, is generally observed in polymeric systems. Among the sources of this hysteresis are chemical attack, dissolution, inhomogeneity of chemical composition of solid surface, surface roughness, and local adsorption.

It is important to realize that wettability and bonding are not synonymous terms. Wettability describes the extent of intimate contact between a liquid and a solid; it does not necessarily mean a strong bond at the interface. One can have excellent

wettability and a weak van der Waals-type low-energy bond. A low contact angle, meaning good wettability, is a necessary but not sufficient condition for strong bonding. Consider again a liquid droplet lying on a solid surface. In such a case, Young's equation, Eq. (4.1), is commonly used to express the equilibrium among surface tensions in the horizontal directions. What is normally neglected in such an analysis is that there is also a vertical force $\gamma_{LV} \sin \theta$, which must be balanced by a stress in the solid acting perpendicular to the interface. This was first pointed out by Bikerman and Zisman in their discussion of the proof of Young's equation by Johnson (1959). The effect of internal stress in the solid for this configuration was discussed by Cahn and Hanneman (1964), Allen and Cahn (1979). In general, Young's equation has been applied to void formation in solids without regard to the precise state of internal stress. Fine et al. (1993) analyzed the conditions for occurrence of these internal stresses and their effect on determining work of adhesion in particle reinforced composites.

Wettability is very important in PMCs because in the manufacturing of PMCs, the liquid matrix must penetrate and wet fiber tows. Among polymeric resins that are commonly used as matrix materials, thermoset resins have a viscosity in the 1–10 *Pas* range. The melt viscosities of thermoplastics are two to three orders of magnitude higher than those of thermosets and they show, comparatively, poorer fiber wetting characteristics. Although the contact angle is a measure of wettability, the reader should realize that its magnitude will depend on the following important variables: time and temperature of contact; interfacial reactions; stoichiometry, surface roughness, and geometry; heat of formation; and electronic configuration.

Example 4.1 Consider a laminated composite made by laminating sheets of two materials (1 and 2), each of volume, v, in an alternating sequence. Let the thickness of the laminae of the two materials be t_1 and t_2 and the number of sheets of each be N_1 and N_2, respectively. For a given volume fraction of component 1, V_1 (remember that $V_1 + V_2 = 1$), derive an expression for the interfacial area as a function of t_1 and t_2.

Solution Let the area of cross section of the laminate be A. Let v, V, N, and t represent the volume, volume fraction, number, and thickness of a lamina, respectively, and let subscripts 1 and 2 denote the two components. Then, we can write

$$\begin{gathered} V_1 = \text{volume of component 1/total volume} = AN_1t_1/v \\ V_2 = \text{volume of component 2/total volume} = AN_2t_2/v \\ V_1 + V_2 = 1 \\ A(N_1t_1/v + N_2t_2/v) = 1 \end{gathered},$$

or

$$A/v = 1/(N_1t_1 + N_2t_2). \tag{4.3}$$

$$\begin{gathered} \text{Total number of interfaces} = (N_1 + N_2 - 1). \\ \text{Total interfacial area per unit volume, } I_a = (N_1 + N_2 - 1)A/v. \end{gathered} \tag{4.4}$$

From Eqs. (4.3) and (4.4), we have

$$I_a = (N_1 + N_2 - 1)/(N_1 t_1 + N_2 t_2).$$

Taking $t_1 = t_2 = t$, we get

$$I_a = (N_1 + N_2 - 1)/(N_1 + N_2)t = k/t,$$

where $k = (N_1 + N_2 - 1)/(N_1 + N_2)$ = a constant. The constant k will be approximately equal to 1 when N_1 and N_2 are very large compared to unity. Thus, the interfacial area is inversely proportional to the thickness of the sheet.

4.1.1 *Effect of Surface Roughness*

Generally, it is implicitly assumed that the substrate is perfectly smooth. This, however, is far from true in practice. More often than not, the interface between fiber and matrix is rather rough instead of the ideal planar interface; see Fig. 4.2. Most fibers or reinforcements show some degree of roughness (Chawla 1997). Surface roughness profiles of the fiber surface obtained by atomic force microscopy (AFM) can provide detailed, quantitative information on the surface morphology and roughness of the fibers. It would appear that AFM can be a useful tool in characterizing the fiber surface roughness (Chawla et al. 1993, 1995; Jangehud et al. 1993; Chawla and Xu 1994). Figure 4.3 shows an example of roughness characterization by AFM of the surface of a polycrystalline alumina fiber (Nextel 610).

Generally, the fiber/matrix interface will assume the same roughness profile as that of the fiber. In the case of polymer matrix composites, an intimate contact at the molecular level between the fiber and the matrix brings intermolecular forces into play with or without causing a chemical linkage between the components. In order

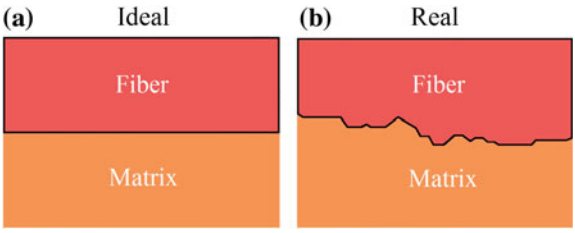

Fig. 4.2 **a** An ideal planar interface between reinforcement and matrix. **b** A more likely jagged interface between a fibrous reinforcement and a matrix

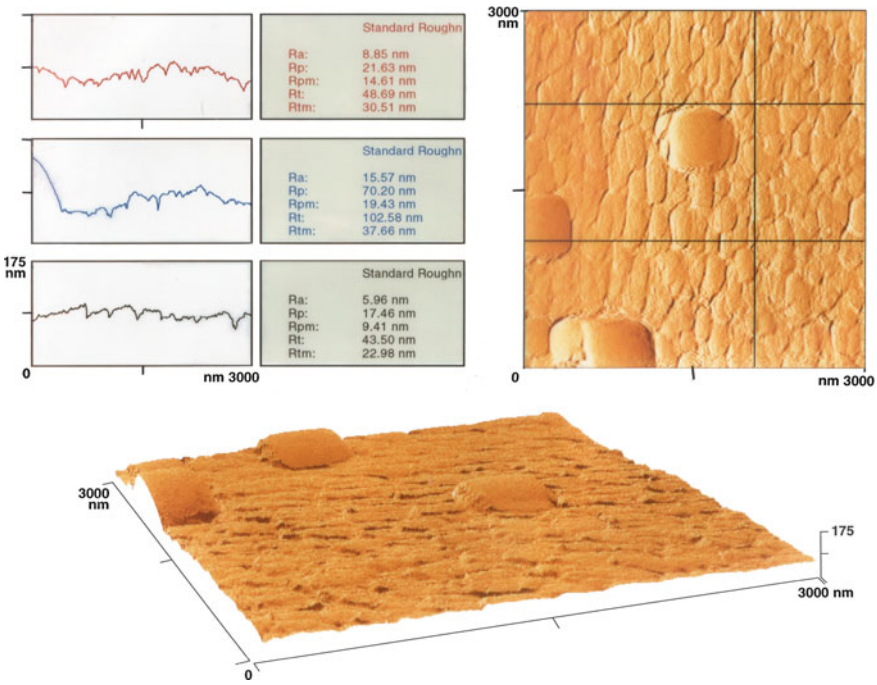

Fig. 4.3 Characterization of surface roughness of a polycrystalline alumina fiber (Nextel 610) by atomic force microscopy. The three profiles on the left-hand side correspond to the two horizonal and one vertical lines on the right-hand side figure. The bottom figure shows a three-dimensional perspective view of surface

to obtain an intimate contact between the fiber and the matrix, the matrix in liquid form must wet the fiber. Coupling agents are frequently used to improve the wettability between the components. At times, other approaches, such as modifying the matrix composition, are used.

Although the contact angle provides a quantitative measure of wettability, it should be emphasized that its value depends on the surface preparation. Surface topography can have a great influence. Wenzel (1936) discussed the effect of surface roughness on wettability and pointed out "within a measured unit on a rough surface, there is actually more surface, and in a sense therefore a greater surface energy, than in the same measured unit area on a smooth surface." Following Wenzel, the effect of surface roughness on wettability can be described in terms of r, the ratio of real area, A_{real}, to projected area, A_{proj}, of the interface. Thus,

$$\cos\theta_0 = r\frac{\gamma_{SV} - \gamma_{LS}}{\gamma_{LV}}, \tag{4.5}$$

where $r = A_{\text{real}}/A_{\text{proj}}$.

If $\theta_o < 90°$, wettability is enhanced by roughness, and if $\theta_0 > 90°$, wettability is reduced by roughness. If wetting is poor ($\theta_0 > 90°$), surface roughness can reduce bonded area and lead to void formation and possible stress concentrations. Cassie and Baxter (1944) considered the case of a flat substrate that consists of randomly distributed n different phases on the surface. Specifically, for a substrate consisting of two components, the contact angle is given by

$$\cos\theta = f_1 \cos\theta_1 + f_2 \cos\theta_2 \text{ and } f_1 + f_2 = 1,$$

where f_1 and f_2 are the volume fractions of the two components.

4.2 Crystallographic Nature of Interface

Most of the physical, chemical, and mechanical discontinuities at the interface mentioned previously are self-explanatory. The concept of atomic registry or the crystallographic nature of an interface needs some elaboration. In terms of the types of atomic registry, we can have a coherent, semicoherent, or incoherent interface. A *coherent* interface is one where atoms at the interface form part of both the crystal lattices, that is, there exists a one-to-one correspondence between lattice planes on the two sides of the interface. A coherent interface thus has some coherency strains associated with it because of the straining of the lattice planes in the two phases to provide the continuity at the interface atomic sites on the two sides of the interface. In general, a perfect atomic registry does not occur between unconstrained crystals. Rather, coherency at the interface invariably involves an elastic deformation of the crystals. A coherent interface, however, has a lower energy than an incoherent one. A classic example of a coherent interface is the interface between Guinier–Preston (G-P) zones and the aluminum matrix. These G-P zones are precursors to the precipitates in aluminum matrix. With increasing size of the crystals, the elastic strain energy becomes more than the interfacial energy, leading to a lowering of the free energy of the system by introducing dislocations at the interface. Such an interface, containing dislocations to accommodate the large interfacial strains and thus having only a partial atomic registry, is called a *semicoherent interface*. Thus, a semicoherent interface is one that does not have a very large lattice mismatch between the phases, and the small lattice mismatch is accommodated by the introduction of dislocations at the interface. As examples, we cite interfaces between a precipitate and a matrix as well as interfaces in some eutectic composites such as NiAl–Cr system (Walter et al. 1969), which has semicoherent interfaces between phases. With still further increase in crystal sizes, the dislocation density at the interface increases, and eventually the dislocations lose their distinct identity, that is, it is no longer possible to specify individual atomic positions at the interface. Such an interface is called an *incoherent interface*. An incoherent interface consists of such severe atomic disorder that no matching of lattice planes occurs across the boundary, i.e., no continuity of lattice planes is maintained across the interface. This

eliminates coherency strains, but the energy associated with the boundary increases because of severe atomic disorder at the grain boundary. The atoms located at such an interface do not correspond to the structure of either of the two crystals or grains. Crystallographically, most of the interfaces that one encounters in fiber, whisker, or particle reinforced composites are incoherent.

4.3 Interactions at the Interface

We mentioned earlier that interfaces are bidimensional regions. An initially planar interface, however, can become an interfacial zone with, possibly, multiple interfaces resulting from the formation of different intermetallic compounds, interdiffusion, and so on. In such a case, in addition to the compositional parameter, we need other parameters to characterize the interfacial zone, for example, geometry and dimensions; microstructure and morphology; and mechanical, physical, chemical, and thermal characteristics of different phases present in the interfacial zone. It commonly occurs that initially the components of a composite system are chosen based on their mechanical and physical characteristics in isolation. It is important to remember, however, that when one puts together two components to make a composite, the composite will rarely be a system in thermodynamic equilibrium. More often than not, there will be a driving force for some kind of interfacial reaction(s) between the two components, leading to a state of thermodynamic equilibrium for the composite system. Of course, thermodynamic information, such as phase diagrams, can help predict the final equilibrium state of the composite. For example, data regarding reaction kinetics, diffusivities of one constituent in another, etc. can provide information about the rate at which the system would tend to attain the equilibrium state. In the absence of thermodynamic and kinetic data, experimental studies would have to be done to determine the compatibility of the components. Quite frequently, the very process of fabrication of a composite can involve interfacial interactions that can cause changes in the constituent properties and/or interface structure. For example, if the fabrication process involves cooling from high temperatures to ambient temperature, the difference in the expansion coefficients of the two components can give rise to thermal stresses of such a magnitude that the softer component (generally the matrix) will deform plastically. Chawla and Metzger (1972) showed in a tungsten fiber/single crystal copper matrix (nonreacting components) that liquid copper infiltration of tungsten fibers at about 1100 $^{\circ}C$ followed by cooling to room temperature resulted in a dislocation density in the copper matrix that was much higher in the vicinity of the interface than away from the interface. The high dislocation density in the matrix near the interface occurred because of plastic deformation of the matrix caused by high thermal stresses near the interface. Arsenault and coworkers (Arsenault and Fisher 1983; Vogelsang et al. 1986) found similar results in SiC whisker/aluminum matrix composite. Many other researchers have observed dislocation generation in the vicinity of reinforcements/matrix interface due to the

thermal mismatch between the reinforcement and metal matrix. In PMCs and CMCs, the matrix is unlikely to deform plastically in response to the thermal stresses. It is more likely to relieve those stresses by matrix microcracking. In powder processing techniques, the nature of the powder surface will influence the interfacial interactions. For example, an oxide film, which is invariably present on the surface of powder particles, will affect the chemical nature of the powder. Topographic characteristics of the components can also affect the degree of atomic contact that can be obtained between the components. This can result in geometrical irregularities (e.g., asperities and voids) at the interface, which can be a source of stress concentrations.

Example 4.2 Distinguish between the terms *surface energy* and *surface tension*.

Answer Surfaces in solids and liquids have special characteristics because surfaces represent the termination of a phase. Consider an atom or a molecule in the interior of an infinite solid. It will be bonded in all directions, and this balanced bonding results in a reduced potential energy of the system. At a free surface, atoms or molecules are not surrounded by other atoms or molecules on all sides; they have no bonds or neighbors above the surface. Thus, there exists an imbalance of forces at the surface (it is true at any interface, really) that results in a rearrangement of atoms or molecules at the surface. We say that a surface has an extra energy called *surface energy*, i.e., surface energy is the excess energy per unit area associated with the surface because of the unsatisfied bonds at the surface. The units of surface energy are Jm^{-2}. We can also define it as the energy needed to create a unit surface area. In a crystalline solid, surface energy depends on the crystallographic orientation. For example, if we hold a single crystal at high temperature, it will assume a shape bounded by low-energy crystallographic planes of minimum surface energy. *Surface tension* is the tendency to minimize the total surface energy by minimizing the surface area. Surface energy and surface tension are numerically equal for isotropic materials. Surface tension is generally given in units of Nm^{-1}, which is the same as Jm^{-2}. This is not true for anisotropic solids. Consider a surface of area A with a surface energy of γ. If we increase the surface area by a small amount, the work done per unit increase of area can be written as

$$d(A\gamma)/dA = \gamma + \partial\gamma/\partial A.$$

The term $\partial\gamma/\partial A$ is zero for liquids because of atomic or molecular mobility in the liquid state. The structure of a liquid surface is unchanged when we increase its surface area. Actually, for any material that is incapable of withstanding shear, $\partial\gamma/\partial A = 0$. In general, such materials include liquids and solids at high temperatures. Thus, for a liquid, the surface tension and surface energy are equal. Because, thermodynamically, the most stable state is the one with a minimum of free energy, isotropic liquids tend toward a minimum area/unit volume, i.e., a sphere. Such equality does not hold for solids that can withstand shear. If we stretch the surface of a solid, the atoms or molecules at the surface are pulled apart, γ decreases, and the quantity $\partial\gamma/\partial A$ becomes negative. Thus, for crystalline solids, the surface

tension is not equal to surface energy. That is why a piece of solid metal does not assume a spherical shape when left to stand at room temperature. In fact, the surface energy of a crystal varies with crystallographic orientation. Generally, the more densely packed planes have a lower surface energy, and they end up forming the stable planes on the surface.

Typically, polymers have surface energies < 100 mJm^{-2}; oxides have between 100–2000 mJm^{-2}; while metals, carbides, and nitrides have > 1000 mJm^{-2}.

4.4 Types of Bonding at the Interface

It is important to be able to control the degree of bonding between the matrix and the reinforcement. To do so, it is necessary to understand all the different possible bonding types, one or more of which may be acting at any given instant. We can conveniently classify the important types of interfacial bonding as follows:

- Mechanical bonding,
- Physical bonding,
- Chemical bonding,
  - Dissolution bonding, and
  - Reaction bonding.

4.4.1 Mechanical Bonding

Simple mechanical keying or interlocking effects between two surfaces can lead to a considerable degree of bonding. In a fiber reinforced composite, any contraction of the matrix onto a central fiber would result in a gripping of the fiber by the matrix. Imagine, for example, a situation in which the matrix in a composite radially shrinks more than the fiber on cooling from a high temperature. This would lead to a gripping of the fiber by the matrix even in the absence of any chemical bonding (Fig. 4.4). The matrix penetrating the crevices on the fiber surface, by liquid or viscous flow or high-temperature diffusion, can also lead to some mechanical bonding. In Fig. 4.4, we show a radial gripping stress, σ_r. This is related to the interfacial shear stress, τ_i, by the following expression:

$$\tau_i = \mu\sigma_r, \tag{4.6}$$

where μ is the coefficient of friction, generally between 0.1 and 0.6.

In general, mechanical bonding is a low-energy bond vis à vis a chemical bond, i.e., the strength of a mechanical bond is lower than that of a chemical bond. Work on metallic wires in metal matrices (Vennett et al. 1970; Schoene and Scala 1970)

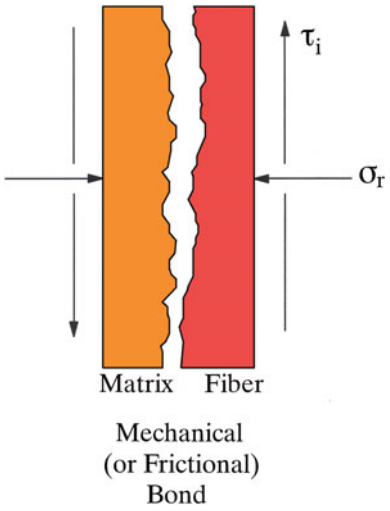

Fig. 4.4 Mechanical gripping due to radial shrinkage of a matrix in a composite on cooling from a high temperature

indicates that in the presence of interfacial compressive forces, a wetting or metallurgical bond is not quite necessary because the mechanical gripping of the fibers by the matrix is sufficient to cause an effective reinforcement, as indicated by the occurrence of multiple necking in fibers when the composite is pulled in tension. Hill et al. (1969) confirmed the mechanical bonding effects in tungsten filament/aluminum matrix composites. Chawla and Metzger (1978) studied bonding between an aluminum substrate and anodized alumina (Al_2O_3) films and found that with a rough interface a more efficient load transfer from the aluminum matrix to alumina occurred. There is only mechanical bond between Al_2O_3 and Al. Pure mechanical bonding alone is not enough in most cases. However, mechanical bonding could add, in the presence of reaction bonding, to the overall bonding. Also, mechanical bonding is efficient in load transfer when the applied force is parallel to the interface. In the case of mechanical bonding, the matrix must fill the hills and valleys on the surface of the reinforcement. Rugosity, or surface roughness, can contribute to bond strength only if the liquid matrix can wet the reinforcement surface. A good example of excellent wetting (contact angle, $\theta = 0°$) is between WC particles and cobalt liquid. If, on the other hand, the matrix, liquid polymer, or molten metal is unable to penetrate the asperities on the reinforcement (fiber or particle) surface, then the matrix will solidify and leave interfacial voids, as shown in Fig. 4.5. Examples of surface roughness contributing to interfacial strength include the following:

1. Surface treatments of carbon fibers, e.g., nitric acid oxidation of carbon fibers, which increase specific surface area and lead to good wetting in PMCs, consequently an improved interlaminar shear strength (ILSS) of the composite (see Chap. 8).

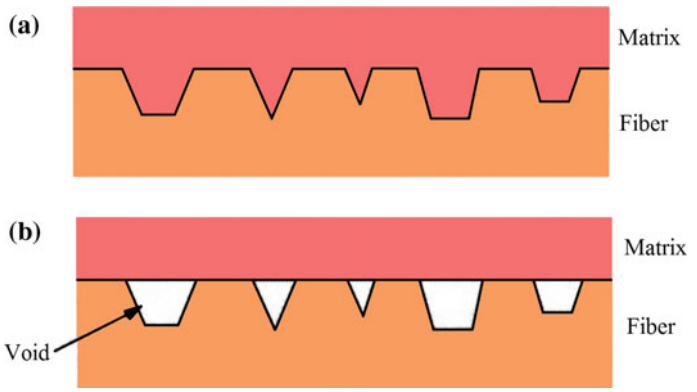

Fig. 4.5 **a** Good mechanical bond. **b** Lack of wettability can make a liquid polymer or metal unable to penetrate the asperities on the fiber surface, leading to interfacial voids

2. Most metal matrix composites will have some roughness-induced mechanical bonding between the ceramic reinforcement and the metal matrix (see Chap. 6).
3. Most CMC systems also show a mechanical gripping between the fiber and the matrix (see Chap. 7).

We can make some qualitative remarks about general interfacial characteristics that are desirable in different composites. In PMCs and MMCs, one would like to have mechanical bonding in addition to chemical bonding. In CMCs, on the other hand, it would be desirable to have mechanical bonding in lieu of chemical bonding. In any ceramic matrix composite, roughness-induced gripping at the interface is quite important. Specifically, in fiber reinforced ceramic matrix composites, interfacial roughness-induced radial stress will affect the interface debonding, the sliding friction between the fiber and the matrix during pullout of debonded fibers, and the fiber pullout length.

4.4.2 Physical Bonding

Any bonding involving weak, secondary or van der Waals forces, dipolar interactions, and hydrogen bonding can be classified as *physical bonding*. The bond energy in such physical bonding is very low, approximately 8–16 *kJ/mol*.

4.4.3 Chemical Bonding

Atomic or molecular transport, by diffusional processes, is involved in chemical bonding. Solid solution and compound formation may occur at the interface, resulting in a reinforcement/matrix interfacial reaction zone having a certain thickness. This encompasses all types of covalent, ionic, and metallic bonding. Chemical bonding involves primary forces and the bond energy is in the range of approximately 40–400 *kJ/mol*.

There are two main types of chemical bonding:

1. *Dissolution bonding*: In this case, interaction between components occurs at an electronic scale. Because these interactions are of rather short range, it is important that the components come into intimate contact on an atomic scale. This implies that surfaces should be appropriately treated to remove any impurities. Any contamination of fiber surfaces, or entrapped air or gas bubbles at the interface, will hinder the required intimate contact between the components.
2. *Reaction bonding*: In this case, a transport of molecules, atoms, or ions occurs from one or both of the components to the reaction site, that is, the interface. This atomic transport is controlled by diffusional processes. Such a bonding can exist at a variety of interfaces, e.g., glass/polymer, metal/metal, metal/ceramic, or ceramic/ceramic.

Two polymer surfaces may form a bond owing to the diffusion of matrix molecules to the molecular network of the fiber, thus forming tangled molecular bonds at the interface. Coupling agents (silanes are the most common ones) are used for glass fibers in resin matrices; see Chap. 5 for details. Surface treatments (oxidative or nonoxidative) are given to carbon fibers to be used in polymeric materials; we describe these in Chap. 5. In metallic systems, solid solution and intermetallic compound formation can occur at the interface. A schematic of the diffusion phenomenon between a fiber and a matrix resulting in a solid solution as well as a layer of an intermetallic compound, M_xF_y is shown in Fig. 4.6. The plateau region of the interfacial zone, which has a constant proportion of the two atomic species, is the region of intermetallic compound formation. The reaction products and the reaction rates can vary, depending on the matrix composition, reaction time, and temperature. Generally, one tries to fit such data to an expression of the form

$$x^2 \approx Dt, \tag{4.7}$$

where x is the thickness of the reaction zone, D is the diffusivity, and t is the time. This expression follows from the theory of diffusion in solids. The diffusivity, D, depends on the temperature in an exponential manner

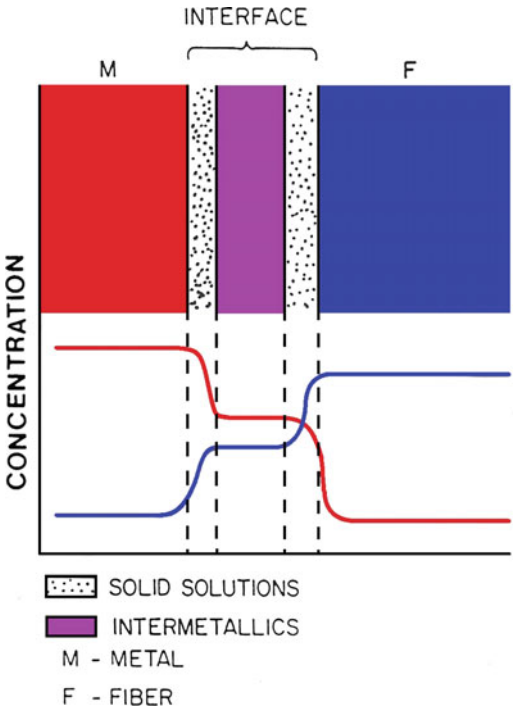

Fig. 4.6 Interface zone in a metal matrix composite showing solid solution and intermetallic compound formation

$$D = A \exp(-\Delta Q/kT), \tag{4.8}$$

where A is a preexponential constant, ΔQ is the activation energy for the rate-controlling process, k is Boltzmann's constant, and T is the temperature in kelvin. This relationship follows from the diffusion-controlled growth in an infinite diffusion couple with planar interface. For a composite containing cylindrical fibers of a small diameter, the diffusion distance is very small, i.e., the condition of an infinite diffusion couple with planar interface is not likely to be valid. However, to a first approximation, we can write

$$x^2 \approx ct, \tag{4.9}$$

where c is a pseudo-diffusivity and has the dimensions of diffusivity ($m^2 s^{-1}$). The reader should bear in mind that this approximate relationship can be expected to work for composites in which the reaction thickness is small compared to the interfiber spacing. Under these conditions, one can use an Arrhenius-type relationship, $c = B \exp(-\Delta Q/kT)$, where B is a preexponential constant. A plot of $\ell n\, c$ versus $1/T$ can be used to obtain the activation energy, ΔQ, for a fiber/matrix reaction in a given temperature range. The preexponential constant B depends on the matrix composition, fiber, and the environment.

4.5 Optimum Interfacial Bond Strength

Two general ways of obtaining an optimum interfacial bond involve treatments of fiber or reinforcement surface or modification of matrix composition. It should be emphasized that maximizing the bond strength is not always the goal. In brittle matrix composites, too strong a bond would cause embrittlement. We can illustrate the situation by examining the following three cases.

4.5.1 Very Weak Interface or Fiber Bundle (No Matrix)

This extreme situation will prevail when we have no matrix and the composite consists of only a fiber bundle. The bond strength in such a composite will only be due to interfiber friction. A statistical treatment of fiber bundle strength (see Chap. 12) shows that the fiber bundle strength is about 70 to 80% of average single fiber strength.

4.5.2 Very Strong Interface

The other extreme in interfacial strength is when the interface is as strong or stronger than the higher strength component of the composite, generally the reinforcement. In this case, of the three components—reinforcement, matrix, and interface—the interface will have the lowest strain-to-failure. The composite will fail when any cracking occurs at a weak spot along the brittle interface. Typically, in such a case, a catastrophic failure will occur, and we will have a composite with very low toughness.

4.5.3 Optimum Interfacial Bond Strength

An interface with an optimum interfacial bond strength will result in a composite with an enhanced toughness, but without a severe penalty on the strength parameters. Such a composite will have multiple failure sites, most likely spread over the interfacial area, which will result in a diffused or global spread of damage, rather than a very local damage.

4.6 Tests for Measuring Interfacial Strength

Numerous tests have been devised to characterize the fiber/matrix interface strength. We briefly describe some of these.

4.6.1 Flexural Tests

Flexural or bend tests are very easy to do and can be used to get a semi-qualitative idea of the fiber/matrix interfacial strength of a composite. There are two basic governing equations for a simple beam elastically stressed in bending:

$$\frac{M}{I} = \frac{E}{R}, \tag{4.10}$$

and

$$\frac{M}{I} = \frac{\sigma}{y}, \tag{4.11}$$

where M is the applied bending moment, I is the second moment of area of the beam section about the neutral plane, E is the Young's modulus of elasticity of the material, R is the radius of curvature of the bent beam, and σ is the tensile or compressive stress on a plane at a distance y from the neutral plane. For a uniform, circular section beam

$$I = \frac{\pi d^4}{64}, \tag{4.12}$$

where d is the diameter of the circular section beam. For a beam of a uniform, rectangular section, we have

$$I = \frac{bh^3}{12}, \tag{4.13}$$

where b is the beam width and h is the height of the beam. Bending takes place in the direction of the depth, i.e., h and y are measured in the same direction. Also, for a beam with a symmetric cross section with respect to the neutral plane, replacing y in Eq. (4.11) by $h/2$ gives the stress at the beam surface. When an elastic beam is bent, the stress and strain vary linearly with thickness, y across the section, with the neutral plane representing the zero level. The material on the outside or above the neutral plane of the bent beam is stressed in tension while that on the inside or below the neutral plane is stressed in compression. In the elastic regime, the stress and strain are related by Hooke's law

$$\sigma = E\varepsilon. \tag{4.14}$$

From Eqs. (4.10), (4.11), and (4.14), we can obtain the following simple relation valid in the elastic regime:

$$\varepsilon = \frac{y}{R}. \tag{4.15}$$

Thus, the strain ε in a beam bent to a radius of curvature R varies linearly with distance y from the neutral axis across the beam thickness. We describe some variants of flexural tests.

4.6.1.1 Three-Point Bending

The bending moment in three-point bending is given by

$$M = \frac{P}{2} \cdot \frac{S}{2} = \frac{PS}{4}, \tag{4.16}$$

where P is the load and S is the span. The important point to note is that the bending moment in a three-point bend test increases from the two extremities of the beam to a maximum value at the midpoint, i.e., the maximum stress is reached along a line at the center of the beam. From Eqs. (4.11), (4.13), and (4.16), and taking $y = h/2$, we get the following expression for the maximum stress for a rectangular beam in three-point bending:

$$\sigma = \frac{6PS}{4bh^2} = \frac{3PS}{2bh^2}, \tag{4.17}$$

where b and h are breadth and height of the beam. We can have the fibers running parallel or perpendicular to the specimen length. When the fibers are running perpendicular to the specimen length, we obtain a measure of transverse strength of the fiber/matrix interface.

The shear stress in a three-point bend test is constant. The maximum in shear stress, τ_{max} will correspond to the maximum in load P_{max} and is given by

$$\tau_{max} = \frac{3P_{max}}{4bh}. \tag{4.18}$$

4.6.1.2 Four-Point Bending

This is also called *pure bending* because there are no transverse shear stresses on the cross sections of the beam between the two inner loading points. For an elastic

beam bent in four-point, the bending moment increases from zero at the two extremities to a constant value over the inner span length. This bending moment in four-point is given by

$$M = \frac{P}{2} \cdot \frac{S}{4} = \frac{PS}{8}, \tag{4.19}$$

where S is the outer span and the stress can be written as

$$\sigma = \frac{6PS}{8bh^2} = \frac{3PS}{4bh^2}. \tag{4.20}$$

4.6.1.3 Short-Beam Shear Test (Interlaminar Shear Stress Test)

This test is a special longitudinal three-point bend test with fibers parallel to the length of the bend bar and the length of the bar being very small. It is also known as the *i*nter*l*aminar *s*hear *s*trength (ILSS) test. The maximum shear stress, τ, occurs at the midplane and is given by Eq. (4.18). The maximum tensile stress occurs at the outermost surface and is given by Eq. (4.17). Dividing Eq. (4.18) by Eq. (4.17), we get

$$\frac{\tau}{\sigma} = \frac{h}{2S}. \tag{4.21}$$

Equation (4.21) says that if we *make the load span, S, very small*, we will maximize the shear stress, τ, so that the specimen fails under shear with a crack running along the midplane. Hence, sometimes we call this test as the short-beam shear test.

The reader should bear in mind that the interpretation of this test is not straightforward. Clearly, the test becomes invalid if the fibers fail in tension before shear-induced failure occurs. The test will also be invalid if shear and tensile failure occurs simultaneously. It is advisable to make an examination of the fracture surface after the test and ensure that the crack is along the interface and not through the matrix. There is an ASTM standard for this test: D2344. Among the advantages of this test are the following:

- Simple test, short span ($S = 5\ h$).
- Easy specimen preparation.
- Good for qualitative assessment of interfacial coatings.

The main disadvantages of this test are the following:

- Meaningful quantitative results on the fiber/matrix interface strength are difficult to obtain.
- It is difficult to ensure a pure shear failure along the interface.

4.6.1.4 Iosipescu Shear Test

This is a special test devised for measuring interfacial shear strength (Iosipescu 1967). In this test, a double-edged notched specimen is subjected to two opposing force couples. This is a special type of four-point bend test in which the rollers are offset, as shown in Fig. 4.7, to accentuate the shear deformation. A state of almost pure and constant shear stress is obtained across the section between the notches by selecting a proper notch angle (90°) and notch depth (22% of full width). The average shear stress in this configuration is given by

$$\tau = \frac{P}{bh}, \tag{4.22}$$

where the symbols have the usual significance. The main advantage of this test is that a large region of uniform shear is obtained vis à vis other tests. However, there can be a substantial stress concentration near the notch tip in orthotropic (not so in isotropic materials) such as fiber reinforced composites. The stress concentration is proportional to the fiber orientation and the fiber volume fraction.

4.6.2 Single Fiber Pullout Tests

Single fiber pullout and pushout tests have been devised to measure interfacial characteristics. These tests result in a peak load corresponding to fiber/matrix

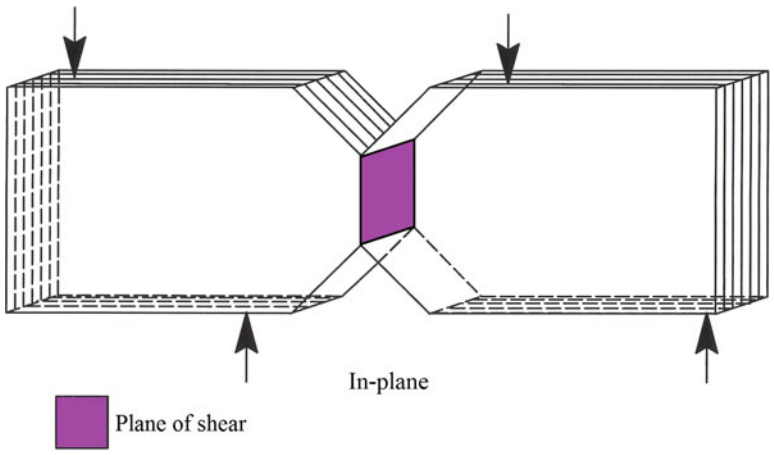

Fig. 4.7 A special type of four-point bend test, called the Iosipescu test, in which the rollers (position indicated by arrows) are offset to accentuate the shear deformation

debonding and a frictional load corresponding to the fiber pullout from the matrix. The mechanics and interpretation of these tests are rather involved, and knowledge of the underlying assumptions is important in order to get useful information from such tests. We describe the salient features of these tests.

These tests can provide useful information about the interface strength in model composite systems. They are not very helpful in the case of commercially available composites. One must also carefully avoid any fiber misalignment and introduction of bending moments. The mechanics of the single fiber pullout test are rather complicated (Chamis 1974; Penn and Lee 1989; Kerans et al. 1989; Marshall et al. 1992; Kerans and Parthasarathy 1991).

The fabrication of the single fiber pullout test sample is often the most difficult part; it entails embedding a part of the single fiber in the matrix. A modified variation of this simple method is to embed both ends of the single fiber in the matrix material, leaving the center region of the fiber uncovered. In all of these methods, the fiber is pulled out of the matrix in a tensile testing machine and a load versus displacement record is obtained.

The peak load corresponds to the initial debonding of the interface. This is followed by frictional sliding at the interface, and finally by the fiber pullout from the matrix, during which a steady decrease in the load versus displacement curve is observed. The steady decrease in the load is attributed to the decreasing area of the interface as the fiber is pulled out. Thus, the test simulates the fiber pullout that may occur in an actual composite, and more importantly, provides the bond strength and frictional stress values.

The effect of different Poisson's contractions of fiber and matrix can result in a radial tensile stress at the interface (see Chap. 10). The radial tensile stress will no doubt aid the fiber/matrix debonding process. The effect of Poisson's contraction, together with the fact that the imposed shear stress is not constant along the interface, complicates the analysis of the fiber pullout test.

These tests, however, can provide useful quantitative information about the interface strength in model composite systems. One must also carefully avoid any fiber misalignment and introduction of bending moments. Figure 4.8a shows the experimental setup for such a test. A portion of fiber, length l, is embedded in a matrix and a pulling tensile force is applied as shown. If we measure the stress required to pull the fiber out of the matrix as a function of the embedded fiber length, we get the plot shown in Fig. 4.8b. The stress required to pull the fiber out, without breaking it, increases linearly with the embedded fiber length, up to a critical length, l_c. At embedded fiber lengths greater than or equal to l_c, the fiber will fracture under the action of the tensile stress, σ, acting on the fiber. Consider Fig. 4.8a again. The tensile stress, σ, acting on the fiber results in a shear stress, τ, at the fiber/matrix interface. A simple force balance along the fiber length gives

$$\sigma\pi r^2 = \tau 2\pi r l.$$

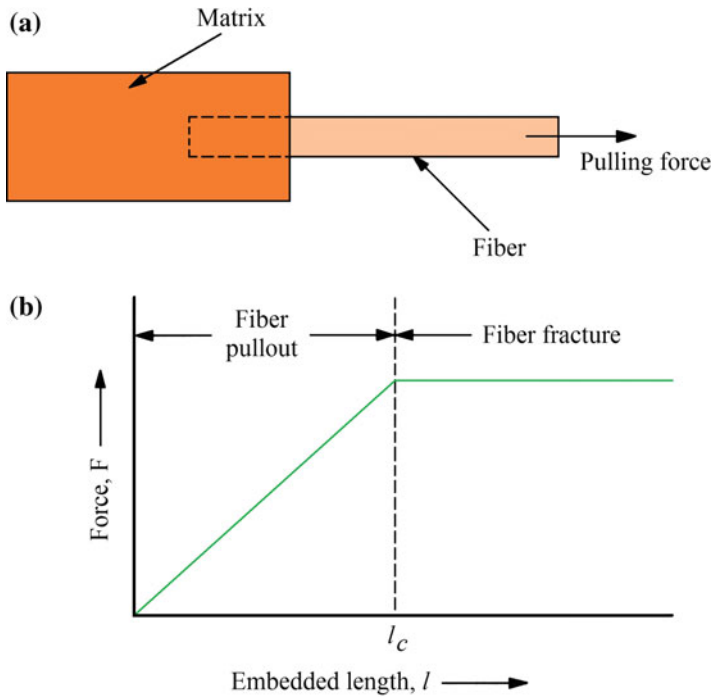

Fig. 4.8 **a** An experimental setup for a single fiber pullout test. A portion of fiber, length l, is embedded in a matrix and a pulling tensile force is applied as shown. **b** The stress required to pull the fiber out of the matrix as a function of the embedded fiber length

For $l < l_c$, the fiber is pulled out and the interfacial shear strength is given by

$$\tau = \frac{\sigma r}{2l}. \tag{4.27}$$

At $l > l_c$, fiber failure rather than pullout occurs. One measures the load required to debond as a function of the embedded fiber length. Then we can write

$$P = 2\pi r l \tau. \tag{4.28}$$

And the interfacial shear strength, τ, can be calculated from the slope of the P versus l. There is an implicit assumption in this analysis, viz., the shear stress acting along the fiber/matrix interface is a constant. In a single fiber embedded test, one obtains the average load value over the entire interfacial surface area to get the interfacial debond strength and/or frictional strength. Analytical and finite element analyses show that the shear stress is a maximum close to the surface ends and falls rapidly within a distance of a few fiber diameters. Thus, one would expect the interface debonding to start near the surface and progressively propagate along the embedded length.

The interfacial shear strength is a function of the coefficient of friction, μ, and any normal compressive stress at the interface, σ_r. The source of radial compressive stress is the shrinkage of the matrix during cooling from the processing temperature.

4.6.3 Curved Neck Specimen Test

This technique was devised for PMCs. A special mold is used to prepare a curved neck specimen of the composite containing a single fiber along its central axis. The specimen is compressed and the fiber/matrix debonding is observed visually. The curved neck shape of the specimen enhances the transverse tensile stress at the fiber/matrix interface. The transverse tensile stress leading to interface debonding results from the fact that the matrix and the fiber have different Poisson's ratios. If the matrix Poisson ratio, v_m, is greater than that of the fiber, v_f, then on compression, there will result a transverse tensile stress at the center of the neck and perpendicular to the interface whose *magnitude* is given by (Broutman 1969)

$$\sigma_i = \frac{\sigma\left(v_m - v_f\right)E_f}{\left[(1+v_m)E_f + \left(1 - v_f - 2v_f^2\right)E_m\right]}, \tag{4.29}$$

where σ is the net section compressive stress (i.e., load/minimum area), E is the Young's modulus, v is the Poisson's ratio, and the subscripts f and m denote fiber and matrix, respectively. Note the expression in Eq. (4.29) gives the magnitude of tensile stress developed perpendicular to the interface when the sample is subjected to a compressive load.

One can measure the net section stress, σ, corresponding to interface debonding and compute the interfacial tensile strength from Eq. (4.29). There are some important points that should be taken into account when using this test. One needs a special mold to prepare the specimen, and a very precise alignment of the fiber along the central axis is a must. Finally, a visual examination is required to determine the interface debonding point. This would limit the technique to transparent matrix materials. Acoustic emission detection techniques may be used to avoid visual examination.

4.6.4 Instrumented Indentation Tests

Many instrumented indentation tests have been developed that allow extremely small forces and displacements to be measured. Indentation instruments have been in use for hardness measurement for quite a long time, but depth sensing instruments with high resolution became available in the 1980s (Doerner and Nix 1986; Ferber et al. 1993, 1995; Janczak et al. 1997). Such instruments allow very small

volumes of a material to be studied, and a very local characterization of microstructural variations is possible by mechanical means. Such an instrument records the total penetration of an indenter into the sample. The indenter position is determined by a capacitance displacement gage. Pointed or conical or rounded indenters can be used to displace a fiber aligned perpendicular to the composite surface. Figure 4.9 shows three different types of indenters available commercially: cylindrical with a flat end, conical with a flat end, and pointed with a flat end. An example of fiber pushin is shown in a series of four photographs in Fig. 4.10. By measuring the applied force and displacement, interfacial stress can be obtained. The indenter can be moved toward the sample or away from the sample by means of a magnetic coil assembly. Such instruments are available commercially. One special instrument (Touchstone Res. Lab., Tridelphia, WV) combines an indentation system within the chamber of an SEM. Such an instrument combines the material characterization ability of an SEM with a fiber pushout apparatus. Commonly, some assumptions are made in making an interpretation of an indentation test to determine the strength characteristics of the interface region. For example:

1. Any elastic depression of the matrix adjacent to the fiber is negligible.
2. There are no surface stress concentrations.
3. There is no change in the fiber diameter due to the Poisson expansion during compression of the fiber.
4. There are no residual stresses.

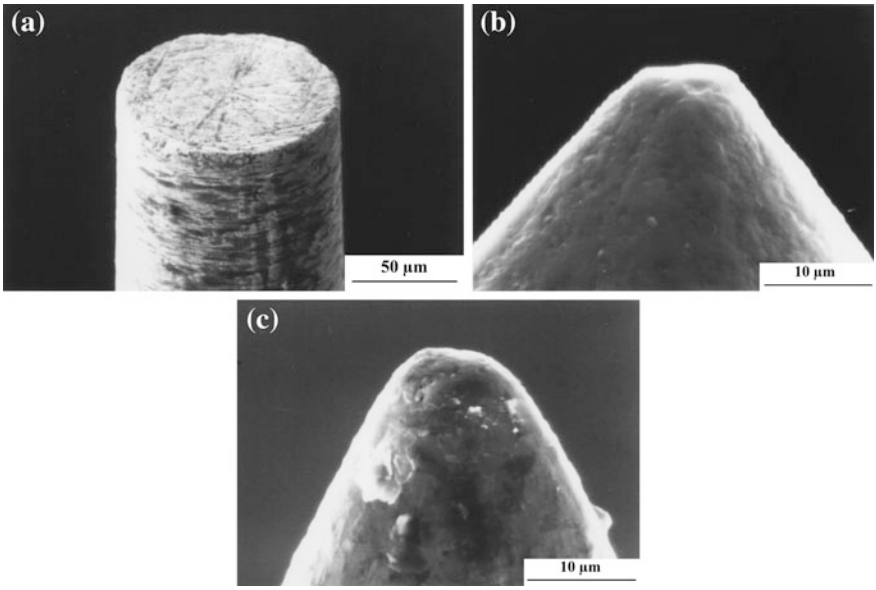

Fig. 4.9 Three different types of indenters: cylindrical with a flat end, conical with a flat end, and pointed (Courtesy of J. Janczak-Rusch and L. Rohr)

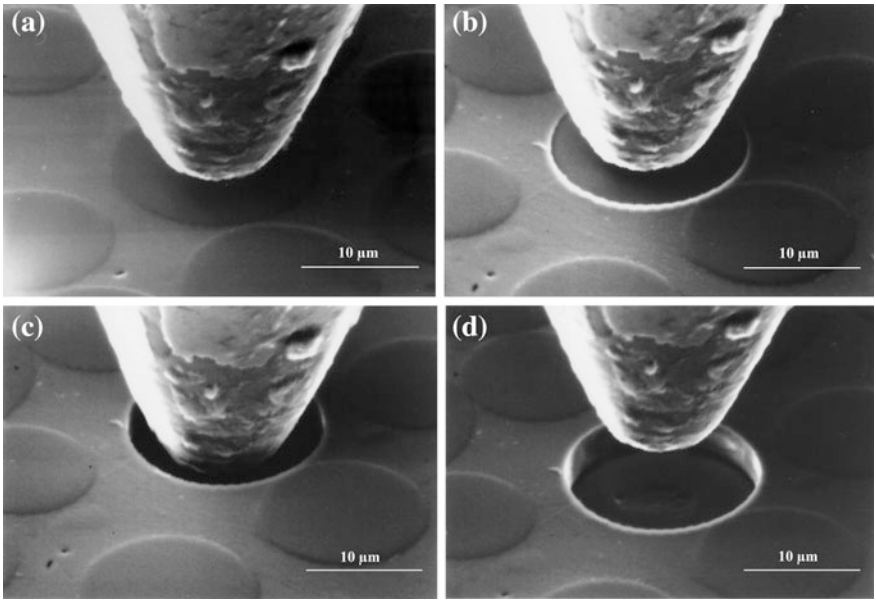

Fig. 4.10 An example of fiber pushin is shown in a series of four photographs, counterclockwise from top left (Courtesy of J. Janczak-Rusch and L. Rohr)

The specimen thickness must be large compared to the fiber diameter for these assumptions to be valid.

Many methods involving the pressing of an indenter on a fiber cross section have been devised for measuring the interfacial bond strength in a fiber reinforced composite. The pushout test uses a thin specimen (1–3 *mm*), with the fibers aligned perpendicular to the viewing surface. The indenter is used to push a series of fibers out. Such a fiber pushout test can give the frictional shear stress, τ, acting at the fiber/matrix interface. An example of a valid pushout test, showing a three-region curve, is shown in Fig. 4.11. In the first region, the indenter is in the contact with the fiber and the fiber sliding is less than the specimen thickness t. This is followed by a horizontal region in which fiber sliding length is greater than or equal to the sample thickness. In the third region, the indenter comes in contact with the matrix. In the horizontal region, the interfacial shear stress is given by

$$\tau_i = \frac{P}{2\pi r t},$$

where P is the applied load, r is the fiber radius, and t is the specimen thickness. The specimen thickness should be much greater than the fiber diameter for this relationship to be valid. In the third region of Fig. 4.11, the value of the interfacial

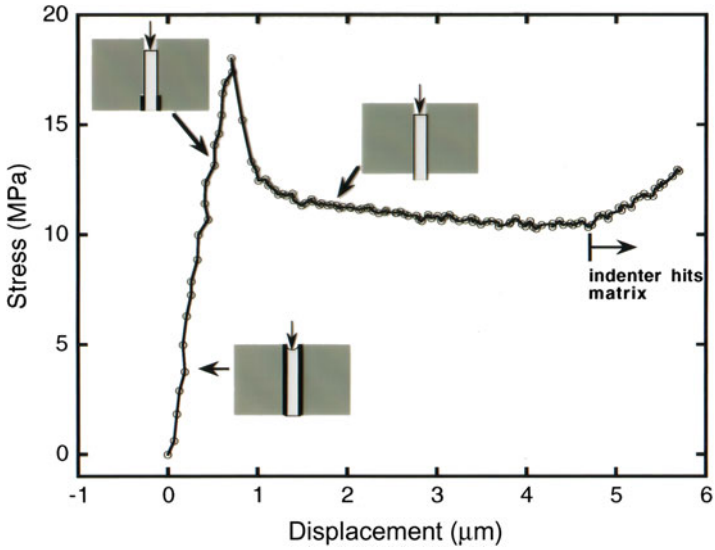

Fig. 4.11 Stress versus displacement obtained in fiber pushout test. (Chawla et al. 2001)

shear stress cannot be determined because the indenter comes in contact with the matrix, i.e., the test is no more valid.

In such indentation tests, after interfacial debonding, the fiber will slide along the interface over a distance that is dependent on the load applied by the indenter. The fiber is elastically compressed by the indenter load over the debonded length, which is assumed to be dependent on the interfacial friction. The axial load on the indenter is assumed to be balanced by the frictional stress at the interface, and the effect of radial expansion during indentation is neglected. There are two analytical models due to Kerans and Parthasarathy (1991) and Hsueh (1992) that take into account progressive debonding and sliding during fiber pushin and pushout. Radial and axial stresses are taken into account in both models and Coulombic friction is assumed at the fiber/matrix interface. Lara-Curzio and Ferber (1994) found that the two models gave almost identical results in Nicalon fiber/calcium aluminosilicate matrix composites.

An instrumented indentation test to be used at high temperature was developed by Eldridge (1995). Such a test is very useful for CMCs. Such a test is also useful to analyze the effect of residual stresses.

4.6.5 Fragmentation Test

In this test, a single fiber is embedded in a dog-bone-type tensile sample of matrix. When a tensile load is applied to such a sample, the load is transferred to the fiber

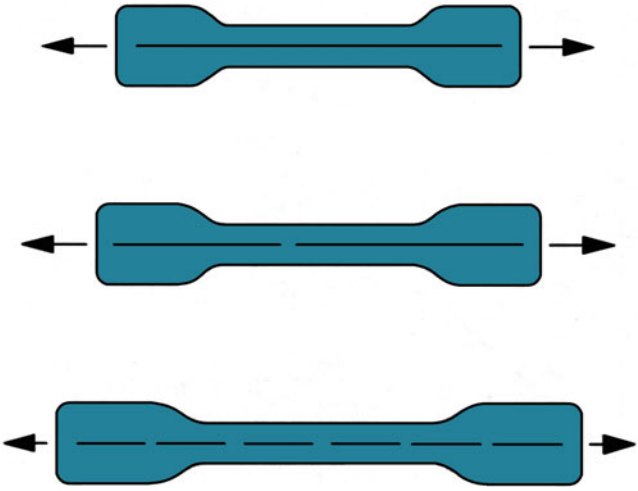

Fig. 4.12 A single fiber fragmentation test. On loading the composite, the load is transferred to the fiber and on continued loading it fragments into smaller pieces until the fiber fragment length becomes too small to enable loading it to fracture

via shear strains and stresses produced on planes parallel to the fiber/matrix interface. We discuss this subject of load transfer in fiber reinforced composites in Chap. 10. When the tensile stress in the fiber reaches its ultimate strength, it fragments into two parts. If we continue loading, this process of fiber fragmentation continues, i.e., the single fiber continues to fragment into even smaller pieces until the fiber fragment length becomes too small to enable loading it to fracture. This fiber length is called the *critical length,* l_c. This is shown schematically in Fig. 4.12. From a consideration of equilibrium of forces over an element dx of the fiber (see Chap. 10 also), we can write

$$\begin{array}{c} \pi r^2 d\sigma = 2\pi r\, dx\, \tau \\ d\sigma/dx = 2\tau/r \end{array} . \tag{4.30}$$

From Eq. (4.30), we obtain the critical length as follows. For simplicity, we consider that the matrix is perfectly plastic, i.e., we ignore any strain hardening effects and that the matrix yields in shear at shear stress of τ_y. We also assume that the shear stress along the fiber/matrix interface is constant over the length of the fiber fragment, l_c. Integrating Eq. (4.30), we get

$$\int_0^{\sigma_{\max}} d\sigma = \int_0^{l_c/2} 2\tau\, dx/r, \qquad \sigma^{\max} = \tau l_c/r \tag{4.31}$$

or

$$\tau = \sigma^{\max} r/l_c = \sigma^{\max} d/2l_c. \tag{4.32}$$

The fiber fragmentation technique is a simple technique that gives us a quantitative measure of the fiber/matrix interfacial strength. Drzal et al. (1983, 1994, 1997) and others have used this technique extensively to characterize carbon fiber reinforced polymer matrix composites. Clearly, a transparent matrix is required. The technique will work only if the fiber failure strain is less than that of the matrix, which is commonly true. The major shortcoming or the doubtful assumption is that the interfacial shear stress is constant over the fiber length. In addition, the real material is rarely perfectly plastic.

4.6.6 Laser Spallation Technique

Gupta et al. (1990, 1992) devised a laser spallation technique to determine the tensile strength of a planar interface between a coating (thickness > 0.5 μm) and a substrate. Figure 4.13 shows their experimental setup. A collimated laser pulse impinges on a thin film sandwiched between the substrate and a confining plate. This plate is made of fused quartz, which is transparent to Nd: YAG laser (wavelength = 1.06 μm). An aluminum film is used as the laser-absorbing medium. Absorption of the laser energy in the constrained aluminum film causes a sudden expansion of the film, which produces a compressive shock wave in the substrate that moves toward the coating/substrate interface. When the compression pulse hits the interface, part of it is transmitted into the coating. This compressive pulse is reflected into a tensile pulse at the free surface of the coating. If this tensile pulse is of a sufficient magnitude, it will remove the coating from the substrate. A laser Doppler displacement interferometer is used to record the time rate of change of the displacement of the coating free surface as the compressive pulse is reflected. By means of a sophisticated digitizer equipment, it is possible to obtain a time resolution of about 0.5 *ns* for recording displacement fringes. This information is then related to the stress pulse history at the interface. A direct recording of the stress pulse makes this technique useful for interface systems involving ductile components. It is a complex technique and gives the strength of flat interface.

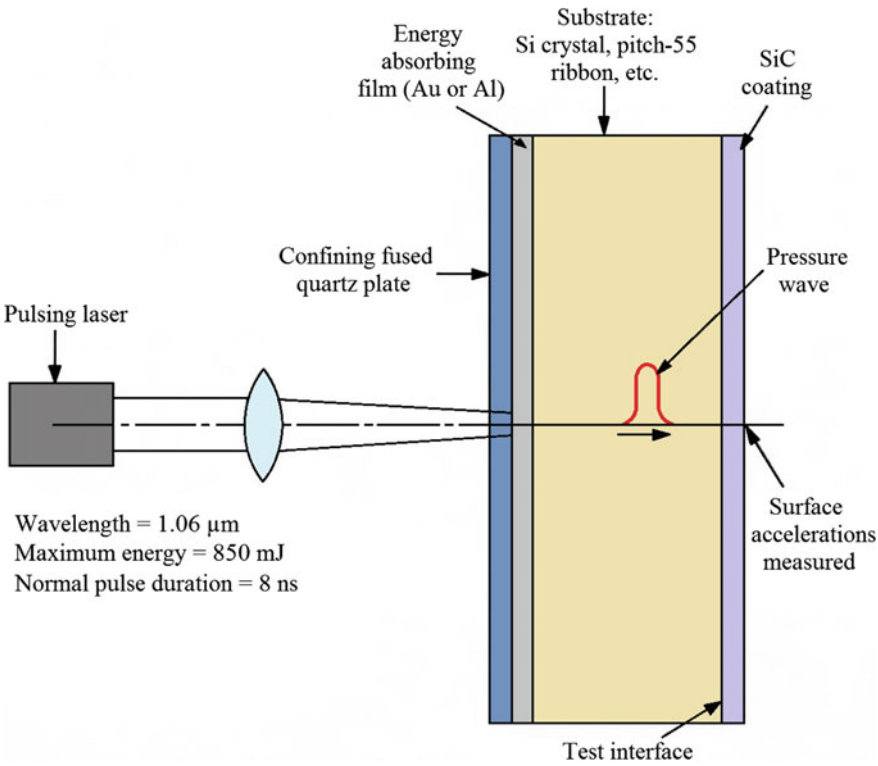

Fig. 4.13 Experimental setup for a laser spallation test. A collimated laser pulse impinges on a thin film sandwiched between the substrate and a confining plate. Absorption of the laser energy in the constrained aluminum film causes a sudden expansion of the film, which produces a compressive shock wave in the substrate that moves toward the coating/substrate interface. This compressive pulse is reflected into a tensile pulse at the free surface of the coating

Problems

4.1. Describe some techniques for measuring interfacial energies in different composite systems.

4.2. In order to study the interfacial reactions between the fiber and matrix, oftentimes one uses very high temperatures in order to reduce the time necessary for the experiment. What are the objections to such accelerated tests?

4.3. What are the objections to the use of short-beam shear test to measure the interlaminar shear strength (ILSS)?

4.4. Diffusion along free surface is faster than in the bulk of a material. Similarly, diffusion along a grain boundary is faster than in the lattice. Taking these factors into account, write expressions for diffusion coefficients, in descending order, for diffusion along lattice, dislocation, grain boundary, reinforcement/matrix interface, and surface. Explain the reason behind your answer.

4.5 Discuss the importance of moisture diffusion in fiber reinforced polymer matrix composites. Recall that moisture absorption in PMCs is largely due to the permeability of the polymer matrix. Suggest some possible effects of moisture absorption in fiber reinforced PMCs in terms of effects on different moduli (along the fiber and perpendicular to the fiber) and ILSS.

References

S.M. Allen, J.W. Cahn, Acta. Met. **27**, 1085–1095 (1979)
R.J. Arsenault, R.M. Fisher, Scripta Met. **17**, 67 (1983)
R.E. Baier, E.G. Sharfin, W.A. Zisman, Science **162**, 1360 (1968)
L.J. Broutman, *Interfaces in Composites*. ASTM STP No. 452 (American Society of Testing & Materials, Philadelphia, 1969)
J.W. Cahn, R.E. Hanneman, Surf. Sci. **1**, 387 (1964)
A.B.D. Cassie, S. Baxter, Trans. Faraday Soc. **40**, 546 (1944)
C.C. Chamis, *Composite Materials*, vol. 6 (Academic Press, New York, 1974), p. 32
K. Chawla, S. Lee, B.P. Lee, J.L. Dalsin, P.B. Messersmith, N.D. Spencer, J. Biomed. Mater. Res. A **90**, 742 (2009)
K.K. Chawla, Compos. Interfaces **4**, 287 (1997)
K.K. Chawla, M. Metzger, J. Mater. Sci. **7**, 34 (1972)
K.K. Chawla, M. Metzger, *Advances in Research on Strength and Fracture of Materials*, vol. 3 (Pergamon Press, New York, 1978), p. 1039
K.K. Chawla, Z.R. Xu, *High Performance Composites: Commonalty of Phenomena* (PA, TMS, Warrendale, 1994), p. 207
K.K. Chawla, Z.R. Xu, J.-S. Ha, E. Lara-Curzio, M.K. Ferber, S. Russ, *Advances in Ceramic Matrix Composites II* (American Ceramic Society, Westerville, OH, 1995), p. 779
K.K. Chawla, Z.R. Xu, A. Hlinak, Y.-W. Chung, *Advances in Ceramic-Matrix Composites* (American Ceramic Society, 1993), p. 725
N. Chawla, K.K. Chawla, M. Koopman, B. Patel, C. Coffin, J. Eldridge, Composites Sci. Tech. **61**, 1923 (2001)
M.F. Doerner, W.D. Nix, J. Mater. Res. **1**, 601 (1986)
L.T. Drzal, M. Madhukar, M. Waterbury, Compos. Sci. Tech. **27**, 65–71 (1994)
L.T. Drzal, M.J. Rich, P.F. Lloyd, J. Adhesion **16**, 1–30 (1983)
L.T. Drzal, N. Sugiura, D. Hook, Compos. Interfaces **4**, 337 (1997)
J.I. Eldridge, *Materials Research Society Symposium Proceedings*, vol. 365 (Materials Research Society, 1995), p. 283
M.K. Ferber, A.A. Wereszczak, L. Riester, R.A. Lowden, K.K. Chawla, *Ceramic Engineering* and *Science Proceeding* (American Ceramic Society, Westerville, OH, 1993)
M.K. Ferber, E. Lara-Curzio, S. Russ, K.K. Chawla, *Ceramic Matrix Composites—Advanced High-Temperature Structural Materials* (Materials Research Society, Pittsburgh, PA, 1995), p. 277
M.E. Fine, R. Mitra, K.K. Chawla, Scripta Met. et Mater. **29**, 221 (1993)
V. Gupta, A.S. Argon, J.A. Cornie, D.M. Parks, Mater. Sci. Eng., A **126**, 105 (1990)
V. Gupta, A.S. Argon, J.A. Cornie, D.M. Parks, J. Mech. Phys. Solids **4**, 141 (1992)
R.G. Hill, R.P. Nelson, C.L. Hellerich, *Proceedings of the Refractory Working Group Meeting* (Seattle, WA, 1969), Oct
C.-H. Hsueh, J. Am. Ceram Soc. **76**, 3041 (1992)
N. Iosipescu, J. Mater. **2**, 537 (1967)
J. Janczak, G. Bürki, L. Rohr, Key Eng. Mater. **127**, 623 (1997)

I. Jangehud, A.M. Serrano, R.K. Eby, M.A. Meador, *Proceedings 21st Biennial Conference on Carbon* (Buffalo, NY, 1993), June 13–18
R.E. Johnson, J. Phys. Chem. **63**, 1655 (1959)
R.J. Kerans, R.S. Hays, N.J. Pagano, T.A. Parthasarathy, Amer. Cer. Soc. Bull. **68**, 429 (1989)
R.J. Kerans, T.A. Parthasarathy, J. Amer. Cer. Soc. **74**, 1585 (1991)
E. Lara-Curzio, M.K. Ferber, J. Mater. Sci. **29**, 6158 (1994)
D.B. Marshall, M.C. Shaw, W.L. Morris, Acta Met et Mater **40**, 443 (1992)
L.S. Penn, S.M. Lee, J. Comp. Tech. Res. **11**, 23 (1989)
C. Schoene, E. Scala, Met. Trans. **1**, 3466 (1970)
R.M. Vennett, S.M. Wolf, A.P. Levitt, Met. Trans. **1**, 1569 (1970)
M. Vogelsang, R.J. Arsenault, R.M. Fisher, Met. Trans. A **17**, 379 (1986)
J.L. Walter, H.E. Cline, E. Koch, Trans. AIME **245**, 2073 (1969)
R.N. Wenzel, Ind. Eng. Chem. **28**, 987 (1936)

Suggested Reading

D.F. Adams, L.A. Carlsson, R.B. Pipes, *Experimental Characterization of Advanced Composite Materials*, 3rd edn. (CRC Press, Boca Raton, Fl, 2003)
K.T. Faber, Annu. Rev. Mater. Sci. **27**, 499 (1997)
J.-K. Kim, Y.-W. Mai, *Engineered Interfaces in Fiber Reinforced Composites* (Elsevier, New York, 1998)
E.P. Plueddemann (ed.), *Interfaces in polymer matrix composites*, vol. 6 of the series Composite Materials (Academic Press, New York, 1974)
R.J. Stokes, D.F. Evans, *Fundmentals of Interfacial Engineering* (Wiley-VCH, New York, 1997)
H.D. Wagner, G. Marom (ed.), *Composite Interfaces (Special Issue—Selected Papers from the Sixth International Conference on Composite Interfaces (ICCI-6), Israel)* (VSP, Zeist, The Netherlands, 1997)

Part II

Chapter 5
Polymer Matrix Composites

Polymer matrix composites (PMCs) have established themselves as engineering structural materials, not just as laboratory curiosities or cheap stuff for making chairs and tables. This came about not only because of the introduction of high performance fibers such as carbon, boron, and aramid, but also because of some new and improved matrix materials (see Chap. 3). Nevertheless, glass fiber reinforced polymers represent the largest class of PMCs. Carbon fiber reinforced PMCs are perhaps the most important structural composites, especially in the aerospace field. In this chapter, we discuss polymer composite systems containing glass, aramid, polyethylene, boron, and carbon fibers.

5.1 Processing of PMCs

Many techniques, originally developed for making glass fiber reinforced polymer matrix composites can also be used with other fibers. Glass fiber reinforced polymer composites represent the largest class of PMCs. As we saw in Chap. 3, polymeric matrix materials can be conveniently classified as thermosets and thermoplastics. Recall that thermosets harden on curing. Curing or crosslinking occurs in thermosets by appropriate chemical agents and/or application of heat and pressure. Conventionally, thermal energy (heating to 200 $^{\circ}C$ or above) is provided for this purpose. This process, however, brings in the problems of thermal gradients, residual stresses, and long curing times. Residual stresses can cause serious problems in nonsymmetric or very thick PMC laminates, where they may be relieved by warping of the laminate, fiber waviness, matrix microcracking, and ply delamination. We mentioned electron beam curing in Chap. 3. Electron beam curing offers an alternative that avoids these problems. It is a non-thermal curing process that requires much shorter cure time cycles. Curing by electron beam occurs by electron-initiated reactions at a selectable cure temperature. We describe different

K. K. Chawla, *Composite Materials*,
https://doi.org/10.1007/978-3-030-28983-6_5

methods of fabrication of polymer matrix composites—first thermoset-based composites and then thermoplastic-based composites.

5.1.1 Processing of Thermoset Matrix Composites

There are many processing methods for composites with thermoset matrix materials including epoxy, unsaturated polyester, and vinyl ester.

5.1.1.1 Hand Layup and Spray Techniques

Hand layup and spray techniques are perhaps the simplest polymer processing techniques. Fibers can be laid onto a mold by hand and the resin (unsaturated polyester is one of the most common) is sprayed or brushed on. Frequently, resin and fibers (chopped) are sprayed together onto the mold surface. In both cases, the deposited layers are densified with rollers. Figure 5.1 shows schematics of these processes. Accelerators and catalysts are frequently used. Curing may be done at room temperature or at a moderately high temperature in an oven.

5.1.1.2 Filament Winding

Filament winding (Shibley 1982; Tarnopol'skii and Bail' 1983) is another very versatile technique in which a continuous tow or roving is passed through a resin impregnation bath and wound over a rotating or stationary mandrel. A roving consists of thousands of individual filaments. Figure 5.2a shows a schematic of this process, while Fig. 5.2b shows a pressure vessel made by filament winding. The winding of roving can be polar (hoop) or helical. In polar winding, the fiber tows do not cross over, while in the helical they do. The helix angle depends on the shape of the object to be made. Successive layers are laid on at a constant or varying angle until the desired thickness is attained. Curing of the thermosetting resin is done at an elevated temperature and the mandrel is removed. Very large cylindrical (e.g., pipes) and spherical (e.g., for chemical storage) vessels are built by filament winding. Glass, carbon, and aramid fibers are routinely used with epoxy, polyester, and vinyl ester resins for producing filament wound shapes.

There are two types of filament winding processes: wet winding and prepreg winding. In wet winding, a low viscosity resin is applied to the filaments during the winding process. Polyesters and epoxies with viscosity less than 2 *Pas* (2000 *cP*) are used in wet winding. In prepreg winding, a hot-melt or solvent-dip process is

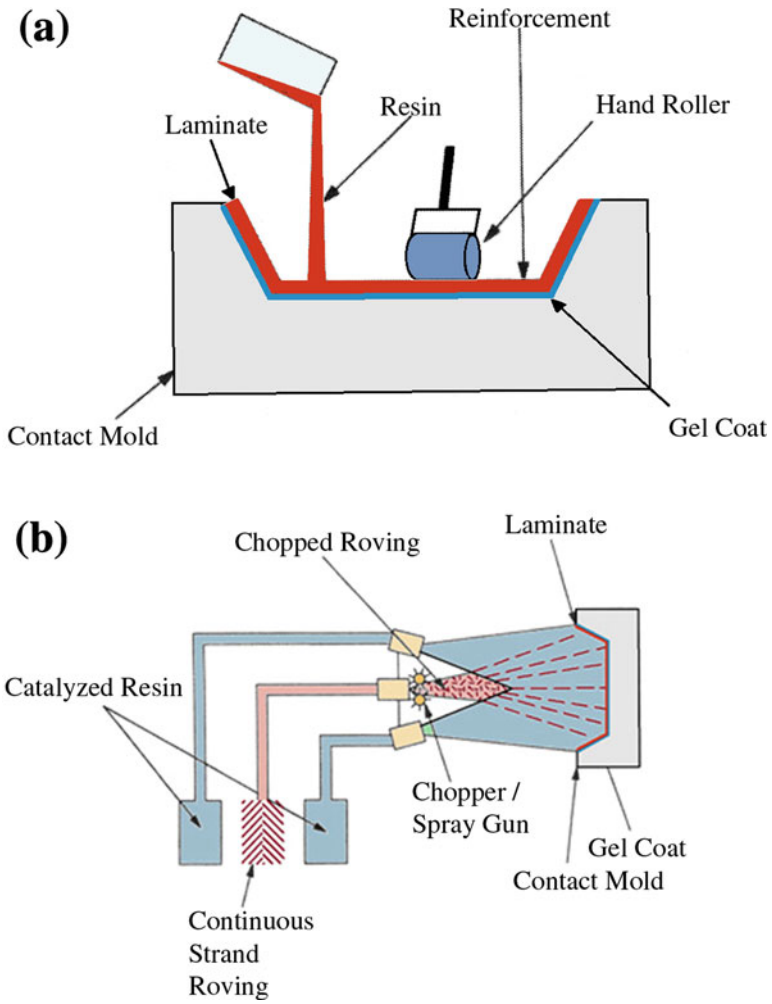

Fig. 5.1 **a** In hand layup, fibers are laid onto a mold by hand, and the resin is sprayed or brushed on. **b** In spray-up, resin and fibers (chopped) are sprayed together onto the mold surface

used to preimpregnate the fibers. Rigid amines, novolacs, polyimides, and higher viscosity epoxies are generally used for this process. In filament winding, the most probable void sites are roving crossovers and regions between layers with different fiber orientations.

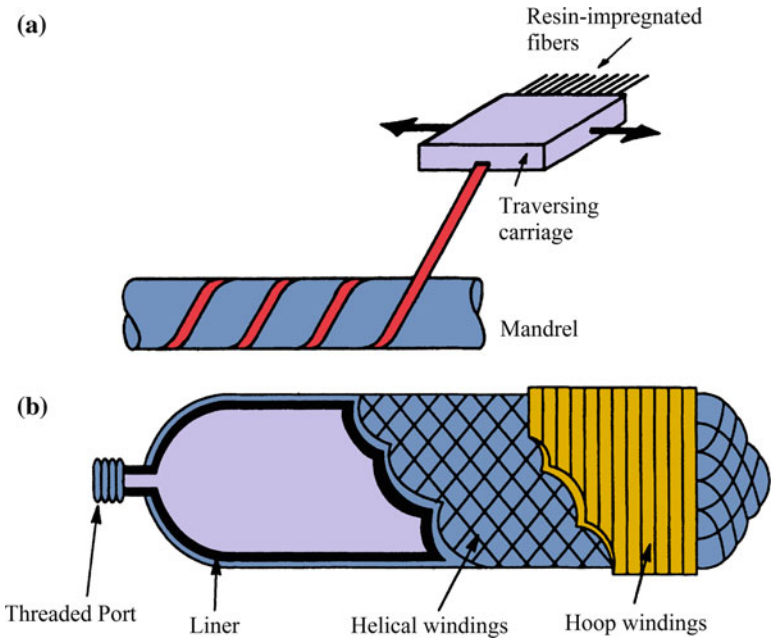

Fig. 5.2 **a** Schematic of filament winding process. **b** Schematic of a filament wound pressure vessel with a liner; helical and hoop winding are shown

5.1.1.3 Pultrusion

In this process, continuous sections of polymer matrix composites with fibers oriented mainly axially are produced. Figure 5.3a shows a schematic of this process. Continuous fiber tows come from various creels. Mat or biaxial fabric may be added to these to provide some transverse strength. These are passed through a resin bath containing a catalyst. After this, the resin impregnated fibers pass through a series of wipers to remove any excess polymer and then through a collimator before entering the heated die. A thorough wet out of the rovings is very important. Stripped excess resin is recirculated to the resin bath. The heated die has the shape of the finished component to be produced. The resin is cured in the die and the composite is pulled out. At the end of the line, the part is cut by a flying saw to a fixed length. Typically, the process can produce continuously at a rate of 10–200 *cm/min*. The exact speed depends on the resin type and the cross-sectional thickness of the part being produced. Pultruded profiles as wide as 1.25 *m* with more than 60% fiber volume fraction can be made routinely. An example of a product obtained by pultrusion is shown in Fig. 5.3b. The hollow trapezoidal-shaped product shown is a helicopter windshield post made of carbon fiber mat and tows in a high temperature vinyl ester resin matrix.

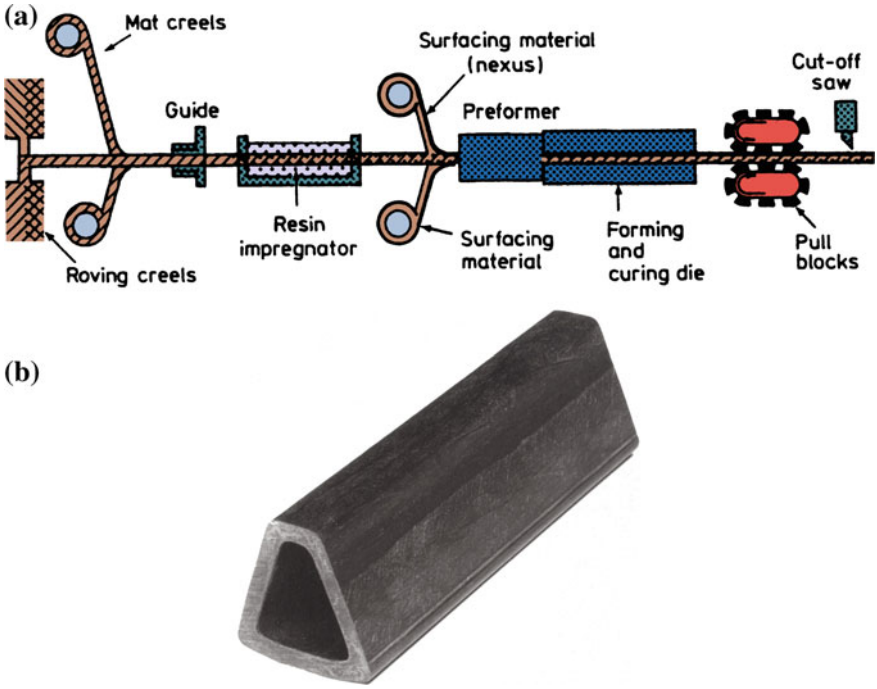

Fig. 5.3 **a** Schematic of the pultrusion process. (Courtesy of Morrison Molded Fiber Glass Co.) **b** A helicopter windshield post made of carbon fibers/vinyl ester resin by pultrusion. The post is 1.5 *m* long. (Courtesy of Morrison Molded Fiber Glass Co.)

Note that the pultrusion process has a continuous molding cycle. This requires that the fiber distribution be constant and that the cross-sectional shapes not vary along the length, i.e., no bends or tapers are allowed. Main advantages of the process are low labor cost and product consistency. Shapes such as rods, channels, and angle and flat stock are easily produced. Fibrous reinforcements in different forms can be used. Roving, i.e., continuous fibers are most commonly used. It is easy to saturate such a bundle of fibers with the resin. Continuous strand mat consisting of continuous fiber lengths with random orientation can also be used. They are used to obtain reinforcement action in the transverse direction. Other forms of materials used include chopped strand mat consisting of short (chopped) fibers that can be bonded or stitched to a carrier material, commonly a unidirectional tape, and woven fabrics and braided tapes. Such forms provide reinforcement at 0°, 90°, or an arbitrary angle θ to the loading direction. Common resins used in pultrusion are polyester, vinyl ester, and epoxy. Meyer (1985) provides the details regarding this process.

5.1.1.4 Resin Transfer Molding (RTM)

Resin transfer molding is a closed-mold, low-pressure process. A preform made of the desired fiber (carbon, glass, or aramid) is placed inside a mold, and liquid resin such as epoxy or polyester is injected into the mold by means of a pump. Reinforcements can be stitched, but more commonly they are made into a preform that maintains its shape during injection of the polymer matrix. The resin is allowed to cure and form a solid composite. The polymer viscosity should be low enough (<1 *Pas*) for the fibers to be wetted easily. Additives to enhance the surface finish, flame retardancy, weather resistance, curing speed, etc. may be added to the resin. Thermoplastics have too high a melting point and too high viscosities (>1 *Pas* or 1000 *cP*) to be processed with RTM. In RTM processing, Darcy's law, which describes the permeability of a porous medium, is of great importance. Darcy's law for single-phase fluid flow says that the volume current density, J, i.e., volume/(area x time), of a fluid is given by

$$J = -\frac{k}{\eta}\nabla P,$$

where k is the permeability of the porous medium, η is the fluid viscosity, and ∇P represents the pressure gradient that drives the fluid flow. It can be recognized that Darcy's law is an analog of Ohm's law for electrical conduction, i.e., hydraulic permeability is an analog of electrical conductivity. Note that the permeability, k, is a function of the properties of the porous medium, i.e., its microstructure; it does not depend on properties of the fluid.

Among the advantages of RTM, one can cite the following:

- Large, complex shapes and curvatures can be obtained.
- A higher level of automation is possible than in many other processes.
- Layup is simpler and the process is speedier than manual operations.
- By using woven, stitched, or braided preforms, fiber volume fractions as high as 65% can be achieved.
- The process involves a closed mold; therefore, styrene emissions can be reduced to a minimum. In general, RTM produces much fewer emissions compared to hand layup or spray up techniques.

Mold design is a critical element in the RTM process. Generally, the fibrous preform is preheated. The mold has built-in heating elements to accelerate the process of resin curing. Resin flow into the mold and heat transfer are analyzed numerically to obtain an optimal mold design.

The automotive industry has found RTM to be a cost-effective, high volume process for large-scale processing. Use of RTM to make automotive parts can result in significant weight reduction. For example, composite parts made by RTM resulted in 90 *kg* reduction in the weight of Dodge Viper automobile.

5.1.1.5 Automated Tape Placement (ATP) and Automated Fiber Placement (AFP)

In general, automation in most any field results in productivity gains. For example, a completely automated process, i.e., no human being is required, has a great attraction for use in radioactive or clean environments. In the area of fabrication of composites, it has led to two very important techniques: automatic tape laying (ATL) and automatic fiber placement (AFP) processing. Another significant advantage is that rather large structures can be made by this process. The hand layup process is limited by the extent of a worker's reach. Clearly, such a restriction would be absent in any automatic process. Most automated machines are large, sophisticated, and represent a major capital investment. Resin choices for tapes can be grouped by processing characteristics. These are commonly thermoset resins such as epoxies; they are cured to B-stage, i.e., tacky, and later fully cured. The second group comprises non-tacky solid resins that melt and flow prior to curing to a thermoset polymer, e.g., bismaleimides and non-tacky thermoplastic resins processed entirely by melting and freezing, e.g., polyether ether ketone (PEEK) and polyphenylene sulfide (PPS).

Capital expenditures for computer-controlled, automated equipment can be significant, however. Understandably, such equipment initially found applications in defense-related applications, e.g., the wing skin panels of F-22 *Raptor* fighter jet. In civilian aerospace industry aircrafts such as Boeing 787 and Airbus 350 and other advanced aircrafts, automated processing techniques have moved well into civilian aircraft construction as well.

Automated Tape Placement (ATP)

In ATP technique, resin preimpregnated high performance reinforcement fibers in the form of a tape are placed in specific directions. It is easy to see that part weight will be minimized by placing fibers only along the directions needed. ATP has gained wide acceptance for part fabrication in the aerospace industry; examples include aircraft wings, body skins, and control surfaces. In ATP, prepregged tape, rather than single fiber tows, is laid down continuously to form parts. It is often used for parts with highly complex contours or angles. Tape layup is versatile; it allows breaks in the process and easy changes in direction. Although the process is commonly used with thermosets, it can be adapted for thermoplastic materials as well.

The ATP technique works as follows. The customer's computer-aided design (CAD) is the starting point. Using the CAD system, the product or component to be manufactured, say a curved part, is developed mathematically onto a flat surface. This is further broken down into layers to be fabricated by laying strips of tape side by side. Sophisticated software is used to translate strips in each layer via a series of numerical control steps to develop the final product shape. A spool of tape (consisting of, say, carbon fiber preimpregnated with a thermosetting resin, commonly epoxy), covered with a protective paper on the top and protective film underneath, is unwound; the film and the paper are peeled off, and the tape suspended in mid air

is cut to correct shape by cutting blades. The cutting blades are very fast; they can make 6000 cuts per minute. A laser beam in the tape laying head is used to accurately lay the tape on the mold.

Automated tape laying machines (ATL) are used to make aircraft parts such as wing stringers, spars, skins and elevators, tail skins and horizontal planes, engine cowls, fuselage skins, and belly fairings. These automated tape laying machines are capable of laying preimpregnated tapes of 75-, 150-, or 300-*mm* width at any orientation and can build up the product consisting of any number of plies. Modern ATL machines have heads that integrate ultrasonic cutting of the laminate, cutter depth-setting, and dockable inkjet marking. Low-rail gantry platforms are available in medium and large size ranges that can be matched to customer part size and floor space requirements. The machines feature tape-deposit speeds of up to 50 *m/min* and a high degree of placement accuracies on complex contours.

Automated Fiber Placement (AFP)

Automated fiber placement (AFP) involves the use of individual fiber tows. Multiple resin preimpregnated fiber tows are placed onto a mandrel at high speed, using a numerically controlled placement head to dispense, clamp, cut, and restart each tow during placement. Minimum cut length (the shortest tow length a machine can lay down) is the essential ply-shape determinant. The fiber placement heads can be attached to a 5-axis gantry or retrofitted to a filament winder. Machines are available with dual mandrel stations to increase productivity. Advantages of fiber placement fabrication include speed, reduced material scrap and labor costs, part consolidation, and improved part-to-part uniformity. The process is employed when producing large thermoset parts with complex shapes.

The fiber tows, preimpregnated with the resin, from spools are fed into the fiber placement head where they are collimated into a single band and laminated onto the work surface. Typically, each tow is about 3 *mm* wide strand of continuous fibers. A strand, in its turn, may consist of 12,000 individual filaments impregnated with an epoxy resin.

Different fiber tows can be delivered at different speeds, thus conforming to a complex structural shape. For example, when a curved surface is to be laminated, the outer tows of the band pull more strand length than the inner tows. It is possible to cut individual tows and restart without stopping the motion of the head. This allows in-process control of the bandwidth, avoiding excess resin buildup and to fill in any gaps. A compaction roller or shoe consolidates the tape pressing it onto the work surface. This pressing action serves to remove any trapped air and any minor gaps between individual tows. Figure 5.4 shows a schematic of the automatic fiber placement process.

High-speed, automatic processing has become very popular with the coming of large-sized civilian aircraft. As an example of a commercially produced AFP machine, we mention VIPER made by MAG Cincinnati (Hebron, Ky.). Such machines are used for automated fabrication of composite fuselage panels for the commercial aircraft. The VIPER 6000 series AFP machines can produce fuselage panels up to 6.3 *m* in diameter. The VIPERs produce 92% of the fuselage for the

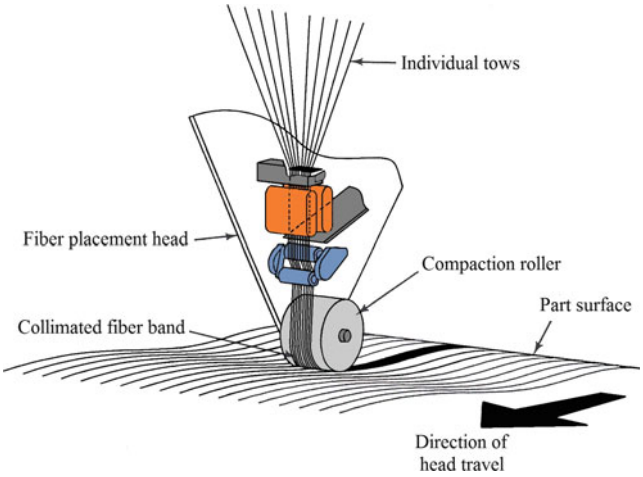

Fig. 5.4 Schematic of automatic fiber placement process

A350 XWB. According to MAG Cincinnati, the company that manufactures the VIPER machines, such machines enable independent control over feed, clamp, cut, and start for up to 32 individual tows or slit tape. Multistrands of carbon fiber/epoxy can be placed around a mandrel to make a single finished part without seams and rivets.

5.1.1.6 Autoclave-Based Methods

Autoclave-based methods or bag molding processes (Slobdzinsky 1982) are used to make large parts. Before we describe this important process, we should digress and describe an important term, although we have used it earlier, viz., prepreg. The term *prepreg* is a short form of preimpregnated fibers. Generally, a prepreg is in the form of a thin sheet or lamina of unidirectional (or occasionally woven) fiber/polymer composite protected on both sides with easily removable separators. Figure 5.5a shows schematic of a prepreg. Prepregs thus represent an intermediate stage in the fabrication of a polymeric composite component. The prepreg generally has the resin in a partially cured state with a moderately self-adhesive tack. This can easily be obtained with epoxies whose cure can be separated into two stages (see Chap. 3). Some composite systems have thermoset matrix materials that do not go through a two-stage cure, such as polyesters and polyimides; in such systems, the tack in the prepreg can be achieved by the addition of liquid rubbers or resins. In prepregs made with a thermoplastic matrix, such a tack is conspicuous by its absence. The reason for this is that thermoplastics do not undergo a curing reaction like thermosets (see Chap. 3). As a consequence, prepregs made with a thermoplastic matrix are quite stiff or *boardy*. A typical unidirectional prepreg is in the form of a long

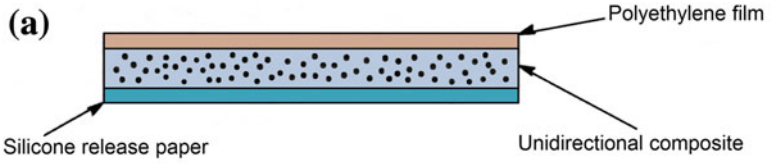
(a)
Polyethylene film
Silicone release paper
Unidirectional composite

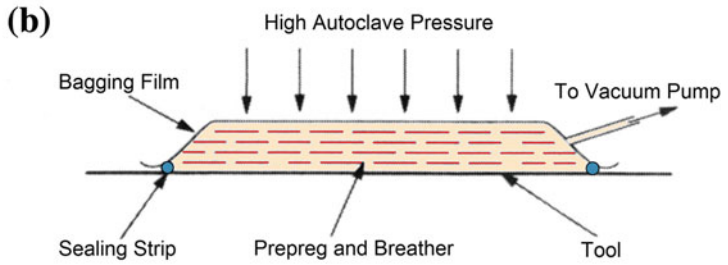
(b)
High Autoclave Pressure
Bagging Film
To Vacuum Pump
Sealing Strip
Prepreg and Breather
Tool

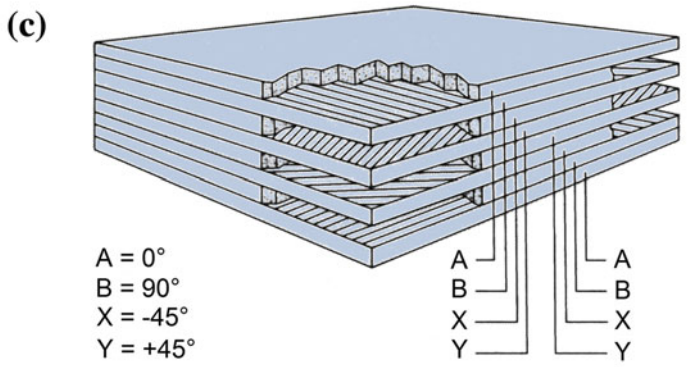
(c)
A = 0°
B = 90°
X = -45°
Y = +45°
A
B
X
Y
A
B
X
Y

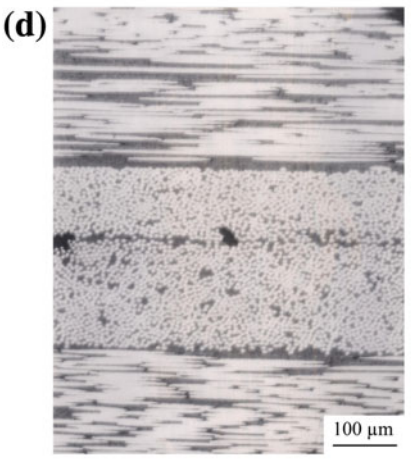
(d)
100 µm

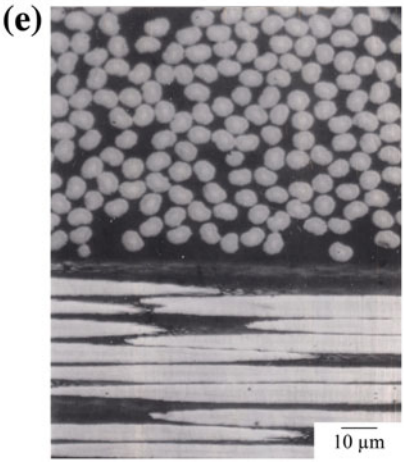
(e)
10 µm

◂**Fig. 5.5** **a** Schematic of a prepreg. **b** Setup in an autoclave to make a laminated composite. **c** Layup of plies with different fiber orientations. **d** Optical micrographs of carbon fiber/epoxy laminated composite made in an autoclave. **e** A higher magnification of e. Note the different fiber orientations in different layers

roll, 300–1500 *mm* wide roll and 0.125 *mm* thick. The length of the roll can be anything, but it is generally 50–250 *m*. The fiber content, by volume, in a unidirectional prepreg is typically is about 65%. It is not uncommon to use 50 or more such plies or laminae in an autoclave processed composite.

Prepregs can be made by a number of techniques. In a process called *solution dip,* the resin ingredients are dissolved in a solvent to 40–50% solid levels. The fiber (in the form of a yarn or a fabric) is passed through the solution, and it picks up an amount of solid that depends on the speed of throughput and the amount of solids in the solution. In another process, *solution spray,* a specified amount of solid resin is sprayed onto the fiber yarn or fabric. In both solution dip and solution spray, the impregnated fiber is put through a heat cycle to remove the solvents and the chemical reaction in the resin proceeds to give the desired tack. In *direct hot-melt,* the resin formulation is incorporated as a high temperature coat on the fiber. At high temperature, the viscosity is low enough for coating the fiber directly. *Film calendaring* involves casting the resin formulation into a film from either hot melt or solution. The fiber yarn is sandwiched between two films and calendared so that the film is worked onto the fiber.

Autoclave-based processing of PMCs results in a very high quality product. That is the reason it is used to make components in the aerospace field. An *autoclave* is a closed vessel (round or cylindrical) in which processes (physical and/or chemical) occur under simultaneous application of high temperature and pressure. Heat and pressure are applied to appropriately stacked prepregs. The combined action of heat and pressure consolidates the laminae, removes the entrapped air, and helps cure the polymeric matrix. Autoclave processing of composites thus involves a number of phenomena: chemical reaction (curing of the thermoset matrix), flow of the resin, and heat transfer. Figure 5.5b shows schematically the setup in an autoclave to make a laminated composite. Bags containing prepregs in predetermined orientations (this is discussed in Chap. 11) are placed in an autoclave (typically a cylindrical oven in which pressure and heat can be applied to the part). The bags consist of thin and flexible membranes made of rubber that separate the layup from the gas used to compress. Densification and curing are achieved by pressure differential across the bag walls. One can use vacuum, in which case the bag contents are evacuated and atmospheric pressure consolidates the composite. Figure 5.5c shows a schematic of the layup of plies with different fiber orientations obtained after consolidation. Optical micrographs of actual carbon fiber/epoxy laminated composite made in an autoclave are shown in Fig. 5.5d, e. Note the different fiber orientations in different layers.

Autoclave-based processing with prepregs is quite versatile. One may use more than one type of reinforcement fiber to produce what is called a *hybrid* composite.

Fig. 5.6 A large autoclave that is used to make the wings of Boeing 787. An idea of the size of the autoclave can be obtained from the height of the person standing inside the autoclave. (Courtesy of ASC Process Systems Inc., Sylmar, California)

A prepreg with fibers running parallel to the long dimension is called a 0^{o} lamina or ply. A prepreg cut with fibers perpendicular to the long dimension is designated as a 90^{o} lamina, while a prepreg with fibers running at an intermediate angle θ is designated a θ-ply. The exact orientation sequence of plies in the laminate is determined from theory of elasticity (see Chap. 11) to obtain appropriate magnitudes and directions of stress and to avoid unwanted twisting and/or torsion. Such laminate construction, mostly done by hand, can result in high fiber volume fractions (60–65%). A nice example of an autoclave, one the largest in the world which is used to process the wings of the Boeing 787 plane is shown in Fig. 5.6. An idea of the physical dimensions can be obtained from the man standing in the cylindrical body of the autoclave. One of the end pieces is shown on the left hand side in the picture.

5.1.2 Thermoplastic Matrix Composites

Thermoplastic matrix composites have several advantages and disadvantages over thermoset matrix composites. We first list these and then we will describe some of the important processes used to form thermoplastic matrix composites.

The advantages of thermoplastic matrix composites include the following:

- Refrigeration is not necessary with a thermoplastic matrix.
- Parts can be made and joined by heating.
- Parts can be remolded, and any scrap can be recycled.
- Thermoplastics have better toughness and impact resistance than thermosets. This can generally also be translated into thermoplastic matrix composites.

The disadvantages include the following:

- The processing temperatures are generally higher than those with thermosets.
- Thermoplastics are stiff and boardy, i.e., they lack the tackiness of the partially cured epoxies.

A good quality laminate must be void-free. This implies that there must be sufficient flow of the thermoplastic matrix between layers as well as within individual tows. Generally, a pressure of 6–12 *MPa*, a temperature between 275 and 350 °*C*, and dwell times of up to 30 *min* are appropriate for thermoplastics such as polysulfones and polyetheretherketone (PEEK). Because no time is needed for any curing reaction, the time length of the molding cycle with a thermoplastic matrix is less than that with a thermoset matrix.

A brief description of processing methods for thermoplastic matrix composites follows.

5.1.2.1 Film Stacking

Laminae of thermoplastic matrix containing fibers with very low resin content (~ 15 *w/o*) are used in this process. Low resin content is used because these are very boardy materials. The laminae containing fibers are stacked alternately with thin films of pure polymer matrix material. The stack of laminae consists of fibers impregnated with insufficient matrix and polymer films of complementary weight to give the desired fiber volume fraction in the end product. These are then consolidated by simultaneous application of heat and pressure.

The impregnation of thermoplastic matrix takes place under the simultaneous application of heat and pressure; the magnitude of pressure and temperature must be sufficient to force the polymeric melt to flow into and through the reinforcement preform. The rate of penetration of a fluid into the fibrous preform structure is described by Darcy's law (see Sect. 5.1.1). Darcy's law says that flow rate is directly proportional to the applied pressure and inversely proportional to the viscosity. Thus, increasing the applied pressure and decreasing the viscosity of the molten polymer (i.e., increasing the temperature) help in the processing.

5.1.2.2 Diaphragm Forming

This process involves the sandwiching of freely floating thermoplastic prepreg layers between two diaphragms (Cogswell 1992). The air between the diaphragms

is evacuated and the thermoplastic laminate is heated above the melting point of the matrix. Pressure is applied to one side, which deforms the diaphragms and makes them take the shape of the mold. The laminate layers are freely floating and very flexible above the melting point of the matrix, and thus they readily conform to the mold shape. After the completion of the forming process, the mold is cooled, the diaphragms are stripped off, and the composite is obtained. One of the advantages of this technique is that components with double curvatures can be formed. The diaphragms are the key to the forming process, and their stiffness is a very critical parameter. Compliant diaphragms do the job for simple components. For very complex shapes requiring high molding pressures, stiff diaphragms are needed. At high pressures, a significant transverse squeezing flow can result, and this can produce undesirable thickness variations in the final composite.

5.1.2.3 Thermoplastic Tape Laying

Thermoplastic tape laying machines are also available, although they are not as common as the thermosetting tape laying machines. Figure 5.7 shows the schematic of one such machine. A controllable tape head has the tape dispensing and shim dispensing/take-up reels and heating shoes. The hot head dispenses thermoplastic tape from a supply reel. There are three heating and two cooling/compaction shoes. The hot shoes heat the tape to molten state. The cold shoes cool the tape instantly to a solid state.

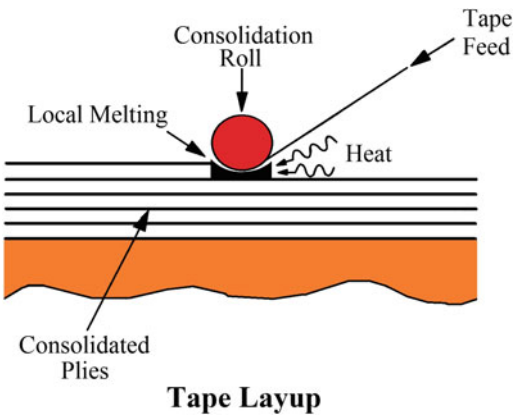

Fig. 5.7 Schematic of a thermoplastic tape laying machine. (Courtesy of Cincinnati Milacron.)

5.1.2.4 Commingled Fibers

The thermoplastic matrix can be provided in the form of a fiber. The matrix fiber and the reinforcement fiber are commingled to produce a yarn that is a blend of the thermoplastic matrix and reinforcement yarn. Such a commingled yarn can be woven, knit, or filament wound. The yarn formed into the appropriate shape is then subjected to heat and pressure to melt the thermoplastic matrix component, wet out the reinforcement fibers, and obtain a composite.

There are many commingled fibers available commercially for processing into a composite. As examples, we cite the following. Vectran is the trade name of a liquid crystal thermoplastic aromatic polyester fiber. The multifilament yarn is produced by melt spinning. It has a low melting point, and thus when commingled with a reinforcement fiber, it can provide the matrix component in the composite. It is available in the form of multifilament yarn that can be commingled with glass or other reinforcement fibers. Twintex is the commercial name that involves commingled polypropylene fibers and glass fibers.

5.1.2.5 Thermoforming, Injection Molding

As pointed out earlier, thermoplastics soften on heating, and therefore melt flow techniques of forming can be used. Such techniques include injection molding, extrusion, and thermoforming. Thermoforming involves the production of a sheet, which is heated and stamped, followed by vacuum or pressure forming. Generally, discontinuous fibrous (principally glass) reinforcement is used, which results in an increase of melt viscosity. Short fiber reinforced thermoplastic resin composites can also be produced by a method called *reinforced reaction injection molding* (RRIM) (Lockwood and Alberino 1981). RRIM is actually an extension of the *reaction injection molding* (RIM) of polymers. In RIM, two liquid components are pumped at high speeds and pressures into a mixing head and then into a mold where the two components react to polymerize rapidly. An important example is a urethane RIM polymer. In RRIM, short fibers (or fillers) are added to one or both of the components. The equipment for RRIM must be able to handle rather abrasive slurries. The fiber lengths that can be handled are generally short, owing to viscosity limitations. Because a certain minimum length of fiber, called the critical length (see Chap. 10), is required for effective fiber reinforcement, more often than not RRIM additives are fillers rather than reinforcements. Most RIM and RRIM applications are in the automotive industry.

5.1.2.6 Long Fiber Thermoplastic (LFT) Compression Molding

The most common way of making thermoplastic composites involves mixing of short length of fibers (about 2–3 *mm* or less) with a thermoplastic matrix and injection molding the composite (see above). The properties of these short fiber reinforced composites are better than those of the unreinforced matrix material, but the full potential of the reinforcing fiber is not achieved. We treat the important subject of critical length of fiber for load transfer in Chap. 11. Suffice it here to state that increasing the length of fibers to greater than 10 *mm* would result in improvements in many mechanical properties of the composites. In the literature, the acronym LFT is used to refer to composites with a thermoplastic matrix containing fibers greater than 10 *mm* in length. Figure 5.8 shows variation of some mechanical characteristics of a composite as a function of fiber length in a schematic manner. Note the increase in stiffness and strength as well as improvement in impact properties with increasing fiber length. This has led to innovations in processing of long fiber thermoplastic matrix composites, commonly referred to as LFT composites (Ning et al. 2019).

The basic process is illustrated in Fig. 5.9. The critical step in processing LFTs is the production of continuous fiber reinforced rods or tapes from which long fiber pellets are cut (Vaidya and Chawla 2008a, b). In this process, continuous fiber tows pass through a bath of molten matrix and the impregnated tows pass through a die for shaping into a rod or ribbon, followed by passage through a chiller to cool. The last stage involves a puller/chopper; the puller pulls the tow at the desired speed while the chopper cuts the continuous, impregnated tow to desired length of pellets suitable for use in an extruder and compression molding. The long fiber pellets are suitable for the conventional injection molding process, injection compression molding as well as the extrusion compression molding process. The LFT pellets made by hot melt impregnation are fed into a plasticator where they are metered in a barrel, heated above the melting point of the thermoplastic resin, and the mixture of polymer plus fiber flows through a low shear plasticator to form a molten charge. The molten charge (it looks like cotton candy) coming out of the plasticator is quickly transferred to a heated mold where it is compressed in a closed tool (generally, a high tonnage press). The part is then removed after sufficient cooling.

Another commercial process called LFT-D-ILC has been used to make LFT composites consisting of glass fibers/styrene copolymers. Polypropylene has also been used as a thermoplastic matrix in this process. Essentially, it is an extrusion/compression molding process. The distinctive feature of the LFT-D-ILC process is that the long fiber composite is produced directly from the basic materials. The polymer matrix material and any modifiers/additives are mixed and melted in a compounding extruder. This mixture is mixed with the reinforcing fibers in a twin screw extruder (Krause et al. 2003). The special screw-design disperses the fibers in the matrix and further fiber breakage is avoided. The extruder machines work continuously and produce a continuous long fiber reinforced extrudate, which is cut into pieces with the desired length and is then directly compression molded.

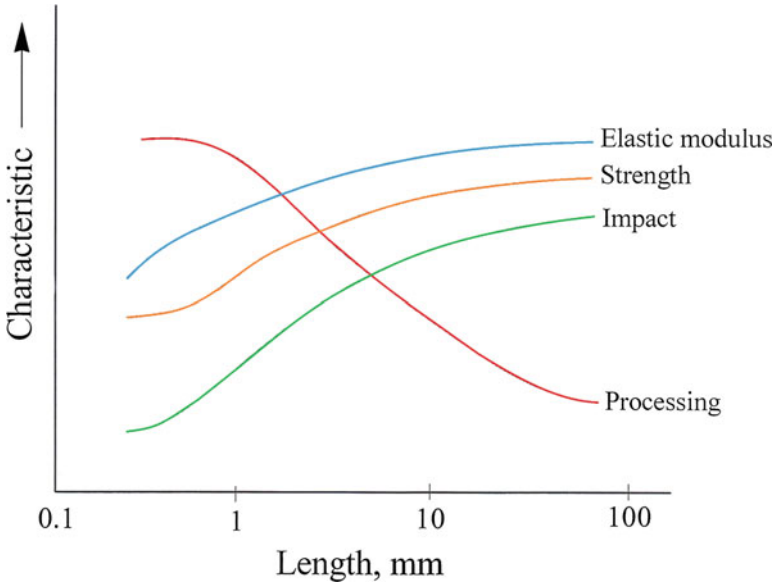

Fig. 5.8 Variation of some mechanical properties of a composite as a function of fiber length

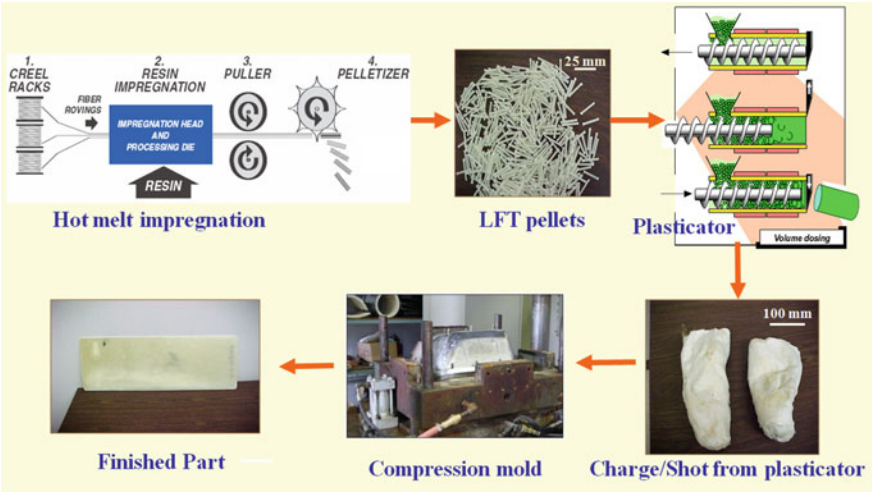

Fig. 5.9 Extrusion/compression molding process for making long fiber reinforced thermoplastic (LFT) composites. Hot melt impregnation of fibers is used to produce tapes, rods, or long pellets of LFT. Pelletized LFT material is fed into an extruder or plasticator. Plasticized LFT charge is compression molded to different product forms

5.1.3 Sheet Molding Compound (SMC)

There are some common PMCs that do not contain long, continuous fibers; hence, we describe them separately in this section. *Sheet molding compound* (SMC) is the name given to a composite that consists of unsaturated polyester resin containing short glass fibers plus some additives called fillers. The additives generally consist of fine calcium carbonate particles and mica flakes. Sometimes calcium carbonate powder is substituted by hollow glass microspheres, which results in a lower density, but makes it more expensive. Figure 5.10 shows a schematic of the SMC processing. Polyester resin can be replaced by vinyl ester to further reduce the weight, but again with a cost penalty. SMC is used in making some auto body parts, such as bumper beams, radiator support panels, and many others. It has been used in the Corvette sports car for many decades. Polypropylene resin can be reinforced with calcium carbonate particles, mica flakes, or glass fibers. Such composites, though structurally not as important as, say, carbon fiber/epoxy composites, do show improved mechanical properties vis à vis unreinforced resin. It should be mentioned that some SMCs containing carbon fiber instead of glass fiber have been developed. Characteristics such as strength, stiffness, and service temperature are improved. These materials are used in automotive parts, appliances, electrical components, and so forth.

5.1.4 Carbon Fiber Reinforced Polymer Composites

Carbon fiber reinforced polymer matrix composites can be said to have had their beginning in the 1950s and to have attained the status of a mature structural material in the 1980s. Not unexpectedly, earlier applications in the defense-related aerospace industry were the main driving force for the carbon fiber reinforced polymer matrix composites, followed by the sporting goods industry. The availability of a large variety of carbon fibers (Chap. 2), coupled with a steady decline in their prices over

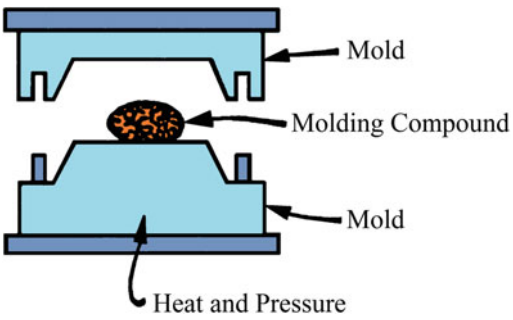

Fig. 5.10 Schematic of SMC processing

the years, and an equally large variety of polymer matrix materials (Chap. 3) made it easier for carbon fiber polymer composites to assume the important position that they have: applications in civilian aircraft, automotive, and civil infrastructure. Epoxy is the most commonly used polymer matrix with carbon fibers. Unsaturated polyester, vinyl ester, polysulfone, polyimide, and thermoplastic resins are also used. Carbon fibers are the major load-bearing components in most such composites. There is, however, a class of carbon fiber composites wherein the excellent thermal and, to some extent, electrical conductivity characteristics of carbon fibers are exploited, for example, in situations where static electric charge accumulation occurs, parts made of thermoplastics containing short carbon fibers are frequently used. Carbon fibers coated with a metal, e.g., nickel, are used for shielding against electromagnetic interference. Mesophase pitch-based carbon fibers show excellent thermal conductivity and thus find applications in thermal management systems.

5.2 Interface in PMCs

We provide below a summary of some important features of the interface region in PMCs with glass, carbon, aramid, and polyethylene fibers.

5.2.1 Glass Fiber/Polymer

The reader will recall from the description given in Chaps. 2 and 3 that inorganic, silica-based glasses are analogous to many organic polymers in that they are amorphous. Recall also that pure, crystalline silica melts at 1800 $^{\circ}C$ and can be worked in the range of 1600–1800 $^{\circ}C$. However, by adding some metal oxides, one can break the Si–O bonds and obtain a series of amorphous glasses with low glass transition temperatures so that they can be processed at much lower temperatures than pure silica. In general, the atomic or molecular arrangement in any material is different at the surface than in the interior. In particular, in the case of silica-based glasses containing a variety of oxides, a complex hydroxyl layer is formed rather easily. Nonhygroscopic oxides absorb water as hydroxyl groups while hygroscopic oxides become hydrated. The activity of a glass surface is thus a function of the hydroxyl content and the cations just below the surface. That is, the surface activity of E glass will be different from that of fused silica. Invariably, glass fibers are surface treated by applying a *size* on the freshly drawn glass fibers to protect them from the environment, for handling ease, and to avoid introducing surface defects. Common sizes are starch gum, hydrogenated vegetable oil, gelatin, polyvinyl alcohol (PVA), and a variety of nonionic emulsifiers. The size is generally incompatible with the matrix resin and is therefore removed before putting the glass fibers in a resin matrix by heat cleaning at $\sim 350\ ^{\circ}C$ for 15–20 h in air, followed by washing with detergent or solvent and drying. After cleaning, organometallic or

organosilane coupling agents are applied; an aqueous solution of silane is commonly used for this purpose. The organosilane compounds have the chemical formula

$$R - \mathrm{Si} - X_3,$$

where R is a resin-compatible group and X represents groups capable of interacting with hydroxylated silanols on the glass surface. Typically, a silane coupling agent will have the following general chemical structure:

$$X_3\mathrm{Si}(\mathrm{CH}_2)_n Y,$$

where n can have a value between 0 and 3, X is a hydrolyzable group on silicon, and Y is an organofunctional group that is resin-compatible. Silane coupling agents are generally applied to glass from an aqueous solution. Hydrolyzable groups are essential for generating intermediate silanols. Examples of coupling agents commonly used are organometallic or organosilane complexes. It is thought by some researchers (Knox 1982) that the coupling agents create a chemical bridge between the glass surface and the resin matrix. Other researchers (Kardos 1985) do not subscribe to this view.

The *chemical bridge theory* goes as follows. Silane molecules, as mentioned earlier, are multifunctional groups with a general chemical formula of R–SiX_3, where X stands for hydrolyzable groups bonded to Si. For example, X can be an ethoxy group, OC_2H_5 and R is a resin-compatible group. They are hydrolyzed in aqueous size solutions to give trihydroxy silanols (Fig. 5.11a). These trihydroxy silanols get attached to hydroxyl groups at the glass surface by means of hydrogen bonding (Fig. 5.11b). During the drying of sized glass fibers, water is removed and a condensation reaction occurs between silanol and the glass surface and between adjacent silanol molecules on the glass surface, leading to a polysiloxane layer bonded to the glass surface (Fig. 5.11c). Now we can see that the silane coating is anchored at one end, through the R group, to the uncured epoxy or unsaturated polyester matrix, and at the other end to the glass fiber through the hydrolyzed silanol groups. On curing, the functional groups R either react with the resin or join the resin molecular network (Fig. 5.11d).

Appealing though this chemical bridge model of silane coupling is, there are certain shortcomings. The interface model shown in Fig. 5.11d will result in such a strong bond that it will fail because of the strains encountered during the curing of the resin and those resulting from differential thermal contraction (see below). Also, under conditions of industrial application of silanes from aqueous solution, a covalent reaction to the glass fiber surface does not occur unless a primary or secondary amine is present (Kardos 1985; Kaas and Kardos 1971).

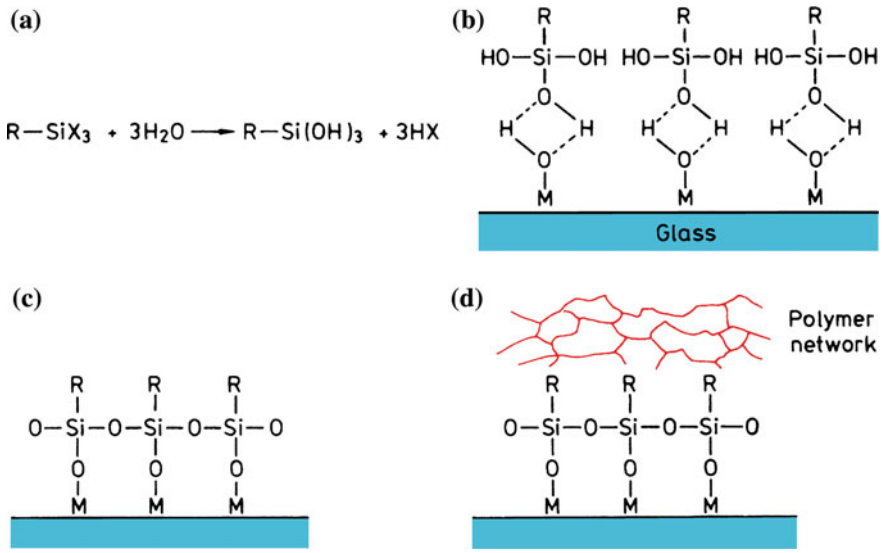

Fig. 5.11 Function of a silane coupling agent (chemical bridge model): **a** hydrolysis of silane to silanol; **b** hydrogen bonding between hydroxy groups of silanol and a glass surface; **c** polysiloxane bonded to a glass surface; and **d** resin-compatible functional groups *R* after reacting with a polymer matrix. (From Hull (1981), reprinted with permission.)

5.2.1.1 Reversible Bond Model

During the processing of PMCs, most polymeric matrix materials will shrink on curing, while the reinforcement fiber remains unaffected. This can lead to large stresses at the fiber/polymer interface. Stresses can also result in cooling due to differences in coefficients of thermal expansion of glass (about 5 10^{-6} K^{-1}) and rigid polymer ($\sim$50–100 10^{-6} K^{-1}). The chemical bridge model provides a rigid bond at the glass/polymer interface that will not be able to withstand the strains involved because of the curing and shrinkage. A clean glass surface under ordinary atmospheric conditions can readily pick up a molecular layer of water. Water can reach the glass/polymer interface by diffusion through the polymer, by penetrating through cracks or by capillary migration along the fibers. Note that hydrophobic mineral fibers such as carbon or silicon carbide are less sensitive to water than glass fiber because there is little tendency for water molecules to cluster at the interface. Thus, the silane coupling agents at the glass/resin interface also have the important function of allowing the composite to accommodate internal stresses.

Plueddeman (1974a, b) pointed out that a silane coupling agent provides a reversible hydrolytic bond between a polymer matrix and an inorganic fiber. Hydrated silanol bonds to the oxides on the glass surface, i.e., –MOH, where *M* stands for Si, Al, Fe, and so on, with the elimination of water. The dynamic equilibrium mechanism of bonding requires water at a hydrophilic interface to

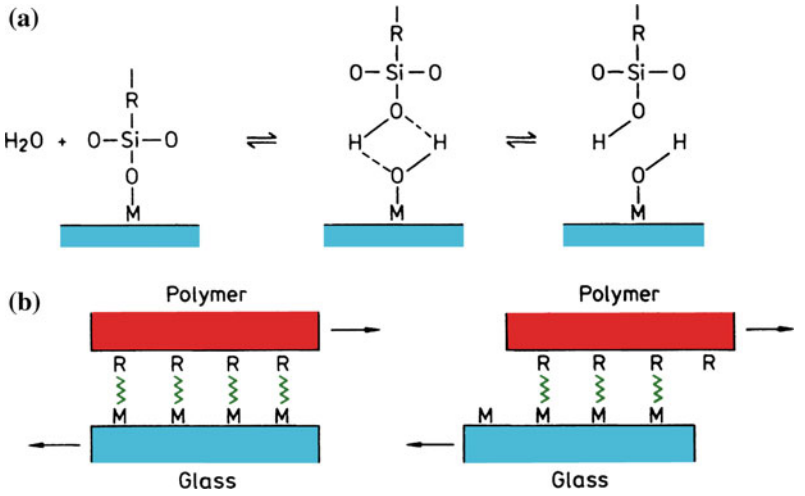

Fig. 5.12 **a** Plueddemann's reversible bond associated with hydrolysis. **b** Shear displacement at a glass/polymer interface without permanent bond rupture. (From Hull (1981), reprinted with permission.)

allow relaxation of thermal stresses generated during cooling. Plueddemann's model is shown in Fig. 5.12. In the presence of water at the interface (it can diffuse in from the resin), the covalent M–O bond hydrolyzes as shown in Fig. 5.12a. If a shear parallel to the interface occurs, the polymer and glass fiber can glide past each other without a permanent bond rupture (Fig. 5.12b). Ishida and Koenig (1978) used infrared spectroscopy to obtain experimental evidence for this reversible bond mechanism. The interface is not a static sandwich of polymer–water–glass. Instead, a dynamic equilibrium prevails that involves making and breaking of bonds, which allows relaxation of internal stresses at a molecular scale. Water is therefore necessary to bond rigid polymers to inorganic surfaces such as glass.

5.2.2 Carbon Fiber/Polymer Interface

As in any other composite, the carbon fiber/polymer matrix interface is very important in determining the final properties of the composite. Carbon fiber is a highly inert material. This makes it difficult to have a strong adhesion between carbon fiber and a polymer matrix. One solution is to make the fiber surface rough by oxidation or etching in an acid. This results in an increased specific surface area and improved wetting, which in turn results in improved interlaminar shear strength because of the mechanical keying effect at the fiber/matrix interface. Recall that the carbon fiber microstructure is inhomogeneous through its cross section. Specifically, in the surface layer, the basal planes are better aligned parallel to the

surface. This surface graphitic layer is very smooth and weak in shear and hard to bind with a matrix. That is the reason that a surface treatment is given to carbon fibers. A variety of surface treatments can be used to accomplish the following:

a. increase the surface roughness and
b. increase the surface reactivity.

The interface region between a carbon fiber and the polymer matrix is quite complex. It is therefore not surprising that a unified view of the interface in such composites does not exist. As pointed out in Chap. 2, the carbon fiber structure, at submicrometer level, is not homogeneous through its cross section. The orientation of the basal planes depends on the precursor fiber and processing conditions. In particular, the so-called onion-skin structure is frequently observed in PAN-based carbon fibers, wherein basal planes in a thin surface layer are aligned parallel to the surface while the basal planes in the core are less well-aligned. Figure 5.13 shows the structure of a carbon fiber/epoxy composite (Diefendorf 1985). The onion-skin zone (C in Fig. 5.13) has a very graphitic structure and is quite weak in shear. Thus, failure is likely to occur in this thin zone. Additionally, the skin can be hard to bind with a polymeric matrix because of the high degree of preferred orientation of the basal planes, thus, facilitating interfacial failure (zone D). The matrix properties in zone E (close to the interface) may be different from those of the bulk epoxy (zone B). Carbon fibers meant for polymer reinforcement invariably receive some form of surface treatment from the manufacturer to improve their compatibility with the polymer matrix and their handleability. Organic *sizes* are commonly applied by passing the fibers through a sizing bath. Common sizes include polyvinyl alcohol, epoxy, polyimide, and titanate coupling agents.

Carbon fibers, especially high modulus carbon fibers that have undergone a high temperature graphitization, are quite smooth. They have a rather low specific area, varying from 0.1 to 2 m^2g^{-1}. Invariably, there is a microscopic scale of roughness; mostly as longitudinal striations (see Fig. 2.20). Carbon fibers are also generally chemically inert, that is, interfacial interactions in carbon fiber-based composites would be rather weak. Generally, a short beam bending test is conducted to measure what is called *interlaminar shear strength*, ILSS (see Chap. 4). Admittedly, such a test is not entirely satisfactory, but for lack of any better, quicker, or more convenient test, the ILSS test value is taken as a measure of bond strength.

Ehrburger and Donnet (Ehrburger and Donnet 1980) point out that there are two principal ways of improving interfacial bonding in carbon fiber composites: increase the fiber surface roughness, and thus the interfacial area, and increase the surface reactivity. Many surface treatments have been developed to obtain improved interfacial bonding between carbon fibers and the polymer matrix (Donnet and Bansal 1984; McKee and Mimeault 1973). A brief description of these follows.

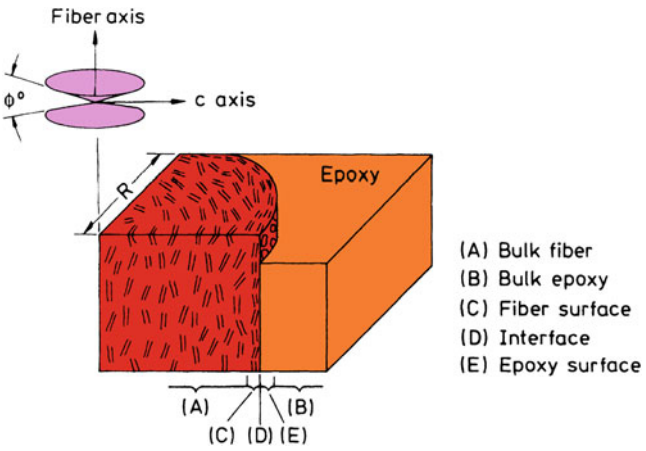

Fig. 5.13 Schematic structure of a carbon fiber/epoxy composite showing carbon fiber, interface, and epoxy matrix. (From Diefendorf (1985), used with permission.)

5.2.2.1 Chemical Vapor Deposition (CVD)

Chemical vapor deposition technique has been used to deposit silicon carbide and pyrocarbon on carbon fibers. Growing whiskers ($\sim 2\ \mu m$ in diameter) on the carbon fiber surface, called *whiskerization* in the literature, can result in a two- to threefold increase of ILSS. The improvement in ILSS is mainly due to the increase in surface area. Whiskerization involving the growth of single crystal SiC whiskers perpendicular to the fiber results in an efficient mechanical keying effect with the polymer matrix. The CVD method of doing this is expensive, and handling of whiskerized fibers is difficult. Although this treatment results in an increase in ILSS, there also occurs a weakening of the fibers. Ehlert et al. (2010) have developed a solution-based technique of growing ZnO nanorods perpendicular to the carbon fiber, which seems to be quite promising inasmuch as it is claimed not to result in a decrease in strength while improving the interfacial strength by mechanical interlocking.

5.2.2.2 Oxidative Etching

Treating carbon fibers with several surface oxidation agents leads to significant increase in the ILSS of composites. This is because the oxidation treatment increases the fiber surface area and the number of surface groups (Ehrburger and Donnet 1980). Figure 5.14 shows a linear relationship between the fiber surface roughness as measured by AFM and interlaminar shear strength in a series of carbon fiber/epoxy composites (Jangehud et al. 1993). Yet another reason for increased ILSS may be the removal of surface defects, such as pores, weakly bonded carbon debris, and impurities (Donnet and Bansal 1984). Oxidation

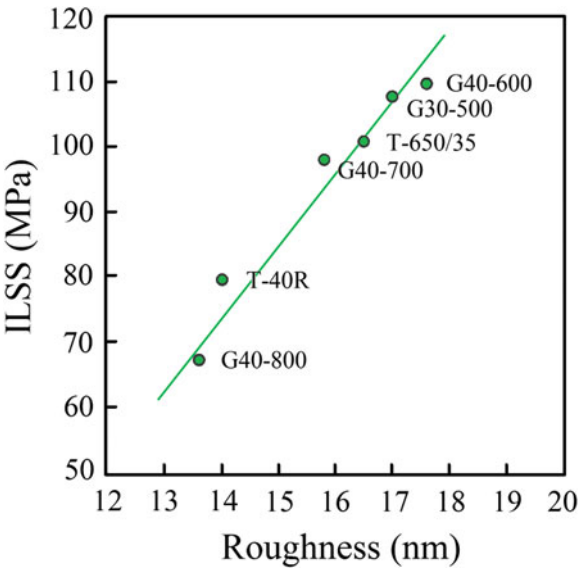

Fig. 5.14 Linear relationship between the carbon fiber surface roughness as measured by AFM and interlaminar shear strength in a series of carbon fiber/epoxy composites (Jangehud et al. 1993)

treatments can be carried out by means of a gaseous or a liquid phase. Gaseous phase oxidation can be done with air or oxygen diluted with an inert gas (Clark et al. 1974). Gas flow rates and the temperature are the important parameters in this process. Oxidation results in an increase in the fiber surface roughness by pitting and increased longitudinal striations (Donnet and Bansal 1984). Too high an oxidation rate will result in nonuniform etching of the carbon fibers and a loss of fiber tensile strength. Since oxidation results in a weight loss, we can conveniently take the amount of weight loss as an indication of the degree of oxidation. Figure 5.15 shows ILSS versus weight loss for high strength and high modulus carbon fiber reinforced composites (Clark et al. 1974). Weight loss being a measure of the oxidation of carbon fiber, the maximum ILSS in Fig. 5.15 corresponds to less than a 10% weight loss in both cases. Overoxidation results in a loss of fiber strength and lower ILSS.

5.2.2.3 Liquid Phase Oxidation

Liquid phase oxidation involves treatments in nitric acid, sodium hypochlorite, potassium permanganate, and anodic etching (Donnet and Bansal 1984). Liquid phase oxidation by nitric acid and sodium hypochlorite results in an increase in the interfacial area and formation of oxygenated surface groups due to fiber etching. Wetting of the carbon fibers by the polymer matrix is enhanced by these.

Graphitic oxides are lamellar compounds having large amounts of hydroxylic and carboxylic groups. The formation of a graphitic oxide layer increases the number of acidic groups on the carbon fibers.

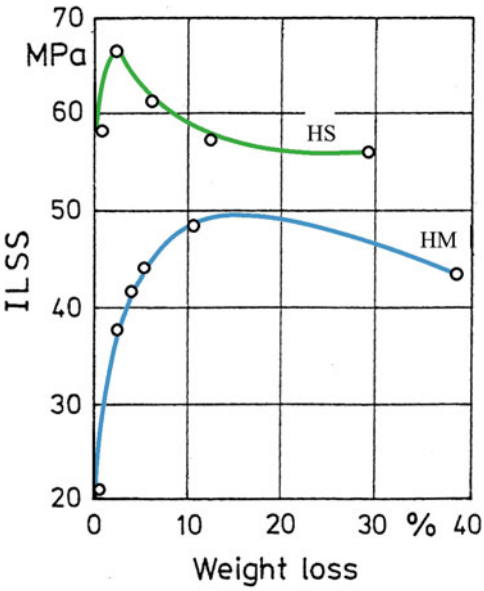

Fig. 5.15 Interlaminar shear strength (ILSS) as a function of weight loss on oxidation. A high weight loss corresponds to a high degree of oxidation. Note that the maximum ILSS corresponds to less than 10% weight loss in both cases. A: high modulus type carbon fiber; B: high strength type carbon fiber. (From Clark et al. (1974), used with permission.)

Anodic etching or electrochemical oxidation using dilute nitric acid or dilute sodium hydroxide solutions results in no significant decrease in tensile strength of the carbon fibers, according to Ehrburger and Donnet (1980). The fiber weight loss is less than 2% and no great change in surface area or fiber roughness occurs, the major change being an increase in the acidic surface groups. Oxidative treatments produce functional groups (e.g., $-CO_2H$, –C–OH, and –C=O) on carbon fiber surfaces. They form at the edges of basal planes and at defects. These functional groups form chemical bonds with unsaturated resins.

According to Drzal et al. (1983a, b), various carbon fiber surface treatments promote adhesion to epoxy materials through a two-pronged mechanism: (a) the surface treatment removes a weak outer layer that is present initially on the fiber and (b) chemical groups are added to the surface which increase interaction with the matrix. When a fiber finish is applied, according to Drzal and coworkers, the effect is to produce a brittle but high modulus interphase layer between the fiber and the matrix. As amine content is reduced, the modulus of epoxy goes up accompanied by lower fracture strength and strain. That is, the interphase being created between the fiber and the matrix has high modulus but low toughness. This promotes matrix fracture as opposed to interfacial fracture.

5.2.3 Aramid Fiber/Polymer Interface

Most polymers show rather poor adhesion to aramid fibers. This is evidenced by the generally poor interlaminar shear strength and transverse tensile strength values obtained with aramid reinforced PMCs. Typically, aramid/epoxy interfacial strengths are about half of the interfacial strengths of glass/epoxy or carbon/epoxy composites. A highly oriented chain microstructure and skin/core heterogeneity are responsible for this poor interfacial strength. This may not be a disadvantage in aramid/polymer composites used to make impact-resistant items such as helmets or body armor, where ease of delamination may be an advantage from a toughness point of view. However, in high strength and high stiffness composites, poor interfacial adhesion can be a disadvantage. Various fiber surface treatments have been tried to alleviate this problem. Among these are the following:

- Bromine water treatment. This also results in reduced fiber strength.
- Silane coupling agents developed for glass fibers.
- Isocyanate-linked polymer.
- Treatment with reactive chemicals such as acetic acid anhydride, methacryloyl chloride, and sulfuric acid, among others. Such treatments, however, result in a decrease in the tensile strength of aramid fiber, attributable to etching of the aramid fiber.
- Acid (HCl, H_2SO_4) or base (NaOH) hydrolysis of aramid fiber yields reactive terminal amino groups to which diepoxide molecules could attach.
- Plasma treatment in vacuum, ammonia, or argon. Plasma treatment in ammonia increases the amine concentration on the fiber surface, which is thought to lead to covalent bonding at the interface. An increase in nitrogen content in the form of amine groups is accompanied by a decrease in oxygen content with increasing exposure time.

5.2.4 Polyethylene Fiber/Polymer Interface

Ultra high molecular weight polyethylene (UHMWPE) fiber is another chemically very inert fiber, and therefore it does not adhere very well to polymeric matrix materials. High modulus polyethylene fibers such as Spectra or Dyneema are hard to bond with any polymeric matrix. Some kind of surface treatment must be given to the polyethylene fiber to bond with resins such as epoxy, PMMA, etc. By far the most successful surface treatment involves a cold gas (such as air, ammonia, or argon) plasma (Kaplan et al. 1988). A plasma consists of gas molecules in an excited state, i.e., it is highly reactive and has dissociated molecules. When the polyethylene, or any other fiber, is treated with a plasma, surface modification occurs by removal of any surface contaminants and highly oriented surface layers, addition of polar and functional groups on the surface, and introduction of surface

roughness; all these factors contribute to an enhanced fiber/matrix interfacial strength (Biro et al. 1992; Brown et al. 1992; Hild and Schwartz 1992a, b; Kaplan et al. 1988; Li et al. 1992). An exposure of just a few minutes to the plasma is sufficient to do the job.

In a UHMWPE fiber/epoxy composite, a plasma treatment of fiber resulted in an increase in fiber surface roughness and an increased bonding area and interfacial shear strength (Kaplan et al. 1988; Biro et al. 1992). In another work (Brown et al. 1992), it was shown that chemical etching of UHMWPE fibers resulted in more than a sixfold increase in interfacial shear strength of UHMWPE/epoxy composites.

Chemical treatment with chromic acid and plasma etching in the presence of oxygen are two treatments that are commonly used to modify the surface characteristics of polyethylene fiber with a view to improve their adhesion to polymeric matrix materials.

5.3 Structure and Properties of PMCs

Continuous fiber reinforced polymer, metal or ceramic, composites show anisotropic properties. The properties of a composite will depend on the matrix type, fiber type, interface, amount or volume fraction of fiber (or that of the matrix), fabrication process, and, of course, the fiber orientation.

5.3.1 Structural Defects in PMCs

The final stage in any PMC fabrication process is called *debulking*, which serves to reduce porosity in PMCs. Nevertheless, there are other common structural defects in PMCs. Following is a list of these:

- Resin-rich (fiber-poor) regions.
- Voids (e.g., at roving crossovers in filament winding and between layers having different fiber orientations, in general). This is a very serious problem; a low void content is necessary for improved interlaminar shear strength. Hence, the importance of the debulking step.
- Microcracks (these may form due to curing stresses or moisture absorption during processing).
- Debonded and delaminated regions.
- Variations in fiber alignment.

5.3.2 Mechanical Properties

Some microstructures of polymer matrices reinforced by continuous and discontinuous fibers are shown in Fig. 5.16. A transverse section of continuous glass fiber in an unsaturated polyester matrix is shown in Fig. 5.16a. Note the resin rich regions. The layer structure in the cross section of an injection molded composite consisting of short glass fibers in a semicrystalline polyethylene terephthalate (PET) is shown in Fig. 5.16b (Friedrich 1985). Ideally, an injection molded should show short fibers distributed in an isotropic manner. Figure 5.16b essentially, it is a three-layer structure showing different orientations of the short fibers. More fibers are parallel to the mold fill direction (MFD) in the two surface layers (marked *S*), than in the transverse direction in the central layer (marked *C*). Note the marked heterogeneity in the microstructure, which results in a characteristically anisotropic behavior.

Laminates of polymer matrix composites made by the stacking of appropriately oriented plies also result in composites with highly anisotropic characteristics. In particular, the properties of continuous fiber reinforced polymers are quite a bit higher in the longitudinal direction than in other directions. It turns out that one generally finds the longitudinal properties of composites quoted in the literature for comparative purposes.

The reader is warned that one must bear in mind this discrepancy when comparing such data of highly anisotropic materials with the data of isotropic materials such as common polycrystalline metals. Besides, composites containing aramid and polyethylene fibers will not have such attractive properties in compression in the longitudinal direction. A summary of some important characteristics of PMCs is presented in Tables 5.1 and 5.2.

Most thermoset matrix composites show essentially elastic behavior right up to fracture, i.e., there is no yield point or plasticity. The strain-to-failure values are rather low, typically, less than 0.5%. Consequently, the work done during fracture is also small. This has some very practical implications for the design engineer, viz., he or she cannot bank on any local yielding in such composites to take care of stress concentrations.

In general, the continuous fiber reinforced composites will be stiff and strong along the fiber axis, but off-angle these properties fall rather sharply. Typically, in a unidirectional PMC, the fiber volume fraction can be 65%. In composites having fibers aligned bidirectionally, this value can fall to 50%, while in a composite containing in-plane random distribution of fibers, the volume fraction will rarely be more than 30%. As a general rule-of-thumb, we can take the Young's modulus of the composite in the longitudinal direction to be given by the following rule-of-mixtures relationship

$$E_{cl} = E_f V_f + E_m V_m,$$

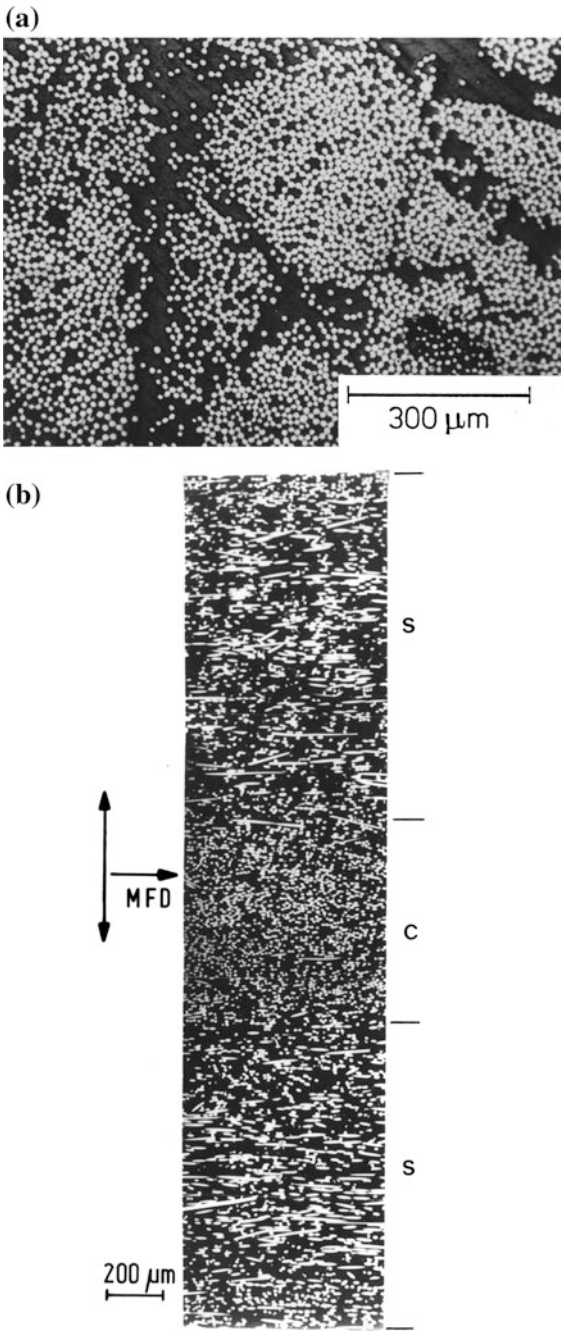

Fig. 5.16 **a** Continuous glass fibers in unsaturated polyester matrix. **b** Discontinuous glass fibers in a semicrystalline polyethylene terephthalate thermoplastic matrix. MFD denotes the mold fill direction. S and C denote the surface and central layers, respectively. (From Friedrich (1985), used with permission.)

Table 5.1 Representative properties of some PMCs[a]

Materials	Density ($g\ cm{-}3$)	Tensile modulus			Tensile strength		Compressive Strength Longitudinal (MPa)	Flexural Modulus (GPa)	Flexural Strength (MPa)	ILSS[b] (MPa)	Longitudinal coefficient of thermal expansion ($10^{-6}\ K^{-1}$)
		Longitudinal (GPa)	Transverse (GPa)	Shear Modulus (GPa)	Longitudinal (MPa)	Transverse (MPa)					
Unidirectional *E* glass 60 *v/o*	2	40	10	4.5	780	28	480	35	840	40	4.5
Bidirectional *E* glass cloth 35 *v/o*	1.7	16.5	16.5	3	280	280	100	15	220	60	11
Chopped strand mat *E* glass 20 *v/o*	1.4	7	7	2.8	100	100	120	7	140	69	30
Boron 60 *v/o*	2.1	215	24.2	6.9	1400	63	1760	–	–	84	4.5
Kevlar 29 60 *v/o*	1.38	50	5	3	1350	–	238	51.7	535	44	–
Kevlar 49 60 *v/o*	1.38	76	5.6	2.8	1380	30	276	70	621	60	−2.3

[a]The values are only indicative and are based on epoxy matrix at room temperatures

[b]ILSS is interlaminar shear strength

Source Adapted with permission from Hancox (1983)

Table 5.2 Typical mechanical properties of some carbon fiber/epoxy composites[a]

Property	AS	HMS	Celion 6000	GY 70
Tensile strength (*MPa*)	1850	1150	1650	780
Tensile modulus (*GPa*)	145	210	150	290–325
Tensile strain-to-fracture (%)	1.2	0.5	1.1	0.2
Compressive strength (*MPa*)	1800	380	1470	620–700
Compressive modulus (*GPa*)	140	110	140	310
Compressive strain-to-fracture (%)	–	0.4	1.7	–
Flexural strength (4-point) (*MPa*)	1800	950	1750	790
Flexural modulus (*GPa*)	120	170	135	255
Interlaminar shear strength (*MPa*)	125	55	125	60

[a]Values given are indicative only and are for a unidirectional composite (62% V_f) in the longitudinal direction

Source Adapted with permission from Riggs et al. (1982)

where E and V denote the Young's modulus and the volume fraction of a component and the subscripts c, f, m, and l indicate composite, fiber, matrix, and the longitudinal direction, respectively. From the data provided in Chap. 2 on the mechanical properties of fibers, the reader can easily verify that glass fiber/polymer will only give a modest increase in modulus while aramid/polymer will provide a significant increase in stiffness. However, aramid, polyethylene, and carbon fiber reinforced polymer composites will show a significant increase in longitudinal stiffness. Aramid fiber/polymer composites are likely to show higher creep rate than glass/polymer composites. Aramid fiber has superior impact characteristics, therefore, aramid fiber-based polymer composites will show good ballistic resistance, and impact resistance in general. Similar observations can be made regarding strength characteristics of the other polymer matrix composites. As should be clear to the reader, these properties are highly dependent on the fiber properties.

5.3.2.1 Damping Characteristics

Damping in material has to do with dissipation of vibrations. High damping or the ability to reduce vibrations can be very important in many applications, for example, in mechanical equipment that is subject to variable speeds, resonance problems lead to unacceptable levels of noise. Also, in sporting goods such as tennis rackets, fishing rods, and golf clubs, it is desirable to have high damping. In a composite, damping will depend on relative proportion of fiber and matrix, orientation of reinforcement with respect to the axis of loading, viscoelastic characteristics of the matrix and the reinforcement, any slipping at the interface between the matrix and the reinforcement, and last but not least, any source of damage such as cracks or environmental attack. In general, aramid fiber/polymer composites

provide good damping characteristics. This, of course, stems from the superior damping of aramid fiber (see Chap. 2).

5.3.2.2 Moisture Effects in Polymer Matrix Composites

Environmental moisture can penetrate organic materials by diffusion. Typically, moisture works as a plasticizer for a polymer, i.e., properties such as stiffness, strength, and glass transition temperature decrease with the ingress of moisture in a polymer. It is now well recognized that the problem of moisture absorption in polymer matrix composites is a very important one. The maximum moisture content under saturated condition, M_m as a function of relative humidity, is given by the following relationship:

$$M_m = A(\%\,\text{relative humidity})^{\text{B}},$$

where A and B are constants. The moisture content in a composite, M, can be written as

$$M = M_i + G(M_m - M_i),$$

where M_i is the initial moisture content (= 0 for a completely dry material) and G is a dimensionless, time-dependent parameter related to the diffusion coefficient. Generally, one assumes that Fickian diffusion prevails, i.e., Fick's law of diffusion is applicable. Under conditions of Fickian diffusion, water diffuses into the laminate from the two surfaces that are in equilibrium with their surroundings, and the parameter G is given by (Chen and Springer 1976)

$$G \approx 1 - \left(8/\pi^2\right)\exp\left(-\pi^2 Dt/S^2\right),$$

where D is the diffusion coefficient ($m^2 s^{-1}$) in the direction normal to the laminate surface; t = time (s); $S = h$ (the laminate thickness), if exposed on both sides; and $S = 2\ h$, if exposed on one side. A dried specimen, usually in the form of a thin sheet, is placed in a humid environment at a constant temperature, and the mass gained is measured as a function of time. If we plot the mass gained (say, as percentage moisture absorbed) as a function of the square root of time, at a given temperature, we obtain a curve with the following characteristics. After an initial linear portion (i.e., $M \propto \sqrt{t}$), the curve assumes a plateau form in an asymptotic manner as shown in Fig. 5.17. The slope of the linear portion can be used to determine the diffusion coefficient as follows:

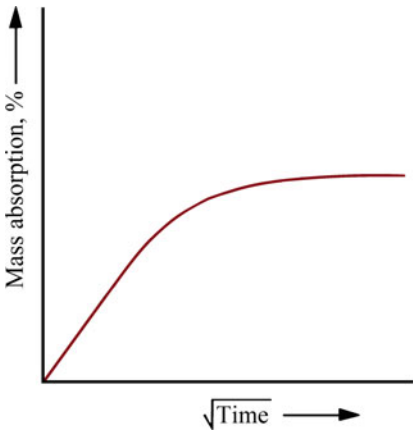

Fig. 5.17 Schematic curve of fractional moisture absorbed as a function of the square root of time, at a given temperature

$$Slope = \frac{M_2 - M_1}{\sqrt{t_2} - \sqrt{t_1}} = \frac{4M_m\sqrt{D}}{h\sqrt{\pi}},$$

where M_1 and M_2 are the moisture contents corresponding to times t_1 and t_2, respectively. Rearranging the above expression, we write for D

$$D = \left[\frac{M_2 - M_1}{\sqrt{t_2} - \sqrt{t_1}}\right]^2 \cdot \pi \left[\frac{h}{4M_m}\right]^2.$$

The epoxy resins commonly employed as matrices in the composites meant for use in the aerospace industry are fairly impervious to the range of fluids commonly encountered in service, for example, jet fuel, hydraulic fluids, and lubricants (Anderson 1984). There are, however, two fundamental effects that must be taken into account when designing components made of PMCs, namely, temperature and humidity. The combined effect of these two, that is, hygrothermal effects, can result in a considerable degradation in the mechanical characteristics of the PMCs. This is especially so in high performance composites such as carbon fiber/epoxy, which are used in the aerospace industry where dimensional tolerances are rather severe. Because aerospace structures are exposed to a range of environments and temperatures, for example, oils, fuels, moisture, acids, and hot gases, the excellent corrosion-resistance characteristics of carbon/epoxy composites are of great value under such conditions. Commonly encountered damage to polymers by ultraviolet rays is minimized by properly painting the exterior of the composite. Moisture is a major damaging agent. Epoxy matrices can absorb water to as much as 1% of the composite weight; however, unlike glass fiber, which is attacked by moisture, the carbon fiber itself is unaffected by moisture. Thus, moisture absorbed in carbon

fiber PMCs opens up the polymer structure and reduces its glass transition temperature, that is, the moisture acts as a plasticizer for the polymeric matrix. Moisture absorption in polymers occurs according to Fick's law, that is, the weight gain owing to moisture intake varies as the square root of the exposure time. This Fickian moisture absorption in a 16-ply carbon epoxy laminate is shown in Fig. 5.18a (Shirrel and Sandow 1980). An example of moisture-induced degradation in a model composite consisting of a single carbon fiber in an epoxy matrix is shown in Figs. 5.18 b–d. A photoelastic technique that shows stress-induced birefringence was used to analyze the stress patterns obtained as a function of immersion time in water. Figure 5.18b shows the initial condition. After an immersion for 10.5 *h*, a net tensile stress birefringence was obtained (Fig. 5.18c). With continued moisture absorption, more swelling of the epoxy matrix occurred, causing an increase in the axial tensile stress in the fiber and eventually leading to fiber fracture after 151 *h*, as shown in Fig. 5.18d (Xu and Ashbee 1994). The moisture absorption problem in PMCs is analogous to that of degradation by temperature effects. Collings and Stone (1985) present a theoretical analysis of strains developed in longitudinal and transverse plies of a carbon/epoxy laminate owing to hygrothermal effects. An interesting finding of theirs is that tensile thermal strains that develop in the matrix after curing are reduced by compressive strains generated in the matrix by swelling resulting from water absorption. It is worth

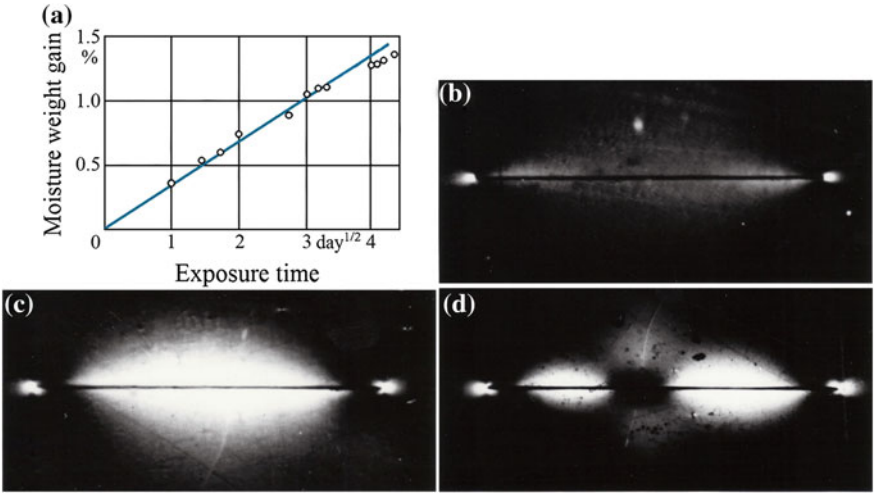

Fig. 5.18 **a** Fickian moisture absorption in a 16-ply carbon epoxy laminate (Shirrel and Sandow 1980). Moisture-induced degradation in a model composite consisting of a single carbon fiber in an epoxy matrix as seen by using photoelasticity to show stress-induced birefringence was used to analyze the stress patterns obtained as a function of immersion time in water. **b** The initial condition in a carbon fiber/epoxy composite. **c** After an immersion for 10.5 *h*, a net tensile stress birefringence was observed. **d** More swelling of the epoxy matrix occurred, causing an increase in the tensile stress in the carbon fiber and eventually leading to fiber fracture after 151 *h* (From Xu and Ashbee 1994)

pointing out that moisture absorption causes compressive stresses in the resin and tensile stresses in the fibers (see Fig. 5.18). Thus, it is understandable that moisture absorption should reduce the residual strains after curing.

5.3.2.3 Environmental Issues Related to PMCs

There are certain environmental issues related to the use of polymer matrix composites. Common polymers are derived from petroleum (a nonrenewable resource). They are also difficult to dispose of at the end of life, especially the thermosets. In short, polymers have a reputation of being environmentally unfriendly. Consequently, there is effort to produce polymers and composites from eco-friendly sources. We discuss these biocomposites in Chap. 15.

Degradation of polymers owing to ultraviolet radiation is another important environmental effect. Ultraviolet radiation breaks the covalent bonds in organic polymers, which can degrade the mechanical behavior of PMCs (Goel et al. 2008). This kind of damage, frequently referred to as photodegradation, is actually quite a complex process. It may involve chemicrystallization, i.e., rearrangement of broken polymer chains, due to photo-oxidation, into crystalline phase, color change, embrittlement, formation of surface cracks, and degradation of mechanical properties. An example of such a loss of mechanical properties is shown in Fig. 5.19. This figure shows the loss of stiffness or modulus as a function of exposure to ultraviolet radiation for glass fiber reinforced polypropylene composites. Crystallinity of PP increases with rate of oxidation (chemicrystallization). Sometimes a prolonged exposure of epoxy laminates to ultraviolet radiation results in a slight increase in strength, attributed to postcuring of the resin, followed by a gradual loss of strength as a result of laminate surface degradation (Bergmann 1984).

Hazardous air pollutants (HAPs) are generated during the curing of thermoset polymers. These include volatile organic compounds (VOCs) and nitrogenous oxides (commonly denoted by NOx). Certain VOCs are thought to interact photo-chemically in the atmosphere and form ozone. HAPs may have long term adverse health effects. Sources of these during processing of PMCs include solvents used to reduce viscosity, gases evolved, and disposal of scrap material. Commonly, styrene is the main culprit. The government regulatory agencies such as the US Environmental Protection Agency (EPA) have set certain regulatory limits on the emission of VOCs and HAPs.

Among the ways to reduce VOC emissions are (Sands et al. 2001): use closed processing, accelerated curing to react or trap VOCs in the curing media, and e-beam curing. Autoclave processing is thought to be a major source of such HAPs, especially NOx. Non-autoclave processing would help in this regard. Substitution of thermosets with thermoplastic is another possibility. E-beam curing of resins is done at room temperature without any solvent; the amount of VOCs is reduced.

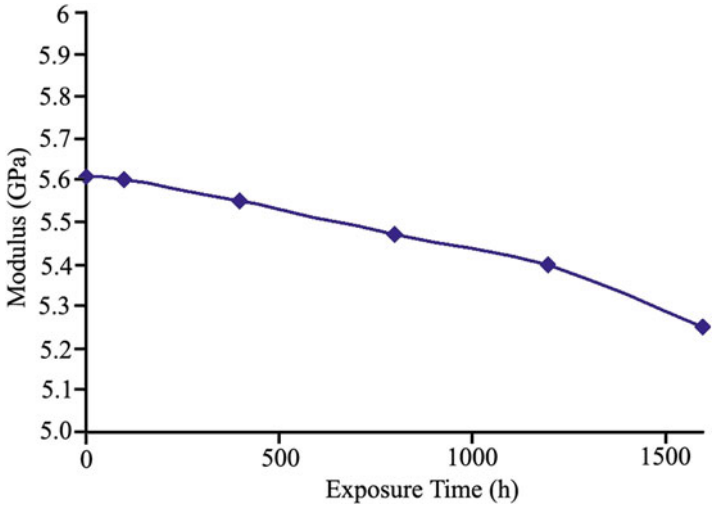

Fig. 5.19 Loss of stiffness or modulus as a function of exposure to ultraviolet radiation for glass fiber reinforced polypropylene composites. (From Goel et al. 2008)

5.3.2.4 Mechanical Behavior

Fracture in PMCs, as in other composites, is associated with the characteristics of the three entities: fibers, matrix, and interface. Specifically, fiber/matrix debonding, fiber pullout, fiber fracture, polymer crazing, and fracture of the matrix are the energy absorbing phenomena that can contribute to the failure process of the composite. Of course, the debonding and pullout processes depend on the type of interface. At low temperatures, the fracture of a PMC involves a brittle failure of the polymeric matrix accompanied by pullout of the fibers transverse to the crack plane. Figure 5.20 shows this kind of fracture at −80 °C in the case of a short glass fiber/polyethylene terephthalate (PET) composite. Note the brittle fracture in the matrix. At room temperature, the same polymeric matrix (PET) deformed locally in a plastic manner, showing crazing (Friedrich, 1985). Generally, stiffness and strength of a PMC increase with the amount of stiff and strong fibers introduced in a polymer matrix. The same cannot be said unequivocally for the fracture toughness. The toughness of the matrix and several microstructural factors related to the fibers and the fiber/matrix interface have a strong influence on the fracture toughness of the composite. Friedrich (1985) describes the fracture toughness of short fiber reinforced thermoplastic matrix composite in an empirical manner by a relationship of the form

$$K_{cc} = MK_{cm},$$

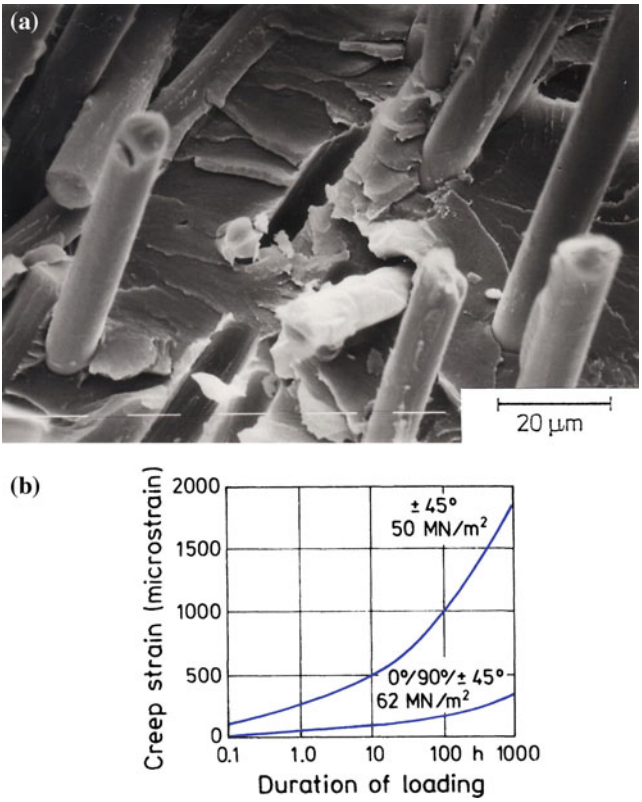

Fig. 5.20 **a** Brittle matrix fracture and fiber pullout in a short glass fiber reinforced polyethylene terephthalate (PET) composite fractured at −80 °C. (From Friedrich (1985), used with permission.] **b** Creep strains at ambient temperature for a ±45° and for a 0/90/±45 carbon/epoxy laminate. (From Sturgeon (1978), used with permission.)

where K_{cm} is the fracture toughness of the matrix and M is a microstructural efficiency factor. M can be larger than 1 and depends on fiber amount, fiber orientation, and the fiber orientation distribution over the fracture plane, as well as the deformation behavior of the matrix and the relative effectiveness of all the energy absorbing mechanisms.

Carbon fiber/epoxy composites exhibit superior properties in creep compared to aramid/epoxy. This is because aramid fibers, similar to other polymeric fibers, creep significantly even at quite low stresses (Eriksen 1976). Additionally, in a laminated composite made by stacking prepregs of different fiber orientations, the ply stacking sequence can affect the composite properties. Figure 5.20b shows tensile creep strain at ambient temperature as a function of time for two different stacking sequences (Sturgeon 1978). The laminate with carbon fibers at ±45° shows more creep strain than one containing plies at 0°/90°/±45°. The reason for this is that in the ±45° sequence, the epoxy matrix undergoes creep strain by tension in the

loading direction, shear in the ±45° directions, and rotation of the plies in a scissor-like action. As we shall see in Chap. 11, 0° and 90° plies do not show this scissor-like rotation, which is a characteristic of the 45° plies. Thus, the addition of 0° and 90° plies reduces the matrix shear deformation. Consequently, the creep resistance of 0°/90°/±45° sequence is better than that of the ±45° sequence.

Carbon fiber reinforced PMCs generally show excellent fatigue strength. Depending on the ply stacking arrangement, their fatigue strength (tension-tension) may vary from 60 to 80% of the ultimate tensile strength for lives over 10^7 cycles (Baker 1983). The higher fatigue strength levels pertain to composites having more than 50% of the fibers in the longitudinal direction (0°), which leads to high longitudinal stiffness and low strains. Pipes and Pagano (1970) showed that certain stacking sequences can result in tensile stresses at the free edges, which can lead to early local delamination effects in fatigue and consequently to lower fatigue lives. Further discussion of these topics can be found in Chap. 11–14.

A considerable amount of work has been done to toughen the carbon fiber reinforced PMCs. This has involved modifying epoxies and using polymeric matrix materials other than epoxies. Among the latter are modified bismaleimides and some new thermoplastic materials (see also Chap. 3). The latter category includes poly (phenylene sulfide) (PPS), polysulfones (PS), and polyetheretherketone (PEEK), among others. PEEK, a semicrystalline polyether, combines excellent toughness with chemical inertness. Typically, PEEK-based carbon fiber composites are equivalent to high performance epoxy-based carbon fiber composites, with the big advantage that the PEEK-based composites have an order-of-magnitude higher toughness than the epoxy-based composites. PEEK matrix composites are more difficult to process and are more expensive than epoxy matrix composites.

Here we should point out an important phenomenon, viz., incorporation of fibers in a thermoplastic polymer can result in alteration of crystallization kinetics of the thermoplastic matrix (Waddon et al. 1987; Hull 1994). Figure 5.21 shows a

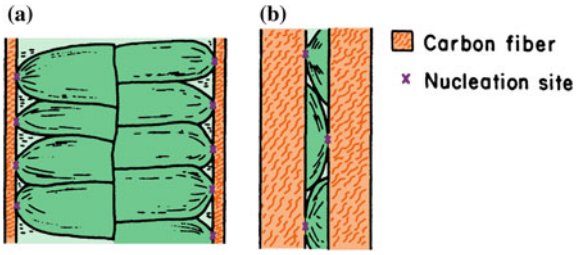

Fig. 5.21 A schematic representation of two possible spherulitic morphologies resulting from constrained growth in PEEK, a thermoplastic matrix, because of the presence of carbon fibers. **a** Low fiber volume fraction **b** high fiber volume fraction. The nucleation density of spherulites on the fibers is the same in the two cases but the fiber volume fraction is different, i.e., the interfiber spacing is smaller for the high fiber volume fraction composite. Hence, the constraint on the growth of spherulites is greater in the high fiber volume fraction case. (After Waddon et al. (1987).)

schematic representation of two possible spherulitic morphologies resulting from constrained growth in PEEK, a thermoplastic matrix, because of the presence of carbon fibers. The nucleation density of spherulites on the fibers is the same in the two cases but the fiber volume fraction is different, i.e., the interfiber spacing is smaller for the high fiber volume fraction composite. Hence, the constraint on the growth of spherulites is greater in the high fiber volume fraction case. This is really a general issue in all kinds of composites, namely, the microstructure and properties of matrix change during processing of the composite. See Chap. 12 for a further discussion of the importance of such structure-sensitive issues in composites.

5.4 Applications

Glass fiber reinforced polymers are used in a wide variety of industries: from sporting goods to civil construction to aerospace. Tanks and vessels (pressure and nonpressure) in the chemical process industry, as well as process and effluent pipelines, are routinely made of glass fiber reinforced polyester resin. Figure 5.22 shows a wide variety of glass fiber/resin matrix structural shapes made by the pultrusion technique. S-2 glass fibers and aramid fibers are used in the storage bins and floorings of civilian aircraft. Other aircraft applications include doors, fairings, and radomes. Aramid fiber is also used in light load-bearing components in helicopters and small planes. In most applications involving glass fiber reinforced polymers, aramid fibers can be substituted for glass without much difficulty. Racing yachts and private boats are examples of aramid fiber making inroads into the glass

Fig. 5.22 Many fiberglass/resin structural shapes made by pultrusion are available. (Courtesy of Morrison Molded Fiber Glass Co.)

Fig. 5.23 Drumsticks made with a pultruded Kevlar aramid fiber core and a thermoplastic injection molded cover. (Courtesy of Morrison Molded Fiber Glass Co.)

fiber fields where performance is more important than cost. Drumsticks made with a pultruded core containing Kevlar aramid fibers and a thermoplastic injection molded cover are shown in Fig. 5.23. These drumsticks last longer than the wooden ones, are lightweight, do not warp, and are more consistent than wooden sticks. Military applications vary from ordinary helmets to rocket engine cases. One has to guard against using aramid reinforcement in situations involving compressive, shear, or transverse tensile loading paths.

5.4.1 Pressure Vessels

A very important application of PMCs is in the use of natural gas for transportation. Use of natural gas as a fuel results in lower emissions (NO_x, CO_2) vis à vis gasoline fuel. It may also be a cheaper fuel in certain locations. The use of compressed natural gas as a vehicle fuel requires onboard storage of gas at high pressure ($\sim 200\ kPa$). Steel cylinders were used as pressure vessels. These metallic gas cylinders are quite heavy and thus result in a reduced payload. Much lighter, filament wound PMC cylinders were developed to replace the steel cylinders. Examples of these include steel or aluminum cylinders hoop wrapped with glass fiber/polyester and hoop- and polar-wound glass or carbon fiber reinforced polymer cylinders with a thermoplastic liner. Other common applications involve pipes for

Fig. 5.24 A filament-wound pipe (diameter = 2 *m*) made for irrigation purposes in Ecuador. (Courtesy of Odebrecht Co.)

transportation of water or petroleum. Figure 5.24 shows a large diameter (2 *m*) glass fiber reinforced filament wound cylinder made for water transport for irrigation purposes in Ecuador.

5.4.1.1 Ballistic Protection

Woven fabrics made of fibers that can deform under impact make an essential constituent of modern ballistic protection systems. Fabrics are commonly used in layers to make what is called concealable body armor, which is used for protection against low- and medium-energy handgun rounds. Ballistic fabrics are made of aramid fiber (Kevlar or Twaron) or polyethylene (Spectra or Dyneema) by many manufacturers in a variety of styles. Typically, concealable body armor is constructed of multiple layers of ballistic fabric, assembled into the "ballistic panel." The ballistic panel is then inserted into the "carrier," which is constructed of conventional garment fabrics such as nylon or cotton. The ballistic panel may be permanently sewn into the carrier or may be removable. Ballistic fabric is available from a number of manufacturers in various styles. Body armor intended for routine use is commonly worn under the normal clothing. Although the overall finished product looks relatively simple in construction, the ballistic panel is very complex.

Kevlar 29, Kevlar 129, and a new line called Kevlar Protera are DuPont aramid fibers meant for this purpose. Spectra fiber is used with resin into a product called

Spectra Shield composite, which is used to make helmets, hard armor for vehicles, and soft body armor. The helmet manufacture involves a special version of Spectra Shield, a special shell design, and a three-way adjustable liner of shock absorbing foam padding.

5.4.1.2 Applications of Composites in Aerospace

It can be said without any exaggeration that the introduction in 2007 of Boeing 787 aircraft represents a watershed event in the use of composites in the civilian aerospace industry. This aircraft has major structural components such as fuselage, wings, floor beams, etc. made of composite materials. In fact, the composites represent 50% by weight. This did not happen overnight though. It should be recognized that Boeing 777 has had composites 9% by weight. Most of the larger components in 787 are carbon fiber reinforced epoxy, with smaller parts made of short fibers in a variety of matrix materials, including thermoplastic matrix materials. Besides the obvious weight savings resulting from the use of composites, allowing fuel savings and extended range of flying, there are other fundamental designs and processing changes made possible by the use of composites.

Modern large airplanes, flying at high altitudes, have pressurized cabins. The limit of pressurization depends on the strength of the fuselage material. In Boeing 787, the fuselage is made of carbon fiber/epoxy composites, which have a higher strength and stiffness than the conventional aluminum. This allows the fuselage to be pressurized to higher stress levels. The use of high strength composites, in turn, allows larger size viewing windows, higher humidity levels in the cabin, etc. than in conventional aircraft. Recall that the cabin of an aircraft undergoes pressurization cycles many thousands of times over its lifetime. A fuselage made of high strength composites can withstand higher pressure (corresponding to 1800 m altitude) than one made of aluminum (corresponding to 2400 m). Recall that it is easier to breathe at an altitude of 1800 m than at 2400 m. In addition, composites are more resistant to moisture than aluminum, which means the level of humidity in the cabin can be increased (more comfortable for the passengers) and bigger windows (better viewing for the passengers) can be used.

Processing and tooling for composites are other areas which saw a tremendous change because of the large size of composite components needed for Boeing 787. An iron–nickel alloy called Invar is used to make tooling for large composites. Boeing uses the tape laying process wherein strips of carbon fiber/epoxy (<30 mm wide) are laid by multiple robotic tape laying heads on a spinning mandrel. The mandrel is made of a special alloy called Invar, which has a constant coefficient of thermal expansion. The mandrel is actually made of six interlocking pieces of Invar. It is etched to provide a mirror image of the plane interior. It has lengthwise grooves which allow composite stringers to be incorporated. Layer upon layer of prepreg strips is laid on the spinning mandrel until the desired shape and thickness are obtained. This is followed by curing for about 2 h in an autoclave at around 250 $°C$.

Figure 5.6 shows a specially built huge autoclave for this purpose. The hat-shaped longitudinal stringers are co-cured with fuselage skin. The strips of composites are laid into etched grooves for structural support. Finally, windows and doors are cut out by abrasive water jets into fuselage after curing.

All of the carbon/epoxy composites for Boeing 787 are supplied by Toray Industries, the world's largest producer of carbon fibers. The demand for ex-PAN carbon fiber has grown tremendously with the advent of Boeing 787. Boeing 787 represented very large-scale application of composites, not seen heretofore. Toray's 3900-Z prepreg consisting of intermediate modulus T800 carbon fiber and a toughened epoxy matrix (cured at 175 $^{\circ}C$) is a major material component. T800 carbon fiber has a tensile strength of 5.49 *GPa* and tensile modulus of 300 *GPa*. Toray's T700 carbon fiber (4.9 *MPa* tensile strength, *235 GPa* tensile modulus) and glass fiber are also used.

Nanoparticles are added to polymers for use in the cabin interior to improve flammability. In some areas, Boeing has used resin film infusion (RFI) for horizontal cross beams that span the fuselage. Tape laying and fiber placement machines allowed high speed production of parts. These machines allowed formation of complex geometric shapes using software tools that translate information from computer aided design (CAD) and laminate data.

Airbus Industrie has a plane, A 350 XWB that is very similar to Boeing 787 in that it consists of 53% by weight of carbon fiber/epoxy composites. It is also made by automatic fiber placement, automatic tape placement, and resin infusion techniques, very similar to the ones used for Boeing 787.

Composite materials enable aircraft such as Boeing 787 to have a high aspect ratio than in a conventional aluminum aircraft. In aerodynamics, the aspect ratio of a wing is defined as the square of the wing span divided by the area of the wing:

$$\text{Aspect ratio, } AR = b^2/A,$$

where b is the span of the wing and A is the area of the wing. A high aspect ratio indicates long, narrow wings, whereas a low aspect ratio implies short, stubby wings. The use of composites allows a high aspect ratio of wing, which together with raked wing tips makes it possible for 787 to cruise at Mach 0.85 and consume less fuel than a conventional aircraft of a comparable size.

Mach number is a dimensionless number in fluid dynamics.[1] It is defined as the ratio of flow velocity past a boundary to the local of sound. Mach 1 corresponds to the speed of sound, a speed less than Mach 1 would be subsonic while a speed greater than Mach 1 would be supersonic. The reason for this is that carbon/epoxy composites have high strength and stiffness and low density, which make it feasible to design long, slender (high AR) wings that would not be possible with

[1]The Mach number is named after the Austrian physicist, Ernst Mach. The Mach number being a dimensionless quantity, the convention is to use it in the format of Mach 1, Mach 2, etc., not 1 Mach, 2 Mach, etc.

conventional aluminum. It is worth pointing out that most birds have wings with a high aspect ratio. The V-formation commonly observed in flights of migratory birds has been regarded as akin to a single swept wing with a very high aspect ratio. It is thought that such a formation confers a high flight efficiency compared to that of a single bird in flight. Composites deliver other benefits besides weight reduction. The structural composite can integrate an acoustic damping system, thermal transfer characteristics, and electrical functions. The use of composites also allowed a large reduction in the numbers of fasteners used. Boeing also claims that there is extended lamellar flow where the inlet of the nacelle meets with the structure of nacelle. The enhanced lamellar flow results in large fuel savings.

The main wing boxes of Boeing 787 are made by Mitsubishi Heavy Industries, Tokyo, Japan. Cured, solid laminate wing skins are cut to shape by abrasive cutters (Flow International Corp, Kent, WA). These waterjet cutters can cut through thick (25 *mm*) laminates very quickly and without overheating. Thick sections can be cut at 0.67 *m/min*. Thinner (6 *mm*) laminates can be cut at *3 m/min*. PMCs such as carbon/epoxy do not undergo corrosion like metals. They do bring in other problems though, such as photo-oxidation. This requires painting and use of intermediate barrier coatings. The thermal and electrical characteristics of PMCs are much inferior from those of aluminum. Electrical shortening is not a problem with aluminum because of its high electrical conductivity. Similarly, metals like aluminum are better against lightning strikes. We discuss the lightning problem below in a separate section.

5.4.1.3 The Lightning Problem

Aircrafts encounter lightning strikes routinely in a given flight. The aircraft is shielded from such events by providing a conductive path, thereby protecting it from a structural damage as well as damage to electronics of the aircraft. In a typical lightning strike, there may be 10–200 *kA* of current and tens of *kV* of voltage. Such strikes occur in a fraction of a second. An all aluminum airplane provides the lowest resistance for the electrical discharge. It is not uncommon for an airplane to be struck by a series of lightning discharges, generally between three and five, in exceptional cases up to 25 per year. The airframe acts as a Faraday cage (an enclosure to block electromagnetic fields.) The aluminum structure, when struck by a lightning, passes the electric energy around the interior and keeps the passengers safe. The technical equipment is kept safe from the high voltage and the aircraft can, generally, proceed normally. Recall the Boeing 787 and Airbus 350 planes are 50% by weight carbon fiber/epoxy composites. They are more sensitive to lightning strikes. The high temperatures generated by the electrical discharge can burn the resin used in composite materials and hence weaken the structure. These composite airplanes require copper or nickel meshes embedded into the surface of the fuselage for protection against lightning strikes. The copper filament mesh minimizes damage to the airplane's skin where lightning attacks, and keeps the electric current

on the exterior of the airplane where it will not harm the passengers and the electrical systems inside. Note that the electrical resistivity of copper is about 1.72×10^{-8} Ωm while that of carbon is between 3 and 60×10^{-5} Ωm. That is, three orders of magnitude difference. Typically, a conductive mesh of copper minimizes damage to the skin, and prevents the buildup of electric current in any one area. The main shell of carbon fiber/epoxy composite forms the fuselage, on that we have a coat of thin corrosion-resistant layer of glass fiber/epoxy composite. On top of that goes the fine copper mesh. This conductive mesh spreads the lightning current to minimize damage to the skin where lightning attaches, and keeps the current on the exterior of the fuselage. This helps reduce any voltages that might build up inside the airplane, which could damage the electrical systems. On top of that goes a thin adhesive film to smoothen the texture of the mesh and then primer and paint. In short, composite fuselage has a sleeve of conductive mesh, which diffuses a lightning strike. Fuel tanks in the wings require protection against arcs and sparks.

We should mention that similar protection against lightning strikes is required in composite wing blades used in windmills. We discuss this later.

5.4.1.4 The Fastener Problem

Fasteners are needed in any aircraft to join different parts. A rivet is a mechanical fastener. It generally consists of a cylindrical shaft with a head on one end. The rivet is placed in a drilled hole and deformed to take the shape of a dumbbell. The rivet can support tensile and shear loads (i.e., loading perpendicular to the shaft of the dumbbell axis.) In a conventional aluminum-based aircraft, there are millions of rivets. These rivets are made of aluminum alloys. An important problem in regard to the use of carbon fiber reinforced epoxy polymers in aircraft is that one may not use aluminum rivets. Although the number of rivets used, in planes such as Boeing 787 and Airbus 350, is much lower than in a conventional aluminum frame aircraft, one runs into the problems of galvanic corrosion between aluminum and carbon. Carbon is cathodic in nature, while aluminum is anodic. Any joining involving localized heating could also be a potential source of problems because aluminum carbide may form as a result of overheating, which will be detrimental to the mechanical and corrosion properties. Aluminum carbide is very brittle and hygroscopic. What makes the galvanic corrosion so bad on an airliner fuselage is the extremely high ratio of cathode (CFRP) surface area to anode (Al) surface area. This, along with a large gap in galvanic potential, can lead to a very high rate of corrosion at the interface. The solution to this problem is to use titanium rivets; titanium has a galvanic potential close to that of carbon. The reader will realize that titanium rivets are a lot more expensive than aluminum rivets.

5.4.1.5 Use of Composites in Jet Engines: GEnx

Composites have been used in the outer parts of a modern jet engine. These include nacelles, fan exit guide vanes, ducts, etc. Attempts to introduce composite materials inside the engine have been made since mid-twentieth century. Rolls Royce tried compressor fan blades made of PMCs; most noteworthy effort being the blades for the RB-211 engine, made of carbon fiber/epoxy. These blades had severe problems in the area of foreign object damage (FOD) and reproducible properties. These problems, unfortunately, led to bankruptcy of the company in 1973. Nevertheless, RB-211 did represent an important advance of composites into the cold sections of the engines. It had a new, wide-chord design, which allowed a smaller number of blades to be used, which reduced the noise. But the FOD or bird strike problem proved to be fatal one for the company.

General Electric has also been involved in this effort to introduce PMCs into the jet engine. It launched the GE 90-768 engine which had fan blades made of polymer matrix composite. This engine was selected for Boeing B777. These fan blades have wide-chord shape. In particular, we wish to describe the GEnx engine which is used in Boeing 787 and 747. A picture of this engine showing the fan blades made of PMCs is shown in Fig. 5.25. Engine fan cases on GEnx jet engine are made by resin infusion process by GKN Aerospace at its Alabama plant. Among the special features GEnx are the following:

- Advanced dual rotor, axial flow, high bypass turbofan engine (used in Boeing 787 and 747).
- Represents an advance over GE90 turbofan, especially the use of PMCs to make fan blades and case fan.
- It is designed to produce a thrust between 240 and 330 *kN*.
- It is a quieter and a more efficient engine compared to the earlier versions.
- Use of composite blades leads to higher bypass ratio.

Following are the dimensions of GEnx:

- *Fan Diameter*: 2.8 *m* for 787 and 2.7 *m* for 747.
- *Fan blades*: carbon fiber/epoxy with titanium leading edges.
- *Fan Case*: carbon fiber/epoxy (braided fabric with optimized braid orientations).

The new fan case, made of composites, results in weight savings of about 150 *kg*/engine. The composite fan case can also survive a blade detachment without requiring an aramid fabric wrapping which is done on conventional aluminum casings. GEnx has only 18 fan blades compared to 36 in CF6. The shape optimization of blades results in this benefit, which leads to a quieter engine.

Fig. 5.25 Blades of GEnx engine are made of carbon fiber/epoxy composites. (Courtesy of General Electric Co.)

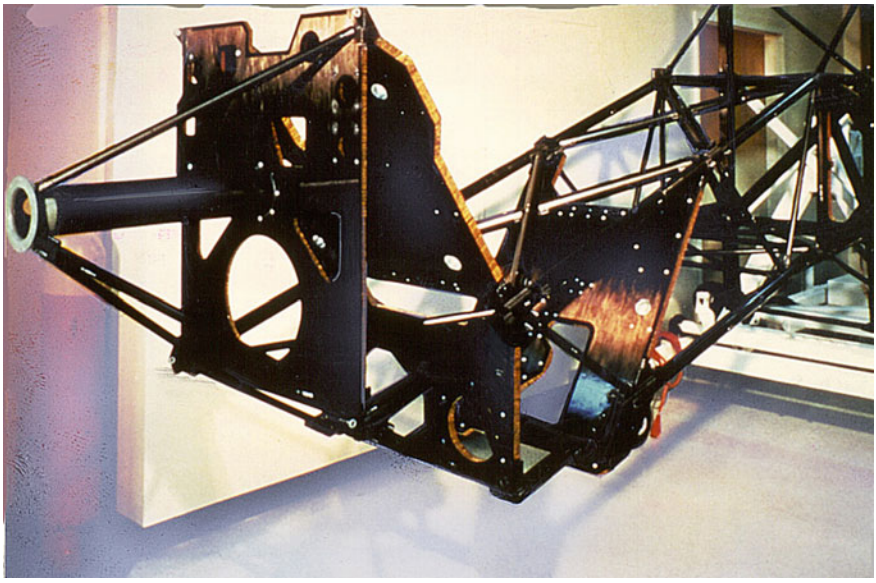

Fig. 5.26 Intelsat 5 used a primary structure and several antennas made of carbon fiber PMCs. (Courtesy of Fiberite Co.)

5.4.1.6 Other Aerospace Applications

The helicopter industry in particular has long been an enthusiastic user of carbon fiber PMCs. It is claimed that composite helicopter rotor blades have lower direct operating costs than aluminum blades (Mayer 1974), and this is without taking into account the intangibles such as longer fatigue life, reduced maintenance, and lower manufacturing costs. Boeing Vertol, Bell Aircraft, and Sikorsky, among others, use composite rotor blades in their helicopters. Cargo bay doors, maneuvering engine pods, arm booms, and booster rocket casings in the U.S. Space Shuttle Orbiter are made of carbon fiber/epoxy composites. Figure 5.26 shows the primary tower structure and several antennas made of carbon fiber/epoxy for use in Intelsat 5. The main attractions for their use are lightness and dimensional stability.

5.4.1.7 Applications in Leisure Industry

The leisure and sporting goods industry is another big market for PMCs. Golf clubs, archery bows, fishing rods, tennis rackets, cricket bats, and skis are commonplace items in which carbon fiber PMCs are used. Figure 5.27a shows a tennis racket, a pair of skis, and a fishing rod while Fig. 5.27b shows a bicycle frame made of carbon fiber/epoxy. Note the sleek lines that have become a hallmark of composite construction. In addition to attractive mechanical characteristics, carbon fiber reinforced thermoplastic composites have excellent electrical properties. This is exploited in situations where a static charge builds up easily, for example, in high speed computer parts and in musical instruments where rubbing, sliding, or separation of an insulating material results in electrostatic voltages. In parts made of insulating polymeric resins, this charge stays localized until the polymer comes in contact with a body at a different potential and the electrostatic voltage discharges via an arc or spark. Voltages as high as 30–40 kV can build up. This electrostatic charge can be painful to a human being or even fatal in extreme circumstances. Some very sensitive microelectronic parts can be damaged by an electrostatic discharge of a mere 20 V. Thus, it is not surprising that carbon fibers dispersed in thermoplastic resins find applications where dissipation of a static charge is important. Of course, conductive fillers of other than carbon fiber can be used to overcome the problem of static electricity, but carbon fibers also serve to reinforce mechanically in situations requiring high strength and wear resistance. Figure 5.28a, b shows a microphone and head shell, the unit that holds the stylus at the end of the turntable arm. Carbon fibers dissipate the static directly, thus eliminating the need for copper conductors. This is coupled with a high stiffness-to-weight ratio of these composites, which allows a weight reduction of the part as well. We should also mention that quite a few companies are making musical instruments such as guitars, violins, and violas as well as bows out of carbon fiber reinforced composites.

Fig. 5.27 Examples of sporting goods made of carbon fiber composites where lightness, good mechanical characteristics, and sleek lines make the items very attractive: **a** tennis racket, a pair of skis, and a fishing rod. (Courtesy of Fiberite Co.), **b** a bicycle frame made of carbon fiber/epoxy. (Courtesy of Trek Co.)

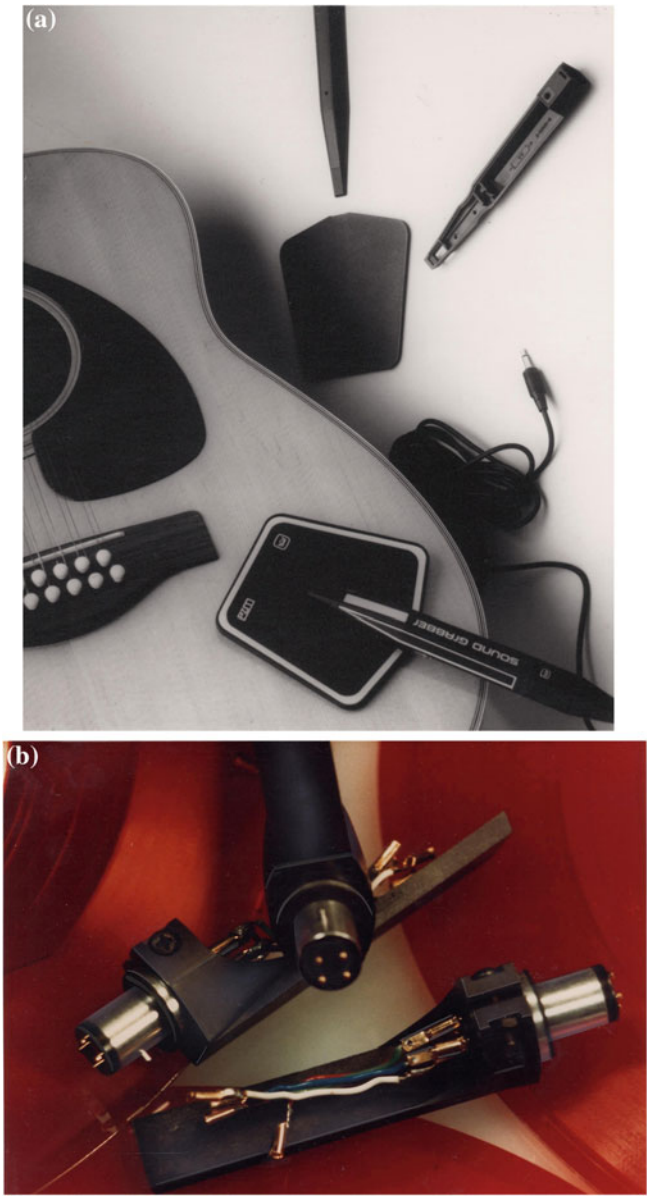

Fig. 5.28 Use of carbon fiber/thermoplastic matrix composites in situations involving static charge: **a** microphone, **b** a head shell unit of a turntable arm. (Courtesy of LNP Corporation.)

5.4.1.8 Electromagnetic Shielding

Shielding against electromagnetic interference (EMI) is another area where highly conductive composites based on carbon fibers are finding applications. EMI is nothing but electronic pollution or noise caused by rapidly changing voltages. Examples include avionic housings, computer enclosures, and any other electronic device that needs protection against stray EMI. Nickel-coated carbon fibers are used in shielding against electromagnetic and radio frequency interference. Nickel confers excellent conductivity while retaining the flexibility of carbon fibers. In aircraft, such a composite can provide protection against lightning strikes. Radar-absorbing materials are used to reduce EMI. Navy ships carry a large number of antennas, computers, and telecommunications equipment. A myriad of EMI problems can arise under such circumstances. Nickel is deposited by chemical vapor deposition on carbon fibers. Nickel-coated carbon fibers can be incorporated into a polymeric matrix by any of the methods described earlier. Finely chopped nickel-coated carbon fibers can be incorporated in adhesives, sealants, gaskets, and battery electrodes for use in aerospace and for electronic applications requiring EMI shielding.

It is convenient to measure shielding effectiveness or attenuation in decibels (*dB*), which is nothing but a logarithmic scale. The decibel scale is preferred when a quantity can vary over several orders of magnitude. Electromagnetic shielding effectiveness (*SE*) can be defined as follows:

$$\textit{Shielding effectiveness}\,(SE) = 20\,\log\left(\frac{\textit{incident field strength}}{\textit{transmitted field strength}}\right).$$

Table 5.3 shows the correspondence between shielding effectiveness in *dB* and signal attenuation in percentage. A shielding level of 80 *dB* implies 99.99% attenuation of the incident electromagnetic radiation. For most business electronic equipment with 30–1000 *MHz* frequency, 35–45 *dB* attenuation is adequate. Requirements of military applications are more stringent, and 60–80 *dB* attenuation is not uncommon.

While there are applications involving the use of the conductive properties of carbon fibers, there are also certain problems associated with this characteristic of carbon fibers. Carbon fibers are extremely fine and light, and if they become accidently airborne, for any reason, and settle on electrical equipment, short circuit can occur. The conclusion of extensive studies conducted at NASA on this problem was that despite the risk, there was no reason to prohibit the use of carbon fibers in structures; see NASA (1980).

Table 5.3 Correspondence between shielding effectiveness in dB and % signal attenuation

Shielding effectiveness (dB)	Attenuation (%)
20	90
40	99
60	99.9
80	99.99

5.4.1.9 Civil Infrastructure Applications

A major development in the 1990s has been the use of fiber reinforced composites in civil infrastructure. Among the major drivers for this are reduced cost, corrosion resistance, improved life and reduced maintenance, and possible reduction in seismic problems. Major effort has been in the area of bridges, new as well repair and retrofit. As an example, concrete and masonry structures can be strengthened by composites rather than steel plates. One such process involves surface preparation and application of an appropriate primer to the concrete structure, application of a resin coat, followed by a sheet of composite and a second coat of resin. Both glass fiber and carbon fiber reinforced composites are used, although carbon fiber reinforced polymer composites give superior results. As an illustrative example, we show in Fig. 5.29a a concrete column wrapped around with a jacket of carbon fiber/epoxy composite, while Fig. 5.29b shows the results after the application of a compressive load. In the part of the concrete column without the composite jacket, the spalling of concrete and buckling of the steel reinforcement bars can be seen. In the portion of the column protected with a composite jacket, there is no visible effect. Potentially, composite wrapping of structural columns for seismic reinforcement would appear to be a huge market. The reader should not get the impression that everything is perfect in this area of use of composites in the civil infrastructure. There are many problems, such as durability, moisture absorption by the polymer matrix, and other environmental effects. In addition, there is a lack of design guidelines and database of material specifications, which makes it difficult for civil engineers to accept the composites.

Carbon fiber is also used to reinforce cement. The resultant brittle composite shows improved tensile and flexural strength, high impact strength, dimensional stability, and high resistance to wear. Another application of carbon fiber PMCs in civil infrastructure has to do with the ability of bridges and other structures to withstand earthquakes. Earthquake-proofing of bridge columns is done by wrapping columns with carbon fiber reinforced composites as described above.

Reinforced concrete is a common building construction material. Since reinforced concrete has high compressive strength but low tensile strength, we use reinforcing bars, often referred to as rebar, on the tensile side of concrete structures. Conventional rebar is made of steel, which is quite an effective and cost-efficient reinforcement material for concrete. The main problem with steel rebar is that it is subject to corrosion by chloride ions. Chloride ions are present in coastal areas, locations where salt is used for deicing, and sites where aggressive chemicals and

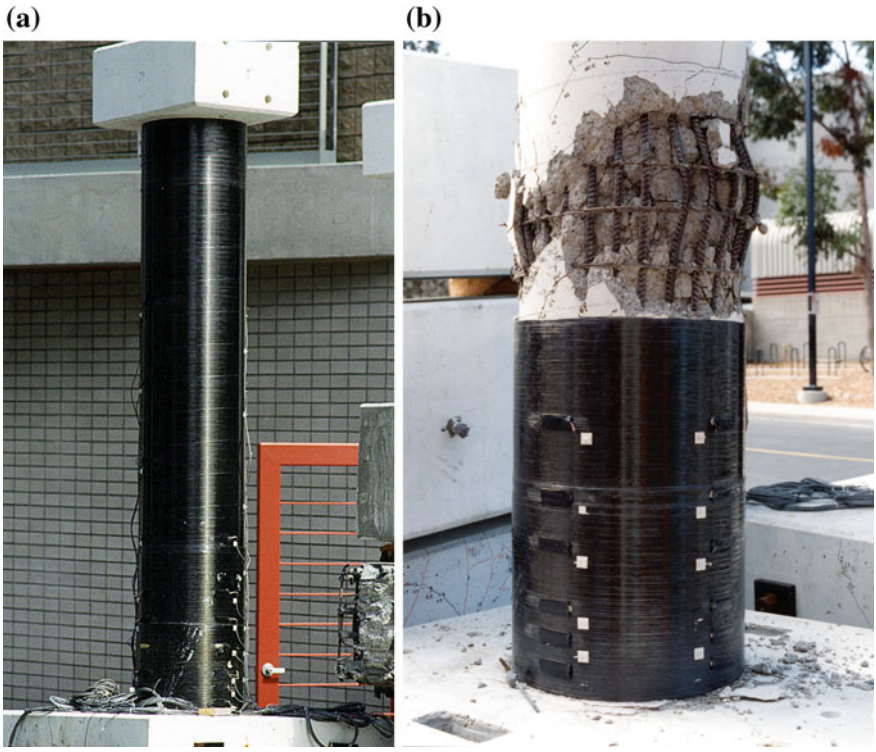

Fig. 5.29 **a** A concrete column wrapped around with a jacket of carbon fiber/epoxy composite while **b** On application of a compressive load, spalling of concrete, and buckling of the steel reinforcement bars can be seen in the part of the concrete column without the composite jacket. In the portion of the column protected with a composite jacket, there is no visible effect. (Courtesy of B. Kad.)

ground conditions provide chloride ions. It turns out that the products of corrosion of rebar have a larger volume (2–5 times) than the original metal that is consumed in the corrosion process. This change in volume leads to tensile loading of the concrete, followed by cracking and spalling. One way out of this problem has been to use epoxy-coated steel rebar. Of course, stainless steel would solve the corrosion problem, but it would be highly uneconomical. A glass fiber reinforced polymer composite rebar can be used as non-prestressed reinforcement in concrete. These composite rebars are resistant to chloride ion attack, have a tensile strength of 1½–2 times that of steel, and weigh only 25% of the weight of equivalent size steel rebar. The elastic modulus of glass fiber polymer is about 50 *GPa*, much less than that of steel, about 210 *GPa*. This lower stiffness causes greater deflection in the structure which can lead to cracking. Other reinforcements such as carbon fiber, aramid fiber, or S glass fiber can be used instead of E glass fiber, but all these fibers are very expensive, so these options are generally not cost-effective compared to steel. Yet

another point that needs to be taken into account is the higher ductility of steel compared to that of composite rebar.

5.4.1.10 PMCs in Wind Energy

Wind energy is an important renewable energy resource. Here, we briefly describe the basic concept of a wind turbine and how and why polymer matrix composites play a vital role in this field.

Windmills of one sort or another have been around for quite a while. Electrical power is produced by the spinning blades of a wind turbine. The basic principle behind the windmill is very simple. Large, multiple airfoil blades (commonly three) move under the action of wind. When the wind blows, it creates positive pressure on the front side of the blade and negative pressure behind it, i.e., the blade moves because of differential air pressure on the airfoil, which makes the rotor turn. The blade movement produces mechanical energy which is converted into electrical energy by a generator.

In the past, windmill blades were made of wood. A typical windmill consists of a rotor with aerodynamically shaped blades (commonly, a set of three) placed on a tower. The rotor blade has the shape of an aerofoil like the wing of an airplane. The material for the skins of the aerofoil needs to be strong, stiff, but light. These requirements lead to wood and fiber reinforced polymer composites as the optimum materials. Wood does not measure up to the composites mainly because of a very large variability in properties and likely environmental damage. Since 1990s, fiber reinforced composites have been increasingly used to make the blades of a windmill. Most common composites used are glass fiber reinforced epoxy composites and carbon fiber/epoxy forms a distant second. Glass fiber composites are cheaper than carbon fiber composites. However, longer blades (60 m) can be made by a judicial mix of glass and carbon fibers to lower the mass of the blade. The longer blades improve the efficiency of turbine (see below). The most common resin matrices are bisphenol-A epoxy or unsaturated polyester or vinyl ester. Three blades are commonly used on a windmill turbine. It should be pointed out that the skins of the turbine blade's fiber are made of fiber reinforced polymers as facings with the core being made of suitable foam.

Figure 5.30 shows an offshore windmill farm. The rotors of such windmills are typically made of glass fiber reinforced epoxy. The rotor blade corresponds to an elastic beam. For such a beam, we can define a figure of merit (Brøndsted et al. 2005)

$$M_b = E^{0.5}/\rho,$$

where E is the Young's modulus or tensile stiffness and ρ is the density of the material. One can have a figure of merit based on fracture toughness as well.

Fig. 5.30 An offshore wind farm at Middelgrunden near Copenhagen, Denmark. Each rotor blade is 36.8 *m* long. (Courtesy of LM Glasfiber, www.lmglasfiber.com)

The blades spin at 25 *rpm* under forces that are equivalent to forces encountered by a widebody jet at takeoff. Some blades are comparable in size to the wing of a Boeing 747 aircraft. In a windmill, a turbine converts the kinetic energy of wind into electrical energy with the power, P, given by (Brøndsted et al. 2005)

$$P = \alpha \rho A v^3,$$

where α is a constant based on aerodynamic efficiency, ρ is the density of air, A is the area of the rotor plane, and v is the wind velocity. We note from the above expression that the power obtained in a windmill is proportional to the square of the radius, r of the windmill, and to the cube of wind velocity, v, i.e.,

$$P \propto r^2 v^3.$$

So, for a given wind velocity, it makes sense to increase the radius of the windmill. In 1990s, wind turbines commonly had 15 *m* long blades and could produce 50 *kW* of power. In modern times, blades of length 60 *m* are not uncommon, while the largest wind turbines could produce 5 *MW* of power.

5.4.1.11 Processing of Rotor Blades

Rotor blades can be made manually (e.g., wet layup), but manual processes are restricted to small blades. Manual processes are cheap but quality control is questionable. Variability of the resin content can be a serious problem in wet layup. Use of prepregs helps to avoid this problem, but one must apply heat and pressure for consolidation, which adds to the cost. Large blades can be made by filament winding or automatic tape placement. Blade skins made by manual processes are made as two half-shells and cured. The skins are then bonded by adhesives.

Automation of the layup process of fiber in the blade mold can lead to economies of processing large blades. In an automatic process automatic tape laying or automatic fiber placement, the blade geometry is programmed into control system. Commonly the molds themselves are made of composite materials.

5.4.1.12 Loading of Rotor Blades in a Windmill

The rotor blades of a wind turbine made of fiber reinforced polymer composites experience gravity, centrifugal forces because of the rotation of the rotor, and cyclic fatigue loading. The blades are commonly designed for a lifetime of about 20 years which translates to 10^8–10^9 cycles (Brøndsted et al. 2005). Fatigue loading of the turbine blade and the gearbox can be a serious problem. One should point out a major difference between the fatigue loading of the wing of an aircraft and the blade of a wind turbine; the loading conditions in a windmill are more strenuous. An aircraft at its cruising speed at high altitudes is not subjected to the same forces as a wind turbine blade on earth. It is important to realize that if, during high-speed spinning of the rotor blades, one of the blades came loose and smashed into the central tower, it could cause the whole structure to collapse. Such incidents have been captured on video.

5.4.1.13 Static Testing of Windmill Blades

Static loading is carried out in a traction rig attached to the blade by steel wires. The blade is loaded in tension to maximum load. According to the practice used at LM Glasfiber, a large manufacturer of windmills, the rotor blade must stay under load for at least 10 *s* without breaking. The tensile test is repeated twice flapwise and then the extreme load is tested in all directions: leading edge, trailing edge, suction side, and pressure side. It can take about a week to do the static testing, and the test is repeated after the blade has been subjected to the dynamic test (see the description of the dynamic test below). This is done to make sure that the dynamic or fatigue loading of the blade has not introduced a subcritical damage.

5.4.1.14 Dynamic Testing of Windmill Blades

Dynamic testing of the rotor blades is very important because they must be able to sustain fatigue loads corresponding to 20 years of life. Every material has a natural frequency of oscillation, f, given by

$$f = \frac{1}{2\pi}\sqrt{\frac{k}{m}},$$

where k is the stiffness (N/m) and m is the mass. The blade sets into oscillation corresponding to its natural frequency. The larger or more massive the blade, the lower the natural frequency. It is not uncommon to subject the blade to five million oscillations edgewise followed by five million oscillations flapwise. A 60 m long blade could easily be fatigue tested for a year. During fatigue testing, nondestructive techniques are used to detect any damage in the blades, e.g., an infrared camera may be used to detect cracks in the laminate. Concurrently, many strain gages, attached to the surface of the blade, are used to track the deformation and deflections.

5.4.1.15 Protection Against Lightning

As is well known, lightning strikes the highest point in a given area. This makes wind turbines a very likely target, because of their height and elevated location. Lightning strikes involve currents of very large amperage (can be up to 200 kA) and they release very large amount of energy in a very short time period (milliseconds). Besides the obvious electrical and magnetic properties, lightning strikes involve X-rays, thunder which is nothing but an acoustic shock wave, and intense heat. Thus, a lightning strike can easily destroy a blade, if it is not protected. Windmills in offshore locations are particularly vulnerable to lightning strikes. Commonly, lightning protection involves several external copper air termination disks called receptors, which are fastened to an aluminum cable in the blade interior running its entire length. Conductors are fastened to the blade and to one another with bolts, near the blade root a portion of the conductor is embedded into the fiber reinforced composite. From the blade root area, the conductor is bonded to the hub and then to the ground. LM Glasfiber uses a system consisting of several receptors placed on both sides of the blade. Each receptor is capable of conducting the energy generated by a lightning strike to the main cable, on its own. Together, the multiple receptors improve the lightning protection along the entire length of the blade.

Problems

5.1. Why are prepregs so important in polymer matrix composites? What are their advantages? Describe the different types of prepregs.

5.2. Randomly distributed short fibers should result in more or less isotropic properties in an injection molded composite. But this is generally not true. Why? What are the other limitations of injection molding process?
5.3. In a thermally cured PMC, the fiber surface treatments have been well established for certain systems. For example, silanes are used on glass fiber in an epoxy matrix while an oxidizing treatment is given to carbon fiber for use in an epoxy matrix. What would be the effect of electron beam curing on the interface development in a PMC?
5.4. Describe the major differences in the processing of composites having a thermoset matrix and those having a thermoplastic matrix.
5.5. What are the important factors in regard to fire resistance of PMCs?

References

B.W. Anderson, *Advances Fracture Research*, ICF4, vol. 1 (New Delhi, Pergamon Press, Oxford, 1984), p. 607
A. Baker, Met. Forum. **6**, 81 (1983)
H.W. Bergmann, *Advances in Fracture Research*, ICF4 (New Delhi, Pergamon Press, Oxford, 1984), p. 569
D.A. Biro, G. Pleizier, Y. Deslandes, J. Mater. Sci. Lett. **11**, 698 (1992)
P. Brøndsted, H. Lilholt, A. Lystrup, Ann. Rev. Mater. Res. **35**, 505 (2005)
J.R. Brown, P.J.C. Chappell, Z. Mathys, J. Mater. Sci. **27**, 3167 (1992)
C.H. Chen, G.S. Springer, J. Compos. Mater. **10**, 2 (1976)
D. Clark, N.J. Wadsworth, W. Watt, *Carbon Fibres, Their Place in Modern Technology* (The Plastics Institute, London, 1974), pp. 44
F.N. Cogswell, *Thermoplastic Aromatic Polymer Composites* (Butterworth-Heinemann, Oxford, 1992), p. 136
T.A. Collings, D.E.W. Stone, Composites **16**, 307 (1985)
R.J. Diefendorf, *Tough Composite Materials* (Noyes Publishing, Park Ridge, NJ, 1985), p. 191
J.-B. Donnet, R.C. Bansal, *Carbon Fibers* (Marcel Dekker, New York, 1984), p. 109
L.T. Drzal, M.J. Rich, P.F. Lloyd, J. Adhes. **16**, 1 (1983a)
L.T. Drzal, M.J. Rich, M.F. Koenig, P.F. Lloyd, J. Adhes. **16**, 133 (1983b)
G.J. Ehlert, Y. Lin, U. Galan, H.A. Sodano, J. Solid. Mech. Mater. Eng. **4**, 1687 (2010)
P. Ehrburger, J.B. Donnet, Philos. Trans. R Soc. London **A294**, 495 (1980)
R.H. Eriksen, Composites **7**, 189 (1976)
K. Friedrich, Compos. Sci. Tech. **22**, 43 (1985)
A. Goel, K.K. Chawla, U.K. Vaidya, M. Koopman, J. Mater. Sci. **43**, 4423 (2008)
N.L. Hancox, *Fabrication of Composite Materials* (North-Holland, Amsterdam, 1983), p. 1
D.N. Hild, P. Schwartz, J. Adhes. Sci. Technol. **6**, 879 (1992a)
D.N. Hild, P. Schwartz, J. Adhes. Sci. Technol. **6**, 897 (1992b)
D. Hull, *An Introduction to Composite Materials* (Cambridge University Press, Cambridge, UK, 1981), p. 42
D. Hull, Mater. Sci. Eng. **A184**, 173 (1994)
H. Ishida, J.L. Koenig, J. Colloid Interface Sci. **64**, 555 (1974)
I. Jangehud, A.M. Serrano, R.K. Eby, M.A. Meador, *Proceedings of 21st Biennial Conference on Carbon* (Buffalo, NY, 13–18 June)
R.L. Kaas, J.L. Kardos, Polym. Eng. Sci. **11**, 11 (1971)

S.L. Kaplan, P.W. Rose, H.X. Nguyen, H.W. Chang, SAMPE. Q. **19**, 55 (1988)
J.L. Kardos, *Molecular Characterization of Composite Interfaces* (Plenum Press, New York, 1985), p. 1
C.E. Knox, *Handbook of Composite Materials* (Van Nostrand Reinhold, New York, 1982), p. 136
W. Krause, F. Henning, S. Troster, O. Geiger, P. Eyerer, J. Thermoplast. Compos. Mater. **16**, 292
Z.F. Li, A.N. Netravali, W. Sachse, J. Mater. Sci. **27**, 4625 (1992)
R.J. Lockwood, L.M. Alberino, *Advances in Urethane Science and Technology* (Technomic Press, Westport, CT, 1981)
N.J. Mayer, *Engineering Applications of Composites* (Academic Press, New York, 1974), p. 24
D. McKee, V. Mimeault, *Chemistry and Physics of Carbon*, vol. 8 (Marcel Dekker, New York, 1973), p. 151
R.W. Meyer, *Handbook of Pultrusion Technology* (Chapman & Hall, New York, 1985)
NASA, *Risk to the Public from Carbon Fibers Released in Civil Aircraft Accidents, SP-448* (NASA, Washington DC, 1980)
H. Ning, N. Lu, A. A. Hassen, K. Chawla, M. Selim, S. Pillay, Int. Mater. Rev. (2019). doi: 10.1080/09506608.2019.1585004
R.B. Pipes, N.J. Pagano, J. Compos. Mater. **1**, 538 (1970)
E.P. Plueddemann, *Interfaces in Polymer Matrix Composites* (Academic Press, New York, 1974a), p. 174
D.M. Riggs, R.J. Shuford, R.W. Lewis, *Handbook of Composites* (Van Nostrand Reinhold, New York, 1982), p. 196
J.M. Sands, B.K. Fink, S.H. McKnight, C.H. Newton, J.W. Gillespie Jr., G.R. Palmese, Clean. Prod. Process. **2**, 228 (2001)
A.M. Shibley, *Handbook of Composite Materials* (Van Nostrand Reinhold, New York, 1982), p. 448
C.D. Shirrel, F.A. Sandow, *Fibrous Composites in Structural Design* (Plenum Press, New York, 1980), p. 795
A. Slobodzinsky, *Handbook of Composite Materials* (Van Nostrand Reinhold, New York, 1982), p. 368
J.B. Sturgeon, Creep of engineering materials. J. Strain. Anal. Monogr. 175 (1978)
Y.M. Tarnopol'skii, Y.M. Bail' AI, *Fabrication of Composites* (North-Holland, Amsterdam, 1983), p. 45
U.K. Vaidya, K.K. Chawla, Int. Mater. Rev. **53**, 185 (2008a)
A.J. Waddon, M.J. Hill, A. Keller, D.J. Blundell, J. Mater. Sci. **27**, 1773 (1987)
Z.R. Xu, K.H.G. Ashbee, J. Mater. Sci. **29**, 394 (1994)

Suggested Reading

E.P. Plueddemann (ed.), *Interfaces in Polymer Matrix Composites* (Academic Press, New York, 1974b)
U.K. Vaidya, K.K. Chawla, Processing of fibre reinforced thermoplastic composites. Int. Mater. Rev. **52**, 185 (2008b)

Chapter 6
Metal Matrix Composites

Metal matrix composites consist of a metal or an alloy as the continuous matrix and a reinforcement that can be particle, short fiber or whisker, or continuous fiber. In this chapter, we first describe important techniques to process metal matrix composites, then we describe the interface region and its characteristics, properties of different metal matrix composites, and finally, we summarize different applications of metal matrix composites.

6.1 Types of Metal Matrix Composites

There are three kinds of metal matrix composites (MMCs):

- Particle reinforced MMCs,
- Short fiber or whisker reinforced MMCs, and
- Continuous fiber or sheet reinforced MMCs.

Table 6.1 provides examples of some important reinforcements used in metal matrix composites and their aspect (length/diameter) ratios and diameters. Particle or discontinuously reinforced MMCs have become very important because they are inexpensive vis à vis continuous fiber reinforced composites and they have relatively isotropic properties compared to fiber reinforced composites. Figure 6.1a, b shows typical microstructures of continuous alumina fiber/magnesium alloy and silicon carbide particle/aluminum alloy composites, respectively. Use of nanometer-sized fullerenes as a reinforcement has been tried. In addition to being very small, fullerenes (of which C_{60} is the most common) are light and hollow. The important question in this regard is whether they remain stable during processing and service. For the interested reader, we cite work by Barrera et al. (1994), who used powder metallurgy, rf sputtering of a composite (multifullerene) target, and thin film codeposition methods to make fullerene/metal composites. Specifically, fullerene/copper composites were processed by sputtering copper during fullerene

K. K. Chawla, *Composite Materials*,
https://doi.org/10.1007/978-3-030-28983-6_6

Table 6.1 Typical reinforcements used in metal matrix composites

Type	Aspect ratio	Diameter, μm	Examples
Particle	~1–4	1–25	SiC, Al_2O_3, WC, TiC, BN, B_4C
Short fiber or whisker	~10–1000	0.1–25	SiC, Al_2O_3, Al_2O_3+SiO_2, C
Continuous fiber	>1000	3–150	SiC, Al_2O_3, Al_2O_3+SiO_2, C, B, W, NbTi, Nb_3Sn

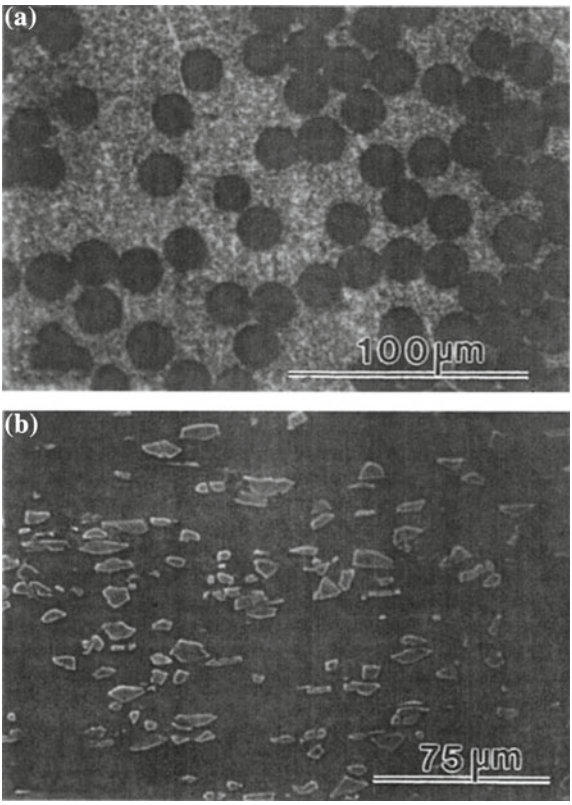

Fig. 6.1 **a** Transverse cross-section of continuous alumina fiber/magnesium alloy composite. **b** Typical microstructure of a silicon carbide particle/aluminum alloy composite (Courtsey of N. Chawla). Note the angular nature of SiC particles and alignment of particles along the long axis

sublimation in an argon atmosphere. Fullerenes were found to withstand the processing. However, in the case of aluminum matrix, brittle Al_4C_3 was observed to form at high temperatures.

6.2 Important Metallic Matrices

A variety of metals and their alloys can be used as matrix materials. We describe briefly the important characteristics of some of the more common ones.

6.2.1 Aluminum Alloys

Aluminum alloys, because of their low density and excellent strength, toughness, and resistance to corrosion, find important applications in the aerospace field. Of special mention in this regard are the Al–Cu–Mg and Al–Zn–Mg–Cu alloys, very important precipitation hardenable alloys. Aluminum–lithium alloys form one of the most important precipitation hardenable aluminum alloys. Lithium, when added to aluminum as a primary alloying element, has the unique characteristic of increasing the elastic modulus and decreasing the density of the alloy. Understandably, the aerospace industry has been the major target of this development. Al–Li alloys are precipitation hardenable, much like the Al–Cu–Mg and Al–Zn–Mg–Cu alloys. The precipitation hardening sequence in Al–Li alloys is, however, much more complex than that observed in conventional precipitation-hardenable aluminum alloys. Generally, these alloys contain, besides lithium, some copper, zirconium, and magnesium. Vasudevan and Doherty (1989) provide an account of the heat treatments and structure/property aspects of various aluminum alloys.

6.2.2 Titanium Alloys

Titanium is one of the important aerospace materials. It has a density of 4.5 gcm^{-3} and a Young's modulus of 115 *GPa*. For titanium alloys, the density can vary between 4.3 and 5.1 gcm^{-3}, while the modulus can have a range of 80–130 *GPa*. High strength/weight and modulus/weight ratios are important. Titanium has a relatively high melting point (1672 °*C*) and retains strength to high temperatures with good oxidation and corrosion resistance. All these factors make it an ideal material for aerospace applications. Titanium alloys are used in jet engines (turbine and compressor blades), fuselage parts, etc. It is, however, an expensive material.

At supersonic speeds, the skin of an airplane heats up so much that aluminum alloys are no good; titanium alloys must be used at such high temperatures. At speeds greater than Mach 2, the temperatures will be even higher than what titanium alloys can withstand. Titanium aluminides are one of the candidate materials in this case.

Titanium has two polymorphs: alpha (α) titanium has a hexagonal close packed (hcp) structure and is stable below 885 °*C* and beta (β) titanium has a bcc structure

and is stable above 885 °*C*. Aluminum raises the $\alpha \rightarrow \beta$ transformation temperature, i.e., aluminum is an alpha stabilizer. Most other alloying elements (Fe, Mn, Cr, Mo, V, No, Ta) lower the $\alpha \rightarrow \beta$ transformation temperature, i.e., they stabilize the β phase. Thus, three general alloy types can be produced, viz., α, $\alpha + \beta$, and β titanium alloys. The Ti–6%Al–4% V, called the *workhorse* Ti alloy of the aerospace industry, belongs to the $\alpha + \beta$ group. Most titanium alloys are not used in a quenched and tempered condition. Generally, hot working in the $\alpha + \beta$ region is carried out to break the structure and distribute the α phase in an extremely fine form.

Titanium has a great affinity for oxygen, nitrogen, and hydrogen. Parts per million of such interstitials in titanium can change mechanical properties drastically; in particular, embrittlement can set in. That is why welding of titanium by any technique requires protection from the atmosphere. Electron beam techniques, in a vacuum, are frequently used.

6.2.3 Magnesium Alloys

Magnesium and its alloys form another group of very light materials. Magnesium is one of the lightest metals; its density is 1.74 gcm^{-3}. Magnesium alloys, especially castings, are used in aircraft gearbox housings, chain saw housings, electronic equipment, etc. Magnesium, being a hexagonal close packed metal, is difficult to cold work.

6.2.4 Copper

Copper has a face centered cubic structure. Its use as an electrical conductor is quite ubiquitous. It has good thermal conductivity. It can be cast and worked easily. One of the major applications of copper in a composite as a matrix material is in niobium-based superconductors.

6.2.5 Intermetallic Compounds

Intermetallic compounds can be ordered or disordered. The structure of ordered intermetallic alloys is characterized by long range ordering, i.e., different atoms occupy specific positions in the lattice. Because of their ordered structure, the motion of dislocations in intermetallics is much more restricted than in disordered alloys. This results in retention (in some cases, even an increase) of strength at elevated temperatures, a very desirable feature. For example, nickel aluminide shows a marked increase in strength up to 800 °*C*. An undesirable feature of

intermetallics is their extremely low ductility. Attempts at ductility enhancement in intermetallics have involved a number of metallurgical techniques. Rapid solidification is one method. Another technique that has met success is the addition of boron to Ni_3Al. With extremely small amounts of boron (0.06 *wt. %*), the ductility increases from about 2% to about 50%. Long range order also has significant effects on diffusion-controlled phenomena such as recovery, recrystallization, and grain growth. The activation energy for these processes is increased, and these processes are slowed down. Thus, ordered intermetallic compounds tend to exhibit high creep resistance. Enhancing toughness by making composites with intermetallic matrix materials is a potential possibility.

An important disordered intermetallic is molybdenum disilicide ($MoSi_2$) (Vasudevan and Petrovic 1992). It has a high melting point and shows good stability at temperatures greater than 1200 °*C* in oxidizing atmosphere. It is commonly used as a heating element in furnaces. The high oxidation resistance comes from a protective SiO_2 film that it tends to form at high temperatures.

6.3 Processing

Many processes for fabricating metal matrix composites are available. For the most part, these processes involve processing in the liquid and solid state. Some processes may involve a variety of deposition techniques or an in situ process of incorporating a reinforcement phase. We provide a summary of these fabrication processes.

6.3.1 Liquid State Processes

Metals with melting temperatures that are not too high, such as aluminum, can be incorporated easily as a matrix by liquid route. A description of some important liquid-state processes is given here.

Casting, or *liquid infiltration*, involves infiltration of a fiber bundle by liquid metal (Divecha et al. 1981; Rohatgi et al. 1986). It is not easy to make MMCs by simple liquid phase infiltration, mainly because of difficulties with wetting of ceramic reinforcement by the molten metal. When the infiltration of a fiber preform occurs readily, reactions between the fiber and the molten metal can significantly degrade fiber properties. Fiber coatings applied prior to infiltration, which improve wetting and control reactions, have been developed and can result in some improvements. In this case, however, the disadvantage is that the fiber coatings must not be exposed to air prior to infiltration because surface oxidation will alter the positive effects of coating (Katzman 1987). One commercially successful liquid infiltration process involving particulate reinforcement is the *Duralcan* process. Figure 6.2 shows a schematic of this process. Ceramic particles and ingot grade

aluminum are mixed and melted. The ceramic particles are given a proprietary treatment. The melt is stirred just above the liquidus temperature—generally between 600 and 700 °*C*. The melt is then converted into one of the following four forms: extrusion blank, foundry ingot, rolling bloom, or rolling ingot. The Duralcan process of making particulate composites by liquid metal casting involves the use of 8–12 μm ceramic particles. Too small particles, e.g., 2–3 μm, will result in a very large interface region and thus a very viscous melt. In foundry grade MMCs, high Si aluminum alloys (e.g., A356) are used, while in wrought MMC, Al–Mg-type alloys (e.g., 6061) are used. Alumina particles are typically used in foundry alloys, while silicon carbide particles are used in the wrought aluminum alloys.

For making continuous fiber reinforced MMCs, tows of fibers are passed through a liquid metal bath, where the individual fibers are wet by the molten metal, excess metal is wiped off, and a composite wire is produced. Figure 6.3 shows a micrograph of one such wire made of SiC fibers in an aluminum matrix. Note the multifiber cross sections in the broken composite wire. A bundle of such wires can be consolidated by extrusion to make a composite. Another pressureless liquid metal infiltration process of making MMCs is Lanxide's Primex™ process, which can be used with certain reactive metal alloys such as Al–Mg to infiltrate ceramic preforms. For an Al–Mg alloy, the process takes place between 750 and 1000 °*C* in a nitrogen-rich atmosphere (Aghajanian et al. 1989). Typical infiltration rates are less than 25 *cm/h*.

Squeeze casting, or *pressure infiltration*, involves forcing the liquid metal into a fibrous preform. Figure 6.4 shows two processes of making a fibrous preform. In the press forming process, an aqueous slurry of fibers is well agitated and poured

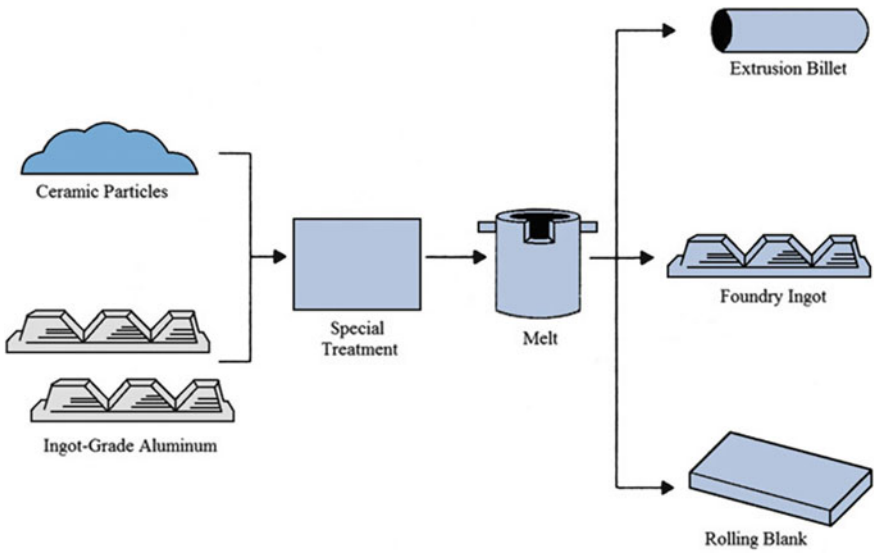

Fig. 6.2 Schematic of the Duralcan process

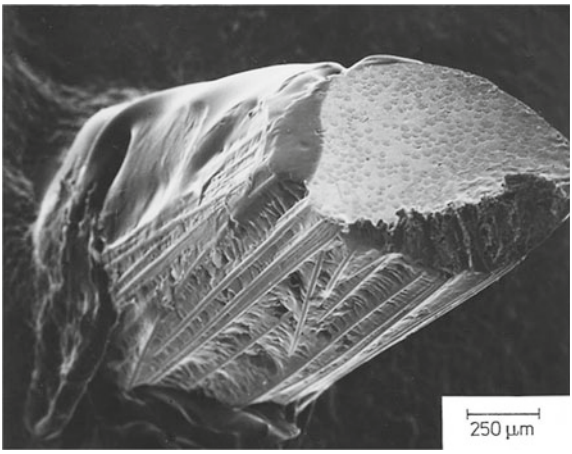

Fig. 6.3 A silicon carbide fiber/aluminum wire preform. SiC fibers can be seen in the transverse section as well as along the length the wire preform

into a mold, pressure is applied to squeeze the water out, and the preform is dried (Fig. 6.4a). In other process, suction is applied to a well-agitated mixture of whiskers, binder, and water. This is followed by demolding and drying of the fiber preform (Fig. 6.4b). A schematic of the squeeze casting process is shown in Fig. 6.5a. Pressure is applied until the solidification is complete. By forcing the molten metal through small pores of fibrous preform, this method obviates the requirement of good wettability of the reinforcement by the molten metal. Figure 6.5b shows the microstructure of Saffil alumina fiber/aluminum matrix composite made by squeeze casting. Composites fabricated with this method have minimal reaction between the reinforcement and molten metal because of short dwell time at high temperature and are free from common casting defects such as porosity and shrinkage cavities. Squeeze casting is really an old process, also called *liquid metal forging* in earlier versions. It was developed to obtain pore-free, fine-grained aluminum alloy components with superior properties than conventional permanent mold casting. In particular, the process has been used in the case of aluminum alloys that are difficult to cast by conventional methods, for example, silicon-free alloys used in diesel engine pistons where high temperature strength is required. Inserts of nickel-containing cast iron, called Ni-resist, in the upper groove area of pistons have also been produced by the squeeze casting technique to provide wear resistance. Use of ceramic fiber reinforced metal matrix composites at locations of high wear and high thermal stress has resulted in a product much superior to the Ni-resist cast iron inserts.

The squeeze casting technique, shown in Fig. 6.5a, has been quite popular in making composites with selective reinforcement. A porous fiber preform (generally of discontinuous Saffil-type Al_2O_3 fibers) is inserted into the die. Molten metal (aluminum) is poured into the preheated die located on the bed of a hydraulic press.

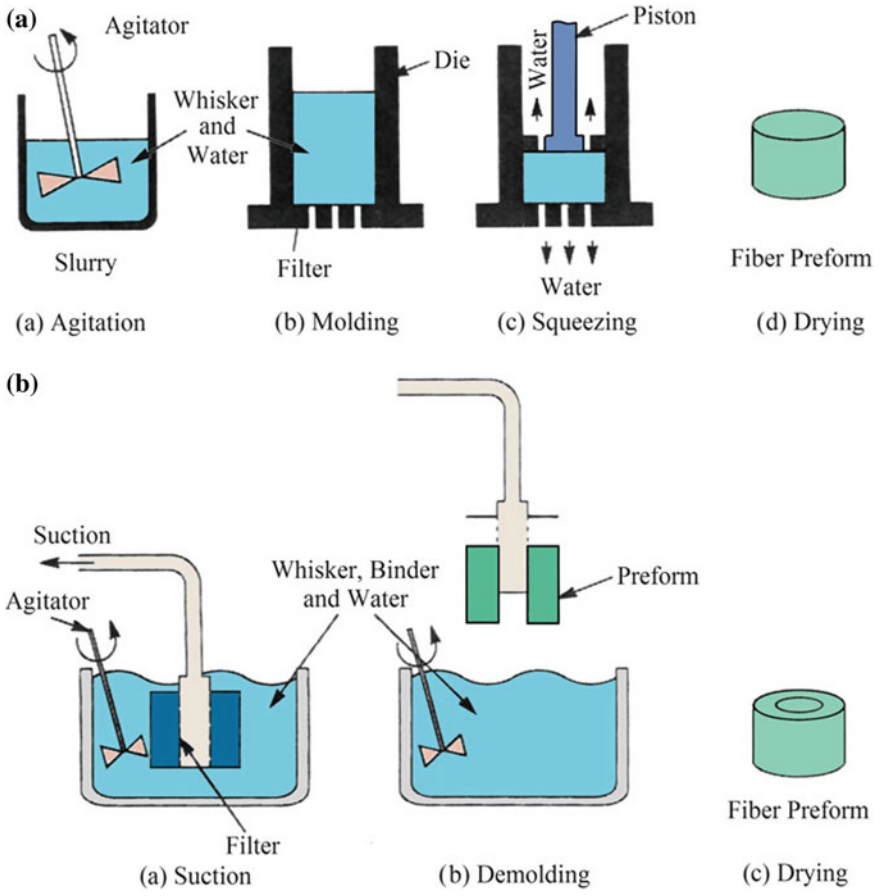

Fig. 6.4 **a** Press forming of a preform. **b** Suction forming of a preform

The applied pressure (70–100 *MPa*) makes the molten aluminum penetrate the fiber preform and bond the fibers. Infiltration of a fibrous preform by means of a pressurized inert gas is another variant of liquid metal infiltration technique. The process is conducted in the controlled environment of a pressure vessel and rather high fiber volume fractions; complex-shaped structures are obtainable (Mortensen et al. 1988; Cook and Warner 1991). Although commonly, aluminum matrix composites are made by this technique, alumina fiber reinforced intermetallic matrix composites (e.g., TiAl, Ni_3Al, and Fe_3Al matrix materials) have been prepared by pressure casting (Nourbakhsh et al. 1990). The technique involves melting the matrix alloy in a crucible in vacuum while the fibrous preform is heated separately. The molten matrix material (at about 100 °*C* above the melting point, T_m) is poured onto the

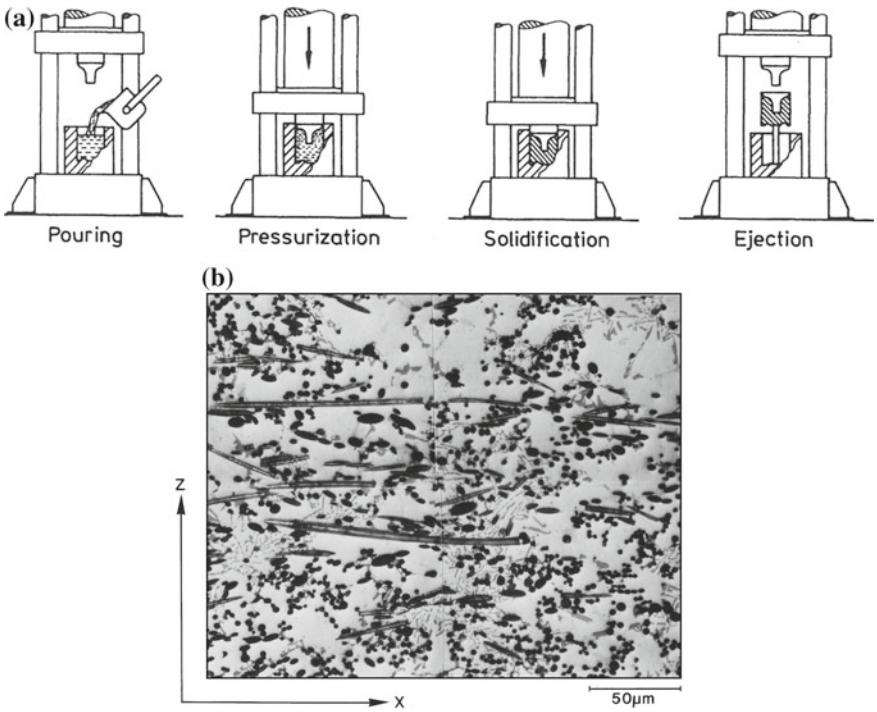

Fig. 6.5 **a** Squeeze casting technique of making a metal matrix composite. **b** The microstructure of Saffil alumina fiber/aluminum matrix composite made by squeeze casting [Courtesy of G. Eggeler]

fibers, and argon gas is introduced simultaneously. Argon gas pressure forces the melt to infiltrate the preform. The melt generally contains additives to aid wetting the fibers.

6.3.1.1 Special Issues in Casting of MMCs

Casting of metal matrix composites consisting of a metal containing particulate or fibrous reinforcement may appear to be superficially similar to casting of metals. Metals can be cast into near net-shape product forms because of their relatively low melt viscosities. In particular, when a metal is heated above its melting point (or in the case of an alloy above its liquidus temperature), we get a low viscosity liquid that has nice fluid flow characteristics such that it can be used to infiltrate a fibrous or particulate preform (Michaud 1993; Cornie et al. 1986). Darcy's law describes the phenomenon of permeability of porous medium by a fluid. Specifically, in the case of MMCs, we can write for the permeability of a porous medium, k, in terms of Darcy's law for single phase fluid flow:

$$J = -\frac{k}{\eta}\nabla P,$$

where J is the volume current density (i.e., volume/area.time) of the fluid, η is the fluid viscosity, and ∇P is the pressure gradient responsible for the fluid flow. One can immediately see that increasing the external pressure and/or decreasing the viscosity of the liquid will increase the volume current density, J.

Liquid phase processing of MMCs, more specifically, casting of aluminum matrix containing ceramic particles, one of the popular systems, requires some modifications to conventional aluminum casting processes, which are summarized as follows:

- Molten aluminum and silicon carbide can react and form Al_4C_3, an undesirable reaction product. Aluminum alloys that minimize reactivity with SiC should be used. Al–Si alloys (with Si levels of up to 9%) are typically used with SiC reinforcement. With increasing temperature, an increase in the amount of silicon is required to prevent Al_4C_3 formation.
- Covering the melt with an inert gas atmosphere will reduce oxidation of the melt.
- Addition of reinforcement particles increases the viscosity of the melt. Several equations have been proposed for the viscosity of particulate composite. The Einstein equation for dilute suspensions of spherical particles is well known, but it is valid for particle concentrations less than 0.1. The Einstein equation is

$$\eta_c = \eta_m(1 + 2.5\, V_p),$$

where η_m is the viscosity of the unreinforced metal and V_p is the volume fraction of particles. Another expression for the viscosity of a viscous melt containing particles is given by (Thomas 1965)

$$\eta_c = \eta_m\left(1 + 2.5\, V_p + 10.05 V_p^2\right).$$

Thus, the temperature of the composite melt should be above a certain limit ($\sim 745\ ^\circ C$ for Al–Si/SiC) to keep the melt from becoming highly viscous.

- Stirring of the composite melt is required (Mehrabian et al. 1974). The density of SiC (3.2 g/cm^3) is higher than that of Al (2.5 g/cm^3), so the particles will sink unless the melt is agitated. Alternating currents in a magnetic field (Katsura 1982) and mechanical vibration (Pennander and Anderson 1991) have also been used to improve wetting and permeability of the reinforcement in the liquid matrix.

6.3.1.2 Centrifugal Casting

One of the disadvantages of MMCs with ceramic reinforcement is that they are typically more difficult to machine than the unreinforced alloy. In centrifugal casting, optimal placement of the reinforcement can be achieved by inducing a centrifugal force immediately during casting which allows one to intentionally obtain a gradient in reinforcement volume fraction (Divecha et al. 1981). Figure 6.6 shows the microstructure of a centrifugally cast WC particle/bronze matrix composite. In brake rotors, for example, wear resistance is needed on the rotor face, but not in the hub area. Thus, in areas where reinforcement is not as crucial, such as in the hub area, easier machining may be obtained.

6.3.1.3 Processing of WC/Co Composites

Tungsten carbide (WC)/cobalt (Co) composites, commonly referred to as cemented carbides, are produced by powder processing. Even though powders are the starting materials in this process, we include this under the liquid phase processing category because, pressureless, liquid phase sintering is used to form the metal matrix in this composite. This is because liquid cobalt wets WC particles very easily; it has a contact angle of zero degree with WC. Tungsten carbide particles are blended with cobalt powder by milling with an organic liquid to minimize heating and prevent oxidation. After milling, the liquid is removed by a spray-drying process, resulting in free-flowing, spherical granules of WC/Co. These granules are compacted under a pressure in the range of 50–150 *MPa*, which results in green compacts having 65% of the theoretical density. This is followed by pressureless, liquid phase sintering. Good infiltration of WC particles by liquid cobalt occurs because of capillary action and enhanced interfacial diffusion. A high density composite, accompanied

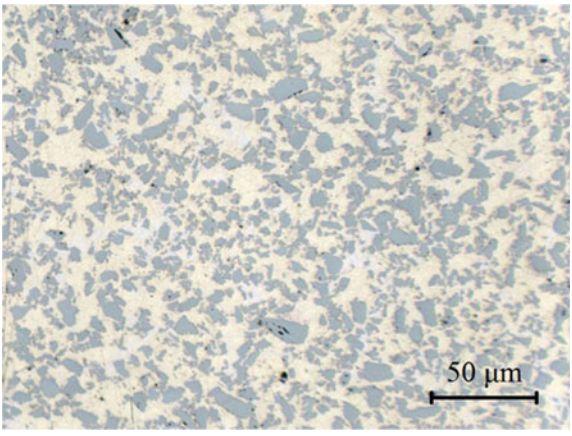

Fig. 6.6 Microstructure of a centrifugally cast WC/bronze composite

by large amount shrinkage, is obtained. The capillary action results in some rearrangement of particles, leading to a closer packing of WC particles in Co matrix.

6.3.1.4 Spray Forming

Spray forming of particulate MMCs involves the use of spray techniques that have been used for some time to produce monolithic alloys (Srivatsan and Lavernia 1992). A spray gun is used to atomize a molten aluminum alloy matrix. Ceramic particles, such as silicon carbide, are injected into this stream. Usually, the ceramic particles are preheated to dry them. Figure 6.7 shows a schematic of this process. An optimum particle size is required for an efficient transfer. Whiskers, for example, are too fine to be transferred. The preform produced in this way is generally quite porous. The co-sprayed metal matrix composite is subjected to scalping, consolidation, and secondary finishing processes, thus making it a wrought material. The process is totally computer-controlled and quite fast. It also should be noted that the process is essentially a liquid metallurgy process. One avoids the formation of deleterious reaction products because the time of flight is extremely short. Silicon carbide particles of an aspect ratio (length/diameter) between 3 and 4 and volume fractions up to 20% have been incorporated into aluminum alloys. A great advantage of the process is the flexibility that it affords in making different

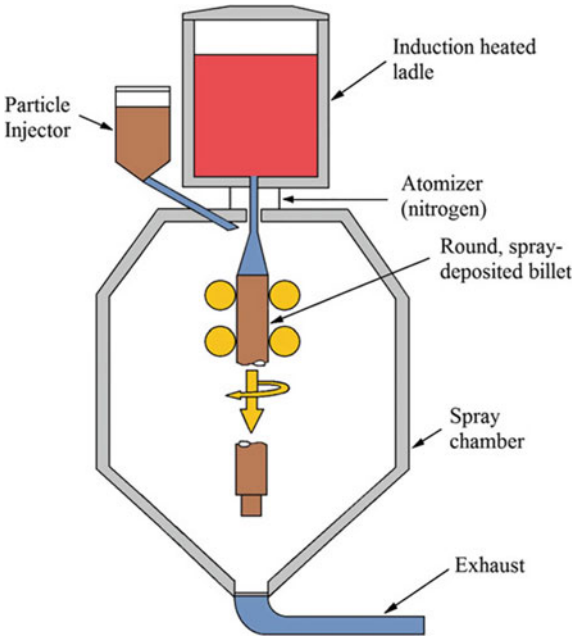

Fig. 6.7 Schematic of the spray forming process

types of composites. For example, one can make in situ laminates using two sprayers or one can have selective reinforcement. This process, however, is quite expensive, mainly because of the high cost of the capital equipment.

6.3.1.5 Modeling of Infiltration

When a metal is heated above its melting point (or in the case of an alloy above the liquidus temperature), we get a low-viscosity liquid that has nice fluid flow characteristics so that it can be used to infiltrate a fibrous preform (Michaud 1993; Cornie et al. 1986). Such an infiltration process can be described by phenomena such as capillarity and permeability. The phenomenon of permeability of a porous medium by a fluid is very important in a variety of fields. Specifically, in the case of MMCs, it is useful to be able to understand the permeability of a porous fibrous or particulate preform by the molten metal. Permeability of a porous medium, k, is commonly described by Darcy's law:

$$J = -\frac{k}{\eta}\nabla P,$$

where J is volume current density (i.e., volume/area time) of the fluid, η is the fluid viscosity, and P is the pressure that drives the fluid flow. Note that the permeability, k, is a function of the properties of the porous medium, i.e., its microstructure; it does not depend on properties of the fluid. The other equation is a continuity equation for the flow of the liquid metal:

$$\left(\frac{dV}{dx}\right) = 0,$$

where V is the velocity of flow and x is the distance. Below the liquid front, in the area of the preform, the pressure is assumed to be equal to 0. At the liquid front, there is a pressure discontinuity which is equal to the capillary pressure. Based on these two equations, it is possible to model the infiltration of liquid metal in a fibrous preform. Squeeze casting involves the application of pressure. Clyne and Mason (1987) have treated this problem.

6.3.2 Solid State Processes

Many solid state techniques to make metal matrix composites are available (Ghosh 1993). We describe some of the important ones.

Diffusion bonding is a common solid state welding technique used to join similar or dissimilar metals. Interdiffusion of atoms from clean metal surfaces in contact at an elevated temperature leads to welding. There are many variants of the basic

diffusion bonding process; however, all of them involve a step of simultaneous application of pressure and high temperature. Matrix alloy foil and fiber arrays, composite wire, or monolayer laminae are stacked in a predetermined order. Figure 6.8a shows a schematic of one such diffusion bonding process, also called the *foil–fiber–foil process*. Figure 6.8b shows the microstructure of SiC fiber/titanium matrix composite made by diffusion bonding. The starting materials in this case were made by sputter coated SiC fibers with titanium. Filament winding was used to obtain panels, about 250 μm thick. Four such panels were stacked and hot pressed at 900 $^{\circ}C$, under a pressure of 105 MPa for 3 h. A careful examination of Fig. 6.8b will show the reader interfaces between sheets of Ti alloy matrix. Vacuum hot pressing is the most important step in the diffusion bonding processes for metal matrix composites. The major advantages of this technique are the ability to process a wide variety of matrix metals and control of fiber orientation and volume fraction. Among the disadvantages are processing times of several hours, high processing temperatures and pressures, all of which make the process quite expensive; besides the fact only objects of limited size can be produced. Hot isostatic pressing (HIP), instead of uniaxial pressing, can also be used. In HIP, gas pressure against a can consolidates the composite piece contained inside the can. With HIP, it is relatively easy to apply high pressures at elevated temperatures over variable geometries.

Deformation processing of metal/metal composites involves mechanical processing (swaging, extrusion, drawing, or rolling) of a ductile two-phase material. The two phases co-deform, causing the minor phase to elongate and become fibrous in nature within the matrix. These materials are sometimes referred to as in situ composites. The properties of a deformation-processed composite depend largely on the characteristics of the starting material, which is usually a billet of a two-phase alloy that has been prepared by casting or powder metallurgy methods. Roll bonding is a common technique used to produce a laminated composite consisting of different metals in the sheet form (Chawla and Collares 1978; Sherby et al. 1985). Such composites are called sheet laminated metal matrix composites. Other examples of deformation-processed metal matrix composites are the niobium-based conventional filamentary superconductors and the silver-based high-T_c superconductors (see Chap. 9).

Deposition techniques for metal matrix composite fabrication involve coating individual fibers in a tow with the matrix material needed to form the composite followed by diffusion bonding to form a consolidated composite plate or structural shape. The main disadvantage of using deposition techniques is that they are very time consuming. However, there are several advantages:

- The degree of interfacial bonding is easily controllable; interfacial diffusion barriers and compliant coatings can be formed on the fiber prior to matrix deposition or graded interfaces can be formed.
- Thin, monolayer tapes can be produced by filament winding; these are easier to handle and mold into structural shapes than other precursor forms—unidirectional or angle-plied composites can be easily fabricated in this way.

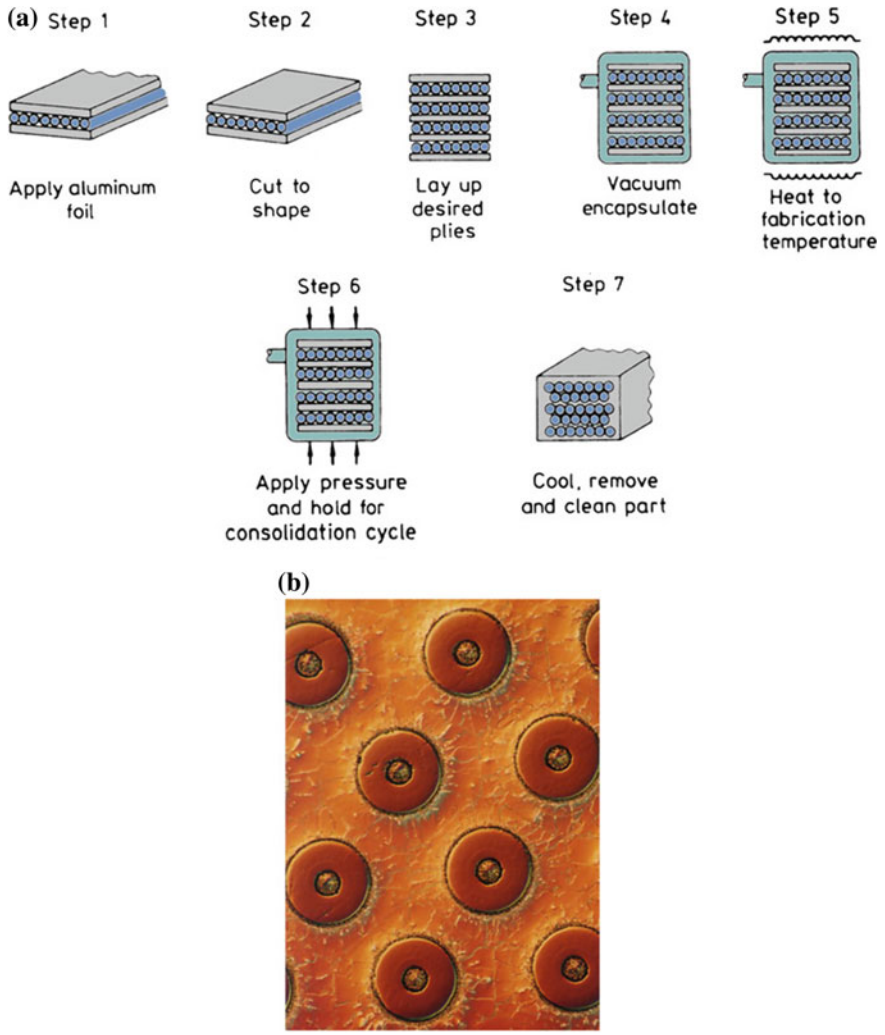

Fig. 6.8 **a** Schematic of diffusion bonding process. **b** The microstructure of SiC fiber/titanium matrix composite made by diffusion. Each fiber is 142 μm in diameter [Courtesy of J. Baughman]

Several deposition techniques are available: immersion plating, electroplating, spray deposition, chemical vapor deposition (CVD), and physical vapor deposition (PVD) (Partridge and Ward-Close 1993). Dipping or immersion plating is similar to infiltration casting except that fiber tows are continuously passed through a bath of molten metal, slurry, sol, or organometallic precursors. Electroplating produces a coating from a solution containing the ion of the desired material in the presence of an electric current. Fibers are wound on a mandrel, which serves as the cathode, and placed into the plating bath with an anode of the desired matrix material. The

advantage of this method is that the temperatures involved are moderate and no damage is done to the fibers. Problems with electroplating involve void formation between fibers and between fiber layers, adhesion of the deposit to the fibers may be poor, and there are limited numbers of alloy matrices available for this processing. A spray deposition operation, typically, consists of winding fibers onto a foil-coated drum and spraying molten metal onto them to form a monotape. The source of molten metal may be powder or wire feedstock, which is melted in a flame, arc, or plasma torch. The advantages of spray deposition are easy control of fiber alignment and rapid solidification of the molten matrix. In a CVD process, a vaporized component decomposes or reacts with another vaporized chemical on the substrate to form a coating on that substrate. The processing is generally carried out at elevated temperatures.

6.3.3 *In Situ Processes*

In in situ techniques, one forms the reinforcement phase in situ. The composite material is produced in one step from an appropriate starting alloy, thus avoiding the difficulties inherent in combining the separate components as in a typical composite processing. Controlled unidirectional solidification of a eutectic alloy is a classic example of in situ processing. A eutectic is an alloy of two or more metals (or compounds) or crystalline substances that have a fixed, lower melting point than that of any of its constituents. The eutectic reaction can be represented as (a liquid, L decomposes to give two solids, α and β):

$$L \rightleftharpoons \alpha + \beta.$$

Unidirectional solidification of a eutectic alloy can result in one phase being distributed in the form of fibers or ribbon in the other. One can control the fineness of distribution of the reinforcement phase by simply controlling the solidification rate. The solidification rate in practice, however, is limited to a range of 1–5 *cm/h* because of the need to maintain a stable growth front. The stable growth front requires a high temperature gradient. Figure 6.9 shows scanning electron micrographs of transverse sections of in situ composites obtained at different solidification rates (Walter 1982). The nickel alloy matrix has been etched away to reveal the TaC fibers. At low solidification rates, the TaC fibers are square in cross section, while at higher solidification rates, blades of TaC form. The number of fibers per square centimeter also increased with increasing solidification rate. Table 6.2 gives some important systems that have been investigated. A precast and homogenized rod of a eutectic composition is melted, in vacuum or inert gas atmosphere. The rod is contained in a graphite crucible, which in turn is contained in a quartz tube. Heating is generally done by induction. The coil is moved up the quartz tube at a fixed rate. Thermal gradients can be increased by chilling the crucible just below the

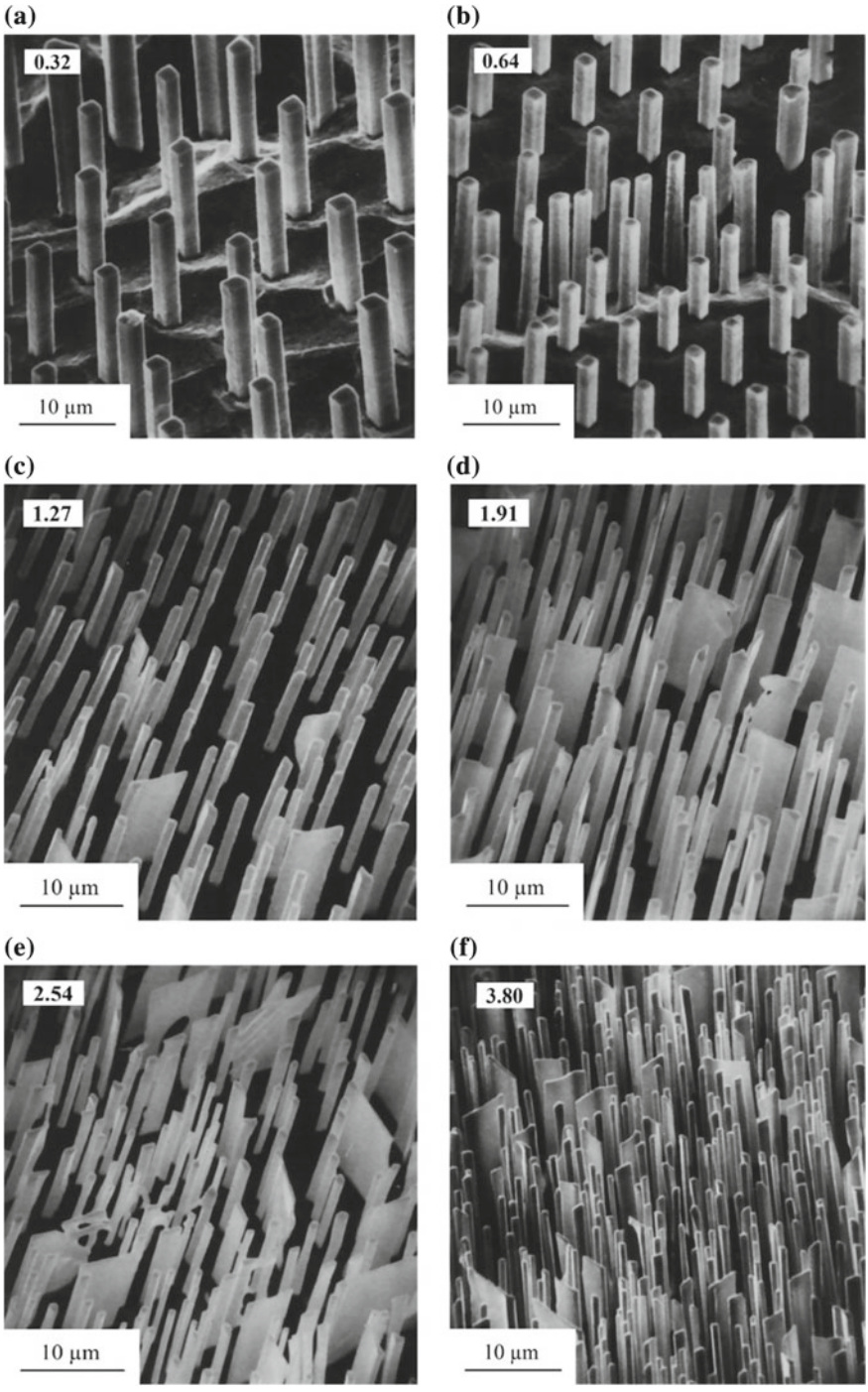
(a)
0.32
10 μm
(b)
0.64
10 μm
(c)
1.27
10 μm
(d)
1.91
10 μm
(e)
2.54
10 μm
(f)
3.80
10 μm

◂**Fig. 6.9** Transverse sections of in situ composites obtained at different solidification rates indicated in left hand top corners (*cm/h*). The nickel alloy matrix has been etched away to reveal the TaC fibers [From Walter (1982), used with permission]

Table 6.2 Some important in situ composite systems

System	Carbide (*vol. %*)	T_E^a (°*C*)
Co–NbC	12	1365
Co–TiC	16	1360
Co–TaC	10	1402
Ni–HfC	15–28	1260
Ni–NbC	11	1330
Ni–TiC	7.5	1307

[a]T_E is the eutectic temperature

induction coil. Electron beam heating can also be used, especially when reactive metals such as titanium are involved. The reader is referred to McLean (1983).

The XD™ process is another in situ process; in this an exothermic reaction between two components is used to produce a third component. Sometimes such processing techniques are referred to as the *self-propagating high-temperature synthesis* (SHS) process. Specifically, the XD™ process produces ceramic particle reinforced metallic alloy. Generally, a master alloy containing rather high volume fraction of reinforcement is produced by the reaction synthesis. This is mixed and remelted with the base alloy to produce a desirable amount of particle reinforcement. Typical reinforcements are SiC, TiB_2, etc. in an aluminum, nickel, or intermetallic matrix (Christodolou et al. 1988).

6.4 Interface in Metal Matrix Composites

As we have repeatedly pointed out, the interface region in any composite is very important in determining the ultimate properties of the composite. In this section, we give examples of the microstructure of the interface region in different metal matrix composite systems and discuss the implications of various interfacial characteristics on the resultant properties of the composite. Recall that we can use contact angle, θ as a measure of wettability; a small θ indicates good wetting. Most often, the ceramic reinforcement is rejected by the molten metal because of non-wettability or high contact angle. Sometimes the contact angle of a liquid drop on a solid substrate can be decreased by increasing the surface energy of the solid (γ_{SV}) or by decreasing the energy of the interface between the liquid and the solid (γ_{SL}). Thus, under certain circumstances, the wettability of a solid ceramic by a molten metal can be improved by making a small alloy addition to the matrix composition. An example of this is the addition of lithium to aluminum to improve the wettability in the alumina fiber/aluminum composite (Champion et al. 1978; Chawla 1989). However, in addition to wettability, there are other important factors such as

chemical, mechanical, thermal, and structural ones that affect the nature of bonding between reinforcement and matrix. As it happens, these factors frequently overlap, and it may not always be possible to isolate these effects.

6.4.1 Major Discontinuities at Interfaces in MMCs

As we said earlier, at the interface a variety of discontinuities can occur. The important parameters that can show discontinuities in MMCs at a ceramic reinforcement/metal matrix interface are as follows:

- *Bonding*: A ceramic reinforcement will have an ionic or a mixed ionic/covalent bonding, while the metal matrix will have a metallic bonding.
- *Crystallography*: The crystal structure and the lattice parameter of the matrix and the reinforcement will be different.
- *Moduli*: In general, the elastic moduli of the matrix and the reinforcement will be different.
- *Chemical potential*: The matrix and the reinforcement will *not* be in thermodynamic equilibrium at the interface, i.e., there will be a driving force for a chemical reaction.
- *Coefficient of thermal expansion* (*CTE*): The matrix and the reinforcement will, in general, have different CTEs.

6.4.2 Interfacial Bonding in Metal Matrix Composites

Here we provide a summary of salient features of the interfacial region in some of the most important metal matrix composites.

6.4.2.1 Crystallographic Nature

In crystallographic terms, ceramic/metal interfaces in composites are, generally, incoherent, high energy interfaces. Accordingly, they can act as very efficient vacancy sinks, providing rapid diffusion paths, segregation sites, sites of heterogeneous precipitation, and sites for precipitate free zones. Among the possible exceptions to this are the eutectic composites (Cline et al. 1971) and the XD™-type particulate composites (Mitra et al. 1993). In eutectic composites, X-ray and electron diffraction studies show preferred crystallographic growth directions, preferred orientation relationships between the phases, and low index habit planes. Boundaries between in situ components are usually semicoherent, and the lattice mismatch across the interfaces can be accommodated by interface dislocations.

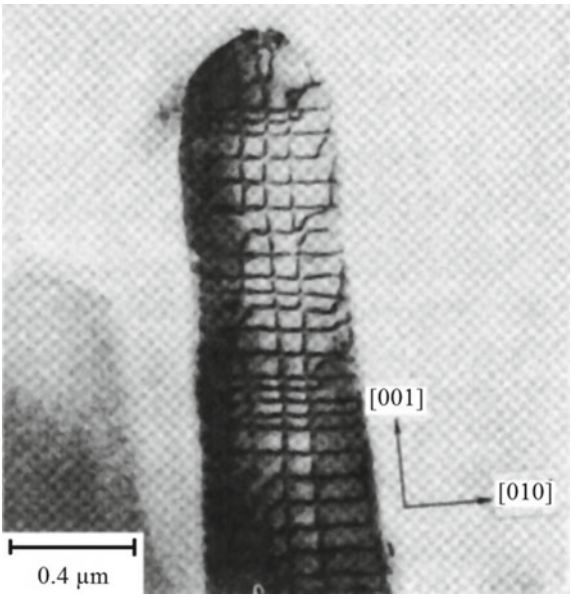

Fig. 6.10 A network of dislocations between the NiAl matrix and a chromium rod in a unidirectionally solidified NiAl–Cr eutectic [Reprinted with permission from H. E. Cline et al. 1971, *Acta Met*., **19**, Pergamon Press Ltd.]

Figure 6.10 shows a network of dislocations between the NiAl matrix and a chromium rod in a unidirectionally solidified NiAl–Cr eutectic (Cline et al. 1971).

6.4.2.2 Mechanical Bonding

Some bonding must exist between the ceramic reinforcement and the metal matrix for load transfer to occur from matrix to fiber. Two main categories of bonding are mechanical and chemical. Mechanical keying between two surfaces can lead to bonding. Hill et al. (1969) confirmed this experimentally for tungsten filaments in an aluminum matrix, while Chawla and Metzger (1978) observed mechanical gripping effects at Al_2O_3/Al interfaces. The results of Chawla and Metzger (1978) are shown in Fig. 6.11 in the form of linear density of cracks (number of cracks per mm) in alumina as a function of strain in an alumina/aluminum composite for different degrees of interface roughness. The main message of this figure is that the crack density continues to increase to larger strain values in the case of a rough interface (deeply etched pits) vis à vis a smooth or not very rough interface, i.e., the rougher the interface, the stronger the mechanical bonding.

We can make an estimate of the radial stress, σ_r, at the fiber/matrix interface due to roughness induced gripping by using the following expression (Kerans and Parthasarathy 1991):

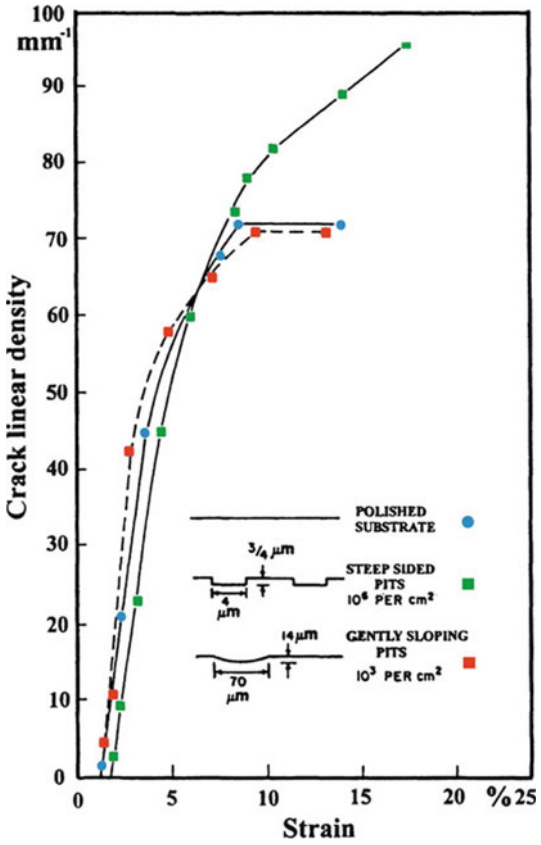

Fig. 6.11 The linear density of cracks in alumina as a function of strain in an alumina/aluminum composite for different degrees of interface roughness. The crack density continues to increase to larger strain values in the case of a rough interface (deeply etched pits) vis à vis a smooth or not very rough interface

$$\sigma_r = \frac{-E_m E_f}{E_f(1+\nu_m) + E_m(1-\nu_f)} \left[\frac{A}{r}\right],$$

where E is the Young's modulus, ν is the Poisson's ratio, A is the amplitude of roughness, r is the radius of the fiber, and the subscripts m and f indicate matrix and fiber, respectively. For a given composite, the compressive radial stress increases with the interface roughness amplitude and decreases with the fiber radius. An important example of such an MMC, i.e., nonreacting components with purely a mechanical bond at the interface, is the filamentary superconducting composite consisting of niobium–titanium alloy filaments in a copper matrix.

6.4.2.3 Chemical Bonding

Ceramic/metal interfaces are generally formed at high temperatures. Diffusion and chemical reaction kinetics are faster at elevated temperatures. One needs to have

knowledge of the chemical reaction products and, if possible, their properties. Molten iron, nickel, titanium, low alloy steels, austenitic and ferritic stainless steels, and nickel-based superalloys react with silicon-containing ceramics to form eutectics, with the reaction products being mainly metal silicides and carbides. It is thus imperative to understand the thermodynamics and kinetics of reactions in order to control processing and obtain optimum properties. We provide some examples.

Most metal matrix composite systems are nonequilibrium systems in the thermodynamic sense; that is, there exists a chemical potential gradient across the fiber/matrix interface. This means that given favorable kinetic conditions (which in practice means a high enough temperature or long enough time), diffusion and/or chemical reactions will occur between the components (see Fig. 4.4 in Chap. 4). Two common morphologies of reaction products at an interface in common metal matrix composites are (a) a reaction layer that covers the ceramic reinforcement more or less uniformly and (b) a discrete precipitation, particle or needle shaped, around the reinforcement. Type (a) reaction is controlled by diffusion of elements in the reaction layer. Typically, such a diffusional growth of the reaction layer scales as $x^2 \simeq Dt$, where x is the reaction layer thickness, t is the time, and D is the diffusion coefficient. Examples of systems showing such interfacial reactions include B/Al and SiC/Ti. Fujiwara et al. (1995) observed such a parabolic growth of the reaction zone in SCS-6 silicon carbide fiber/Ti–4.5Al–3V–2Fe–2Mo (*wt. %*) composites at three different temperatures. Figure 6.12 shows the reaction zone thickness squared (x^2) as a function of reaction time for three different boron fiber/titanium matrix composites. Note that the B_4C coating is more effective for the B/Ti system.

Silicon carbide fiber reinforced titanium matrix composites are attractive for some aerospace applications. Titanium and its alloys are very reactive in the liquid state; therefore, only solid state processing techniques such as diffusion bonding are used to make these composites (Partridge and Ward-Close 1993). In particular, a titanium alloy matrix containing SCS-6-type silicon carbide fiber can have a very complex interfacial chemistry and microstructure. A schematic of the interface region in these composites is shown in Fig. 6.13 (Gabryel and McLeod 1991). The

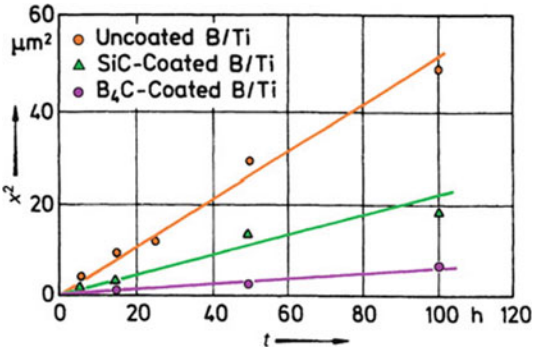

Fig. 6.12 Reaction zone thickness squared (x^2) as a function of reaction time for three different boron fibers in a titanium matrix. A B_4C carbide coating on the boron is most effective for the B/Ti system [From Naslain et al. (1976), used with permission]

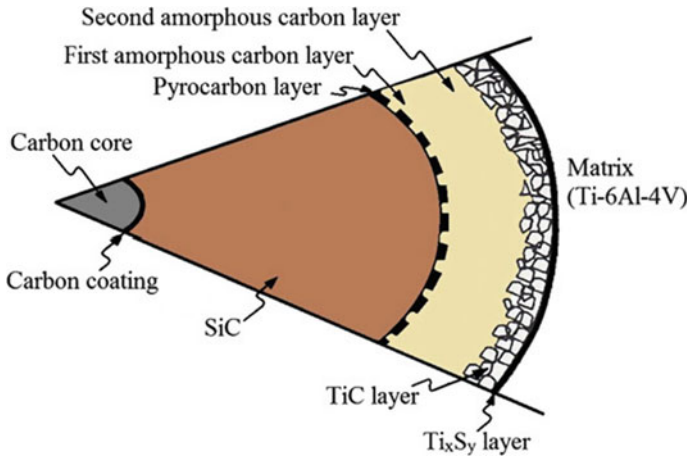

Fig. 6.13 Schematic of the interface region in silicon carbide fiber reinforced titanium matrix composites [Adapted from Gabryel and McLeod (1991)]

pyrocarbon layer and the amorphous carbon layers are provided on the fiber surface, while the Ti silicides form during processing of the MMC.

Type (b) reaction involving precipitation at the interface is controlled by the nucleation process, followed by discrete precipitation at the reinforcement/matrix interface. Examples include alumina/magnesium, carbon/aluminum, and alumina–zirconia/aluminum. Figure 6.14 shows an example, a dark field TEM micrograph, of the reaction zone between alumina fiber and magnesium matrix. Also to be seen

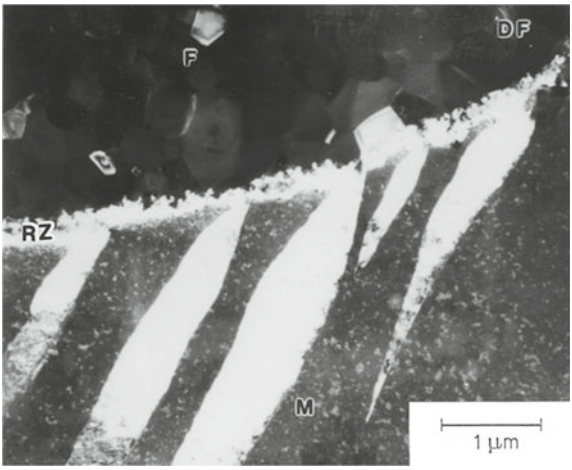

Fig. 6.14 A controlled amount of interfacial reaction at the Al_2O_3 fiber/Mg alloy matrix interface. *M, F*, and *RZ* denote matrix, fiber, and reaction zones, respectively. Dark field (DF) transmission electron micrograph

in this figure are the deformation twins in the matrix, the result of thermal stresses on cooling down from the liquid metal infiltration temperature. Aluminum oxide can react with magnesium present in an aluminum alloy (Jones et al. 1993):

$$3\,Mg + Al_2O_3 \leftrightarrow 3\,MgO + 2\,Al$$
$$3\,Mg + 4Al_2O_3 \leftrightarrow 3\,MgOAl_2O_3 + 2Al$$

At high levels of Mg and low temperatures, MgO is expected to form, while the spinel forms at low levels of magnesium (Pfeifer et al. 1990).

A good example of obtaining a processing window by exploiting the kinetics of interfacial reaction between the fiber and matrix can be seen in the work of Isaacs et al. (1991). These authors examined the interface structure in an aluminum matrix reinforced with an (alumina + zirconia) fiber. The composite made by pressure infiltration of the fibrous preform by liquid aluminum at 973 K (700 $°C$), with a dwell time of 13 *min*, showed faceted $ZrAl_3$ platelets growing from the fiber into a matrix. However, they could suppress the kinetics of interfacial reaction by minimizing the high temperature exposure. No interfacial reaction product was observed when they processed the composite with the initial fibrous preform temperature below the melting point of aluminum and the solidification time less than 1 minute.

Carbon fiber reacts with molten aluminum to form aluminum carbide, which is a very brittle compound and highly susceptible to corrosion in humid environments. Thus, it becomes imperative to use a barrier coating on carbon fibers before bringing them in contact with the molten aluminum. The carbon fibers are coated with a co-deposition of Ti + B (presumably giving TiB_2). The starting materials for the coating process are $TiCl_4$ (g), BCl_3 (g), and Zn (v); the possible reaction products are TiB_2, $TiCl_2$, $TiCl_3$, and $ZnCl_3$. Any residual chloride in the coating is highly undesirable from a corrosion-resistance point of view.

In the case of carbon fibers in aluminum, poor wettability is a major problem. The wettability seems to improve somewhat when temperature increases above 1000 $°C$ (Manning and Gurganus 1969; Rhee 1970), but it turns out that above 500 $°C$ a deleterious reaction occurs between the carbon fibers and the aluminum matrix, whereby Al_4C_3, a very brittle intermetallic compound, is known to form (Baker and Shipman 1972). Fiber surface coatings have also been tried. Such coatings do allow wetting by low melting-point metals, but these coatings are also unstable in molten metals. Fiber degradation leading to reduced composite strength generally results. In the case of carbon fiber/aluminum composites, co-deposition of titanium and boron onto carbon fibers before incorporating them into an aluminum matrix came to be established as a commercial method for carbon fiber surface treatment. Figure 6.15 shows a schematic of this process (Meyerer et al. 1978). Multiple yarn creels result in increased capacity over single yarn creels. The common size on carbon fibers such as polyvinyl alcohol (PVA) (meant for polymeric matrices) is removed in a furnace, designated as a PVA furnace in Fig. 6.15. The first CVD furnace in Fig. 6.15 is a precoat furnace for cleaning and activating the carbon yarn surface. The Ti/B coating is deposited in the second CVD furnace, followed by drawing through a molten aluminum bath.

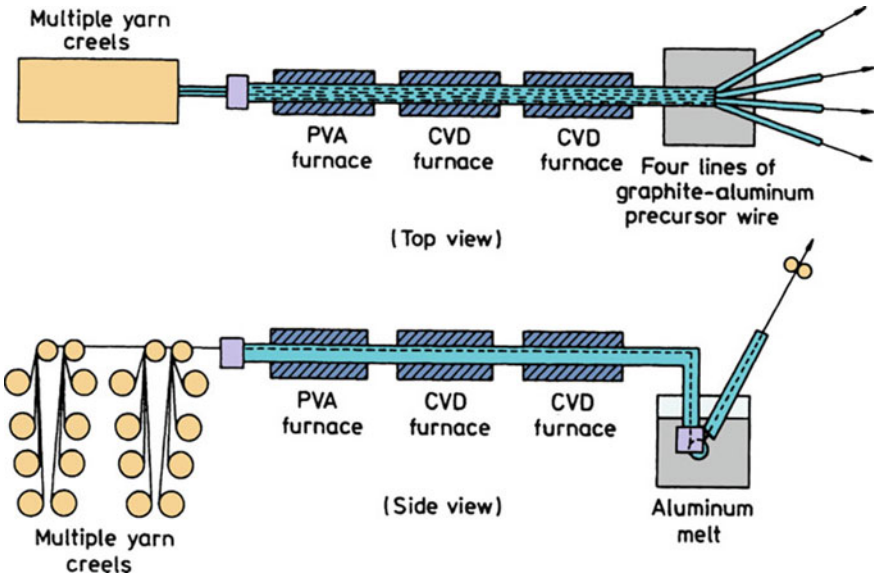

Fig. 6.15 Schematic of the Ti/B co-deposition process for making carbon fiber/aluminum compsites. [From Meyerer et al. (1978), used with permission]

Warren and Andersson (1984) have reviewed the thermodynamics of chemical equilibria between SiC and some common metals. They divide these systems into *reactive* and *stable* types. In reactive systems, SiC reacts with the metal to form silicides and/or carbides and carbon. No two-phase field exists in the ternary phase diagram showing SiC and the metal in equilibrium. For example, with nickel and titanium, the following reactions are possible:

$$\begin{gathered} \mathrm{SiC} + \mathrm{Ni} \rightarrow \mathrm{Ni}_x\mathrm{Si}_y + \mathrm{C} \\ \mathrm{SiC} + \mathrm{Ti} \rightarrow \mathrm{Ti}_x\mathrm{Si}_y + \mathrm{TiC} \quad (\text{low SiC fractions}) \end{gathered}.$$

Such reactions are thermodynamically possible between SiC and nickel or titanium, but in practice, reaction kinetics determine the usefulness of the composite. In stable systems, SiC and a metallic matrix alloy can coexist thermodynamically, that is, a two-phase field exists. Examples are SiC fibers in alloys of aluminum, gold, silver, copper, magnesium, lead, tin, and zinc. This does not imply that SiC will not be attacked. In fact, a fraction of SiC fibers in contact with molten aluminum can dissolve and react to give Al_4C_3:

$$\mathrm{SiC} + \mathrm{Al} \rightarrow \mathrm{SiC} + (\mathrm{Si}) + \mathrm{Al}_4\mathrm{C}_3.$$

This reaction can happen because the section SiC–Al lies in a three-phase field. Such reactions can be avoided by prior alloying of aluminum with silicon.

The interface product(s) formed because of a reaction will generally have characteristics different from those of either component. It should be pointed out, however, that at times, some controlled amount of reaction at the interface, such as that shown in Fig. 6.14, may be desirable for obtaining strong bonding between the fiber and the matrix, but, too thick an interaction zone will adversely affect the composite properties.

Silicon carbide particle reinforced aluminum composites have been investigated extensively. An important processing technique for these MMCs involves liquid metal infiltration of a particulate preform. In a silicon-free aluminum alloy matrix, silicon carbide and molten aluminum can react as follows:

$$4\,\mathrm{Al}(l) + 3\mathrm{SiC}(s) \leftrightarrow \mathrm{Al_4C_3}(s) + 3\mathrm{Si}(s).$$

The forward reaction will add silicon to the matrix. As the silicon level increases in the molten matrix, the melting point of the alloy decreases with time. The reaction can be made to go leftward by using high silicon alloys. This, of course, restricts the choice of Al alloys for liquid route processing. Table 6.3 gives a summary of interfacial reactions in some important MMCs.

In general, ceramic reinforcements (fibers, whiskers, or particles) have a coefficient of thermal expansion smaller than that of most metallic matrices. This means that when the composite is subjected to a temperature change, thermal stresses will be generated in both of the components. This observation is true for all composites —polymer, metal, and ceramic matrix composites. What is unique of metal matrix composites is the ability of a metal matrix to undergo plastic deformation in response to the thermal stresses generated and thus alleviate them. Chawla and Metzger (1972), working with a single crystal copper matrix containing large diameter tungsten fibers, showed the importance of thermal stresses in MMCs. Specifically, they employed a dislocation etch-pitting technique to delineate dislocations in single crystal copper matrix and showed that near the fiber the dislocation density was much higher in the matrix than the dislocation density far away from the fiber. The use of single crystal avoided complications from grain boundaries and the W/Cu system has not interfacial reaction; thus the system allows

Table 6.3 Interfacial reaction products in some important MMCs

Reinforcement	Matrix	Reaction Product(s)
SiC	Ti alloy	TiC, Ti_5Si_3
	Al alloy	Al_4C_3
Al_2O_3	Mg alloy	MgO, $MgAl_2O_4$ (spinel)
C	Al alloy	Al_4C_3
B	Al alloy	AlB_2
Al_2O_3 + ZrO_z	Al alloy	$ZrAl_3$
W	Cu	None
C	Cu	None
Al_2O_3	Al	None

pure fiber reinfroment to be studied. The situation in the as-cast composite can be depicted as shown schematically in Figure 6.16, where a primary plane section of the composite is shown having a hard zone (high dislocation density) around each fiber and a soft zone (low dislocation density) away from the fiber (Chawla 1975). The enhanced dislocation density in the copper matrix near the fiber arises because of the matrix plastic deformation in response to the thermal stresses generated by the thermal mismatch between the fiber and the matrix. The intensity of the gradient in dislocation density will depend on the interfiber spacing. The dislocation density gradient will decrease with a decrease in the interfiber spacing. The existence of a plastically deformed zone containing high dislocation density in the metallic matrix in the vicinity of the reinforcement has since been confirmed by transmission electron microscopy by a number of researchers, both in fibrous and particulate metal matrix composites (Arsenault and Fisher 1983; Rack 1987; Christman and Suresh 1988). Such high dislocation density in the matrix can alter the precipitation behavior, and, consequently, the aging behavior in MMCs in those composites that have a precipitation hardenable alloy matrix (see Sect. 6.5).

We mentioned the roughness induced radial compression stress at the fiber/matrix interface in Sect. 4.2. As discussed earlier, the thermal mismatch between the components can lead to thermal residual stresses. Specifically, a radial stress component will be introduced which can be positive or negative. To obtain the net radial stress at the fiber/matrix interface, one should add the stresses algebraically from the two sources, viz., the contribution due to thermal mismatch between the reinforcement and the matrix and the stress arising due to the roughness induced gripping, as mentioned previously. A combined expression for the radial stress from these two sources can be written as (Kerans and Parthasarathy 1991)

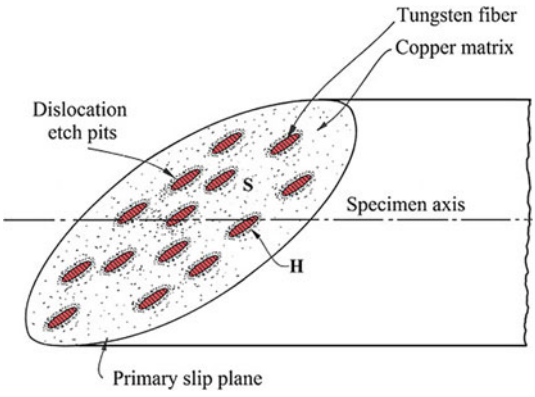

Fig. 6.16 A primary plane section of a metal matrix composite W/Cu is shown as having a hard zone (H) around each fiber and a soft zone (S) away from the fiber

$$\sigma_r = \frac{-qE_{\mathrm{m}}EE}{E_{\mathrm{f}}(1+\nu_{\mathrm{m}}) + E_{\mathrm{m}}(1-\nu_{\mathrm{f}})}\left[\Delta\alpha\Delta T + \frac{A}{r}\right],$$

where q is an adjustable parameter (equal to 1 for an infinite matrix), E is the Young's modulus, v is the Poisson's ratio, ΔT is the temperature change, $\Delta\alpha$ is the thermal mismatch between the fiber and the matrix = ($\alpha_{\mathrm{m}} - \alpha_{\mathrm{f}}$), A is the amplitude of interfacial roughness, r is the radius of the fiber, and the subscripts m and f refer to matrix and fiber, respectively. Thus, in the absence of chemical bonding, one can control the degree of interfacial bonding by controlling the degree of interfacial roughness, the thermal mismatch between the matrix and the reinforcement, and the amplitude of temperature change.

Metal matrix composites with reinforcement in the form of a short fiber, whisker, or particle (also called *discontinuously reinforced MMCs*), especially aluminum matrix composites can be subjected to conventional metalworking processes (e.g., rolling, forging, extrusion, machining, and swaging). Figure 6.17a shows a perspective montage (SEM) of a rolled plate of SiC (20 *v/o*)/2124 Al. The rolling direction is perpendicular to the original extrusion direction. The very small particles in Fig. 6.17a are the precipitates in the matrix after aging, while the large irregular particles are probably (Fe, Mn) Al_6. The distribution of SiC whiskers in the aluminum matrix, as seen in a transmission electron microscope, is shown in Fig. 6.17b, while a closeup of the whisker/matrix interface region is shown in Fig. 6.17c. Note the waviness of the interface. Fu et al. (1986) examined the interface chemistry and crystallography of C/Al and SiC_w/Al MMCs in the TEM. They observed an oxide at some of the SiC/Al interfaces. Figure 6.18a and b shows the TEM bright and dark field micrographs of the interface region of 20 *v/o* SiC_w/Al. The crystalline γ-Al_2O_3 phase is about 30 *nm*. It was, however, not uniformly present at every interface. In C/Al composites, both fine-grained γ-Al_2O_3 and coarse-grained Al_4C_3 were found at the interfaces. On heat treating, some of the Al_4C_3 grew into and along the porous sites at the carbon fiber surface.

6.5 Properties

We describe some of the important mechanical and physical properties of metal matrix composites in this section.

6.5.1 Modulus

Unidirectionally reinforced continuous fiber reinforced metal matrix composites show a linear increase in the longitudinal Young's modulus of the composite as a function of the fiber volume fraction. Figure 6.19 shows an example of modulus

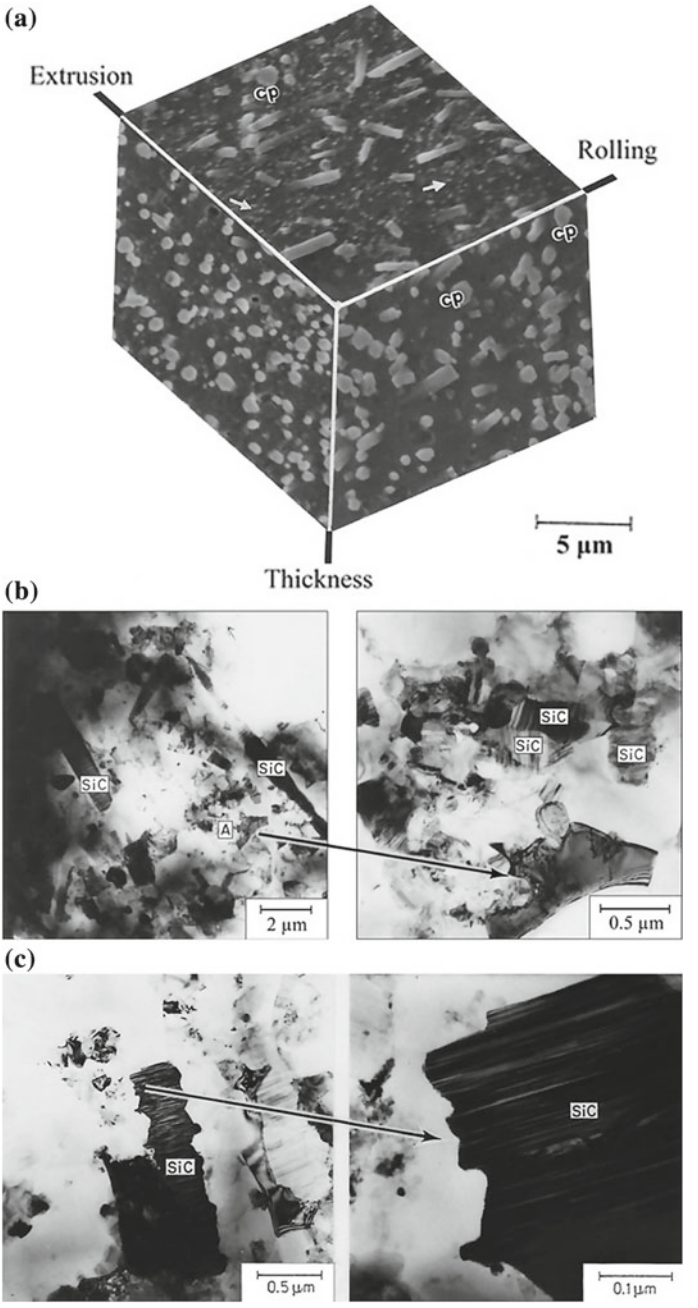
(a)
Extrusion
Rolling
Thickness
CP
CP
CP
5 μm
(b)
SiC
SiC
A
2 μm
SiC
SiC
SiC
0.5 μm
(c)
SiC
0.5 μm
SiC
0.1 μm

◂**Fig. 6.17** **a** A perspective montage of a SiC/Al composite. The smallest particles (indicated by arrows on the top face) are precipitates from the matrix as a result of aging. Silicon carbide whiskers are the intermediate particles, both long and narrow and equiaxial ones having a diameter similar to the width of the long, narrow ones. The large irregular particles are (Fe, Mn) Al_6-type constituent particles (some of these are marked cp). The liquid-phase hot-pressed billet was first extruded in the extrusion direction, forged along the thickness direction, and finally rolled along the rolling direction. [Courtesy of D.R. Williams and M.E. Fine]. **b** Distribution of SiC_w in an aluminum matrix (TEM). **c** A higher magnification of the whisker/matrix interface (TEM) [Courtesy of J.G. Greggi and P.K. Liaw]

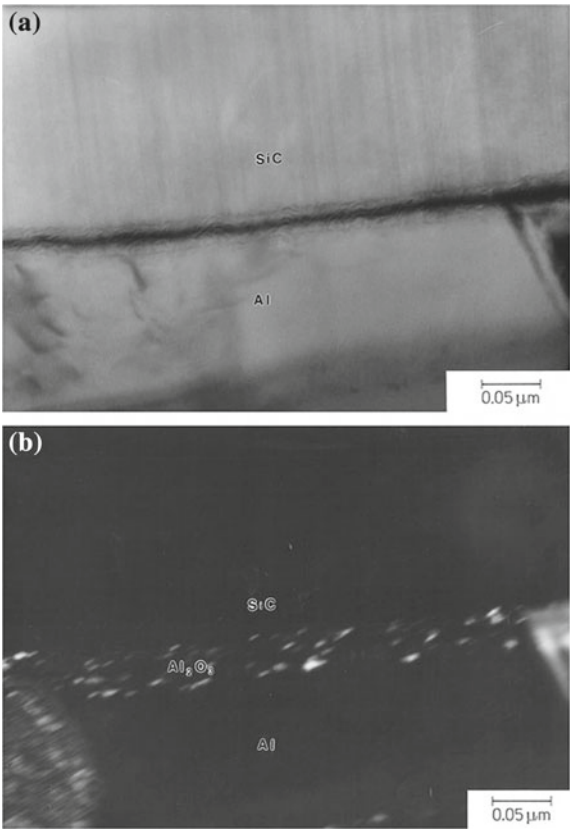

Fig. 6.18 Interface in SiC_w/Al composite: **a** bright field TEM, **b** dark field TEM showing the presence of $A1_2O_3$ at the interface [From Fu et al. (1986), ©ASTM, reprinted with permission]

and strength increase as a function of fiber volume fraction for alumina fiber reinforced aluminum–lithium alloy matrix (Champion et al. 1978). The increase in the longitudinal Young's modulus is in agreement with the rule-of-mixtures value, while the modulus increase in a direction transverse to the fibers is very low. Rule-of-mixtures nothing but a volume weighted average of a property. Particle

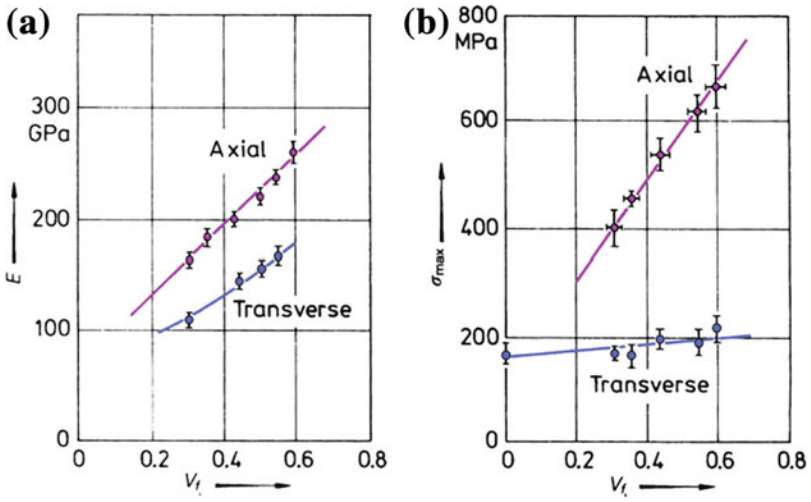

Fig. 6.19 Properties of Al_2O_3/Al-Li composites as a function of fiber volume fraction (V_f): **a** axial and transverse Young's modulus versus fiber volume fraction, **b** axial and transverse ultimate tensile strength versus fiber volume fraction [From Champion et al. (1978), used with permission]

reinforcement also results in an increase in the modulus of the composite, the increase, however, is much less than that predicted by the rule-of-mixtures. This is understandable inasmuch as the rule-of-mixtures is valid only for continuous fiber reinforcement. Figure 6.20 shows schematically increase in Young's modulus of an MMC as a function of reinforcement volume fraction for different forms of reinforcement, viz., continuous fiber, whisker, or particle. Note the loss of reinforcement efficiency as one goes from continuous fiber to particle. Metal matrix particulate composites, such as SiC particle reinforced aluminum, can offer a 50–100% increase in modulus over that of unreinforced aluminum, i.e., a modulus

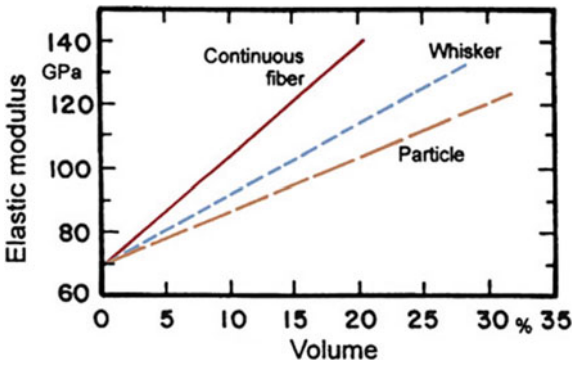

Fig. 6.20 Increase in Young's modulus of an MMC as a function of reinforcement volume fraction for continuous fiber, whisker, or particle reinforcement

equivalent to that of titanium but density about 33% less. Also, unlike the fiber reinforced composites, the stiffness enhancement in particulate composites is reasonably isotropic.

6.5.2 Strength

Prediction of strength of an MMC is more complicated than the prediction of modulus. This is so because there can be direct and indirect strengthening. The direct strengthening involves the strength contribution of the fiber and the metal matrix. It does not include any strength contribution stemming from processing induced microstructural changes in the metal matrix.

The direct strengthening is described as follows. Consider an aligned fiber reinforced metal matrix composite under a load P_c in the direction of the fibers. This load is distributed between the fiber and the matrix. Thus,

$$P_c = P_m V_m + P_f V_f,$$

where P_m and P_f are the loads on the matrix and the fiber, respectively. This equation can be converted to the following rule-of-mixtures (we discuss this in more detail in Chap. 10) relationship under conditions of isostrain (i.e., the strain in the fiber, matrix, and composite is the same):

$$\sigma_c = \sigma_f V_f + \sigma_m V_m,$$

where σ is the stress, V is the volume fraction, and the subscripts c, f, and m denote the composite, fiber, and matrix, respectively. This equation, commonly referred to as the *rule-of-mixtures*, says that the strength of the composite is a volume-weighted average of the strengths of the fiber and the matrix.

On the face of it, there is nothing wrong with rule-of-mixtures as written above for strength. The problem is that one needs the in situ values of σ_f and σ_m. If the fiber remains essentially elastic up to the point of fracture, then σ_f, the fiber strength in the composite, is the same as that determined in an isolated test of the fiber. This is particularly true of ceramic fibers. The same, however, cannot be said for the metallic matrix. The matrix strength in the composite (the in situ strength) will, in all likelihood, not be the same as that determined from a test of an unreinforced matrix sample in isolation. This is because the metal matrix can suffer several microstructural alterations during processing and, consequently, changes in its mechanical properties. This is what is called indirect strengthening. In view of the fact that, in general, ceramic reinforcements have a coefficient of thermal expansion smaller than that of most metallic matrices, thermal stresses will be generated in the two components, the fiber and the matrix. A series of events can take place in response to the thermal stresses (Chawla and Metzger 1972; Chawla 1973a, b, 1974):

Table 6.4 Representative properties of some continous fiber reinforced MMCs

Composite and direction	Fiber volume fraction (%)	Density ($g\ cm^{-3}$)	σ_{max} (MPa)	E (GPa)
B/Al				
0°	50	2.65	1500	210
90°	50	2.65	140	150
SiC/Al				
0°	50	2.84	250	310
90°	50	2.84	105	–
SiC/Ti–6A1–4V				
0°	35	3.86	1750	300
90°	35	3.86	410	–
Al_2O_3/Al–Li				
0°	60	3.45	690	262
90°	60	3.45	172–207	152
C (Thornel 50)/Mg alloy	38	1.8	510	–
C/Al	30	2.45	690	160

1. Plastic deformation of the ductile metal matrix (slip, twinning, cavitation, grain boundary sliding, and/or migration).
2. Cracking and failure of the brittle fiber.
3. An adverse reaction at the interface.
4. Failure of the fiber/matrix interface.

In particular, plastic deformation (item #1 above) can result in an increased dislocation density in the metal matrix because of thermal stresses. Item 3 can also affect the strength depending on the nature and extent of the reaction product. We will discuss the subject of thermal stresses in Chap. 10. A discussion of the effect of thermal stresses on the strength properties of composites will be presented in Chap. 12. A summary of typical properties of long or continuous fiber reinforced MMCs is given in Table 6.4.

The indirect strengthening appears to be more important in particle reinforced composites. Arsenault and Shi (1986) and Shi and Arsenault (1991, 1993) analyzed various contributing factors in particulate MMCs, in the absence of a shear lag strengthening mechanism, which would be more effective in the case of long fibrous reinforcement. They enumerated the following strengthening mechanisms in particulate MMCs:

- Orowan strengthening, σ_o, which is given by Gb/l, where G is the shear modulus of the matrix, b is the Burgers vector of the matrix, and l is the particle spacing.
- Grain and substructure strengthening, σ_{gb}, in the metal matrix, following a Hall–Petch type relationship, i.e., strength varying as $d^{-1/2}$, where d is the grain or subgrain size in the matrix. The Hall–Petch slope k for Al is in the range of 0.1–0.15, i.e., it is very low, while for steels, k is very high. Thus, a grain diameter

$d < 10\ \mu m$ will give significant strengthening, while $d < 1\ \mu m$ can give much better strengthening.

- Quench strengthening, σ_q, with thermal strain in the matrix given by $e_m = \Delta\alpha\Delta T$. According to the model of Arsenault and Shi (1986), dislocation punching occurs in the matrix due to thermal mismatch. The dislocation density resulting from the coefficient of thermal expansion mismatch is given by

$$\rho_{\mathrm{CTE}} = (AeV_p)/b(1 - V_p)d,$$

where A is a geometric constant, e is the thermal misfit strain, A is the particle area, b is the Burgers vector, and V_p is the particle volume fraction.

The corresponding stress is given by

$$\sigma_q = \alpha Gb(\rho_{\mathrm{CTE}})^{1/2},$$

where α is a constant. This contribution to strength can be significant.

- The contribution to strength by work hardening of the matrix, σ_{wh}. Particles affect the matrix work hardening rate.

Thus, for total strength of the particulate MMC from all these contributions, we can write

$$\sigma_{\mathrm{c}} = \sigma_{\mathrm{o}} + \sigma_{\mathrm{gb}} + \sigma_{\mathrm{q}} + \sigma_{\mathrm{WH}} + \sigma_{\mathrm{m}},$$

where σ_{m} is the matrix strength.

In powder metallurgy processed composites, fine oxide from the SiC particle's surface can enter the matrix. For a 20% particle volume fraction, V_p, 10 μm diameter particle, the estimated Orowan strength, σ_{o}, is about 10 MPa. The contribution of grain boundary strengthening is given by

$$\sigma_{\mathrm{gb}} = kd^{-1/2}.$$

Grain boundary strengthening can be high in spray cast and powder metallurgy processed composites.

An analysis (Nardone and Prewo 1986) that takes into account tensile loading at the particle ends gives the following expression for the yield strength of a particulate composite

$$\sigma_{\mathrm{yc}} = \sigma_{\mathrm{ym}}[1 + (L + t)/4L]V_{\mathrm{p}} + \sigma_{\mathrm{ym}}(1 - V_{\mathrm{p}}),$$

where σ_{ym} is the yield stress of the unreinforced matrix, V_{p} is the particle volume fraction, L is the length of the particle perpendicular to the applied load, and t is the length of the particle parallel to the loading direction (see also Chap. 10).

6.5.2.1 Effect of Thermal Stresses

It is important to realize that the matrix in composites is not merely a kind of glue or cement to hold the reinforcement in place (Chawla 1985). The characteristics of the matrix, as modified by the introduction of reinforcement, must be evaluated and exploited to obtain an optimum set of properties of the composite. The nature of the fibers or particles, fiber or particle diameter, and distribution, as well as conventional solidification parameters, all influence the final matrix microstructure. Porosity is one of the major defects in cast MMCs, owing to the shrinkage of the metallic matrix during solidification. At high fiber volume fractions, the flow of interdendritic liquid becomes difficult, and large scale movement of semisolid metal may not be possible. More importantly, the microstructure of the metallic matrix in a fiber composite can differ significantly from that of the unreinforced metal. Mention has been made of higher dislocation density in the metal matrix because of plastic deformation originating in thermal stresses (Chawla and Metzger 1972). Mortensen et al. (1986) showed that the presence of fibers influences the solidification of the matrix alloy. Figure 6.21a shows a cross section of an SCS-2 silicon carbide fiber/Al–4.5 % Cu matrix. Note the normal dendritic cast structure in the unreinforced region, whereas in the reinforced region the dendritic morphology is controlled by the fiber distribution. Figure 6.21b shows the same system at a higher magnification. The second phase (θ) appears preferentially at the fiber/matrix interface or in the narrow interfiber spaces. Kohyama et al. (1985) observed that shrinkage cavities present in the matrix in SiC/Al composites were the predominant crack initiation sites. They also observed a wavy interface structure between SiC and the aluminum matrix, indicating some mechanical bonding in addition to any chemical and physical bonding. In the system SiC/Mg (AZ19C), they observed a magnesium rich interfacial layer that acted as the fracture initiating site.

Frequently the metal matrix alloy used in an MMC has precipitation hardening characteristics, i.e., such an alloy can be hardened by a suitable heat treatment, called *aging treatment*. It has been shown by many researchers (Dunand and Mortensen 1991a, b; Dutta et al. 1988; Dutta and Bourell 1990; Esmaeili et al. 1991; Nieh and Karlak 1984; Parrini and Schaller 1994) that the microstructure of the metallic matrix is modified by the presence of ceramic reinforcement and consequently the standard aging treatment for, say, an unreinforced aluminum alloy will not be valid (see Suresh and Chawla (1993) for a review of this topic). The reinforcements (particle or whisker), such as SiC, B_4C, and Al_2O_3, are unaffected by the aging process. These reinforcements, however, can affect the precipitation behavior of the matrix quite significantly. In particular, as we pointed out earlier, a higher dislocation density in the matrix metal or alloy than that in the unreinforced metal or alloy is produced. The higher dislocation density in the matrix has its origin in the thermal mismatch ($\Delta\alpha$) between the reinforcement and the metallic matrix. This thermal mismatch can be quite large, for example, in the case of SiC and aluminum, it has a high value of $21 \times 10^{-6}/K$. The precipitate hardenable aluminum alloy matrix has a more important role to play in these composites than a nonhardenable matrix material. A considerable strength increment results due to the

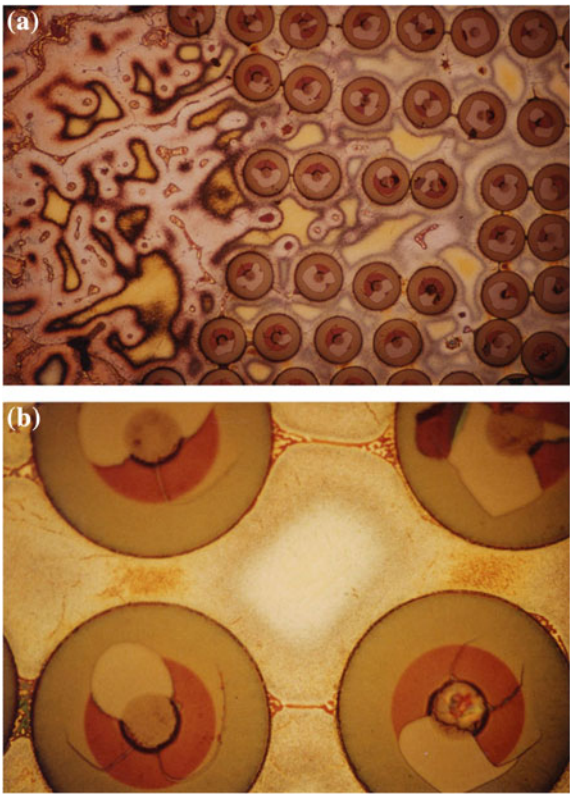

Fig. 6.21 Transverse section of an SCS–2 SiC fiber in an Al–4.5 % Cu matrix. **a** Note the difference in the dendritic structure of the unreinforced and the fiber-rich regions of the matrix. **b** The second phase appears preferentially at the fiber/matrix interface or in the narrow interfiber region. The fiber diameter is 142 *μm* in both **a** and **b** [Reprinted with permission from *Journal of Metals*, Vol. 37, No. 6, pp. 45, 47, and 48, a publication of the Metallurgical Society, Warrendale, Pennsylvania]

age hardening treatments. One would expect that the high dislocation density will also affect the precipitation kinetics in a precipitation hardenable matrix such as 2XXX series aluminum alloy. Indeed, faster precipitation kinetics have been observed in the matrix than in the bulk unreinforced alloy. This has very important practical implications. One may not use the standard heat treatments commonly available in various handbooks, say, for monolithic aluminum alloys for the same alloy used as a matrix in an MMC.

6.5.2.2 Properties of In Situ Composites

We mentioned earlier the class of MMCs called in situ composites. An important example of such a system is a composite made by directional solidification of a eutectic alloy. The strength, σ, of such an in situ metal matrix composite is given by a relationship similar to the Hall–Petch relationship used for grain boundary strengthening of metals (Meyers and Chawla 1984):

$$\sigma = \sigma_o + k\lambda^{-1/2},$$

where σ_o is a friction stress term, k is a material constant, and λ is the spacing between rods or lamellae. It turns out that one can vary the interfiber spacing, λ, rather easily by controlling the solidification rate, R, because

$$\lambda^2 R = \text{constant}.$$

van Suchtelen (1972) has classified eutectic or in situ composites into two broad categories from an electronic property viewpoint:

1. *Combination-type properties*. This can be further subdivided into (a) sum type and (b) product type. In *sum type*, properties of the constituent phases contribute proportionately to their amount. Examples are heat conduction, density, and elastic modulus. In the *product type*, the physical output of one phase serves as input for the other phase, for example, conversion of a magnetic signal into an electrical signal in a eutectic composite consisting of a magnetostrictive phase and a piezoelectric phase.
2. *Morphology-dependent properties*. In this case, the properties depend on the periodicity and anisotropy of the microstructure, the shape and size of the phases, and the amount of interface area between the phases. A good example is InSb-NiSb, which is a quasibinary system with a eutectic at 1.8% NiSb. Unidirectional solidification of a eutectic melt at a growth rate of 2 cmh^{-1} results in an aligned composite consisting of an InSb semiconducting matrix containing long hexagonal fibers of the NiSb phase. The magnetoresistance of the InSb–NiSb composite becomes extremely large if the directions of the metallic fibers, the electric current, and the magnetic field are mutually perpendicular. This characteristic has been exploited in making contactless control devices; a practical example is described in Sect. 6.6.

6.5.2.3 Properties of Particulate Composites

Tensile stress–strain curves of SiC_p/Al composites are shown in Fig. 6.22 (Chawla et al. 1998). Figure 6.22a shows the true stress–true strain curves for one particle size (6 μm) but different volume fractions of the SiC particles. As the particle volume fraction increases, the strength of the composite increases but the ductility

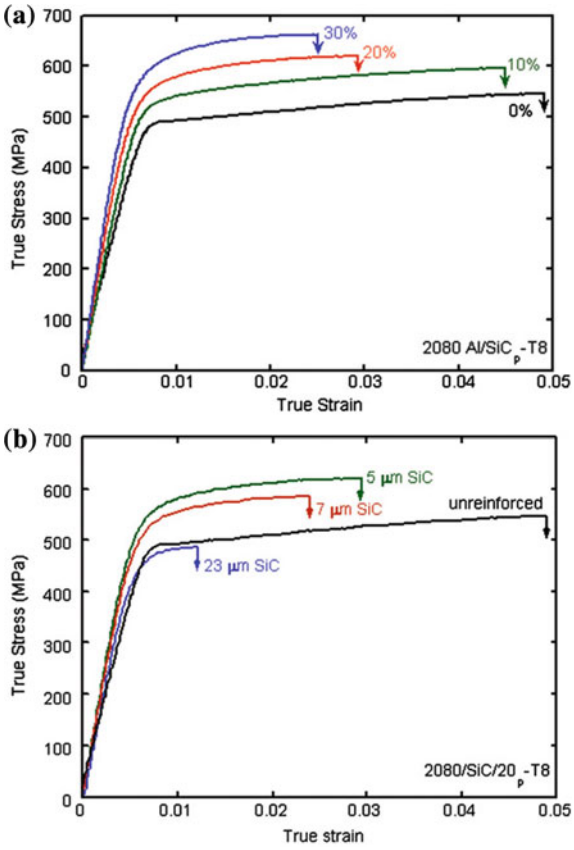

Fig. 6.22 **a** True stress–true strain curves for different volume fractions of the SiC particles (6 μm) in aluminum matrix. As the particle volume fraction increases, the strength of the composite increases but the ductility decreases. **b** True stress–true strain curves for different particle sizes but for a fixed volume fraction (20% by volume). The strength increases as the particle size decreases [Courtesy of N. Chawla]

decreases. Figure 6.22b shows the true stress–true strain curves for different particle sizes but for a fixed volume fraction (20% by volume). The strength increases as the particle size decreases.

Toughness can be regarded as a measure of energy absorbed in the process of fracture, or more specifically as the critical stress intensity factor in plane strain (denoted by K_{Ic}), which is quantitative measure of the resistance to crack propagation. The toughness of MMCs depends on the following factors:

- matrix alloy composition and microstructure;
- reinforcement type, size, and orientation;
- processing, insofar as it affects microstructural variables (e.g., distribution of reinforcement, porosity, segregation, and so on.).

For a given fiber volume fraction, V_f, the larger the diameter of the fiber, the tougher the composite. This is because the larger the fiber diameter, for a given fiber volume fraction, the larger the amount of tough, metallic matrix in the interfiber region that can undergo plastic deformation and thus contribute to the toughness.

Unidirectional fiber reinforcement can lead to easy crack initiation and easy propagation vis à vis the unreinforced alloy matrix. Braiding of fibers can make the crack propagation toughness increase tremendously due to extensive matrix deformation, fiber bundle debonding, and fiber pullout (Majidi and Chou 1987). The general range of K_{Ic} values for particle reinforced aluminum-type MMCs is between 15 and 30 $MPam^{1/2}$, while short fiber or whisker reinforced MMCs have $K_{Ic} \simeq 5$–$10\ MPam^{1/2}$.

The fracture toughness of particle reinforced MMCs is controlled by (a) volume fraction of reinforcement, (b) interparticle spacing and strength of particles, (c) spatial distribution of particles (i.e., particle clustering), and (d) matrix microstructure (as controlled by heat treatment in age hardenable alloys). Figure 6.23 shows toughness in several particulate composite systems as a function of reinforcement volume fraction. All the composites show a decrease in toughness with increasing volume fraction of reinforcement. The toughness appears to reach a "plateau" at volume fraction of 20% and above. The decrease in toughness is attributed to an increase in stress triaxiality with increasing volume fraction of particles.

Among the explanations for low toughness values of the composites are the following variables: the type of intermetallic particles, inhomogeneous internal stress, and particle or whisker distribution. Improvements in fracture toughness of SiC_w/Al composites and K_{Ic} values levels equivalent to those of 7075 A1(T6) have

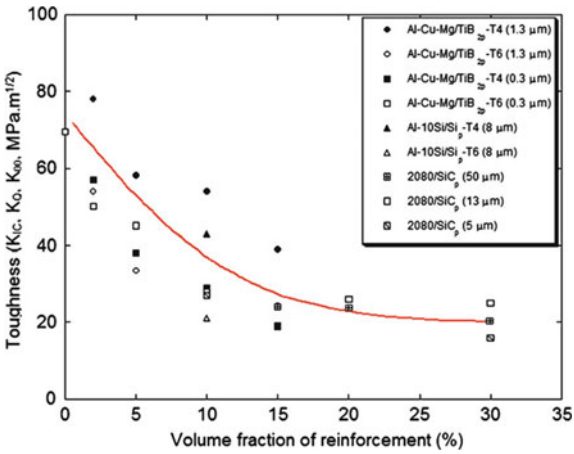

Fig. 6.23 Toughness in several particulate composite systems as a function of reinforcement volume fraction. All the composites show a decrease in toughness with increasing volume fraction of reinforcement [After Manoharan et al. 1990; Hunt et al. 1991]

been obtained by using a cleaner matrix powder, better mixing, and increased mechanical working during fabrication (McDanels 1985). McDanels' work also reinforces the idea that the metallic matrix is not merely a medium to hold the fibers together. Figure 6.23 shows that the type of aluminum matrix used in 20 v/o SiC_w/Al composites was the most important factor affecting yield strength and ultimate tensile strength of these composites. Higher strength aluminum alloys showed higher strengths but lower ductilities. Composites with 6061 Al matrix showed good strength and higher fracture strain.

6.5.3 Thermal Characteristics

In general, ceramic reinforcements (fibers, whiskers, or particles) have a coefficient of thermal expansion smaller than that of most metallic matrices. This means that when the composite is subjected to a temperature change (deliberate or inadvertent), thermal stresses will be generated in both the components because of the constraint imposed by the interfacial bonding.

Chawla and Metzger (1972), working with a single crystal copper matrix containing large diameter tungsten fibers showed the importance of thermal stresses in MMCs. Specifically, they employed a dislocation etch-pitting technique to delineate dislocations in the single crystal copper matrix. This system has the advantage of showing pure fiber reinforcement, i.e., no interfacial reaction, no grain boundaries in the matrix, etc. They showed that, in their low fiber volume fraction composites, near the fiber the dislocation density was much higher in the matrix than the dislocation density far away from the fiber. The situation in the as-cast composite can be depicted as is shown schematically in Figure 6.15, where a primary plane section of the composite is shown having a hard zone (high dislocation density) around each fiber and a soft zone (low dislocation density) away from the fiber. The enhanced dislocation density in the copper matrix near the fiber arises because of the plastic deformation in the matrix in response to the thermal stresses generated by the thermal mismatch between the fiber and the matrix. The intensity of the gradient in dislocation density will depend on the interfiber spacing. The dislocation density gradient will decrease with a decrease in the interfiber spacing. The existence of a plastically deformed zone containing high dislocation density in the metallic matrix near the reinforcement has also been confirmed by transmission electron microscopy by a number of researchers, both in fibrous and particulate metal matrix composites.

Thermal mismatch is indeed something that is difficult to avoid in any composite. By the same token, however, one can control the overall thermal expansion characteristics of a composite by controlling the proportion of reinforcement and matrix and the distribution of the reinforcement in the matrix. Many researchers

have proposed models to predict the coefficients of thermal expansion of composites, determined experimentally these coefficients, and analyzed the general thermal expansion characteristics of metal matrix composites; we describe some of these in Chap. 10. It would be appropriate to point out here some special aspects of thermal characteristics of MMCs, especially particulate MMCs. This is because of their applications in electronic packaging, where their superior thermal characteristics play an important role; this makes it very important to understand the effects of thermal stresses and thermal cycling in MMCs. Prediction of coefficient of thermal expansion (CTE) is complicated because of the structure of the composite (particles, whiskers, or fibers), interface, and the matrix plastic deformation due to internal thermal stresses. Expansion characteristics of isotropic composites are a function of V_p or V_f, size, and morphology of the reinforcement. Phenomena such as hysteretic deformation during thermal cycling, microcracking, and fiber extrusion/intrusion on the surface lead to surface roughness. Rezai-Aria et al. (1993) observed surface roughness when they subjected Saffill alumina fiber reinforced aluminum to thermal cycling. It is important to realize that the CTE of a material is not an absolute physical constant, but that it varies with temperature. This is especially so with MMCs, where the matrix can undergo plastic deformation as a result of thermal stresses (Vaidya and Chawla 1994). In addition, there are many microstructural factors that come into play. For example, a micromechanical analysis of the thermal expansion of two-dimensional SiC_p/Al composites showed the importance of reinforcement continuity (Shen et al. 1994). Balch et al. (1996) investigated the role of reinforcement continuity on the thermal expansion of SiC/Al and the effect of the presence of voids on CTE. Their analysis showed that a high matrix yield strength, a high interfacial strength, and a convex reinforcement shape would minimize variations in CTE of a SiC_p/Al-type composite during any thermal excursion. In foam reinforced composites, a weak interface could be exploited to produce void and thus minimize the average CTE of the composite, but hysteretic thermal expansion would be observed.

6.5.4 *High temperature properties, creep, and fatigue*

Superior high temperature properties of MMCs have been demonstrated in a number of systems. For example, silicon carbide whiskers (SiC_w) improve the high temperature properties of aluminum considerably. Figure 6.24 compares the elastic modulus, yield stress, and ultimate tensile strength of SiC_w (21% V_f)/2024 aluminum alloy composites to those of the unreinforced aluminum alloy (Phillips 1978). Figure 6.25 shows the fracture surface after tensile testing of a Nicalon fiber/aluminum composite at two temperatures. Note the more or less planar fracture with no fiber pullout at room temperature (Fig. 6.25a). At 500 °*C*, a loss of adhesion between the fiber and the matrix occurs with the accompanying fiber/matrix separation and fiber pullout. The fiber pullout has left a hole in the center; see Fig. 6.25b.

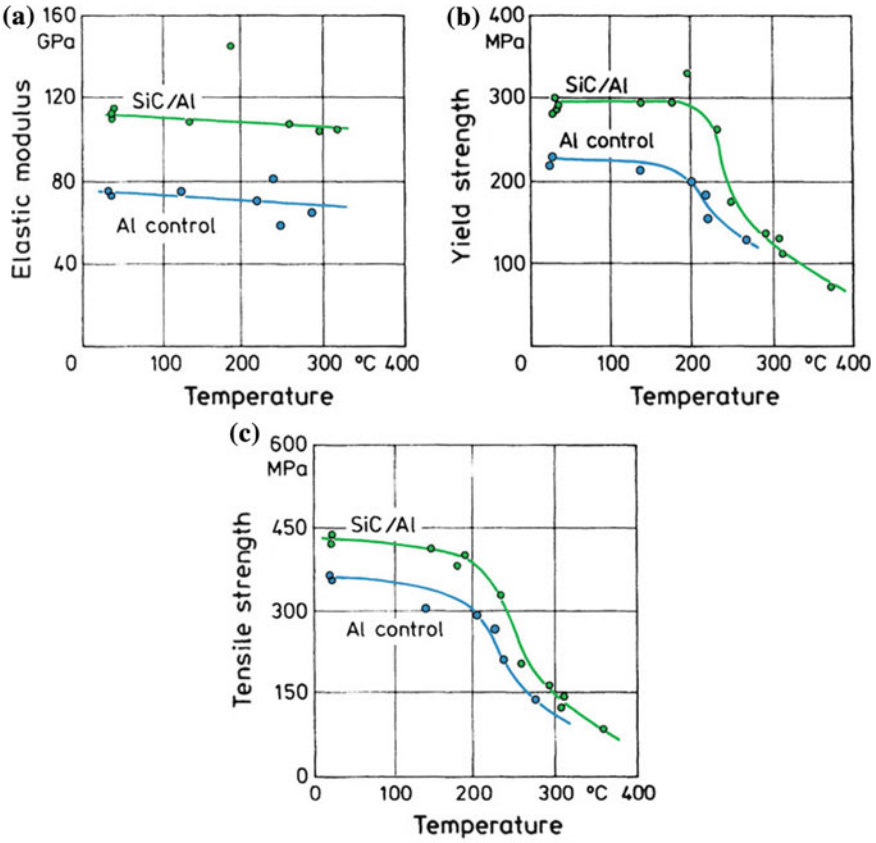

Fig. 6.24 Comparison of high-temperature properties of SiC_w/Al composites and aluminum: **a** elastic modulus, **b** yield stress, **c** ultimate tensile strength [From Phillips (1978), used with permission]

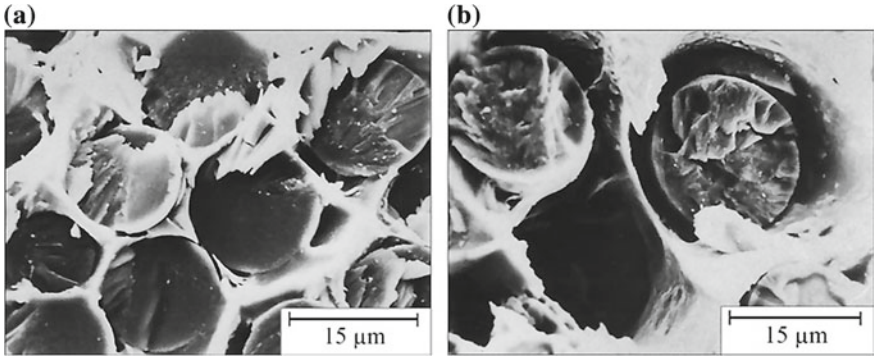

Fig. 6.25 Tensile fracture in Nicalon fiber/aluminum: **a** at room temperature showing a planar fracture, **b** at 500 °*C* showing fiber/matrix separation and fiber pullout leaving a hole [Courtesy of K. Okamura]

High modulus carbon fiber/aluminum composites combine a very high stiffness with a very low thermal expansion due mainly to the almost zero longitudinal expansion coefficient of carbon fibers. Carbon/aluminum composites, however, are susceptible to galvanic corrosion between carbon and aluminum. Carbon is cathodic in nature, while aluminum is anodic. Thus, galvanic corrosion can be a serious problem in joining aluminum to a carbon fiber composite. A common solution is to have an insulating layer of glass between the aluminum and the carbon composite. Any welding or joining involving localized heating could also be a potential source of problems because aluminum carbide may form as a result of overheating, which will be detrimental to the mechanical and corrosion properties.

The phenomenon of creep refers to time dependent deformation. In practice, at least for most metals and ceramics, the creep behavior becomes important at high temperatures and, thus, sets a limit on the maximum application temperature. In general, this limit increases with the melting point of a material. We describe the creep behavior of MMCs along with that of other composites in Chap. 12.

Fatigue is the phenomenon of mechanical property degradation leading to failure of a material or a component under cyclic loading. Many large volume applications of composite materials involve cyclic loading situations, e.g., automobile components. For a general discussion of fatigue behavior of composites, see Chap. 12. We mention here but one example of the importance of matrix microstructure on the fatigue behavior of MMCs. Williams and Fine (1985a) investigated the fatigue

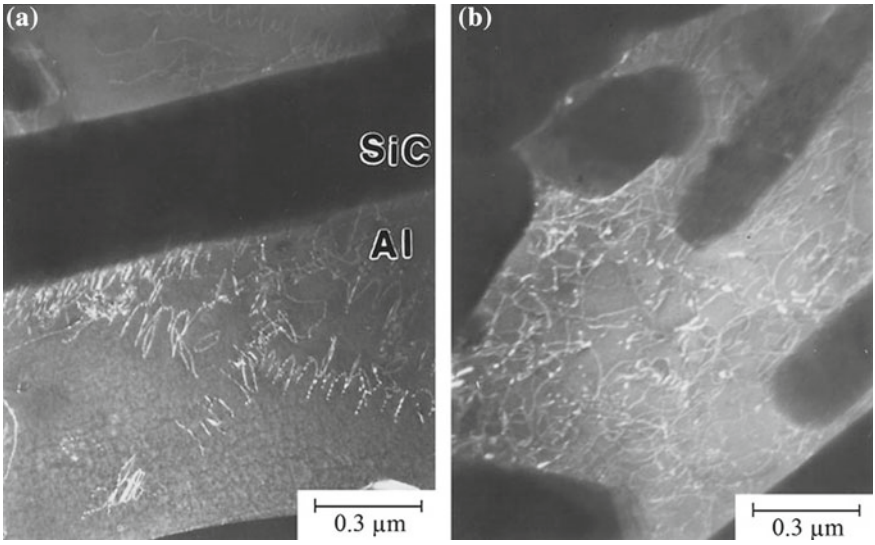

Fig. 6.26 Dislocation distribution in the aluminum matrix of a SiC_w/Al composite: **a** inhomogeneous dislocation distribution before testing, **b** uniform dislocation distribution after fatigue testing [From Williams and Fine (1985b), used with permission]

behavior of SiC whisker reinforced 2124 Al alloy composites. They found that unbonded SiC_p and non-SiC intermetallics were the fatigue crack initiation sites. The unbonded SiC particles occur when clusters of SiC are present. Thus, not unexpectedly, reducing the clustering of SiC and the number and size of the intermetallics resulted in increased fatigue life. Cyclic loading results in a uniform distribution of dislocations in the metal matrix. Figure 6.26 shows the dislocation distribution in an aluminum matrix before and after fatigue testing of a SiC_w/Al composite (Williams and Fine 1985b). Note the uniform dislocation distribution after fatigue testing.

6.6 Applications

It is convenient to divide the applications of metal matrix composites into aerospace and nonaerospace categories. In the category of aerospace applications, low density and other desirable features such as a tailored coefficient of thermal expansion and thermal conductivity, high stiffness, and strength are the main drivers. Performance rather than cost is the important item. Inasmuch as continuous fiber reinforced MMCs deliver superior performance than particle reinforced composites, the former are frequently used in aerospace applications. In the nonaerospace applications, cost and performance are important, i.e., an optimum combination of these items is required. It is thus understandable that particle reinforced MMCs find more structural and nonstructural applications in nonaerospace fields. By far, the largest commercial application of MMCs is in the form of filamentary superconducting composites. We devote a whole chapter to such composites (Chap. 9) because of their commercial importance. Here, we provide a brief description of various other applications of MMCs.

Reduction in the weight of a component is a major driving force for any application in the aerospace field. For example, in the Hubble telescope, pitch-based continuous carbon fiber reinforced aluminum was used for waveguide booms because this composite is very light, has a high elastic modulus, E, and has a low coefficient of thermal expansion, α. Other aerospace applications of MMCs involve replacement of light but toxic beryllium. For example, in the US Trident missile, beryllium has been replaced by SiC_p/Al composite.

One of the important applications of MMCs in the automotive area is in diesel piston crowns (Donomoto et al. 1983). This application involves incorporation of short fibers of alumina or alumina + silica in the crown of the piston. The conventional diesel engine piston has an Al–Si casting alloy with crown made of a nickel cast iron. The replacement of the nickel cast iron by aluminum matrix composite resulted in a lighter, more abrasion-resistant, and cheaper product. Figure 6.27 shows a picture of such a piston; the arrow indicates the piston crown that is made of short fiber reinforced aluminum composite. Another application in

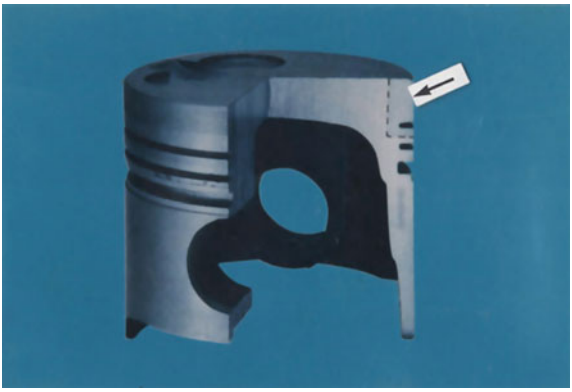

Fig. 6.27 A cutout of a squeeze cast piston with MMC inserts indicated by dotted lines [Courtesy of Toyota Motor Co.]

the automotive sector involves the use of carbon fiber and alumina fibers in an aluminum alloy matrix for use as cylinder liners in the Prelude model of Honda Motor Co. Figure 6.28 shows the microstructure of the cylinder liner showing the unreinforced and fiber reinforced portions.

Continuous alumina fiber (Nextel 610) reinforced Al composites are used to make power transmission cables. The cable consists of a composite core, consisting of Al_2O_3/Al composite wrapped with Al–Zr wires. The composite core bears most of the load as it has much higher stiffness and strength. Several tests were conducted on the actual conductor, including sag-tension behavior, vibration fatigue, thermal expansion, lightning resistance, and electrical resistance. Figure 6.29a shows these cables, while Fig. 6.29b shows the advantage in reducing the sag by using the 3M's Aluminum Conductor Composite Reinforced (ACCR) instead of the conventional aluminum-steel reinforced conductor (ACSR).

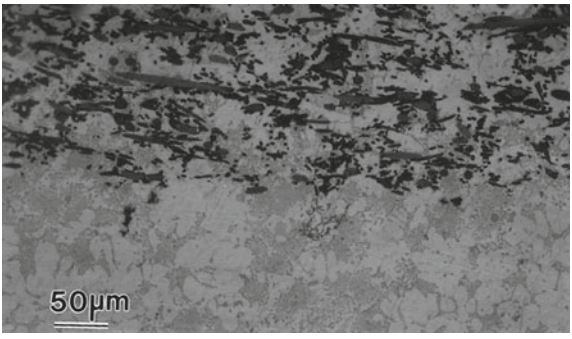

Fig. 6.28 Microstructure of the cylinder liner showing the unreinforced Al alloy (bottom) and fiber (alumina + carbon) reinforced (top) portions

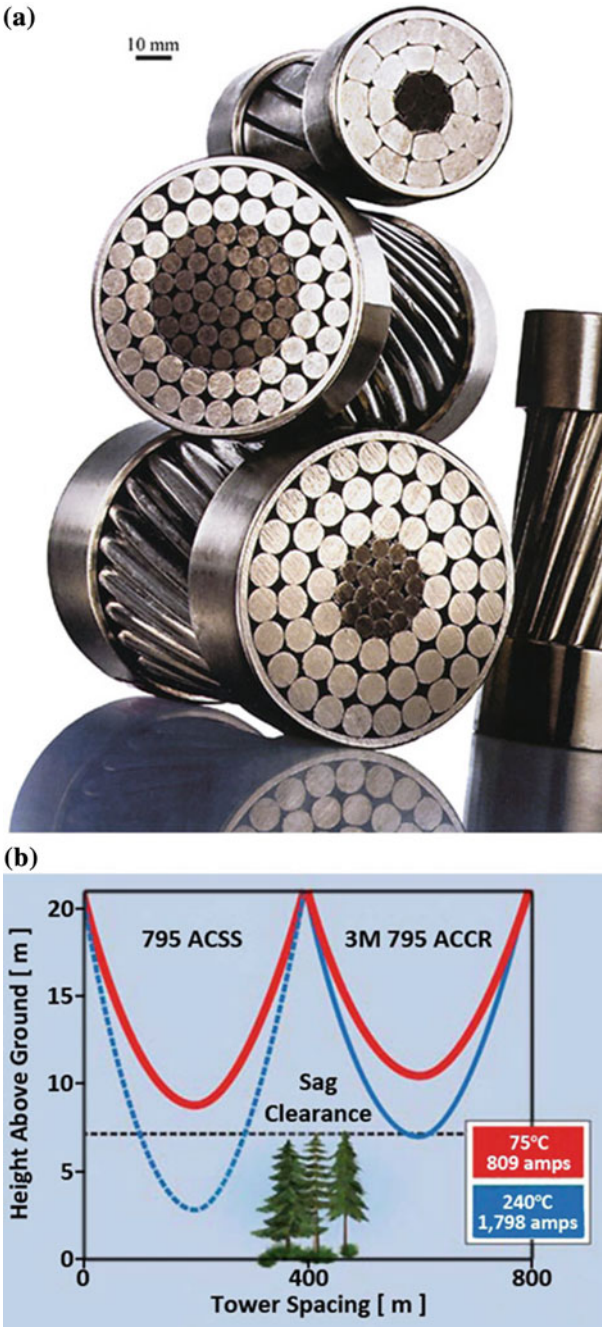

Fig. 6.29 **a** 3M's power transmission cable with composite core. **b** Reduction in sag by using the 3M's aluminum conductor composite reinforced (ACCR) instead of the conventional aluminum–steel reinforced conductor (ACSR) [Courtesy of 3M Corp.]

An important potential commercial application of particle reinforced aluminum composite is to make automotive driveshafts. In the design of a driveshaft, one needs to consider the speed at which it becomes dynamically unstable. It turns out that in terms of geometric parameters, a shorter shaft length and larger diameter will give a higher critical speed, N_c, while in terms of material parameters, the higher the specific stiffness (E/ρ), the higher N_c will be. One can make changes in the driveshaft geometry (increase the length or reduce the diameter) while maintaining a constant critical speed. A decrease in the driveshaft diameter can be important because of under-chassis space limitations.

Particulate metal matrix composites, especially with light metal matrix composites such as aluminum and magnesium, also find applications in automotive and sporting goods. In this regard, the price per kilogram becomes the driving force for application. At one time, particulate MMCs were used to make mountain bicycles. These bicycles had frames made from extruded tubes of 6061 aluminum containing about 10% alumina particles. The major advantage is the gain in stiffness.

An interesting example of a sheet laminate composite is a nonvibration sheet steel, made by Kawasaki Steel under the tradename Nonvibra™. A thin film of resin is sandwiched between two metal sheets. A chromate coating is applied on the inner surface of the skin metal. The chromate coating is conducive to cementing the bond between the resin and the outer skin metal. Such a laminated composite muffles noise over a broad range of frequencies, and it can be used in the temperature range of 0–100 °*C*. Examples of applications include oil pans, locker covers, dashboard panels, floor panels, electrical machinery and appliances, and office equipment.

6.6.1 Electronic Grade MMCs

Metal matrix composites can be tailored to have optimal thermal and physical properties to meet the requirements of electronic packaging systems (e.g., cores, substrates, carriers, and housings). Continuous boron fiber reinforced aluminum composites made by diffusion bonding have been used as heat sinks in chip carrier multilayer boards.

Unidirectionally aligned, pitch-based carbon fibers in an aluminum matrix can have very high thermal conductivity along the fiber direction. The conductivity transverse to the fibers is about two-thirds that of aluminum. Such a C/Al composite can find applications in heat transfer applications where weight reduction is an important consideration, for example, in high-density, high-speed integrated-circuit packages for computers and in base plates for electronic equipment. Can the reader think of a potential application in the disk drive of a computer?

Example Discuss the use of carbon fiber/copper matrix as a high thermal conductivity metal matrix composite for applications that require high thermal conductivity and high strength.

Answer Pitch-based carbon fibers can have very high thermal conductivity along the fiber axis, higher than even that of copper. Putting such fibers in a copper matrix will result in a high strength, high thermal conductivity metal matrix composite. The problem with carbon fibers and metallic matrixes is that the surface energy considerations preclude wetting of the carbon fibers by the molten metals. The surface energy of carbon fiber is about 100 mJ/m^2, while most molten metals have surface energy of about 1000 mJ/m^2. Recall from Chap. 2 that wetting occurs when the surface energy of the substrate (fiber) is higher than that of the molten metal. Thus, one does not expect the wetting of carbon fibers by molten copper. Two possible routes around this difficulty are

- Fiber surface modification and
- Matrix modification.

It would appear that modification of carbon fiber surface by making it rough could result in a reasonable mechanical bond between carbon fiber and copper matrix.

Problems

6.1. Pressure casting is frequently used to prepare metal matrix composite. Explain why.

6.2. Describe some of the advantages of metal matrix composites over monolithic metals.

6.3. Discuss the advantages of metal matrix composites vis à vis polymer matrix composite.

6.4. Discuss the advantages and disadvantages of liquid metal processing vis à vis other methods of fabricating metal matrix composites.

6.5. Silicon carbide (0.1 μm thick) coated boron fiber was used to reinforce a metallic matrix. The SiC coating serves as a diffusion barrier coating. Estimate the time for dissolution of this coating at 700 K if the diffusion coefficient at 700 K is $10^{-16}\ m^2 s^{-1}$.

6.6. The metallic matrix will generally undergo constrained plastic flow in the presence of a moderately high volume fraction of high modulus fibers. Draw schematically the stress–strain curves of a constrained metal matrix (i.e., in situ behavior) and an unconstrained metal (i.e., 100% matrix metal). Explain the difference.

6.7. Aluminum and magnesium are two common metal matrix materials. What is the viscosity of molten aluminum and magnesium?

6.8. What is the effect on viscosity of adding ceramic particles to a molten metal such as aluminum or magnesium? Discuss its implications in the processing of MMCs with respect to features such as particle size, volume fraction, etc.

6.9. Discuss the problem of thermal stability of unidirectionally solidified eutectic (in situ) metallic composites.

6.10. Discuss the use of silicon carbide particle reinforced aluminum composites in braking applications.

6.11. Discuss the use of alumina particle reinforced aluminum composites in bicycle frames. Do include the effect of welding for joining such composites.

References

M.K. Aghajanian, J.T. Burke, D.R. White, A.S. Nagelberg, SAMPE Quart. **34**, 817–823 (1989)
R.J. Arsenault, R.M. Fisher, Scripta Met. **17**, 67 (1983)
R.J. Arsenault, N. Shi, Mater. Sci. Eng. **81**, 175 (1986)
D.K. Balch, T.J. Fitzgerald, V.J. Michaud, A. Mortensen, Y.-L. Shen, S. Suresh, Metall. Mater. Trans. A. **27A**, 3700 (1996)
A.A. Baker, C. Shipman, Fibre Sci. Tech. **5**, 282 (1972)
E.V. Barrera, J. Sims, D.L. Callahan, V.J. Provenzano, J. Milliken, R.L. Holtz, J. Mater. Res. **9**, 2662 (1994)
A.R. Champion, W.H. Krueger, H.S. Hartman, A.K. Dhingra (1978), in *Proceedings of International Conference on Composite Materials (ICCM/2)*, TMS-AIME, New York, p. 883
K.K. Chawla, Metallography **6**, 155 (1973a)
K.K. Chawla, Philos. Mag. **28**, 401 (1973b)
K.K. Chawla (1974), in *Grain Boundaries in Eng. Mater*., Claitor's Publishing, Baton Rouge, LA, p. 435
K.K. Chawla, Fibre Sci. Tech. **8**, 49 (1975)
K.K. Chawla, J. Metals **37**, 25 (1985)
K.K. Chawla, *Precious and Rare Metal Technologies* (Elsevier, Amsterdam, 1989), p. 639
K.K. Chawla, C.E. Collares (1978), In *Proceedings of the 1978 International Conference on Composite Materials (ICCM/2)*, TMS-AIME, New York, p. 1237
K.K. Chawla, M. Metzger, J. Mater. Sci. **7**, 34 (1972)
K.K. Chawla, M. Metzger (1978), in *Fracture 1977: Proceedings of the 4th International Conference on Fracture*. Pergamon Press, vol. 3, p. 1039
N. Chawla, C. Andres, J.W. Jones, J.E. Allison, Metall. Mater. Trans. **29A**, 2843 (1998)
T. Christman, S. Suresh, Mater. Sci. Eng. **A102**, 211 (1988)
L. Christodolou, P.A. Parrish, C.R. Crowe, Mat. Res. Soc. Symp. Proc. **120**, 29 (1988)
H.E. Cline, J.L. Walter, E.F. Koch, L.M. Osika, Acta. Met. **19**, 405 (1971)
T.W. Clyne, J.F. Mason, Met. Trans. A **18**, 1519 (1987)
A.J. Cook, P.S. Warner, Mater. Sci. Eng. **A144**, 189 (1991)
J.A. Cornie, Y.-M. Chiang, D.R. Uhlmann, A.S. Mortensen, J.M. Collins, Ceram. Bull. **65**, 293 (1986)
A.P. Divecha, S.G. Fishman, S.D. Karmarkar, J. Metals **33**(9), 12–17 (September 1981)
T. Donomoto, N. Miura, K. Funatani, N. Miyake (1983) *SAE Tech. Paper* No. 83052, Detroit, MI
D.C. Dunand, A. Mortensen, Acta Metall. Mater. **39**, 127 (1991a)
D.C. Dunand, A. Mortensen, Acta Metall. Mater. **39**, 1405 (1991b)
I. Dutta, D.L. Bourell, D. Latimer, J. Comp. Mater. **22**, 829 (1988)
I. Dutta, D.L. Bourell, Acta Metall. **38**, 2041 (1990)
A.H. Esmaeili, K.K. Chawla, A.K. Datye, A.K. Vasudevan (1991), in *Proceedings of the International Conference on Composite Materials, ICCM/VII*, Honolulu, HI, p. 17F1
L.-J. Fu, M. Schmerling, H.L. Marcus (1986), in *Composite Materials: Fatigue and Fracture*, ASTM STP 907, ASTM, Philadelphia p. 51
C. Fujiwara, M. Yoshida, M. Matsuhama, S. Ohama (1995), in *Proceedings of International Conference on Composite Materials (ICCM-10)*, pp. II–687

C.M. Gabryel, A.D. McLeod, Met Trans. **23A**, 1279 (1991)
A.K. Ghosh, *Metal Matrix Composites* (Butterworth-Heinemann, Boston, MA, 1993), p. 119
R.G. Hill, R.P. Nelson, C.L. Hellerich (1969), in *Proceedings of the 16th Refractory Working Group Meeting*, Seattle, WA
W.H. Hunt, T.M. Osman, J.J. Lewandowski (1991) J. Miner. Metal Mater. Soc. **30**
J.A. Isaacs, F. Taricco, V.J. Michaud, A. Mortensen, Met. Trans. **22A**, 2855 (1991)
C. Jones, C.J. Kiely, S.S. Wang, J. Mater. Res. **4**, 327 (1993)
H.A. Katzman, J. Mater. Sci. **22**, 144 (1987)
M. Katsura (1982) Japan Pat. 57-25275
R.J. Kerans, T.A. Parthasarathy, J. Am. Ceram. Soc. **74**, 1585 (1991)
A. Kohyama, N. Igata, Y. Imai, H. Teranishi, T. Ishikawa (1985), in *Proceedings of Fifth International Conference on Composite Materials (ICCM/V)*, TMS-AIME, Warrendale, PA, p. 609
A.P. Majidi, T.W. Chou, Proc. ICCM VI **2**, 422 (1987)
M. Manoharan, L. Ellis, J.J. Lewandowski, Scripta Met. et Mater. **24**, 1515 (1990)
C. Manning, T. Gurganus, J. Am. Ceram. Soc. **52**, 115 (1969)
D.L. McDanels, Met. Trans. **16A**, 1105 (1985)
M. McLean, *Directionally Solidified Materials for High Temperature Service* (The Metals Soc, London, 1983)
R. Mehrabian, R.G. Riek, M.C. Flemings, Metall Trans **5**, 1899 (1974)
W. Meyerer, D. Kizer, S. Paprocki, H. Paul (1978), in *Proceedings of 1978 International Conference on Composite Materials (ICCM/2)*, TMS-AIME, New York, p. 141
M.A. Meyers, K.K. Chawla, *Mechanical Metallurgy* (Prentice-Hall, Englewood Cliffs, NJ, 1984), p. 494
V.J. Michaud, *Metal Matrix Composites* (Butterworth-Heinemann, Boston, MA, 1993), p. 3
R. Mitra, W.A. Chiou, M.E. Fine, J.R. Weertman, J. Mater. Res. **8**, 2300 (1993)
A. Mortensen, J.A. Cornie, M.C. Flemings, J. Metals **40**, 12 (1988)
A. Mortensen, M.N. Gungor, J.A. Cornie, M.C. Flemings, J. Metals **38**, 30 (1986)
V.C. Nardone, K.M. Prewo, Scipta Met **20**, 43 (1986)
R. Naslain, J. Thebault, R. Pailler (1976), in *Proceedings of the 1975 International Conference on Composite Materials*, vol. 1, TMS-AIME, New York, p. 116
T.G. Nieh, R.F. Karlak, Scripta Met. **17**, 67 (1984)
S. Nourbakhsh, F.L. Liang, H. Margolin, Met. Trans. A **21A**, 213 (1990)
L. Parrini, R. Schaler, J. Alloys Comp. **211**, 402 (1994)
P.G. Partridge, C.M. Ward-Close, Int. Mater. Rev. **38**, 1 (1993)
L. Pennander, C.-H. Anderson (1991) in *Metal Matrix Composites —Processing, Microstructure and Properties*, *12th Riso International Symposium on Materials Science* ed. by Hansen et al., p. 575
M. Pfeifer, J.M. Rigsbee, K.K. Chawla, J. Mater. Sci. **25**, 1563 (1990)
W.L. Phillips (1978), in *Proceedings of 1978 International Conference on Composite Materials (ICCM/2)*, TMS-AIME, New York, p. 567
H.J. Rack (1987), in *Sixth International Conference on Composite Materials*. Elsevier Applied Science, New York, p. 382
F. Rezai-Aria, T. Liechti, G. Gagnon, Scripta Metall. Mater. **28**, 587 (1993)
S. Rhee, J. Am. Ceram. Soc. **53**, 386 (1970)
P.K. Rohatgi, R. Asthana, S. Das, Intl. Met. Rev. **31**, 115 (1986)
Y.-L. Shen, A. Needleman, S. Suresh, Metall. Mater. Trans. A **25A**, 839 (1994)
O. Sherby, S. Lee, R. Koch, T. Sumi, J. Wolfenstine, Mater. Manufact. Process. **5**, 363 (1985)
N. Shi, R.J. Arsenault, J. Comp. Tech. Res. **13**, 211 (1991)
N. Shi, R.J. Arsenault, Met. Trans. **24A**, 1879 (1993)
J. van Suchtelen, Philips Res. Rep. **27**, 28 (1972)
T.S. Srivatsan, E.J. Lavernia, J. Mater. Sci. **27**, 5965 (1992)
S. Suresh, K.K. Chawla, *Metal Matrix Composites* (Butterworth-Heinemann, Boston, MA, 1993), p. 119

D.G. Thomas, J. Colloid. Sci. **20**, 267 (1965)
R.U. Vaidya, K.K. Chawla, Compos. Sci. Tech. **50**, 13 (1994)
A.K. Vasudevan, R.D. Doherty (eds.), *Aluminum Alloys—Contemporary Research and Applications* (Academic Press, Boston, 1989)
A.K. Vasudevan, J.J. Petrovic (eds.), *High temperature structural silicides* (Elsevier, Amsterdam, 1992)
J.L. Walter, *In Situ Composites IV* (Elsevier, New York, 1982), p. 85
R. Warren, C.-H. Andersson, Composites **15**, 101 (1984)
D.R. Williams, M.E. Fine (1985a), in *Proceedings of 5th International Conference on Composite Materials* (*ICCM/V*), TMS, Warrendale, PA. p. 275
D.R. Williams, M.E. Fine (1985b), in *Proceedings of Fifth International Conference on Composite Materials* (*ICCM/V*), Warrendale, PA, TMS-AIME, p. 369

Suggested Reading

N. Chawla, K.K. Chawla, *Metal Matrix Composites*, 2nd edn. (Springer, New York, 2006)
T.W. Clyne, P.J. Withers, *An Introduction to Metal Matrix Composites* (Cambridge University Press, Cambridge, 1993)
A. Mortensen, J. Llorca, Ann. Rev. Mater. Res. **40**, 243 (2010)
S. Suresh, A. Needleman, A. Mortensen (eds.), *Metal Matrix Composites* (Butterworth-Heinemann, Boston, 1993)
M. Taya, R.J. Arsenault, *Metal Matrix Composites* (Pergamon Press, Oxford, 1990)

Chapter 7
Ceramic Matrix Composites

Ceramic materials in general have a very attractive package of properties: high strength and high stiffness at very high temperatures, chemical inertness, low density, and so on. This attractive package is marred by one deadly flaw, namely, an utter lack of toughness. They are prone to catastrophic failures in the presence of flaws (surface or internal). They are extremely susceptible to thermal shock and are easily damaged during fabrication and/or service. It is therefore understandable that an overriding consideration in ceramic matrix composites (CMCs) is to toughen the ceramics by incorporating fibers in them and thus exploit the attractive high temperature strength and environmental resistance of ceramic materials without risking a catastrophic failure. It is worth pointing out at the very outset that there are certain basic differences between CMCs and other composites. The general philosophy in nonceramic matrix composites is to have the fiber bear a greater proportion of the applied load. This load partitioning depends on the ratio of fiber and matrix elastic moduli, E_f/E_m. In nonceramic matrix composites, this ratio can be very high, while in CMCs, it is rather low and can be as low as unity; think of alumina fiber reinforced alumina matrix composite. Another distinctive point regarding CMCs is that because of limited matrix ductility and generally high fabrication temperature, thermal mismatch between components has a very important bearing on CMC performance. The problem of chemical compatibility between components in CMCs has ramifications similar to those in, say, MMCs. We first describe some of the processing techniques for CMCs, followed by a description of some salient characteristics of CMCs regarding interface and mechanical properties and, in particular, the various possible toughness mechanisms, and finally a description of some applications of CMCs.

K. K. Chawla, *Composite Materials*,
https://doi.org/10.1007/978-3-030-28983-6_7

7.1 Processing of CMCs

Ceramic matrix composites (CMCs) can be processed either by conventional powder processing techniques used for making polycrystalline ceramics or by some new techniques developed specifically for making CMCs. We describe below some of the important processing techniques for CMCs.

7.1.1 Cold Pressing and Sintering

Cold pressing of the matrix powder and fiber followed by sintering is a carryover from conventional processing of ceramics. Generally, in the sintering step, the matrix shrinks considerably and the resulting composite has many cracks. In addition to this general problem of shrinkage associated with sintering of any ceramic, certain other problems arise when we put high aspect ratio (length/diameter) reinforcements in a glass or ceramic matrix material and try to sinter. Fibers and whiskers can form a network that may inhibit the sintering process. Depending on the difference in thermal expansion coefficients of the reinforcement and matrix, a hydrostatic *tensile* stress may develop in the matrix on cooling, which will counter the driving force (surface energy minimization) for sintering (Raj and Bordia 1989; Kellet and Lange 1989). Thus the densification rate of the matrix will, in general, be retarded in the presence of reinforcements (Bordia and Raj 1988; De Jonghe et al. 1986; Sacks et al. 1987; Rahaman and De Jonghe 1987; Prewo 1986). Whiskers or fibers may also give rise to the phenomenon of bridging, which is a function of the orientation and aspect ratio of the reinforcement.

7.1.2 Hot Pressing

Some form of hot pressing is frequently resorted to in the consolidation stage of CMCs. This is because a simultaneous application of pressure and high temperature can accelerate the rate of densification and a pore-free and fine-grained compact can be obtained. A common variant, called the *slurry infiltration* process, is one of the most important techniques used to produce continuous fiber reinforced glass and glass–ceramic composites (Sambell et al. 1974; Phillips 1983a, b; Cornie et al. 1986; Prewo and Brennan 1980; Brennan and Prewo 1982; Chawla et al. 1993a, b). The slurry infiltration process involves two stages:

1. Incorporation of a reinforcing phase into an unconsolidated matrix.
2. Consolidation of matrix by hot pressing.

Figure 7.1 shows a schematic of this process. In addition to incorporation of the reinforcing phase, the first stage involves some kind of fiber alignment. A fiber tow

or a fiber preform is impregnated with matrix containing slurry by passing it through a slurry tank. The impregnated fiber tow or preform sheets are similar to the prepregs used in polymer matrix composites. The slurry consists of the matrix powder, a carrier liquid (water or alcohol), and an organic binder. The organic binder is burned out prior to consolidation. Wetting agents may be added to ease the infiltration of the fiber tow or preform. The impregnated tow or prepreg is wound on a drum and dried. This is followed by cutting and stacking of the prepregs and consolidation in a hot press. The process has the advantage that, as in PMCs, the prepregs can be arranged in a variety of stacking sequences, e.g., unidirectional, cross-plied (0°/90°/0°/90°, etc.), or angle-plied ($+\theta/-\theta/+\theta/-\theta$, etc.). Figure 7.2a shows an optical micrograph of a transverse section of a unidirectional Nicalon fiber/glass matrix composite. In general, such glass matrix composites are well consolidated, i.e., there is hardly any porosity. Porosity can be a problem with crystalline ceramics. Figure 7.2b shows the pressure and temperature schedule used during hot pressing of a typical CMC.

The slurry infiltration process is well suited for glass or glass–ceramic matrix composites, mainly because the processing temperatures for these materials are lower than those used for crystalline matrix materials and glassy phase has good flow properties. Any hot pressing process has certain limitations on producing complex shapes. The fibers should suffer little or no damage during handling. Application of a very high pressure can easily damage fibers. Refractory particles of

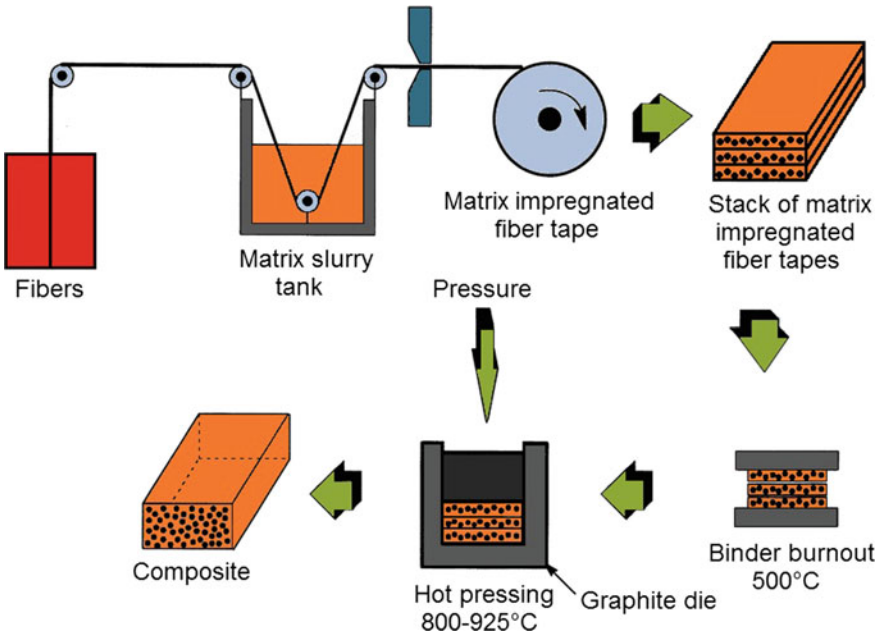

Fig. 7.1 Schematic of the slurry impregnation process

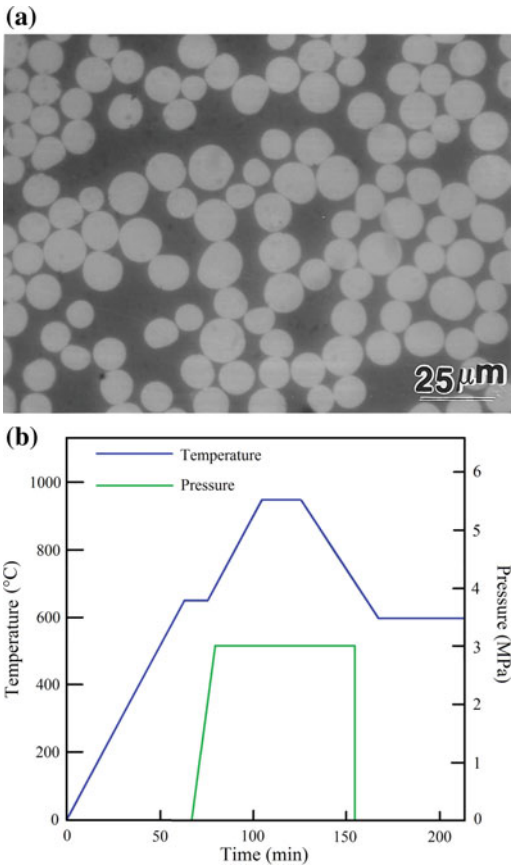

Fig. 7.2 **a** An optical micrograph of a transverse section of a unidirectional Nicalon fiber/glass matrix composite. **b** Pressure and temperature schedule used during hot pressing of a typical CMC

a crystalline ceramic can damage fibers by mechanical contact. The reinforcement can also suffer damage from reaction with the matrix at very high processing temperatures. The matrix should have as little porosity as possible in the final product as porosity in a structural ceramic material is highly undesirable. To this end, it is important to completely remove the fugitive binder and use a matrix powder particle smaller than the fiber diameter. The hot pressing operational parameters are also important. Precise control within a narrow working temperature range, minimization of the processing time, and use of a pressure low enough to avoid fiber damage are important factors in this final consolidation part of the process. Fiber damage and any fiber/matrix interfacial reaction, along with its detrimental effect on the bond strength, are unavoidable attributes of the hot pressing operation.

In summary, the slurry infiltration process generally results in a fairly uniform fiber distribution; low porosity and high strength values can be obtained. The main disadvantage of this process is that one is restricted to relatively low melting or low softening point matrix materials.

Whisker reinforced CMCs are generally made by mixing the whiskers with a ceramic powder slurry, followed by drying and hot pressing. Sometimes hot isostatic pressing (HIPing) rather than uniaxial hot pressing is used. Whisker agglomeration in a green body is a major problem. Mechanical stirring and adjustment of pH level of the suspension (matrix powder + whiskers in water) can be of help in this regard. The addition of whiskers to slurry can result in very high viscosity. Also, whiskers with large aspect ratios (>50) tend to form bundles and clumps (Liu et al. 1991). Obtaining well-separated and deagglomerated whiskers is of great importance for reasonably high density composites. Use of organic dispersants (Barclay et al. 1987), techniques such as agitation mixing assisted by an ultrasonic probe, and deflocculation by a proper pH control (Yang and Stevens 1990) can be usefully employed. Most whisker reinforced composites are made at temperatures in the 1500–1900 $^{\circ}C$ range and pressures in the 20–40 MPa range (Homeny et al. 1987; Shalek et al. 1986).

7.1.3 Reaction Bonding Processes

Reaction bonding involves the use of components in a powder form and then using a chemical reaction to form the ceramic compound. Reaction bonding processes similar to the ones used for monolithic ceramics can be used to make ceramic matrix composites. Reaction bonding process has the following advantages:

- Problems with matrix shrinkage during densification can be avoided.
- Rather large volume fractions of whiskers or fiber can be used.
- Multidirectional, continuous fiber preforms can be used.
- The reaction bonding temperatures for most systems are generally lower than the sintering temperatures, so that fiber degradation can be avoided.

One great disadvantage of this process is that high porosity is difficult to avoid.

A hybrid process involving a combination of hot pressing and reaction bonding techniques can also be used (Bhatt 1986, 1990). A silicon cloth is prepared by attrition milling a mixture of silicon powder, a polymer binder, and an organic solvent to obtain a dough of proper consistency. This dough is then rolled to make a silicon cloth of desired thickness. Fiber mats are made by filament winding of silicon carbide with a fugitive binder. The fiber mats and silicon cloth are stacked in an alternate sequence, debinderized (the step of binder removal), and hot pressed in a molybdenum die in a nitrogen or vacuum environment. The temperature and pressure are adjusted to produce a handleable preform. At this stage, the silicon matrix is converted to silicon nitride by transferring the composite to a nitriding

furnace between 1100 and 1400 °*C*. Typically, the silicon nitride matrix has about 30% porosity, which is not unexpected in reaction bonded silicon nitride.

Reaction bonding processing can also be used to make oxide fiber/oxide matrix composites, which are very attractive for high temperature applications in air. Specifically, the technique has been applied to alumina (Claussen et al. 1989, 1994; Kristofferson et al. 1993) and mullite (Wu and Claussen 1994) systems. Mullite is an important technological ceramic that forms as an intermediate phase in the SiO_2–Al_2O_3 system. The chemical composition of mullite is commonly denoted as $3Al_2O_3.2SiO_2$ (which corresponds to 60 *mol*% Al_2O_3); in reality, it refers to a solid solution in the range of 60–63 *mol*% Al_2O_3 below 1600 °*C* (Schneider and Komarneni 2005). In the case of producing an oxide matrix in a preform of oxide fibers, reaction bonding process involves direct oxidation of starting powders to create the matrix. The process has a shorter processing time than forming matrix by infiltration techniques. For the case of alumina, a starting powder consisting of Al–Al_2O_3 or a slurry infiltrated compact is heat-treated in an oxidizing atmosphere. The aluminum powder oxidizes to Al_2O_3. The key point, however, is that in this process of oxidation, there occurs a 28% volume expansion, which partially compensates for the sintering shrinkage. Oxidation is usually completed below 1100 °*C*, where sintering does not take place. Mullite matrix can be obtained by adding SiC to the starting powder, which is then oxidized during processing to form the SiO_2 component. An alternative technique of producing mullite involves the use of an Al–Si alloy as a starting material. Because problems with shrinkage during densification are avoided, reaction bonding is an attractive and fast method of producing fiber reinforced, ceramic composites.

7.1.4 Infiltration

Infiltration of a preform made of reinforcement can be done with a matrix material in solid, liquid, or gaseous form.

7.1.4.1 Liquid Infiltration

This technique is very similar to liquid polymer or liquid metal infiltration (Fig. 7.3). Proper control of the fluidity of the liquid matrix is, of course, the key to this technique. It yields a high density matrix, i.e., no pores in the matrix. Almost any reinforcement geometry can be used to produce a virtually flaw-free composite. The temperatures involved in the case of CMCs, however, are much higher than those encountered in polymer or metal processing. Processing at such high temperatures can lead to deleterious chemical reactions between the reinforcement and the matrix. Thermal expansion mismatch between the reinforcement and the matrix, the rather large temperature interval between the processing temperature and room temperature, and the low strain to failure of ceramics can add up to a formidable set

of problems in producing a crack-free CMC. Viscosities of ceramic melts are generally quite high, which makes the infiltration of preforms rather difficult. Wettability of the reinforcement by the molten ceramic is another item to be considered. Hillig (1988) has discussed the melt infiltration processing of ceramic matrix composites in regard to chemical reactivity, melt viscosity, and wetting of the reinforcement by the melt. A preform made of reinforcement in any form (for example, fiber, whisker, or particle) having a network of pores can be infiltrated by a ceramic melt by using capillary pressure. Application of pressure or processing in vacuum can aid in the infiltration process. Assuming that the preform consists of a bundle of regularly spaced, parallel channels, one can use Poiseuilles's equation to obtain the infiltration height, h:

$$h = \sqrt{\frac{\gamma r t \cos\theta}{2\eta}},$$

where r is the radius of the cylindrical channel, t is the time, γ is the surface energy of the liquid infiltrant, θ is the contact angle of wetting, and η is the viscosity. The penetration height is proportional to the square root of time, and the time required to penetrate a given height is inversely proportional to the viscosity of the melt. Penetration will also be easier if the contact angle is low (i.e., better wettability),

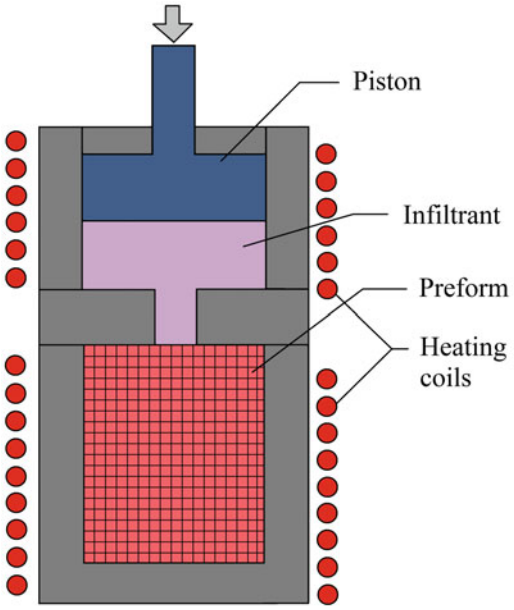

Fig. 7.3 Schematic of the melt infiltration process. After Cornie et al. (1986), used with permission

and the surface energy, γ, and the pore radius, r, are large. If the radius, r, of the channel is made too large, the capillarity effect will be lost.

Infiltration of a fibrous preform by a molten intermetallic matrix material under pressure has been successfully done (Nourbakhsh and Margolin 1989). Alumina fiber reinforced intermetallic matrix composites (e.g., TiAl, Ni_3Al, and Fe_3Al matrix materials) have been prepared by *pressure casting*, also called *squeeze casting* (Nourbakhsh and Margolin 1989, 1990). The matrix alloy is melted in a crucible in a vacuum, while the fibrous preform is heated separately. The molten matrix material (at about 100 °C above the melting temperature, T_m) is poured onto the fibers, and argon gas is introduced simultaneously. Argon gas pressure forces the melt to infiltrate the preform. The melt generally contains additives to aid wetting of the fibers.

We may summarize the advantages and disadvantages of various melt infiltration techniques as follows. The advantages are as follows:

- The matrix is formed in a single processing step.
- A homogeneous matrix can be obtained.

The disadvantages of infiltration techniques are as follows:

- High melting points of ceramics mean a greater likelihood of reaction between the melt and the reinforcement.
- Ceramics have higher melt viscosities than metals; therefore, infiltration of preforms is relatively difficult.
- The matrix is likely to crack because of the differential shrinkage between the matrix and the reinforcement on solidification. This can be minimized by choosing components with nearly equal coefficients of thermal expansion.

7.1.5 *Directed Oxidation or the Lanxide™ Process*

Yet another version of liquid infiltration is the directed oxidation process, also known as the Lanxide™ process, developed by erstwhile Lanxide Corp. (Urquhart 1991). One of the Lanxide processes is called DIMOX™, which stands for directed metal oxidation process. A schematic of the directed metal oxidation process is shown in Fig. 7.4. The first step in this process is to make a preform, which in the case of a particulate composite can be a ceramic green body. In the case of a fibrous composite, filament winding or a fabric lay-up may be used to make a preform. A barrier to stop the growth of the matrix material is placed on the preform surfaces. In this method, a molten metal is subjected to directed oxidation, i.e., the desired reaction product forms on the surface of the molten metal and grows outward. The metal is supplied continuously to the reaction front by a wicking action through channels in the oxidation product. For example, molten aluminum in air will get

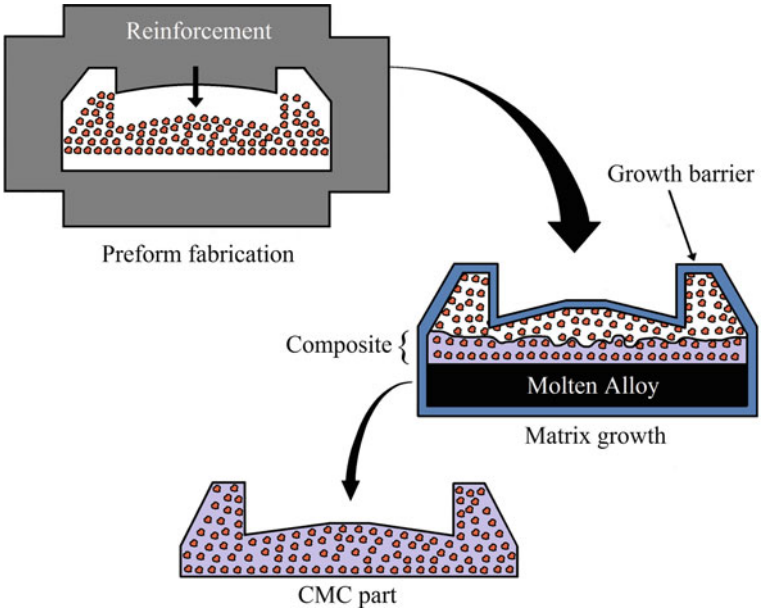

Fig. 7.4 Schematic of the directed metal oxidation process of Lanxide Corp (Courtesy Lanxide Corp.)

oxidized to aluminum oxide. If one wants to form aluminum nitride, then molten aluminum is reacted with nitrogen. The reaction can be represented as follows:

$$\mathrm{Al} + \mathrm{air} \rightarrow \mathrm{Al_2O_3}$$
$$\mathrm{Al} + \mathrm{nitrogen} \rightarrow \mathrm{AlN}.$$

The end product in this process is a three-dimensional, interconnected network of a ceramic material plus about 5–30% of unreacted metal. When filler particles are placed next to the molten metal surface, a ceramic network forms around these particles. As we said earlier, a fabric made of a continuous fiber can also be used. The fabric is coated with a proprietary coating to protect the fiber from highly reducing aluminum and to provide a weak interface, which is desirable for enhanced toughness in CMCs. Some aluminum (6–7 *wt%)* remains at the end of the process. This must be removed if the composite is to be used at temperatures above the melting point of aluminum (660 °*C*). On the other hand, the presence of a residual metal can be exploited to provide an increment of fracture toughness in these composites.

Proper control of the reaction kinetics is of great importance in this process. The process is potentially a low-cost process because near-net shapes of the final product are possible. Also, good mechanical properties (such as strength and toughness) have been reported (Urquhart 1991). Figure 7.5 shows some fiber reinforced

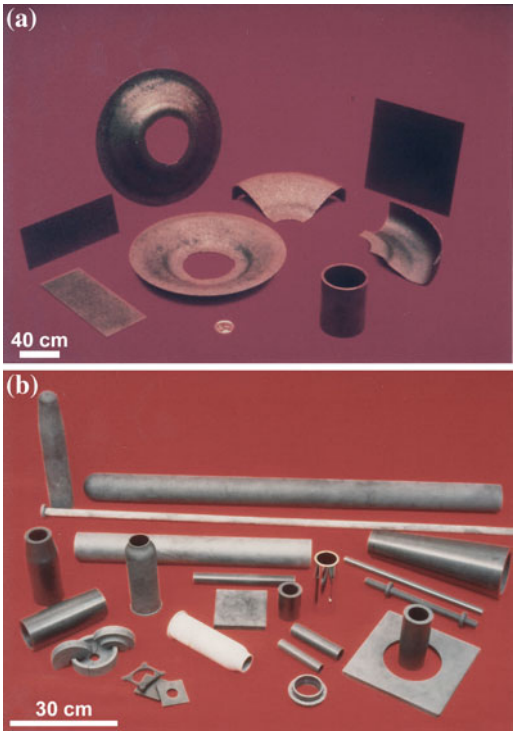

Fig. 7.5 Some fiber reinforced ceramic components made by Dimox process. **a** Fiber reinforced ceramic composites for applications in high temperature gas turbine engine components. **b** Heat exchanger and radiant burner tubes, flame tubes, and other high temperature furnace parts made of particle reinforced ceramic composites (Courtesy of Lanxide Corp.)

ceramic components made by this process. Figure 7.5a shows some fiber reinforced ceramic composites for applications in high temperature gas turbine engine components, while Fig. 7.5b shows heat exchanger and radiant burner tubes, flame tubes, and other high temperature furnace parts made of particle reinforced ceramic composites.

The main disadvantages of the Lanxide processes are as follows:

- It is difficult to control the chemistry and produce an all-ceramic matrix by this method. There is always some residual metal, which is not easy to remove completely.
- It is difficult to envision the use of such techniques for large, complex parts, such as those required, say, for aerospace applications.

7.1.6 In Situ Chemical Reaction Techniques

In situ chemical reaction techniques to produce CMCs are extensions of those used to produce monolithic ceramic bodies. We describe below some of the more important techniques, viz., chemical vapor deposition (CVD) and chemical vapor infiltration (CVI) and different types of reactive consolidation techniques.

7.1.6.1 Chemical Vapor Deposition and Chemical Vapor Impregnation

When the chemical vapor deposition (CVD) technique is used to impregnate rather large amounts of matrix material in fibrous preforms, it is called *chemical vapor impregnation* (CVI). Common ceramic matrix materials used are SiC, Si_3N_4, and HfC. The CVI method has been used successfully by several researchers to impregnate fibrous preforms (Fitzer and Hegen 1979; Fitzer and Schlichting 1980; Fitzer and Gadow 1986; Stinton et al. 1986; Burkland et al. 1988). The preforms can consist of yarns, woven fabrics, or three-dimensional shapes.

In very simple terms, in the CVI process, a solid material is deposited from gaseous reactants onto a heated substrate. A typical CVD or CVI process would require a reactor with the following parts:

1. A vapor feed system.
2. A CVD reactor in which the substrate is heated and gaseous reactants are fed.
3. An effluent system where exhaust gases are handled.

The chemistry for making ceramic fibers by CVD was given in Chap. 2. The basic chemistry to make a bulk ceramic matrix in and around fibers in a preform remains the same. One can synthesize a variety of ceramic matrices such as oxides, glasses, ceramics, and intermetallics by CVD. Commonly, the process involves an isothermal decomposition of a chemical compound in the vapor form to yield the desired ceramic matrix on and in between the fibers in a preform. Figure 7.6 shows a schematic of such an isothermal process. For example, methyltrichlorosilane (CH_3SiCl_3), the starting material to obtain SiC, is decomposed at a temperature between 1200 and 1400 K as per the following reaction:

$$CH_3Cl_3Si(g) \rightarrow SiC(s) + 3HCl(g).$$

The vapors of SiC deposit as solid phase on and in between the fibers in a free-standing preform to make the matrix. An example of the microstructure of an SiC/SiC composite obtained by CVI is shown in Fig. 7.7. The CVI process is very slow because it involves diffusion of the reactant species to the fibrous substrate, followed by outflow of the gaseous reactant products. The CVI process of making a ceramic matrix is, indeed, a kind of low-stress and low-temperature CVD process, and thus avoids some of the problems associated with high temperature ceramic processing. However, when the CVI process is carried out isothermally,

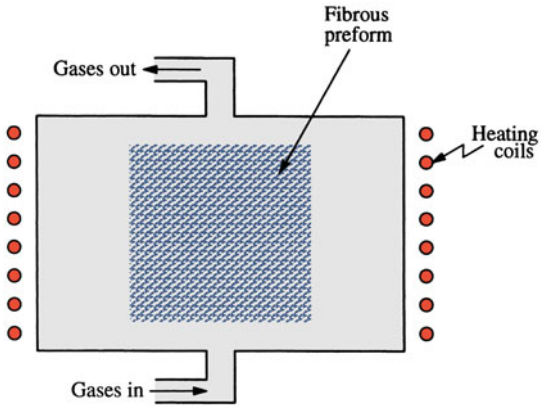

Fig. 7.6 Schematic of an isothermal chemical vapor infiltration process

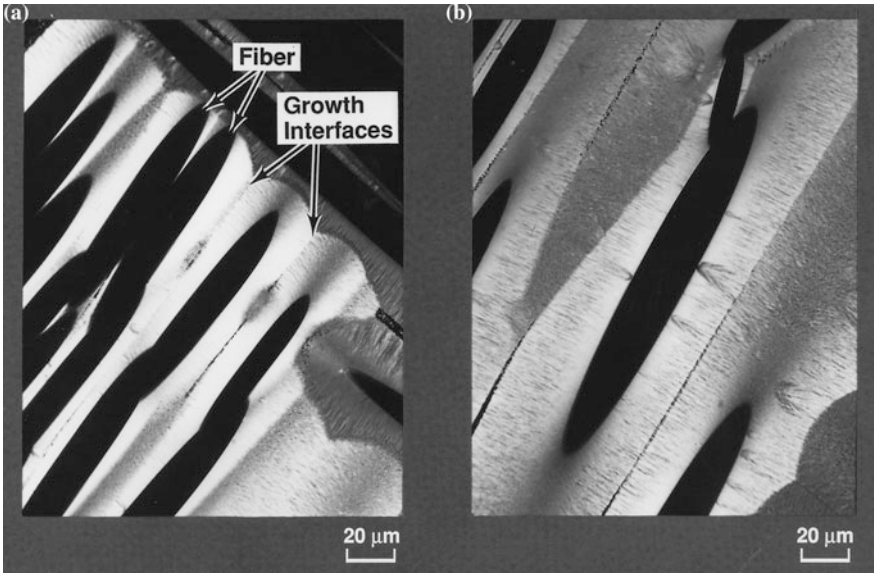

Fig. 7.7 An example of the microstructure of a Nicalon fiber/SiC matrix composite obtained by CVI (Courtesy of R.H. Jones.) Note the growth interfaces within the matrix indicated by arrows

near-surface pores tend to close first, restricting the gas flow to the interior of the preform. This necessitates multiple cycles of impregnation, surface machining, and reinfiltration to obtain an adequate density. One can avoid some of these problems to some extent by using a forced gas flow and a temperature gradient.

A schematic of one version of this process is shown in Fig. 7.8 (Stinton et al. 1986). A graphite holder in contact with a water-cooled metallic gas distributor holds the fibrous preform. The bottom and side surfaces thus stay cool, while the

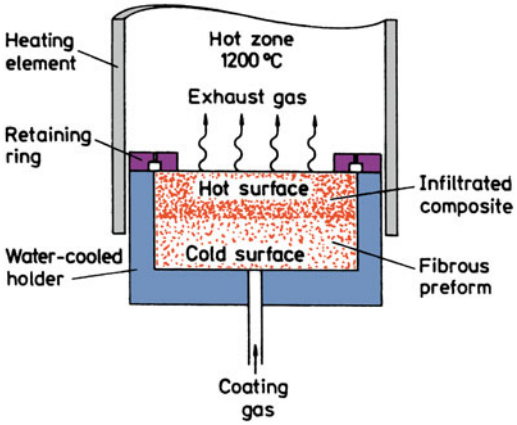

Fig. 7.8 Schematic of a chemical vapor infiltration process with pressure and temperature gradients. [After Stinton et al. (1986)]

top of the fibrous preform is exposed to the hot zone, creating a steep thermal gradient. The reactant gaseous mixture passes unreacted through the fibrous preform because of the low temperature. When these gases reach the hot zone, they decompose and deposit on and in between the fibers to form the matrix. As the matrix material gets deposited in the hot portion of the preform, the preform density and thermal conductivity increase, and the hot zone moves progressively from the top of the preform toward the bottom. When the composite is formed completely at the top and is no longer permeable, the gases flow radially through the preform, exiting from the vented retaining ring.

This variant of CVI, which combines forced gas flow and temperature gradient, avoids some of the problems mentioned earlier. Under these modified conditions, 70–90% dense SiC and Si_3N_4 matrices can be impregnated in SiC and Si_3N_4 fibrous preforms in less than a day. Under conditions of plain CVI, it would take several weeks to achieve such densities, i.e., one can reduce the processing time from several days to less than 24 *h*. One can also avoid using binders in this process with their attendant problems of incomplete removal. The use of a graphite holder simplifies the fabrication of the preform, and the application of a moderate pressure to the preform can result in a higher-than-normal fiber volume fraction in the final product. The final obtainable density in a ceramic body is limited by the fact that closed porosity starts at about 93–94% of theoretical density. It is difficult to impregnate past this point.

Advantages of a CVI technique or any variant thereof include the following:

- Good mechanical properties at high temperatures.
- Large, complex shapes can be produced in a near-net shape.
- Considerable flexibility in the fibers and matrices that can be employed (oxide and nonoxide).

7.1.6.2 Reactive Consolidation or Liquid-Phase Sintering

Siliconized silicon carbide is the name given to a composite of SiC fibers in a silicon matrix. Molten silicon reacts with carbon fibers to form SiC. The original geometry of the carbon fibers is retained. Carbon fiber in the form of cloth, tow, felt, or matte is used as a precursor. A preform is made of carbon fiber and infiltrated with liquid silicon. Silicon reacts with carbon fibers to form SiC fibers in an Si matrix. Typical composition of the resultant composite is Si (30–50%) + SiC fiber. The silicon matrix limits the use temperature to about 1400 °*C*. A big advantage of SiC/Si composites is that the constituents are in chemical equilibrium and they have closely matched thermal expansion coefficients. A version of this siliconized silicon process is used by GE, which we describe separately in Sect. 7.1.11.

In another version of this process, a liquid phase forms as a result of an exothermic reaction between elemental powders. A good example is from the field of intermetallics, e.g., nickel aluminides. The following steps are involved:

1. Mix nickel and aluminum in stoichiometric proportions.
2. Cold isostatic press to 70% theoretical density to obtain a green body.
3. Vacuum encapsulate the green body in a 304 stainless-steel can.
4. Subject the canned material to reactive hot isostatic pressing.

7.1.7 Sol–Gel

Sol–gel techniques, which have been used to make conventional ceramic materials, can also be used to make ceramic matrix materials in the interstices of a fibrous preform. We described the sol–gel technique in Chap. 2. To recapitulate, a metal compound, e.g., a metal alkoxide, acetate, or halide, is converted to a sol. The sol is the precursor to form a gel (a network of particles), which in turn is subjected to controlled heating to produce the desired end product: a glass, a glass–ceramic, or a ceramic. Characteristically, the gel-to-ceramic conversion temperature is much lower than that required in a conventional melting or sintering process. Some of the advantages of the sol–gel techniques for making composites are the same as the ones for monolithic ceramics, viz., lower processing temperatures, greater compositional homogeneity in single-phase matrices, potential for producing unique multiphase matrix materials, etc. Specifically, in regard to composite material fabrication, the sol–gel technique allows processing via liquids of low viscosity such as the ones derived from alkoxides. Among the disadvantages of sol–gel are high shrinkage and low yield compared to slurry techniques. The fiber network provides a very high surface area to the matrix gel. Consequently, the shrinkage during the drying step, frequently, results in a large density of cracks in the matrix. Generally, repeated impregnations are required to produce a substantially dense matrix.

It is easy to see that many of the polymer handling and processing techniques can be used for sol–gel as well. Impregnation of fibrous preforms in vacuum and filament winding are two important techniques. In filament winding, fiber tows or rovings are passed through a tank containing the sol, and the impregnated tow is wound on a mandrel to a desired shape and thickness. The sol is converted to gel, and the structure is removed from the mandrel. A final heat treatment then converts the gel to a ceramic or glass matrix.

The sol–gel technique can also be used to prepare prepregs by the slurry infiltration method. The sol in the slurry acts as a binder and coats fibers and glass particles. The binder burnout step is thus eliminated because the binder, being of the same composition as the matrix, becomes part of the glass matrix. An advantage of this sol–gel-based slurry method is that consolidation can be done at lower temperatures. Among the problems, one should mention that the coating layer on the fiber is porous, frequently carbon-rich, and nonuniform.

7.1.8 Polymer Infiltration and Pyrolysis (PIP)

Just as polymeric precursors can be used to make ceramic fibers (see Chap. 2), we can use polymeric precursors to form a ceramic matrix in a composite. This technique is called polymer infiltration and pyrolysis (PIP). It is an attractive processing route because of its relatively low cost, small amounts of residual porosity, and minimal degradation of the fibers. Moreover, this approach allows near-net-shape molding and fabrication technology that is able to produce nearly fully dense composites. In PIP, the fibers are infiltrated with an organic polymer, which is heated to fairly high temperatures and pyrolyzed to form a ceramic matrix. Due to the relatively low yield of polymer to ceramic, multiple infiltrations are used to densify the composite.

Polymeric precursors for ceramic matrices allow one to use conventional polymer composite fabrication technology that is readily available, and take advantage of processes used to make polymer matrix composites (French 1996; Hurwitz et al. 1989). These include complex shape forming and fabrication. Furthermore, by processing and pyrolyzing at lower temperatures (compared to sintering and hot pressing, for example), one can avoid fiber degradation and the formation of unwanted reaction products at the fiber/matrix interface.

Among the desirable characteristics of a preceramic polymer are as follows (more of wish list):

- High ceramic yield from polymer precursor.
- Precursor that yields a ceramic with low free carbon content (which will oxidize at high temperatures).
- Controllable molecular weight, which allows for solvent solubility and control over viscosity for fabrication purposes.

- Low-temperature crosslinking of the polymer, which allows the resin to harden and maintain its dimensions during the pyrolysis process.
- Low cost and toxicity.

Most preceramic polymer precursors are formed from chloro-organosilicon compounds to form poly(silanes), poly(carbosilanes), poly(silazanes), poly (borosilanes), poly(silsesquioxanes), and poly(carbosiloxanes). The synthesis reaction involves the dechlorination of the chlorinated silane monomers. Since a lot of the chlorosilane monomers are formed as by-products in the silicone industry, they are inexpensive and readily available. The monomers can be further controlled by an appropriate amount of branching which controls important properties such as the viscosity of the precursor as well as the amount of ceramic yield. All silicon-based polymer precursors lead to an amorphous ceramic matrix, where silicon atoms are tetrahedrally arranged with non-silicon atoms. This arrangement is similar to that found in amorphous silica. High temperature treatments typically lead to crystallization and slight densification of the matrix, which results in shrinkage. At high temperatures, the amorphous ceramic begins to form small domains of crystalline phase, which are more thermodynamically stable. Si–C matrices derived from polycarbosilane begin to crystallize at 1100–1200 $^{\circ}C$, while Si–C–O (polysiloxanes) and Si–N–C (polysilazanes) remain amorphous to 1300–1400 $^{\circ}C$.

Typically the range of the molecular weight of the polymer is tailored, followed by shaping of the product. The polymer is then crosslinked and finally pyrolyzed in an inert or reactive atmosphere (e.g., NH_3) at temperatures between 1000 and 1400 $^{\circ}C$. The pyrolysis step can be further subdivided into three steps. In the first step, between 550 and 880 $^{\circ}C$, an amorphous hydrogenated compound of the type $Si(C_aO_bN_cB_d)$ is formed. The second step involves nucleation of crystalline precipitates such as SiC, Si_3N_4, and SiO_2 at temperatures between 1200 and 1600 $^{\circ}C$. Grain coarsening may also result from consumption of any residual amorphous phase and reduction of the amount of oxygen due to vaporization of SiO and CO. Porosity is typically in the order of 5–20 *vol%* with pore sizes of the order of 1–50 *nm*. It should be noted that the average pore size and volume fraction of pores decrease with increasing pyrolysis temperature, since the amount of densification (and shrinkage) becomes irreversible at temperatures above the maximum pyrolysis temperature

Among the disadvantages of PIP, we can list the following:

- Low yield accompanies the polymer-to-ceramic transformation.
- Large shrinkage, which typically causes cracking in the matrix during fabrication. Due to shrinkage and weight loss during pyrolysis, residual porosity after a single impregnation is on the order of 20–30%.
- To reduce the amount of residual porosity, multiple impregnations are needed.
- Reimpregnation is typically conducted with a very low-viscosity prepolymer, so that the slurry may wet and infiltrate the small micropores that exist in the preform. Usually, reimpregnation is done by immersing the part in the liquid

polymer in a vacuum bag, while higher viscosity polymers require pressure impregnation. Typically, the amount of porosity will reduce from 35% to less than 10% after about 5 impregnations.

Significant gas evolution also occurs during pyrolysis (French 1996). Thus, it is advisable to allow these volatile gases to slowly diffuse out of the matrix, especially for thicker parts. Typically, pyrolysis cycles ramp to somewhere between 800 and 1400 $°C$ over periods of 1–2 days, to avoid delamination. Recall that pyrolysis must be done at a temperature below the crystallization temperature of the matrix (or large volume changes will occur) and below the degradation temperature of the reinforcing fibers. The pyrolysis atmosphere is most commonly argon or nitrogen, although in ammonia, we obtain a pure amorphous silicon nitride with low amounts of free carbon. Fitzer and Gadow (1986) used repeated infiltration and in situ thermal decomposition of porous reaction-bonded ceramics to process Si_3N_4/SiC composites. The following steps are taken in processing the composites:

(i) Prepare a porous SiC or Si_3N_4 fibrous preform with some binder phase.
(ii) Fibrous preform is evacuated in an autoclave.
(iii) Samples are infiltrated with molten precursors, silazanes, or polycarbosilanes, at high temperature (780 K), and the argon or nitrogen pressure is slowly increased from 2 to 40 MPa. The high temperature results in a transformation of the oligomer silane to polycarbosilane and simultaneous polymerization at high pressures.
(iv) Infiltrated samples are cooled and treated with solvents.
(v) Samples are placed in an autoclave, and the organosilicon polymer matrix is thermally decomposed in an inert atmosphere at a high pressure and at temperature in the 800–1300 K range.
(vi) Steps (ii) through (v) are repeated to attain an adequate density. To produce an optimum matrix crystal structure, the material is annealed in the 1300–1800 K range.

Polymer-derived ceramic matrix composites, similar to carbon/carbon composites (see Chap. 8), typically have a cracked matrix from processing as well as a number of small pores. The large amount of shrinkage and cracking in the matrix can be contained, to some extent, by the additions of particulate fillers to the matrix, which, when added to the polymer, reduce shrinkage and stiffen the matrix material in the composite. Figure 7.9 shows schematically the role of fillers in reducing the porosity and cracking in the final product. Particulate or whisker ceramics used as fillers in the polymeric matrix can serve a variety of purposes:

- Reduce and disrupt the formation of matrix cracks that form during shrinkage of the polymer.
- Enhance ceramic yield by forming reaction products during pyrolysis.
- Strengthen and toughen the weak amorphous matrix and increase the interlaminar shear strength of the composite.

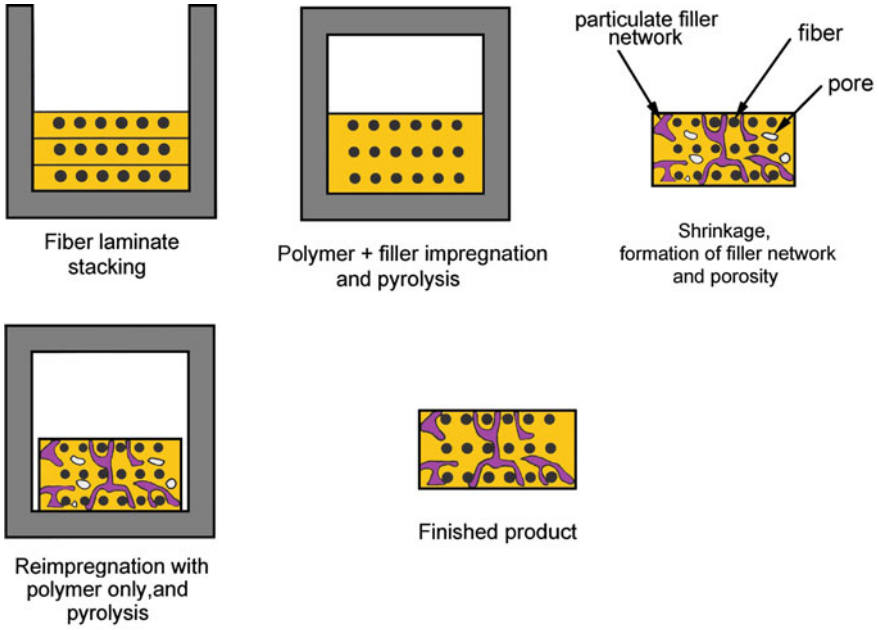

Fig. 7.9 The role of fillers in reducing the porosity and cracking in the final CMC product

The filler must be submicrometer in size in order to penetrate the tow bundle and the filler's coefficient of thermal expansion must match that of the polymeric matrix. The filler must not be used in very high fractions and the slurry should not be forced into the reinforcing fibers since abrasion of the fiber fabric may take place. This is especially true with hard, angular fillers or ceramic whiskers. Typically, the volume fraction of filler is 15–25% of the matrix volume fraction. High filler loading may result in an increase in interply spacing and lower volume fraction of fibers.

When an "active" filler phase is added to the polymer, the following generic reaction can take place to form a new carbide phase (Greil 1995):

$$P(s,l) + T(s) \xrightarrow{\Delta} C(s) + M(s) + G(g),$$

where P is the polymer, T is the active filler, C is the ceramic, G is the gaseous by-product, and M is the carbide phase formed. By controlling the amount of filler, the degree of shrinkage can be controlled.

Fiber architecture may have an impact with regard to polymer infiltration and pyrolysis (PIP). One of the key factors is wetting of the fiber bundles. During pyrolysis, the precursor shrinks around the fibers, so cracks are introduced. For example, two-dimensional woven fabrics seem to have less propensity in developing interlaminar cracks than do cross-ply or unidirectional architectures. Satin

weaves are preferred over plain weaves because more uniform cracking is achieved and large cracks between weave crossover points are avoided (Hurwitz 1992). Due to the looser nature of the satin weave (it is more drapeable), better wetting and densification may take place, although the loose nature of the weave also makes it more difficult to handle.

7.1.9 Electrophoretic Deposition

The phenomenon of electrophoresis has been known since the beginning of the nineteenth century, but its applications in processing of ceramics and ceramic composites are relatively recent. Electrophoretic deposition (EPD) should not be confused with electroplating. In electroplating, ions are the moving species and they undergo ion reduction on deposition. In EPD, on the other hand, solid particles migrate with no charge reduction on deposition. Also, the deposition rate in EPD is ≈ 1 *mm/min* while in electroplating it is ≈ 0.1 *μm/min*. Electrophoretic deposition is a relatively simple and inexpensive technique, which can be profitably exploited for infiltration of tightly woven preforms made of fibers (Illston et al. 1993). EPD makes use of nanoscale ceramic particles in a stable non-agglomerated form (such as in a sol or colloidal suspension) and exploits their net surface electrostatic charge characteristics while in suspension. On application of an electric field, such surface charge carrying particles will migrate toward and deposit on an electrode. If the deposition electrode is replaced by a conducting fibrous preform, the suspended particles will be attracted into and deposited within it, providing an appropriate means of effectively infiltrating densely packed fibrous bundles. A schematic of the basic EPD cell is shown in Fig. 7.10a, while an example of the microstructure of Nextel 720 fiber reinforced mullite matrix composite, obtained by EPD, is shown in Fig. 7.10b. The movement of ceramic sol particles in an aqueous suspension within an electric field is governed by the field strength, and the pH, ionic strength, and viscosity of the solution (Illston et al. 1993). The electrophoretic mobility of charged particles in a suspension is given by the following equation called the Smoluchowski equation (Brown and Salt 1965):

$$\text{electrophoretic mobility} = \frac{\mathrm{U}}{\mathrm{E}} = \frac{\varepsilon\zeta}{4\pi\eta},$$

where U is the velocity, E is the field strength, ε is the dielectric constant, ζ is the zeta potential, and η is the viscosity. The zeta potential is a parameter that characterizes a suspension. It can be determined by measuring particle velocity in an electric field. According to the above equation, a suitable suspension for EPD should have the following characteristics: a high particle surface charge, a high dielectric constant of the liquid phase, and a low viscosity. In addition, a low conductivity of the suspending medium to minimize solvent transport would be desirable (Boccaccini et al. 2000; Kaya et al. 2009).

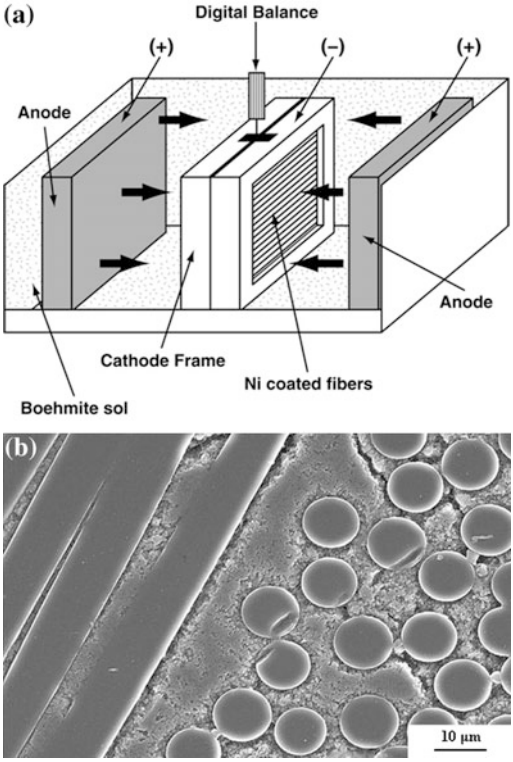

Fig. 7.10 **a** Schematic of the basic electrophoretic deposition (EPD) cell. **b** Microstructure of Nicalon 720 fiber/mullite composite made by electrophoretic deposition [From Kaya et al. (2009)]

7.1.10 Self-propagating High-Temperature Synthesis (SHS)

The SHS technique involves the synthesis of compounds without an external source of energy. One exploits exothermic reactions to synthesize ceramic compounds, which are difficult to fabricate by conventional techniques. For example, one can mix titanium powder and carbon black, cold press the mixture, and ignite the compact at the top in a cold-walled vessel. A combustion wave will pass through the compact, giving titanium carbide.

Among the salient features of SHS are as follows:

- High combustion temperature (up to 4000 °*C*).
- Simple, low cost equipment.
- Good control of chemical composition.
- Different shapes and forms can be obtained.

This technique can be used to produce a variety of refractory materials. The main disadvantage is that SHS products are very porous, because of the fairly large

porosity in the original mix of reactants and because of the large volume change that results when the reactants transform to the products. Any adsorbed gases at the elevated temperatures used during this process can also add to the porosity of the final product. Synthesis concomitant with densification can improve the situation to some extent. This involves the application of high pressure during the combustion or immediately after the completion of the combustion reaction, when the product temperature is still quite high. Hot pressing, rolling, and shock waves are some of the techniques used to apply the necessary pressure.

Many ceramics, such as borides, carbides, nitrides, silicides, and sialons, and composites, such as $SiC_w + Al_2O_3$, have been synthesized by means of SHS. The SHS process gives a weakly bonded compact. Therefore, the process is generally followed by breaking the compact, milling, and consolidation by some techniques such as HIPing. Explosive or dynamic compaction can result in a relatively dense product. A good example of an SHS process to make composites is the XD™ process, wherein exothermic reactions are used to produce multiphase alloy powders. These are hot-pressed at $\sim 1450\ ^\circ C$ to full density. Reinforcement in the form of particles, whiskers, and platelets can be added to the master alloy to make a composite. A good example is that of TiB_2 particles, about 1 μm in diameter, distributed in intermetallic matrices such as TiAl, TiAl + Ti_3Al, and NiAl.

7.1.11 GE's Melt Infiltration Process

We devote this section to GE's melt infiltration process of making CMC components, mainly because it represents a successful commercial venture that involves entry of CMC into high temperature part of an aircraft turbine engine. They are replacing parts made of nickel-based superalloy. The big driving force behind this effort is the low density of the CMC parts (about one-third of Ni-based superalloy parts) and higher operating temperatures. Figure 7.11 shows the melt infiltration process used by GE to make SiC fiber (Hi Nicalon S2) fiber reinforced silicon carbide (sometimes referred to as SiC/SiC composites). GE calls it melt infiltration (MI) process because molten silicon is used to infiltrate the fiber tow at about 1500 °C. The fibers are coated with BN, SiC particles, and carbon particles. On infiltration, silicon reacts with carbon to form SiC, and the pores are filled with silicon, resulting in an SiC–Si matrix. The fiber can be either woven or uniaxially aligned. The BN coating on the Nicalon fiber is done by CVD. The coated fibers are passed through a slurry bath containing molten silicon, carbon particles, some binders, and additives. These fibers are wound on a drum and made into a unidirectional prepreg. The prepreg sheets are then stacked, similar to the PMC laminates, compacted and densified in an autoclave, followed by pyrolysis to remove organic binders and silconization, i.e., combining carbon and silicon to make silicon carbide matrix. The last step, not shown in this figure, is the application of environmental barrier coating and inspection of the part.

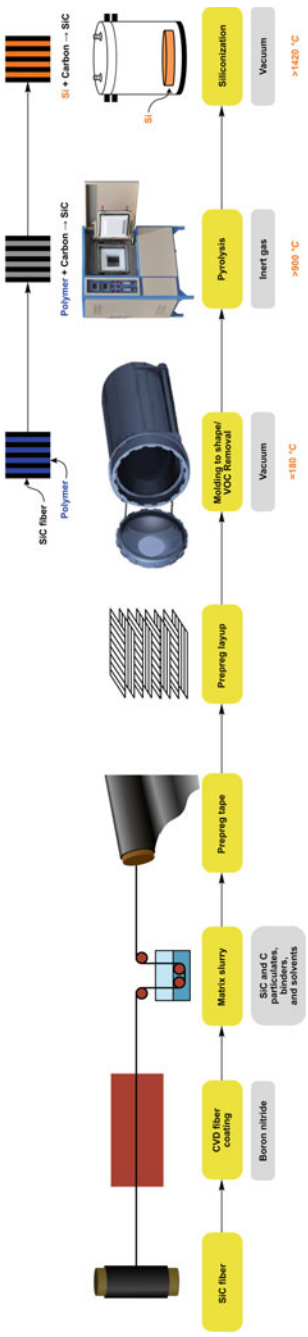

Fig. 7.11 Melt infiltration process used by GE to make CMC shrouds consisting of SiC fiber (Hi Nicalon S2) fiber reinforced silicon carbide (sometimes referred to as SiC/SiC composites) After Gardiner (2018)

7.2 Interface in CMCs

In general, for CMCs one must satisfy the following compatibility requirements: thermal expansion compatibility and chemical compatibility. Ceramics have a limited ductility, and in the fabrication of CMCs one uses high temperatures. Thus, thermal mismatch on cooling from high temperatures can cause cracking in matrix (or fiber). Thermal strain in composites is proportional to $\Delta\alpha\Delta T$, where $\Delta\alpha = \alpha_f - \alpha_m$, α_f and α_m being the linear expansion coefficients of the fiber and matrix, respectively, and ΔT is the temperature interval. There is, of course, another complication, namely, fiber expansion coefficients are also sometimes not equal in the axial and radial directions. Carbon fiber in particular has the following axial and radial coefficients:

$$\alpha_a \approx 0$$
$$\alpha_r \approx 8 \times 10^{-6} K^{-1}.$$

If $\Delta\alpha$ is positive, i.e., $\alpha_f > \alpha_m$, the matrix is compressed on cooling, which is beneficial because it leads to an increase in the tensile stress at which matrix cracking will occur. Conversely, if $\Delta\alpha$ is negative, i.e., $\alpha_f < \alpha_m$, the matrix experiences tension, which, if ΔT is sufficiently large, can cause matrix cracking. In the radial direction, if $\Delta\alpha$ is positive, the fibers tend to shrink away from the matrix on cooling, which results in a reduced interfacial bond strength. If, however, $\Delta\alpha$ is negative, the fiber/matrix bond strength can even be improved.

Matrix cracking resulting from thermal mismatch is, comparatively speaking, a more serious problem in short fiber composites than in continuous fiber composites. The reason is that in a ceramic matrix containing aligned continuous fibers, transverse microcracks appear in the matrix, but fibers continue to hold the various matrix blocks together and the composite can still display a reasonable amount of strength. In a randomly oriented short fiber composite, owing to increased stress at the fiber ends, matrix cracking occurs in all directions and the composite is very weak. We can define a thermal expansion mismatch parameter for axial and radial directions in an aligned fiber composite as (Sambell et al. 1972):

$$\phi_a, \phi_r = \Delta\alpha\Delta T(E_m/\sigma_m).$$

Table 7.1 makes a comparison of damage resulting from thermal expansion mismatch in some carbon fiber reinforced ceramic matrix composites. Note that only glass and glass–ceramic matrices (low modulus materials) show no damage.

Chemical compatibility between the ceramic matrix and the fiber involves the same thermodynamic and kinetic considerations as with other composite types. Quite frequently, the bond between fiber and ceramic matrix is simple mechanical interlocking. During fabrication (by hot pressing) or during subsequent heat treatments, the fiber/matrix bond could be affected by the high temperatures attained because of any chemical reaction between the fiber and matrix or because of any phase changes in either one of the components. Sambell et al. (1972) studied the

Table 7.1 A comparison of damage resulting from the thermal expansion mismatch in some carbon fiber reinforced systems[a]

Matrix	α_m^b (10^{-6} K^{-1})	T_c^c(°C)	E (GPa)	σ_{mu}^d (MPa)	ϕ_a^e	ϕ_r^e	Damage
MgO	13.6	1200	300	200	25	10	Severe cracking
Al_2O_3 (80% dense)	8.3	1400	230	300	9	0.3	Severe cracking
Sodalime glass	8.9	480	60	100	2.6	0.3	Localized cracks
Borosilicate glass	3.5	520	60	100	1.1	−1.4	Uncracked
Glass–ceramic	1.5	1000	100	100	1.5	−6.5	Uncracked

[a]Type I carbon fibers $\alpha_a \approx 0$, $\alpha_r \approx 8 \times 10^{-6}$ K^{-1}
[b]α_m is the matrix thermal expansion coefficient
[c]T_c is the temperature below which little stress relaxation can occur
[d]σ_{mu} is the matrix strength
[e]ϕ_a and ϕ_r are the thermal expansion mismatch parameters
Source Adapted with permission from Phillips (1983a, b)

zirconia reinforced magnesia composite system in which there occurs a chemical reaction at 1600 °C. At temperatures less than 1600 °C, the composites showed a weak fiber/matrix interface and fiber pullout occurred during mechanical polishing. Upon heat treating at 1600 °C, however, because of the interfacial reaction and the resultant improved bonding, no damage was observed upon mechanical polishing. Heat treatment at 1700 °C resulted in the complete destruction of the zirconia fibers and the distribution of zirconia to grain boundaries in magnesia. Thus, as we noted in the case of MMCs (Chap. 6), it is important to be able to control the interfacial bond by means of controlled chemical reactions between components. Chokshi and Porter (Chokshi and Porter 1985), working with SiC/Al_2O_3 system, observed a reaction layer on the fiber surface after creep testing in air. Auger electron microscopy analysis showed a mullite layer with large glassy phase regions along grain boundaries. The following interfacial reaction was proposed:

$$2SiC + 3Al_2O_3 + 4O = Al_6Si_2O_{13} + 2C,$$

and reaction kinetics were modeled by an equation of the form

$$x^2 \approx Dt,$$

where x is the reaction zone thickness, $D = D_o \exp(-Q/kT)$, Q is the activation energy, k is Boltzmann's constant, T is the temperature in kelvin, and t is the time in seconds.

The nature of the bond between fiber and ceramic matrix is thought to be predominantly mechanical. In carbon fiber reinforced glass or glass–ceramics, there

is little or no chemical bonding (Davidge 1979; Phillips et al. 1972; Prewo 1982). Evidence for this is the low transverse strength of these composites and the fact that one does not see matrix material adhering to the fibers on the fracture surface. The bond is thought to be entirely mechanical with the ceramic matrix penetrating the irregularities present on the carbon surface. Shear strength data on carbon fiber in borosilicate glass and lithium-aluminosilicate glass–ceramics (LAS) show that the borosilicate glass composites have double the shear strength of LAS composites. The reason for this is the different radial shrinkages of fibers from the matrix during cooling. Calculated radial contractions of fiber from the matrix are $2.4 \times 10^{-8}\ m$ for the LAS ceramic and $0.9 \times 10^{-8}\ m$ for the glass–ceramic composite (Phillips 1983a, b). Shrinkage reduces the mechanical interlocking and thus the fiber/matrix bond.

In ceramic matrix composites, interfacial roughness-induced radial stress becomes quite important because it affects the interface debonding, the sliding friction of debonded fibers, and the fiber pullout length. Fiber pullout is one of the important energy-dissipating fracture processes in fiber reinforced ceramic or glass matrix composites. An absence of strong chemical bond and a purely mechanical bond at the fiber/matrix interface is highly desirable for the fiber pullout to occur. In regard to the mechanical bonding, a number of researchers have pointed out the importance of interfacial roughness in ceramic matrix composites (CMCs) (Jero 1990; Jero and Kerans 1990; Carter et al. 1991; Jero et al. 1991; Kerans and Parthasarathy 1991; Mackin et al. 1992; Mumm and Faber 1992; Venkatesh and Chawla 1992; Chawla et al. 1993a, b; Sorensen 1993). If an interfacial coating is used, its coefficient of expansion must also be taken into account. As shown by Chawla and coworkers (Venkatesh and Chawla 1992; Chawla et al. 1993a, b), even when the coefficients of thermal expansion of the coating, fiber, and matrix are such that a radial tensile stress exists at the fiber/coating interface after cooling from an elevated processing temperature, fiber pullout may not occur because of a strong mechanical bonding due to a roughness-induced clamping at the fiber/matrix. Thus, a tensile thermal stress in the radial at the interface is a desirable factor. A radial tensile stress at the interface will encourage fiber debonding and slippage, which in turn result in high toughness and high work of fracture. We can express the interfacial sliding resistance in terms of interfacial shear stress as follows (Hutchinson and Jenson 1990):

$$\tau = \tau_{\mathrm{o}} - \mu\sigma_{\mathrm{n}} \quad (\sigma_{\mathrm{n}} < 0)$$

$$\tau = \tau_{\mathrm{o}} \quad (\sigma_{\mathrm{n}} \geq 0),$$

where σ_n is the stress normal to the interface, μ is the coefficient of friction, and τ_o is the sliding resistance when σ_{n} is positive (tensile). Kerans and Parthasarathy (1991) included interface surface roughness in a detailed treatment of fiber debonding and sliding during both pushout and pullout experiments. They modeled the effect of fiber surface roughness as an increase in the interfacial strain mismatch, leading to an increase in the interfacial normal pressure. The effective normal stress σ_n at the

interface is the algebraic sum of the two radial components: residual thermal stress and roughness-induced stress. We can write

$$\sigma_n = \sigma_t + \sigma_r,$$

where σ_t and σ_r are thermal and roughness-induced stresses, respectively.

The thermal stress and roughness-induced stress can be expressed as

$$\sigma_t = \beta(\Delta\alpha\Delta T)$$
$$\sigma_r = \beta(A/r),$$

where $\Delta\alpha$ is the difference in thermal expansion coefficients between matrix and fiber, ΔT is the temperature differential ($T_2 - T_1$), β is a term containing elastic constants, A is the amplitude of roughness, and r is the fiber radius.

The conventional SiC/SiC composite has a brittle SiC matrix and brittle SiC fiber with a BN interphase. Raj (2019) has proposed an engineered matrix approach, which involves thermal expansion of the engineered matrix to be close to that of the SiC fibers to minimize the thermal strains developed during thermal fatigue and to possess sufficient high temperature plasticity to minimize crack propagation, relatively high fracture toughness, and self-healing capabilities to prevent oxygen ingress to the BN coated fibers through surface-connected cracks. He examined different silicide-based engineered matrix materials. Isothermal oxidation tests showed that some of the matrices exhibited either catastrophic oxidation ("pesting") or spalling of the oxide scale. Based on these oxidation tests, he downselected two engineered matrices, $CrSi_2$/SiC/Si_3N_4 and CrMoSi/SiC/Si_3N_4. Four-point bend tests were conducted on these two engineered matrices between ambient temperature and 1698 *K*. These matrices, as expected, were brittle at low temperatures, but they showed increased four-point bend strengths and bend ductility at high temperatures as the silicide particles became more ductile, which was qualitatively consistent with the theoretically expected behavior that crack blunting at these particles should increase the matrix strength. The presence of Cr works as a getter to any oxygen ingress into the matrix through surface-connected cracks, thereby protecting the BN coating on the SiC fibers. The second-phase particles are ductile at the application temperatures to enable ductile phase toughening. His work showed that additions of 5(*wt%*) CrB_2 to $CrSi_2$–SiC and CrMoSi–SiC matrices were effective in healing scratches and in partially closing ~ 1 *mm* diameter holes.

7.3 Properties of CMCs

An important feature of CMCs is matrix microcracking, which does not have a parallel in MMCs or PMCs. As mentioned earlier, the relative elastic modulus values of fiber, E_f and matrix, E_m are very important in CMCs. The ratio E_f/E_m determines the extent of matrix microcracking. Typically, the strain-to-fracture

value of a ceramic matrix is very low. Thus, in MMCs and in thermoplastic PMCs, the matrix failure strain (ε_m) is considerably greater than that of fibers. Most unreinforced metals show that a strain-to-fracture $\varepsilon_m > 10\%$, while most polymers fail between 3 and 5% strain. Thus, in both MMCs and PMCs, fiber failure strain controls the composite failure strain. Typically, fibers such as boron, carbon, and silicon carbide show failure strain values of $\sim$1–2%. Compare this with the failure strains of less than 0.05% for most ceramic matrix materials. The situation in regard to fiber and/or matrix failure is shown in a simplified manner in Fig. 7.12. The crack-free original situation is shown in Fig. 7.12a. In the case of MMCs and PMCs, fibers fail first at various weak points distributed along their lengths; see Fig. 7.12b. The final failure of the composite will occur along a section that has the most fiber fractures. In a strongly bonded CMC, fiber and matrix would fail simultaneously at matrix failure strain and a situation similar to that shown in Fig. 7.12c will prevail. In a weakly bonded CMC, however, the matrix will start cracking first and the fibers will be bridging the matrix blocks; Fig. 7.12d shows an idealized situation. Thus, from a toughness point of view, in general, we do not want too strong a bond in a CMC because it would make a crack run through the specimen. A weak interface, however, would lead to fiber bridging of matrix microcracks.

A CMC with even a microcracked ceramic matrix can retain some reasonable strength ($\sigma_c \simeq \sigma_f V_f$) and there are applications, such as bushings, where such a damage-tolerant characteristic would be very valuable because in the absence of fibers bridging the cracks, the monolithic matrix would simply disintegrate. The disadvantage, of course, is that matrix microcracking provides an easy path for environmental attack of the fibers and the fiber/matrix interface. Let us consider an idealized situation of a fiber reinforced, unidirectionally aligned, CMC, loaded in the longitudinal direction. Assume that the CMC has proper interface, i.e., it is damage-tolerant. At a stress σ_0, the stress–strain curve will show a dip, indicating

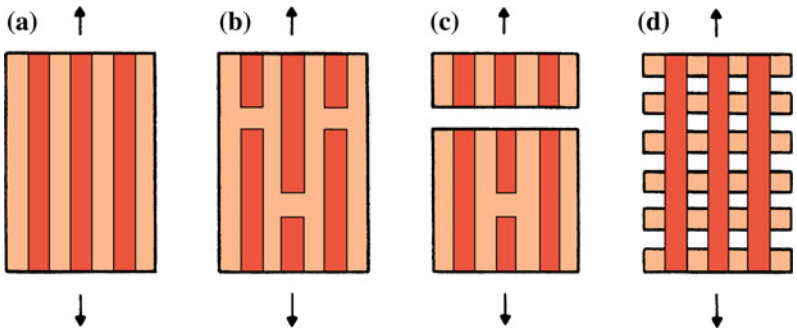

Fig. 7.12 **a** Original crack-free situation. **b** In the case of MMCs and PMCs, fibers fall first at various weak points distributed along their lengths. The composite will fail along a section that has the maximum number of fiber fractures. **c** In a strongly bonded CMC, fiber and matrix would fail simultaneously at matrix failure strain. **d** In a weakly bonded CMC, however, the matrix will start cracking first and the fibers will be bridging the matrix blocks

the incidence of periodic matrix cracking. Because the fibers have enough strength to support the load in the presence of a damaged matrix (a very desirable feature indeed), the stress–strain curve will continue to rise until, at a stress marked σ_u, the fiber bundle fails. At this point, the phenomenon of fiber pullout starts. The extent of this fiber pullout region depends critically on the interfacial frictional resistance. The fiber/matrix interface has a lot to do with the form of the stress–strain curve. If the bonding is too strong, matrix cracking will be accompanied by a small amount of fiber pullout, which is an undesirable characteristic from the toughness viewpoint, as we shall see in Sect. 7.4. Both σ_0 and σ_u are insensitive to specimen or component size because both strength levels are independent of matrix flaws (Evans 1985). This is in distinct contrast to the behavior of monolithic ceramic materials, which show significant size dependence. Increased stiffness and strength were observed in a unidirectionally aligned composite consisting of continuous carbon fibers (50% V_f) in a glass matrix compared to the unreinforced glass matrix (Davidge 1979). But more importantly, a large increase in the work of fracture occurred. The increased work of fracture is a result of the controlled fracture behavior of the composite, while the unreinforced matrix failed in a catastrophic manner.

Fiber length, or more precisely, the fiber aspect ratio (length/diameter), fiber orientation, relative strengths and moduli of fiber and matrix, thermal expansion mismatch, matrix porosity, and fiber flaws are the important variables that control the performance of CMCs. Sambell et al. (1974) showed that, for ceramic matrix materials containing short, randomly distributed carbon fibers, a weakening effect occurred rather than a strengthening effect. This was attributed to the stress concentration effect at the extremities of randomly distributed short fibers and thermal expansion mismatch. Aligned continuous fibers do lead to a real fiber reinforcement

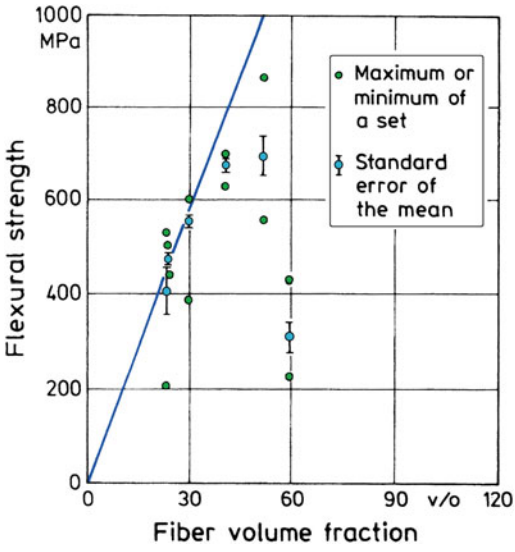

Fig. 7.13 Linear increase in strength with fiber volume fraction V_f up to ~55% in carbon fiber/glass matrix composites. [After Phillips et al. (1972), used with permission]

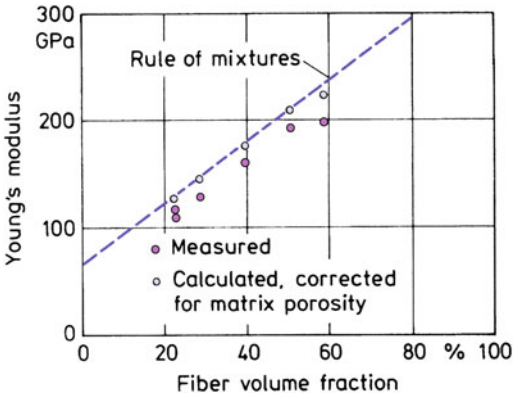

Fig. 7.14 Linear increase in Young's modulus with fiber volume fraction, V_f. At higher V_f, it deviates from linear owing to matrix porosity and possible fiber misalignment [Phillips et al. (1972)]

effect. The stress concentration at fiber ends is minimized and higher fiber volume fractions can be obtained. At very high fiber volume fractions, however, it becomes difficult to eliminate the porosity in the ceramic matrix. Figure 7.13 shows that the strength increases in a linear fashion for carbon fiber/glass matrix composites, for up to $\sim$55% V_f (Phillips et al. 1972). Beyond 55% V_f, the high matrix porosity led to a drop in the strength. The Young's modulus also increased linearly with V_f, as shown in Fig. 7.14; at higher V_f it deviated from linearity owing to matrix porosity and possible fiber misalignment (Phillips et al. 1972).

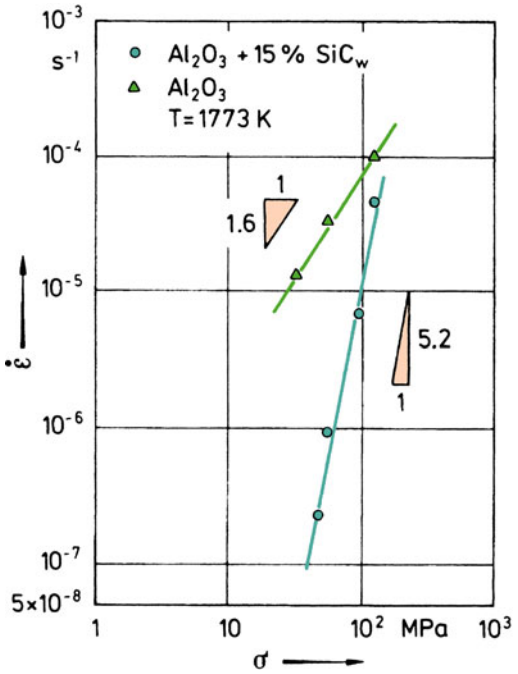

Fig. 7.15 Plots of creep strain rate as function of stress at constant temperature for silicon carbide whisker reinforced alumina and unreinforced alumina. SiC_w/Al_2O_3 is more creep-resistant than unreinforced polycrystalline alumina [Chokshi and Porter 1985]. Note that the composite has a higher stress exponent than the unreinforced matrix

Creep resistance of a ceramic such as alumina can be improved by adding fibers or whiskers. Silicon carbide SiC whisker reinforced alumina showed superior creep resistance than polycrystalline alumina (Chokshi and Porter 1985); see Fig. 7.15. This figure shows, on a log–log plot, the creep strain rate as a function of stress at a constant temperature. Note that the composite has a higher stress exponent than the unreinforced matrix. The higher stress exponent indicates a change in the operating creep mechanism.

The exponent for polycrystalline alumina is about 2, and this is rationalized in terms of some kind of diffusion creep being the controlling mechanism. A stress exponent of about 5, which was observed for the composite, is indicative of a dislocation creep mechanism being in operation. Observation of the specimens deformed in creep in transmission electron microscope showed dislocation activity.

7.4 Toughness of CMCs

Many concepts have been proposed for augmenting the toughness of ceramic matrix materials (see Chawla 2003, for a summary). Table 7.2 lists some of these concepts and gives the basic requirements for the models to be valid. Clearly, more than one toughness mechanism may be in operation at a given time. Matrix microcracking, fiber/matrix debonding leading to crack deflection and fiber pullout, and phase transformation toughening are all basically energy-dissipating processes that can result in an increase in toughness or work of fracture. Figure 7.16 shows schematically some of these toughness mechanisms or energy-dissipating mechanisms that can be brought to play in CMCs.

Table 7.2 Ceramic matrix composite toughening mechanisms

Mechanism	Requirement
1. Compressive prestressing of the matrix	$\alpha_f > \alpha_m$ will result in an axial compressive prestressing of the matrix after fabrication
2. Crack impeding	Fracture toughness of the second phase (fibers or particles) is greater than that of the matrix locally. Crack is either arrested or bows out (line tension effect)
3. Fiber (or whisker) pullout	Fibers or whiskers having high transverse fracture toughness will cause failure along fiber/matrix interface leading to fiber pullout on further straining
4. Crack deflection	Weak fiber/matrix interfaces deflect the propagating crack away from the principal direction
5. Phase transformation toughening	The crack tip stress field in the matrix can cause the second-phase particles (fibers) at the crack tip to undergo a phase transformation causing expansion ($\Delta V > 0$). The volume expansion can squeeze the crack shut

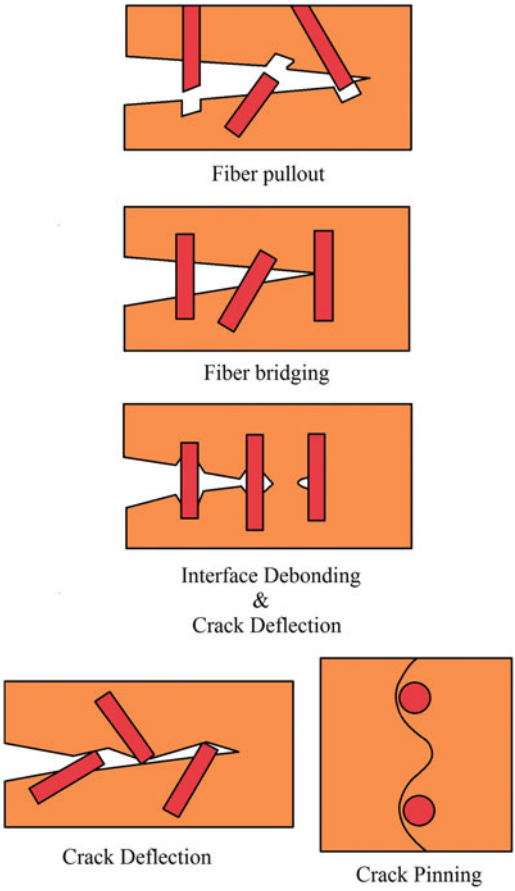

Fig. 7.16 Schematic of some toughness or energy-dissipating mechanisms that can be brought to play in CMCs

Work on carbon and SiC fiber reinforced glass and glass–ceramic composites (Brennan and Prewo 1982; Prewo et al. 1986; Fitzer and Hegen 1979; Prewo 1982) has shown that tough and strong CMCs could be made if extensive fiber pullout and a controlled fracture behavior of the CMC (i.e., a damage-tolerant fracture behavior) could be brought to play. Let us examine a Nicalon fiber/glass–ceramic composite. A scanning electron micrograph of a hot-pressed Ba–Si–Al–O–N glass–ceramic containing Nicalon fiber composite is shown in Fig. 7.17 (Herron and Risbud 1986). Note the crystalline nature of the matrix. The fracture surface of this composite (Fig. 7.18) showed the phenomenon of fiber pullout, indicating a weak fiber/matrix bond. The fibers were bonded to the matrix by an amorphous layer whose characteristics changed with heat treatment; a carbon-rich layer was also observed on the fiber surface (Herron and Risbud 1986). Remnants of the interfacial amorphous layer

adhering to the Nicalon fibers can be seen in Fig. 7.18. One can accentuate the propensity for fiber pullout by applying a suitable coating on the fiber, which would control the interfacial characteristics. This was observed in the composite system Nicalon/pyrolytic carbon coating/SiC, as shown in Fig. 7.19 wherein we see Nicalon fibers pulled out of the matrix (Chawla et al. 1994). Among oxide ceramic matrix materials, alumina and mullite are quite important. In particular, SiC whisker reinforced alumina composites (20–30% by volume of SiC whiskers in alumina, made by hot pressing) showed impressive gains in toughness and strength (Becher and Wei 1984; Wei and Becher 1984; Tiegs and Becher 1986); see Figs. 7.20 and 7.21. A typical fine-grained monolithic alumina has toughness (K_{Ic}) of 4–5 $MPam^{1/2}$ and flexural strength between 350 and 450 MPa. Al_2O_3 containing 20% by volume of SiC whiskers showed a K_{Ic} of 8–8.5 $MPam^{1/2}$ and a flexural strength of 650 MPa; these levels were maintained up to about 1000 $°C$.

It is worth reemphasizing that the main goal in CMCs is to increase the toughness; modulus and strength are already high in most ceramics. If the crack growth in a ceramic can be impeded by some means, then a higher stress would be required to make it move. Fibers (metallic or ceramic) can play the role of toughening agents in ceramic matrices. Metallic fiber reinforced ceramics will clearly be restricted to lower temperatures than ceramic fiber reinforced ceramic matrices. As described above, glass and glass–ceramic matrices containing carbon fibers (Phillips et al. 1972; Davidge 1979; Prewo and Brennan 1980; Prewo 1982; Brennan and Prewo 1982; Prewo et al. 1986) have been shown to have fiber pullout as the dominant toughening mechanism. Basically, fiber pullout requires that the strength transferred to the fiber during the ceramic matrix fracture be less than the fiber ultimate strength, σ_{fu}, and that an interfacial shear stress be developed that is greater than the fiber/matrix interfacial strength, τ_i; that is the interface must fail in shear. For a given fiber of radius r, we have the axial tensile stress in the fiber given by (we derive this expression in Chap. 10)

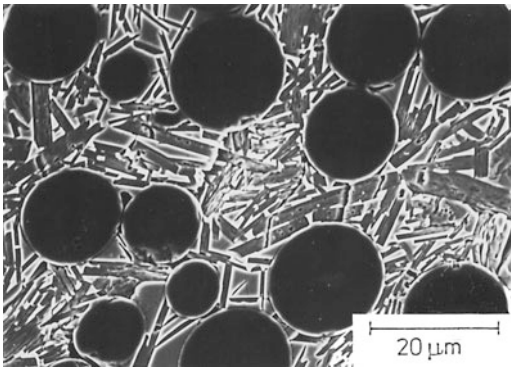

Fig. 7.17 Scanning electron micrograph of a hot-pressed Nicalon fiber/Ba–Si–Al–O–N glass–ceramic matrix composite. [From Herron and Risbud (1986), used with permission]

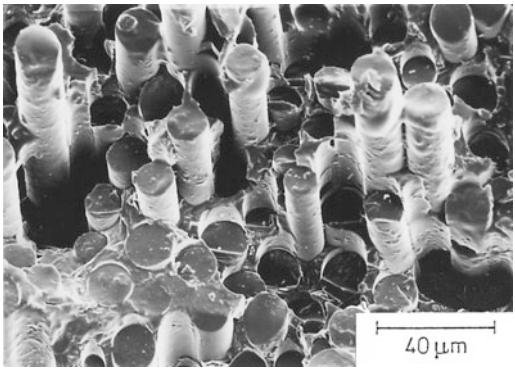

Fig. 7.18 Fracture surface of Nicalon/Ba–Si–AI–O–N glass–ceramic matrix composite showing fiber pullout. [Herron and Risbud (1986), used with permission]

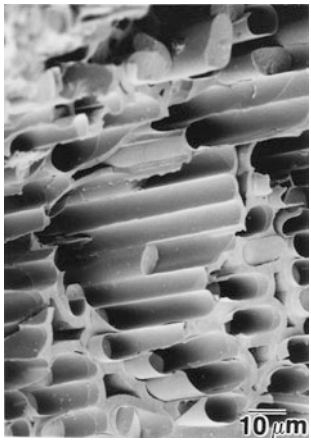

Fig. 7.19 Fiber pullout in a Nicalon/pyrolytic carbon coating/SiC matrix composite. Some broken fibers can be seen inside the cylindrical cavities left by the pulled out fibers [Courtesy of N. Chawla.]

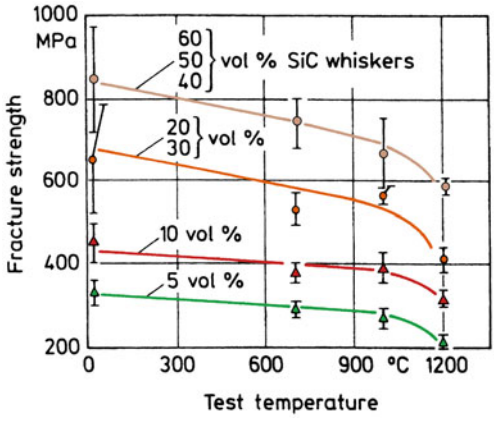

Fig. 7.20 High temperature strength increases as a function of the SiC whiskers volume fraction in SiC_w/Al_2O_3. [From Tiegs and Becher (1986), used with permission]

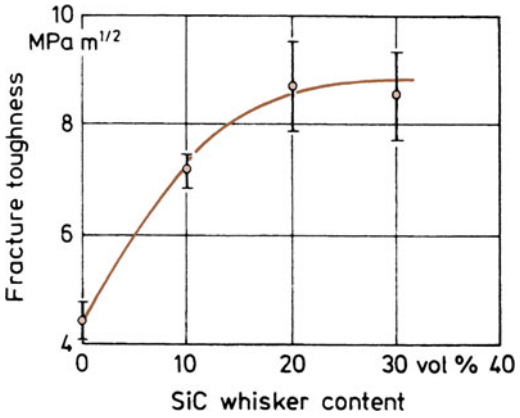

Fig. 7.21 Toughness gains are obtained by incorporating SiC whiskers in alumina. Tiegs and Becher (1986), used with permission

$$\sigma_f = 2\tau_i\left(\frac{l_c}{r}\right),$$

where l_c is the critical fiber length and $\sigma_f < \sigma_{fu}$. The tensile stress increases from a minimum at both fiber ends and attains a maximum along the central portion of the fiber (see Fig. 10.13). Fibers that bridge the fracture plane and whose ends terminate within $l_c/2$ from the fracture plane will undergo pullout, while those with ends further away will fracture when $\sigma_f = \sigma_{fu}$. A crack deflection mechanism also requires that as a matrix crack reaches the interface, it gets deflected along the interface rather than passing straight through the fiber. Consider a fiber reinforced ceramic that has mechanical bonding at the interface, i.e., frictional gripping of the fiber by the matrix. When we load this composite, a crack initiates in the matrix and starts propagating in the matrix normal to the interface. If the fiber/matrix interface is weak, then interfacial shear and lateral contraction of fiber and matrix will result in fiber/matrix debonding and crack deflection away from its principal direction (normal to the interface). A further increment of crack extension in the principal direction will occur after some delay. On continuing stressing of the composite, the fiber/matrix interface delamination continues and fiber failure will occur at some weak point along its length. This is followed by broken fiber ends being pulled out against the frictional resistance of the interface and finally causing a total separation. We discuss this process in terms of crack deflection criteria further in next section.

Let us summarize the requirements for strong and tough CMCs. Avoiding processing-related flaws in the matrix and in the fiber would appear to be an elementary and straightforward recommendation. If processing results in large flaws in the matrix, the composite fracture strain will be low. In this respect, fiber bridging of cracks in a CMC will result in a reduced flaw size in the matrix. This, in turn, will help achieve higher applied strains before crack propagation in the matrix than in an unreinforced, monolithic ceramic (Aveston et al. 1971). A weak interfacial bond, as pointed out earlier, leads to crack deflection at the fiber/matrix

interface and/or fiber pullout. Use of a high volume fraction of continuous fibers stiffer than the matrix will give increased stiffness, which results in a higher stress level being needed to produce matrix microcracking and a higher composite ultimate tensile stress, as well as a high creep resistance (DiCarlo 1985). A high volume fraction and a small fiber diameter also provide a sufficient number of fibers for crack bridging and postponing crack propagation to higher strain levels. A small-diameter fiber also translates into a small l_c, the critical length for effective load transfer from matrix to fiber (see Chap. 10). Although a weak interface is desirable from a toughness point of view, it provides a short circuit for environmental attack. An ability to maintain a high strength level and high inertness at high temperatures and in aggressive atmospheres is highly desirable.

An interesting technique to obtain enhanced toughness in CMCs involves coatings that undergo phase transformation involving volume change. Kriven and colleagues (Kriven1995; Zhu and Kriven 1996; Kriven and Lee 1998) have exploited interfacial coatings with compositions that have multiple polymorphs wherein transformations can be triggered by shear stress. Under the action of shear stress at the tip of an oncoming crack, a transformation is induced in the coating, causing a volume or shape change at the fiber/matrix interface. Energy from the crack is then dissipated by the following means:

(i) dissipation of crack energy through nucleation,
(ii) possible autocatalytic nucleation of transformation along the interface promoting interfacial debonding and fiber pullout,
(iii) increased surface energy contribution from interfacial microcracking or shearing from the transformation, and
(iv) increased frictional work that the crack must do to achieve interfacial debonding, i.e., optimal results will require control of coating thickness.

7.4.1 Crack Deflection at the Interface in a CMC

The phenomenon of crack deflection at the fiber/matrix has been analyzed by many researchers. Cook and Gordon (1964) analyzed the phenomenon of crack deflection or the formation of secondary cracks at a weak interface in terms of the state of stress at the crack tip. Let us consider a crack advancing in the matrix in a direction perpendicular to the fiber/matrix interface. Cook and Gordon estimated the strength of the interface necessary to cause a diversion of the crack from its original direction when both fiber and matrix have the same elastic constant. At the tip of any crack, a triaxial state of stress (plane strain) or a biaxial stress (plane stress) is present. Figure 7.22 shows schematically the stress distribution at a crack tip. The main applied stress component, σ_y, has a very high value at the crack tip and decreases sharply with distance from the crack tip. The stress component acting normal to the interface, σ_x, is zero at the crack tip; it rises to a maximum value at a small distance from the crack tip and then falls off in a manner similar to σ_y. It is

easy to visualize that if the tensile strength of the fiber/matrix interface is less than the maximum value of σ_x, then the interface will fail in front of the crack tip. According to the estimates of Cook and Gordon, an interfacial strength of 1/5 or less than that of the main stress component, σ_y, will cause the opening of the interface in front of the crack tip.

More sophisticated analyses of crack interaction with an interface, based on the fracture energy considerations, have been proposed (He and Hutchinson 1989; Evans and Marshall 1989; Ruhle and Evans 1988; Gupta 1991; Gupta et al. 1993). He and Hutchinson's results give the conditions for fiber/matrix debonding in terms of the fracture of the interface and that of the fiber; see Fig. 7.23. We obtain a plot of G_i/G_f vs. α, where G_i is the mixed-mode interfacial fracture energy of the interface, G_f is the mode I fracture energy of the fiber, and α is a measure of elastic anisotropy. The parameter α is defined as

$$\alpha = \frac{\overline{E_1} - \overline{E_2}}{\overline{E_1} + \overline{E_2}},$$

where

$$\bar{E} = \frac{E}{1 - \nu^2},$$

where E is the Young's modulus and ν is the Poisson's ratio and the subscripts 1 and 2 refer to the matrix and fiber, respectively. The plot in Fig. 7.23 shows the conditions under which the crack will deflect along the interface or propagate through the interface into the fiber. For all values of G_i/G_f below the shaded line, interface debonding is predicted. In area above the shaded line, the crack will penetrate through the interface into the fiber. Consider the special case of zero elastic mismatch, i.e., for $\alpha = 0$. In this case, the fiber/matrix interface will debond for G_i/G_f less than about 0.25. Conversely, for G_i/G_f greater than 0.25, the crack will propagate across the interface into fiber. In general, for the elastic mismatch, α greater than zero, the minimum interfacial toughness, G_i, required for interface

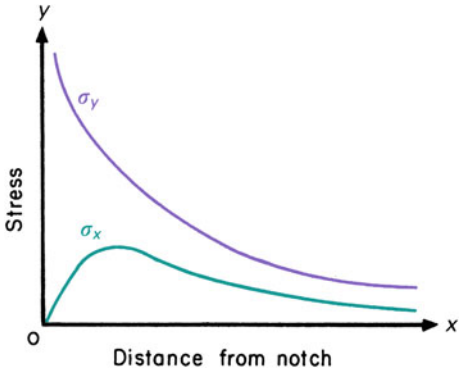

Fig. 7.22 Stress distribution at a crack tip. The stress is applied along the y-axis and the crack is propagating along the x-axis. [After Cook and Gordon (1964)]

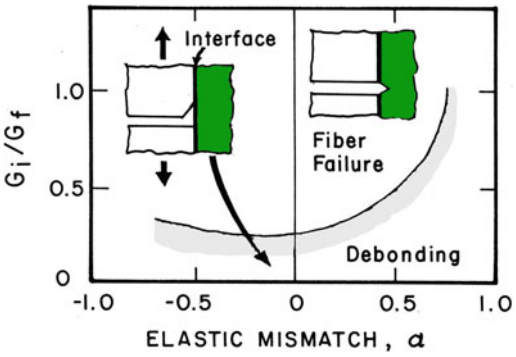

Fig. 7.23 Fiber/matrix debonding criterion in terms of the energy requirements. G_i is the mixed-mode interfacial fracture energy of the interface, G_f is the mode I fracture energy of the fiber, and α is a measure of elastic anisotropy, $\bar{E} = \frac{E}{1-\nu^2}$. After He and Hutchinson (1989)

debonding increases, i.e., high modulus fiber tends to favor debonding. One shortcoming of this analysis is that it treats both the fiber and matrix as isotropic materials. This is not always true, especially for the fiber. Also, in practice, it is difficult to obtain the values of quantities such as the interfacial fracture energy. Gupta et al. (1993) have derived strength and energy criteria for crack deflection at a fiber/matrix interface for several composite systems, taking due account of the anisotropic nature of the fiber. Their experimental technique, laser spallation experiment using a laser Doppler displacement interferometer, was described in Chap. 4. By this technique, they could measure the tensile strength of a planar interface. They have tabulated the required values of the interface strength and fracture toughness for delamination in a number of ceramic, metal, intermetallic, and polymer matrix composites.

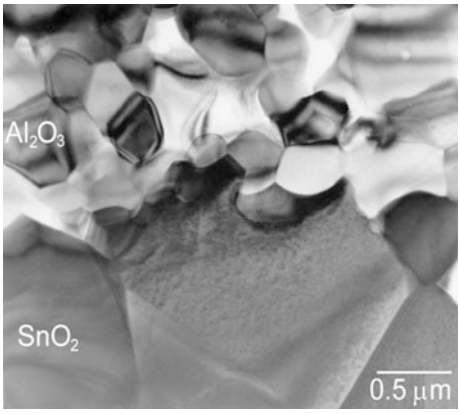

Fig. 7.24 Roughness-induced mechanical keying at the interface between alumina and SnO_2. Note the tortuous nature of the interface. TEM [Gladysz et al. (1999)]

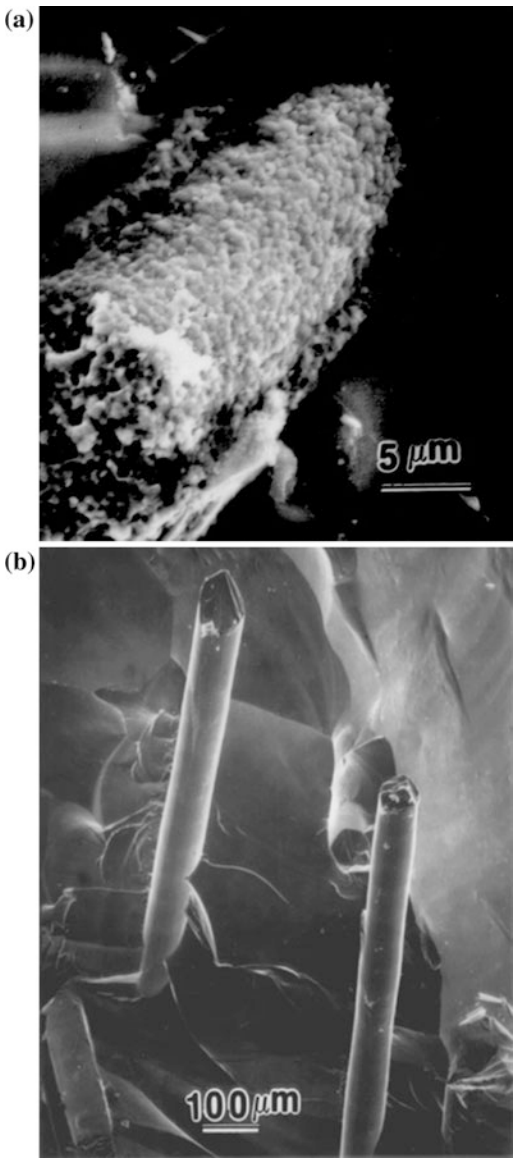

Fig. 7.25 **a** Fracture surface of alumina fiber/SnO_2 coating/glass matrix composite showing partial fiber pullout. Note the rough surface of the alumina fiber due to its small grain size. **b** Fracture surface single crystal alumina fiber/SnO_2/glass composite showing fiber pullout. This fiber is single crystal alumina, which has no grain boundaries and is, therefore, very smooth. Crack deflection at the interface leads to fiber pullout

We end this section by describing a simple and practical way of analyzing the crack deflection problem at the interface in a CMC. This involves evaluation of the state of stress at the interface. In Sect. 7.2, we discussed the state of stress at the fiber/matrix interface taking into account the thermal stresses induced by processing and interfacial roughness-induced stresses. Taking into account the overall stress state at the interface, one can modify the roughness-induced radial stress by choosing a fiber with a smooth surface or by applying a smooth coating on the fiber

(Chawla et al. 2000). A rough interface results in strong mechanical keying, which can prevent interfacial debonding and fiber pullout. A smooth interface, on the other hand, leads to weak keying, which is desirable for crack deflection and fiber pullout. For example, one can use coatings that bond weakly with alumina (e.g., SnO_2, $LaPO_4$), fugitive coatings, layered oxides (mica type) with easy cleavage planes, etc. It is important that there should not be any chemical reaction between the coating and fiber or matrix. Also, thermal mismatch between fiber and matrix should result, in the as-fabricated state, a residual tensile stress at the interface in the radial direction. Figure 7.24 brings home the idea of roughness-induced mechanical keying at the interface. It shows a TEM micrograph of the interface region between alumina fiber and SnO_2 coating. Note the tortuous nature of the interface. Such a high degree of roughness will result in a partial fiber pullout, even when the thermal stress state is favorable. Figure 7.25a shows this for an alumina fiber/glass matrix composite. Note the rough surface of the alumina fiber due to its small grain size. The situation changes dramatically, if we choose an alumina fiber with a smooth surface. This is shown in Fig. 7.25b where the fiber is single crystal alumina, which has no grain boundaries and is, therefore, very smooth. Crack deflection at the interface leads to fiber pullout, etc., which contribute to toughness (see also Chap. 10). For a detailed analysis of this important topic of interface engineering for toughness, the reader is referred to a review by Chawla et al. (2000).

7.5 Thermal Shock Resistance

Thermal shock resistance is a very important characteristic of ceramics and ceramic composites that are meant to be used at high temperatures and are likely to undergo thermal cycling. We define a thermal shock resistance (TSR) parameter as

$$Thermal\ Shock\ Resistance = \frac{\sigma k}{E\alpha},$$

where σ is the fracture strength, k is the thermal conductivity, E is the Young's modulus, and α is the coefficient of thermal expansion. Most ceramics have low thermal conductivity which is one problem. But high a coefficient of thermal expansion, α, will aggravate the situation further. Thus, common sodalime glass and alumina have a high α, about $9 \times 10^{-6}\ K^{-1}$. This makes them very poor in TSR. If we reduce CaO and Na_2O in the common glass, and add B_2O_3 to form a borosilicate, we get a special glass that has an $\alpha = 3 \times 10^{-6}\ K^{-1}$. Such a glass will show superior TSR and is commercially available under the trade names, Pyrex or Duran glass. Glass–ceramics such as lithium aluminosilicates (LAS) have an α close to zero and thus excellent TSR. LAS are used to make the CorningWare which can be taken directly from the freezer to the cooking range or oven without causing it to shatter!

Boccaccini et al. (1997) studied the cyclic thermal shock behavior of Nicalon fiber reinforced Duran glass matrix composites. The thermal mismatch between the fiber and the matrix in this system is almost zero. A decrease in Young's modulus and a simultaneous increase in internal friction as a function of thermal cycles were observed. The magnitude of internal friction was more sensitive to microstructural damage than Young's modulus. An interesting finding of theirs involved the phenomenon of crack healing when the glass matrix composite was cycled above the glass transition temperature of the matrix. We discuss this topic further in Chap. 13.

7.6 Applications of CMCs

Ceramic matrix composites find applications in many areas. A convenient classification of the applications of CMCs is aerospace and nonaerospace. Material related drivers for applications of CMCs in the aerospace field are as follows:

- High specific stiffness and strength leading to a weight reduction, and, consequently, decreased fuel consumption.
- Reduction in fabrication and maintenance cost.
- Higher operating temperatures leading to a greater thermal efficiency.
- Longer service life.
- Signature reduction, which is valuable in stealth technology (reduce the distance at which a vehicle can be detected).

CMCs can lead to improvements in aerospace vehicles including aircraft, helicopters, missiles, and reentry vehicles. Projected skin temperatures in future hypersonic aircraft are higher than 1600 °*C*. Other parts, such as radomes, nose tips, leading edges, and control surfaces, will experience only slightly lower temperatures. Currently, one uses sacrificial, nonload-bearing thermal protection materials on load-bearing components.

A picture of the GEs LEAP engine that uses open- and box-type shrouds made of SiC fiber/SiC matrix is shown in Fig. 7.26a, while the shrouds are shown in Fig. 7.26b. These are components that are used in hot section of the turbine engines (LEAP and GE9X) in commercial, civilian aircraft. In Fig. 7.26a, they will be located toward the right in the high pressure part of the turbine indicated by the arrow. We should mention that the blades in the front of this engine are made of carbon fiber/epoxy composites (see Chap. 5). LEAP engine is the first commercial jet engine to use CMC shrouds in the high pressure part of the turbine. The GE9X engine expands CMC use to the inner and outer combustor liners, HPT stage 1 and stage 2 nozzles and stage 1 shrouds. With one-third the density of nickel-based superalloys, these lightweight CMC components reduce an engine's overall weight resulting in improved fuel efficiency. CMC's high temperature properties greatly enhance engine performance, durability, and fuel economy. The superior heat resistance of CMCs allows for less cooling air requirement in the engine's hot

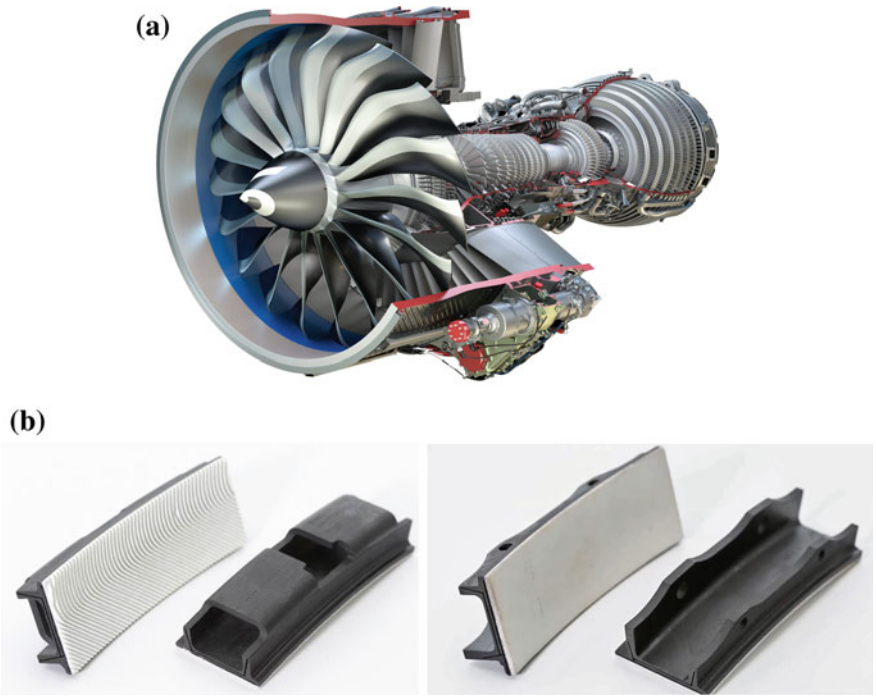

Fig. 7.26 **a** A cutout of LEAP engine, the first commercial jet engine to use CMC (silicon carbide fiber/silicon carbide matrix) shrouds in the high pressure part of the turbine, on the right hand side in this picture indicated by the arrow. **b** The CMC (SiC/SiC) shrouds used in high pressure turbine part of the engine [Courtesy of General Electric Co.]

section. It is worth pointing out here that the great success of introduction of CMC pars in engines is predicated on years of basic research work funded by the US Department of Energy at the national laboratories as well as basic research work done in France, Japan, and UK.

Next, we give a description of some nonaerospace applications of CMCs.

7.6.1 Cutting Tool Inserts

An important area of CMC applications is that of cutting tool inserts. Silicon carbide whisker reinforced alumina (SiC_w/Al_2O_3) composites are used as cutting tool inserts for high-speed cutting of superalloys. For example, in the cutting of Inconel 718, SiC_w/Al_2O_3 composite tools show performance that is three times better than conventional ceramic tools, and eight times better than cemented carbides. Among the characteristics that make CMCs good candidates for cutting tool inserts are

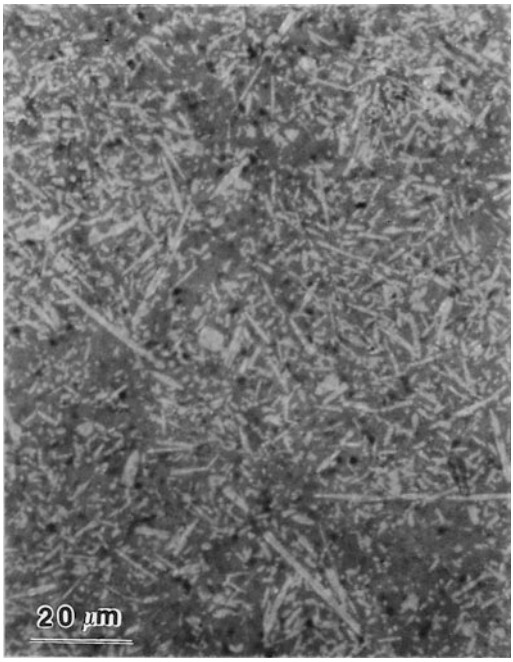

Fig. 7.27 Microstructure of SiC whisker reinforced alumina composite tool insert made by hot pressing

- Abrasion resistance,
- Thermal shock resistance,
- Strength,
- Fracture toughness, and
- Thermal conductivity.

Commonly, the volume fraction of SiC_w is 30–45%, and they are made by hot pressing. Figure 7.27 shows the microstructure of such a composite.

7.6.2 Ceramic Composite Filters

Candle type filters consisting of Nextel™ 312 ceramic fibers in a silicon carbide matrix (see Fig. 7.28) can be used to remove particulate matter from high temperature gas streams up to 1000 °*C*. The collected particles are removed by reverse pulse jet cleaning. The high temperature capability of such filters can eliminate the

Fig. 7.28 A candle type filter consisting of Nextel™ 312 ceramic fibers in a silicon carbide matrix. The filter is 1.3 *m* long. Such filters are used to remove particulate matter from high temperature gas streams up to 1000 °*C* [Courtesy of 3M Co.]

need to cool the gas stream prior to filtration, which may increase process efficiency and eliminate the cost and complexity of gas dilution, air scrubbers, or heat exchangers. The ceramic fibers toughen the composite construction and result in a filter with excellent resistance to thermal shock and catastrophic failure. The lightweight (900 *g*) of such a filter reduces the strength requirements of the tube sheet, and the excellent thermal shock resistance provides protection during temperature changes. The 3M ceramic composite filter is designed for advanced coal-fired power-generation systems, such as pressurized fluidized bed combustion (PFBC), and integrated gasification combined cycle (IGCC). Among its features are

- High temperature capability,
- Resistance to thermal shock,
- Lightweight, and
- Resistance to catastrophic failure.

Potential applications of such filters include

- Pressurized fluidized bed combustion (PFBC),
- Integrated gasification combined cycle (IGCC), and
- Incineration.

Supports made of Nicalon fiber reinforced glass matrix composites are used as pad inserts and takeout paddles in direct hot glass-contact equipment (Beier and Markmann 1997).

7.6.3 Other Applications of CMCs

Potentially, CMCs can find applications in heat engines, components requiring resistance to aggressive environments, special electronic/electrical applications, energy conversion, and military systems (Schioler and Stiglich 1986).

An interesting application is a radiant burner tube made of CMCs. Heat transfer between two objects can occur by conduction when the two objects are in contact, by convection such as by mixing of hot and cold fluids, or by radiation which involves transmission of electromagnetic waves through space (even vacuum). In a radiant burner tube, heat is transferred from combustion gases to the radiant tube and then by radiation that energy is transferred to the load (the material to be heated). Radiant tube burners are useful in situations where combustion products must not come in contact with the material to be heated, i.e., they are an indirect heating burner meaning the heat is transferred without any direct flame or combustion exhaust. Radiant tube burner systems are designed to reduce nitrous oxide in the burner process. This radiant heat transfer from the tube to the object to be heated is proportional to the fourth power of the temperature. Thus a ceramic radiant burner tube that can be operated at a higher temperature than say a metallic alloy tube will be more efficient. The problem is that monolithic ceramics lack adequate toughness and thermal shock resistance to be of much use. Hence, the effort to use the radiant tubes made of continuous fiber reinforced ceramic composites that show superior toughness and thermal shock resistance.

Among the barriers that need to be overcome for large-scale applications of CMCs are the high production costs, accepted design philosophy, and the lack of models for strength and toughness. Complicated shapes are difficult to make economically by hot pressing. Sintering or sintering followed by hot isostatic pressing (HIP) are the alternate routes for non-glassy matrices.

Problems

7.1. What are the sources of fiber degradation during the processing of ceramic matrix composites?
7.2. Describe the advantages of using sol–gel and polymer pyrolysis techniques to process the ceramic matrix in CMCs.
7.3. Explain how a carbon fiber reinforced glass–ceramic composite can be obtained with an almost zero in-plane coefficient of thermal expansion.
7.4. Chemically, what is an alkoxide? Describe some of the alkoxides that can be used to obtain different ceramic matrices in CMC.
7.5. Distinguish between interphase and interface.
7.6. Why is thermal shock resistance more of a problem in CMCs than in MMCs? Explain.

References

J. Aveston, G.A. Cooper, A. Kelly, *The Properties of Fibre Composites* (IPC Science & Technology Press, Guildfort, UK, 1971), p. 15
S.J. Barclay, J.R. Fox, H.K. Bowen, J. Mater. Sci. **22**, 4403 (1987)
P.F. Becher, G.C. Wei, Comm. Am. Ceram. Soc. **67**, 259 (1984)
W. Beier, S. Markmann, Adv. Mater. Process. **152**, 37 (1997)
R.T. Bhatt, *NASA TN-88814* (1986)
R.T. Bhatt, J. Mater. Sci. **25**, 3401 (1990)
A.R. Boccaccini, C.B. Ponton, K.K. Chawla, Mater. Sci. Eng. **A241**, 142 (1997)
R.K. Bordia, R. Raj, J. Am. Ceram. Soc. **71**, 302 (1988)
J.J. Brennan, K.M. Prewo, J. Mater. Sci. **17**, 2371 (1982)
C.V. Burkland, W.E. Bustamante, R. Klacka, J.M. Yang, *Whisker- and Fiber-Toughened Ceramics* (ASM International, Mater Park, OH, 1988), p. 225
W.C. Carter, E.P. Butler, E.R. Fuller Jr., Scripta Metall et Mater. **25**, 579–584 (1991)
K.K. Chawla, *Ceramic Matrix Compos*, 2nd edn. (Kluwer Academic Publisher, Boston, 2003)
K.K. Chawla, M.K. Ferber, Z.R. Xu, R. Venkatesh, Mater. Sci. Eng. **A162**, 35–44 (1993)
K.K. Chawla, Z.R. Xu, A. Hlinak, Y.W. Chung, Advances in ceramic-matrix composites. Am. Ceram. Soc., 725–736 (1993b)
N. Chawla, P.K. Liaw, E. Lara-Curzio, R.A. Lowden, M.K. Ferber, *High Performance Composites: Commonalty of Phenomena* (The Minerals, Metals & Materials Society, Warrendale, PA, 1994), p. 291
A.H. Chokshi, J.R. Porter, J. Am. Ceram. Soc. **68**, c144 (1985)
N. Claussen, T. Le, S. Wu, J. Eur. Ceram. Soc. **5**, 29 (1989)
N. Claussen, S. Wu, D. Holtz, J. Eur. Ceram. Soc. **14**, 209 (1994)
J. Cook, J.E. Gordon, Proc. R Soc., London **A228**, 508 (1964)
J.A. Cornie, Y.-M. Chiang, D.R. Uhlmann, A. Mortensen, J.M. Collins, Am. Ceram. Soc. Bull. **65**, 293 (1986)
R.W. Davidge, *Mechanical Behavior of Ceramics* (Cambridge University Press, Cambridge, 1979), p. 116
L.C. De Jonghe, M.N. Rahaman, C.H. Hseuh, Acta. Metall. **39**, 1467 (1986)
J.A. DiCarlo, J. Metall. **37**, 44 (1985)
A.G. Evans, Mater. Sci. Eng. **71**, 3 (1985)
A.G. Evans, D.B. Marshall, Acta. Metall. **37**, 2567 (1989)
E. Fitzer, R. Gadow, Am. Ceram. Soc. Bull. **65**, 326 (1986)
E. Fitzer, D. Hegen, Angew. Chem. **91**, 316 (1979)
E. Fitzer, J. Schlichting, Z. Werkstofftech. **11**, 330 (1980)
J.E. French, *Handbook of continuous fiber ceramic composites* (Ceramic. Soc., Westerville, OH, Amer, 1996), p. 269
G. Gardiner, Composite World, July 2018
P. Greil, J. Am. Ceram. Soc. **78**, 835 (1995)
V. Gupta, MRS Bull. **XVI**(4), 39 (1991)
V. Gupta, J. Yuan, D. Martinez, J. Am. Ceram. Soc. **76**, 305 (1993)
M.Y. He, J.W. Hutchinson, J. Appl. Mech. **56**, 270 (1989)
M. Herron, S.H. Risbud, Am. Ceram. Soc. Bull. **65**, 342 (1986)
W.B. Hillig, J. Am. Ceram. Soc. **71**, C-96 (1988)
J. Homeny, W.L. Vaughn, M.K. Ferber, Am. Ceram. Soc. Bull. **67**, 333 (1987)
J.W. Hutchinson, H.M. Jensen, Mech. Mater. **9**, 139–163 (1990)
F.I. Hurwitz, NASA Tech. Memo. 105754 (1992)
F.I. Hurwitz, J.Z. Gyekenyesi, P.J. Conroy, Ceram. Eng. Sci. Proc. **10**, 750 (1989)
T.J. Illston, C.B. Ponton, P.M. Marquis, E.G. Butler, Third Euroceramics, in *Faenza Editrice Iberica*, ed. by P. Duran, J.F. Fernandez, vol. 1 (Madrid, 1993), p. 419
P.D. Jero, Am. Ceram. Soc. Bull. **69**, 484 (1990)

P.D. Jero, R.J. Kerans, Scripta. Metall. **24**, 2315–2318 (1990)
P.D. Jero, R.J. Kerans, T.A. Parthasarathy, J. Am. Ceram. Soc. **74**, 2793–2801 (1991)
C. Kaya, F. Kaya, E.G. Butler, A.R. Boccaccini, K.K. Chawla, J. Euro. Ceram. Soc. **29**, 1631 (2009)
B. Kellett, F.F. Lange, J. Am. Ceram. Soc. **67**, 369 (1989)
R.J. Kerans, T.A. Parthasarathy, J. Am. Ceram. Soc. **74**, 1585–1596 (1991)
W.M. Kriven, J. Phys. (France) **5**, C8–C101 (1995)
W.M. Kriven, S.J. Lee, Ceram. Eng. Sci. Proc. **19**, 305 (1998)
A. Kristofferson, A. Warren, J. Brandt, R. Lundberg, in *Proceedings of International Conference on HTCMC-1*, ed. by R. Naslain et al. (Woodhead Publication, Cambridge, UK, 1993), p. 151
H.Y. Liu, N. Claussen, M.J. Hoffmann, G. Petzow, J. Eur. Ceram. Soc. **7**, 41 (1991)
T.J. Mackin, P.D. Warren, A.G. Evans, Acta. Metall. Mater. **40**, 1251–1257 (1992)
D.R. Mumm, K.T. Faber, Ceram. Eng. Sci. Proc. **7–8**, 70–77 (1992)
S. Nourbakhsh, F.L. Liang, H. Margolin, Metall. Trans. A. **21A**, 213 (1990)
S. Nourbakhsh, H. Margolin, Metall. Trans. A. **20A**, 2159 (1990)
D.C. Phillips, *Fabrication of Composites* (North-Holland, Amsterdam, 1983), p. 373
D.C. Phillips, R.A.J. Sambell, D.H. Bowen, J. Mater. Sci. **7**, 1454 (1972)
K.M. Prewo, J. Mater. Sci. **17**, 3549 (1982)
K.M. Prewo, *Tailoring Multiphase and Composite Ceramics*, vol. 20 (Materials Science Research, Plenum Press, New York, 1986), p. 529
K.M. Prewo, J.J. Brennan, J. Mater. Sci. **15**, 463 (1980)
K.M. Prewo, J.J. Brennan, G.K. Layden, Am. Ceram. Soc. Bull. **65**, 305 (1986)
M.N. Rahaman, L.C. De Jonghe, J. Am. Ceram. Soc. **70**, C-348 (1987)
R. Raj, R.K. Bordia, Acta. Metall. **32**, 1003 (1989)
S. Raj, Ceram. Int. **45**, 3608 (2019)
M. Ruhle, A.G. Evans, Mater. Sci. Eng. **A107**, 187 (1988)
M.D. Sacks, H.W. Lee, O.E. Rojas, J. Am. Ceram. Soc. **70**, C-348 (1987)
R.A.J. Sambell, D.H. Bowen, D.C. Phillips, J. Mater. Sci. **7**, 773 (1972)
R.A.J. Sambell, D.C. Phillips, D.H. Bowen, *Carbon Fibres: Their Place in Modern Technology* (The Plastics Institute, London, 1974), p. 16/9
L.J. Schioler, J.J. Stiglich, Am. Ceram. Soc. Bull. **65**, 289 (1986)
H. Schneider, S. Komarneni, *Mullite* (Wiley, VCH, 2005), p. 509
P.D. Shalek, J.J. Petrovic, G.F. Hurley, F.D. Gac, Am. Ceram. Soc. Bull. **65**, 351 (1986)
B.F. Sorensen, Scripta. Metall. et Mater. **28**, 435–439 (1993)
D.P. Stinton, A.J. Caputo, R.A. Lowden, Am. Ceram. Soc. Bull. **65**, 347 (1986)
T.N. Tiegs, P.F. Becher, *Tailoring Multiphase and Composite Ceramics* (Plenum Press, New York, 1986), p. 639
A.W. Urquhart, Mater. Sci. Eng. A **144**, 75 (1991)
R. Venkatesh, K.K. Chawla, J. Mater. Sci. **11**, 650–652 (1992)
G.C. Wei, P.F. Becher, Am. Ceram. Soc. Bull. **64**, 298 (1984)
S. Wu, N. Claussen, J. Am. Ceram. Soc. **77**, 2898 (1994)
M. Yang, R. Stevens, J. Mater. Sci. **25**, 4658 (1990)
D. Zhu, W.M. Kriven, Ceram. Eng. Sci. Proc. **17**, 383 (1996)

Suggested Reading

D.C. Phillips, Fiber reinforced ceramics, in *Fabricution of Ceramics of Handbook of Composites*, vol. 4, (North-Holland, Amsterdam, 1983), p. 373
K.K. Chawla, Ceramic Matrix Compos, 2nd edn. (Kluwer Academic Publisher, Boston, 2003)

Chapter 8
Carbon Fiber/Carbon Matrix Composites

We devote this chapter to a very special kind of composite that consists of carbon fibers embedded in a carbonaceous matrix. The carbon fiber in these composites can be continuous or short. We described the processing of carbon fibers in Chap. 2. Carbon is a very versatile material. It can exist in a variety of forms: amorphous, graphite, diamond, fullerenes, graphene, nanotubes, etc. Below we summarize the salient features of some important forms of carbon.

Diamond: Carbon in the diamond form has an FCC structure; it is also called diamond cubic. Each C atom is covalently bonded to four carbon atoms at the vertices of a tetrahedron, and the interatomic distance is 0.154 *nm*. Carbon in the diamond form has isotropic properties. It is one of the hardest materials.

Graphite: Graphitic form of carbon has a hexagonal structure. Carbon atoms are arranged in layers. The bonding between atoms in the plane of the layer is covalent but the bonding between layers is weak, van der Waals type. This difference in the bonding in *a* and *c* directions makes graphite highly anisotropic. Young's modulus in the basal plane (*a* direction) is ~ 1000 *GPa,* while in a direction perpendicular to the basal plane (*c* direction) it is ~ 35 *GPa*. Tensile strength, thermal expansion, and thermal conduction are also anisotropic in a similar manner.

Pyrolytic Graphite: Pyrolytic graphite is produced from a gaseous phase via pyrolysis of hydrocarbons. The pyrolysis of hydrocarbons results in carbon, which is deposited on a hot substance. Pyrolytic graphite has a highly oriented structure and therefore is highly anisotropic.

Carbon Black: This is a generic term for carbon powder of extremely fine size (*nm* range) and very high surface area. It is essentially elemental carbon (>97%), electrically conductive, and finds extensive use as a reinforcement in tires and other rubber products as well as in printing inks and paints.

Carbon nanotubes: These are hollow, cylindrical tubes of carbon atoms with diameter in the range of 5–20 *nm*. They are frequently referred to as CNTs. CNTs can have very large aspect ratios. They show some very unusual properties, such as extremely high stiffness and strength.

K. K. Chawla, *Composite Materials*,
https://doi.org/10.1007/978-3-030-28983-6_8

Carbon is an excellent high temperature material when used in an inert or nonoxidizing atmosphere. Potential high temperature applications call for 10 h to a few 1000 h at greater than 1000 °C and at times approaching 2200 °C. The major drawback of carbon is that it reacts with oxygen, forming gaseous oxides of carbon. Unlike other nonoxide ceramics, carbon powder cannot be sintered. Thus, the carbon matrix in a carbon fiber/carbon matrix composite is generally obtained by chemical vapor deposition (CVD) of carbon or thermal decomposition of a source of carbon such as pitch or phenolic resin. Generally, many pores form during this conversion of a hydrocarbon to carbon. Thus, a dense and strong pore-free carbon/carbon composite is not easy to fabricate. A very wide range of characteristics, however, can be obtained in these composites, the principal characteristic being the high temperature capability of these composites in *inert* environments. Being very light, carbon/carbon composites show superior specific strength at high temperatures in *inert* atmospheres.

Although carbon/carbon composites were originally developed for the space program, they have now become high performance engineering materials, with special high-temperature applications. More specifically, these high temperature applications involve brakes for aircraft and automobiles, dies for use in hot-pressing, high temperature fasteners, heating elements in furnaces, liners and protection tubes, etc. Carbon/carbon composites are expensive mainly because of the long processing times involved. Essentially, we take a carbon fiber reinforced polymer matrix composite and convert the polymer matrix by pyrolysis to carbon or we deposit carbon from gaseous reactants into interstices in a woven carbon fiber preform. The process can take days, making the final product very expensive. In what follows we describe the processing techniques, properties, and major applications of carbon/carbon (C/C) composites.

8.1 Processing of Carbon/Carbon Composites

The following three methods are commonly used to fabricate carbon/carbon composites:

(i) A woven preform of carbon fiber is impregnated, under heat and pressure, with thermoplastic pitch, followed by pyrolysis of pitch into carbon. Generally, the cycle is repeated to obtain the desired density. A special version of this technique is called high pressure impregnation carbonization or HIPIC (see below). Pitches are mixtures of hydrocarbons of different molecular weights. Yield of carbon from the pitch precursor increases with increasing average molecular weight of the pitch but high molecular weight means high viscosity which makes penetration of the fibrous preform difficult.

(ii) A carbon fiber/polymer matrix composite is made by one of the conventional PMC fabrication techniques (see Chap. 5), followed by conversion of the

resin, generally a thermoset, to carbon by pyrolysis. Again, reimpregnation and repyrolysis are used to attain the desired density of the composite. Phenolics are one of the common resins used because of the comparatively high carbon yield.

(iii) Chemical vapor deposition (CVD) of carbon is made from a gaseous phase onto and in between the carbon fibers in a preform. Hydrocarbon gases become unstable with respect to carbon at high temperatures (>550 °*C*).

Methane, a common precursor for CVD, decomposes as per the following reaction:

$$CH_4(g) \rightarrow C(s) + 2H_2(g).$$

Low pressure (or addition of inert diluent gases such as H_2, N_2, or Ar to the gaseous stream) is used to improve diffusion because it increases the mean free path of the gaseous molecules.

Figure 8.1 shows the process corresponding to the first two, while Fig. 8.2 shows the CVD process. In both processes, multiple impregnation cycles are required to increase the density of the composites, i.e., reduce the amount of porosity in the composite to an acceptable level. Invariably, in all the processes, there occurs a large weight loss (between 10 and 60%) during the pyrolysis step, which results in a large amount of shrinkage porosity. In addition, there is the complexity of the anisotropic nature of the carbon fiber (properties are different in the axial and radial directions). The carbon matrix, obtained by pyrolysis, is

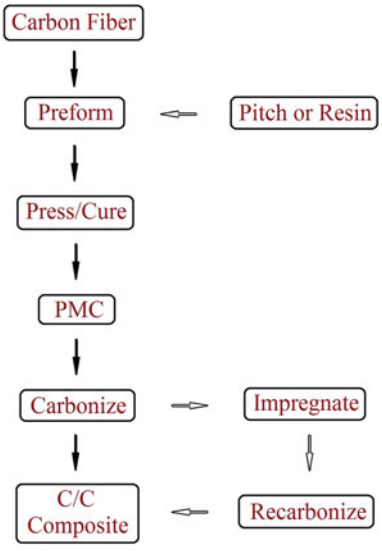

Fig. 8.1 Processing of carbon/carbon composites by pyrolysis of carbon fiber/polymer composites

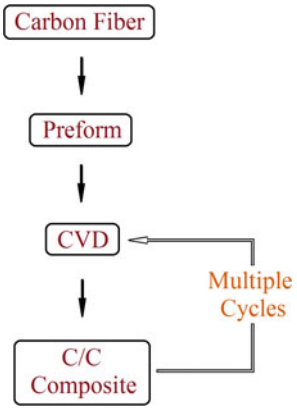

Fig. 8.2 Processing of carbon/carbon composites by chemical vapor deposition (CVD) process

essentially isotropic. This leads to the generation of thermal stresses in each cycle, because of thermal mismatch between the fiber and the matrix, which leads to the formation of microcracks in the C/C composites after multiple cycles of impregnation and pyrolysis.

8.1.1 High Pressure Processing

Application of isostatic pressure in an autoclave during carbonization of pitch can increase the yield of carbon from 50% at atmospheric pressure to over 90% at 100 *MPa*. This high pressure processing is also called high pressure impregnation carbonization or HIPIC. Commonly, partially impregnated preform and excess pitch are placed in a sealed metal can, which in turn is placed in the pressure vessel. The temperature is increased to 550–650 $^{\circ}C$ and pressure in the range of 5–100 *MPa* is applied. The thin metal can acts like a rubber bag in the processing of PMCs in an autoclave. The process can take as much as 24 *h*. After HIPIC, the metal container is stripped off and the impregnated composite is generally subjected to a graphitization treatment at temperatures above 2300 $^{\circ}C$.

Properties of C/C composites depend a great deal on the volume fraction of porosity present. Essentially, the pores present are of open-cell type. An easy parameter to follow the evolution of porosity in C/C composites is the density of the composite. One generally starts with a carbon fiber preform of density of 1 gcm^{-3}. After about four cycles of impregnation, we attain a density of 1.4 gcm^{-3}. However, under conditions of HIPIC, it is possible to reach a density of 1.8 gcm^{-3} after four or five cycles, see Fig. 8.3. It is worth pointing out here that the theoretical density of carbon is 2.25 gcm^{-3}. Carbon fiber itself can have density between 1.6 and 2.2 gcm^{-3}. A value of 2.2 gcm^{-3} for carbon fiber is very uncommon; only mesophase pitch-based carbon fiber can show such a value after high temperature

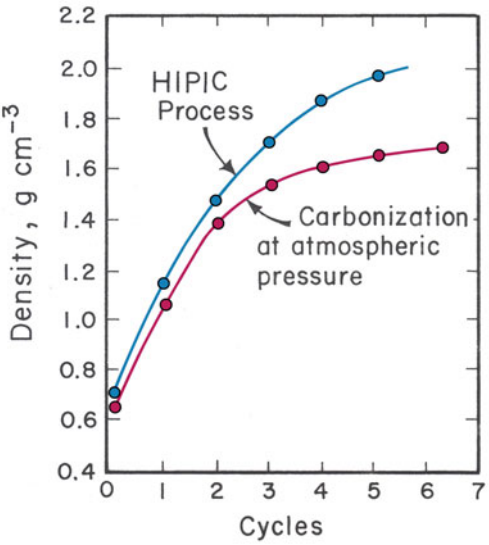

Fig. 8.3 Change in density of carbon/carbon composites as function of number of impregnation cycles. Under conditions of high pressure impregnation (HIPIC), higher density is achieved than under atmospheric impregnation [After Taverna and McAllsiter (1971)]

graphitization treatment. For the fabrication of C/C composites, up to a density 1.4 gcm^{-3}, atmospheric processing and HIPIC have about the same efficiency. For density values greater than 1.4 gcm^{-3}, HIPIC shows much better efficiency than processing at atmospheric pressure.

8.2 Oxidation Protection of Carbon/Carbon Composites

By far, the greatest drawback of carbon/carbon composites is the formation of gaseous oxides of carbon upon reaction with oxygen in air at temperatures as low as 450 °*C*. Potential applications of carbon/carbon composites may call for use in service at temperatures exceeding 1000 °*C* and even approaching 2200 °*C* for times ranging from 10 *h* to a few thousand hours. There are two main approaches to protect carbon/carbon composites against oxidation (Buckley 1988; Luthra 1988; McKee 1986, 1987; Strife and Sheehan 1988):

(i) Use inhibitors to slow down the rate of reaction between carbon and oxygen. This involves modification of matrix through the addition of some oxidation inhibitors (e.g., B, Si, Zr, or their compounds).
(ii) Use diffusion barriers to prevent oxygen from reaching carbon and reacting with it. This involves the deposition of ceramic coatings on the surface. These coatings are generally multilayer coatings of functionally graded materials of carbides, nitrides, and oxides of Si, Zr, Ta, Al, etc.

The diffusion barrier coating should have the following characteristics:

- Oxidation resistance,
- Low oxygen permeability and volatility,
- Good adhesion to carbon,
- Chemical compatibility with carbon, and
- Thermal expansion match with carbon.

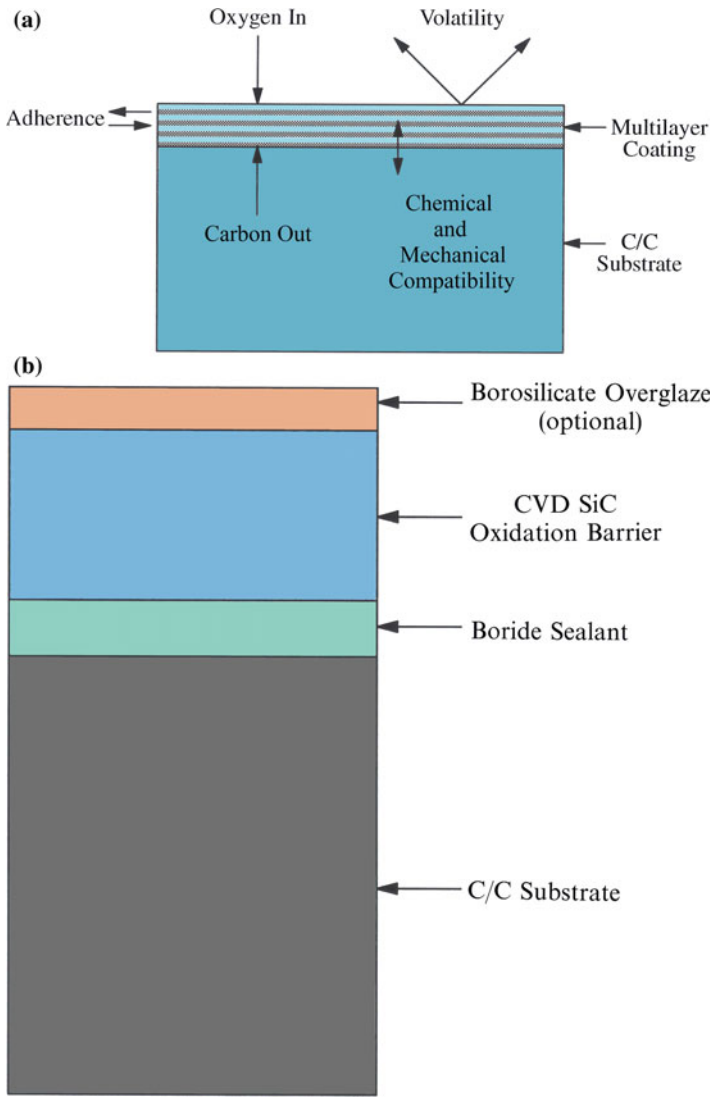

Fig. 8.4 **a** Critical factors that should be taken into account for an oxidation protection system for carbon/carbon composites [after Strife and Sheehan (1988)]. **b** Schematic of a typical multilayer oxidation protection system on a C/C substrate

Figure 8.4a shows the critical factors that should be considered in an oxidation protection system for carbon/carbon composites (Strife and Sheehan 1988), while Fig. 8.4b shows, schematically, a typical multilayer oxidation protection system on a C/C substrate.

The two approaches involving the use of inhibitors and diffusion barriers are frequently combined: use diffusion barriers and internal glass-forming inhibitors and sealants. Silicon-based ceramics, such as SiC and Si_3N_4, are commonly used as the primary oxygen barrier coatings. Sealants have the added advantage that they also seal thermal stress cracks originating because of the thermal mismatch between C/C composite and silicon carbide coating. Tetraethylorthosilicate (TEOS) is commonly used to impregnate such cracks (McKee 1986, 1987). TEOS leaves oxidation-resistant silica in the cracks. Addition of boria B_2O_3 can inhibit the oxidation (Ehrburger et al. 1986; McKee 1986).

Extended oxidation protection of carbon/carbon composites can be obtained by using boria containing dense Si_3N_4 or SiC coatings and boron-rich inner coating. Borate glasses act as sealants and fill up the cracks that form in the outer coatings because of thermal expansion mismatch. An oxidation protection system used for extended protection under thermal cycling conditions, with peak temperatures reaching 1400 °*C*, is shown in Fig. 8.5 (Strife and Sheehan 1988). Moisture sensitivity of borate glasses, corrosion of outer coatings by glasses, glass volatilization, and unacceptably high oxygen permeability are some of the negative factors. Alvey and George (1991) used multilayer Zr/Pt coating that formed $ZrPt_3$ on annealing on carbon/carbon composites. Their results showed that this coating protected carbon and a carbon fiber/phenolic resin composite from a 2800 °*C* flame. They attributed this performance to the oxidation resistance of $ZrPt_3$ and to the reflectivity of the coating, which reduced the thermal flux on the substrate to a short time.

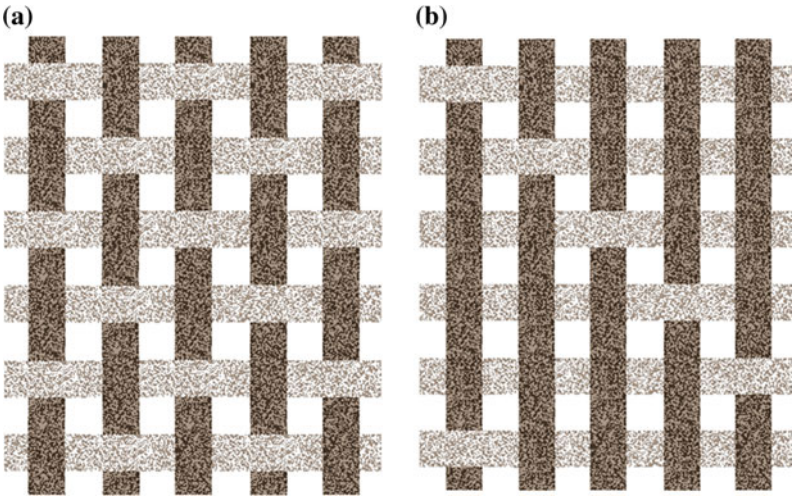

Fig. 8.5 Two-dimensional fabric: **a** plain weave; **b** five-harness satin

8.3 Properties of Carbon/Carbon Composites

Properties of carbon/carbon composites depend on the type of carbon fiber used (high modulus or high-strength type), fiber volume fraction, fiber distribution, and the amount of porosity. One-, two-, and three-dimensionally woven carbon fibers may be used. Carbon fiber can be woven in a variety of weaves for reinforcement in two or more dimensions. Two main types of weave are plain and satin. A *plain weave* has one warp yarn running over and under one fill yarn and is the simplest weave. *Satin-type weaves* are more flexible; that is, they can conform to complicated shapes easily. Figure 8.5 shows a two-dimensional (2-D) plain weave and a five-harness satin weave (McAllister and Lachman 1983). Modifications of the basic 3-D orthogonal weave involving fiber directions, as many as 5, 7, or 11, are possible, which give a highly isotropic final composite (McAllister and Lachman 1983). A five-harness satin weave, shown in Fig. 8.5b, has one warp yarn running over four fill yarns and under one fill yarn.

The precursor, processing, and high temperature involved all influence the carbonaceous matrix significantly. Table 8.1 summarizes the room temperature properties of some carbon/carbon composites. The values refer to a high modulus carbon fiber, a final heat treatment at 1000 °*C*, four to six densification cycles, and a fiber volume fraction as indicated in the table. The properties of a woven carbon fabric depend on the weave pattern and the amount of fibers in the *x*-, *y*-, and *z*-directions. Figure 8.6 shows schematically the stress–strain curves, at room temperature, of 1-D, 2-D, and 3-D carbon/carbon composites (Fritz et al. 1979). The fracture mode changes from semibrittle (1-D) to non-brittle (3-D). The latter is due to the existence of the continuous crack pattern in the composites. Because carbon/carbon composites are meant for high-temperature applications, their thermal expansion behavior is of great importance. As expected, fibers control the thermal expansion behavior parallel to the fibers, while perpendicular to the fiber axis the carbonaceous matrix controls the expansion behavior. The amount of porosity in the matrix will also influence the thermal expansion behavior.

Table 8.1 Mechanical properties of carbon/carbon composites at room temperature

Weave	Flexural strength (*MPa*)	Young's modulus (*GPa*)	Interlaminar shear strength (*MPa*)
1-D, 55% V_f	1200–1400	150–200	20–40
2-D, 8H/S weave, 35% V_f	300	60	20–40
3-D, felt, 35% V_f	170	15–20	20–30

Source Adapted with permission from Fritz et al. (1979)

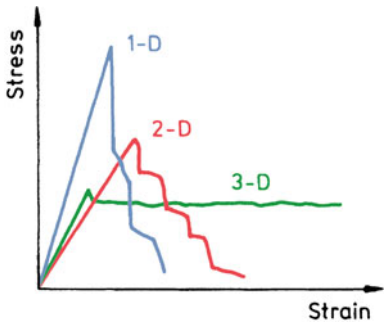

Fig. 8.6 Stress–strain curves (schematic), at room temperature, of 1-D, 2-D, and 3-D carbon/carbon composites [From Fritz et al. (1979), used with permission]

8.3.1 Thermal Properties

Carbon/carbon composites can have high thermal conductivity, especially if mesophase pitch-based carbon fibers are used. Recall that pitch-based carbon fibers have highly oriented carbon fibers with a highly oriented graphitic structure. These composites show highly anisotropic properties, high thermal conductivity along the fiber, and low conductivity in transverse direction. This means that one must have proper fiber configuration to obtain the desired thermal conductivity.

8.3.2 Frictional Properties

Carbon/carbon composites have good tribological properties against most surfaces, in addition to adequate strength, good toughness, and high thermal conductivity. These characteristics make it possible to use them in applications such as bearing seals, electrical brushes, and brakes for aircraft and automobiles.

8.3.3 Ablative Properties

Space vehicles, on reentry into the atmosphere, are subjected to intense aerothermal loads (external surface pressure, skin friction, and aerodynamic heating). Intense heating occurs which lead to extremely high temperatures. We use thermal protection systems (TPS) made of suitable materials in order to keep space vehicle, occupants, and equipment safe. Ablative TPS is commonly used because it is quite effective in expending thermal energy. In an ablative TPS, we sacrifice the material and thus absorb the thermal energy. There is a variety of ablative materials available. The one of interest to us here is the high temperature ablative material of which C/C composites are a prime example. They are used in manned space vehicles, hypersonic vehicles, and missiles.

Please see Problem 8.6 at the end of this chapter about the Columbia shuttle disaster which involved C/C composites.

8.4 Applications of Carbon/Carbon Composites

Major applications of carbon/carbon composites involve uses at high temperatures, for example, as heat shields for reentry vehicles, aircraft brakes, hot-pressing dies, and high-temperature parts such as nozzles. Figure 8.7 shows a fully processed three-dimensional carbon/carbon frustum. Hot-pressing dies made of carbon/carbon composites are commercially available, while brake disks are used in aircraft. It should be mentioned that the first use of carbon/carbon brakes in civilian aircraft occurred in the now-defunct Concorde supersonic aircraft. Brakes for racing cars and some high-end luxury cars are the latest entry. Heat shields and nozzles are made of multidirectionally reinforced carbon/carbon composites. As pointed out, carbon/carbon composites can withstand high temperatures in an inert atmosphere. Lack of oxidation resistance is a major problem, and a great deal of effort has been put into the development of oxidation-resistant coating for carbon fibers, with SiC coating being the primary coating material.

Other applications of carbon/carbon composites include their use as implants and internal repair of bone fractures because of their excellent biocompatibility. They

Fig. 8.7 A three-dimensional carbon/carbon frustum [Courtesy of Fiber Materials Inc.]

are also used to make molds for hot pressing. Carbon/carbon molds can withstand higher pressures and offer a longer use life than polycrystalline graphite.

8.4.1 Carbon/Carbon Composite Brakes

Brakes of any kind use friction between contact surfaces to stop a moving component. In the process, the kinetic energy of the moving object is converted into heat, which needs to be absorbed by the brake materials. Most commonly, the essential components of a braking system are a rotating part (such as a wheel, axle, disk, or brake drum) and a stationary part that is pressed against the rotating part to slow or stop the moving object. The transmission of kinetic energy from the moving vehicle to the brake pads results in heat, which leads to high temperatures in the friction pad material and brake components. Efficient brake systems must be able to withstand the thermal shock, dissipate heat quickly (i.e., high thermal conductivity or more appropriately high thermal diffusivity is needed) and maintain consistent braking performance. Any brake design must consider the following items (Awasthi and Wood 1988):

- Friction members must generate stopping torque (over a range of environmental conditions: rain, snow, dust storms, etc.).
- Heat sinks must absorb the kinetic energy of the aircraft.
- Structural elements should be able to transfer torque to the tires.

Brakes are one of the major applications of carbon/carbon composites. An example of a carbon/carbon brake assembly used on a Boeing 767 plane is shown in Fig. 8.8. Brakes, aircraft or automobile, must have the following general requisites (Awasthi and Wood 1988):

(a) Oxidation resistance;
(b) High thermal capacity;
(c) Good strength, impact resistance, strain-to-failure;
(d) Adequate and consistent frictional characteristics;
(e) High thermal conductivity.

When the brakes are applied, multiple-disk brakes with alternating rotors and stators are forced against adjacent members by hydraulic pressure. Friction between rotating and stationary disks causes them to heat up to 1500 °*C* (surface temperature can be as high as 3000 °*C*) over a short time period, i.e., one needs excellent thermal shock resistance. In commercial processing of carbon/carbon brakes, a fabric made of woven carbon fibers with fiber tows inserted in the thickness (or z-direction) direction is used.

In view of the requisites listed above, any braking material must be a good structural material, an efficient heat sink, and must have excellent abrasion resistance. Let us consider an example from the aircraft field, which will help illustrate

Fig. 8.8 A carbon/carbon brake assembly used on a Boeing 767 airplane [Courtesy of Allied-Signal Corp.]

the formidable demands made on a braking material. Many civilian aircraft use carbon/carbon composite brakes. Let us take Boeing 767 airplane as an example. In the event of an aborted takeoff, an extremely large amount of kinetic energy must be dissipated in about 30 *s* by the eight brakes on the aircraft (see the example below for an estimate of the temperature rise in a rejected takeoff (RTO). A rejected takeoff (RTO) is, indeed, the worst-case scenario but then the braking material must be able to meet such requirements. It is estimated that about 3000 RTOs occur every year in the US.

The weight savings that result from the replacement of conventional brakes by carbon/carbon brakes help one understand why the aircraft industry has taken up the C/C brakes (Awasthi and Wood 1988). In a large aircraft, a conventional multiple stator and rotor arrangement (a sintered high friction material sliding against a high-temperature steel) weighs about 1100 *kg*. Carbon/carbon brakes (both the stator and the rotor being made of carbon/carbon composite) weigh about 700 *kg,* resulting in a weight savings of 400 *kg*. Also, as a braking material, carbon/carbon composites are superior to high-strength bulk graphite. Carbon/carbon composites have much higher strength at the same density.

Example One of the functions of the brake system is to absorb the heat energy developed during braking. Consider the Boeing 777 plane. Find out its mass and takeoff speed from the web. Compute the kinetic energy of the plane when it is about to takeoff. Assume that the plane has carbon/carbon brakes. The pilot is asked to abort the takeoff for some reason. Under these conditions, assuming that all of the kinetic energy is converted to thermal energy, compute the temperature rise in this aborted takeoff.

Answer From the website of Boeing, we find that the maximum takeoff weight of a Boeing 777 plane is 247,000 *kg*. The takeoff speed can range from 270 to 345 *km/h*. Let us take a speed of 78.6 *m/s*. Putting these values into the equation for kinetic energy (*K.E.*)

$$K.E. = \frac{1}{2}mv^2,$$

where m is the mass of the plane and v is its velocity. Substituting the values of mass and velocity in the above expression, we get the kinetic energy to be 763 *MJ*.

This is the kinetic energy that is converted into heat and must be absorbed in the carbon/carbon composite brakes during a rejected takeoff. To find the change in temperature, we use the following relationship:

$$Q = \Delta T C_p m,$$

where Q is the kinetic energy converted to heat, ΔT is the change in temperature, m is the mass of the brakes, and C_p is the specific heat of the carbon brakes. The mass of the brakes is 700 *kg*. The specific heat of the carbon brakes is 1.6 $\frac{kJ}{kg\,K}$. Putting all these values in the above expression, we get

$$\Delta T = \frac{Q}{C_p m} = \frac{763 \times 1000}{1.6 \times 700} = 681.25\ ^\circ C,$$

i.e., a change in temperature of close to 700 °*C*.

8.5 Other Applications of Carbon/Carbon Composites

Among other aerospace applications of carbon/carbon composites, one may cite their use in rocket propulsion components and reentry thermal protection of a spacecraft. Figure 8.7 shows the frustum of a cone of a rocket made of a three-dimensional carbon/carbon composite. A three-dimensional composite has fibers in x-, y-, and z-directions. The concept of thermal protection is illustrated in Fig. 8.8 (Meetham 1989). The top layer in contact with the high temperature environment gets eventually sacrificed. Among nonaerospace applications, there are examples of the use of carbon/carbon composites as implants as well as internal fixation of bone fractures because of their excellent biocompatibility. They are also used for making molds for hot pressing. Carbon/carbon molds can withstand higher pressures and offer a longer life than polycrystalline graphite. Figure 8.9 shows an example of a mold made of carbon/carbon composite that replaced a conventional heat-resistant tool steel material. In general, the high cost of carbon/carbon composites limits applications to aerospace and other specialty applications. The

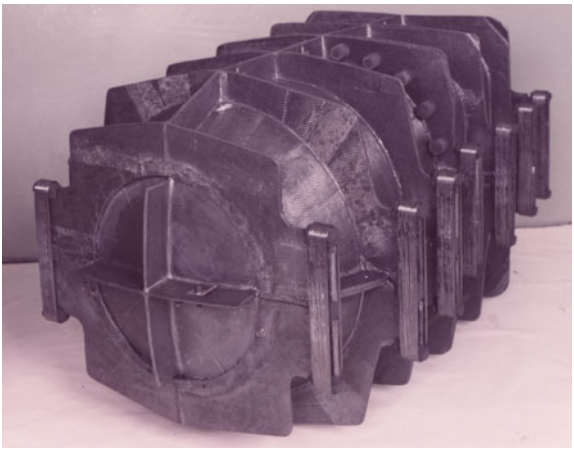

Fig. 8.9 A mold made of carbon/carbon composite [Courtesy of SIGRI]

limitation of low oxidation resistance is a serious one, and most applications do need some sort of protection against oxidation. The Formula 1 racing cars usually use a new set of brake linings for each race. Aircraft brakes, on the other hand, are required to survive 2000–4000 landings. An Airbus A380 has 16 sets of brakes; each brake costs something between US$35,000 and 45,000. However, use of carbon/carbon composite brakes results in weight savings relative to the conventional steel brakes; a saving of 250 *kg* on a plane such as Boeing 737. This allows more payload and/or fuel savings.

8.5.1 Carbon/SiC Brake Disks

This is another type of brake, developed by SGL Co. The matrix consists of silicon carbide (SiC) and elemental silicon (Si). The reinforcement fiber is carbon (C). Silicon carbide provides the hardness required for wear resistance, while the carbon fibers provide the fracture toughness. The strain at fracture of such C/SiC composites ranges from 0.1 to 0.3%, which is reasonably high for ceramics. The low weight, high hardness, resistance to thermal shock, and non-brittle fracture behavior make for an excellent braking material.

Problems

8.1 The terms voids and cracks are frequently used interchangeably but in reality they are not synonyms. Specifically, in regard to C/C composites, distinguish between voids and microcracks in terms of their form and origin.

8.2 TEOS is often used as a glass-forming sealant to heal the microcracks in C/C composites. However, there are some limitations on efficiency. Explain what the limitations are and why.

8.3 Invariably C/C composites will need to be joined to other conventional materials. Describe the different joining approaches that can be used to accomplish this; give the pros and cons of each technique.

8.5 C/C composites are frequently made carbon fibers woven in more than three directions. What effect does this have on crack propagation, fracture surface appearance, and toughness of C/C composite?

8.5 Glass-forming sealants help close the crack-like defects in C/C composites. Are there any deleterious effects of such sealants?

8.6 Describe the NASA's Columbia shuttle disaster in which all seven astronauts lost their lives in 2003. Highlight the role of carbon/carbon composites in this disaster. How and why did the disaster occur? Describe the modifications instituted by NASA to prevent such a disaster in the future.

References

M.D. Alvey, P.M. George, Carbon **29**, 523 (1991)
S. Awasthi, J.L. Wood, Adv. Ceram. Mater. **3**, 449 (1988)
J.D. Buckley, Am. Ceram. Soc. Bull. **67**, 364 (1988)
P. Ehrburger, P. Baranne, J. Lahaye, Carbon **24**, 495 (1986)
W. Fritz, W. Hüttner, G. Hartwig, *Nonmetallic Materials and Composites at Low Temperatures* (Plenum Press, New York, 1979), p. 245
K.L. Luthra, Carbon **26**, 217 (1988)
L.E. McAllister, W.L. Lachman, *Fabrication of Composites* (North-Holland, Amsterdam, 1983), p. 109
D.W. McKee, Carbon **24**, 737 (1986)
D.W. McKee, Carbon **25**, 551 (1987)
G.W. Meetham, Mater. Des. **10**, 197 (1989)
J.R. Strife, J.E. Sheehan, Am. Ceram. Soc. Bull. **67**, 369 (1988)
A.R. Taverna, L.E. McAllister, *Advanced Materials: Composites and Carbon* (American Ceramic Society, Columbus, 1971), p. 199

Suggested Reading

K.K. Chawla, *Ceramic Matrix Composites*, 2nd edn. (Kluwer Academic Publishers, Boston, 2003)
J.-B. Donnet, R.C. Bansal, *Carbon Fibers*, 2nd edn. (Marcel Dekker, New York, 1984)
E. Fitzer, *Carbon Fibres and Their Composites* (Springer, Berlin, 1985)
G. Savage, *Carbon-Carbon Composites* (Chapman & Hall, London, 1992)
C.R. Thomas (ed.), *Essentials of Carbon-Carbon Composites* (Royal Society of Chemistry, Cambridge, 1993)

Chapter 9
Multifilamentary Superconducting Composites

9.1 Introduction

Certain materials lose all resistance to the flow of electricity when cooled to within a few degrees of absolute zero. The phenomenon is called *superconductivity*, and the materials exhibiting this phenomenon are called *superconductors*. Superconductors can carry a high current density without any electrical resistance; thus, they can generate the very high magnetic fields that are desirable in many applications: magnetic resonance imaging, high energy physics, and fusion energy programs. Other fields of application include magnetic levitation vehicles, magnetohydrodynamic generators, rotating machines, and magnets in general. Kammerlingh Onnes discovered the phenomenon of superconductivity in mercury in 1911. Since then, some 27 elements and hundreds of solid solutions or compounds have been discovered that show this phenomenon of total disappearance of electrical resistance below a critical temperature, T_c. Figure 9.1 shows the variation of electrical resistivity with temperature of a normal metal and that of a superconducting material, Nb_3Sn. The critical temperature is a characteristic constant of each material. Kunzler et al. (1961) discovered the high critical field capability of Nb_3Sn and thus opened up the field of practical, high field superconducting magnets. It turns out that most of the superconductors came into the realm of economic viability when techniques were developed to put the superconducting species in the form of ultra-thin filaments in a copper matrix as described below. A similar development route is used for the newer oxide superconductors.

Multifilamentary composite superconductors started becoming available in the 1970s. These are niobium-based (Nb–Ti and Nb_3Sn) superconductors, also referred to as *conventional* superconductors. The erstwhile record of critical temperature at which a conventional material became a superconductor was 23 *K* and was set in 1974. These conventional superconductors require liquid helium as a coolant, which is expensive. In 1986, there began a new era in the field of superconductivity, called high temperature superconductivity (HTS), which started with the now

K. K. Chawla, *Composite Materials*,
https://doi.org/10.1007/978-3-030-28983-6_9

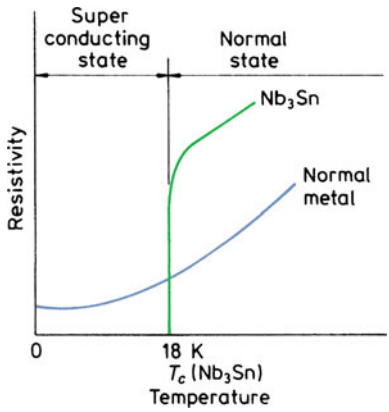

Fig. 9.1 Variation of electrical resistivity with temperature for a normal metal and a superconducting material, Nb_3Sn

well-known work of Bednorz and Muller. They reported of superconductivity at 30 *K* in a ceramic containing lanthanum, copper, oxygen, and barium. This original discovery, for which Bednorz and Muller received a Nobel prize, set off a storm of activity. In 1987, Chu and Wu found a related oxide superconductor with a critical temperature above 77 *K*, the boiling point of liquid nitrogen. This had the chemical composition of $YBa_2Cu_3O_{7-x}$ and is commonly referred to as the *1–2–3 superconductor* because of the Y:Ba:Cu ratio. Since then other ceramic compounds with critical temperatures above 77 *K* have been discovered.

The oxide superconductors have the great advantage of having a T_c around 90 *K*, i.e., above the liquid nitrogen temperature (77 *K*). Thus, potentially, liquid nitrogen, a cheap and easily available cooling medium, could replace liquid helium, which is expensive and limited in supply. There are, however, many problems with these superconductors. These new ceramic superconductors have a layered, perovskite body centered tetragonal structure and, not surprisingly, are very brittle. This problem of brittleness, as was pointed out in 1987 by some researchers including this author, makes it very difficult to make thin filaments of these oxide superconductors for use in, for example, magnet windings. Besides the inherent brittleness of ceramics, these superconductors carry very low current densities. It is true that the electrical resistance goes to zero around 90 *K*, but the troublesome fact is that these materials lose their superconductivity at very modest current densities, of the order of a few hundred $A\ cm^{-2}$. This has been attributed to impurities, misaligned grains, and the like. It turns out that the layered perovskite cuprates are all anisotropic, difficult to prepare in desirable shapes such as long continuous wires, and very poor at carrying current. In particular, the grain boundaries in a polycrystalline sample block the current. This is attributed to the extremely short (a few *nm*) coherence length in these oxides (Larbalestier 1996). Coherence length is a term that is related to the Fermi velocity for the material and the energy gap associated with the condensation to the superconducting state. A transition from the superconducting state to a normal state will have a transition layer of finite thickness which is related to the coherence length. Yet another problem is that the

performance of these oxide superconductors deteriorates drastically as the applied magnetic field increases. At a magnetic field of 1 T, the critical current density, J_c, is about 1–10 $A\ cm^{-2}$. For any reasonable commercial application, one needs a J_c of about $10^5\ A\ cm^{-2}$. The critical current density, J_c, is a function of the processing and, consequently, of the microstructure of the superconductor. This is where some innovative processing can be of great value. Heine et al. (1989) took just such a step when they partially melted Bi–Sr–Ca–Cu–O (BSCCO) in a silver sheath and observed that the resultant superconductor showed high J_c in the grains. There remains a large gap to be bridged between producing a small sample for testing in the laboratory and making a viable commercial product. We need superconductors (Larbalestier 1996) that "… must be electrically continuous, otherwise there can be no applications." They must also be strong and tough, amenable to being economically made into long lengths, and possess high overall J_c values. The term *overall* implies that all of the space required to make the superconductor must be taken into account when critical current density is computed (Larbalestier 1996). It should be pointed out that the Nb–Ti system took 15–20 years between its discovery and commercial availability. The new high temperature oxide superconductors hold great promise, and it would appear that eventually some kind of composite superconductors will be used commercially as are the Nb-based conventional superconductors. Thus, it is quite instructive to review the composite material aspects of niobium-based superconductors, which we do first in this chapter. We describe the processing, structure, and properties of the conventional and high-T_c superconductors. Both are truly multifilamentary metal matrix composites. But first let us describe why we need these superconductors in the form of multifilamentary metal matrix composites.

9.1.1 The Problem of Flux Pinning

For a variety of applications, we need long-length superconductors of uniform properties, for example, large solenoids and coils for rotating machinery and magnets for plasma confinement in a fusion reactor. In conventional superconductors, ultra-thin superconducting filaments are incorporated in a copper matrix to form a filamentary fibrous composite. In the high-T_c superconductors, we have ceramic superconducting material in the form of thin filaments in a metal matrix. Small diameter, continuous, superconducting filaments distributed in a high conductivity (electrical and thermal) matrix constitute nothing but a superconducting metal matrix composite (MMC). The main reason for using superconductors in the form of filamentary composites is that flux jumps can be avoided if the diameter of superconducting filaments is below a certain value (Irie 1994). It is important to realize that stable, superconducting magnets need flexible and continuous wires that can be wound; this became possible only after wires and cables were made of such MMC composites.

Superconducting filaments have a micrometer-size diameter that helps to reduce the risk of flux jump in any given filament. If a superconductor is perturbed, say, by motion or a change in the applied field, it leads to a rearrangement of magnetic flux lines in the superconductor. This phenomenon is called *flux motion* and is an energy-dissipative or heat-producing process. When a current density J flows in a superconductor in the presence of a magnetic field, B, it experiences a Lorentz force per unit volume F_L, given by the cross product of J and B:

$$F_L = J \times B$$

The Lorentz force acts in a direction perpendicular to both J and B. This force can result in motion of flux lines. Whenever the flux lines move (no matter what the source of this motion), they produce resistance. Hence, we need to pin the flux lines in a superconductor, which is done by appropriate microstructural control. The critical current density, J_c, corresponds to the Lorentz force that unpins the flux lines and makes them move. Thus, the pinning force is equal to $J_c \times B$. Any heat generated by flux motion will result in a temperature increase, which in turn will lead to a reduced critical current and more flux motion will result. The net result is that the superconductor is heated above T_c and reverts to the normal state. A practical solution to this problem is to make the superconductor in the form of ultra-thin filaments so that the amount of energy (heat) dissipated by flux motion is too small to cause this runaway behavior; see Fig. 9.2. The high-purity copper or some other metal matrix provides a high-conductivity alternate path for the current. In the case of a *quench*, that is, superconductor reverting to the normal state, the metal matrix carries the current without getting excessively hot. The superconductor is cooled again below its T_c and carries the electric current again. This is the

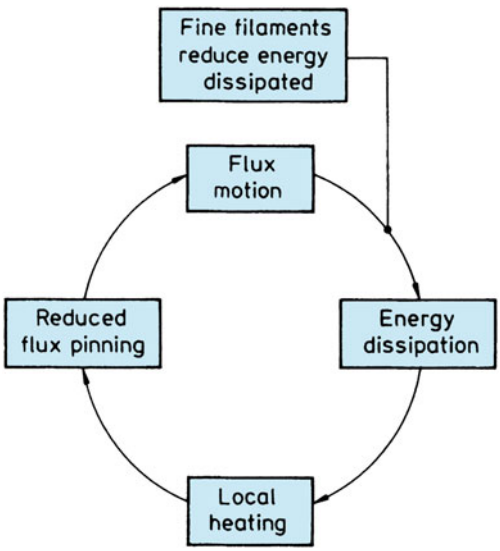

Fig. 9.2 Flux movement in a superconductor is caused by any change in current or field

so-called *cryogenic stability* or *cryostabilization* design concept, namely, the superconductor is embedded in a large volume of low-resistivity metal and a coolant (liquid helium or liquid nitrogen) is in intimate contact with all windings.

9.2 Types of Superconductor

The technologically most important property of a superconductor is its capacity to carry an electric current without normal I^2R losses up to a critical current density, J_c. I^2R losses are known as Joule heating, with I and R representing the electric current and resistance, respectively. The critical current density, J_c, is a function of the applied field and temperature. The commercially available superconductors in the 1980s could demonstrate critical current densities of $J_c > 10^6\ A\ cm^{-2}$ at 4.2 K, the liquid helium temperature, and an applied field of 5 T.

There are three parameters that limit the properties of a superconductor, namely, the critical temperature (T_c), the critical electrical current density (J_c), and the critical magnetic field (H_c); see Fig. 9.3. As long as the material stays below the shaded area indicated in Fig. 9.3, it will behave as a superconductor.

There are two types of superconductor:

Type I: These are characterized by low T_c values, and they lose their superconductivity abruptly at H_c.

Type II: These behave as diamagnetic materials up to a field H_{c1}. Above this field, the magnetic field penetrates gradually into the material, and

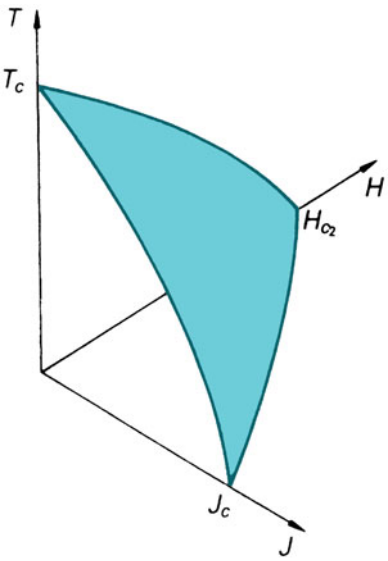

Fig. 9.3 The state of superconductivity in a material is described by three critical parameters: magnetic field (H), temperature (T), and current density (J). The material will remain in a superconducting state as long as it is below the shaded portion

concomitantly the superconductivity is gradually lost, until at the critical magnetic field H_{c2} the material reverts to the normal state.

All major applications of superconductivity involve the use of these type II superconductors. The magnetic field penetrates a type II superconductor in the form of thin filaments called *magnetic vortices*, which are fixed by what are called *pinning centers*. When an electric current is applied, the Lorentz force exerted by current tends to move these vortices. If there is no pinning or if the pinning is weak such that the Lorentz force moves the vortices, then the motion of these vortices generates voltage and the resultant heat will destroy the superconducting state. An interesting demonstration of such a dynamic interaction of vortices with pinning centers was done by Matsuda et al. (1996) by means of a technique called *Lorentz microscopy*. They studied a niobium film sample in which they had made a square lattice of defects by ion irradiation. The sample was placed in a low-temperature specimen stage of a 300 *kV* field emission transmission electron microscope. The objective lens of TEM was replaced by an intermediate lens to make an out-of-focus image (i.e., a Lorentz micrograph) in which vortices appear as dark spots. Thus, one needs microstructural pinning of flux lines in a filamentary superconductor embedded in a metal matrix.

In the following sections, we describe processing, microstructure, and properties of some important superconducting composite systems. Finally, we provide a summary of their applications.

9.3 Processing and Structure of Multifilamentary Superconductors

There are three main categories of multifilamentary superconductors: Nb–Ti-based ductile alloy superconductors, Nb_3Sn-type brittle superconductors, and ceramic oxide brittle superconductors.

9.3.1 Niobium–Titanium Alloys

Niobium–titanium alloys provide a good combination of superconducting and mechanical properties. A range of compositions is available commercially: Nb–44% Ti, Nb–46.5% Ti, and Nb–50% Ti (all atomic percents).

In all these alloys, a $J_c > 10^6\ A\ cm^{-2}$ at 4.2 *K* and an applied field of 7 *T* can be obtained by a suitable combination of mechanical working and annealing treatments. Strong flux pinning and therefore high J_c are obtained in these alloys by means of dislocation of cell walls and precipitates. The flux pinning by precipitates becomes important in high-Ti alloys because the Nb–Ti phase diagram indicates precipitation of α-Ti in these alloys; see Fig. 9.4. As pointed out earlier, the

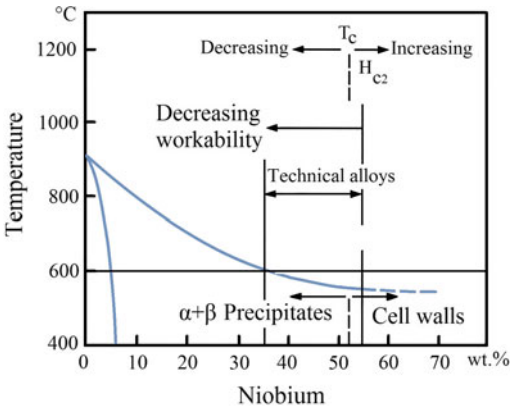

Fig. 9.4 Nb–Ti phase diagram showing the range of compositions used to make Nb–Ti superconductors [After Hillmann 1981]

condition of stability against flux motion requires that the superconductor be manufactured in the form of a composite system: extremely fine superconducting filaments embedded in a copper matrix provide flux stability and reduced losses caused by varying magnetic fields. Fortunately, Nb–Ti and copper are compatible, chemically and otherwise, and amenable to making filamentary composites. Figure 9.5 shows the essential steps in the fabrication of Nb–Ti composite superconductors. Annealed Nb–Ti rods are inserted into hexagonal-shaped high-purity copper tubes. These rods are next loaded into an extrusion billet of copper, evacuated, sealed, and extruded. The extruded rods are cold drawn to an intermediate size and annealed to provide the necessary dislocation cell walls and precipitates for flux pinning. This is followed by more cold drawing passes to the appropriate final size and a final anneal to get back the high conductivity of the copper matrix. Consider the specific case of Nb–50% Ti alloy. Its initial microstructure consists of a β solid solution. The necessary cell structure and dislocation density for flux pinning purposes depend on the purity of the alloy and the size and distribution of the α particles after precipitation heat treatment. The α phase is non-superconducting; its main function is to aid dislocation cell structure formation. Dislocations and α particles are responsible for flux pinning and thus contribute to high J_c values. The amount and distribution of α particles depend on the alloy chemical composition, processing, and annealing temperature and time. For an Nb–50% Ti alloy, a heat treatment of 48 h at 375 °C is generally used and results in about 11% of α particles. A greater amount of α will reduce the ductility of the alloy. Higher annealing temperatures result in excessive softening, fewer dislocations, and lower J_c. The precipitation treatment is generally followed by some cold working to refine the microstructure and obtain a high J_c. The precise amount of strain given in this last step is a function of the superconductor design, that is, the distribution of Nb–Ti filaments and the ratio of Nb–Ti/Cu in the cross section.

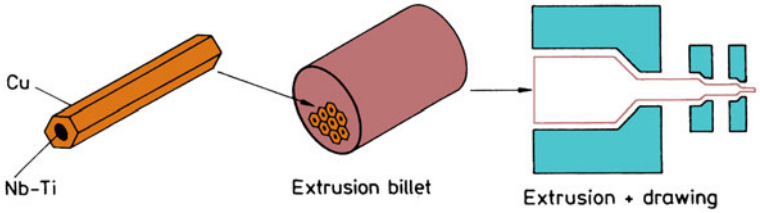

Fig. 9.5 Fabrication route for Nb–Ti/Cu composite superconductors

The interfacial bonding is essentially mechanical. However, undesirable intermetallic compounds can form from any scratches on the surface of NbTi rod (Hillmann 1981). A hardball of oxidized NbTi, about 1 μm in diameter, can form at a scratch on the surface of an NbTi rod. During extrusion, there is a snowball-like effect causing mechanical alloying and formation of an NbTi + Cu mixture. During subsequent annealing treatment, this mixture can turn into $(NbTi)Cu_2$ and/or $(NbTi)_2Cu$ intermetallic compounds. These brittle compounds can eventually easily crack and cause rupture of the superconducting filament.

Figure 9.6a shows a compacted strand cable superconductor made from 15 fine multifilamentary strands (strand diameter = 2.3 mm). Each strand in this figure consists of 1060 filaments of Nb–Ti (diameter = 50 μm) embedded in a copper matrix. A magnified picture of one of the strands is shown in Fig. 9.6b, while a scanning electron microscope picture is shown in Fig. 9.7. The Cu–Ni layers shown in Fig. 9.7 provide the low conductivity barriers to prevent eddy current losses in alternating fields.

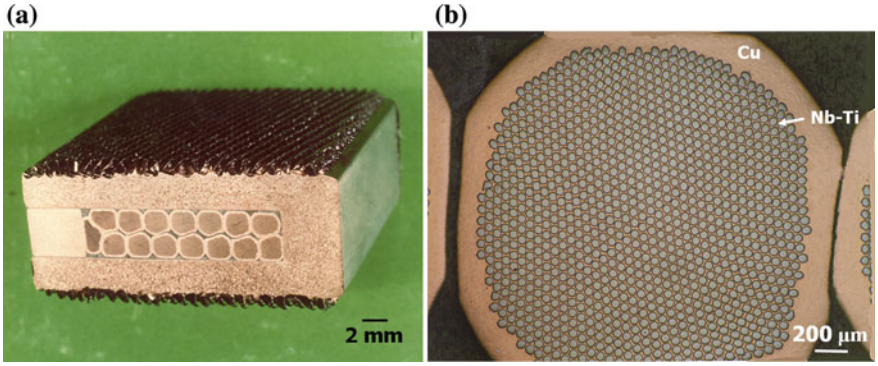

Fig. 9.6 **a** Compacted strand cable superconductor made from 15 multifilamentary strands each of diameter = 2.3 mm. **b** Magnified picture of one of the strands in **a** containing 1060 filaments (diameter = 50 μm). [Courtesy of Hitachi Cable Co.]

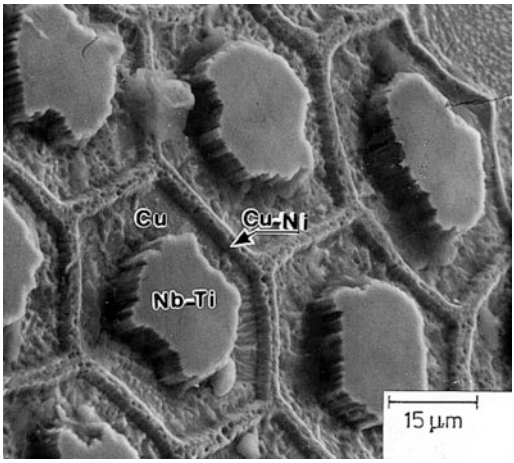

Fig. 9.7 Scanning electron microscope picture of Nb–Ti/Cu superconductor

9.3.2 A15 Superconductors

For applications involving fields greater than 12 *T* and temperatures higher than 4.2 *K*, the ordered intermetallic compounds having an A15 crystal structure (Nb_3Sn, V_3Ga) are better suited than the Nb–Ti type. The A15 compounds have the chemical formula A_3B, where A is a transition element and B can be either a transition or a nontransition element. In particular, Nb_3Sn has a T_c of 18 *K*. The higher the T_c, the lower the refrigeration costs will be, hence, the tremendous interest in high-T_c oxide superconductors. Superconducting magnets form an integral part of any thermonuclear fusion reactor for producing plasma-confining magnetic fields. Nb_3Sn is the most widely used superconductor for high fields and high temperatures. A characteristic feature of these intermetallic compounds having an A15 crystal structure is their extreme brittleness (typically, a strain-to-fracture of 0.2% with no plasticity). Compare this to Nb–Ti, which can be cold worked to a reduction in area over 90%. Initially, the compound Nb_3Sn was made in the form of wires or ribbons either by diffusion of tin into niobium substrate in the form of a ribbon or by chemical vapor deposition. V_3Ga on a vanadium ribbon was also produced in this manner. The main disadvantages of these ribbon-type superconductors were (1) flux instabilities due to one wide dimension in the ribbon geometry, and (2) limited flexibility in the ribbon width direction. Later, with the realization that flux stability could be obtained by the superconductors in the form of extremely fine filaments, the filamentary composite approach to A-15 superconductor fabrication was adopted. This breakthrough involving the composite route came through early in the 1970s. Tachikawa (1970) showed that V_3Ga could

be produced on vanadium filaments via a Cu–Ga matrix, while Kaufmann and Pickett (1970) demonstrated that Nb_3Sn could be obtained on niobium filaments from a bronze (Cu–Sn) matrix.

The process of producing Nb_3Sn is shown schematically in Fig. 9.8. Sometimes, this process is referred to as the *bronze route*; the reason for this name will become clear presently. Niobium rods are inserted into a bronze (Cu–13 wt% Sn) extrusion billet. This billet is sealed and extruded into rods. This is called the *first-stage extrusion*. The rods obtained after the first-stage extrusion are loaded into a copper can that has a tantalum or niobium barrier layer and extruded again, the *second-stage* extrusion. The second-stage extruded composite is cold drawn and formed into a cable, clad with more copper, and compacted to form a monolithic conductor. This is finally given a heat treatment to convert the very fine niobium filaments into Nb_3Sn. A similar process can be used to make a V_3Ga superconductor, but it is not available commercially. Specifically, for the Nb_3Sn superconductors, the ratio of cross-sectional area of bronze matrix to that of niobium, called R ratio (= Cu–Sn/Nb), is an important design parameter that strongly affects the J_c value. It is important that a right amount of tin be available to form the stoichiometric Nb_3Sn phase. Too much of the bronze matrix will reduce the J_c value. Thus, one uses a bronze with about 13 wt% tin, the limit of solubility of tin in copper, which yields enough tin without affecting the formability. Arriving at an optimum value of the ratio R is critical because the resultant Nb_3Sn must be stoichiometric. One ensures this by using a high ratio of R (>3) and sufficiently long diffusion times. An example of an Nb_3Sn monolithic superconductor used in high field magnets is shown in Fig. 9.9. Each little dot in this photograph (Fig. 9.9a) is a 4 μm Nb_3Sn filament. Wide strips in the hexagonal form are niobium; they serve as barriers to tin diffusion from the bronze into the copper. Tantalum is also used as a diffusion barrier. Figure 9.9b shows a scanning electron micrograph of a niobium/bronze

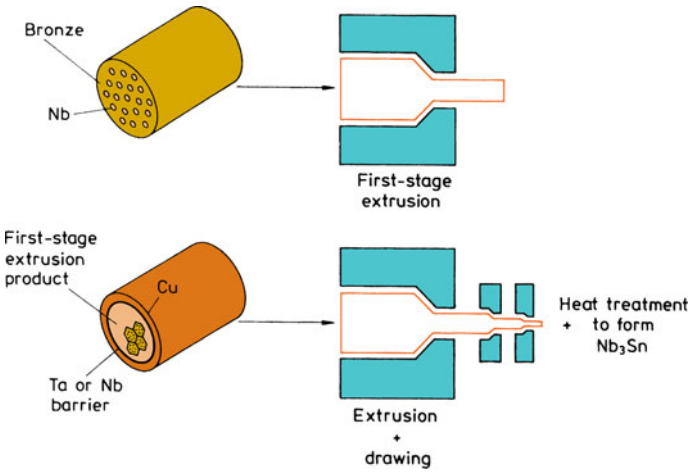

Fig. 9.8 Schematic of the bronze method of fabricating Nb_3Sn/Cu superconductor

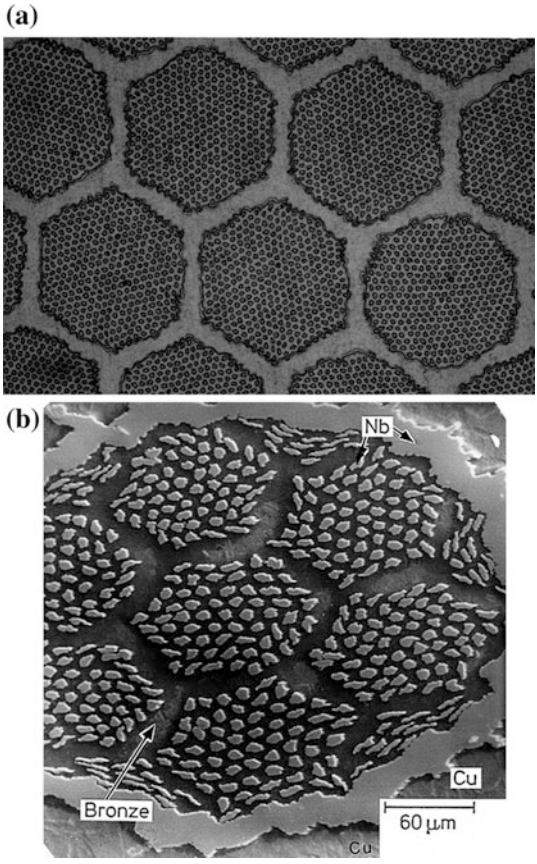

Fig. 9.9 **a** An Nb_3Sn/Cu composite superconductor used in high field magnets. Each little dot in this picture is a 4 μm diameter Nb_3Sn filament. Hexagonal strips are niobium diffusion barriers for tin. [Courtesy of Hitachi Cable Co.] **b** Scanning electron micrograph of a niobium/bronze composite before the heat treatment to form Nb_3Sn

composite before heat treatment to form Nb_3Sn. The good flux pinning and the consequent high critical currents in these superconductors are due to the grain boundaries (Scanlan et al. 1975; Nembach and Tachikawa 1979). At a heat treatment temperature of about 650–700 $°C$, the Nb_3Sn forms and consists of very fine grains, less than 80 nm (0.08 μm) in diameter. The critical current density for Nb_3Sn under these conditions is more than 2×10^5 $A\ cm^{-2}$ at 10 T and 4.2 K.

The problem of thermal mismatch, i.e., the differential expansion or contraction between the components of a composite (Chawla, 1973a, b), something very much inherent to composites, also exists in superconductors. In the case of A15 type composite superconductors, their brittle nature makes this thermal mismatch problem of great importance. It turns out that in this case, when cooled from the reaction temperature (~ 1000 K) to 4.2 K, the different coefficients of thermal

expansion of copper and Nb_3Sn lead to rather large compressive strains in the brittle Nb_3Sn filament. Luhman and Suenaga (1976) showed that the T_c of Nb_3Sn varied with the strain applied to the Nb_3Sn filament by the copper matrix. Later, measurements of critical currents as a function of applied strain confirmed these results, and one could explain the strain–critical current behavior in terms of the effects of strain on T_c and H_{c2}. This understanding of strain–critical current behavior is used to good effect in the design of Nb_3Sn superconducting magnets. As pointed out, Nb_3Sn filaments fail at a tensile strain of about 0.2%. Thus, if the superconductor is designed so that the Nb_3Sn filaments in the bronze matrix experience compression between 0.4 and 0.6%, then one can expect these composites to withstand applied strains of between 0.6 and 0.8% before fracture ensues in the Nb_3Sn filaments.

Although the bronze route of manufacturing the superconductor is a commercial process now, there are some disadvantages involved. One must have frequent interruptions for annealing the work-hardened bronze matrix. To shorten this process of fabrication, a number of in situ and powder metallurgy techniques have been tried (Roberge and Foner 1980). These in situ techniques involve melting of copper-rich Cu–Nb mixtures ($\sim$1800–1850 °C), homogenization, and casting. Niobium is practically insoluble in copper at ambient temperature. Thus, the casting has a microstructure consisting of niobium precipitates in a copper matrix. When this is cold drawn into wire, niobium is converted into fine filaments in the copper matrix. Tin is then plated onto the wire and diffused to form Nb_3Sn. The different melting and cooling techniques used include chill casting, continuous casting, levitation melting, and consumable electrode arc melting. The powder metallurgy techniques involve mixing of copper and niobium powder, pressing, hot or cold extrusion, and drawing to a fine wire that is coated or reacted with tin. The contamination of niobium with oxygen causes embrittlement and prevents its conversion into fine filaments. This has led to the addition of a third element (Al, Zr, Mg, or Ca) to the Cu–Nb mixture. This third element preferentially binds oxygen and leaves the niobium ductile.

A summary of characteristics of Nb/Ti and Nb_3Sn multifilamentary composites is provided in Table 9.1.

9.3.3 Ceramic Superconductors

The ceramic oxide superconductors with a transition temperature higher than the conventional superconductors were discovered in late 1986 and early 1987. Since then many oxide superconductors have been discovered, and they have a range of critical transition temperatures. There are two classes of high temperature superconductors (HTS): First generation (1G) and second generation (2G). Also, there is a rather complex notation that is commonly used in the ceramic oxide superconductor literature. For example, the oxides used in 1G HTS are bismuth-based, the one-layer compound $Bi_2Sr_2Cu_1O_y$ is denoted by (2210), the two-layer compound $Bi_2Sr_2Ca_1Cu_2O_y$ is designated by (BSCCO) or (2212), and the three-layer

Table 9.1 A summary of characteristics of Nb–Ti and Nb_3Sn-type multifilamentary composites (after Hillmann 1981)

Characteristic	Nb–Ti	Nb_3Sn
T_c (K)	≈9	18.1
B_{c2}	≈14.5	24.5
Stabilization	Simple, coextrusion with high purity Cu matrix	Complex, coprocessing with bronze matrix, followed by heat treatment to obtain Nb_3Sn in a Cu matrix
Insulation	Conventional, varnish, cotton, and polymeric tape can be used	Complex, in prereaction insulated conductors, high thermal stability of insulation is needed; in post-reaction insulated conductors, careful mechanical handling is required
Advantages	Fabrication process is cheap; insensitive to mechanical handling, simple magnet technology	Applications to high magnetic fields and high temperatures
Disadvantages	Applications limited to 8 T at 4.2 K	Brittleness of the Nb_3Sn, restricted mechanical handling, large number of very fine filaments (diameter $\leq$ 5 μm) is required, complicated magnet winding

compound $Bi_{2-x}Pb_xSr_2Ca_2Cu_3O_y$ is denoted by (Pb) (2223). 2G HTS are yttrium-based, specifically YBa_2Cu_3O (referred to as YBCO). In fact, YBCO was one of the earlier oxide superconductors; interest in it waned when it was discovered that bismuth-based superconductors could carry more current in the presence of low magnetic fields. Oxide superconductors with a transition temperature around 90 K are available. The reader will recall that such high transition temperatures enable the use of liquid nitrogen (boiling point 77 K), a cheap and easily available coolant. With conventional superconductors, one must use liquid helium as a coolant. There are still many problems with these high-T_c superconductors; one of the major ones is that they carry very low current densities, especially in the presence of magnetic fields. The electrical resistance goes to zero at a T_c of 90 K, but the supercurrents have difficulty going from one grain to another. Various explanations, such as impurities and misaligned grains, have been put forth to explain this behavior. The performance of these new superconductors deteriorates with increasing magnetic field. At a magnetic field of 1 T, the critical current density, J_c, is between 1 and 10 $A\ cm^{-2}$. The conventional superconductors, on the other hand, can carry as much as 10^5 $A\ cm^{-2}$.

Understandably, a large amount of research and development effort has been focused on wire and system development. HTS wire must be flexible and strong and capable of carrying large currents in the presence of a magnetic field. The key parameters in making an HTS wire system commercially successful are critical current density, operating temperature (related to but less than the critical temperature), magnetic field, and last but not least, cost. Critical current is the amount

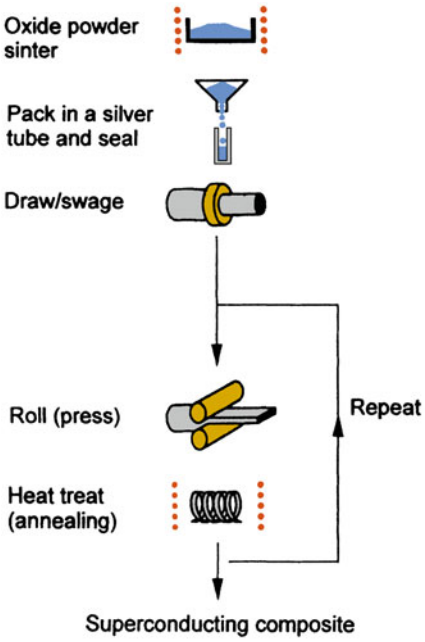

Fig. 9.10 Schematic of the oxide powder in the tube method of making high temperature superconducting composite [After Sandhage et al. 1991]

of current a given wire can carry without losing superconductivity. It would be desirable to have a J_c value between 10^3 and 10^5 $A\ cm^{-2}$. HTS wires must be able to carry current at relatively high temperatures to decrease the difficulties associated with cooling. The anticipated range for HTS operating temperature (depending on the application) is 4.2–77 *K*. Superconducting devices also require tolerance to surrounding magnetic fields and should be able to operate in the presence of magnetic fields. The goal for a cost-effective HTS wire is $0.01/ampere-meter.

We alluded earlier to the extreme brittleness of the ceramic superconductors. Very powerful tensile and shear forces develop in dipole magnets due to the phenomenon of Lorentz force, enough to literally explode the ceramic oxides. This also means that processing of such superconductors into long lengths is much more difficult than is the case with a ductile Nb–Ti system. Since the discovery of HTS, many techniques have been tried to make HTS in the form of flexible, long conductor wires. One method called the *oxide-powder-in-tube* (OPIT) method (Sandhage et al. 1991) involved the use of oxide powder of appropriate composition (stoichiometry, phase content, purity, etc.) packed in silver tube (4–7 *mm* inside diameter and 6–11 *mm* outside diameter). The silver tube is sealed after packing and degassed. The deformation processing techniques commonly used are swaging and drawing for wires and rolling is used for tapes. Heat treatments, intermediate and/or subsequent to deformation, are given to form the correct phase, promote grain interconnectivity, crystallographic alignment of the oxide, and to obtain proper oxygenation (Sandhage et al. 1991). Figure 9.10 shows a schematic of this process. What we need is a high degree of crystallographic alignment of the

superconducting oxide grains. It is known that the critical current density in HTS is increased with the alignment of oxide grains (Osamura et al. 1990; Uno et al. 1991). A major obstacle in the manufacture of long lengths of YBCO wire is the existence of weak links, such as a grain boundary. Also, the use of silver as the matrix makes it very expensive.

In a manner similar to the so called bronze route of making conventional superconductors, where the superconductor is a very brittle intermetallic, Nb_3Sn, one must avoid the synthesis of the brittle ceramic until the very end. The sintering step should be carried after the formation of the desired shape. This technique, called the *metallic precursor* (MP) method, involves melting the metallic elements (e.g., Y, Ca, Ba, Cu, and Ag), melt spinning, i.e., rapidly solidifying, the molten alloy into a ribbon form, and then pulverizing it to obtain homogeneous alloy powder. This precursor alloy powder is then packed into a silver can, sealed, and extruded into a hexagonal rod. Pieces of the extruded rod are packed into another bundle and further extruded. The final step in this process involves a very large reduction, up to 300:1, and results in round wire or tape (Masur et al. 1994). Figure 9.11a shows a low magnification cross sectional picture of a cable made by the MP process. Higher magnification views of the longitudinal section and transverse cross section of Y-124 (or more precisely, $Y_{0.9}Ca_{0.1}Ba_2Cu_4Ag_{0.65}$) metallic precursor/silver composite containing 962,407 filaments are shown in Fig. 9.11 b and c, respectively. The uniformity of deformation is excellent. The extruded composites are then internally oxidized to form oxides: Y_2O_3, BaO, CuO, and Ba_2Cu_3O. These are then reacted to give the Y-124 phase. The precursor oxides are approximately 50% converted to Y-124 after 100 *min* at 700 $^\circ C$ and 80% converted after 300 minutes at 750$^\circ C$ (Masur et al. 1994). The tapes, after the oxidation treatment, are subjected to a thermomechanical treatment (TMT) to obtain suitable textures. The TMT involves multiple heat treatments in the 600–825 $^\circ C$ range, uniaxial pressings at a pressure of up to 2 *GPa*, and the final heat treatment at 750 $^\circ C$ for 100 *h* in one-atmosphere oxygen. Recall the similarity between this and the bronze process used for Nb_3Sn.

One of the key developments in regard to HTS was the demonstration that crystallographic texture could be introduced into metal by rolling and annealing the metal into a thin tape, and this texture could be transferred to a superconducting oxide coating through buffer layers deposited on the metallic template. The buffer layers also serve to prevent any unwanted coating–substrate chemical reactions. The result was a superconducting oxide, such as yttrium–barium–copper oxide (YBCO), with oriented crystals. Such a tape can conduct large electrical currents without resistance at liquid nitrogen temperature (77 *K*). Although American Superconductor's first-generation, or 1G, HTS wires are in commercial use, second-generation (2G) wires are expected to be a formed-fit replacement for 1G wire. Eliminating silver in the manufacturing process will make the 2G wire less expensive. In addition, 2G wire will work better than 1G wire in the presence of a strong magnetic field in a motor, generator, or transformer.

We now briefly describe two important processes of obtaining aligned grains of oxide superconductors. The first one, called ion beam assisted deposition technique

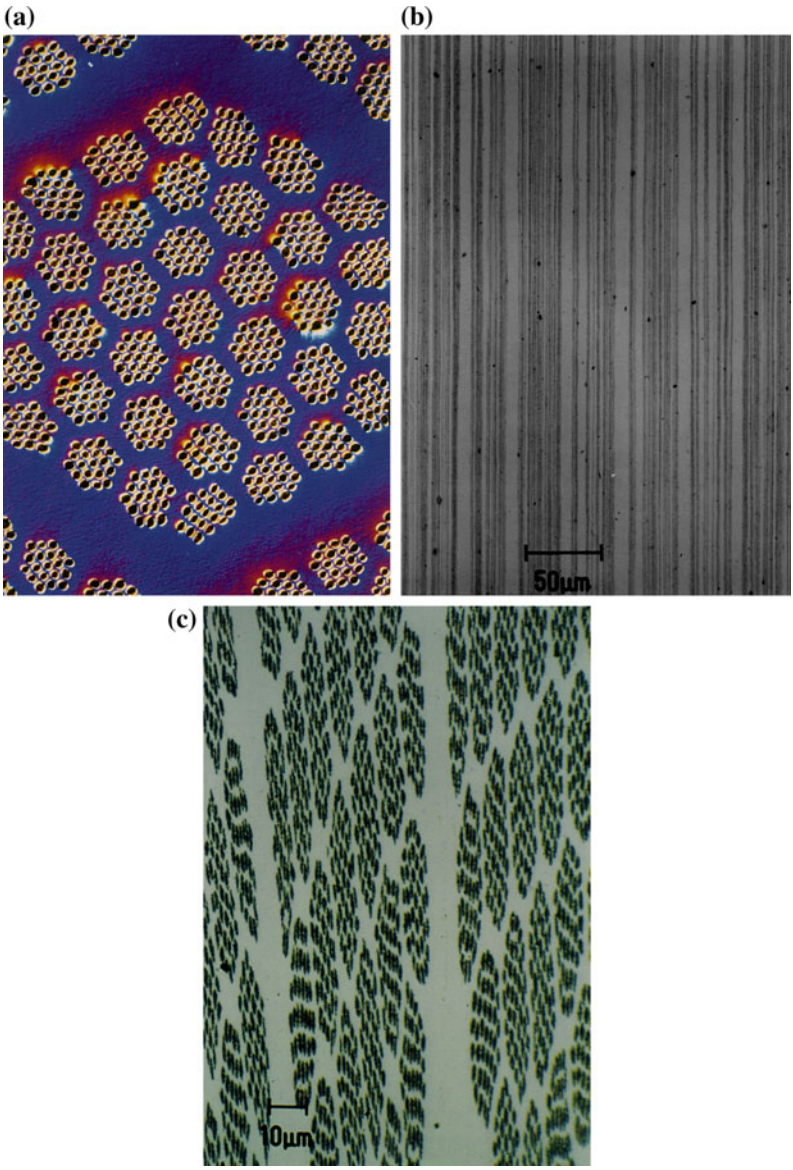

Fig. 9.11 **a** Low-magnification cross-sectional picture of a cable made by the MP process. **b** Longitudinal section **c** transverse section. The superconductor is $Y_{0.9}Ca_{0.1}Ba_2$ $Cu_4Ag_{0.65}$ metallic precursor/silver composite containing 962,407 filaments [Courtesy of American Superconductor Co.]

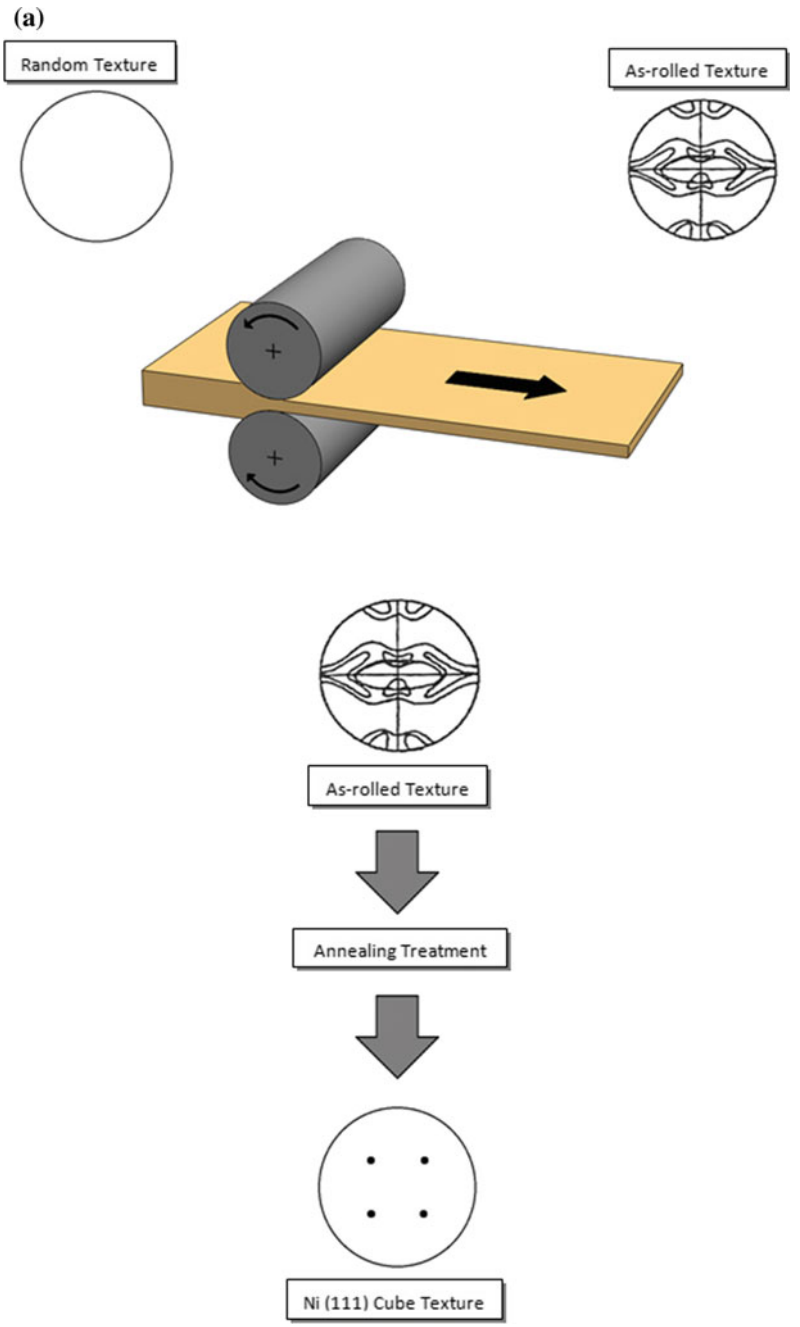

Fig. 9.12 The RABiTS process. A metallic substrate is prepared by rolling and heat treatments to serve as a structural template for the superconducting YBCO layer, which has substantially fewer weak links than the substrate. The circles show the pole figures showing the specific type of grain texture obtained

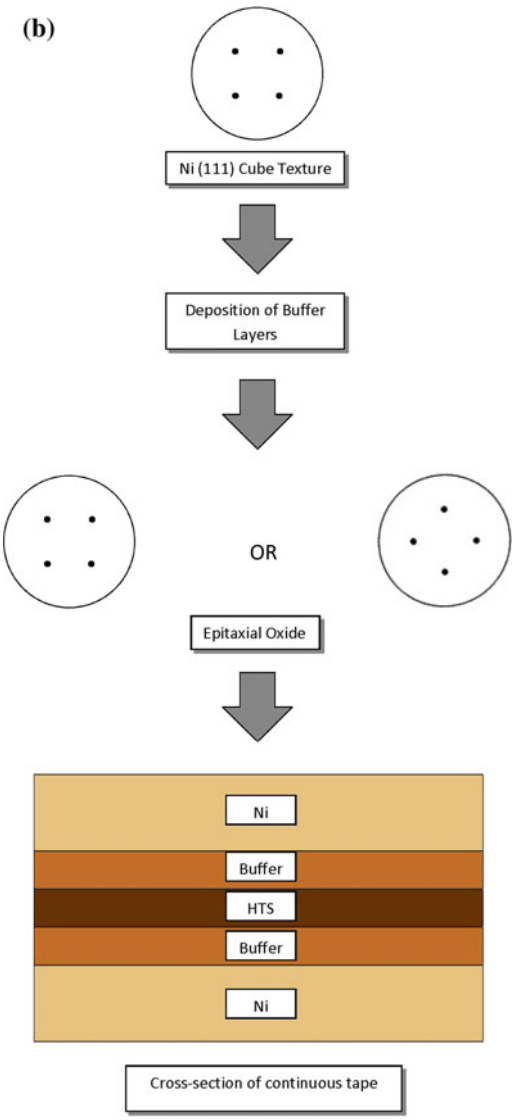

Fig. 9.12 (continued)

(IBAD), starts with a randomly oriented sheet of Hastelloy (a nickel alloy) on which a yttrium-stabilized zirconia (YSZ) layer is deposited as a buffer. The ion beam selectively removes the YSZ atoms that are not aligned at certain orientations biaxially. YBCO film is then deposited on this template. This process is based on some earlier Japanese work and the work done at the Los Alamos National Laboratory in the US. The second process, developed at the Oak Ridge National

Laboratory, is called "rolling assisted biaxially textured substrates," or RABiTS (Goyal et al. 1999; Bhattacharjee et al. 2007). This results in a biaxial texture in a range of metals. On this textured metallic substrate, oxide superconductors are deposited epitaxially. These textured substrates serve as structural templates for the final superconductor layer, which has substantially fewer weak links. In the RABiTS process, silver is replaced by nickel or nickel alloys, eliminating the expensive silver. The RABiTS process consists of the following steps:

i. Thermomechanical processing (rolling, heat treatments, and annealing) is used to obtain flexible, biaxially oriented Ni or Ni alloy substrates. The substrate serves as a structural template for the superconducting YBCO layer, which has substantially fewer weak links than the substrate. This is shown in Fig. 9.12. The circles show the pole figures showing the specific type of grain texture obtained.
ii. Deposit a series of buffer layers on the substrate. YBCO superconductors are then deposited epitaxially on the buffer layer. The buffer layers transfer the texture of the metal substrate to the superconductor and prevent any reaction between the substrate and the superconductor. The final composite superconducting tape is shown schematically in Fig. 9.13.

American Superconductor Co. makes HTS wires that are high performance, long length, RABiTS-based, nickel–tungsten substrate coated with very thin buffer layers. The company produces wide ribbons of material that are slit into 100-meter-long, 4-millimeter-wide wires. Figure 9.14 shows such a superconducting cable, trade name Amperium. An impressive array of different materials is used to make the superconducting cable.

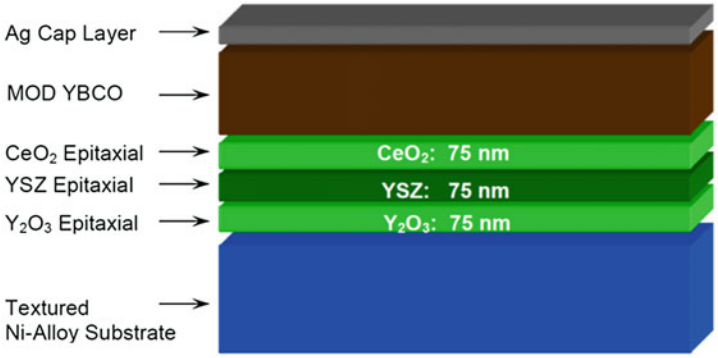

Fig. 9.13 A schematic of final composite superconducting tape obtained by the RABiTS process. The series of buffer layers and the YBCO superconductor are deposited epitaxially on the substrate. The buffer layers transfer the texture of the metal substrate to the superconductor and prevent any reaction between the substrate and the superconductor

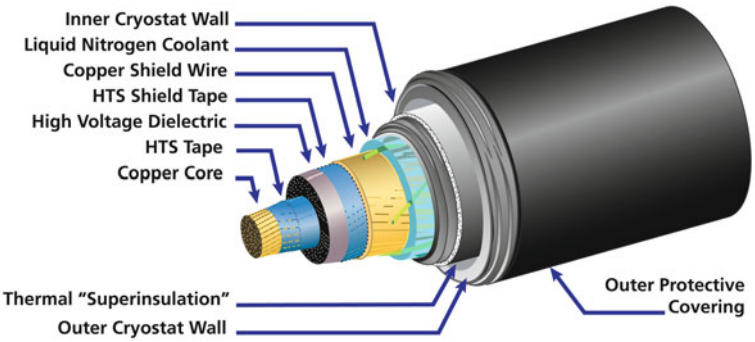

Fig. 9.14 A schematic of a 2G superconducting cable, trade name Amperium. Note the number of different materials used [Courtesy of American Superconductor Co.]

9.4 Applications

Filamentary superconducting composites have some very important applications. Examples of applications of metal matrix composite superconducting coils include (Cyrot and Pavuna 1992) the following:

- Magnetic resonance imaging (MRI), which requires extremely uniform magnetic fields of $\sim$1–2 T. This is perhaps the largest commercial application of metal matrix composites.
- High field magnets for research in high energy and in condensed matter physics.
- Coils for windings in motors and generators.
- Magnetic levitating (MAGLEV) coils for high speed trains.
- Magnetohydrodynamic and electromagnetic thrust systems for propulsion in ships and submarines.

Since the discovery of HTS, much emphasis has been placed on the high T_c of these superconductors. It is good to remember a rule of thumb for most superconductor applications, which says that critical temperature T_c of a technological superconductor should be about twice the use temperature (Cyrot and Pavuna 1992), i.e.,

$$T_{\text{use}} \sim T_c/2.$$

This implies that superconductors that are used with liquid helium (4.2 K) as a coolant should have a $T_c > 8$ K. In fact, due to the heating of the magnet, the actual operational temperature is closer to $\sim$7 K, so one needs a $T_c \sim 15$ K. Thus, to use the oxide high temperature superconductors (HTS) in applications at 77 K, one needs a superconductor with a $T_c \sim 150$ K. Such a material has not yet been synthesized; the thallium compound with $T_c \sim 125$ K would appear to be the best candidate for the "true" technological material at liquid nitrogen temperature. For

most electronic-type applications, the rule of thumb is less stringent, and we can write

$$T_{\text{use}} \sim 2/3\, T_c.$$

Nb_3Sn/Cu superconducting composites are used for magnetic fields greater than 12 *T*. Such high fields are encountered in thermonuclear fusion reactors, and superconducting composite magnets would represent a sizable fraction of the capital cost of such a fusion power plant. Table 9.2 shows the requirements for critical current density in a given magnetic field for several applications of superconductors. It is estimated that these superconducting magnets will represent a large portion of the capital cost of a fusion power plant. Their performance will affect the plasma as well as the plasma density—hence, the importance of materials research aimed at improving the performance limits of these superconducting magnets. The main difference between the magnets used in a fusion reactor and in power transmission is that in a fusion reactor we use superconductors at very high magnetic fields while in power transmission the use is at relatively low fields.

A large scale potential application of Nb–Ti/Cu superconducting magnets is in magnetically levitated trains. The principle is to put superconducting magnets on the train and copper coils in the track which would cause repulsion between the two and make the train levitate. Various test maglev tracks have been built, in UK, Japan, and Germany. Japan National Railways has tested such trains over a small stretch at speeds over 500 $km\ h^{-1}$. Nb–Ti/Cu superconductor composites are also employed in pulsed magnets for particle accelerators in high energy physics. Other applications of these superconductors include the fields of magnetohydrodynamics and power. Superconducting electric generators for utility applications allow two times or more kilovoltamperes of electricity to be produced than by a conventional generator of a comparable size. The field windings can be made from an Nb–Ti/Cu composite or HTS composites. By using superconducting materials, the designers could make a generator that developed a much stronger magnetic field than a conventional generator, permitting a significant reduction in the size of the generator for the same power output. Superconducting magnets do require cryogenic temperatures to operate, but the cost of this refrigeration is more than compensated by the energy savings. One has only to remember that, in a superconducting machine working with almost zero resistance, the normal losses associated with the

Table 9.2 Critical current density in a given magnetic field for several applications of superconductors [after Cyrot and Pavuna 1992]

Application	B (T)	J_c (A/cm^2)
Interconnects	0.1	5×10^6
AC transmission lines	0.2	10^5
DC transmission lines	0.2	2×10^4
SQUIDs	0.1	2×10^2
Motors and generators	~ 4	$\sim 10^4$
Fault current limiters	>5	$>10^5$

flow of electricity in rotor windings of a conventional machine are absent, resulting in a higher efficiency and reduced operating costs. A major problem in this development of superconducting generators is to prevent the movement of rotor windings under the intense centrifugal and magnetic forces exerted on them. The rotor spins at a speed of 360 *rpm*. Thus, even an infinitesimally small movement of these components would generate enough heat by friction to quench the superconductors. One solution used by GE researchers involved a special vacuum epoxy-impregnation process to bond the Nb–Ti superconductors into rock-solid modules and strong aluminum supports to hold the windings rigidly.

An electrical transformer, built by ABB, using 1G HTS wires has been in use in Geneva, Switzerland since 1997. This transformer used the flexible HTS wires made by American Superconductor. The process involves packing of the raw material into hollow silver tubes, drawing into fine filaments, grouping the multifilaments in another metal jacket, further drawing and heat treating to convert the raw material into the oxide superconductor (see Sect. 9.3.3). The wire is then flattened into a ribbon (2.5×0.25 *mm*) that is used to make the transformer coils. The transformer contains 6 *km* of HTS wires wound into coils, immersed in liquid nitrogen. According to ABB, this transformer loses only about one-fifth of the AC power losses of the conventional transformers made of conventional conductors. Because HTS wires can carry a higher current density, this new transformer is more compact and lighter than a conventional transformer. It should also be mentioned that liquid nitrogen used as a coolant in the HTS transformer is safer than oils used as insulators in conventional transformers.

Finally, we will describe a very important application of Nb-based superconducting composites.

9.4.1 Magnetic Resonance Imaging

The phenomenon of nuclear magnetic resonance (NMR) is exploited in the technique of magnetic resonance imaging (MRI). This technique has a major advantage over X-ray radiography in that it is a noninvasive diagnostic technique, and thus the human body is not exposed to an ionizing radiation. It would be useful to briefly explain the principle behind this important technique. Use is made of the electromagnetic characteristics of the nuclei of elements such as hydrogen, carbon, and phosphorus that are present in the human body. The nuclei of these elements act as bar magnets when placed in a strong magnetic field. The patient is placed in the center of a very powerful magnet. When the magnetic field is turned on, the nuclei of the elements in the patient's body part under examination realign along the magnetic field direction. If we apply a radio frequency field, the nuclei will reorient. And if we repeat this process over and over again, the nuclei will resonate. The resonance frequency is picked up by a sensitive antenna, amplified, and processed by a computer into an image. The MRI images, obtained from the resonance patterns, are more detailed and have a higher resolution than traditional techniques

of visualization of soft tissues. And best of all, these images are obtained without exposing the patient to a radiation or performing biopsy.

MRI became a major diagnostic tool after solenoids made of metal matrix composites consisting of continuous fiber (Nb–Ti) in copper matrix became commercially available. Of course, MRI techniques do not have to use superconducting magnets, i.e., conventional non-superconducting magnets can be used. There are, however, certain advantages with superconductors: better homogeneity and resolution of magnetic fields and higher field strengths than are available with conventional magnets. The disadvantage is that higher fields with superconductors lead to greater shielding problems. The superconducting solenoid, made from Nb–Ti/Cu composite wire, is immersed in a liquid helium cryogenic Dewar. The liquid helium is consumed at about 4 *ml* per hour, and each refill of the Dewar lasts about 3 months. Commercially manufactured nuclear magnetic resonance (NMR) spectrometer systems, also called magnetic resonance imaging systems, for medical diagnostics became available in the 1980s. Figure 9.15 shows a picture of one such system (more details are given below). It is worth repeating that the great advantage of magnetic resonance imaging in clinical diagnostics is that it does not expose the patient to ionizing radiation and its possible harmful side effects. It should be pointed out no ferromagnetic articles should be brought in the vicinity of an MRI superconductor.

Figure 9.15a shows an MRI scanner installed in the Center of Magnetic Resonance Imaging at the University of Minnesota in 2018. It represents a big step forward in the MRI scanner technology, so we provide some details. As we mentioned earlier, MRI scanners represent the largest application of metal matrix composites; specifically the Nb–Ti/Cu composites. Figure 9.15 shows a 10.5 *T* machine installed at the Center for Magnetic Resonance Imaging at the University of Minnesota. Most common MRI machines are rated between 0.5 and 2.0 *T* (1 *T* = 10,000 *G*). For reference, the earth's magnetic field is only 0.5 *G*. In an MRI machine, the patient lies inside a cylindrical bore of about 60 *cm* diameter. By far, the largest and the most expensive component of an MRI scanner is the superconducting magnet, which is responsible for producing a very high and stable magnetic field. The superconducting magnets are made of many windings of Nb–Ti/Cu wire. The Minnesota machine has windings that are more than one kilometer long. When we pass an electric current through these windings, we produce a magnetic field. **S**uperconducting composites make the resistance in the wires go to zero at liquid helium temperature. These windings are kept cold by insulating in vacuum. While superconducting magnets are expensive, the strong magnetic field allows for very high-quality imaging, and superconductivity makes the system economical to operate.

In the 10.5 *T* machine at the University of Minnesota's Center for Magnetic Resonance Research, the patient lies down inside a 4-*m*-long cylinder for the whole body scan. 10.5 *T* magnet is quite heavy (weighs about 110 tons, 3 times more than a Boeing 737 aircraft). The big machine allows extremely fine resolution that can reveal the intricate details of human brain and thin cartilage that lines the hip socket. Of course, there are biological side effects at these high magnetic fields. Although

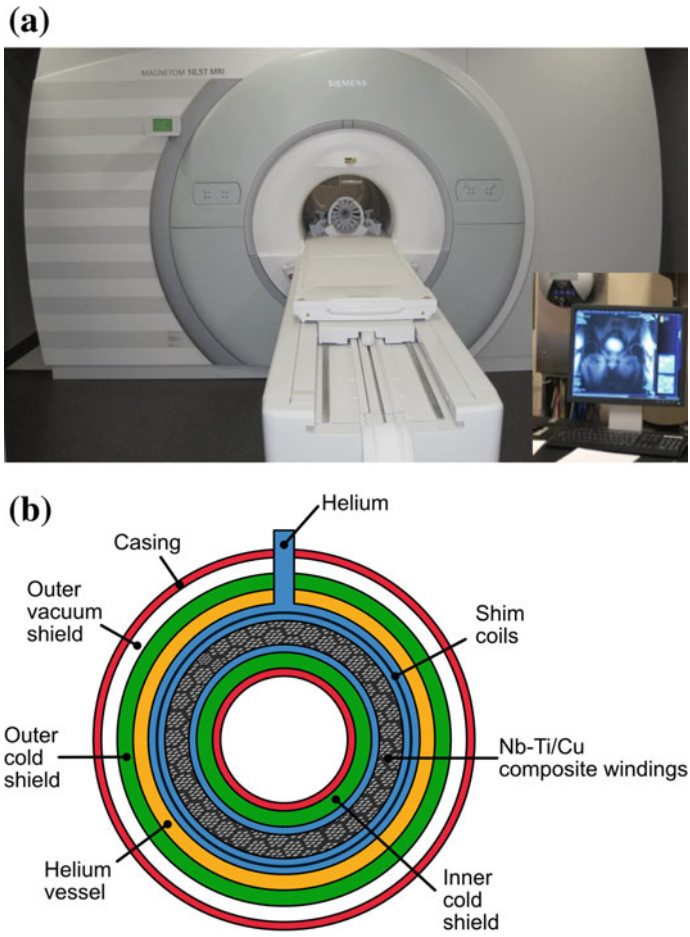

Fig. 9.15 **a** A 10.5 *T* magnetic resonance imaging system for clinical diagnostics at the University of Minnesota. [Courtesy of Center of Magnetic Resonance Imaging, University of Minnesota] **b** schematic arrangement of the cross section of an MRI machine

the effects are temporary, people can experience dizziness and vertigo when their body is moved in and out of the scanner. It is also said that when people move inside the machine, they can sometimes taste metal, see white flashes or experience involuntary eye movements called nystagmus.

Figure 9.15b shows a schematic arrangement of the cross section of an MRI machine. Shim coils is a new term that we should explain. They are nothing but a device to adjust the homogeneity of the magnetic field, a very important feature of any MRI scanner.

The term shim coils comes from the mechanical shims that are used to adjust the position and the degree of parallelism of the pole faces of an electromagnet. Shim

coils in an MRI scanner adjust the homogeneity of the magnetic field by changing the current flowing through it. They are not mechanical shims but electrical current shims.

Problems

9.1. There are many known superconducting A15 compounds. Of these Nb_3Al, Nb_3Ga, and Nb_3Ge have higher values of T_c and H_{c2} than do Nb_3Sn and V_3Ga. How then does one explain the fact that only Nb_3Sn and to a lesser extent V_3Ga are available commercially?
9.2. It is believed that grain boundaries are the imperfections responsible for the flux pinning in high-J_c materials like Nb_3Sn and V_3Ga. How does J_c vary with grain size?
9.3. What is the effect of any excess unreacted bronze leftover in the manufacture of Nb_3Sn superconductor composite via the bronze route?
9.4. Examine the Nb–Sn phase diagram. At what temperature does the A15 compound (Nb_3Sn) become unstable? Nb_3Sn is formed by solid-state diffusion in Nb/Cu–Sn composites at 700 °C or below. Is this in accord with information from the phase diagram? Explain.
9.5. Do you think it is important to study the effect of irradiation on superconducting materials? Why?
9.6. In the high magnetic field coils of large dimensions, rather large tensile and compressive loads can be encountered during energizing and de-energizing. Discuss the effects of cyclic stress on the superconducting coil materials.
9.7. Superconducting composites in large magnets can be subjected to high mechanical loads. Describe the sources of such loadings.

References

P.K. Bhattacharjee, R.K. Ray, A. Upadhyaya, J. Mater. Sci. **42**, 1984 (2007)
K.K. Chawla, Metallography **6**, 55 (1973a)
K.K. Chawla, Philos. Mag. **28**, 401 (1973b)
M. Cyrot, D. Pavuna, *Introduction to Superconductivity and High T_c Materials* (World Scientific, Singapore, 1992), p. 202
A. Goyal, S.X. Ren, E.D. Specht, D.M. Kroeger, R. Feenstra, D. Norton, M. Paranthaman, D.F. Lee, D.K. Christen, Micron **30**, 463 (1999)
K. Heine, N. Tenbrink, M. Thoerer, App. Phys. Lett. **55**, 2441 (1989)
H. Hillmann, *Superconductor Materials Science* (Plenum, New York, 1981), p. 275
F. Irie, in *Composite Superconductors*, ed. by K. Osamura. (Marcel Dekker, New York, 1994), p. 7
A.R. Kaufmann, J.J. Pickett, Bull. Am. Phys. Soc. **15**, 833 (1970)
J.E. Kunzler, E. Bachler, F.S.L. Hsu, J.E. Wernick, Phys. Rev. Lett. **6**, 89 (1961)
D. Larbalestier, Science **274**, 736 (1996)
T. Luhman, M. Suenaga, Appl. Phys. Lett. **29**, 1 (1976)
L.J. Masur, E.R. Podtburg, C.A. Craven, A. Otto, Z.L. Wang, D.M. Kroeger, J. Miner. Met. Mater. Soc. **46**, 28 (1994)

T. Matsuda, K. Harada, H. Kasai, O. Kamimura, A. Tonomura, Science **271** (1996)
E. Nembach, K. Tachikawa, J. Less Common Met. **19**, 1962 (1979)
K. Osamura, S.S. Oh, S. Ochiai, Supercond. Sci. Technol. **3**, 143 (1990)
R. Roberge, S. Foner, *Filamentary A15 Superconductors* (Plenum Press, New York, 1980), p. 241
R.H. Sandhage, G.N. Riley Jr., W.L. Carter, J. Miner. Met. Mater. Soc. **21**, 25 (1991)
R.M. Scanlan, W.A. Fietz, E.F. Koch, J. Appl. Phys. **46**, 2244 (1975)
K. Tachikawa, in *Proceedings of the 3rd ICEC* (Illife Science and Technology Publishing, Surrey, UK, 1970)
N. Uno, N. Enomoto, H. Kikuchi, K. Matsumoto, M. Mimura, M. Nakajima, Adv. Supercond. **2**, 341 (1991)

Suggested Reading

K. Osamura (ed.), *Composite Superconductors* (Marcel Dekker, New York, 1994)

Part III

Chapter 10
Micromechanics of Composites

In this chapter, we consider the results of incorporating a reinforcement (fibers, whiskers, particles, etc.) in a matrix to make a composite. It is of great importance to be able to predict the properties of a composite, given the properties of the components and the geometric arrangement of the components in the composite. We examine various micromechanical aspects of composites. A particularly simple case is the *rule-of-mixtures*, a rough tool that considers the composite properties as volume-weighted averages of the component properties. It is important to realize that the rule-of-mixtures works in only certain simple situations. The density of the composite is an example where the rule-of-mixtures is applied readily. In the case of mechanical properties, there are certain restrictions to its applicability. When more precise information is desired, it is better to use more sophisticated approaches based on the theory of elasticity.

10.1 Density

Consider a composite of mass m_c and volume v_c. The total mass of the composite is the sum total of the masses of fiber and matrix, that is,

$$m_c = m_f + m_m. \tag{10.1}$$

The subscripts c, f, and m indicate composite, fiber, and matrix, respectively. We use fiber, but it could be any form of reinforcement, particle, short fiber, whisker, etc. Note that Eq. (10.1) is valid even in the presence of any voids in the composite. The volume of the composite, however, must include the volume of voids, v_v. Thus,

$$v_c = v_f + v_m + v_v. \tag{10.2}$$

K. K. Chawla, *Composite Materials*,
https://doi.org/10.1007/978-3-030-28983-6_10

Dividing Eq. (10.1) by m_c and Eq. (10.2) by v_c and denoting the mass and volume fractions by M_f, M_m and V_f, V_m, V_v, respectively, we can write

$$M_f + M_m = 1, \tag{10.3}$$

and

$$V_f + V_m + V_v = 1. \tag{10.4}$$

The composite density ρ_c (= m_c/v_c) is given by

$$\rho_c = \frac{m_c}{v_c} = \frac{m_f + m_m}{v_c} = \frac{\rho_f v_f + \rho_m v_m}{v_c},$$

or

$$\rho_c = \rho_f V_f + \rho_m V_m. \tag{10.5}$$

We can also derive an expression for ρ_c in terms of mass fractions. Thus,

$$\begin{aligned}
\rho_c &= \frac{m_c}{v_c} = \frac{m_c}{v_f + v_m + v_v} = \frac{m_c}{m_f/\rho_f + m_m/\rho_m + v_v} \\
&= \frac{1}{M_f/\rho_f + M_m/\rho_m + v_v/m_c} \\
&= \frac{1}{M_f/\rho_f + M_m/\rho_m + v_v/\rho_c v_c} \\
&= \frac{1}{M_f/\rho_f + M_m/\rho_m + V_v/\rho_c}.
\end{aligned} \tag{10.6}$$

We can use Eq. (10.6) to indirectly measure the volume fraction of voids in a composite. Rewriting Eq. (10.6), we obtain

$$\rho_c = \frac{\rho_c}{\rho_c\left[M_f/\rho_f + M_m/\rho_m\right] + V_v},$$

or

$$V_v = 1 - \rho_c\left(\frac{M_f}{\rho_f} + \frac{M_m}{\rho_m}\right). \tag{10.7}$$

Example 10.1 A thermoplastic matrix contains 40 wt% glass fiber. If the density of the matrix, ρ_m, is 1.1 gcm^{-3} while that of glass fiber, ρ_f, is *2.5* gcm^{-3}, what is the density of the composite? Assume that no voids are present.

Solution Consider 100 g of the composite:

$$\text{Amount of glass fiber}, m_f = 40\,g$$
$$\text{Amount of matrix}, m_m = 60\,g.$$

Volume of the composite, v_c, is the sum of the volumes of fiber, v_f, and matrix, v_m,

$$\begin{aligned} v_c &= v_m + v_f \\ &= (m_m/\rho_m) + \left(m_f/\rho_f\right) = (60/1.1 + 40/2.5)\,cm^3 \\ &= 54.5 + 16 = 70.5\,cm^3. \end{aligned}$$

The density of the composite is

$$\rho_c = 100\,g/70.5\,cm^3 = 1.42\,g\,cm^{-3}.$$

10.2 Mechanical Properties

In this section, we first describe some of the methods for predicting elastic constants, thermal properties, and transverse stresses in fibrous composites and then we treat the mechanics of load transfer.

10.2.1 Prediction of Elastic Constants

Consider a unidirectional composite such as the one shown in Fig. 10.1. Assume that plane sections of this composite remain plane after deformation. This is called the *isostrain* or *action-in-parallel* situation. It was first treated by Voigt (1910). Let us apply a force, P_c, in the fiber direction. Now, if the two components adhere perfectly and if they have the same Poisson's ratio, then each component will undergo the same longitudinal elongation, Δl. Thus, we can write for the strain in each component

$$\varepsilon_f = \varepsilon_m = \varepsilon_{cl} = \frac{\Delta l}{l}, \tag{10.8}$$

where ε_{cl} is the strain in the composite in the longitudinal direction. If both fiber and matrix are elastic, we can relate the longitudinal stress σ in the two components to the longitudinal strain ε_l by Young's modulus E. Thus,

$$\sigma_f = E_f \varepsilon_{cl} \quad \text{and} \quad \sigma_m = E_m \varepsilon_{cl}.$$

Let A_c be the cross sectional area of the composite, A_m, that of the matrix, and A_f, that of all the fibers. The applied load on the composite, P_c, is shared between the fiber and the matrix. We can write

$$P_c = P_f + P_m,$$

where P_f and P_m are the loads on the fiber and the matrix, respectively. Converting into stress components, we can write

$$\sigma_{cl} A_c = \sigma_f A_f + \sigma_m A_m. \tag{10.9}$$

From Eqs. (10.8) and (10.9), we get

$$\sigma_{cl} A_c = \left(E_f A_f + E_m A_m\right) \varepsilon_{cl}$$

or

$$E_{cl} = \frac{\sigma_{cl}}{\varepsilon_{cl}} = E_f \frac{A_f}{A_c} + E_m \frac{A_m}{A_c},$$

where E_{cl} is the longitudinal Young's modulus of the composite.

Now, for a given length of a composite, $A_f/A_c = V_f$ and $A_m/A_c = V_m$. Then the preceding expression can be simplified to

$$E_{cl} = E_f V_f + E_m V_m = E_{11}. \tag{10.10}$$

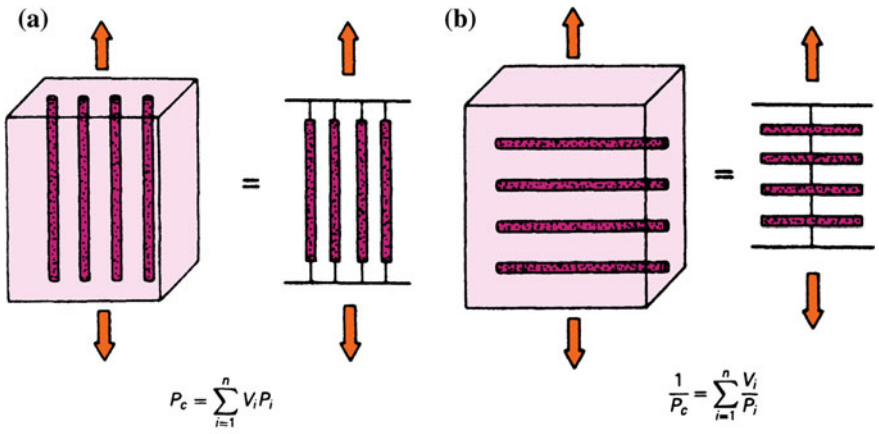

Fig. 10.1 Unidirectional composite: **a** isostrain or action in parallel, **b** isostress or action in series

The longitudinal modulus is also denoted by E_{11}. Equation (10.10) is called the rule-of-mixtures for Young's modulus in the fiber direction.

A similar expression can be obtained for the composite longitudinal strength from Eq. (10.9), namely,

$$\sigma_{cl} = \sigma_f V_f + \sigma_m V_m. \tag{10.11}$$

For properties in the transverse direction, we can represent the simple unidirectional composite by what is called the *action-in-series* or *isostress* situation; see Fig. 10.1b. In this case, we group the fibers together as a continuous phase normal to the stress. Thus, we have equal stresses in the two components and the model is equivalent to that treated by Reuss (1929). For loading transverse to the fiber direction, isostress condition prevails, and we have

$$\sigma_{ct} = \sigma_f = \sigma_m,$$

while the total displacement of the composite in the thickness direction, Δt_c, is the sum of displacements of the matrix and fiber, that is,

$$\Delta t_c = \Delta t_m + \Delta t_f.$$

Dividing throughout by t_c, the gage length of the composite, we obtain

$$\frac{\Delta t_c}{t_c} = \frac{\Delta t_m}{t_c} + \frac{\Delta t_f}{t_c}.$$

Now $\Delta t_c/t_c = \varepsilon_{ct}$, strain in the composite in the transverse direction, while Δt_m and Δt_f are equal to the strains in the matrix and fiber times their respective gage lengths, that is, $\Delta t_m = \varepsilon_m t_m$ and $\Delta t_f = \varepsilon_f t_f$. Then

$$\varepsilon_{ct} = \frac{\Delta t_c}{t_c} = \frac{\Delta t_m}{t_m}\frac{t_m}{t_c} + \frac{\Delta t_f}{t_f}\frac{t_f}{t_c},$$

or

$$\varepsilon_{ct} = \varepsilon_m \frac{t_m}{t_c} + \varepsilon_f \frac{t_f}{t_c}. \tag{10.12}$$

For a given cross sectional area of the composite under the applied load, the volume fractions of fiber and matrix can be written as

$$V_m = \frac{t_m}{t_c} \quad \text{and} \quad V_f = \frac{t_f}{t_c}.$$

This simplifies Eq. (10.12) to

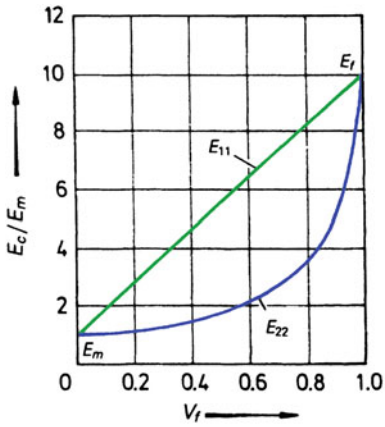

Fig. 10.2 Variation of longitudinal modulus (E_{11}) and transverse modulus (E_{22}) with fiber volume fraction (V_f)

$$\varepsilon_{ct} = \varepsilon_m V_m + \varepsilon_f V_f. \tag{10.13}$$

Considering both components to be elastic and remembering that $\sigma_{ct} = \sigma_f = \sigma_m$ in this case, we can write Eq. (10.13) as

$$\frac{\sigma_{ct}}{E_{ct}} = \frac{\sigma_{ct}}{E_m} V_m + \frac{\sigma_{ct}}{E_f} V_f,$$

or

$$\frac{1}{E_{ct}} = \frac{V_m}{E_m} + \frac{V_f}{E_f} = \frac{1}{E_{22}}. \tag{10.14}$$

The relationships given by Eqs. (10.5), (10.10), (10.11), (10.13), and (10.14) are commonly referred to as rules-of-mixtures (volume-weighted averages). Figure 10.2 shows the plots of Eqs. (10.10) and (10.14). The reader should appreciate that these relationships and their variants are but rules-of-thumb obtained from a simple, strength of materials approach. More comprehensive micromechanical models, based on the theory of elasticity, can and should be used to obtain the elastic constants of fibrous composites. We describe below, albeit very briefly, some of these.

10.2.2 Micromechanical Approaches

The states of stress and strain can each be described by six components. An anisotropic body with no symmetry elements present requires 21 independent elastic constants to relate stress and strain (Nye 1985). This is the most general case of elastic anisotropy. An elastically isotropic body, on the other hand, is the simplest

case; it needs only two independent elastic constants. In such a body, when a tensile stress σ_z is applied in the z-direction, a tensile strain ε_z results in that direction. In addition to this tensile strain, there are two equal compressive strains ($\varepsilon_x = \varepsilon_y$) in the x- and y-directions. In a generally anisotropic body, the two transverse strain components are not equal. In fact, as we shall see in Chap. 11, in such a body, tensile loading can result in tensile and shear strains. The large number of independent elastic constants (21 in the most general case, i.e., no symmetry elements) represents the degree of elastic complexity in a given system. Any symmetry elements present will reduce the number of independent elastic constants (Nye 1985).

A composite containing uniaxially aligned fibers will have a plane of symmetry perpendicular to the fiber direction (i.e., material on one side of the plane will be the mirror image of the material on the other side). Figure 10.3 shows square, hexagonal, and random fiber arrays in a matrix. A square array of fibers, for example, will have symmetry planes parallel to the fibers as well as perpendicular to them. Such a material is an orthotropic material (it has three mutually perpendicular planes of symmetry) and possesses nine independent elastic constants (Nye 1985). Hexagonal and random arrays of aligned fibers are transversely isotropic and have five independent elastic constants. These five constants as well as the stress–strain relationships, as derived by Hashin and Rosen (1964) and Rosen (1973), are given in Table 10.1. There are two Poisson's ratios: one gives the transverse strain caused by an axially applied stress, and the other gives the axial strain caused by a transversely applied stress. The two are not independent but are related (see Sect. 11.3). Thus, the number of independent elastic constants for a transversely isotropic composite is five. Note that the total number of independent elastic constants in Table 10.1 is five (count the number of *Cs*).

More accurate results can be obtained if we take into account the inevitable scatter in the distribution of fibers, i.e., in reality, they never have an idealized distribution in the matrix. This approach involves the use of a representative element of volume. Ignoring the length, we can write for fiber volume fraction in the composite

$$V_f = s_f^2/s_c^2,$$

where s is the equivalent side and the subscripts f and c represent fiber and composite, respectively. A summary of the elastic constants for a transversely isotropic composite in terms of the elastic constants of the two components is given in

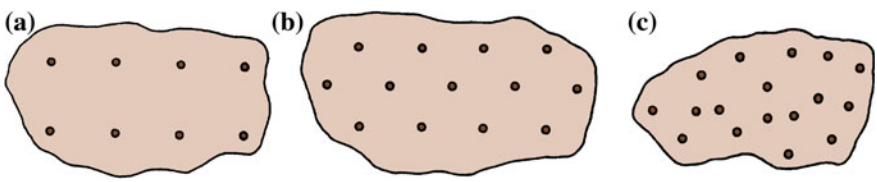

Fig. 10.3 Various fiber arrays in a matrix: **a** square, **b** hexagonal, and **c** random

Table 10.1 Elastic moduli of a transversely isotropic fibrous composite

$E = C_{11} - \dfrac{2C_{12}^2}{C_{22} + C_{23}}$	$K_{23} = \frac{1}{2}(C_{22} + C_{23})$
$G = G_{12} = G_{13} = C_{44}$	$G_{23} = \frac{1}{2}(C_{22} + C_{23})$
$v = v_{13} = v_{31} = \frac{1}{2}\left(\dfrac{C_{11} - E}{K_{23}}\right)^{1/2}$	$v_{23} = \dfrac{K_{23} - \phi G_{23}}{K_{23} + \phi G_{23}}$
$E_2 = E_3 = \dfrac{4G_{23}K_{23}}{K_{23} + \phi G_{23}}$	$\phi = 1 + \dfrac{4K_{23}v^2}{E}$
Stress–strain relationships	
$\varepsilon_{11} = \dfrac{1}{E_1}[\sigma_{11} - v(\sigma_{22} + \sigma_{33})]$	$\varepsilon_{22} = \varepsilon_{33} = \dfrac{1}{E_2}(\sigma_{22} - v\sigma_{33}) - \dfrac{v}{E}\sigma_{11}$
$\gamma_{12} = \gamma_{13} = \dfrac{1}{G}\sigma_{12}$	$\gamma_{23} = \dfrac{2(1 + v_{23})}{E_2}\sigma_{23}$

Source Adapted with permission from Hashin and Rosen (1964)

Table 10.2 (Chamis 1983). Note the use of $\sqrt{V_f}$ in these expressions. Because the plane 2–3 is isotropic in Fig. 10.4, the properties in directions 2 and 3 are identical. The matrix is treated as an isotropic material, while the fiber is treated as an anisotropic material. Thus, E_m and v_m are the two constants required for the matrix, while five constants (E_{f1}, E_{f2}, G_{f12}, G_{f23}, and v_{f12}) are required for the fiber. The expressions for the five independent constants (E_{11}, E_{22}, G_{12}, G_{23}, and v_{12}) are given in Table 10.2.

Frequently, composite structures are fabricated by stacking thin sheets of unidirectional composites called *plies* in an appropriate orientation sequence dictated by elasticity theory (see Chap. 11). It is of interest to know properties, such as the elastic constants and the strength characteristics of a ply. In particular, it is very valuable if we are able to predict the lamina characteristics starting from the characteristics of the individual components. Later in the macromechanical analysis (Chap. 11), we treat a ply as a homogeneous but thin orthotropic material. Elastic constants in the thickness direction can be ignored in such a thin ply, leaving four independent elastic constants, namely, E_{11}, E_{22}, v_{12}, and G_{12}, i.e., one less than the number of constants required for a thick but transversely isotropic material. The missing constant is G_{23}, the transverse shear modulus in the 2–3 plane, normal to the fiber axis. A brief description of the various micromechanical techniques used to

Table 10.2 Elastic constants of a transversely isotropic composite in terms of component constants (matrix isotropic, fiber anisotropic)

Longitudinal modulus	$E_{11} = E_{f1}\ V_f + E_m V_m$
Transverse modulus	$E_{22} = E_{33} = \dfrac{E_m}{1 - \sqrt{V_f}\left(1 - E_m/E_{f2}\right)}$
Shear modulus	$G_{12} = G_{13} = \dfrac{G_m}{1 - \sqrt{V_f}\left(1 - G_m/G_{f12}\right)}$
Shear modulus	$G_{23} = \dfrac{G_m}{1 - \sqrt{V_f}\left(1 - G_m/G_{f23}\right)}$
Poisson's ratio	$v_{12} = v_{13} = v_{f12}V_f + v_m V_m$
Poisson's ratio	$v_{23} = \dfrac{E_{22}}{2G_{23}} - 1$

Source Adapted with permission from Chamis (1983)

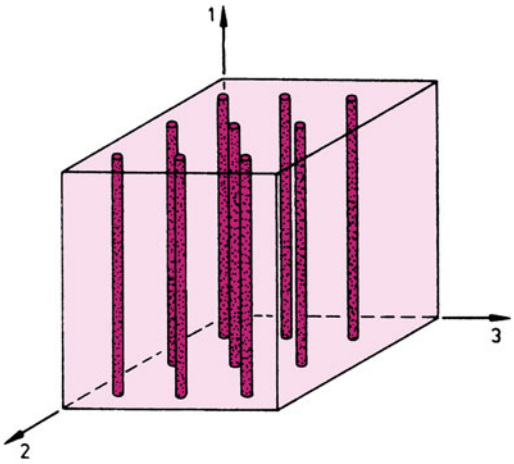

Fig. 10.4 A transversely isotropic fiber composite: plane transverse to fibers (2–3 plane) is isotropic

predict the elastic constants follows and then we give an account of a set of empirical equations, called *Halpin–Tsai equations*, that can be used under certain conditions to predict the elastic constants of a fiber reinforced composite.

In the so called self-consistent field methods (Chamis and Sendecky 1968), approximations of phase geometries are made and a simple representation of the response field is obtained. The phase geometry is represented by one single fiber embedded in a matrix cylinder. This matrix cylinder is embedded in an unbounded homogeneous material whose properties are taken to be equivalent to those of average composite properties. The matrix under a uniform load at infinity introduces a uniform strain field in the fiber. Elastic constants are obtained from this strain field. The results obtained are independent of fiber arrangements in the matrix and are reliable at low fiber volume fractions (V_f), reasonable at intermediate V_f, and unreliable at high V_f (Hill 1964). Exact methods deal with specific geometries, for example, fibers arranged in a hexagonal, square, or rectangular array in a matrix. The elasticity problem is then solved by a series development, a complex variable technique, or a numerical solution. The approach of Eshelby (1957, 1959) considers an infinite matrix containing an ellipsoidal inclusion. Modifications of the Eshelby method have been made by Mori and Tanaka (1973).

The variational or bounding methods focus on the upper and lower bounds on elastic constants. When the upper and lower bounds coincide, the property is determined exactly. Frequently, the upper and lower bounds are well separated. When these bounds are close enough, we can safely use them as indicators of the material behavior. It turns out that this is the case for longitudinal properties of a unidirectional lamina. Hill (1965) derived bounds for the ply elastic constants that are analogous to those derived by Hashin and Rosen (1964) and Rosen (1973). In particular, Hill put rigorous bounds on the longitudinal Young's modulus, E_{11}, in

terms of the bulk modulus inplane strain (k_p), Poisson's ratio (v), and the shear modulus (G) of the two phases. No restrictions were made on the fiber form or packing geometry. The term k_p is the modulus for lateral dilation with zero longitudinal strain and is given by

$$k_p = \frac{E}{2(1-2v)(1+v)}.$$

The bounds on the longitudinal modulus, E_{11}, are

$$\begin{aligned} \frac{4V_f V_m (v_f - v_m)^2}{(V_f/k_{pm}) + (V_m/k_{pf}) + 1/G_m} &\leq E_{11} - E_f V_f - E_m V_m \\ &\leq \frac{4V_f V_m (v_f - v_m)^2}{(V_f/k_{pm}) + (V_m/k_{pf}) + 1/G_f}. \end{aligned} \tag{10.15}$$

Equation (10.15) shows that the deviations from the rule-of-mixtures [Eq. (10.10)] are quite small (<2%). We may verify this by substituting some values of practical composites such as carbon or boron fibers in an epoxy matrix or a metal matrix composite such as tungsten in a copper matrix. Note that the deviation from the rule-of-mixtures value comes from the $(v_m - v_f)^2$ factor, i.e., square of a very small quantity. For $v_f = v_m$, we have E_{11} given exactly by the rule-of-mixtures.

Hill (1965) also showed that for a unidirectionally aligned fiber composite

$$v_{12} \lessgtr v_f V_f + v_m V_m \text{ accordingly as } (v_f - v_m)(k_{pf} - k_{pm}) \lessgtr 0. \tag{10.16}$$

Generally, $v_f < v_m$ and $E_f \gg E_m$. Then, v_{12} will be less than that predicted by the rule-of-mixtures. It is easy to see that the bounds on v_{12} are not as close as the ones on E_{11}. This is because $v_f - v_m$ appears in the case of v_{12} Eq. (10.16), while $(v_f - v_m)^2$ appears in the case of E_{11} Eq. (10.15). In the case where $v_f - v_m$ is very small, the bounds are close enough to allow us to write

$$v_{12} \approx v_f V_f + v_m V_m. \tag{10.17}$$

10.2.3 Halpin–Tsai Equations

Halpin, Tsai, and Kardos (Halpin and Tsai 1967; Halpin and Kardos 1976; Kardos 1971) empirically developed some generalized equations that readily give satisfactory results compared to the complicated expressions. They are also useful in determining the properties of composites that contain discontinuous fibers oriented in the loading direction. One writes a single equation of the form

$$\frac{p}{p_m} = \frac{1 + \xi\eta V_f}{1 - \eta V_f}, \tag{10.18}$$

$$\eta = \frac{p_f/p_m - 1}{p_f/p_m + \xi}, \tag{10.19}$$

where p represents one of the moduli of composite, for example, E_{11}, E_{22}, G_{12}, or G_{23}; p_m and p_f are the corresponding modulus of the matrix and fiber, respectively; V_f is the fiber volume fraction; and ξ is a measure of the reinforcement that depends on boundary conditions (fiber geometry, fiber distribution, and loading conditions). The term ξ is an empirical factor that is used to make Eq. (10.18) conform to the experimental data.

The function η in Eq. (10.19) is constructed in such a way that when $V_f = 0$, $p = p_m$ and when $V_f = 1$, $p = p_f$. Furthermore, the form of η is such that

$$\frac{1}{p} = \frac{V_m}{p_m} + \frac{V_f}{p_f} \quad \text{for } \xi \to 0$$

and

$$p = p_f V_f + p_m V_m \quad \text{for } \xi \to \infty.$$

These two extremes (not necessarily tight) bound the composite properties. Thus, values of ξ between 0 and ∞ will give an expression for p between these extremes. Some typical values of ξ are given in Table 10.3. Thus, we can cast the Halpin–Tsai equations for the transverse modulus as

$$\frac{E_{22}}{E_m} = \frac{1 + \xi\eta V_f}{1 - \eta V_f} \quad \text{and} \quad \eta = \frac{E_f/E_m - 1}{E_f/E_m + \xi}. \tag{10.20}$$

Comparing these expressions with exact elasticity solutions, one can obtain the value of ξ. Whitney (1973) suggested $\xi = 1$ or 2 for E_{22}, depending on whether a hexagonal or square array of fibers was used.

Nielsen (1974) modified the Halpin–Tsai equations to include the maximum packing fraction $\phi_{\max}$ of the reinforcement. His equations are

Table 10.3 Values of ξ for some uniaxial composites

Modulus	ξ
E_{11}	$2(l/d)$
E_{22}	0.5
G_{12}	1.0
G_{21}	0.5
K	0

Source Adapted from Nielsen (1974), courtesy of Marcel Dekker, Inc.

$$\begin{aligned}\frac{p}{p_m} &= \frac{1+\xi\eta V_f}{1-\eta\Psi V_f}\\ \eta &= \frac{p_f/p_m - 1}{p_f/p_m + \xi}\\ \Psi &\simeq 1 + \left(\frac{1-\phi_{\max}}{\phi_{\max}^2}\right) V_f,\end{aligned} \tag{10.21}$$

where $\phi_{\max}$ is the maximum packing factor. It allows one to take into account the maximum packing fraction. For a square array of fibers, $\phi_{\max} = 0.785$, while for a hexagonal arrangement of fibers, $\phi_{\max} = 0.907$. In general, $\phi_{\max}$ is between these two extremes and near the random packing, $\phi_{\max} = 0.82$.

Example 10.2 Consider a unidirectionally reinforced glass fiber/epoxy composite. The fibers are continuous and 60% by volume. The tensile strength of glass fibers is 1 *GPa,* and the Young's modulus is 70 *GPa*. The tensile strength of the epoxy matrix is 60 *MPa,* and its Young's modulus is 3 *GPa*. Compute the Young's modulus and the tensile strength of the composite in the longitudinal direction.

Solution Young's modulus of the composite in the longitudinal direction is given by

$$E_{cl} = 70 \times 0.6 + 3 \times 0.4 = 42 + 1.2 = 43.2\,GPa.$$

To calculate the tensile strength of the composite in the longitudinal direction, we need to determine which component, fiber or matrix, has the lower failure strain. The failure strain of the fiber is

$$\varepsilon = \sigma_f / E_f = 1/70 = 0.014,$$

while that of the matrix is

$$\varepsilon_m = \left(60 \times 10^{-3}\right)/3 = 0.020.$$

Thus, $\varepsilon_f < \varepsilon_m$, i.e., fibers fail first. At that strain, assuming a linear stress–strain curve for the epoxy matrix, the matrix strength is

$$\sigma_m' = E_m \varepsilon_f = 3 \times 0.014 = 0.042\,GPa.$$

Then, we get the composite tensile strength as

$$\begin{aligned}\sigma_c &= 0.6 \times 1 + 0.4 \times 0.042\\ &= 0.6 + 0.0168 = 617\,MPa.\end{aligned}$$

10.2.4 Transverse Stresses

When a fibrous composite consisting of components with different elastic moduli is uniaxially loaded, stresses in transverse directions arise because of the difference in Poisson's ratio of the matrix and the fiber, that is, because the two components have different contractile tendencies. Here, we follow Kelly's (1970) treatment of this important but, unfortunately, not well-appreciated subject. This problem in elasticity is very useful in computing thermal stresses in composites, in which case the two components have different thermal expansion coefficients.

Consider a unit fiber reinforced composite consisting of a single fiber (radius a) surrounded by its shell of matrix (outer radius b) as shown in Fig. 10.5. The composite as a whole is thought to be built of an assembly of such unit composites, a reasonably valid assumption at moderate fiber volume fractions. We axially load the composite, taking the axis to be along the direction z. Owing to the obvious cylindrical symmetry, we treat the problem in polar coordinates, r, θ, and z. It follows from the axial symmetry that the stress and strain are independent of angle θ and are functions only of r, which simplifies the problem. We can write the Hooke's law for this situation as

$$\begin{bmatrix} e_r & 0 & 0 \\ 0 & e_\theta & 0 \\ 0 & 0 & e_z \end{bmatrix} = \frac{1+\nu}{E} \begin{bmatrix} \sigma_r & 0 & 0 \\ 0 & \sigma_\theta & 0 \\ 0 & 0 & \sigma_z \end{bmatrix} - \frac{\nu}{E}(\sigma_r + \sigma_\theta + \sigma_z) \begin{bmatrix} 1 & 0 & 0 \\ 0 & 1 & 0 \\ 0 & 0 & 1 \end{bmatrix}, \quad (10.22)$$

where e is the strain, σ is the stress, ν is the Poisson's ratio, E is Young's modulus in the longitudinal direction, and the subscripts r, θ, and z refer to the radial, circumferential, and axial directions, respectively. The only equilibrium equation for this problem is

$$\frac{d\sigma_r}{dr} + \frac{\sigma_r - \sigma_\theta}{r} = 0. \quad (10.23)$$

Also, for the plane strain condition, we can write for the strain components, in terms of displacements,

$$e_r = \frac{du_r}{dr} \quad e_\theta = \frac{u_r}{r} \quad e_z = \text{const}, \quad (10.24)$$

where u_r is the radial displacement.

From Eq. (10.22), we have, after some algebraic manipulation,

$$\begin{aligned} \frac{\sigma_\theta}{K} &= (1-\nu)e_\theta + \nu(e_r + e_z) \\ \frac{\sigma_r}{K} &= (1-\nu)e_r + \nu(e_\theta + e_z), \end{aligned} \quad (10.25)$$

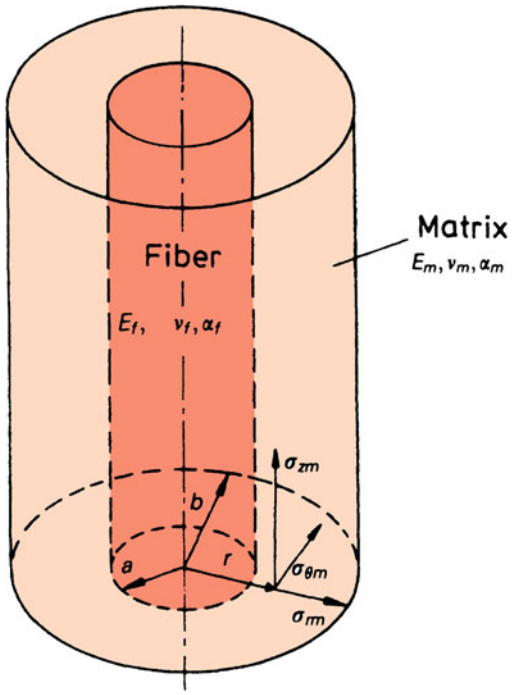

Fig. 10.5 A single fiber surrounded by its matrix shell

where

$$K = \frac{E}{(1+v)(1-2v)}.$$

From Eqs. (10.24) and (10.25), we get

$$\begin{aligned} \frac{\sigma_\theta}{K} &= v\frac{du_r}{dr} + (1-v)\frac{u_r}{r} + ve_z \\ \frac{\sigma_r}{K} &= (1-v)\frac{du_r}{dr} + v\frac{u_r}{r} + ve_z. \end{aligned} \tag{10.26}$$

Substituting Eq. (10.26) in Eq. (10.23), we obtain the following differential equation in terms of the radial displacement u_r:

$$\frac{d^2u_r}{dr^2} + \frac{1}{r}\frac{du_r}{dr} - \frac{u_r}{r^2} = 0. \tag{10.27}$$

Equation (10.27) is a common differential equation in elasticity problems with rotational symmetry (Love 1952), and its solution is

$$u_r = Cr + \frac{C'}{r}, \tag{10.28}$$

where C and C' are the constants of integration to be determined by using boundary conditions. Now, Eq. (10.28) is valid for displacements in both components, that is, fiber and matrix. Let us designate the central component by subscript 1 and the sleeve by subscript 2. Thus, we can write the displacements in the two components as

$$\begin{aligned} u_{r1} &= C_1 r + \frac{C_2}{r} \\ u_{r2} &= C_3 r + \frac{C_4}{r}. \end{aligned} \tag{10.29}$$

The boundary conditions for our problem can be expressed as follows:

1. At the free surface, the stress is zero, that is, $\sigma_{r2} = 0$ at $r = b$.
2. At the interface, the continuity condition requires that at $r = a$, $u_{r1} = u_{r2}$ and $\sigma_{r1} = \sigma_{r2}$.
3. The radial displacement must vanish along the symmetry axis, that is, at $r = 0$, $u_{r1} = 0$.

The last boundary condition immediately gives $C_2 = 0$, because otherwise u_{r1} will become infinite at $r = 0$. By applying the other boundary conditions to Eqs. (10.26) and (10.29), we obtain three equations with three unknowns. Knowing these integration constants, we obtain u_r and thus the stresses in the two components. It is convenient to develop an expression for radial pressure p at the interface. At the interface $r = a$, if we equate σ_{r2} to $-p$, then after some tedious manipulations it can be shown that

$$p = \frac{2e_2(v_2 - v_1)V_2}{V_1/k_{p2} + V_2/k_{p1} + 1/G_2}, \tag{10.30}$$

where k_p is the plane strain bulk modulus equal to $E/2(1 + v)(1 - 2v)$, while the subscripts 1 and 2 refer to the two components. The expressions for the stresses in the components involving radial pressure, p, are

Component 1:

$$\begin{aligned} \sigma_{r1} &= \sigma_{\theta 1} = -p \\ \sigma_{z1} &= E_1 e_z - 2v_1 p. \end{aligned} \tag{10.31}$$

Component 2:

$$\sigma_{r2} = p\left(\frac{a^2}{b^2 - a^2}\right)\left(1 - \frac{b^2}{r^2}\right)$$
$$\sigma_{\theta 2} = p\left(\frac{a^2}{b^2 - a^2}\right)\left(1 + \frac{b^2}{r^2}\right) \tag{10.32}$$
$$\sigma_{z2} = E_2 e_z + 2\nu_2 p\left(\frac{a^2}{b^2 - a^2}\right).$$

Note that p is positive when the central component 1 is under compression, that is, when $\nu_1 < \nu_2$.

Figure 10.6 shows the stress distribution schematically in a fiber composite (1 = fiber, 2 = matrix). We can draw some inferences from Eqs. (10.31) and (10.32) and Fig. 10.6.

1. Axial stress is uniform in components 1 and 2, although its magnitude is different in the two and depends on the respective elastic constants.
2. In the central component 1, σ_{r1} and $\sigma_{\theta 1}$ are equal in magnitude and sense. In the sleeve component 2, σ_{r2} and $\sigma_{\theta 2}$ vary as $1 - b^2/r^2$ and $1 + b^2/r^2$, respectively.
3. When the Poisson's ratio difference ($\nu_2 - \nu_1$) goes to zero, σ_r and σ_θ go to zero, that is, the rheological interaction will vanish.
4. Because of the relatively small difference in the Poisson's ratio of the components of a composite, the transverse stresses that develop in the elastic regime

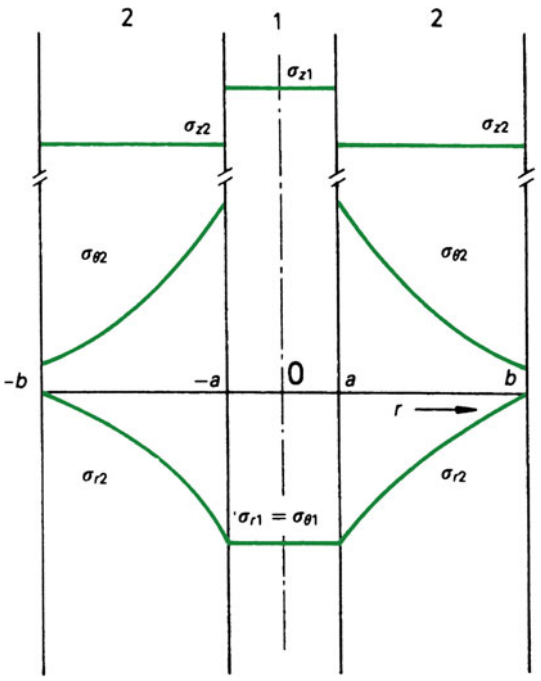

Fig. 10.6 Three-dimensional stress distribution (schematic) in the unit composite shown in Fig. 10.5. In this case, the transverse stresses (σ_r and σ_θ) result from the differences in the Poisson's ratios of the fiber and matrix

will be relatively small. If one of the components deforms plastically ($v \rightarrow 0.5$), then Δv can become significant and so will the transverse stresses.

10.3 Thermal Properties

Thermal energy is responsible for the atomic or molecular vibration about a mean position in any material. As the temperature of a material is increased, the amplitude of thermal energy-induced vibrations is increased and the interatomic or intermolecular spacing increases, i.e., an expansion of the body occurs. Most materials show such an expansion with increasing temperature. In general, the thermal expansion of a material is greater in the liquid state than in the crystalline state, with the transition occurring at the melting point. In the case of a glassy material, such a transition occurs at the glass transition temperature, although it is not as well defined as the one at the melting point. Over a certain range of temperature, one can relate the temperature interval and thermal strain by a coefficient, called the *coefficient of thermal expansion*. In the case of a linear strain, the linear thermal expansion coefficient, α, is a second rank symmetric tensor, and is related to the strain tensor, ε, by the following relationship:

$$\varepsilon_{ij} = \alpha_{ij} \Delta T, \tag{10.33}$$

where ΔT is the temperature change. The two indexes indicate the second rank tensor. The thermal expansion coefficient, α, generally does not have a constant value over a very large range of temperature. Thus, we can define α_{ij} in a more general way by taking into account this variation with temperature as follows:

$$\alpha_{ij} = \delta \varepsilon_{ij} / \delta T,$$

where $\delta \varepsilon_{ij}$ and δT are small strain and temperature intervals, respectively. If we consider a volumetric strain, the volumetric coefficient of thermal expansion, β, is given by

$$\beta_{ij} = \frac{1}{V} \left(\frac{\delta V}{\delta T} \right),$$

where δV is the small volume interval and δT is the small temperature interval. For small strains, it can be easily shown that

$$\beta_{ij} = 3\alpha_{ij}.$$

Recall that the sum of the diagonal terms of the strain tensor is equal to volume change. Hence, the volumetric expansion coefficient, β, is equal to the sum of the diagonal terms of the strain tensor, i.e.,

$$\beta = \varepsilon_{11} + \varepsilon_{22} + \varepsilon_{33} = 3\alpha, \tag{10.34a}$$

or

$$\alpha = \frac{1}{3}[\varepsilon_{11} + \varepsilon_{22} + \varepsilon_{33}]. \tag{10.34b}$$

As we said earlier, only over some specified range of temperature, the coefficient of thermal expansion can be treated as a constant. Consider a temperature range ΔT over which α is a constant. We can write Eq. (10.33) in an extended form as

$$\begin{vmatrix} \varepsilon_{11} & \varepsilon_{12} & \varepsilon_{13} \\ & \varepsilon_{22} & \varepsilon_{23} \\ & & \varepsilon_{33} \end{vmatrix} = \begin{vmatrix} \alpha_{11} & \alpha_{12} & \alpha_{13} \\ & \alpha_{22} & \alpha_{23} \\ & & \alpha_{23} \end{vmatrix} \Delta T. \tag{10.35a}$$

Or, using the contracted notation (see Sect. 11.1), we can write

$$\begin{vmatrix} \varepsilon_1 \\ \varepsilon_2 \\ \varepsilon_3 \\ \varepsilon_4 \\ \varepsilon_5 \\ \varepsilon_6 \end{vmatrix} = \begin{vmatrix} \alpha_1 \\ \alpha_2 \\ \alpha_3 \\ \alpha_4 \\ \alpha_5 \\ \alpha_6 \end{vmatrix} \Delta T. \tag{10.35b}$$

If an arbitrary direction $[hkl]$ has direction cosines n_1, n_2, and n_3, then we can write for the linear thermal expansion coefficient, α_{hkl}, in that direction

$$\alpha_{hkl} = n_1^2\alpha_1 + n_2^2\alpha_2 + n_3^2\alpha_3. \tag{10.36}$$

In a transversely isotropic fibrous composite (i.e., hexagonal symmetry), we have $\alpha_1 = \alpha_2 = \alpha_\perp$, perpendicular to the fiber axis and $\alpha_3 = \alpha_{||}$, parallel to the fiber axis. Then, remembering the property of direction cosines that $n_1^2 + n_2^2 + n_3^2 = 1$, Eq. (10.36) becomes

$$\alpha_{hkl} = \left(n_1^2 + n_2^2\right)\alpha_1 + n_3^2\alpha_3$$

$$\alpha_{hkl} = \alpha_\perp \sin^2\theta + \alpha_{||}\cos^2\theta \tag{10.37a}$$

$$\alpha_{hkl} = \alpha_\perp + \left(\alpha_{||} - \alpha_\perp\right)\cos^2\theta, \tag{10.37b}$$

where θ is the angle between direction $[hkl]$ and the fiber axis.

10.3.1 Expressions for Coefficients of Thermal Expansion (CTE) of Composites

Various equations have been proposed that give the thermal expansion coefficients of a composite, knowing the material constants of the components and their geometric arrangements. Different equations predict very different values of expansion coefficients for a given composite. Almost all expressions, however, predict expansion coefficient values that are different from those given by a simple rule-of-mixtures (= $\alpha_f V_f + \alpha_m V_m$). This is because these equations take into account the important fact that the presence of a reinforcement, with an expansion coefficient less than that of the matrix, introduces a mechanical constraint on the matrix. A fiber will cause a greater constraint on the matrix than a particle. Let us consider the expansion coefficients of particulate and fibrous composites.

One can regard a particulate composite as a homogeneous material in a statistical sense, assuming a uniform distribution of the particles in the matrix. Let us denote the volume fractions of the two phases making a particulate composite by V_1 and V_2 (= 1 − V_1). Various researchers have derived bounds and given expressions for the expansion coefficients and other transport properties such as thermal conductivity. Kerner (1956) developed the following expression for the volumetric expansion coefficient, β_c, of a composite consisting of spherical particles dispersed in a matrix:

$$\beta_c = \beta_m V_m + \beta_p V_p - (\beta_m - \beta_p) V_p \left[\frac{1/K_m - 1/K_p}{V_m/K_p + V_p/K_m + 0.75 G_m} \right],$$

where subscripts c, m, and p denote the composite, matrix, and particle, respectively; β is the volumetric expansion coefficient, and K denotes the bulk modulus. Kerner's expression does not differ significantly from the rule-of-mixtures because the particle reinforcement constrains the matrix much less than fibers. The coefficient of linear thermal expansion according to Turner (1946) is given by

$$\alpha_c = \frac{\alpha_m V_m K_m + \alpha_p V_p K_p}{V_p K_p + V_m K_m},$$

where the symbols have the significance given earlier. Turner's expression, generally, gives an expansion coefficient much lower than the rule-of-mixtures value.

Unidirectionally aligned fibrous composites have two (or sometimes three) thermal expansion coefficients: α_{cl} in the longitudinal direction and α_{ct} in the transverse direction. Fibers generally have a lower expansion coefficient than that of the matrix, and thus the fibers mechanically constrain the matrix. The constraint is more along the length of the fiber than in the radial direction. This results in the longitudinal coefficient of expansion of the composite, α_{cl} being smaller than the transverse coefficient, α_{ct} for the composite. At low fiber volume fractions, it is not unusual to find the transverse expansion of a fibrous composite, α_{ct}, greater than that of the matrix in isolation. The reason for this is as follows. The long, stiff, low CTE

fibers prevent the matrix from expanding in the longitudinal direction, and as a result the matrix is forced to expand more than normal in the transverse direction. It should be pointed out that in the case of some CMCs, this situation can be reversed. For example, in the case of alumina fibers ($\alpha = 8 \times 10^{-6}\ K^{-1}$) in a low-expansion glass or ceramic matrix, it is the matrix that will constrain the fibers, i.e., the situation in this case is the reverse of the one commonly encountered.

We give below some expressions for the coefficients of thermal expansion of unidirectionally reinforced fibrous composites. All of these analyses involve the following assumptions:

1. The bonding between the fiber and matrix is perfect and mechanical in nature, i.e., no chemical interaction is allowed.
2. The fibers are continuous and perfectly aligned.
3. The properties of the constituents do not change with temperature.

Schapery (1969) used energy methods to derive the following expressions for expansion coefficient of a fiber reinforced composite, assuming Poisson's ratios of the components are not very different. The longitudinal expansion coefficient for the composite is

$$\alpha_{cl} = \frac{\alpha_m E_m V_m + \alpha_f E_f V_f}{E_m V_m + E_f V_f}, \tag{10.38}$$

and the transverse expansion coefficient is

$$\alpha_{ct} \simeq (1+\nu_m)\alpha_m V_m + (1+\nu_f)\alpha_f V_f - \alpha_{cl}\bar{\nu} \tag{10.39a}$$
$$\bar{\nu} = \nu_f V_f + \nu_m V_m$$

For high fiber volume fractions, $V_f > 0.2$ or 0.3, α_{ct} can be approximated by

$$\alpha_{ct} = (1+\nu_m)\alpha_m V_m + \alpha_f V_f. \tag{10.39b}$$

The longitudinal and transverse coefficients of thermal expansion for a composite made of alumina fibers in an aluminum matrix are plotted in Fig. 10.7. Note the marked anisotropy in the expansion for aligned fibrous composites.

The anisotropy in expansion can be reduced somewhat if the composite contains randomly oriented short fibers or whiskers in three dimensions. We can write its isotropic thermal expansion coefficient

$$\alpha = \frac{\alpha_{cl} + 2\alpha_{ct}}{3}, \tag{10.40}$$

where α_{cl} and α_{ct} are given by Eqs. (10.38) and (10.39a, 10.39b).

It should be pointed out that the length of fiber as well as fiber orientation has an effect on the coefficients of thermal expansion (Marom and Weinberg 1975; Vaidya et al. 1994). It would appear that the fiber length has a more sensitive effect on the

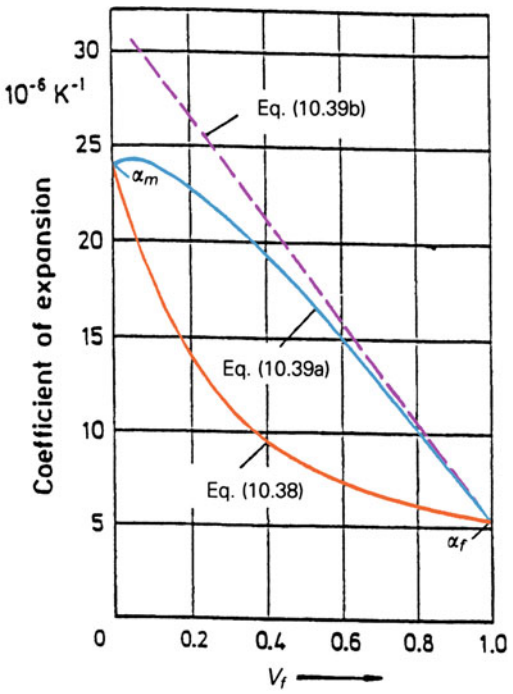

Fig. 10.7 Longitudinal and transverse linear thermal expansion coefficients versus fiber volume fraction for a composite of alumina fiber in an aluminum matrix

expansion characteristics because the constraint on the matrix is highest when the fibers are continuous. An extreme case of a low constraint is one of the matrix containing spherical particles, i.e., aspect ratio = 1. Continuous fibers with an aspect ratio of infinity represent the other extreme in constraint.

The effect of the fiber length on the thermal expansion can be incorporated into Schapery's equation as (Marom and Weinberg 1975; Vaidya and Chawla 1994)

$$\alpha_{11} = \frac{k\alpha_f V_f E_f + \alpha_m V_m E_m + \alpha_i V_i E_i}{kV_f E_f + V_m E_m + V_i E_i},$$

where the value of k is given by

$$\begin{aligned} k &= \tfrac{l}{2l_c} \quad (l < l_c, 0 < k < 0.5) \\ k &= 1 - l_c/2l \quad (l > l_c, 0 < k < 1) \end{aligned},$$

where l is the length and l_c is the critical length of the fiber (see Sect. 10.4).

Chamis (1983) used a simple force balance to arrive at the following expressions for α_1 and α_2:

$$\alpha_1 = \left[\frac{E_{f1}\alpha_{f_1}V_f + E_m\alpha_m V_m}{E_{f1}V_f + E_m V_m}\right]$$
$$\alpha_2 = \alpha_{f2}\sqrt{V_f} + \left(1 - \sqrt{V_f}\right)\left(1 + V_f v_m \frac{E_{f1}}{E_c}\right)\alpha_m.$$

Rosen and Hashin (1970) used a plane strain model to derive expressions for α_1 and α_2:

$$\alpha_1 = \bar{\alpha} + \left[\frac{\alpha_f - \alpha_m}{1/K_f - 1/K_m}\right]\left[\frac{3(1-3v_c)}{E_c} - \frac{1}{K_c}\right]$$
$$\alpha_2 = \bar{\alpha} + \left[\frac{\alpha_f - \alpha_m}{1/K_f - 1/K_m}\right]\left[\frac{3}{2k_c} - \frac{3(1-2v_c)v_c}{E_c} - \frac{1}{K_c}\right],$$

where $\bar{\alpha} = \alpha_f V_f + \alpha_m V_m$, K_c is the composite bulk modulus, E_c is the composite elastic Young's modulus, v_c is the composite Poisson's ratio, and k_c is the composite transverse bulk modulus.

Many applications of composites require controlled thermal expansion characteristics. All the expressions given above predict thermal expansion coefficients of composites based on continuum mechanics. That is, no account is taken of the effect of fiber or particle size on the coefficient of thermal expansion (CTE). Xu et al. (1994) examined the effect of particle size on the CTE of TiC/Al composite, with two TiC particle sizes, 0.7 and 4 μm. The results of this work showed the effect of particle size on the thermal expansion coefficient of particle reinforced aluminum composites in terms of the degree of constraint on the matrix expansion. Careful TEM work showed lattice distortion at the interfacial zone. The effect of particle size on the CTE of composite was related to the volume fraction of interfacial zone through which the constraint occurs. A phenomenological approach that takes into account the different degrees of constraint on the matrix expansion based on the TEM work was used to compute the CTE of this composite with different particle sizes.

10.3.2 Expressions for Thermal Conductivity of Composites

Thermal conductivity is an important physical property. The heat flow in a material is proportional to the temperature gradient, and the constant of proportionality is called the *thermal conductivity*. Thus, in the most general form, using indicial notation, we can write

$$q_i = -k_{ij}dT/dx_j,$$

where q_i is the heat flux along the x_i-axis, dT/dx_j is the temperature gradient across a surface perpendicular to the x_j-axis, and k_{ij} is the thermal conductivity. As should be

evident from the two indexes, thermal conductivity is also a second rank tensor. Although k_{ij} is not a symmetric tensor in the most general case, it is a symmetric tensor for most crystal systems. For an isotropic and a cubic material, k_{ij} reduces to a scalar number, k. For an orthotropic material, we have three constants along the three principal axes, viz., k_{11}, k_{22}, and k_{33}. For a transversely isotropic material such as a unidirectionally reinforced fibrous composite, there will be two constants: thermal conductivity in the axial direction, k_{cl}, and that in the transverse direction, k_{ct}. The thermal conductivity in the axial direction, k_{cl}, can be predicted by a rule-of-mixtures type expression (Behrens 1968)

$$k_1 = k_{cl} = k_{f1}V_f + k_m V_m, \tag{10.41}$$

where k_{f1} is the thermal conductivity of the fiber in the axial direction, k_m is that of the isotropic matrix, and V_f and V_m are the volume fractions of the fiber and matrix, respectively.

In a transverse direction, the thermal conductivity of a unidirectionally aligned fiber composite (i.e., transversely isotropic) can be approximated by the action-in-series model discussed earlier. This would give

$$k_{ct} = k_2 = k_{f2}k_m/\left(k_{f2}V_f + k_m V_m\right).$$

More complicated expressions have been derived for the transverse thermal conductivity. These expressions have implicit assumption of perfect contact between the fiber and the matrix. In real composites, it is likely that the thermal contact at the fiber/matrix interface will be less than perfect because of any microvoids, thermal mismatch, etc. An expression for the transverse thermal conductivity that takes into account the fact that the interface region may have a different thermal conductance than the matrix or the fiber is as follows (Hasselman and Johnson 1987):

$$\begin{aligned} k_{ct} = k_2 = k_m\big[&\left(k_f/k_m - 1 - k_f/ah_i\right)V_f \\ &+ \left(1 + k_f/k_m + k_f ah_i\right)\big]/\big[\left(1 - k_f/k_m + k_f/ah_i\right)V_f. \\ &+ \left(1 + k_f/k_m + k_f/ah_i\right) \end{aligned} \tag{10.42}$$

where k_m is the matrix thermal conductivity, k_f is the transverse thermal conductivity of the fibers, V_f is the fiber volume fraction, a is the fiber radius, and h_i is the thermal conductance of the interface region. Note that the units of thermal conductivity are W/mK, while for thermal conductance the units are W/K. The effect of interfacial conductivity is governed by the magnitude of nondimensional parameter, k_f/ah_i. h_i will have a value of infinity for perfect thermal contact and it will be equal to zero for a pore. Bhatt et al. (1992) studied the important role of interface in controlling the effective thermal conductivity of composites. In particular, one can use the measurement of thermal conductivity as a nondestructive tool to determine the integrity of the fiber/matrix interface.

We can also use Halpin–Tsai–Kardos equations to obtain the following expression for the transverse thermal conductivity of a composite containing unidirectionally aligned fibers:

$$k_{c2} = k_{c3} = k_{ct} = \left(1 + \eta V_f\right)/\left(1 - \eta V_f\right)k_m,$$

and

$$\eta = \left[\left(k_{f2}/k_m\right) - 1\right]/\left[\left(k_{f2}/k_m\right) + 1\right],$$

where we have taken ζ equal to 1 in the Halpin–Tsai–Kardos equation.

Similar to the description of the coefficient of thermal expansion, we can find thermal conductivity of a unidirectionally reinforced fiber composite if we know the thermal conductivity in directions 1 (longitudinal) and 2 (transverse). The thermal conductivity k_x and k_y in any arbitrary directions, x and y, respectively, are given by the following equations:

$$\begin{aligned} k_x &= k_1 \cos^2\theta + k_2 \sin^2\theta \\ k_y &= k_1 \sin^2\theta + k_2 \cos^2\theta \\ k_{xy} &= (k_2 - k_1)\sin\theta\cos\theta \end{aligned},$$

where θ is the angle between longitudinal (1) axis and the x-axis, and k_{xy} can be considered to be a thermal coupling coefficient.

A summary of the general expressions for the thermal properties of a transversely isotropic fiber composite is given in Table 10.4.

Example 10.3 A unidirectional glass fiber reinforced epoxy has 50 vol% of fiber. Estimate its thermal conductivity parallel to the fibers. Given $k_{\text{glass}} = 0.9$ *W/mK*, $k_{\text{epoxy}} = 0.15$ *W/mK*.

Solution Glass fiber is isotropic, i.e., $k_{f1} = k_{f2} = k_f$. The longitudinal thermal conductivity is given by

Table 10.4 Thermal properties of a transversely isotropic composite (matrix isotropic, fiber anisotropic)

Heat capacity	$C = \frac{1}{\rho}\left(V_f \rho_f C_f + V_m \rho_m C_m\right)$
Longitudinal conductivity	$k_{11} = V_f k_{f1} + V_m k_m$
Transverse conductivity	$k_{22} = k_{33} = \left(1 - \sqrt{V_f}\right)k_m + \frac{k_m\sqrt{V_f}}{1 - \sqrt{V_f\left(1 - k_m/k_{f2}\right)}}$
Longitudinal thermal expansion coefficient	$\alpha_{11} = \frac{V_f E_{f1}\alpha_{f1} + V_m E_m \alpha_m}{E_{f1}V_f + E_m V_m}$
Transverse thermal expansion coefficient	$\alpha_{22} = \alpha_{33} = \alpha_{f2}\sqrt{V_f} + \alpha_m\left(1 - \sqrt{V_f}\right)\left(1 + \frac{V_f \nu_m E_{f1}}{E_{f1}V_f + E_m V_m}\right)$

Source Adapted with permission from Chamis (1983)

$$\begin{aligned} k_{ct} &= V_m k_m + V_f k_f \\ &= 0.5 \times 0.15 + 0.5 \times 0.9 \\ &= 0.075 + 0.45 = 0.525\, W/mK. \end{aligned}$$

Example 10.4 Derive an expression for the heat capacity, C_{pc}, of a composite.

Solution The total quantity of heat in the composite, Q_c, is the sum of heats in the fiber (Q_f) and matrix (Q_m). Thus,

$$Q_c = Q_f + Q_m.$$

The quantity of heat is heat capacity times the mass, i.e.,

$$Q = mC_p = v\rho C_p,$$

where m is the mass, v is the volume, ρ is the density, and C_{pc} is the heat capacity. Heat capacity is the amount of heat or thermal energy (J) required to raise the temperature of one mole of the material through one degree. It has the units of *J/mol K*. The specific heat of a material is the heat capacity per unit mass, and it has the units of *J/g K*.

Using the subscripts c, f, and m for composite, fiber, and matrix, respectively, we can write

$$v_c \rho_c C_{pc} = v_f \rho_f C_{pf} + v_m \rho_m C_{pm}.$$

Remembering that $v_f/v_c = V_f$, the fiber volume fraction, and $v_m/v_c = V_m$, the matrix volume fraction, we can write

$$\rho_c C_{pc} = V_f \rho_f C_{pf} + V_m \rho_m C_{pm}$$

or

$$C_{pc} = \frac{1}{\rho_c}\left[V_f \rho_f C_{pf} + V_m \rho_m C_{pm}\right].$$

10.3.3 Electrical Conductivity

Electrical conductivity (or its inverse electrical resistivity) is another important physical property. In terms of electrical conductivity, composites represent a mixed bag. PMCs and CMCs are generally poor electrical conductors. The electrical conductivity of polymers can be increased by the addition of carbon fibers, carbon black, and graphite particles. Such composites care used for situations involving

electromagnetic and radio frequency interference (EMI/RFI) shielding for electronic devices and for dissipation of static charge (Clingerman et al. 2002). Most metal matrix composites are mixtures of good electrical conductors (e.g., Cu, Al, etc.) and insulators (e.g., B, SiC, Al_2O_3, etc.), with W/Cu composite being a notable exception. We can write for the resistivity of a fiber reinforced composite in the axial direction a simple rule-of-mixtures type expression

$$\rho_{c\ell} = \rho_1 V_1 + \rho_2 V_2,$$

where ρ is the electrical resistivity, V is volume fraction, and the subscripts cℓ, 1, and 2 designate the composite in the longitudinal direction and the two components of the composite, respectively. Or in terms of electrical conductivity in the axial direction, σ, we can write

$$\sigma_{c\ell} = \sigma_1 V_1 + \sigma_2 V_{2.}.$$

In the transverse direction, we have

$$\frac{1}{\sigma_{ct}} = \frac{V_1}{\sigma_1} + \frac{V_2}{\sigma_2},$$

where the symbols have the usual significance.

There is a logarithmic expression also for electrical conductivity,

$$\log \sigma_c = V_1 \log \sigma_1 + V_2 \log \sigma_{2,}$$

where the symbols have the significance given above. Of course, one can generalize these expressions to more than two components in the composite, should that be the case. Self-consistent models can also be used to get expressions for the electrical conductivity of a composite (Hale 1976).

The electrical resistivity (and therefore electrical conductivity) of the metal matrix in a composite is likely to be different from that of the unreinforced metal because of possible plastic deformation during processing which will introduce dislocations due to thermal mismatch between the matrix and the reinforcement; the dislocations in turn will increase the resistivity of the matrix. It should be pointed out that unlike the unreinforced metal, one cannot recover electrical conductivity by resorting to an annealing treatment. Physical properties such as thermal and electrical conductivity of composites depend on the properties of the matrix and reinforcement, their volume fractions, characteristics of the interface region, shape of the reinforcement, and the connectivity of the phases (Weber et al. 2003a, b; Weber 2005). The conductivity (thermal or electrical) of a composite will depend on conductivity characteristics of the matrix, reinforcement, volume fraction and aspect ratio of the reinforcement, and, of course, the interfacial characteristics. In particular, interfacial resistance will vary with the form and size of reinforcement.

10.3.4 Hygral and Thermal Stresses

Hygroscopy, the ability of a substance to absorb water, can be a problem with polymeric resins and natural fibers because it can lead to swelling. Swelling can lead to stresses if, as is likely in a composite, the material is not allowed to expand freely because of the presence of a second component. Such stresses resulting from moisture absorption or hygroscopy are called *hygral stresses*. Thermal stresses will result in a material when the material is not allowed to expand or contract freely because of a constraint. When both hygral and thermal stresses are present, we call them *hygrothermal stresses.* Mathematically, these two types of internal stresses are quite similar, and we can treat them together.

Consider the passage of a composite from a reference state, where the body is stress-free and relaxed at a temperature T, concentration of moisture $C = 0$, and external stress $\sigma = 0$, to a final state where the body has hygrothermal as well as external stresses. We can consider that the final state of the composite with hygrothermal stresses and external loading is attained via two intermediate stages shown in Fig. 10.8. The final strain in the body can then be written as the sum of nonmechanical (thermal strain, e_i^T, and hygral strain, e_i^H) and mechanical strains. The mechanical strain is given by the Hooke's law (compliance times the stress). Thus,

$$e_t = \underbrace{e_i^T + e_i^H}_{\text{nonmechaical strains}} + \underbrace{S_{ij}\sigma_j}_{\text{mechanical strain}}, \tag{10.43}$$

where S_{ij} is the compliance. If we regard the composite as transversely isotropic, we can immediately write the following relationships for the strain components:

$$\begin{gathered} e_{xy}^T = e_{xy}^H = 0 \\ e_y^T = e_z^T \quad \text{and} \quad e_y^H = e_z^H \\ e_i^T = \alpha_i (T - T_0) \\ e_i^H = \beta_i C \end{gathered}, \tag{10.44}$$

where the α_i are thermal expansion coefficients (K^{-1}), the β_i are nondimensional swelling coefficients, T is the temperature, T_0 is the equilibrium temperature, C is the concentration of water vapor, and the superscripts H and T indicate hygral and thermal strain components, respectively.

Total volumetric hygrothermal strain can be expressed as the sum of the diagonal terms of the strain matrix. It is important to note that the thermal and hygral effects are dilational only, i.e., they cause only expansion or contraction but do not affect the shear components. Thus,

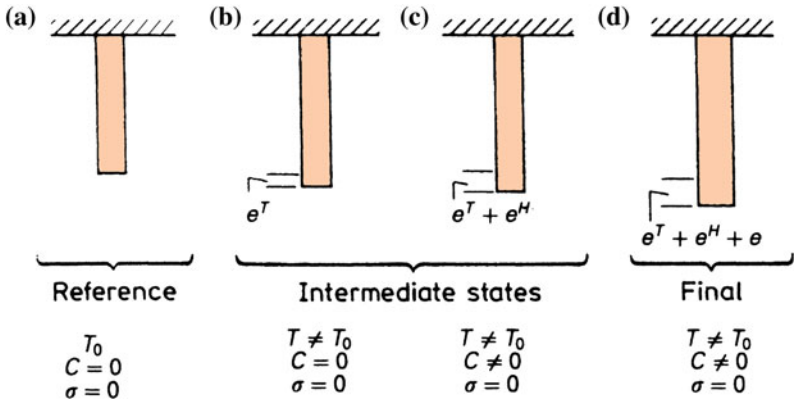

Fig. 10.8 **a** Strain-free reference state; **b** thermal strain (e^T); **c** hygral (e^H) and thermal (e^T) strains; and **d** final state: hygral (e^H), thermal (e^T), and mechanical strain

$$\begin{aligned}\frac{\Delta V}{V} &= e_x^T + e_y^T + e_z^T + e_x^H + e_y^H + e_z^H \\ &= e_x^T + 2e_y^T + e_x^H + 2e_y^H .\end{aligned} \tag{10.45}$$

Hygrothermal stresses are very important in polymer matrix composites (see also Chaps. 3 and 4).

We first consider the constitutive equations for an isotropic material and then for an anisotropic material. Consider an isotropic material, inplane stress, subjected to a temperature change, ΔT, and a change in moisture content, ΔC. We can write the constitutive equations for this case as follows:

$$\begin{aligned}\varepsilon_1 &= \sigma_1/E - \nu\sigma_2/E + \beta\Delta C + \alpha\Delta T \\ \varepsilon_2 &= \nu\sigma_1/E - \sigma_2/E + \beta\Delta C + \alpha\Delta T . \\ \varepsilon_6 &= \sigma_6/G\end{aligned}$$

Note that, as pointed out earlier, ΔC and ΔT do not produce shear strains. For a specially orthotropic, unidirectionally reinforced fiber reinforced lamina (i.e., one in which material and geometric axes coincide, see also Chap. 11), we can write

$$\begin{bmatrix}\varepsilon_1 \\ \varepsilon_2 \\ \varepsilon_6\end{bmatrix} = \begin{bmatrix}S_{11} & S_{12} & 0 \\ & S_{22} & 0 \\ & & S_{66}\end{bmatrix}\begin{bmatrix}\sigma_1 \\ \sigma_2 \\ \sigma_6\end{bmatrix} + \begin{bmatrix}\alpha_1 \\ \alpha_2 \\ 0\end{bmatrix}\Delta T + \begin{bmatrix}\beta_1 \\ \beta_2 \\ 0\end{bmatrix}\Delta C.$$

In this expression, the subscript 6 indicates inplane shear. We explain this notation in detail in Chap. 11. In a PMC, the matrix is likely to absorb more moisture than the fiber, which will lead to $\beta_2 > \beta_1$. In an off-axis, generally orthotropic, unidirectionally reinforced fiber reinforced lamina, the material and geometric axes do not coincide, and the strain components take the following form:

$$\begin{bmatrix} \varepsilon_x \\ \varepsilon_y \\ \varepsilon_s \end{bmatrix} = \begin{bmatrix} \overline{S_{11}} & \overline{S_{12}} & \overline{S_{16}} \\ \overline{S}_{21} & \overline{S_{22}} & \overline{S_{26}} \\ \overline{S}_{61} & \overline{S}_{62} & \overline{S_{66}} \end{bmatrix} \begin{bmatrix} \sigma_x \\ \sigma_y \\ \sigma_s \end{bmatrix} + \begin{bmatrix} \alpha_x \\ \alpha_y \\ \alpha_s \end{bmatrix} \Delta T + \begin{bmatrix} \beta_x \\ \beta_y \\ \beta_s \end{bmatrix} \Delta C,$$

where $\overline{S_{ij}}$ designate the compliance matrix for the generally orthotropic lamina.

10.3.5 Thermal Stresses in Composites

During curing or solidification of the matrix around reinforcement fibers or particles, a large magnitude of shrinkage stresses can result. The interfacial pressure developed during curing is akin to that obtained upon embedding a cylinder (sphere) of radius $r + \delta r$ in a cylindrical (spherical) hole of radius r. The thermal stresses generated depend on the reinforcement volume fraction, reinforcement geometry, thermal mismatch ($\Delta\alpha$), and the modulus ratio, E_r/E_m where E is the Young's modulus and the subscripts r and m refer to the reinforcement and matrix, respectively. Generally, $\alpha_m > \alpha_f$, that is, on cooling from T_0 to T ($T_0 > T$), the matrix would tend to contract more than the fibers, causing the fibers to experience axial compression. In extreme cases, fiber buckling can also lead to the generation of interfacial shear stresses. This problem of thermal stresses in composite materials is a most serious and important problem. It is worth repeating that thermal stresses are internal stresses that arise whenever there is a constraint on the free dimensional change of a body (Chawla 1973a). In the absence of this constraint, the body can experience free thermal strains without any accompanying thermal stresses. The constraint can have its origin in (1) a temperature gradient, (2) crystal structure anisotropy (e.g., a noncubic structure), (3) phase transformations resulting in a volume change, and (4) a composite material made of dissimilar materials (i.e., materials having different CTEs). The thermal gradient problem is a serious one in ceramic materials in general. A thermal gradient ΔT is inversely related to the thermal diffusivity, a of a material. Thus,

$$\Delta T = \phi\left(\frac{1}{a}\right) = \phi\left(\frac{C_p p}{k}\right), \tag{10.46}$$

where C_p is the specific heat, ρ is the density, and k is the thermal conductivity. Metals generally have high thermal diffusivity and any thermal gradients that might develop are dissipated rather quickly. It should be emphasized that in composite materials even a uniform temperature change (i.e., no temperature gradient) will result in thermal stresses owing to the ever present thermal mismatch (Chawla 1973a). Thermal stresses resulting from a thermal mismatch will generally have an expression of the form

$$\sigma = f(E\Delta\,\alpha\,\Delta T). \tag{10.47}$$

We describe below first the three-dimensional thermal stress state in a composite consisting of a central fiber surrounded by its shell of matrix; see Fig. 10.5. After this, we derive the three-dimensional stress state for a particulate composite.

The elasticity problem is basically the same as the one we discussed for transverse stresses (see Sect. 10.2.4). We use polar coordinates; r, θ, and z (see Fig. 10.5). Axial symmetry makes shear stresses go to zero, and the principal stresses are independent of θ. At low volume fractions, the outer cylinder is the matrix and the inner cylinder is the fiber. The expressions for strain in the generalized Hooke's law contain an $\alpha\Delta T$ term. Thus, for component 2,

$$\begin{aligned}
e_{r2} &= \frac{\sigma_{r2}}{E_2} - \frac{\nu_2}{E_2}(\sigma_{\theta 2} + \sigma_{r2}) + \alpha_2 \Delta T \\
e_{\theta 2} &= \frac{\sigma_{\theta 2}}{E_2} - \frac{\nu_2}{E_2}(\sigma_{r2} + \sigma_{z2}) + \alpha_2 \Delta T \\
e_{z2} &= \frac{\sigma_{z2}}{E_2} - \frac{\nu_2}{E_2}(\sigma_{r2} + \sigma_{\theta 2}) + \alpha_2 \Delta T.
\end{aligned}$$

The resultant stresses in 1 and 2 will have the form (see Sect. 10.2.4)

$$\begin{array}{ll}
\textit{Component}\ 1 & \textit{Component}\ 2 \\
\sigma_{r1} = A_1 & \sigma_{r2} = A_2 - \frac{B_2}{r^2} \\
\sigma_{\theta 1} = A_1 & \sigma_{\theta 2} = A_2 + \frac{B_2}{r^2} \\
\sigma_{z1} = C_1 & \sigma_{z2} = C_2
\end{array}. \tag{10.48}$$

Here, A_1, A_2, B_2, C_1, and C_2 are constants. The following boundary conditions exist for our problem:

1. At the interface $r = a$, $\sigma_{r1} = \sigma_{r2}$ for stress continuity.
2. At the free surface $r = b$, $\sigma_{r2} = 0$.
3. The resultant of axial stress σ_z on a section z = constant is zero.
4. Radial displacements in the two components are equal at the interface, that is, at $r = a$, $u_{r1} = u_{r2}$.
5. The radial displacement in component 1 must vanish at the symmetry axis, that is, at $r = 0$, $u_{r1} = 0$.

Using these boundary conditions, it is possible to determine the constants given in Eq. (10.48). The final equations for the matrix sleeve are given here (Poritsky 1934; Chawla 1973b):

$$\sigma_r = A\left(1 - \frac{b^2}{r^2}\right) \quad \sigma_\theta = A\left(1 + \frac{b^2}{r^2}\right) \quad \sigma_z = B, \tag{10.49}$$

where we have omitted the subscript 2 for the matrix for simplicity and the constants A and B have the following expressions:

$$A = -\left[\frac{E_m(\alpha_m - \alpha_f)\Delta T(a/b)^2}{1+(a/b)^2(1-2v)\left[(b/a)^2-1\right]E_m/E_f}\right]$$

$$B = \frac{A}{(a/b)^2} \times \left[2v\left(\frac{a}{b}\right)^2 + \frac{1+(a/b)^2(1-2v)+(a/b)^2(1-2v)\left[(b/a)^2-1\right]E_m/E_f}{1+\left[(b/a)^2-1\right]E_m/E_f}\right]$$

$$v_m = v_f = v.$$

A plot of σ_r, σ_θ, and σ_z against r/a, where r is the distance in the radial direction and a is the fiber radius, is shown in Fig. 10.9 for the system W fiber/Cu matrix for two fiber volume fractions (Chawla and Metzger 1972). Note the change in stress level of σ_z with V_f. This thermoelastic solution can provide information about the magnitude of the elastic stresses involved. A comparison with the yield or fracture strength of the matrix can inform us whether or not plastic deformation or fracture of matrix will occur. Also, if the matrix deforms plastically in response to these thermal stresses, the plots of thermal stress distribution can tell where the plastic deformation will begin. Chawla and Metzger (1972) and Chawla (1973a, b, 1974, 1976a, b), in a series of studies with metal matrix composites, showed that the magnitude of the thermal stresses generated is large enough to deform the soft metallic matrix plastically. Depending on the temperatures involved, the plastic deformation of the metal matrix could involve slip, twinning, cavitation, grain boundary sliding and/or migration. They measured the dislocation densities in the copper matrix of tungsten filament/copper single crystal composites by the etch-pitting technique and showed that the dislocation densities were higher near the fiber/matrix interface than away from the interface, indicating that the plastic deformation, in response to thermal stresses, initiated at the interface. Figure 10.10 shows the variation of dislocation density ($\simeq$ etch pit density) versus distance from the interface. The increase in the dislocation density in the plateau region with V_f (in Fig. 10.10) is due to a higher σ_z with higher V_f value (see Fig. 10.9). Tresca or von Mises yield criteria applied to the stress situation shown in Fig. 10.9 will indicate that the matrix plastic flow starts at the interface. Dislocation generation due to thermal mismatch between reinforcement and a metallic matrix has also been observed in TEM by many researchers (e.g., Arsenault and Fisher 1983; Vogelsang et al. 1986); see Fig. 10.11a. In the case of a fiber reinforced CMC, the ceramic matrix is unlikely to undergo plastic deformation; it is more likely to suffer microcracking as result of thermal stresses. As an example of this, consider a composite made of $CaTiO_3$ and Al_2O_3. The laminated composite was made by hot pressing of these two ceramic components, which involved a cooldown of about 1000 °C. Such a temperature excursion would result in tensile stress in $CaTiO_3$ because $CaTiO_3$ has a larger CTE ($13 \times 10^{-6}\ K^{-1}$) compared to Al_2O_3 ($8 \times 10^{-6}\ K^{-1}$). The magnitude of tensile stress is large enough to cause cracks in

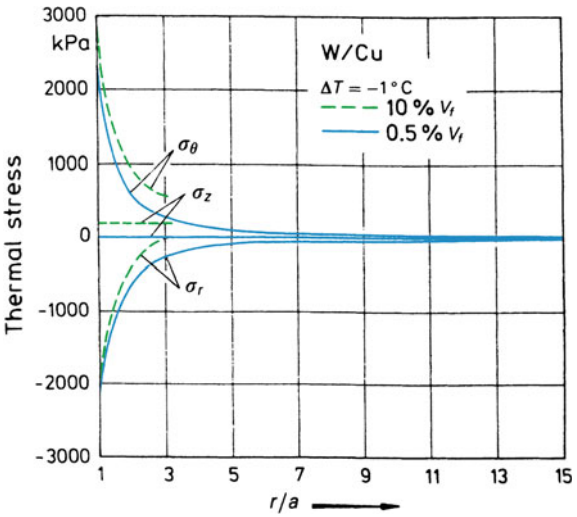

Fig. 10.9 Three-dimensional thermal stress state in a tungsten fiber/copper matrix composite for two different volume fractions. Note the change in σ_z level with V_f. (From Chawla and Metzger 1972, used with permission)

$CaTiO_3$ during cooldown after hot pressing; see the cracks in the $CaTiO_3$ layer in Figure 10.11b (Gladysz and Chawla 2001).

The particulate form of reinforcement can result in a considerably reduced degree of anisotropy. However, so long as a thermal mismatch exists between the particle and the matrix, thermal stresses will be present in such composites as well. Consider a particulate composite consisting of small particles distributed in a matrix. If we regard this composite as an assembly of elastic spheres of uniform size embedded in an infinite elastic continuum, then it can be shown from the theory of elasticity (see, for example, Timoshenko and Goodier 1951) that an axially symmetrical stress distribution will result around each particle. Figure 10.12 shows a schematic of such a particle reinforced composite. The particle radius is *a,* while the surrounding matrix sphere has a radius *b*. This elasticity problem has spherical symmetry; therefore, the use of spherical coordinates, r, θ, and ϕ as indicated in Fig. 10.13a makes for a simple analysis. We have the following components of stress, σ, strain, ε, and displacement, u:

$$\begin{aligned} &\sigma_r, \sigma_\theta = \sigma_\phi \\ &\varepsilon_r, \varepsilon_\theta = \varepsilon_\phi \\ u_r = u, \quad &\text{independent of } \theta \text{ or } \phi \end{aligned} .$$

The equilibrium equation for this spherically symmetric problem is

$$\frac{d\sigma_r}{dr} + \frac{2}{r}(\sigma_r - \sigma_\theta) = 0, \tag{10.50}$$

while the strain–displacement relationships are

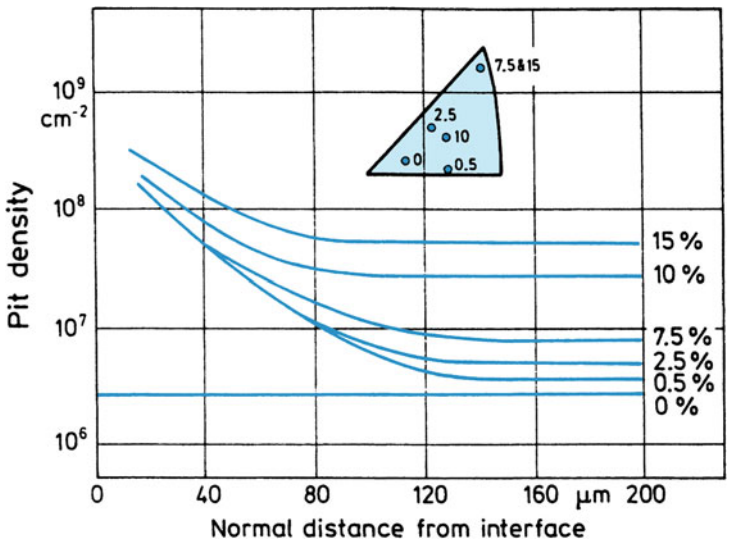

Fig. 10.10 Variation of dislocation density ($\simeq$ pit density) with distance from the interface. The higher dislocation density in the plateau region with high V_f is due to a higher σ_z with higher V_f (Fig. 10.9). (From Chawla and Metzger 1972, used with permission)

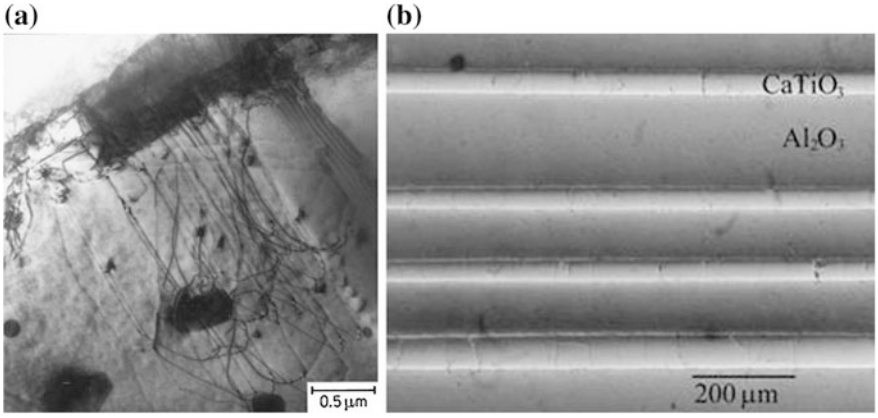

Fig. 10.11 **a** Dislocations generated at SiC whiskers in an aluminum matrix in an in situ thermal cycling experiment done in a high-voltage electron microscope. (From Vogelsang et al. 1986, used with permission) **b** Cracking in the $CaTiO_3$ layer in a $CaTiO_3/Al_2O_3$ composite due to thermal stresses generated during cooldown from the processing temperature. (From Gladysz and Chawla 2001)

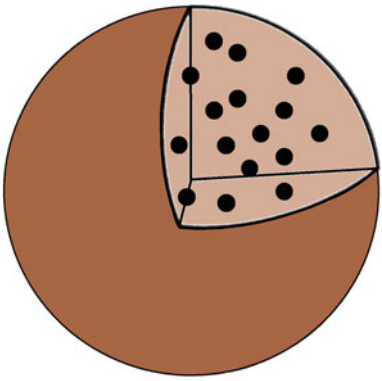

Fig. 10.12 A particle reinforced composite

$$\varepsilon_r = \frac{du}{dr} \quad \varepsilon_\theta = \frac{u}{r}. \tag{10.51}$$

Substituting Eq. (10.51) in Eq. (10.50), we get the governing differential equation for our problem:

$$\frac{d^2u}{dr^2} + \frac{2}{r}\frac{du}{dr} - \frac{2}{r^2}u = 0. \tag{10.52}$$

The solution to this differential equation is

$$u = Ar + \frac{C}{r^2},$$

where A and C are constants.

We apply the following boundary conditions:

1. Stress vanishes at the free surface (i.e., at $r = b$).
2. The radial stress at the interface ($r = a$) is the interfacial pressure, P, i.e.,

$$\sigma_r(a) = P,$$

The particle has a hydrostatic state of stress with the radial and circumferential stress components being equal, i.e.,

$$\sigma_{rp} = -P = \text{constant} = \sigma_{\theta p}, \tag{10.53}$$

while the stresses in the matrix are

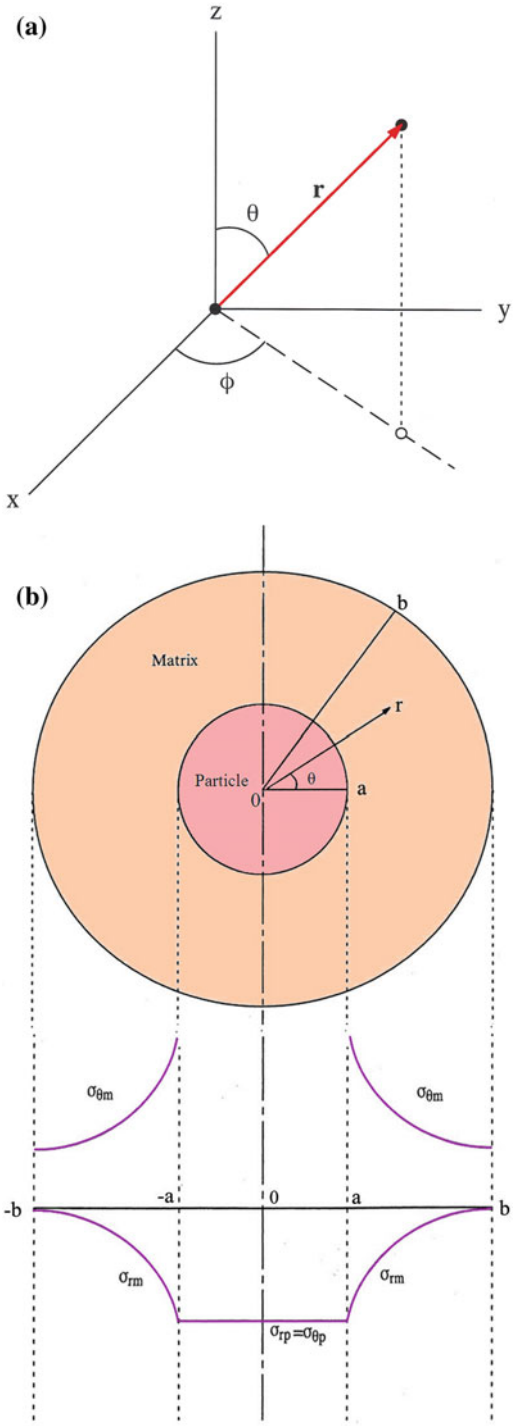

Fig. 10.13 **a** Spherical coordinate system. **b** Stress distribution in a particulate composite for cooldown from the processing temperature

$$\sigma_{rm} = \frac{P}{1 - V_p}\left[\frac{a^3}{r^3} - V_p\right] \tag{10.54}$$

$$\sigma_{\theta m} = -\frac{P}{1 - V_p}\left[\frac{1}{2}\frac{a^3}{r^3} + V_p\right] \tag{10.55}$$

$$p = \frac{(\alpha_m - \alpha_p)\Delta T}{\left[\dfrac{0.5(1 + \nu_m) + (1 - 2\nu_m)V_p}{E_m(1 - V_p)} + \dfrac{1 - 2\nu_p}{E_p}\right]} \tag{10.56}$$

$$V_p = \left(\frac{a}{b}\right)^3.$$

where V_p is the particle volume fraction, a is the particle radius, b is the matrix radius, and other symbols have the significance given earlier. Figure 10.13b shows the stress distribution in a particulate composite when cooled down from the processing temperature and for $\alpha_m > \alpha_p$. Note the different stress distributions in a particulate composite from that in a fibrous composite. The particle is under a uniform pressure, P, while the matrix has different radial and tangential stress components. The radial and tangential components in the matrix vary with distance, as shown in Fig. 10.13b. The radial component goes to zero at the free surface, $r = b$, as per our boundary conditions. The tangential component has a nonzero value at the free surface.

10.4 Mechanics of Load Transfer from Matrix to Fiber

The topic of load transfer from the matrix to the fiber has been treated by a number of researchers (Cox 1952; Dow 1963; Schuster and Scala 1964; Kelly 1973a, b). The matrix holds the fibers together and transmits the applied load to the fibers, the real load-bearing component in most cases. Let us focus our attention on a high modulus fiber embedded in a low modulus matrix. Figure 10.14a shows the situation prior to the application of an external load. We assume that the fiber and matrix are perfectly bonded and that the Poisson's ratios of the two are the same. Imagine vertical lines running through the fiber/matrix interface in a continuous manner in the unstressed state, as shown in Fig. 10.14a. Now let us load this composite axially as shown in Fig. 10.14b. We assume that no direct loading of the fibers occurs. Then the fiber and the matrix experience locally different axial displacements because of the different elastic moduli of the components. Different axial displacements in the fiber and the matrix mean that shear strains are being produced in the matrix on planes parallel to the fiber axis and in a direction parallel to the fiber axis. Under such circumstances, our imaginary vertical lines of the unstressed state will become distorted, as shown in Fig. 10.14b. Transfer of the

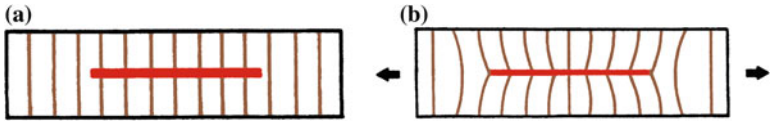

Fig. 10.14 A high modulus fiber embedded in a low modulus matrix: **a** before deformation, **b** after deformation

applied load to the fiber thus occurs by means of these shear strains in the matrix. Termonia (1987) used a finite difference numerical technique to model the elastic strain field perturbance in composite consisting of an embedded fiber in a matrix when a uniform far-field strain was imposed on the matrix. An originally uniform orthogonal mesh around the fiber became distorted when an axial tensile stress was applied.

It is instructive to examine the stress distribution along the fiber/matrix interface. There are two important cases: (1) both the matrix and fiber are elastic, and (2) the matrix is plastic and the fiber is elastic. Fibers such as boron, carbon, and ceramic fibers are essentially elastic right up to fracture. Metallic matrices show elastic and plastic deformation before fracture, while thermoset polymeric and ceramic matrices can be treated, for all practical purposes, as elastic up to fracture.

10.4.1 Fiber Elastic–Matrix Elastic

Consider a fiber of length l embedded in a matrix. Let us subject this composite to a strain, e; see Fig. 10.15. We assume that (1) there exists a perfect bonding between the fiber and matrix (i.e., there is no sliding between them) and (2) the Poisson's ratios of the fiber and matrix are equal, which implies an absence of transverse stresses when the load is applied along the fiber direction. Let the displacement of a point at a distance x from one extremity of the fiber be u in the presence of a fiber and v in the absence of a fiber. Then we can write for the transfer of load from the matrix to the fiber

$$\frac{dP_f}{dx} = B(u - v), \tag{10.57}$$

where P_f is the load on the fiber and B is a constant that depends on the geometric arrangement of fibers, the matrix type, and moduli of the fiber and matrix. Differentiating Eq. (10.57), we get

$$\frac{d^2P_f}{dx^2} = B\left(\frac{du}{dx} - \frac{dv}{dx}\right). \tag{10.58}$$

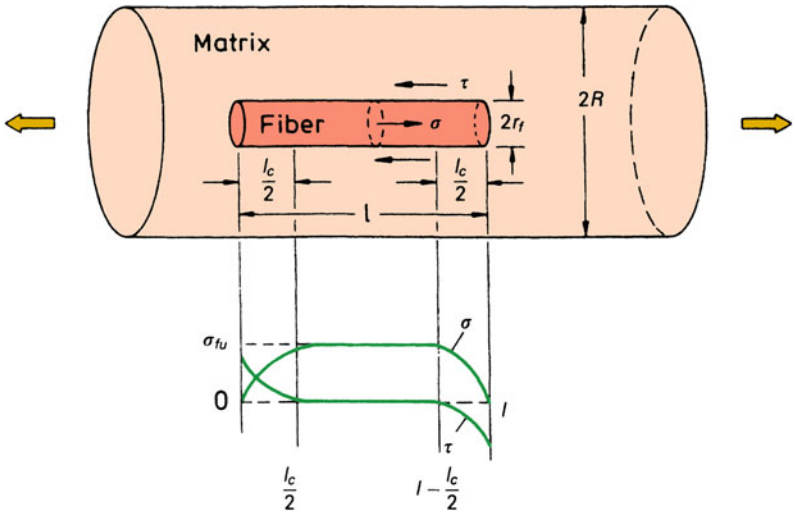

Fig. 10.15 Load transfer in a fiber/matrix composite: Variation of tensile stress (σ_f) in the fiber and interfacial shear stress (τ) with distance along the interface

We have

$$\frac{du}{dx} = \text{strain in the fiber} = \frac{P_f}{A_f E_f}$$
$$\frac{dv}{dx} = \text{strain in matrix away from the fiber}$$
$$= \text{imposed strain}, e.$$

Thus, Eq. (10.58) can be rewritten as

$$\frac{d^2 P_f}{dx^2} = B\left(\frac{P_f}{A_f E_f} - e\right). \tag{10.59}$$

A solution to this differential equation is

$$P_f = E_f A_f e + S \sinh \beta x + T \cosh \beta x, \tag{10.60}$$

where S and T are constants of integration and

$$\beta = \left(\frac{B}{A_f E_f}\right)^{1/2}. \tag{10.61}$$

We use the following boundary condition to evaluate the constants S and T:

$$P_f = 0 \quad \text{at} \quad x = 0 \quad \text{and} \quad x = l.$$

Putting in these values and using the half-angle trigonometric formulas, we get the following result:

$$P_f = E_f A_f e \left[1 - \frac{\cosh \beta(l/2 - x)}{\cosh(\beta l/2)}\right] \quad \text{for} \quad 0 < x < l/2, \tag{10.62}$$

or

$$\sigma_f = \frac{P_f}{A_f} = E_f e \left[1 - \frac{\cosh \beta(l/2 - x)}{\cosh(\beta l/2)}\right] \quad \text{for} \quad 0 < x < l/2. \tag{10.63}$$

The maximum possible value of strain in the fiber is the imposed strain e, and thus the maximum stress is $E_f\, e$. Therefore, if we have a long enough fiber, the stress in the fiber will increase from the two ends to a maximum value, $\sigma_{fu} = E_f e$. It can be shown readily that the average stress in the fiber is

$$\bar{\sigma}_f = \frac{E_f e}{l} \int_0^l \left[1 - \frac{\cosh \beta(l/2 - x)}{\cosh(\beta l/2)}\right] dx = E_f e \left[1 - \frac{\tanh(\beta l/2)}{\beta l/2}\right]. \tag{10.64}$$

We can obtain the variation of shear stress, τ along the fiber/matrix interface by considering the equilibrium of forces acting over an element, dx of fiber (radius r_f). Thus, from Fig. 10.15 we can write

$$\frac{dP_f}{dx} dx = 2\pi r_f\, dx\, \tau. \tag{10.65}$$

Now P_f, the tensile load on the fiber, is equal to $\pi r_f^2 \sigma_f$. Substituting this in Eq. (10.65), we get

$$\tau = \frac{1}{2\pi r_f} \frac{dP_f}{dx} = \frac{r_f}{2} \frac{d\sigma_f}{dx}. \tag{10.66}$$

From Eqs. (10.63) and (10.66), we obtain

$$\tau = \frac{E_f r_f e \beta}{2} \frac{\sinh \beta(l/2 - x)}{\cosh(\beta l/2)}. \tag{10.67}$$

Figure 10.15 shows the variation of τ and σ_f with distance x. The maximum shear stress, in Eq. (10.67), will be the smaller of the following two shear strength values: (1) the shear yield strength of the matrix or (2) the shear strength of the

fiber/matrix interface. Whichever of these two shear strength values is attained first will control the load transfer phenomenon and should be used in Eq. (10.67).

Now we can determine the constant B. The value of B depends on the fiber packing geometry. Consider Fig. 10.15 again and let the fiber length l be much greater than the fiber radius r_f. Let $2R$ be the average fiber spacing (center to center). Let us also denote the shear stress in the fiber direction at a distance r from the axis by $\tau(r)$. Then, at the fiber surface ($r = r_f$), we can write

$$\frac{dP_f}{dx} = -2\pi r_f \tau\left(r_f\right) = B(u - v).$$

Thus,

$$B = -\frac{2\pi r_f \tau\left(r_f\right)}{u - v}. \tag{10.68}$$

Let w be the real displacement in the matrix. Then at the fiber/matrix interface, no sliding being permitted, $w = u$. At a distance R from the center of a fiber, the matrix displacement is unaffected by the fiber presence and $w = v$. From the equilibrium of forces acting on the matrix volume between r_f and R, we can write

$$2\pi r\tau(r) = \text{constant} = 2\pi r_f \tau(r_f)$$

or

$$\tau(r) = \frac{\tau\left(r_f\right) r_f}{r}. \tag{10.69}$$

The shear strain γ in the matrix is given by $\tau(r) = G_m\,\gamma$, where G_m is the matrix shear modulus. Then

$$\gamma = \frac{dw}{dr} = \frac{\tau(r)}{G_m} = \frac{\tau(r_f) r_f}{G_m r}. \tag{10.70}$$

Integrating from r_f to R, we obtain

$$\int_{r_f}^{R} dw = \Delta w = \frac{\tau\left(r_f\right) r_f}{G_m} \int_{r_f}^{R} \frac{1}{r}\, dr = \frac{\tau\left(r_f\right) r_f}{G_m} \ln\left(\frac{R}{r_f}\right). \tag{10.71}$$

But, by definition,

$$\Delta w = v - u = -(u - v). \tag{10.72}$$

From Eqs. (10.71) and (10.72) we get

$$\frac{\tau(r_f)r_f}{u-v} = -\frac{G_m}{\ln(R/r_f)}. \tag{10.73}$$

From Eqs. (10.68) and (10.73), one obtains

$$B = \frac{2\pi G_m}{\ln(R/r_f)}, \tag{10.74}$$

and from Eq. (10.61), one can obtain an expression for the load transfer parameter β:

$$\beta = \left(\frac{B}{E_f A_f}\right)^{1/2} = \left[\frac{2\pi G_m}{E_f A_f \ln(R/r_f)}\right]^{1/2}. \tag{10.75}$$

The value of R/r_f is a function of fiber packing. For a square array of fibers, we have $\ln(R/r_f) = \frac{1}{2}\ln(\pi/V_f)$. For a hexagonal packing of fibers, we have $\ln(R/r_f) = \frac{1}{2}\ln(2\pi/\sqrt{3}V_f)$. We can define $\ln(R/r_f) = \frac{1}{2}\ln(\phi_{\max}/V_f)$, where $\phi_{\max}$ is the maximum packing factor. Substituting this in Eq. (10.75), we get

$$\beta = \left[\frac{4\pi G_m}{E_f A_f \ln(\phi_{\max}/V_f)}\right]^{1/2}.$$

We note from this expression that the greater the value of the ratio G_m/E_f, the greater the value of β and the more rapid the stress increase in the fiber from either end.

More rigorous analyses give results similar to the one above and differ only in the value of β. In all analyses, β is proportional to $(G_m/E_f)^{1/2}$, and differences occur only in the term involving fiber volume fraction, $\ln(R/r_f)$, in the preceding equation.

Termonia (1987) used the finite difference method to show the high shear strains in the matrix near the fiber extremities. Micro-Raman spectroscopy has been used to study the deformation behavior of organic and inorganic fiber reinforced composites (Galiotis et al. 1985; Day et al. 1987, 1989; Schadler and Galiotis 1995; Yang et al. 1992; Young et al. 1990). Characteristic Raman spectra can be obtained from these fibers in the undeformed and the deformed states. Under tension, the peaks of the Raman bands shift to lower frequencies. The magnitude of frequency shift is a function of the material, Raman band under consideration, and the Young's modulus of the material. The shift in Raman bands results from changes in force constants due to changes in molecular or atomic bond lengths and bond angles. Micro-Raman spectroscopy is a very powerful technique that allows us to obtain point-to-point variation in strain along the fiber length embedded in a transparent matrix. An example of this for Kevlar aramid 149/epoxy composite is shown in Fig. 10.16 (Young 1994). In Fig. 10.16a, b, we see that up to 1% strain,

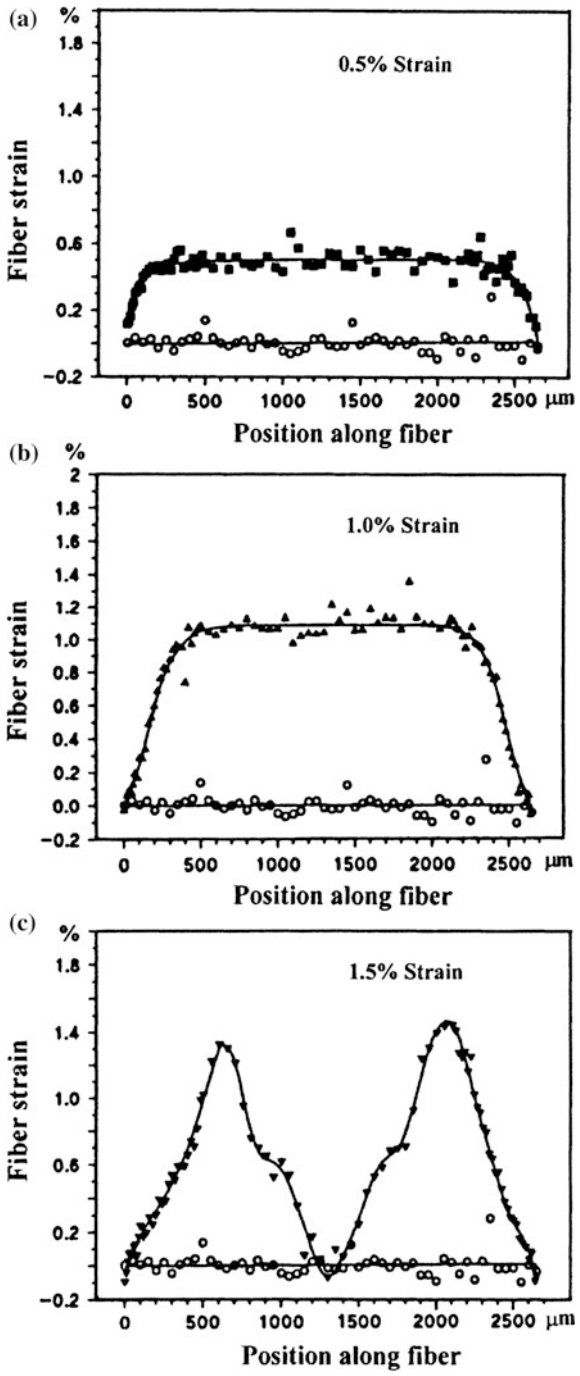

Fig. 10.16 Micro-Raman spectra of Kevlar aramid 149 when the Kevlar/epoxy composite is loaded axially. **a**, **b** strain buildup in the fiber from the two ends. **c**, **d** fiber fracture leads to a drop in strain at those sites. (After Young 1994)

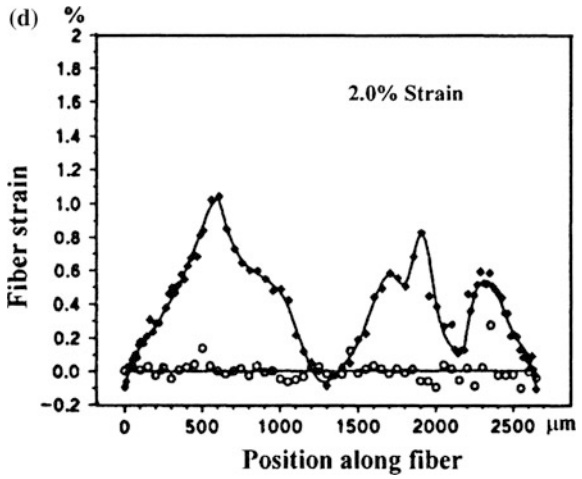

Fig. 10.16 (continued)

the strain in the fiber builds from the two ends as predicted by the shear lag analysis described earlier, while in the middle of the fiber length the strain in the fiber and matrix are equal. In Fig. 10.16c, d, we see that as fiber fractures at different sites along its length, the strain (and the stress) in the fiber drops at those sites.

Let us reexamine Fig. 10.15. As per our boundary condition, the normal stress is zero at the two extremities of the fiber. The normal stress in the fiber, σ, rises from the two ends to a maximum value along most of the fiber length, provided we have a long enough fiber. This gives rise to the concept of a critical fiber length for load transfer (see the next section). The shear stress is maximum at the fiber ends. Matrix yielding or interfacial failure would be expected to start at the fiber ends.

10.4.2 Fiber Elastic–Matrix Plastic

It should be clear from the preceding discussion that in order to load high strength fibers in a ductile matrix to their maximum strength, the matrix shear strength must be large. A metallic matrix will flow plastically in response to the high shear stresses developed. Of course, if the shear strength fiber/matrix interface is less than the shear yield strength of the matrix, then the interface will fail first. In MMCs, assuming that the plastically deforming matrix does not work harden, the shear stress at the fiber surface, $\tau(r_f)$, will have an upper limit of τ_y, the matrix shear yield strength. In PMCs and CMCs, frictional slip at the interface is more likely than plastic flow of the matrix. In the case of PMCs and CMCs, therefore, the limiting shear stress will be the interface strength in shear, τ_i. The term τ_i should replace τ_y in what follows for PMCs and CMCs. If the polymer shrinkage during curing

results in a radial pressure p on the fibers, then τ_y should be replaced by μp because $\tau_i = \mu p$, where μ is the coefficient of sliding friction between the fiber and matrix (Kelly 1973a, b). The equilibrium of forces, then, over a fiber length of $l/2$ gives

$$\sigma_f \frac{\pi d^2}{4} = \tau_y \pi d \frac{l}{2}.$$

Or

$$\frac{l}{d} = \frac{\sigma_f}{2\tau_y}.$$

We consider $l/2$ and not l because the fiber is being loaded from both ends. Given a sufficiently long fiber, it should be possible to load it to its breaking stress σ_{fu} by means of load transfer through the matrix flowing plastically around it. Let $(l/d)_c$ be the minimum fiber length-to-diameter ratio necessary to accomplish this. We call this ratio (l/d) the aspect ratio of a fiber and $(l/d)_c$ is the critical aspect ratio necessary to attain the breaking stress of the fiber, σ_{fu}. Then we can write

$$\left(\frac{l}{d}\right)_c = \frac{\sigma_{fu}}{2\tau_y}. \tag{10.76}$$

For a given fiber diameter d, we can think of a critical fiber length l_c. Thus

$$\frac{l_c}{d} = \frac{\sigma_{fu}}{2\tau_y}. \tag{10.77}$$

Over a length l_c, the load in the fiber builds up from both ends. Strain builds in a likewise manner. Beyond l_c (i.e., in the middle portion of the fiber), the local displacements in the matrix and fiber are the same, and the fiber carries the major load while the matrix carries only a minor portion of the applied load. Equation (10.77) tells us that the fiber length l must be equal to or greater than l_c for the fiber to be loaded to its maximum stress, σ_{fu}. For $l < l_c$, the matrix will flow plastically around the fiber and will load it to a stress in its central portion given by

$$\sigma_f = 2\tau \frac{l}{d} < \sigma_{fu}. \tag{10.78}$$

This is shown in Fig. 10.17. An examination of this figure shows that even for $l/d > (l/d)_c$ the average stress in the fiber will be less than the maximum stress to which it is loaded in its central region. In fact, one can write for the average fiber stress

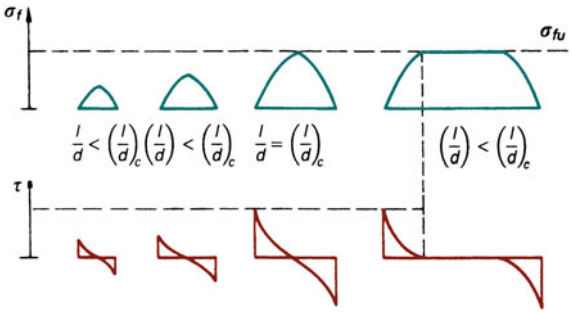

Fig. 10.17 Schematic of variation of tensile stress in a fiber (σ_f) and interface shear stress (τ) with different fiber aspect ratios (l/d)

$$\bar{\sigma}_f = \frac{1}{l}\int_0^l \sigma_f dx = \frac{1}{l}\left[\sigma_f(l - l_c) + \beta\sigma_f l_c\right] = \frac{1}{l}\left[\sigma_f l - l_c(\sigma_f - \beta\sigma_f)\right]$$

or

$$\bar{\sigma}_f = \sigma_f\left(1 - \frac{1-\beta}{l/l_c}\right), \tag{10.79}$$

where $\beta\sigma_f$ is the average stress in the fiber over a portion $l_c/2$ of its length at both ends. One can thus regard β as a load transfer function. Its value will be precisely 0.5 for an ideally plastic material, that is, the increase in stress in the fiber over the portion $l_c/2$ will be linear. The longitudinal strength of a composite containing short but well-aligned fibers will always be less than that of a composite containing unidirectionally aligned continuous fibers. For the strength of short fiber composite, per rule-of-mixtures, we can write

$$\begin{aligned} \sigma_c &= \bar{\sigma}_f V_f + \sigma'_m V_m \\ \sigma_c &= \sigma_f V_f\left(1 - \tfrac{1-\beta}{l/l_c}\right) + \sigma'_m(1 - V_f) \end{aligned}. \tag{10.80}$$

If $\beta = 0.5$,

$$\sigma_c = \sigma_f V_f\left(1 - \frac{l_c}{2l}\right) + \sigma'_m(1 - V_f),$$

where σ'_m is the in situ matrix stress at the strain under consideration. Suppose that in a whisker reinforced metal the whiskers have an $l/l_c = 10$; then it can easily be shown that the strength of such a composite containing discontinuous but aligned fibers will be 95% of that of a composite containing continuous fibers. Thus, as long as the fibers are reasonably long compared to the load transfer length, there is not much loss of strength owing to their discontinuous nature. The stress concentration effect at the ends of the discontinuous fibers has been neglected in this simple analysis.

10.5 Load Transfer in Particulate Composites

The shear lag model described in the previous section is suitable for explaining the load transfer from the matrix to a high aspect ratio reinforcement via shear along the interface parallel to the loading direction. No direct tensile loading of the reinforcement occurs. Such a model will not be expected to work for a particulate composite. A modified shear lag model (Fukuda and Chou 1981; Nardone and Prewo 1986) takes into account tensile loading at the particle ends. According to this modified shear lag model, the yield strength of a particulate composite is given by

$$\sigma_{yc} = \sigma_{ym}[1 + (L + t)/4L]V_p + \sigma_{ym}(1 - V_p),$$

where σ_{ym} is the yield stress of the unreinforced matrix, V_p is the particle volume fraction, L is the length of the particle perpendicular to the applied load, and t is the length of the particle parallel to the loading direction.

For the case of a composite with equiaxed particles (aspect ratio = 1), the above expression reduces to

$$\sigma_{yc} = \sigma_{ym}(1 + 0.5V_p).$$

Note that this expression predicts a linear but modest increase in the strength of the composite with particle volume fraction. However, no account is taken of the particle size or other microstructural parameters.

Models involving the modified shear lag model, Eshelby's equivalent inclusion approach, and Weibull statistics have been proposed (Lewis and Withers 1995; Song et al. 2010). Incorporation of Weibull statistics (see Chap. 12) makes sense because the brittle, ceramic particles in a metallic matrix can debond and/or crack during deformation. The yield strength of ceramic particle reinforced MMC increases as the volume fraction and aspect ratio of the particles increase, while it decreases as the size of the ceramic particles increases.

Problems

10.1. Describe some experimental methods of measuring void content in composites. Give the limitations of each method.

10.2. Consider a 40% V_f SiC whisker reinforced aluminum composite. $E_f = 400\ GPa$, $E_m = 70\ GPa$, and $(l/d) = 20$. Compute the longitudinal elastic modulus of this composite if all the whiskers are aligned in the longitudinal direction. Use Halpin–Tsai–Kardos equations. Take $\xi = 2(l/d)$.

10.3. A composite has 40% V_f of a 150 μm diameter fiber. The fiber strength is 2 GPa, the matrix strength is 75 MPa, while the fiber/matrix interfacial strength is 50 MPa. Assuming a linear buildup of stress from the two ends of a fiber, estimate the composite strength for (a) 200 mm long fibers and (b) 3 mm long fibers.

10.4. Derive the load transfer expression (Eq. 10.62) using the boundary conditions. Show that average tensile stress in the fiber is given by Eq. (10.63).

10.5. Consider a fiber composite system in which the fiber has an aspect ratio of 1000. Estimate the minimum interfacial shear strength τ_i, as a percentage of the tensile stress in fiber, σ_f, which is necessary to avoid interface failure in the composite.

10.6. Show that as $\xi \to 0$, the Halpin–Tsai equations reduce to

$$l/p = V_m/P_m + V_f/P_f$$

while as $\xi \to \infty$, they reduce to

$$p = V_m + V_f P_f.$$

10.7. Consider an alumina fiber reinforced magnesium composite. Calculate the composite stress at the matrix yield strain. The matrix yield stress is 180 MPa, E_m = 70 GPa, and v = 0.3. Take V_f = 50%.

10.8. Estimate the aspect ratio and the critical aspect ratio for aligned SiC whiskers (5 μm diameter and 2 mm long) in an aluminum alloy matrix. Assume that the matrix alloy does not show much work hardening.

10.9. Alumina whiskers (density = 3.8 gcm^{-3}) are incorporated in a resin matrix (density = 1.3 gcm^{-3}). What is the density of the composite? Take V_f = 0.35. What is the relative mass of the whiskers?

10.10. Consider a composite made of aligned, continuous boron fibers in an aluminum matrix. Compute the elastic moduli, parallel, and transverse to the fibers. Take V_f = 0.50.

10.11. Fractographic observations on a fiber composite showed that the average fiber pullout length was 0.5 mm. If σ_{fu} = 1 GPa and the fiber diameter is 100 μm, calculate the strength of the interface in shear.

10.12. Consider a tungsten/copper composite with the following characteristics: fiber fracture strength = 3 GPa, fiber diameter = 200 μm, and the matrix shear yield strength = 80 MPa. Estimate the critical fiber length which will make it possible that the maximum load bearing capacity of the fiber is utilized.

10.13. Carbon fibers (V_f = 50%) and polyimide matrix have the following parameters:

$$\begin{array}{ll} E_f = 280\,GPa & E_m = 276\,MPa \\ v_f = 0.2 & v_m = 0.3 \end{array}.$$

(a) Compute the elastic modulus in the fiber direction, E_{11}, and transverse to the fiber direction, E_{22}.

(b) Compute the Poisson ratios, v_{12} and v_{21}.

10.14. Copper or aluminum wires with steel cores are used for electrical power transmission. Consider a Cu/steel composite wire having the following data:

$$\text{inner diameter} = 1\,mm$$
$$\text{outer diameter} = 2\,mm$$

$$E_{\text{Cu}} = 150\,GPa \qquad \alpha_{\text{Cu}} = 16 \times 10^{-6}\,K^{-1}$$
$$E_{\text{steel}} = 210\,GPa \qquad \alpha_{\text{steel}} = 11 \times 10^{-6}\,K^{-1}$$
$$\sigma_{y\text{Cu}} = 100\,MPa \qquad v_{\text{Cu}} = v_{\text{steel}} = 0.3$$
$$\sigma_{y\text{steel}} = 200\,MPa.$$

(a) The composite wire is loaded in tension. Which of the two components will yield plastically first? Why?
(b) Compute the tensile load that the wire will support before any plastic strain occurs.
(c) Compute the Young's modulus and coefficient of thermal expansion of the composite wire.

10.15. A composite is made of unidirectionally aligned carbon fibers in a glass–ceramic matrix. The following data are available:

$$E_{f1} = 289\,GPa, E_{f2} = 40\,GPa, E_m = 70\,GPa$$
$$G_{f12} = 18\,GPa,\ v_{f1} = 0.2, v_m = 0.3$$

(a) Compute the elastic modulus in the longitudinal and transverse directions.
(b) Compute the two Poisson's ratios.
(c) Compute the principal shear modulus, G_{12}.

References

R.J. Arsenault, R.M. Fisher, Scripta Met. **17**, 67 (1983)
E. Behrens, J. Compos. Mater. **2**, 2 (1968)
H. Bhatt, K.Y. Donaldson, D.P.H. Hasselman, R.T. Bhatt, J. Mater. Sci. **27**, 6653 (1992)
C.C. Chamis, NASA Tech. Memo. 83320 (NASA, Washington, DC, 1983)
C.C. Chamis, G.P. Sendecky, J. Compos. Mater. **2**, 332 (1968)
K.K. Chawla, Metallography **6**, 155 (1973a)
K.K. Chawla, Philos. Mag. **28**, 401 (1973b)
K.K. Chawla, in *Grain Boundaries in Engineering Materials* (Claitor's Publishing Division, Baton Rouge, LA, 1974), p. 435
K.K. Chawla, J. Mater. Sci. **11**, 1567 (1976)
K.K. Chawla, in *Proceedings of the International Conference on Composite Materials/1975* (TMS-AIME, New York, 1976b), p. 535
K.K. Chawla, M. Metzger, J. Mater. Sci. **7**, 34 (1972)

H.L. Cox, Brit. J. Appl. Phys. **3**, 122 (1952)
M.L. Clingerman, J.A. King, K.H. Schulz, J.D. Meyers, J. Appl. Polym. Sci. **83**, 1341 (2002)
R.J. Day, I.M. Robinson, M. Zakikhani, R.J. Young, Polymer **28**, 1833 (1987)
R.J. Day, V. Piddock, R. Taylor, R.J. Young, M. Zakikhani, J. Mater. Sci. **24**, 2898 (1989)
N.F. Dow, General Electric Report No. R63-SD-61 (1963)
J.D. Eshelby, Proc. R. Soc. **A241**, 376 (1957)
J.D. Eshelby, Proc. R. Soc. **A252**, 561 (1959)
H. Fukuda, T.W. Chou, J. Compos. Mater. **15**, 79 (1981)
C. Galiotis, I.M. Robinson, R.J. Young, B.J.E. Smith, D.N. Batchelder, Polym. Commun. **26**, 354 (1985)
G.M. Gladysz, K.K. Chawla, Composites A **32**, 173 (2001)
D.K. Hale, J. Mat. Sci. **11**, 2105 (1976)
J.C. Halpin, J.L. Kardos, Polym. Eng. Sci. **16**, 344 (1976)
J.C. Halpin, S.W. Tsai, Environmental factors estimation in composite materials design. *AFML TR 67-423* (1967)
Z. Hashin, B.W. Rosen, J. Appl. Mech. **31**, 233 (1964)
D.P.H. Hasselman, L.F. Johnson, J. Compos. Mater. **27**, 508 (1987)
R. Hill, J. Mech. Phys. Solids **12**, 199 (1964)
R. Hill, J. Mech. Phys. Solids **13**, 189 (1965)
J.L. Kardos, CRC Crit. Rev. Solid State Sci. **3**, 419 (1971)
A. Kelly, *Chemical and Mechanical Behavior of Inorganic Materials* (Wiley-Interscience, New York, 1970), p. 523
A. Kelly, *Strong Solids*, 2nd edn. (Clarendon Press, Oxford, 1973a), p. 157
A. Kelly, H. Lilbolt, Philos. Mag. **20**, 175 (1971)
E.H. Kerner, Proc. Phys. Soc. Lond. **B69**, 808 (1956)
C.A. Lewis, P.J. Withers, Acta Metall. Mater. **43**, 3685 (1995)
A.E.H. Love, *A Treatise on the Mathematical Theory of Elasticity*, 4th edn. (Dover, New York, 1952), p. 144
G.D. Marom, A. Weinberg, J. Mater. Sci. **10**, 1005 (1975)
T. Mori, K. Tanaka, Acta Met. **21**, 571 (1973)
V.C. Nardone, K.M. Prewo, Scripta Met **20**, 43 (1986)
L.E. Nielsen, *Mechanical Properties of Polymers and Composites*, vol. 2 (Marcel Dekker, New York, 1974)
J.F. Nye, *Physical Properties of Crystals* (Oxford University Press, London, 1985), p. 131
H. Poritsky, Physics **5**, 406 (1934)
A. Reuss, Z. Angew. Math. Mech. **9**, 49 (1929)
B.W. Rosen, Composites **4**, 16 (1973)
B.W. Rosen, Z. Hashin, Int. J. Eng. Sci. **8**, 157 (1970)
L.S. Schadler, C. Galiotis, Int. Mater. Rev. **40**, 116 (1995)
R.A. Schapery, J. Compos. Mater. **2**, 311 (1969)
D.M. Schuster, E. Scala, Trans. Met. Soc.-AIME **230**, 1635 (1964)
M. Song, Y. He, S. Fang, J. Mater. Sci. **45**, 4097 (2010)
Y. Termonia, J. Mater. Sci. **22**, 504 (1987)
S. Timoshenko, J.N. Goodier, *Theory of Elasticity* (McGraw-Hill, New York, 1951), p. 416
P.S. Turner, J. Res. Natl. Bur. Stand. **37**, 239 (1946)
M. Vogelsang, R.J. Arsenault, R.M. Fisher, Met. Trans. A **7A**, 379 (1986)
W. Voigt, *Lehrbuch der Kristallphysik* (Teubner, Leipzig, 1910)
R.U. Vaidya, K.K. Chawla, Compos. Sci. Technol. **50**, 13 (1994)
R.U. Vaidya, R. Venkatesh, K.K. Chawla, Composites **25**, 308 (1994)
L. Weber, Acta Mater. **53**, 1945 (2005)
L. Weber, J. Dorn, A. Mortensen, Acta Mater. **51**, 3199 (2003a)
L. Weber, C. Fischer, A. Mortensen, Acta Mater. **51**, 495 (2003b)
J.M. Whitney, J. Struct. Div. 113 (1973)
Z.R. Xu, K.K. Chawla, R. Mitra, M.E. Fine, Scripta Met. et Mater. **31**, 1525 (1994)

X. Yang, X. Hu, R.J. Day, R.J. Young, J. Mater. Sci. **27**, 1409 (1992)
R.J. Young, R.J. Day, M. Zakikhani, J. Mater. Sci. **25**, 127 (1990)
R.J. Young, in *High-Performance Composites: Commonalty of Phenomena*, ed. by K.K. Chawla, P.K. Liaw, S.G. Fishman (TMS, Warrendale, PA, 1994), p. 263

Suggested Reading

C.T. Herakovich, *Mechanics of Fibrous Composites* (Wiley, New York, 1998)
A. Kelly, *Strong Solids*, 2nd edn. (Clarendon Press, Oxford, 1973b)
S. Nemat-Nasser, M. Hori, *Micromechanics: Overall Properties of Heterogenous Materials* (North-Holland, Amsterdam, 1993)
V.K. Tewary, *Mechanics of Fibre Composites* (Halsted Press, New York, 1978)

Chapter 11
Macromechanics of Composites

Laminated fibrous composites are made by bonding together two or more laminae. These composites, frequently referred to as laminates, are different from sheet laminates made by bonding flat sheets of isotropic materials. In a laminated fibrous composite, the individual unidirectional laminae or plies are oriented in such a manner that the resulting structural component has the desired mechanical and/or physical characteristics in different directions. Thus, one exploits the inherent anisotropy of fibrous composites to design a composite material with appropriate properties.

In Chap. 10, we treated the micromechanics of fibrous composites, that is, how to obtain the composite properties when the properties of the matrix and the fiber and their geometric arrangements are known. While micromechanics is very useful in analyzing the composite behavior, we use the information obtained from a micromechanical analysis of a thin unidirectional lamina (or in the case of a lack of such analytical information, we must determine experimentally the properties of the lamina) as input for a macromechanical analysis of a laminated composite. Figure 11.1 shows this concept schematically (McCullough 1971). Once we have determined, analytically or otherwise, the characteristics of a fibrous lamina, we ignore its detailed microstructural nature and simply treat it as a homogeneous, orthotropic sheet. A laminated fibrous composite is made by stacking a number of such orthotropic fiber reinforced plies or sheets at specific orientations to get composite laminate with the desired characteristics. We then use the well established theory of laminated plates or shells to analyze macromechanically such laminated composites.

To appreciate the significance of such a macromechanical analysis, we first review the basic ideas of the elastic constants of a bulk isotropic material and a lamina, a lamina as an orthotropic sheet, and finally the use of classical laminated plate theory to analyze macromechanically the laminated composites. The reader is referred to some standard texts on elasticity (Love 1952; Timoshenko and Goodier 1951; Nye 1985) for a detailed review of elasticity.

K. K. Chawla, *Composite Materials*,
https://doi.org/10.1007/978-3-030-28983-6_11

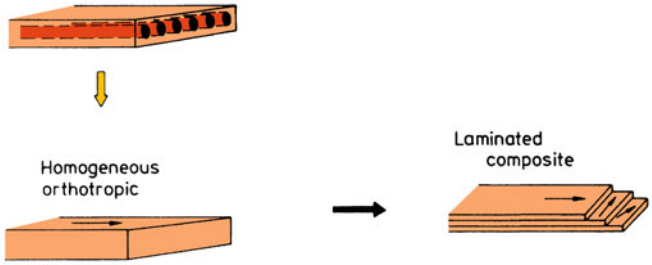

Fig. 11.1 Macromechanical analysis of laminate composites. A unidirectional ply is treated as a homogeneous, orthotropic material. Many such plies are stacked in an appropriate order (following laminated plate or shell theory) to make the composite [Reprinted from McCullough (1971), courtesy of Marcel Dekker, Inc.]

11.1 Elastic Constants of an Isotropic Material

Stress is defined as force per unit area of a body. We can represent the stress acting at a point in a solid by the stress components acting on the surfaces of an elemental cube at that point. There are nine stress components (three normal and six shear) acting on the front faces of an elemental cube. The component σ_{ij} represents the force per unit area in the i direction on a face whose normal is the j direction. Rotational equilibrium requires that $\sigma_{ij} = \sigma_{ji}$. Thus, we are left with six stress components; $i = j$ gives the normal stresses while $i \neq j$ gives three shear stresses.

The displacement of a point in a deformed body with respect to its original position in the undeformed state can be represented by a vector $\boldsymbol{u}$ with components u_1, u_2, and u_3; these components are the projections of $\boldsymbol{u}$ on the x_1, x_2, and x_3 axes. *Strain* is defined as the ratio of change in length to original length. We can define the strain components in terms of the first derivatives of the displacement components as follows:

$$\varepsilon_{ij} = \frac{1}{2}\left(\frac{\partial u_i}{\partial x_j} + \frac{\partial u_j}{\partial x_i}\right).$$

Similar to stress components, when the subscripts $i = j$, we have normal strains while $i \neq j$ gives shear strains. It should be noted, however, that ε_{ij} for $i \neq j$ gives half of the engineering shear strain, γ_{ij}; that is,

$$\gamma_{ij} = 2\varepsilon_{ij} = \frac{\partial u_i}{\partial x_j} + \frac{\partial u_j}{\partial x_i}.$$

The relationship between stress and strain in linear elasticity is described by Hooke's law. Hooke's law states that, for small strains, stress is linearly proportional to strain. For the simple case of a uniaxial stress applied to an isotropic solid, we can write Hooke's law as

$$\sigma = E\varepsilon, \tag{11.1}$$

where σ is the uniaxial stress, ε is the strain in the applied stress direction, and E is Young's modulus. We have omitted the indices in this simple unidirectional case.

In its most generalized form, Hooke's law can be written in the indicial or tensorial notation as

$$\sigma_{ij} = C_{ijkl}\varepsilon_{kl}, \tag{11.2}$$

where C_{ijkl} are the elastic constants or stiffnesses. Equation (11.2), when written out in an expanded form, will have 81 elastic constants. It is a general practice to use a contracted matrix notation for writing stresses, strains, and elastic constants. The contracted notation is especially useful for matrix algebra operations.

We use C_{mn} for C_{ijkl}, σ_m for σ_{ij}, and ε_n for ε_{kl} as per the following scheme:

ij or *kl*	11	22	33	23	31	12
m or *n*	1	2	3	4	5	6

Then Eq. (11.2) can be rewritten as

$$\sigma_m = C_{mn}\varepsilon_n. \tag{11.3}$$

It can be shown from symmetry considerations that $C_{mn} = C_{nm}$.

Conversely, we can write

$$\varepsilon_m = S_{mn}\sigma_n, \tag{11.4}$$

where S_{mn}, the compliance matrix, is the inverse of the stiffness matrix C_{mn}.

In the expanded form, we have

$$\begin{bmatrix}\sigma_1\\ \sigma_2\\ \sigma_3\\ \sigma_4\\ \sigma_5\\ \sigma_6\end{bmatrix} = \begin{bmatrix} C_{11} & C_{12} & C_{13} & C_{14} & C_{15} & C_{16}\\ & C_{22} & C_{23} & C_{24} & C_{25} & C_{26}\\ & & C_{33} & C_{34} & C_{35} & C_{36}\\ & & & C_{44} & C_{45} & C_{46}\\ & & & & C_{55} & C_{56}\\ & & & & & C_{66}\end{bmatrix} \begin{bmatrix}\varepsilon_1\\ \varepsilon_2\\ \varepsilon_3\\ \varepsilon_4\\ \varepsilon_5\\ \varepsilon_6\end{bmatrix} \tag{11.5}$$

Note that σ_4, σ_5, and σ_6 now represent the shear stresses, while ε_4, ε_5, and ε_6 represent the engineering shear strains. The dashed line along the diagonal indicates

that the matrix is symmetric. Equation (11.5) thus gives 21 independent elastic constants in the most general case, i.e., with no symmetry elements present.

For most materials, the number of independent elastic constants is further reduced because of the various symmetry elements present. For example, only three elastic constants are independent for the cubic system. For isotropic materials where elastic properties are independent of direction, only two constants are independent. For isotropic materials, Eq. (11.5) reduces to

$$\begin{bmatrix} \sigma_1 \\ \sigma_2 \\ \sigma_3 \\ \sigma_4 \\ \sigma_5 \\ \sigma_6 \end{bmatrix} = \begin{bmatrix} C_{11} & C_{12} & C_{12} & 0 & 0 & 0 \\ & C_{11} & C_{12} & 0 & 0 & 0 \\ & & C_{11} & 0 & 0 & 0 \\ & & & \frac{C_{11}-C_{12}}{2} & 0 & 0 \\ & & & & \frac{C_{11}-C_{12}}{2} & 0 \\ & & & & & \frac{C_{11}-C_{12}}{2} \end{bmatrix} \begin{bmatrix} \varepsilon_1 \\ \varepsilon_2 \\ \varepsilon_3 \\ \varepsilon_4 \\ \varepsilon_5 \\ \varepsilon_6 \end{bmatrix} \tag{11.6}$$

In terms of the compliance matrix, for isotropic materials, we can write

$$\begin{bmatrix} \varepsilon_1 \\ \varepsilon_2 \\ \varepsilon_3 \\ \varepsilon_4 \\ \varepsilon_5 \\ \varepsilon_6 \end{bmatrix} = \begin{bmatrix} S_{11} & S_{12} & S_{12} & 0 & 0 & 0 \\ & S_{11} & S_{12} & 0 & 0 & 0 \\ & & S_{11} & 0 & 0 & 0 \\ & & & 2(S_{11}-S_{12}) & 0 & 0 \\ & & & & 2(S_{11}-S_{12}) & 0 \\ & & & & & 2(S_{11}-S_{12}) \end{bmatrix} \begin{bmatrix} \sigma_1 \\ \sigma_2 \\ \sigma_3 \\ \sigma_4 \\ \sigma_5 \\ \sigma_6 \end{bmatrix} \tag{11.7}$$

Only C_{11} and C_{12} (or S_{11} and S_{12}) are the independent constants for an isotropic material. In engineering practice, we frequently use elastic constants such as Young's modulus E, Poisson's ratio v, shear modulus G, and bulk modulus K. Only two of these four constants are independent because E, G, v, and K are interrelated:

$$E = 2G(1+v) \quad \text{and} \quad K = \frac{E}{3(1-2v)}.$$

The relationships between these engineering constants and compliances are as follows:

$$E = \frac{1}{S_{11}} \quad v = -\frac{S_{12}}{S_{11}} \quad G = \frac{1}{2(S_{11} - S_{12})}$$

and the compliances are related to the stiffnesses as follows:

$$S_{11} = \frac{C_{11} + C_{12}}{(C_{11} - C_{12})(C_{11} + 2C_{12})}$$
$$S_{12} = -\frac{C_{12}}{(C_{11} - C_{12})(C_{11} + 2C_{12})} - .$$

11.2 Elastic Constants of a Lamina

We can make a laminated composite by stacking a sufficiently large number of laminae. A *lamina*, the unit building block of a composite, can be considered to be in a state of generalized plane stress. Plane stress condition implies that the through thickness stress components are zero (hence, the term plane stress). Thus $\sigma_3 = \sigma_4 = \sigma_5 = 0$. Then Eqs. (11.6) and (11.7) are reduced, for an isotropic lamina, to

$$\begin{bmatrix} \sigma_1 \\ \sigma_2 \\ \sigma_6 \end{bmatrix} = \begin{bmatrix} C_{11} & C_{12} & 0 \\ C_{12} & C_{11} & 0 \\ 0 & 0 & \frac{C_{11} - C_{12}}{2} \end{bmatrix} \begin{bmatrix} \varepsilon_1 \\ \varepsilon_2 \\ \varepsilon_6 \end{bmatrix} \tag{11.8}$$

$$\begin{bmatrix} \varepsilon_1 \\ \varepsilon_2 \\ \varepsilon_6 \end{bmatrix} = \begin{bmatrix} S_{11} & S_{12} & 0 \\ S_{12} & S_{11} & 0 \\ 0 & 0 & 2(S_{11} - S_{12}) \end{bmatrix} \begin{bmatrix} \sigma_1 \\ \sigma_2 \\ \sigma_6 \end{bmatrix} \tag{11.9}$$

Note that the subscript 6 indicates the inplane shear component. Equations (11.8) and (11.9) describe the stress–strain relationships for an isotropic lamina, for example, an aluminum sheet. A fiber reinforced lamina, however, is not an isotropic material. It is an orthotropic material; that is, it has three mutually perpendicular axes of symmetry. Relationships become slightly more complicated when we have orthotropy rather than isotropy.

Recall that a fiber reinforced lamina or ply is a thin sheet (~ 0.1 *mm*) containing oriented fibers. Generally, the fibers are oriented unidirectionally as in a prepreg but fibers in the form of a woven fabric may also be used. Several such thin laminae are stacked in a specific order of fiber orientation, cured, and bonded into a laminated

composite. Because the behavior of a laminated composite depends on the characteristics of individual laminae, and with due regard to their directionality, we now discuss the elastic behavior of an orthotropic lamina.

For the case of an orthotropic material with the coordinate axes parallel to the symmetry axes of the material, the array of elastic constants is given by

$$[S_{ij}] = \begin{bmatrix} S_{11} & S_{12} & S_{13} & 0 & 0 & 0 \\ & S_{22} & S_{23} & 0 & 0 & 0 \\ & & S_{33} & 0 & 0 & 0 \\ & & & S_{44} & 0 & 0 \\ & & & & S_{55} & 0 \\ & & & & & S_{66} \end{bmatrix} \tag{11.10}$$

A similar expression can be written for C_{ij}. We now take into account the fact that a lamina is a thin orthotropic material, that is, through thickness components are zero. We can obtain the compliance matrix for an orthotropic lamina by simply eliminating the terms involving the z-axis:

$$[S_{ij}] = \begin{bmatrix} S_{11} & S_{12} & 0 \\ & S_{22} & 0 \\ & & S_{66} \end{bmatrix} \tag{11.11}$$

We can rewrite in full form Hooke's law for a thin orthotropic lamina, with natural and geometric axes coinciding, as follows:

$$\begin{bmatrix} \varepsilon_1 \\ \varepsilon_2 \\ \varepsilon_6 \end{bmatrix} = \begin{bmatrix} S_{11} & S_{12} & 0 \\ S_{12} & S_{22} & 0 \\ 0 & 0 & S_{66} \end{bmatrix} \begin{bmatrix} \sigma_1 \\ \sigma_2 \\ \sigma_6 \end{bmatrix}. \tag{11.12}$$

Conversely,

$$\begin{bmatrix} \sigma_1 \\ \sigma_2 \\ \sigma_6 \end{bmatrix} = \begin{bmatrix} Q_{11} & Q_{12} & 0 \\ Q_{12} & Q_{22} & 0 \\ 0 & 0 & Q_{66} \end{bmatrix} \begin{bmatrix} \varepsilon_1 \\ \varepsilon_2 \\ \varepsilon_6 \end{bmatrix}. \tag{11.13}$$

It is customary to use the symbol Q_{ij} rather than C_{ij} for thin material. The Q_{ij} are called *reduced stiffnesses*. The relationships between Q_{ij} and S_{ij} are as follows:

$$\begin{aligned} Q_{11} &= \frac{S_{22}}{S_{11}S_{22}-S_{22}^2} \\ Q_{12} &= -\frac{S_{12}}{S_{11}S_{22}-S_{12}^2} \\ Q_{22} &= \frac{S_{11}}{S_{11}S_{22}-S_{12}^2} \\ Q_{66} &= \frac{1}{S_{66}} \end{aligned} \quad . \tag{11.14}$$

Also,

$$Q_{ij} = C_{ij} - \frac{C_{i3}C_{j3}}{C_{33}} \quad (i,j = 1,2,6)$$

Note that three-dimensional orthotropy requires nine independent elastic constants (Eq. 11.10), while bidimensional orthotropy requires only four (Eqs. 11.11 or 11.14). For an isotropic material (two- or three-dimensional), one just needs two independent elastic constants (Eqs. 11.6–11.9).

It is worth emphasizing that Eqs. (11.12) and (11.13), showing terms with indices 16 and 26 to be zero, represent a special case of orthotropy when the principal material axes of symmetry the fiber direction and the direction transverse to it coincide with the geometric directions. If this is not so, that is, if the material symmetry axes and the geometric axes do not coincide, then we have the more general case of orthotropy. In the case of two-dimensional orthotropy, we shall have a fully populated elastic constant matrix and the stress–strain relationships become

$$\begin{bmatrix} \sigma_x \\ \sigma_y \\ \sigma_s \end{bmatrix} = \begin{bmatrix} \bar{Q}_{11} & \bar{Q}_{12} & \bar{Q}_{16} \\ \bar{Q}_{12} & \bar{Q}_{22} & \bar{Q}_{26} \\ \bar{Q}_{16} & \bar{Q}_{26} & \bar{Q}_{66} \end{bmatrix} \begin{bmatrix} \varepsilon_x \\ \varepsilon_y \\ \varepsilon_s \end{bmatrix}, \tag{11.15}$$

where the $\bar{Q}_{ij}$ matrix is called the transformed reduced stiffness matrix because it is obtained by transforming Q_{ij} (specially orthotropic) to $\bar{Q}_{ij}$ (generally orthotropic), the subscripts x and y represent the geometric axes x and y, and the subscript s refers to inplane shear components. We can perform the transformation of axes as will be shown presently and obtain $\bar{Q}_{ij}$ from Q_{ij}.

Figure 11.2 shows the situation for a unidirectional composite lamina where the two sets of axes do not coincide. The properties in the 1–2 or material system of axes are known, and we wish to determine them in the x-y or geometric system or vice versa. In order to carry out the transformation of axes, we need to bring in the concept of direction cosines, a_{ij}. Table 11.1 gives the direction cosines for the transformation of axes shown in Fig. 11.2. Angle θ is positive when the x–y-axes are rotated counterclockwise with respect to the 1–2 axes. This transformation of axes is carried out easily in the matrix form (see Appendix A). For stresses, we can write

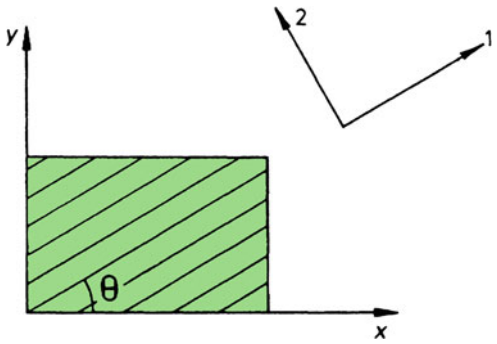

Fig. 11.2 An off-axis unidirectional lamina

Table 11.1 Direction cosines

Direction	x	y	
1	$a_{11} = m$	$a_{12} = n$	$m = \cos\theta$
2	$a_{21} = -n$	$a_{22} = m$	$m = \sin\theta$

$$\begin{bmatrix} \sigma_1 \\ \sigma_2 \\ \sigma_6 \end{bmatrix} = [T]_\sigma \begin{bmatrix} \sigma_x \\ \sigma_y \\ \sigma_s \end{bmatrix}, \tag{11.16}$$

while for strains,

$$\begin{bmatrix} \varepsilon_1 \\ \varepsilon_2 \\ \varepsilon_6 \end{bmatrix} = [T]_\varepsilon \begin{bmatrix} \varepsilon_x \\ \varepsilon_y \\ \varepsilon_s \end{bmatrix}, \tag{11.17}$$

where $[T]_\sigma$ and $[T]_\varepsilon$ are the transformation matrices for stress and strain transformations, respectively, and are given by

$$[T]_\sigma = \begin{bmatrix} m^2 & n^2 & 2mn \\ n^2 & m^2 & -2mn \\ -mn & mn & m^2 - n^2 \end{bmatrix} \tag{11.18}$$

$$[T]_\varepsilon = \begin{bmatrix} m^2 & n^2 & mn \\ n^2 & m^2 & -mn \\ -2mn & 2mn & m^2 - n^2 \end{bmatrix}, \tag{11.19}$$

where $m = \cos\theta$ and $n = \sin\theta$. This method of using different transformation matrices for stress and stain transformations avoids the need of putting the factor $\frac{1}{2}$ before the engineering shear strains to convert them to tensorial strain components suitable for transformation. Multiplying both sides of Eq. (11.16) by $[T]_\sigma^{-1}$ and remembering that $[T]_\sigma[T]_\sigma^{-1} = [I]$, the identity matrix, we get

$$\begin{bmatrix} \sigma_x \\ \sigma_y \\ \sigma_s \end{bmatrix} = [T]_\sigma^{-1} \begin{bmatrix} \sigma_1 \\ \sigma_2 \\ \sigma_6 \end{bmatrix}. \tag{11.20}$$

$[T]_\sigma^{-1}$ can be obtained from $[T]_\sigma$ by simply substituting $-\theta$ for θ. Appendix A gives the procedure for obtaining the inverse of a given matrix. In this particular case, substituting $-\theta$ for θ in Eq. (11.18) results in

$$[T]_\sigma^{-1} = \begin{bmatrix} m^2 & n^2 & -2mn \\ n^2 & m^2 & 2mn \\ mn & -mn & m^2 - n^2 \end{bmatrix}, \tag{11.21}$$

where $m = \cos\theta$ and $n = \sin\theta$. Substituting Eq. (11.13) in Eq. (11.20), we obtain

$$\begin{bmatrix} \sigma_x \\ \sigma_y \\ \sigma_s \end{bmatrix} = [T]_\sigma^{-1}[Q] \begin{bmatrix} \varepsilon_1 \\ \varepsilon_2 \\ \varepsilon_6 \end{bmatrix}. \tag{11.22}$$

If we now substitute Eq. (11.17) in Eq. (11.22), we arrive at

$$\begin{bmatrix} \sigma_x \\ \sigma_y \\ \sigma_s \end{bmatrix} = [T]_\sigma^{-1}[Q][T]_\varepsilon \begin{bmatrix} \varepsilon_x \\ \varepsilon_y \\ \varepsilon_s \end{bmatrix} = |\bar{Q}| \begin{bmatrix} \varepsilon_x \\ \varepsilon_y \\ \varepsilon_s \end{bmatrix}, \tag{11.23}$$

where

$$[\bar{Q}] = [T]_\sigma^{-1}[Q][T]_{\varepsilon!}. \tag{11.24}$$

$[\bar{Q}]$ is the stiffness matrix for a generally orthotropic lamina whose components in the expanded form are written as follows ($m = \cos\theta$, $n = \sin\theta$):

$$\begin{aligned}
\bar{Q}_{11} &= Q_{11}m^4 + 2(Q_{12} + 2Q_{66})m^2n^2 + Q_{22}n^4 \\
\bar{Q}_{12} &= (Q_{11} + Q_{22} - 4Q_{66})m^2n^2 + Q_{12}\left(m^4 + n^4\right) \\
\bar{Q}_{22} &= Q_{11}n^4 + 2(Q_{12} + 2Q_{66})m^2n^2 + Q_{22}m^4 \\
\bar{Q}_{16} &= (Q_{11} - Q_{12} - 2Q_{66})m^3n^2 + (Q_{12} - Q_{22} + 2Q_{66})mn^3 \\
\bar{Q}_{26} &= (Q_{11} - Q_{12} - 2Q_{66})mn^3 + (Q_{12} - Q_{22} + 2Q_{66})m^3n \\
\bar{Q}_{66} &= (Q_{11} + Q_{22} - 2Q_{12} - 2Q_{66})m^2n^2 + Q_{66}\left(m^4 + n^4\right).
\end{aligned} \tag{11.25}$$

Note that although $\bar{Q}_{ij}$ is a completely filled matrix, only four of its components are independent: $\bar{Q}_{16}$ and $\bar{Q}_{26}$ are linear combinations of the other four.

A corresponding stress–strain relationship in terms of compliances of a generally orthotropic lamina can be obtained:

$$\begin{bmatrix} \varepsilon_x \\ \varepsilon_y \\ \varepsilon_s \end{bmatrix} = \begin{bmatrix} S_{11} & S_{12} & S_{16} \\ S_{12} & S_{22} & S_{26} \\ S_{16} & S_{26} & S_{66} \end{bmatrix} \begin{bmatrix} \sigma_x \\ \sigma_y \\ \sigma_s \end{bmatrix}. \tag{11.26}$$

In a generally orthotropic lamina wherein we have nonzero 16 and 26 terms, a unidirectional normal stress σ_x has both normal and shear strains as responses and vice versa; that is, there is a coupling between the normal and shear components. In the case of a specially orthotropic lamina where the 16 and 26 terms are zero, we have normal stresses producing normal strains and shear stresses producing shear strains and vice versa. Thus, in the specially orthotropic case, there is no coupling between the normal and shear components. We present more information about such coupling effects in Sect. 11.5.

11.3 Relationships Between Engineering Constants and Reduced Stiffnesses and Compliances

Consider the thin lamina shown in Fig. 11.3 with the natural or material axes coinciding with the geometric axes. The conventional engineering constants in this case are Young's moduli in direction 1 (E_1) and direction 2 (E_2), the principal shear

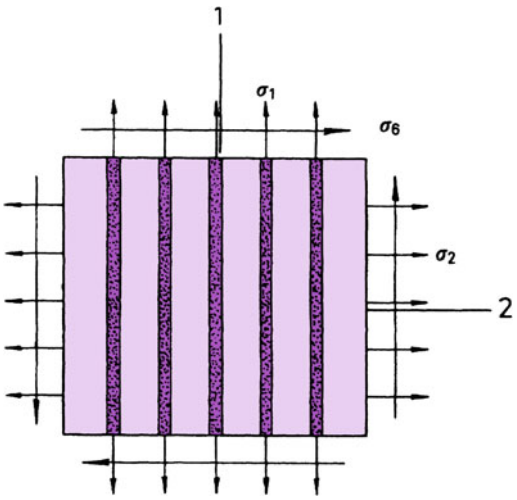

Fig. 11.3 A thin lamina with natural (or material) axes coinciding with the geometric axes

modulus G_6, and the principal Poisson's ratio v_1. The Poisson's ratio v_1, when the lamina is strained in direction 1, is equal to $-\varepsilon_2/\varepsilon_1$. The Poisson's ratio v_2, when the lamina is strained in direction 2, is equal to $-\varepsilon_1/\varepsilon_2$.

We wish to relate these five conventional engineering constants to the four independent elastic constants, the reduced stiffnesses Q_{ij}. Let us consider that σ_1 is the only nonzero component in Eq. (11.13). Then we can write

$$\sigma_1 = Q_{11}\varepsilon_1 + Q_{12}\varepsilon_2$$
$$\sigma_2 = Q_{12}\varepsilon_1 + Q_{22}\varepsilon_2 = 0.$$

Solving for ε_1 and ε_2, we get

$$\varepsilon_1 = \frac{Q_{22}}{Q_{11}Q_{22} - Q_{12}^2}\sigma_1$$

and

$$\varepsilon_2 = \frac{Q_{12}}{Q_{11}Q_{22} - Q_{12}^2}\sigma_1.$$

By definition, we have $E_1 = \sigma_1/\varepsilon_1$. Thus,

$$E_1 = \frac{Q_{11}Q_{22} - Q_{12}^2}{Q_{22}} \tag{11.27}$$

and

$$v_1 = -\frac{\varepsilon_2}{\varepsilon_1} = \frac{Q_{12}}{Q_{22}}. \tag{11.28}$$

If we repeat this procedure with σ_2 as the only nonzero stress component in Eq. (11.13), we obtain

$$E_2 = \frac{\sigma_2}{\varepsilon_2} = \frac{Q_{11}Q_{22} - Q_{12}^2}{Q_{11}} \tag{11.29}$$

and

$$v_2 = -\frac{\varepsilon_1}{\varepsilon_2} = \frac{Q_{12}}{Q_{11}}. \tag{11.30}$$

If we consider that σ_6 is the only nonzero component, we can get

$$G_6 = \frac{\sigma_6}{\varepsilon_6} = Q_{66}. \tag{11.31}$$

Note that only four of the five constants are independent because

$$v_1 E_2 = v_2 E_1 \tag{11.32}$$

or

$$\frac{E_1}{E_2} = \frac{v_1}{v_2}. \tag{11.33}$$

We can solve Eqs. (11.27)–(11.30) for the Q_{ij} to give

$$Q_{11} = \frac{E_1}{1 - v_1 v_2} \quad Q_{22} = \frac{E_2}{1 - v_1 v_2} \quad Q_{12} = \frac{v_1 E_2}{1 - v_1 v_2} = \frac{v_2 E_1}{1 - v_1 v_2},$$

and $Q_{66} = Q_6$ is given by Eq. (11.31). Similarly, we can show that the relationships between compliances and engineering constants are as follows:

$$S_{11} = \frac{1}{E_1} \quad S_{22} = \frac{1}{E_2} \quad S_{12} = -\frac{v_1}{E_1} = -\frac{v_2}{E_2} \quad S_{66} = \frac{1}{G_6}.$$

11.4 Variation of Lamina Properties with Orientation

In Sect. 11.2, we obtained the relationships between Q_{ij} and $\bar{Q}_{ij}$. It is of interest to obtain similar relationships for conventional engineering constants referred to geometric axes x–y (E_x, E_y, G_s, and v_x) in terms of engineering constants referred to material symmetry axes 1–2 (E_1, E_2, G_6, and v_1). Consider Eqs. (11.16) and (11.18) and let σ_x be the only nonzero stress component. Then

$$\sigma_1 = \sigma_x m^2 \tag{11.34a}$$

$$\sigma_2 = \sigma_x n^2 \tag{11.34b}$$

$$\sigma_6 = -\sigma_x mn. \tag{11.34c}$$

By Hooke's law, we can write for the strains in a lamina

$$\varepsilon_1 = \frac{1}{E_1}(\sigma_1 - v_1 \sigma_2) \tag{11.35a}$$

$$\varepsilon_2 = \frac{1}{E_2}(\sigma_2 - \nu_2\sigma_2) \tag{11.35b}$$

$$\varepsilon_6 = \frac{\sigma_6}{G_6}. \tag{11.35c}$$

From Eqs. (11.34a, 11.34b, 11.34c) and (11.35a, 11.35b, 11.35c), we get

$$\varepsilon_1 = \sigma_x\left(\frac{m^2}{E_1} - \nu_1\frac{n^2}{E_1}\right) = \sigma_x\left(\frac{m^2}{E_1} - \frac{\nu_2}{E_2}n^2\right) \tag{11.36a}$$

$$\varepsilon_2 = \sigma_x\left(\frac{n^2}{E_2} - \nu_2\frac{m^2}{E_2}\right) = \sigma_x\left(\frac{n^2}{E_2} - \frac{\nu_1}{E_1}m^2\right) \tag{11.36b}$$

$$\varepsilon_6 = -\frac{\sigma_x mn}{G_6}. \tag{11.36c}$$

Because we have the strain transformation given by Eq. (11.17), we can write the inverse of Eq. (11.17) as

$$\begin{bmatrix}\varepsilon_x\\ \varepsilon_y\\ \varepsilon_s\end{bmatrix} = [T]_\varepsilon^{-1}\begin{bmatrix}\varepsilon_1\\ \varepsilon_2\\ \varepsilon_6\end{bmatrix},$$

where $[T]_\varepsilon^{-1}$ can be obtained by substituting $-\theta$ for θ in Eq. (11.19). In the expanded form, we can write the above expression as

$$\varepsilon_x = m^2\varepsilon_1 + n^2\varepsilon_2 - mn\varepsilon_6 \tag{11.37a}$$

$$\varepsilon_y = n^2\varepsilon_1 + m^2\varepsilon_2 + mn\varepsilon_6 \tag{11.37b}$$

$$\varepsilon_s = 2(\varepsilon_1 - \varepsilon_2)mn + \varepsilon_6\left(m^2 - n^2\right). \tag{11.37c}$$

Substituting Eqs. (11.36a, 11.36b, 11.36c) in Eqs. (11.37a, 11.37b, 11.37c), we obtain

$$\varepsilon_x = \sigma_x\left[\frac{m^4}{E_1} + \frac{n^4}{E_2} + \left(\frac{1}{G_6} - \frac{2\nu_1}{E_1}\right)m^2n^2\right] \tag{11.38a}$$

$$\varepsilon_y = -\sigma_x\left[\frac{\nu_1}{E_1} - \left(\frac{1}{E_1} + \frac{2\nu_1}{E_1} + \frac{1}{E_2} - \frac{1}{G_6}\right)m^2n^2\right] \tag{11.38b}$$

$$\varepsilon_s = -\sigma_x(2mn)\left[\frac{\nu_1}{E_1} + \frac{1}{E_2} - \frac{1}{2G_6} - m^2\left(\frac{1}{E_1} + \frac{2\nu_1}{E_1} + \frac{1}{E_2} - \frac{1}{G_6}\right)\right]. \tag{11.38c}$$

Combining this with Eq. (11.38a), we obtain

$$\frac{1}{E_x} = \frac{m^4}{E_1} + \frac{n^4}{E_2} + \left(\frac{1}{G_6} - \frac{2\nu_1}{E_1}\right) m^2 n^2. \tag{11.39}$$

E_y can be obtained from E_x by substituting $\theta + 90°$ for θ in Eq. (11.39):

$$\frac{1}{E_y} = \frac{n^4}{E_1} + \frac{m^4}{E_2} + \left(\frac{1}{G_6} - \frac{2\nu_1}{E_1}\right) m^2 n^2. \tag{11.40}$$

Now, $\nu_x = -\varepsilon_y/\varepsilon_x$ when σ_x is the applied stress. Then, from Eqs. (11.38b) and (11.39), we obtain

$$\frac{\nu_x}{E_x} = -\frac{\varepsilon_y}{E_x \varepsilon_x} = -\frac{\varepsilon_y}{\sigma_x} = \frac{\nu_1}{E_1} - \left(\frac{1}{E_1} + \frac{2\nu}{E_1} + \frac{1}{E_2} - \frac{1}{G_6}\right) m^2 n^2$$

or

$$\nu_x = E_x \left[\frac{\nu_1}{E_1} - \left(\frac{1}{E_1} + \frac{2\nu_1}{E_1} + \frac{1}{E_2} - \frac{1}{G_6}\right) m^2 n^2\right]. \tag{11.41}$$

Similarly, it can be shown that

$$\nu_y = E_y \left[\frac{\nu_2}{E_2} - \left(\frac{1}{E_1} + \frac{1}{E_2} + \frac{2\nu_1}{E_1} - \frac{1}{G_6}\right) m^2 n^2\right]. \tag{11.42}$$

Taking σ_s to be the only nonzero stress component, noting that $\varepsilon_s = \sigma_s/G_s$, and applying Hooke's law, we obtain

$$\frac{1}{G_s} = \frac{1}{G_6} + 4m^2 n^2 \left(\frac{1+\nu_1}{E_1} + \frac{1+\nu_2}{E_2} - \frac{1}{G_6}\right). \tag{11.43}$$

Equations (11.39) through (11.43) give as the expressions for the variations of elastic constants of a unidirectional composite with fiber orientation. These are very useful expressions. Figure 11.4 shows the variations of E_x, E_y, G_s, ν_x, and ν_y with fiber orientation θ for a 50% V_f carbon/epoxy composite. The other relevant data used in Fig. 11.4 are $E_1 = 240\ GPa$, $E_2 = 8\ GPa$, $G_6 = 6\ GPa$, and $\nu_1 = 0.26$.

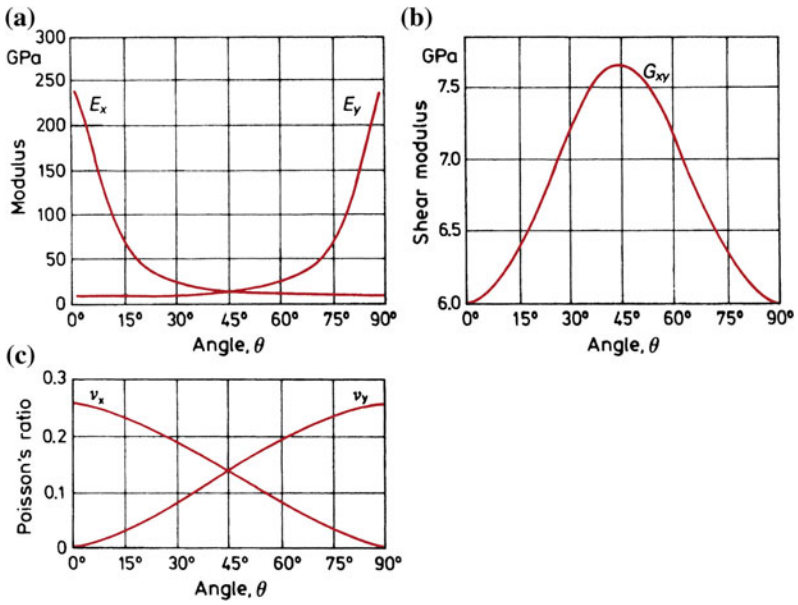

Fig. 11.4 Variation of elastic constants with fiber orientation angle for a 50 v/o carbon/epoxy composite: **a** longitudinal and transverse Young's moduli (E_x and E_y), **b** shear modulus (G_{xy}), and **c** Poisson's ratio (ν_x and ν_y)

11.5 Analysis of Laminated Composites

Now that we have discussed the analysis of an individual lamina, we proceed to discuss the macroscopic analysis of laminated composites (Jones 1975; Christensen 1979; Tsai and Hahn 1980; Halpin 1984; Daniel and Ishai 1994). In this analysis, the individual identities of fiber and matrix are ignored. Each individual, fiber reinforced lamina (also called ply) is treated as a homogeneous, orthotropic sheet, and the laminated composite is analyzed using the classical theory of laminated plates.

It would be in order at this point to describe how a multidirectional laminate can be defined by using a code to designate the stacking sequence of laminae. Figure 11.5 shows an example of a stacking sequence. The stacking sequence shown in Fig. 11.5 can be described by the following code:

$$[0_2/90_2/-45_3/45_3]_s.$$

This code says that starting from the bottom of the laminate, that is, at $z = -h/2$, we have a two plies at 0° orientation; then two plies at 90° orientation; followed by a group of three plies at −45° orientation; and lastly, a group of three plies at +45° orientation. The subscript s indicates that the laminate is symmetric with respect to the midplane ($z = 0$); that is, the top half of the laminate is a mirror image of the

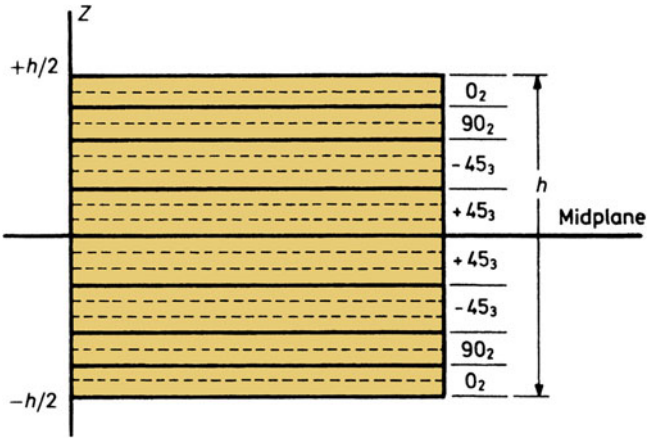

Fig. 11.5 A laminate composite with the stacking sequence given by $[0_1/90_2/–45_3/45_3]_s$

bottom half. It is not necessary that a laminate composite by symmetric. If the top half has the sequence opposite to that of the bottom half, then we shall have an asymmetric laminate. In any event, we may represent the total stacking sequence of the laminate shown in Fig. 11.5 in the following way:

$$[0_2/90_2/-45_3/45_6/-45_3/90_2/0_2]_T,$$

where the subscript T indicates that the code represents the total or the whole thickness of the laminate. Note that we have merged the two middle groups of the same ply orientation into one group. If the laminate composite consists of an odd number of laminae, the midplane will lie in the central ply.

11.5.1 Basic Assumptions

We assume that the laminate thickness is small compared to its lateral dimensions. Therefore, stresses acting on the interlaminar planes in the interior of the laminate, that is, away from the free edges, are negligibly small (we shall see later that the situation is different at the free edges). We also assume that there exists a perfect bond between any two laminae. That being so, the laminae cannot slide over each other, and we have continuous displacements across the bond. We make yet another important assumption, namely, a line originally straight and perpendicular to the laminate midplane remains so after deformation. Actually, this follows from the perfect bond assumption, which does not allow sliding between the laminae.

Finally, we have the so called Kirchhoff assumption, which states that inplane displacements are linear functions of the thickness, and therefore the interlaminar

shear strains, ε_{xz} and ε_{yz}, are negligible. With these assumptions, we can reduce the laminate behavior to a two-dimensional analysis of the laminate midplane.

We have the following strain–displacement relationships:

$$\begin{aligned} \varepsilon_x &= \frac{\partial u}{\partial x} \quad \varepsilon_{xy} = \frac{\partial u}{\partial y} + \frac{\partial v}{\partial x} \\ \varepsilon_y &= \frac{\partial v}{\partial y} \quad \varepsilon_{xz} = \frac{\partial u}{\partial z} + \frac{\partial w}{\partial x} \\ \varepsilon_z &= \frac{\partial w}{\partial z} \quad \varepsilon_{yz} = \frac{\partial v}{\partial z} + \frac{\partial w}{\partial y}. \end{aligned} \tag{11.44}$$

Here, u, v, and w are the displacements in the x-, y-, and z-directions, respectively. For $i \neq j$, the ε_{ij} represent engineering shear strain components equal to twice the tensorial shear components. As per Kirchhoff's assumption, the inplane displacements are linear functions of the thickness coordinate, z. Then

$$u = u_0(x, y) + zF_1(x, y) \qquad v = v_0(x, y) + zF_2(x, y), \tag{11.45}$$

where u_0 and v_0 are displacements of the midplane and F_1 and F_2 are functions to be determined, see below. It also follows from Kirchhoff's assumptions that interlaminar shear strains ε_{xz} and ε_{yz} are zero. Therefore, from Eqs. (11.44) and (11.45) we obtain

$$\begin{aligned} \varepsilon_{xz} &= F_1(x, y) + \frac{\partial w}{\partial x} = 0 \\ \varepsilon_{yz} &= F_2(x, y) + \frac{\partial w}{\partial y} = 0. \end{aligned}$$

It therefore follows that

$$F_1(x, y) = -\frac{\partial w}{\partial x} \quad \text{and} \quad F_2(x, y) = -\frac{\partial w}{\partial y}. \tag{11.46}$$

The normal strain in the thickness direction, ε_z, is negligible: thus we can write

$$w = w(x, y).$$

That is, the vertical displacement of any point does not change in the thickness direction.

Substituting Eq. (11.46) into Eq. (11.45), we obtain

$$\varepsilon_x = \frac{\partial u}{\partial x} = \frac{\partial u_0}{\partial x} - z\frac{\partial^2 w}{\partial x^2} = \varepsilon_x^0 + zK_x \tag{11.47a}$$

$$\varepsilon_y = \frac{\partial v}{\partial y} = \frac{\partial v_0}{\partial y} - z\frac{\partial^2 w}{\partial y^2} = \varepsilon_y^0 + zK_y \tag{11.47b}$$

$$\varepsilon_{xy} = \frac{\partial u}{\partial y} + \frac{\partial v}{\partial x} = \frac{\partial u_0}{\partial y} + \frac{\partial v_0}{\partial x} - 2z\frac{\partial^2 w}{\partial x \partial y} = \varepsilon_{xy}^0 + zK_{xy}. \tag{11.47c}$$

Denoting ε_{xy} by ε_s and K_{xy} by K_s, as per our notation, we can rewrite the expression for ε_{xy} as

$$\varepsilon_s = \varepsilon_s^0 + zK_s. \tag{11.47d}$$

Here, ε_x^0, ε_y^0, and ε_s^0 are the midplane strains, while K_x, K_y, and K_s are the plate curvatures. We can represent these quantities in a compact form as follows:

$$\begin{bmatrix} \varepsilon_x^0 \\ \varepsilon_y^0 \\ \varepsilon_s^0 \end{bmatrix} = \begin{bmatrix} \partial u_0/\partial x \\ \partial v_0/\partial y \\ \partial u_0/\partial y + \partial v_0/\partial x \end{bmatrix} \tag{11.48}$$

and

$$\begin{bmatrix} K_x \\ K_y \\ K_s \end{bmatrix} = -\begin{bmatrix} \partial^2 w/\partial x^2 \\ \partial^2 w/\partial y^2 \\ 2\partial^2 w/\partial x \partial y \end{bmatrix}. \tag{11.49}$$

Equations (11.47a, 11.47b, 11.47c, 11.47d) can be put into the following form:

$$\begin{bmatrix} \varepsilon_x \\ \varepsilon_y \\ \varepsilon_s \end{bmatrix} = \begin{bmatrix} \varepsilon_x^0 \\ \varepsilon_y^0 \\ \varepsilon_s^0 \end{bmatrix} + z\begin{bmatrix} K_x \\ K_y \\ K_s \end{bmatrix}. \tag{11.50}$$

11.5.2 Constitutive Relationships for Laminated Composites

Consider a composite made of n stacked layers or plies; see Fig. 11.6a. Let h be the thickness of the laminated composite. Then we can write, for the kth layer, the following constitutive relationship:

$$[\sigma]_k = [\bar{Q}]_k[\varepsilon]_k. \tag{11.51}$$

From the theory of laminated plates, we have strain–displacement relationships given by Eq. (11.50). We can rewrite Eq. (11.50) as

$$[\varepsilon] = \left[\varepsilon^0\right] + z[K]. \tag{11.52}$$

Substituting Eq. (11.52) in Eq. (11.51), for the kth ply we get

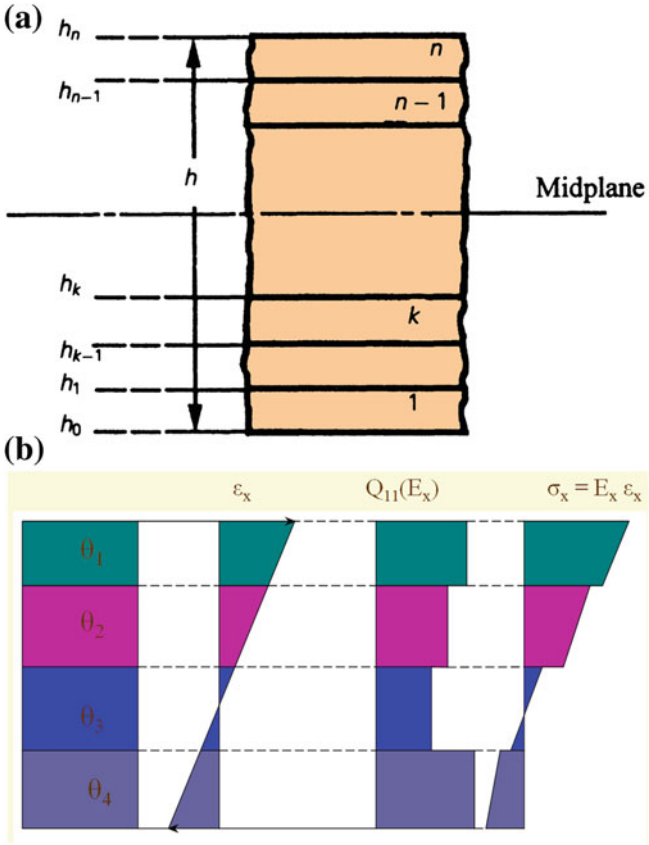

Fig. 11.6 **a** A laminated composite made up of n stacked plies. **b** Variation of strain and stress through the thickness in a 4-ply laminated composite

$$[\sigma]_k = [\bar{Q}]_k [\varepsilon^0] + z[\bar{Q}]_k [K]. \tag{11.53}$$

It is worth emphasizing that strains vary through the thickness of laminated composite linearly with thickness; the stresses do not. This is easy to visualize if we recall that stiffness of each ply will be different; being a function of the fiber orientation. This is shown schematically in a four-ply laminated composite in Fig. 11.6b. Because the stresses in a laminated composite vary from ply to ply, it is convenient to define laminate force and moment resultants as shown in Fig. 11.7. These resultants of stresses and moments acting on a laminate cross section, defined as follows, provide us with a statically equivalent system of forces and moments acting at the midplane of the laminated composite. In the most general case, such a composite will have σ_x, σ_y, σ_z, σ_{xy}, σ_{yz}, and σ_{zx} as the six stress components. Our laminated composite, however, is in a state of plane stress. Thus, we shall have only three stress components: σ_x, σ_y, and σ_{xy} (= σ_s). Accordingly, we define the three corresponding stress resultants as

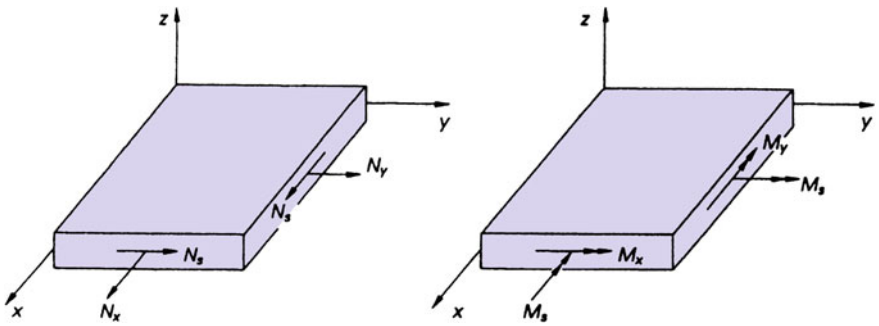

Fig. 11.7 Force (N) and moment (M) resultants in a laminated composite

$$N_x = \int_{-h/2}^{k/2} \sigma_x dz$$
$$N_y = \int_{-h/2}^{h/2} \sigma_y dz \tag{11.54}$$
$$N_s = \int_{-h/2}^{h/2} \sigma_s dz.$$

These stress resultants have the dimensions of force per unit length and are positive in the same direction as the corresponding stress components. These resultants give the total force per unit length acting at the midplane. Additionally, moments are applied at the midplane, which are equivalent to the moments produced by the stresses with respect to the midplane. We define the moment resultants as

$$M_x = \int_{-h/2}^{h/2} \sigma_x z\, dz$$
$$M_y = \int_{-h/2}^{h/2} \sigma_y z\, dz \tag{11.55}$$
$$M_{xy} = M_s = \int_{-h/2}^{h/2} \sigma_s z dz.$$

This system of three stress resultants (Eq. 11.54) and three moment resultants (Eq. 11.55) is statically equivalent to actual stress distribution through the thickness of the composite laminate.

From Eqs. (11.52) and (11.53), we can write for the stress resultants a summation over the n plies:

$$\begin{aligned}\begin{bmatrix} N_x \\ N_y \\ N_s \end{bmatrix} &= \sum_{k=1}^{n} \int_{h_{k-1}}^{h_k} \begin{bmatrix} \sigma_x \\ \sigma_y \\ \sigma_s \end{bmatrix} dz \\ &= \sum_{k=1}^{n} \left(\int_{h_{k-1}}^{h_k} \begin{bmatrix} \bar{Q}_{11} & \bar{Q}_{12} & \bar{Q}_{16} \\ \bar{Q}_{12} & \bar{Q}_{22} & \bar{Q}_{26} \\ \bar{Q}_{16} & \bar{Q}_{26} & \bar{Q}_{66} \end{bmatrix} \begin{bmatrix} \varepsilon_x^0 \\ \varepsilon_y^0 \\ \varepsilon_s^0 \end{bmatrix} dz \right. \\ &\quad \left. + \int_{h_{k-1}}^{h_k} \begin{bmatrix} \bar{Q}_{11} & \bar{Q}_{12} & \bar{Q}_{16} \\ \bar{Q}_{12} & \bar{Q}_{22} & \bar{Q}_{26} \\ \bar{Q}_{16} & \bar{Q}_{26} & \bar{Q}_{66} \end{bmatrix} \begin{bmatrix} K_x \\ K_y \\ K_x \end{bmatrix} z\, dz \right). \end{aligned} \tag{11.56}$$

Note that $[\varepsilon^0]$ and $[K]$ are not functions of z and in a given ply $[\bar{Q}]$ is not a function of z. Thus, we can simplify the preceding expression to

$$\begin{aligned}\begin{bmatrix} N_x \\ N_y \\ N_s \end{bmatrix} &= \sum_{k=1}^{n} \left(\begin{bmatrix} \bar{Q}_{11} & \bar{Q}_{12} & \bar{Q}_{16} \\ \bar{Q}_{12} & \bar{Q}_{22} & \bar{Q}_{26} \\ \bar{Q}_{16} & \bar{Q}_{26} & \bar{Q}_{66} \end{bmatrix} \begin{bmatrix} \varepsilon_x^0 \\ \varepsilon_y^0 \\ \varepsilon_s^0 \end{bmatrix} \int_{h_{k-1}}^{h_k} dz \right. \\ &\quad \left. + \begin{bmatrix} \bar{Q}_{11} & \bar{Q}_{12} & \bar{Q}_{16} \\ \bar{Q}_{12} & \bar{Q}_{22} & \bar{Q}_{26} \\ \bar{Q}_{16} & \bar{Q}_{26} & \bar{Q}_{66} \end{bmatrix} \begin{bmatrix} K_x \\ K_y \\ K_s \end{bmatrix} \int_{h_{k-1}}^{h_k} z\, dz \right). \end{aligned} \tag{11.57}$$

We can rewrite Eq. (11.57) as

$$\begin{bmatrix} N_x \\ N_y \\ N_s \end{bmatrix} = \begin{bmatrix} A_{11} & A_{12} & A_{16} \\ A_{12} & A_{22} & A_{26} \\ A_{16} & A_{26} & A_{66} \end{bmatrix} \begin{bmatrix} \varepsilon_x^0 \\ \varepsilon_y^0 \\ \varepsilon_s^0 \end{bmatrix} + \begin{bmatrix} B_{11} & B_{12} & B_{16} \\ B_{22} & B_{22} & B_{26} \\ B_{16} & B_{26} & B_{66} \end{bmatrix} \begin{bmatrix} K_x \\ K_y \\ K_s \end{bmatrix} \tag{11.58}$$

or

$$[N] = [A]\left[\varepsilon^0\right] + [B][K], \tag{11.59}$$

where

$$A_{ij} = \sum_{k=1}^{n} \left(\bar{Q}_{ij}\right)_k (h_k - h_{k-1}) \tag{11.60}$$

and

$$B_{ij} = \frac{1}{2}\sum_{k=1}^{n} \left(\bar{Q}_{ij}\right)_k \left(h_k^2 - h_{k-1}^2\right). \tag{11.61}$$

Similarly, from Eqs. (11.52) and (11.55), we can write for the moment resultants

$$\begin{bmatrix} M_x \\ M_y \\ M_s \end{bmatrix} = \begin{bmatrix} B_{11} & B_{12} & B_{16} \\ B_{12} & B_{22} & B_{26} \\ B_{16} & B_{26} & B_{66} \end{bmatrix} \begin{bmatrix} \varepsilon_x^0 \\ \varepsilon_y^0 \\ \varepsilon_s^0 \end{bmatrix} + \begin{bmatrix} D_{11} & D_{12} & D_{16} \\ D_{12} & D_{22} & D_{26} \\ D_{16} & D_{26} & D_{66} \end{bmatrix} \begin{bmatrix} K_x \\ K_y \\ K_z \end{bmatrix} \tag{11.62}$$

or

$$[M] = [B]\left[\varepsilon^0\right] + [D][K], \tag{11.63}$$

where

$$D_{ij} = \frac{1}{3}\sum_{k=1}^{n} \left(\bar{Q}_{ij}\right)_k \left(h_k^3 - h_{k-1}^3\right) \tag{11.64}$$

and the B_{ij} are given by Eq. (11.61).

We may combine Eqs. (11.59) and (11.63) and write the constitutive equations for the laminate composite in a more compact form. Thus,

$$\left[\frac{N}{M}\right] = \begin{bmatrix} A & B \\ B & D \end{bmatrix} \left[\frac{\varepsilon^0}{K}\right]. \tag{11.65}$$

To appreciate the significance of the preceding expressions, let us examine the expression for N_x:

$$N_x = A_{11}\varepsilon_x^0 + A_{12}\varepsilon_y^0 + A_{16}\varepsilon_s^0 + B_{11}K_x + B_{12}K_y + B_{16}K_s.$$

We note that the stress resultant is a function of the midplane tensile strains (ε_x^0 and ε_y^0), the midplane shear strain $\left(\varepsilon_s^0\right)$, the bending curvatures (K_x and K_y), and the twisting (K_s). This is a much more complex situation than that observed in a homogeneous plate where tensile loads result in only tensile strains. In a laminated plate, we have coupling between tensile and shear, tensile and bending, and tensile and twisting effects. Specifically, the terms A_{16} and A_{26} bring in the tension–shear coupling, while the terms B_{16} and B_{26} represent the tension–twisting coupling. The D_{16} and D_{26} terms in a similar expression for M_x represent flexure–twisting coupling.

Under certain conditions, the stress and moment resultants become uncoupled. It is instructive to examine the conditions under which some of these simplifications can result. The A_{ij} terms are the sum of ply $\bar{Q}_{ij}$ times the ply thickness (Eq. 11.60).

Thus, the A_{ij} will be zero if the positive contributions of some laminae are nullified by the negative contributions of others. Now the Q_{ij} terms of a ply are derived from orthotropic stiffnesses and, because of the form of transformation Eq. (11.25), $\bar{Q}_{11}$, $\bar{Q}_{12}$, $\bar{Q}_{22}$, and $\bar{Q}_{66}$ are always positive. This means that A_{11}, A_{12}, A_{22}, and A_{66} are always positive. $\bar{Q}_{16}$ and $\bar{Q}_{26}$, however, are zero for 0° and 90° orientations and can be positive or negative for θ between 0° and 90°. In fact, $\bar{Q}_{16}$ and $\bar{Q}_{26}$ are odd functions of θ; that is, for equal positive and negative orientations, they will be equal in magnitude but opposite in sign. In particular, $\bar{Q}_{16}$ and $\bar{Q}_{26}$ for a $+\theta$ orientation are equal to but opposite in sign to $\bar{Q}_{16}$ and $\bar{Q}_{26}$ values for a $-\theta$ orientation. Thus, *if for each $+\theta$ ply, we have another identical ply of the same thickness at $-\theta$, then we shall have what is called a specially orthotropic laminate with respect to inplane stresses and strains; that is, $A_{16} = A_{26} = 0$. The relative position of such plies in the stacking sequence does not matter.*

The B_{ij} terms are sums of terms involving $\bar{Q}_{ij}$ and differences of the square of z terms for the top (h_k) and bottom (h_{k-1}) of each ply. Thus, the B_{ij} terms are even functions of h_k, which means that they are zero if the laminate composite is symmetric with respect to thickness. In other words, *the B_{ij} are zero if we have for each ply above the midplane a ply identical in properties and orientation and at an equal distance below the midplane.* Such a laminate is called a *symmetric laminate* and will have B_{ij} identically zero. This simplifies the constitutive equations, and symmetric laminates are considerably easier to analyze. Additionally, because of the absence of bending–stretching coupling in symmetric laminates, they do not have the problem of warping encountered in nonsymmetric laminates and caused by inplane forces induced by thermal contractions occurring during the curing of the resin matrix. Symmetric laminates will only experience tensile strains at the midplane but no flexure. The reader should realize that the origin of the $[B]$ matrix lies not in the intrinsic orthotropy of the laminae, but in the heterogeneous (nonsymmetric) stacking sequence of the plies. Thus, a two-ply composite consisting of isotropic materials such as aluminum and steel will show a nonzero $[B]$.

The terms in the D_{ij} matrix are defined in terms of $\bar{Q}_{ij}$ and the difference between h_k^3 and h_{k-1}^3. The geometrical contribution $\left(h_k^3 - h_{k-1}^3\right)$ is always positive. Thus, as explained above for A_{ij}, D_{11}, D_{12}, D_{22}, and D_{66} are always positive. Recall that $\bar{Q}_{16}$ and $\bar{Q}_{26}$ are odd functions of θ. D_{16} and D_{26} are zero for all plies oriented at 0° or 90° because these plies have $\bar{Q}_{16} = \bar{Q}_{26} = 0$. D_{16} and D_{26} can also be made zero if, for each ply oriented at $+\theta$ and at a given distance above the midplane, we have an identical ply at an equal distance below the midplane but oriented at $-\theta$. This follows from the property of the odd function of θ that is, $\bar{Q}_{16}(+\theta) = -\bar{Q}_{16}(-\theta)$, and $\bar{Q}_{26}(+\theta) = -\bar{Q}_{26}(-\theta)$, while $\left(h_k^3 - h_{k-1}^3\right)$ is the same for both plies. Note, however, that such a laminated composite does not have a midplane of symmetry; that is, $B_{ij} \neq 0$. In fact, D_{16} and D_{26} are not zero for any midplane symmetric laminate except for unidirectional laminates (0° or 90°) and cross-plied laminates (0°/90°). We can make D_{16} and D_{26} arbitrarily small, however, by using a large enough number of plies stacked at $\pm\ \theta$. This is because the contributions of $+\theta$ plies to D_{16} and D_{26} are opposite in sign to those of $-\theta$ plies, and although their

locations are different distances from the midplane, given large enough number of plies, they will practically cancel each other.

Yet another simple stacking sequence is the quasi-isotropic sequence. Such a laminated composite can be made by having plies of identical properties oriented in such a way that the angle between any two adjacent layers is $2\pi/n$, where n is the number of plies. Such a laminate has $[A]$ independent of orientation in the plane. We call such a stacking sequence *quasi-isotropic*, because $[B]$ and $[D]$ are not necessarily isotropic. We provide a summary of some of these special laminates that we have discussed in Fig. 11.8. Note the coupling coefficients that go to zero for each case.

The important results of this section can be summarized as follows:

$$[\sigma]_k = [\bar{Q}]_k [\varepsilon]_k,$$

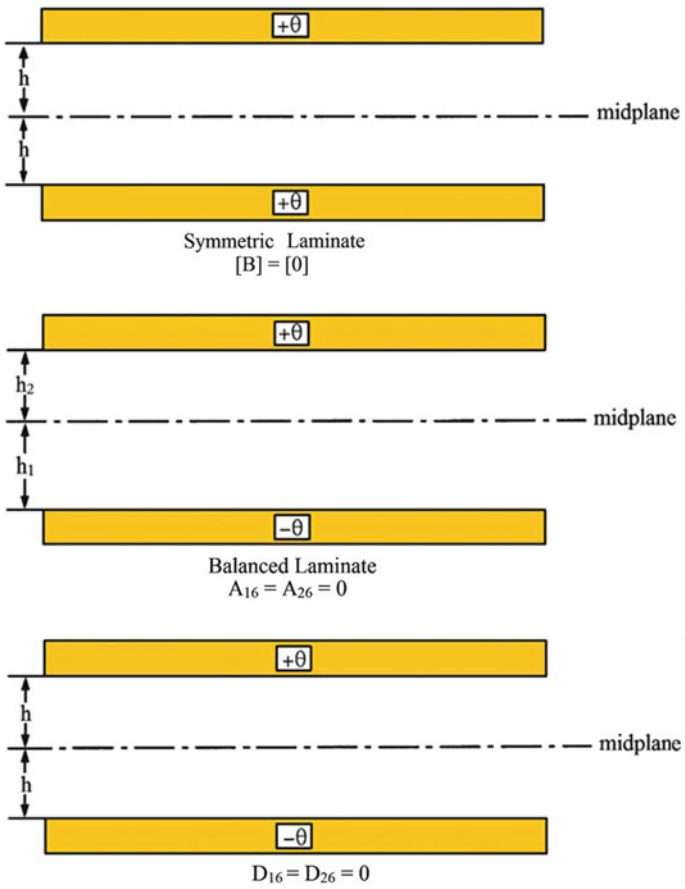

Fig. 11.8 Some special laminates

where $1 \leq k \leq n$ and $i, j = 1, 2, 6$.

$$\varepsilon_i = \varepsilon_i^0 + zK_i$$
$$N_i = \int_{-h/2}^{h/2} \sigma_i \, dz$$
$$M_i = \int_{-h/2}^{h/2} \sigma_i dz$$
$$N_i = A_{ij}\varepsilon_j^0 + B_{ij}K_j$$
$$M_i = B_{ij}\varepsilon_j^0 + D_{ij}K_j$$
$$A_{ij} = \sum_{k=1}^{n} \left(\bar{Q}_{ij}\right)_k (h_k - h_{k-1})$$
$$B_{ij} = \tfrac{1}{2}\sum_{k=1}^{n} \left(\bar{Q}_{ij}\right)_k \left(h_k^2 - h_{k-1}^2\right)$$
$$D_{ij} = \tfrac{1}{3}\sum_{k=1}^{n} \left(\bar{Q}_{ij}\right)_k \left(h_k^3 - h_{k-1}^3\right).$$

Symmetric laminates

$$\bar{Q}(z) = \bar{Q}(-z)$$

Antisymmetric laminates

$$\bar{Q}(z) = -\bar{Q}(-z)$$

Example 11.1 A laminate is made up by stacking 0° and 45° plies as shown below:

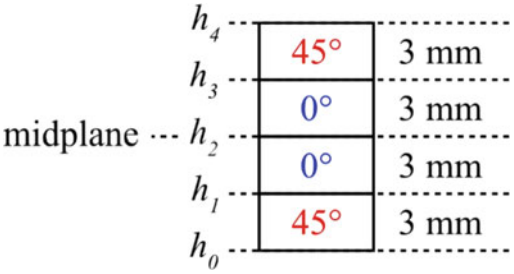

The $[Q_{ij}]_{0^\circ}$ and $\left[\bar{Q}_{ij}\right]_{45^\circ}$ matrices are

$$[Q_{ij}]_{0^\circ} = \begin{bmatrix} 140 & 5 & 0 \\ & 5 & 0 \\ & & 5 \end{bmatrix} GPa$$

$$[\bar{Q}_{ij}]_{45^\circ} = \begin{bmatrix} 50 & 35 & 30 \\ & 50 & 30 \\ & & 35 \end{bmatrix} GPa.$$

Compute the [A], [B], and [D] matrices for this laminate.

Solution

$$(\bar{Q}_{ij})_{45^\circ} = \begin{bmatrix} 50 & 35 & 30 \\ & 50 & 30 \\ & & 35 \end{bmatrix}$$

$$(\bar{Q}_{ij})_{0^\circ} = (Q_{ij})_{0^\circ} = \begin{bmatrix} 140 & 5 & 0 \\ & 5 & 0 \\ & & 5 \end{bmatrix}'.$$

Let us now compute the submatrices, [A], [B], and [D].

$$\begin{aligned} A_{ij} &= \sum_{k=1}^{4} (\bar{Q}_{ij})_k (h_k - h_{k-1}) \\ &= (\bar{Q}_{ij})_t (h_1 - h_0) + (\bar{Q}_{ij})_2 (h_2 - h_1) + (\bar{Q}_{ij})_3 (h_3 - h_2) \\ &\quad + (\bar{Q}_{ij})_4 (h_4 - h_3) \\ A_{ij} &= (\bar{Q}_{ij})_1 [(-3) - (-6)] + (\bar{Q}_{ij})_2 [0 - (-3)] + (\bar{Q}_{ij})_3 [3 - 0] \\ &\quad + (\bar{Q}_{ij})_4 [6 - 3] \\ &= 3\left[(\bar{Q}_{ij})_1 + (\bar{Q}_{ij})_2 + (\bar{Q}_{ij})_3 + (\bar{Q}_{ij})_4 \right] \\ (\bar{Q}_{ij})_1 &= (\bar{Q}_{ij})_4 = (\bar{Q}_{ij})_{45^\circ} \\ (\bar{Q}_{ij})_2 &= (\bar{Q}_{ij})_3 = (\bar{Q}_{ij})_{0^\circ} \\ A &= 6\left[(\bar{Q}_{ij})_{45^\circ} + (\bar{Q}_{ij})_{0^\circ} \right] \\ &= 6\left\{ \begin{bmatrix} 50 & 35 & 30 \\ & 50 & 30 \\ & & 35 \end{bmatrix} + \begin{bmatrix} 140 & 5 & 0 \\ & 5 & 0 \\ & & 5 \end{bmatrix} \right\} \\ &= \begin{bmatrix} 1140 & 240 & 180 \\ & 330 & 180 \\ & & 240 \end{bmatrix} \times 10^6 \text{ N/m}. \end{aligned}$$

We have a symmetric laminate, therefore

$$
\begin{aligned}
[B] &= [0] \\
3D &= \sum_{k=1}^{4} (\bar{Q}_{ij})_k (h_k^3 - h_{k-1}^3) \\
&= (\bar{Q}_{ij})_l (h_1^3 - h_0^3) + (\bar{Q}_{ij})_2 (h_2^3 - h_1^3) + (\bar{Q}_{ij})_3 (h_3^3 - h_2^3) \\
&\quad + (\bar{Q}_{ij})_4 (h_4^3 - h_3^3) \\
&= (\bar{Q}_{ij})_1 \left[(-3)^3 - (-6)^3\right] + (\bar{Q}_{ij}) \left[0 - (-3)^3\right] + (\bar{Q}_{ij}) \left[3^3 - 0\right] \\
&\quad + (\bar{Q}_{ij})_4 \left[6^3 - 3^3\right] \\
&= (\bar{Q}_{ij})_1 (-27 + 216) + (\bar{Q}_{ij})_2 (0 + 27) + (\bar{Q}_{ij})_3 (27 - 0) \\
&\quad + (\bar{Q}_{ij})_4 (216 - 27) \\
3D &= 189 (\bar{Q}_{ij})_1 + 27 (\bar{Q}_{ij})_2 + 27 (\bar{Q}_{ij})_3 + 189 (\bar{Q}_{ij})_4 \\
(\bar{Q}_{ij})_1 &= (\bar{Q}_{ij})_4 = (\bar{Q}_{ij})_{45^\circ} \\
(\bar{Q}_{ij})_2 &= (\bar{Q}_{ij})_3 = (\bar{Q}_{ij})_{0^\circ} \\
D &= 126 (\bar{Q}_{ij})_{45^\circ} + 18 (\bar{Q}_{ij})_{0^\circ} \\
D &= \left\{ 126 \begin{bmatrix} 50 & 35 & 30 \\ & 50 & 30 \\ & & 35 \end{bmatrix} + 18 \begin{bmatrix} 140 & 5 & 0 \\ & 5 & 0 \\ & & 5 \end{bmatrix} \right\} \times 10^9 \frac{\mathrm{N}}{\mathrm{m}^2} \times 10^{-9} \mathrm{m}^3 \\
D &= \begin{bmatrix} 8820 & 4500 & 3780 \\ & 6390 & 3780 \\ & & 4500 \end{bmatrix} \mathrm{N \cdot m}.
\end{aligned}
$$

11.6 Stresses and Strains in Laminate Composites

We saw in Sect. 11.5 that strains produced in a lamina under load depend on the midplane strains, plate curvatures, and distances from the midplane. Midplane strains and plate curvatures can be expressed as functions of an applied load system, that is, in terms of stress and moment resultants. We derived the general constitutive Eq. (11.65) for laminate composites. We can invert Eq. (11.65) partially or fully and obtain explicit expressions for $[\varepsilon^0]$ and $[K]$. We use Eqs. (11.59) and (11.63) for this purpose. Solving Eq. (11.59) for midplane strains, we obtain

$$
\left[\varepsilon^0\right] = [A]^{-1}[N] - [A]^{-1}[B][K]. \tag{11.66}
$$

Substituting Eq. (11.66) in Eq. (11.63), we obtain

$$[M] = [B][A]^{-1}[N] - \Big([B][A]^{-1}[B] - [D]\Big)[K]. \tag{11.67}$$

Combining Eqs. (11.66) and (11.67), we obtain a partially inverted form of the constitutive equation:

$$\begin{bmatrix} \varepsilon^0 \\ \overline{M} \end{bmatrix} = \begin{bmatrix} A^* & B^* \\ C^* & D^* \end{bmatrix} \begin{bmatrix} N \\ \overline{K} \end{bmatrix}, \tag{11.68}$$

where

$$\begin{aligned} [A^*] &= [A]^{-1} \\ [B^*] &= -[A]^{-1}[B] \\ [C^*] &= [B][A]^{-1} = -[B^*]^T \\ [D^*] &= [D] - [B][A]^{-1}[B]. \end{aligned} \tag{11.69}$$

From Eqs. (11.66) and (11.69), we can write

$$\left[\varepsilon^0\right] = [A^*][N] + [B^*][K] \tag{11.70}$$

$$[M] = [C^*][N] + [D^*][K]. \tag{11.71}$$

From Eq. (11.71), we solve for [K] and obtain

$$[K] = [D^*]^{-1}[M] - [D^*]^{-1}[C^*][N]. \tag{11.72}$$

Substituting this value of [K] (Eq. 11.72) in Eq. (11.70), we obtain

$$\begin{aligned} \left[\varepsilon^0\right] &= [A^*][N] + [B^*]\Big([D^*]^{-1}[M] - [D^*]^{-1}[C^*][N]\Big) \\ &= \Big([A^*] - [B^*][D^*]^{-1}[C^*]\Big)[N] + [B^*][D^*]^{-1}[M]. \end{aligned} \tag{11.73}$$

We can combine Eqs. (11.72) and (11.70) to obtain the fully inverted form:

$$\begin{bmatrix} \varepsilon^0 \\ \overline{K} \end{bmatrix} = \begin{bmatrix} A' & B' \\ C' & D' \end{bmatrix} \begin{bmatrix} N \\ \overline{M} \end{bmatrix} = \begin{bmatrix} A' & B' \\ C' & D' \end{bmatrix} \begin{bmatrix} N \\ \overline{M} \end{bmatrix}, \tag{11.74}$$

where

$$
\begin{aligned}
[A'] &= [A^*] - [B^*][D^*]^{-1}[C^*] \\
&= [A^*] + [B^*][D^*]^{-1}[B^*]^T \quad \left([C^*] = -[B^*]^T\right) \\
[B'] &= [B^*][D^*]^{-1} \\
[C'] &= -[D^*]^{-1}[C^*] = [D^*]^{-1}[B^*]^T = [B']^T = [B'] \\
[D'] &= [D^*]^{-1}.
\end{aligned}
$$

Equations (11.65), (11.68), and (11.74) are useful forms of the laminate constitutive relationships. We note that each form involves using the elastic properties of the lamina (from the $\bar{Q}_{ij}$ values for each lamina) and the ply stacking sequence (z coordinate).

11.7 Interlaminar Stresses and Edge Effects

The classical lamination theory used in Sect. 11.5 to describe the laminate composite behavior is rigorously correct for an infinite laminate composite. It turns out that the assumption of a generalized plane stress state is quite valid in the interior of the laminate, that is, away from the free edges. At and near the free edges (extending a distance approximately equal to the laminate thickness) there exists, in fact, a three-dimensional state of stress. Under certain circumstances, there can be rather large interlaminar stresses present at the free edges, which can lead to delamination of plies or matrix cracking at the free edges and thereby cause failure. Researchers studied these aspects quite extensively and have clarified a number of issues. Pipes and Pagano [1970] considered a four-ply laminate, with plies oriented at $\pm\ \theta$ and each ply of thickness h_0, total laminate thickness $4h_0$, under a uniform axial strain as shown in Fig. 11.9. They used a finite difference method to obtain the numerical results for a carbon/epoxy composite system. The classical lamination theory states that in each ply there exists a state of plane stress with σ_x as the axial component and σ_{xy} (= σ_s) as the inplane shear stress component. As per the lamination theory, the stress components vary from layer to layer, but they are constant within each layer, see Fig. 11.6b. This is correct for an infinitely wide laminate. It is not correct for a finite-width laminate because the inplane shear stress does not vanish at the free edge surface. Figure 11.9 shows the stress distribution at the interface $z = h_0$ as a function of y/b, where $2b$ is the laminate width. The inplane shear stress σ_{xy} (=σ_s) converges to the value predicted by the lamination theory for $y/b < 0.5$, that is, away from the free edge. The axial stress component σ_x is also in accord with the lamination theory prediction for $y/b < 0.5$. The stress components σ_y, σ_z, and σ_{yz} increase near the free edge but they are quite small. The interlaminar shear stress σ_{xz}, however, has a very high value at the free edge and it falls approximately to zero at $y/b = 0.5$. As can be seen from Fig. 11.10, the perturbance owing to the free edge runs through a distance approximately equal to the laminate

thickness. Thus, we may regard the interlaminar stresses as a *boundary layer phenomenon* restricted to the free edge and extending inward a distance equal to the laminate thickness. Pipes and Daniel (1971) confirmed these results experimentally. They used the Moiré technique to observe the surface displacements of a symmetric angle-ply laminate subjected to axial tension. Figure 11.11 shows that the agreement between experiment and theory is excellent.

An important result of this phenomenon of edge effects is that the laminate stacking sequence can influence the magnitude and nature of the interlaminar stresses (Pagano and Pipes 1971; Pipes and Pagano 1974; Pipes et al. 1973; Whitney 1973; Oplinger et al. 1974). It had been observed in some earlier work that identical angle-ply laminates stacked in two different sequences had different properties: the $[\pm 15°/\pm 45°]_s$ sequence had poor mechanical properties compared to the $[\pm 45°/\pm 15°]_s$ sequence. Pagano and Pipes (1971) showed that interlaminar normal stress σ_z changed from tension to compression as the ply sequence was inverted. A tensile interlaminar stress at the free edge would initiate delamination there, which would account for the observed difference in the mechanical properties. Whitney (1973) observed the same effect in carbon/epoxy composites in fatigue testing, namely, a specimen having a stacking sequence causing a tensile interlaminar stress at the free edge showed delaminations well before the fracture, while a specimen with a stacking sequence causing compressive interlaminar stress at the free edge showed little incidence of delaminations.

We can summarize the edge effects in laminated composites as follows:

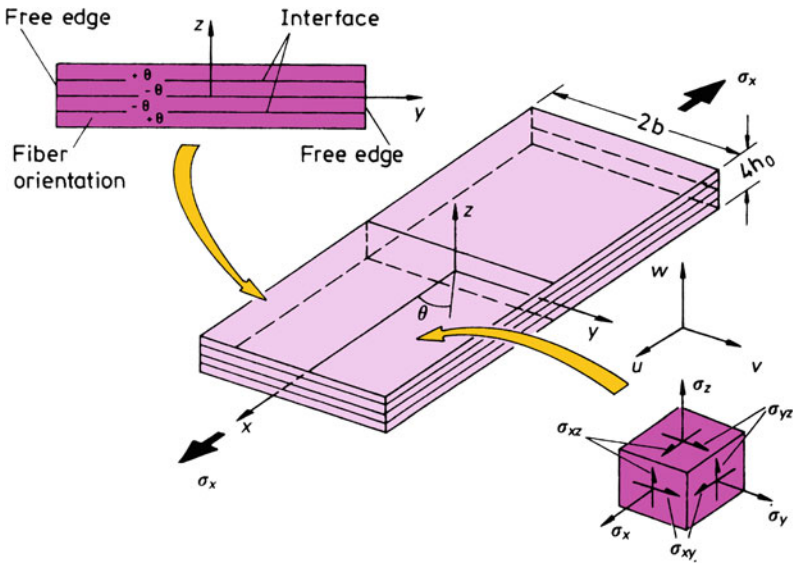

Fig. 11.9 A four-ply laminate ($\pm\theta$, thickness $4h_0$) under a uniform axial strain [From Pipes and Pagano (1970), used with permission.]

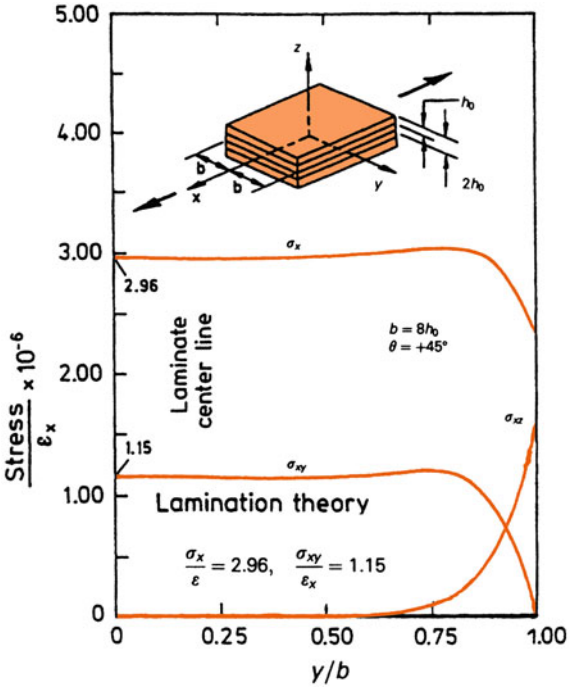

Fig. 11.10 Stress distribution at the interface $z = h_0$ as a function of y/b, where $2b$ is the laminate width. Note the high value of σ_{xy} at the free edge; σ_{xy} falls approximately to zero at $y/b = 0.5$ [From Pipes and Pagano (1970), used with permission.]

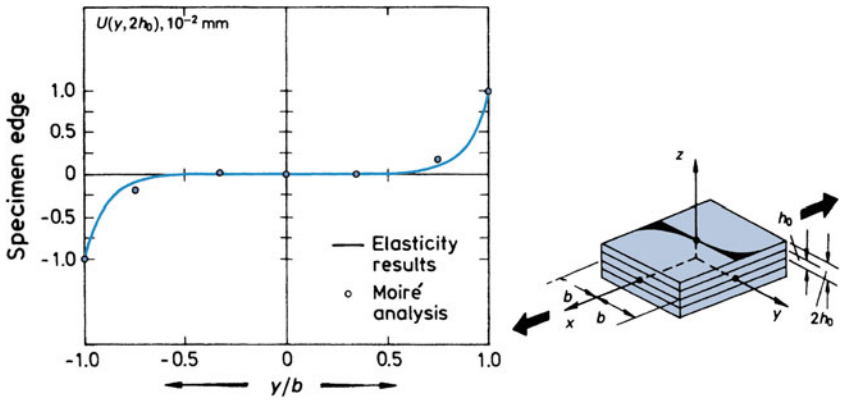

Fig. 11.11 Surface displacements of a symmetric angle-ply laminate subjected to axial tension. Experimental data points were determined by the Moiré technique [From Pipes and Daniel (1971), used with permission.]

1. The classical lamination theory of plates inplane stress is valid in the laminate interior, provided the laminate is sufficiently wide (i.e., $b/4h_0 \gg 2$).
2. Interlaminar stresses are confined to narrow regions of dimensions comparable to the laminate thickness and adjoining the free edges (i.e., $y = \pm b$).
3. The ply stacking sequence in a laminate affects the magnitude as well as the sign of the interlaminar stresses, which in turn affects the mechanical performance of the laminate. Specifically, a tensile interlaminar stress at the free edge is likely to cause delaminations.

Problems

11.1. An isotopic material is subjected to a uniaxial stress. Is the stain state also uniaxial? Write the stress and strain in matrix form.

11.2. For a symmetric laminated composite, we have $\bar{Q}_{ij}(+z) = \bar{Q}_{ij}(-z)$, i.e., the moduli are even functions of thickness z. Starting from this definition, split the integral and show that B_{ij} is identically zero for a symmetric laminate.

11.3. An orthotropic lamina has the following characteristics: $E_{11} = 210\ GPa$, $E_{22} = 8\ GPa$, $G_{12} = 5\ GPa$, and $v_{12} = 0.3$. Consider a three-ply laminate made of such laminae arranged at $\theta = \pm 60°$. Compute the submatrices [A], [B], and [D]. Take the ply thickness to be 1 *mm*.

11.4. Enumerate the various phenomena which can cause microcracking in a fiber composite.

11.5. A thin lamina of a composite with fibers aligned at 45° to the lamina major axis is subjected to the following stress system along its geometric axes:

$$[\sigma_i] = \begin{bmatrix} \sigma_x \\ \sigma_y \\ \sigma_s \end{bmatrix} = \begin{bmatrix} 10 \\ 2 \\ 3 \end{bmatrix} MPa.$$

Compute the stress components along the material axes (i.e., σ_1, σ_2, and σ_6).

11.6. A two-ply laminate composite has the top and bottom ply orientations of 45° and 0° and thicknesses of 2 and 4 *mm*, respectively. The stiffness matrix for the 0° ply is

$$[Q_{ij}] = \begin{bmatrix} 20 & 1 & 0 \\ 1 & 3 & 0 \\ 0 & 0 & 1 \end{bmatrix} GPa.$$

Find the $[\bar{Q}_{ij}]_{45}$ and then compute the matrices [A], [B], and [D] for this laminate.

11.7. A two-ply laminate composite is made of polycrystalline, isotropic aluminum and steel sheets, each 1 *mm* thick. The constitutive equations for the two sheets are

$$\text{A1}: \begin{bmatrix} \sigma_1 \\ \sigma_2 \\ \sigma_6 \end{bmatrix} = \begin{bmatrix} 70 & 26 & 0 \\ 26 & 70 & 0 \\ 0 & 0 & 26 \end{bmatrix} \begin{bmatrix} \varepsilon_1 \\ \varepsilon_2 \\ \varepsilon_6 \end{bmatrix} MPa$$

$$\text{Steel}: \begin{bmatrix} \sigma_1 \\ \sigma_2 \\ \sigma_6 \end{bmatrix} = \begin{bmatrix} 210 & 60 & 0 \\ 60 & 210 & 0 \\ 0 & 0 & 78 \end{bmatrix} \begin{bmatrix} \varepsilon_1 \\ \varepsilon_1 \\ \varepsilon_6 \end{bmatrix} MPa.$$

Compute the matrices [*A*], [*B*], and [*D*] for this laminated composite. Point out any salient features of this laminate.

References

R.M. Christensen, *Mechanics of Composite Materials* (Wiley, New York, 1979)

I.M. Daniel, O. Ishai, *Engineering Mechanics of Composite Materials* (Oxford University Press, New York, 1994)

J.C. Halpin, *Primer on Composite Materials*, 2nd edn. (Technornic, Lancaster, PA, 1984)

R.M. Jones, *Mechanics of Composite Materials* (Scripta Book Co., Washington, DC, 1975)

A.E.H. Love, *A Treatise On the Mathematical Theory of Elasticity*, 4th edn. (Dover, New York, 1952)

R.L. McCullough, *Concepts of Fiber-Resin Composites* (Marcel Dekker, New York, 1971), p. 16

J.F. Nye, *Physical Properties of Crystals* (Oxford University Press, London, 1985)

D.W. Oplinger, B.S. Parker, F.P. Chiang, Exp. Mech. **14**, 747 (1974)

N.J. Pagano, R.B. Pipes, J. Compos. Mater. **5**, 50 (1971)

R.B. Pipes, I.M. Daniel, J. Compos. Mater. **5**, 255 (1971)

R.B. Pipes, B.E. Kaminski, N. J. Pagano, in *Analysis of the Test Methods for High Modulus Fibers and Composites*, ASTM STP 521 (ASTM, Philadelphia, 1973), p. 218

R.B. Pipes, N.J. Pagano, J. Compos. Mater. **4**, 538 (1970)

R.B. Pipes, N.J. Pagano, J. Appl. Mech. **41**, 668 (1974)

S. Timoshenko, J.N. Goodier, *Theory of Elasticity* (McGraw-Hill, New York, 1951)

S.W. Tsai, H.T. Hahn, *Introduction to Composite Materials* (Technomic, Westport, CT, 1980a)

J.M. Whitney, in *Analysis of the Test Methods for High Modulus Fibers and Composites*, ASTM STP 521 (ASTM, Philadelphia, 1973), p. 167

Suggested Reading

A.R. Bunsell, J. Renard, *Fundamentals of Fibre Reinforced Composites* (Institute of Physics Pub, Bristol, 2005)

L.R. Calcote, *Analysis of Laminated Composite Structures* (Van Nostrand Reinhold, New York, 1969)

I.M. Daniel, O. Ishai, *Engineering Mechanics of Composite Materials*, 2nd edn. (Oxford University Press, New York, 2006)
C.T. Herakovich, *Mechanics of Fibrous Composites* (Wiley, New York, 1998)
M.W. Hyer, *Stress Analysis of Fiber-Reinforced Composite Materials* (McGraw-Hill, New York, 1997)
R.M. Jones, *Mechanics of Composite Materials*, 2nd edn. (Taylor & Francis, Philadelphia, 1999)
S.W. Tsai, H.T. Hahn, *Introduction to Composite Materials* (Technomic, Westport, CT, 1980b)

Chapter 12
Monotonic Strength and Fracture

In this chapter, we describe the monotonic strength and fracture behavior of fiber reinforced composites at ambient temperatures. The term *monotonic behavior* means behavior under an applied stress that increases in one direction, i.e., not a cyclic loading condition. We discuss the behavior of composites under fatigue or cyclic loading as well as under conditions of creep in Chap. 13.

12.1 Tensile Strength of Unidirectional Fiber Composites

In Chap. 10 we discussed the prediction of elastic and physical properties when the properties of the components are known. A particularly simple but crude form of this is the rule-of-mixtures, which works reasonably well for predicting the longitudinal elastic constants. Unfortunately, the same cannot be said for the strength of a fiber reinforced composite. It is instructive to examine why the rule-of-mixtures approach does not always work for strength properties of a composite. For a composite containing continuous fibers, unidirectionally aligned and loaded in the fiber direction (isostrain condition), we can write for the stress in the composite,

$$\sigma_c = \sigma_f V_f + \sigma_m (1 - V_f), \tag{12.1}$$

where σ is the axial stress, V_f is the volume fraction, and the subscripts c, f, and m refer to composite, fiber, and matrix, respectively. The important question here is: What is the value of the matrix stress, σ_m? Ideally, it should be the in situ value of the stress on the matrix at a given strain. The main reason that the rule-of-mixtures does not always work for predicting the strength of a composite, while it works reasonably well for Young's modulus in the longitudinal direction, is that the elastic modulus is a relatively microstructure-insensitive property while strength is a highly microstructure-sensitive property. For example, the grain size of a polycrystalline material affects its strength but not its modulus. Thus, the response of a

K. K. Chawla, *Composite Materials*,
https://doi.org/10.1007/978-3-030-28983-6_12

composite for elastic modulus is nothing but the volume-weighted average of the individual responses of the isolated components. Because the strength is an extremely structure-sensitive property, synergism can occur in regard to composite strength. Consider the various factors that may influence the composite strength properties. First, matrix or fiber structure may be altered during fabrication. Second, composite materials consist of two components whose thermomechanical properties are generally quite different and thus may have residual stresses and/or undergo structural alterations owing to these internal stresses. We discussed at length in Chap. 10 the effects of differential contraction during cooling from the fabrication temperature to ambient temperature, which leads to thermal stresses large enough to deform the matrix plastically, which leads to high dislocation density and work hardening of the matrix (Chawla and Metzger 1972; Chawla 1973a, b; Arsenault and Fisher 1983; Vogelsang et al. 1986).

Yet another source of microstructural modification of a component is a phase transformation induced by the fabrication process. In a metallic laminate composite made by roll-bonding aluminum and austenitic stainless steel (type 304), it was observed that the fabrication procedure work hardened the steel and partially transformed the austenite to martensite (Chawla et al. 1986).

The matrix stress state may also be influenced by rheological interaction between the components during straining (Ebert and Gadd 1965; Kelly and Lilholt 1969). The plastic constraint on the matrix owing to the large differences in the Poisson's ratios of the matrix and the fiber, especially in the stage wherein the fiber deforms elastically while the matrix deforms plastically, can considerably alter the stress state in the composite. Thus, microstructural changes in one or both of the components, or rheological interaction between the components during straining can lead to the phenomenon of synergism in the strength properties. In view of this, the rule-of-mixtures should be regarded, in the best of circumstances, as an order of magnitude indicator of the strength of a composite.

12.2 Compressive Strength of Unidirectional Fiber Composites

Fiber reinforced composites under compressive loading can be regarded, as a first approximation, as elastic columns under compression. Thus, the main failure modes in the failure of a composite are the ones that occur in the buckling of columns. Buckling occurs when a slender column under axial compression becomes unstable against lateral movement of the central portion. The critical stress corresponding to failure by buckling of a column with ends-pinned is given by the Euler buckling formula:

$$\sigma_c = \frac{\pi^2 E}{16}\left(\frac{d}{l}\right)^2, \tag{12.2}$$

where d is the diameter and l is the length of the column. It is easy to see that a high aspect ratio (l/d) will result in a low σ_c. Of course, in a fiber reinforced composite we do not load a fiber directly and the conditions of ends-pinned do not prevail. The main effect of different end conditions of the column is that the length of the column should be replaced with an effective length. In a composite, the matrix provides some stability in the lateral direction. Rosen (1965a) showed by means of photoelasticity that fiber reinforced composites fail, in compression, by periodic buckling of the fibers, with the buckling wavelength being proportional to the fiber diameter. This is not surprising in view of the fact that in the analysis of a column on an elastic foundation, it is observed that the buckling wavelength depends on the column diameter. Figure 12.1 shows schematically the three situations: an unbuckled fiber composite, in-phase buckling, and out-of-phase buckling. The in-phase buckling of fibers involves shear deformation of the matrix. In such a case the composite strength in compression is proportional to the matrix shear modulus G_m; that is, $\sigma_c = G_m/V_m$, where V_m is the matrix volume fraction. For an isotropic matrix, we have $G_m = E_m/2(1 + \nu_m)$, where E_m and ν_m are the matrix Young's modulus and Poisson's ratio, respectively. Thus,

$$\sigma_c = \frac{E_m}{2(1+\nu_m)V_m}. \tag{12.3}$$

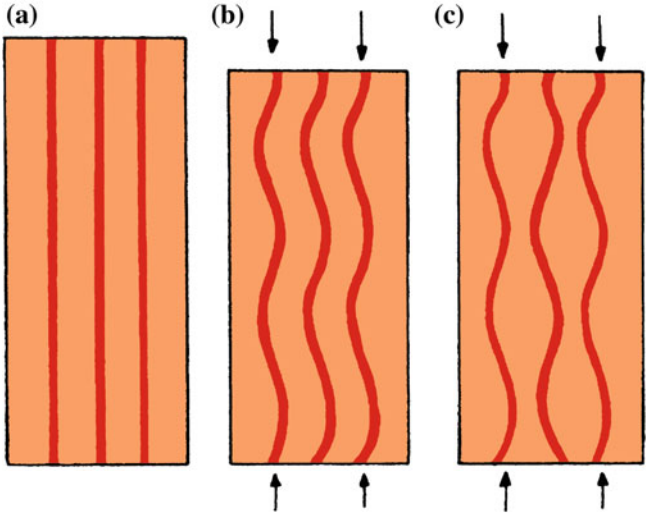

Fig. 12.1 **a** Unbuckled fiber reinforced composite, **b** in-phase buckling of fibers under compression, and **c** out-of-phase buckling of fibers under compression

Out-of-phase buckling of fibers involves transverse compressive and tensile strains. The compressive strength in such a case is proportional to the geometric mean of the fiber and matrix Young's moduli (Rosen 1965a):

$$\sigma_c = 2V_f \left(\frac{V_f E_m E_f}{3V_m} \right)^{1/2}, \tag{12.4}$$

where V and E denote the volume fraction and Young's modulus, respectively, and the subscripts f and m denote fiber and matrix, respectively.

From Eqs. (12.3) and (12.4), we can see that the two failure modes in compression have a different dependence on the moduli of the components, that is,

$$\begin{array}{ll} \sigma_c \propto \left(E_m E_f\right)^{1/2} & \text{out-of-phase} \\ \sigma_c \propto G_m & \text{in-phase} \end{array}. \tag{12.5}$$

Thus, if we were to put the same fiber in two different matrices (i.e., with different matrix moduli), we should be able to distinguish between these two compressive failure modes. Lager and June (1969) did just that with boron fibers in two different polymer matrices. An out-of-phase buckling mode predominated at low fiber volume fractions. At high fiber volume fractions, fibers exerted more influence on each other and a coupled or in-phase buckling mode prevailed. The approximate nature of Eqs. (12.3) and (12.4) is easy to see. Both imply that as $V_m \to 0$ (or $V_f \to 1$), $\sigma_c \to \infty$, that is, the fibers are infinitely strong. Of course, no fibers are infinitely strong. Fiber/matrix adhesion (Hancox 1975) and matrix yielding (Piggott and Harris 1980) also affect the compressive strength of fiber composites. Naryanan and Schadler (1999) observed that kink bands initiate from a damage zone comprising crushed and broken fibers. When the damage zone reached a critical size, the unsupported column of matrix caused a local matrix shear instability (or microbuckling). This local instability propagated as a kink band. The damage zone angle was found to depend on the interface properties, and it affected the strain to form kink bands. In the case of a laminated composite, poor interlaminar bonding can result in easy buckling of fibers (Piggott 1984). Kyriakides et al. (1995) investigated the failure in compression unidirectionally reinforced AS4 carbon fiber/PEEK matrix composites. The failure load of the composite depended on geometric imperfections such as fiber waviness, and failure occurred via formation of kink bands. They modeled the composite as a two-dimensional solid with alternating fiber and matrix layers and investigated numerically the response in compression with different imperfections of various spatial distributions. The calculated responses were characterized by an initially elastic regime that ended at a limit load instability (the instability or limit load is the peak point on the system's load-deflection curve), following which the deformation localized into inclined bands. As the localization process progressed, the fiber bending stresses at the ends of these bands grew to values comparable to those of the fiber strength. Heat and moisture as well as the ply stacking sequence can also

affect the compressive strength. Budiansky and Fleck (1993) proposed a fiber microbuckling model, which predicts a kinking stress as a function of the shear modulus of the composite, shear yield strain, and the strain hardening exponent. Gupta and coworkers (Gupta et al. 1994; Anand et al. 1994; Grape and Gupta 1995a, b) examined the behavior under uniaxial and biaxial compression of laminated carbon/carbon and carbon/polyimide composites. Carbon/carbon laminates under uniaxial stress showed the formation of a diagonal shear fault, which consisted of a mixture of fiber bundle kinks and interply delaminations. Carbon/polyimide composites under in-plane biaxial loading showed a new failure mechanism where the shear in the off-axis plies led to axial interply delaminations which were very similar to wing cracks observed in deformation of brittle materials under compression. Compressive strength of MMCs is generally higher than that of PMCs. Dève (1997) observed a compressive strength ≥ 4 *GPa* for aluminum alloy matrix containing high fiber volume fraction (55–65%) Nextel 610 alumina fibers. Fiber microbuckling was the observed failure mode. For a review of various models and experimental techniques related to compressive failure of fiber reinforced composites, see Schultheisz and Waas (1996) and Waas and Schultheisz (1996).

12.3 Fracture Modes in Tension

A large variety of deformation modes can lead to failure of the composite. The operative failure mode depends, among other things, on loading conditions and the microstructure of a particular composite system. By *microstructure*, we mean fiber diameter, fiber volume fraction, fiber distribution, and damage resulting from thermal stresses that may develop during fabrication and/or in service. In view of the fact that many factors can and do contribute to the fracture process in composites, it is not surprising that a multiplicity of failure modes is observed in a given composite system.

12.3.1 Single and Multiple Fracture

In general, the fiber and matrix will have different values of strain at fracture. When the component that has the smaller breaking strain fractures, for example, a brittle fiber or a brittle ceramic matrix, the load carried by this component is thrown onto the other one. If the component with a higher strain of fracture can bear this additional load, the composite will show multiple fractures of the brittle component. A manifestation of this phenomenon is fiber bridging of the ceramic matrix (see Chap. 7). Eventually, a particular transverse section of the composite becomes so weak that the composite is unable to carry the load any further and it fails.

Consider the case of a fiber reinforced composite in which the fiber fracture strain is less than that of the matrix, for example, a ceramic fiber in a metallic matrix. The composite will then show a single fracture (Hancox 1975) when

$$\sigma_{\mathrm{fu}} V_f > \sigma_{\mathrm{mu}} V_m - \sigma'_m V_m, \tag{12.6}$$

where σ'_m is the matrix stress corresponding to the fiber fracture strain and σ_{fu} and σ_{mu} are the ultimate tensile stresses of the fiber and matrix, respectively. Equation (12.6) states that when the fibers break, the matrix will not be able to support the additional load. This is commonly the case with composites containing a large volume fraction of brittle fibers in a ductile matrix. All the fibers break in more or less one plane and the composite fails in that plane.

If we have a composite that satisfies the condition

$$\sigma_{\mathrm{fu}} V_f < \sigma_{\mathrm{mu}} V_m - \sigma'_m V_m, \tag{12.7}$$

then the fibers will break into small segments until the matrix fracture strain is reached.

In the case where the fibers have a fracture strain greater than that of the matrix (e.g., a ceramic matrix reinforced with ductile fibers), we will have multiple fractures in the matrix. We can write the expression for this as (Hale and Kelly 1972)

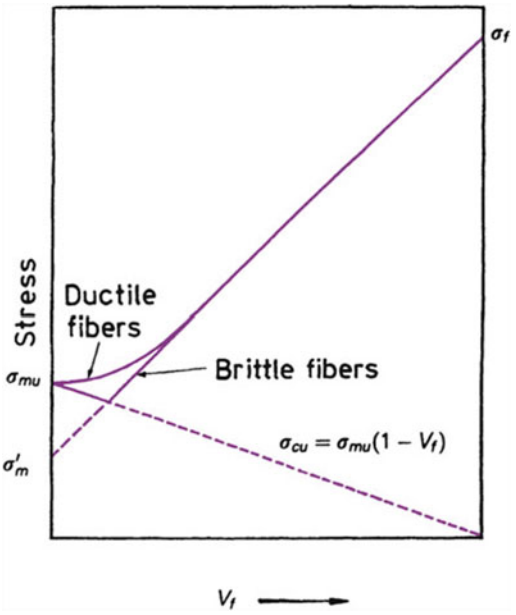

Fig. 12.2 Strength of the composite versus fiber volume fraction showing the conditions for single and multiple fiber fracture

$$\sigma_{\mathrm{fu}} V_f < \sigma_{\mathrm{mu}} V_m + \sigma'_f V_f, \tag{12.8}$$

where σ'_f is the stress in the fiber at the matrix fracture strain. Figure 12.2 shows schematically the conditions for single and multiple fracture in fiber reinforced composites under tension.

12.3.2 Debonding, Fiber Pullout, and Delamination Fracture

Debonding of the fiber/matrix interface, fiber pullout, and delamination fracture are some of the features that are commonly observed in fiber reinforced composites; these modes of fracture are not observed in conventional, monolithic materials. Consider the situation wherein a crack originates in the matrix and approaches the fiber/matrix interface. In a short fiber composite with a critical length l_c, fibers with extremities within a distance $l_c/2$ from the plane of the crack will debond and pull out of the matrix (see Fig. 10.13). These fibers will not break. In fact, the fraction of fibers pulling out will be l_c/l. Continuous fibers ($l > l_c$) invariably have flaws distributed along their length. Thus, some of them may fracture in the plane of the crack while others may fracture away from the crack plane. This is treated in some detail later in this section.

The final fracture of the composite will generally involve some fiber pullout. Consider a model composite consisting of a fiber of length l embedded in a matrix; see Fig. 12.3. If this fiber is pulled out, the bonding between the matrix and the fiber will produce a shear stress τ parallel to the fiber surface. The shear force acting on the fiber as a result of this stress is given by $2\pi r_f \tau l$, where r_f is the fiber radius. Note that $2\pi r_f l$ is the cylindrical area on which shear stress τ is acting, giving the shear force $2\pi r_f \tau l$. Let τ_i be the maximum shear stress that the interface can support and let σ_{fu} be the fiber fracture stress in tension. The maximum force caused by this normal stress on the fiber is $\pi r_f^2 \sigma_{\mathrm{fu}}$. For maximum fiber strengthening, we would like the fiber to break rather than be pulled out of the matrix. From a toughness point of view, however, fiber pullout may be more desirable. We can then write

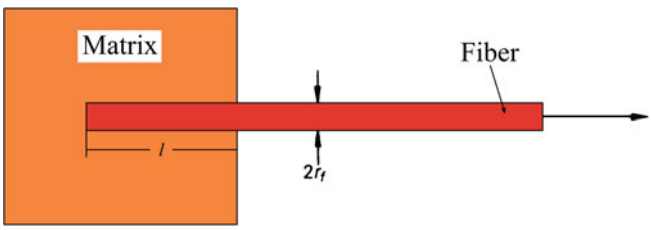

Fig. 12.3 A fiber of length l, embedded in a matrix, being pulled out

from the balance of forces the following condition for the fiber to be fractured under tension:

$$\pi r_f^2 \sigma_{\text{fu}} < 2\pi r_f \tau_i l,$$

or

$$\frac{\sigma_{\text{fu}}}{4\tau_i} < \frac{l}{2r_f} = \frac{l}{d}, \tag{12.9}$$

where d is the fiber diameter and the ratio l/d is the aspect ratio of the fiber.

On the other hand, for fiber pullout to occur, we can write

$$\frac{l}{d} \leq \frac{\sigma_{\text{fu}}}{4\tau_i}. \tag{12.10}$$

The equality in this expression gives us the critical fiber length l_c for a given fiber diameter. Thus,

$$\frac{l_c}{d} = \frac{\sigma_{\text{fu}}}{4\tau_i}. \tag{12.11}$$

This equation provides us with a means of obtaining the interface strength, namely, by embedding a single fiber in a matrix and measuring the load required to pull the fiber out. The load–displacement curve shows a peak corresponding to debonding, followed by an abrupt fall and wiggling about a constant stress level. Note that Eq. (12.11) gives l_c/d to be half that given by Eq. (10.65). This is because in the present case the fiber is being loaded from one end only.

A point that has not been mentioned explicitly so far is that real fibers do not have uniform properties but rather show a statistical distribution. Weak points are distributed along the fiber length. We will treat these statistical aspects of fiber strength in detail in Sect. 12.4. Suffice it to say that it is more than likely that a fiber would break away from the main fracture plane. Interfacial debonding occurs around the fiber breakpoint. The broken fiber parts are pulled out from their cylindrical holes in the matrix during further straining. Figure 12.4a shows schematically the fiber pullout in a continuous fiber reinforced composite, while a practical example of fiber pullout in a boron fiber/aluminum matrix is shown in Fig. 12.4b. Work is done in the debonding process as well as in fiber pullout against frictional resistance at the interface. Outwater and Murphy (1969) showed that the maximum energy required for debonding is given by

$$W_d = \left(\frac{\pi d^2}{24}\right)\left(\frac{\sigma_{\text{fu}}^2}{E_f}\right)x, \tag{12.12}$$

where x is the debond length.

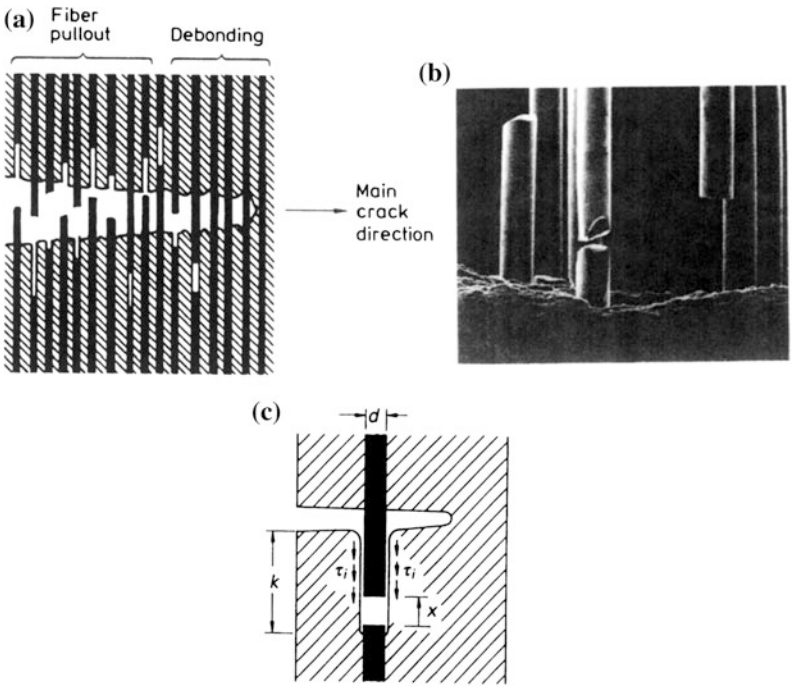

Fig. 12.4 **a** Schematic of fiber pullout in a continuous fiber composite. **b** Fiber pullout in a B/Al system. Fiber diameter is 140 μm. **c** Schematic of an isolated fiber pullout through a distance x against an interfacial shear stress, τ_i

This phenomenon of fiber pullout is very important in regard to toughness (Cottrell 1964). The fiber length l should be large but close to l_c for maximizing the fiber pullout work and to prevent the composite from separating into two halves. It should be recognized at the same time that for $l < l_c$, the fiber will not get loaded to its maximum possible strength level and thus full fiber strengthening potential will not be realized.

We can estimate the work done in pulling out an isolated fiber in the following way (Fig. 12.4c). Let the fiber be broken a distance k below the principal crack plane, where k is between 0 and $l_c/2$, i.e., $0 < k < l_c/2$. Now let the fiber be pulled out through a distance x against an interfacial frictional shear stress, τ_i. Then the total force at that instant on the debonded fiber surface, which is opposing the pullout, is $\tau_i \pi d(k - x)$. When the fiber is further pulled out a distance dx, the work done by this force is $\tau_i \pi d(k - x)\, dx$. We can obtain the total work done in pulling out the fiber over the distance k by integrating. Thus,

$$\text{Work of fiber pullout} = \int_0^k \tau_i \pi d(k - x) dx = \frac{\tau_i \pi d k^2}{2}. \tag{12.13}$$

The reader should be careful with our use of d as a symbol for the fiber diameter and differentiation. Now the pullout length of the fiber can vary between a minimum of 0 and a maximum of $l_c/2$. The average work of pullout per fiber is then

$$W_{fp} = \frac{1}{l_c/2} \int_0^{l_c/2} \frac{\tau_i \pi d k^2}{2} dk = \frac{\tau_i \pi d l_c^2}{24}.$$

This analysis assumes that all fibers are pulled out. In a discontinuous fiber composite, it has been observed experimentally (Kelly 1970) that only the fibers with ends within a distance $l_c/2$ of the main fracture plane and that cross this fracture plane undergo pullout. Thus, it is more likely that a fraction (l_c/l) of fibers will be pulled out. The above expression for average work done per fiber can then be modified as

$$W_{\text{fp}} = \left(\frac{l_c}{l}\right) \frac{\pi d \tau_i l_c^2}{24}. \tag{12.14}$$

In general, fiber pullout provides a more significant contribution to composite fracture toughness than fiber/matrix debonding. The reader should appreciate the fact that debonding must precede pullout. Figure 12.5 shows schematically the variation of work of fracture with fiber length. For $l < l_c$, W_{fp} increases as l^2 (substitute l for k in Eq. 12.17a). Physically, this makes sense because as the fiber length increases, an increasing fiber length will be pulled out. For $l > l_c$, as pointed out earlier, some fibers will fracture in the plane of fracture of the composite and thus their contribution to W_{fp} will be nought. Those fibers whose ends are within a distance of $l_c/2$ from the fracture plane, they will undergo the process of fiber pullout. In this case, the average work of fracture is given by Eq. 12.14, i.e., W_{fp}

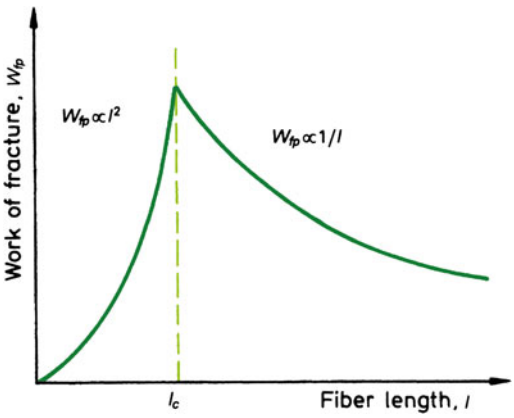

Fig. 12.5 Variation of work done in fiber pullout with fiber length

varies as $1/l$ because with increasing fiber length, fiber breaks intervene and the fiber pullout decreases. The work of fracture, W_{fp} peaks at $l = l_c$. The reader can easily show that for $l = l_c$, the average stress in the fiber will only be half that in an infinitely long fiber.

One measure of fracture toughness can loosely be defined as resistance to crack propagation. Consider a fiber reinforced composite containing a crack transverse to the fibers. In such a situation, we can increase the crack propagation resistance by one of the following means, each of which involves additional work:

1. Plastic deformation of the matrix (applicable in a metal matrix).
2. Presence of weak interfaces, fiber/matrix separation, and deflection of the crack.
3. Fiber pullout.

For a metal matrix composite, the work of fracture is mostly the work done during plastic deformation of the matrix. The work of fracture is proportional to $d(V_m/V_f)^2$ (Cooper and Kelly 1967), where d is the fiber diameter and V_m and V_f are the matrix and fiber volume fractions, respectively. This is understandable because, for a given V_f, the larger the fiber diameter, the greater the amount of plastically deformed matrix. Thus, an advancing crack will result in large work of fracture for a large diameter fiber.

Crack deflection along an interface frequently follows separation of the fiber/matrix interface. This provides us with a potent mechanism of increasing the crack propagation resistance in composites; we discussed this topic in Chap. 7. This improvement in fracture toughness owing to the presence of weak interfaces has been confirmed experimentally. This crack deflection mechanism can be a major source of toughness in ceramic matrix composites (Chawla 2003). Yet another related failure mode in laminated composites is the delamination failure associated with the plies and the fiber/matrix interface. This fracture mode is of importance in structural applications involving long-term use, for example, under fatigue conditions and where environmental effects are important. Highly oriented fibers such as aramid can also contribute to the work of fracture. Figure 12.6 shows a delamination-type fracture in a Kevlar aramid/epoxy composite (Saghizadeh and Dharan 1985) and the characteristic fibrillation of the Kevlar fiber, which stems from its structure as described in Chap. 2. Carbon/epoxy composites, when tested for delamination fracture, showed clean exposed fiber surfaces (Saghizadeh and Dharan 1985). For details regarding this subject of delamination, the reader is referred to Johnson (1985) in suggested reading.

Fiber pullout increases the work of fracture by causing a large deformation before fracture. In this case, the controlling parameter for work of fracture is the ratio d/τ_i, where d is the fiber diameter and τ_i is the interface shear strength. In the case of short fibers, the work of fracture resulting from fiber pullout also increases with the fiber length, reaching a maximum at l_c. In the case of continuous fibers, the work of fracture increases with an increase in spacing between the defects

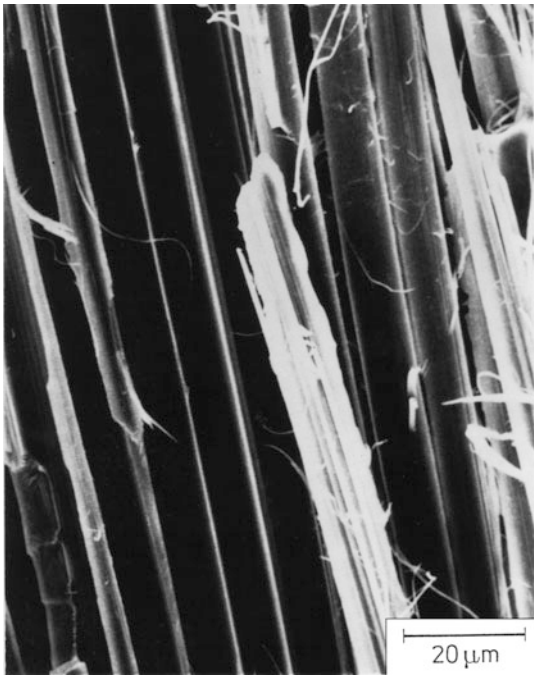

Fig. 12.6 A delamination-type fracture of Kevlar/epoxy composite. Note the characteristic fibrillation in the fiber [From Saghizadeh and Dharan (1985), used with permission]

(Kelly 1971; Cooper 1970). It would thus appear that one can increase the work of fracture by increasing the fiber diameter. This was discussed in Sect. 6.5 in regard to the toughness of metal matrix composites.

12.4 Effect of Variability of Fiber Strength

Most high performance fibers are brittle. Thus, their strength must be characterized by a statistical distribution function. Figure 12.7a shows the strength distribution for a material that shows a large statistical variation in strength, while Fig. 12.7b shows an example of the strength of material in which the variability of strength is insignificant. We can safely put most metallic fibers or wires in the latter category. Most high strength and high stiffness fibers (aramid, polyethylene, B, C, SiC, Al_2O_3, etc.), however, follow some kind of statistical distribution of strength such as the one shown in Fig. 12.7a.

There are many statistical distribution functions for the strength of a material. For brittle materials, a distribution function called the Weibull statistical distribution function (named after the Swedish engineer who first proposed it) has been found to characterize the strength of fairly well. For high strength fibers also, the Weibull treatment of strength has been found to be quite adequate (Coleman 1958). Here we follow the treatment, due to Rosen (Rosen 1965a, b, 1983), of this fiber strength

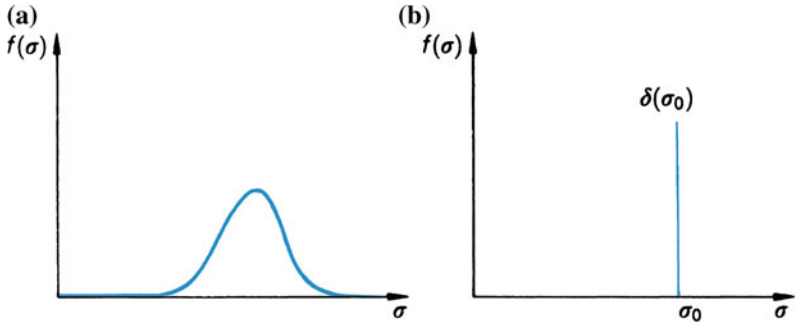

Fig. 12.7 **a** Strength distribution for a brittle material. **b** Strength distribution for material with insignificant variability of strength

variability and its effect on the properties of a fiber reinforced composite. We can express the dependence of fiber strength on its length in terms of the following distribution function:

$$f(\sigma) = L\alpha\beta\sigma^{\beta-1}\exp\left(-L\alpha\sigma^{\beta}\right), \tag{12.15}$$

where L is the fiber length, σ is the fiber strength, and α and β are statistical parameters. $f(\sigma)$, a probability density function, gives the probability that the fiber strength is between σ and $\sigma + d\sigma$.

We define the kth moment, M_k of a statistical distribution function as

$$M_k = \int_0^{\infty} \sigma^k f(\sigma) d\sigma. \tag{12.16}$$

Knowing that the mean strength of the fiber is given by $\bar{\sigma} = \int_0^{\infty} \sigma f(\sigma)\, d\sigma$, we can write

$$\bar{\sigma} = M_1, \tag{12.17}$$

and the standard deviation s can be expressed as

$$s = \left(M_2 - M_1^2\right)^{1/2}. \tag{12.18}$$

From the Weibull distribution (Eq. 12.15) and Eqs. (12.17) and (12.18), we obtain

$$\bar{\sigma} = (\alpha L)^{-1/\beta}\Gamma\left(1 - \frac{1}{\beta}\right), \tag{12.19}$$

and

$$s = (\alpha L)^{-1/\beta}\left[\Gamma\left(1+\frac{2}{\beta}\right) - \Gamma^2\left(1+\frac{1}{\beta}\right)\right]^{1/2}, \tag{12.20}$$

where $\Gamma(n)$ is the gamma function given by $\int_0^\infty \exp(-x)x^{n-1}\,dx$. Note that x in this integral is a general, mathematical variable. The reader should not confuse ti with the fiber length, x in Fig. 12.4. The coefficient of variation μ for this distribution then follows from the expression given below

$$\mu = \frac{s}{\bar{\sigma}} = \frac{\left[\Gamma(1+2/\beta) - \Gamma^2(1+1/\beta)\right]^{1/2}}{\Gamma(1+1/\beta)}. \tag{12.21}$$

We note that μ is a function only of the parameter β. Rosen showed that for $0.05 \leq \mu \leq 0.5$, $\mu \simeq \beta^{-0.92}$ or $\mu \simeq 1/\beta$. In other words, parameter β is an inverse measure of the coefficient of variation μ. For fibers that are characterized by the Weibull distribution [Eq. (12.15)], $\beta > 1$. For glass fibers, μ can be about 0.1, which would correspond to $\beta = 11$. For boron and SiC fibers, μ can be between 0.2 and 0.4 and β will be between 2.7 and 5.8.

Let us consider Eq. (12.19). We can write for a unit length of fiber

$$\bar{\sigma}_1 = k\alpha^{-1/\beta}, \tag{12.22}$$

where

$$k = \Gamma\left(1+\frac{1}{\beta}\right). \tag{12.23}$$

For $\beta > 1$, we have $0.88 \leq k \leq 1.0$. Thus, we can regard the quantity $\alpha^{-1/\beta}$ as the reference strength level. We can plot Eq. (12.19) in the form of curves of $\bar{\sigma}/\alpha^{-1/\beta}$ (a normalized mean strength) against fiber length L for different β values. In Fig. 12.8, $\beta = \infty$ corresponds to a spike distribution function such as the one shown in Fig. 12.7b. In such a case, all the fibers have identical strength, and there

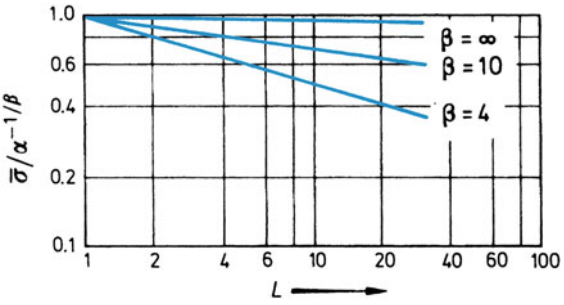

Fig. 12.8 Normalized mean fiber strength versus fiber length L

is no fiber length dependence. For $\beta = 10$, which corresponds to a $\mu \simeq 12\%$, an order of magnitude increase in fiber length produces a 20% fall in average strength. For $\beta = 4$, the corresponding fall in strength is about 50%.

We can obtain the statistical mode σ^*, which is the most probable strength value by differentiating Eq. (12.15) and equating it to zero. Thus,

$$\sigma^* \approx \left(\frac{\beta - 1}{\beta}\right)^{1/\beta} (\alpha L)^{-1/\beta}. \tag{12.24}$$

For large β,

$$\sigma^* \approx (\alpha L)^{-1/\beta}, \tag{12.25}$$

$(\alpha L)^{-1/\beta}$, as mentioned earlier, is a reference stress level. The values of α and β can be obtained from experimental $\bar{\sigma}$ and μ values.

If we use Weibull statistics to characterize ceramic fibers, we can answer the following important question: For making tough, strong fiber reinforced ceramic matrix composites, would we want fibers with small or large Weibull modulus? Lara-Curzio et al. at Oak Ridge National Laboratory examined this problem. Figure 12.9 shows their results in the form of fiber bundle strength versus strain in a CMC for different Weibull modulus values. The takeaway message from this figure is that the lower the Weibull modulus of ceramic fibers (i.e., the less uniformity in their properties), the more graceful failure of the CMC. It is understandable if we recall that a low Weibull modulus fiber will fracture in the composite at different strain values and thus spread the damage, which would lead to final non-catastrophic failure of the CMC.

There is yet another important statistical point with regard to this variability of fiber strength. This has to do with the fact that in a unidirectionally aligned fiber

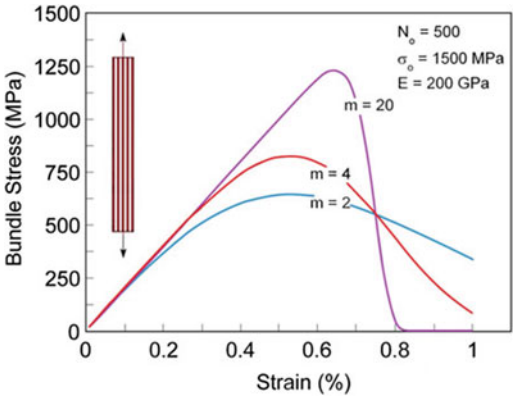

Fig. 12.9 Fiber bundle strength versus strain in a CMC for different Weibull modulus values [Courtesy of E. Lara-Curzio]

composite, the fibers act in a bundle in parallel. It turns out that the strength of a bundle of fibers whose elements do not possess a uniform strength is not the average strength of the fibers. Coleman (1958) investigated this nontrivial problem, which we now describe.

In the simplest case, we assume that all fibers have the same cross section and the same stress–strain curve but with different strain-to-fracture values. Let the strength distribution function for the fiber be $f(\sigma)$ (Eq. 12.15), then the probability that a fiber will break before a certain value σ is attained is given by the cumulative strength distribution function $F(\sigma)$. We can write

$$F(\sigma) = \int_0^{\sigma} f(\sigma) d\sigma. \tag{12.26}$$

One makes a large number of measurements of strength of individual packets or bundles of fibers. Each bundle has the same large number of fibers of identical cross section and they are loaded from their extremities. From such tests, we can obtain the mean fiber strength in the bundle. Daniels (1945) showed that, for a very large number of fibers in the bundle, the distribution of the mean fiber strength at bundle failure attains a normal distribution, with the expectation or mean value being given by

$$\bar{\sigma}_B = \sigma_{\text{fu}}[1 - F(\sigma_{\text{fu}})], \tag{12.27}$$

where σ_{fu} is the maximum fiber strength, i.e., σ_{fu} corresponds to the condition where the bundle supports the maximum load. Thus, we obtain σ_{fu} by taking the derivative of Eq. (12.27) and equating it to zero,

$$\frac{d}{d\sigma}\{\sigma[1 - F(\sigma)]\}_{\sigma=\sigma_{\text{fu}}} = 0. \tag{12.28}$$

The fiber bundle strength, σ_B values are characterized by the following density function for normal distribution function:

$$\omega(\sigma_B) = \frac{1}{\Psi_B\sqrt{2\pi}} \exp\left[-\frac{1}{2}\left(\frac{\sigma_B - \bar{\sigma}_B}{\Psi_B}\right)^2\right], \tag{12.29}$$

where Ψ_B is the standard deviation given by

$$\Psi_B = \sigma_{\text{fu}}\{F(\sigma_{\text{fu}})[1 - F(\sigma_{\text{fu}})]\}^{1/2} N^{-1/2}, \tag{12.30}$$

where N is the number of fibers in the bundle.

As N becomes very large, not unexpectedly, the standard variation Ψ_B becomes small. That is, the larger the number of fibers in the bundle, the more reproducible is

the bundle strength. For bundles characterized by Eq. (12.29), we can define a cumulative distribution function $\Omega(\sigma_B)$. Thus,

$$\Omega(\sigma_B) = \int_0^{\sigma_B} \omega(\sigma_B) d\sigma_B. \tag{12.31}$$

Consider the Weibull distribution [Eq. (12.15)], then we have from Eq. (12.28)

$$\sigma_{\text{fu}} = (L\alpha\beta)^{-1/\beta}. \tag{12.32}$$

Substituting this in Eq. (12.27), we get the following expression (left as an exercise for the reader to do) for the mean fiber bundle strength:

$$\bar{\sigma}_B = (L\alpha\beta e)^{-1/\beta}. \tag{12.33}$$

In Eq. (12.33), e is the constant, called Euler's number, equal to 2.718. If we compare this mean fiber bundle strength value [Eq. (12.33)] to the mean value of the fiber strength obtained from equal length fibers tested individually [Eq. (12.19)], we note the following important items. When there is no dispersion in fiber strength, i.e., all fibers show the same strength value, the mean bundle strength equals the mean fiber strength; see Fig. 12.10. As the coefficient of variation of fiber strength increases above zero, the mean bundle strength decreases and, in the limit of an infinite dispersion, tends to zero. For a 10% variance, the mean bundle strength is about 80% of the mean fiber strength, while for a variance of 25%, the bundle strength is about 60% of the mean fiber strength.

In view of the statistical distribution of fiber strength, it is natural to extend these ideas to composite strength. We present here the treatment called *cumulative weakening model of failure,* introduced by Rosen and coworkers (1965b, 1983). When we load a fiber reinforced composite, fibers (assuming they are more brittle than the matrix) fracture at various points before a complete failure of the composite occurs. There occurs an accumulation of fiber fractures with increasing load. At a certain point, one transverse section will be weakened as a result of the statistical accumulation of fiber fractures, hence the name *cumulative weakening model of failure*. Because the fibers have nonuniform strength, it is expected that some fibers

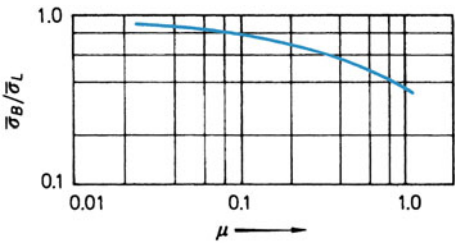

Fig. 12.10 Normalized fiber bundle strength versus variance μ of the fiber population

will break at very low stress levels. Figure 12.11 shows the perturbation in stress state when a fiber fracture occurs. At the point of fiber fracture, the tensile stress in the fiber drops to zero (see also Fig. 10.16). From this point onward, the tensile stress in the fiber increases along the fiber length along the two fiber segments as per the load transfer mechanism by interfacial shear described in Chap. 10. As a result, either the matrix would yield in shear or an interfacial failure would occur. Additionally, this local drop in stress caused by a fiber break will throw the load onto adjoining fibers, causing stress concentrations there. Upon continued straining, progressive fiber fractures cause a cumulative weakening and a redistribution of the load in the composite, see Fig. 12.12. Let us explore the different possibilities. After the first fiber fracture, the interfacial shear stresses may cause delamination between this broken fiber and the matrix, as shown in Fig. 12.12a. When this happens, the broken and delaminated fiber becomes totally ineffective and the composite behaves as a bundle of fibers. The second alternative is that a crack, starting from the first fiber break, propagates through the other fibers in a direction normal to the fibers; see Fig. 12.12b. Such a situation will occur only if the fiber and matrix are very strongly bonded and if the major component is very brittle. In the absence of these two modes, cumulative damage results. With increased loading, additional fiber fractures occur and a statistical distribution is obtained; see Fig. 12.12c.

Rosen (1983) considers in this model that the composite strength is controlled by a statistical accumulation of failures of individual volume elements that are separated by barriers to crack propagation; thus, these elements fail independently. The load on the matrix is ignored. Increased loading leads to individual fiber breaks at loads less than the ultimate fracture load of the composite. An individual fiber break does not make the whole fiber length ineffective, it only reduces the capacity of the fiber being loaded in the vicinity of fiber failure. The stress distribution in the fiber is one of full load over its entire length less a length near the break over which the load is zero. This length is called the *ineffective length*. Thus, the composite is considered to be made up of a series of layers, each layer consisting of a packet of fiber elements embedded in the matrix. The length of the fiber element or the packet height is equal to the ineffective length.

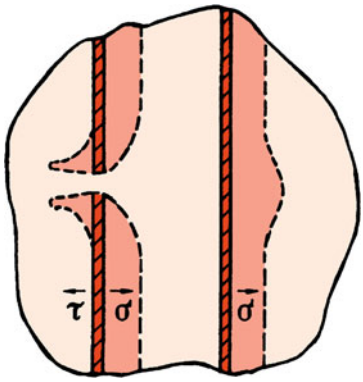

Fig. 12.11 Perturbation of stress state caused by a fiber break

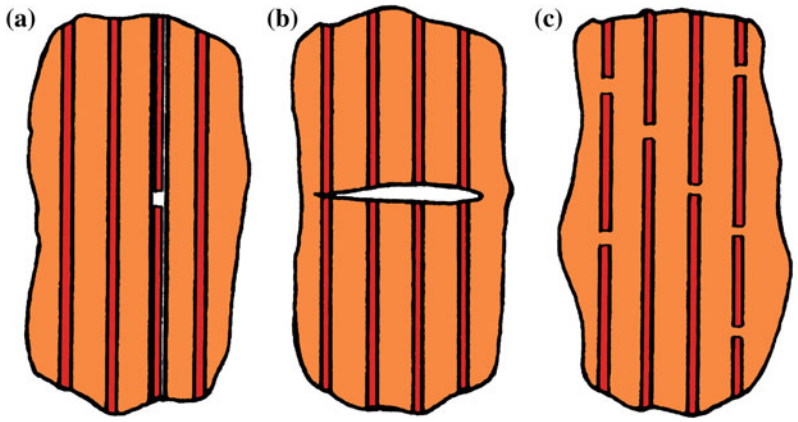

Fig. 12.12 Fracture models: **a** fiber fracture leading to interfacial delamination, **b** first fiber fracture leading to a complete fracture of the composite, and **c** cumulative damage by multiple fiber fracture leading to a statistical distribution of fiber breaks

As the load is increased, fiber breaks accumulate until at a critical load a packet of elements is unable to transmit the applied load and the composite fails. Thus, composite failure occurs because of this weakened section. A characteristic length δ corresponding to the packet height must be chosen. The term δ is defined as the length over which the stress attains a certain fraction ϕ of the unperturbed stress in the fiber. Rosen took ϕ equal to that length over which the stress increases elastically from zero (at a fiber end) to 90% of the unperturbed level. One then derives the stress distribution in the fiber elements and packets. The theory of the weakest link is then applied to obtain the composite strength. In the case of fibers characterized by the Weibull distribution, the stress distribution in the fiber elements is

$$w(\sigma) = \delta\alpha\beta\sigma^{\beta-1}\exp\left(-\delta\alpha\sigma^{\beta}\right), \tag{12.34}$$

where δ is the fiber element length (i.e., the ineffective length).

The composite is now a chain, the strength of whose elements is given by a normal distribution function $w(\sigma_B)$. The strength of a chain having m links (do not confuse with the Weibull modulus) of this population is characterized by a distribution function $\lambda(\sigma_c)$:

$$\lambda(\sigma_c) = mw(\sigma_c)[1 - \Omega(\sigma_c)]^{m-1}, \tag{12.35}$$

where

$$\Omega(\sigma_c) = \int_0^{\sigma_c} w(\sigma_c)d\sigma. \tag{12.36}$$

Suppose now that the number of elements N (i.e., the number of fibers in the bundle) in a composite is so large that the standard deviation of the packet tends to zero. Then the statistical mode of composite strength is equal to $\bar{\sigma}_B$ [Eq. (12.27)].

In the case of a Weibull distribution, it follows from Eq. (12.33) that

$$\sigma_c^* = (\delta\alpha\beta e)^{-1/\beta} \tag{12.37}$$

and the statistical mode of the tensile strength of the composite is

$$\sigma^* = V_f(\delta\alpha\beta e)^{-1/\beta}, \tag{12.38}$$

where V_f is the fiber volume fraction and $e = 2.718$.

It should be pointed out that δ will be of the order of 10–100 fiber diameters and thus much smaller than the gage length used for individual tests.

If we compare the (cumulative) average strength of a group of fibers of length L with the expected fiber strength from Eqs. (12.21) and (12.37), we get

$$\frac{\sigma_c^*}{\bar{\sigma}_L} = \left(\frac{L}{\delta\beta e}\right)^{1/\beta} \frac{1}{\Gamma(1+1/\beta)}. \tag{12.39}$$

For $\beta = 5$ and $L/\delta = 100$, we have $\sigma_c^*/\bar{\sigma}_L = 1.62$; that is, the composite will be much stronger than what we expect from individual fiber tests. We can plot the composite strength σ_c^*, normalized with respect to the average strength $\bar{\sigma}_L$, of individual fibers of length L against μ, the variance of individual fiber strengths; see Fig. 12.13. The curves shown are for different values of the ratio L/δ. For $L/\delta = 1$, that is, the fiber length is equal to the ineffective length, the statistical mode of composite strength is less than the average fiber strength. This difference between

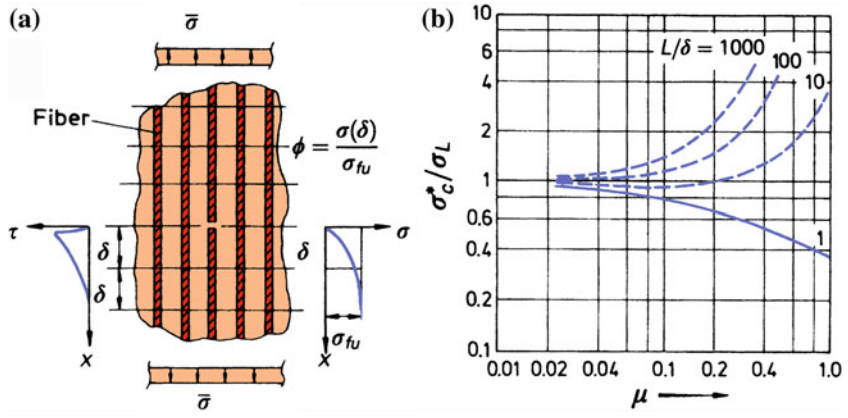

Fig. 12.13 Normalized composite strength $\sigma_C^*/\bar{\sigma}_L$ versus variance μ (From Fiber Composite Materials, ASM, 1965, pp. 39, 38, used with permission)

the two increases with an increase in μ of the fibers. For a more realistic ratio, for example, $L/\delta > 10$, we note that the composite strength is higher than the average fiber strength.

A modification of this cumulative weakening model was proposed by Zweben and Rosen (1970), which takes into account the redistribution of stress that results at each fiber break; that is, there is greater probability that fracture will occur in immediately adjacent fibers because of a stress magnification effect.

12.5 Strength of an Orthotropic Lamina

We saw in Chaps. 10 and 11 that fiber reinforced composites have anisotropic properties. This results from the fact that the fibers are aligned in the matrix. Additionally, the fibers are, generally, a lot stiffer and stronger than the matrix. Therefore, not unexpectedly, fiber reinforced composites also show anisotropy in strength properties. Quite frequently, the strength in the longitudinal direction is as much as an order of magnitude greater than that in the transverse direction. It is of great importance for design purposes to be able to predict the strength of a composite under the loading conditions prevailing in service. The use of a failure criterion gives us information about the failure strength under combined stresses. We assume, for simplicity, that the material is homogeneous; that is, its properties do not change from point to point. In other words, we treat a fiber reinforced lamina as a homogeneous, orthotropic material (Rowlands 1985). We present below a brief account of different failure criteria.

12.5.1 Maximum Stress Criterion

Failure of fiber reinforced lamina will occur when any one of the stress components is equal to or greater than its corresponding allowable or intrinsic strength. Thus, failure will occur if the following conditions are satisfied:

$$\begin{array}{ll} \sigma_1 \geq X_1^T & \sigma_1 \leq -X_1^C \\ \sigma_2 \geq X_2^T & \sigma_2 \leq -X_2^C \\ \sigma_6 \geq S & \sigma_6 \leq S \end{array}, \tag{12.40}$$

where X_1^T is the ultimate uniaxial tensile strength in the fiber direction, X_1^C is the ultimate uniaxial compressive strength in the fiber direction, X_2^T is the ultimate uniaxial tensile strength transverse to the fiber direction, X_2^C is the ultimate uniaxial compressive strength transverse to the fiber direction, and S is the ultimate planar shear strength. When any one of the inequalities indicated in Eq. (12.40) is attained, the material will fail by the failure mode related to that stress inequality. No

interaction between different failure modes is permitted in this criterion. Consider an orthotropic lamina, that is, a unidirectional fiber reinforced prepreg subjected to a uniaxial tensile stress σ_x in a direction making an angle θ with the fiber direction. We then have, for the stress components in the 1–2 system,

$$\begin{bmatrix} \sigma_1 \\ \sigma_2 \\ \sigma_6 \end{bmatrix} = [T]_\sigma \begin{bmatrix} \sigma_x \\ \sigma_y \\ \sigma_s \end{bmatrix}, \tag{12.41a}$$

where the transformation matrix is given by

$$[T]_\sigma = \begin{bmatrix} m^2 & n^2 & 2mn \\ n^2 & m^2 & -2mn \\ -mn & mn & m^2 - n^2 \end{bmatrix} \quad m = \cos\theta,\ n = \sin\theta.$$

Using the fact that only σ_x is nonzero, we obtain

$$\begin{aligned} \sigma_1 &= \sigma_x m^2 \\ \sigma_2 &= \sigma_x n^2 \\ \sigma_6 &= -\sigma_x mn. \end{aligned} \tag{12.41b}$$

Using these expressions for σ_x in conjunction with ith Eq. (12.40), we get, according to the maximum stress criterion, the following three independent failure modes:

$$\begin{aligned} \sigma_x &= \frac{X_1^T}{\sqrt{m}} \quad \text{(longitudinal tensile)} \\ \sigma_x &= \frac{X_2^T}{\sqrt{n}} \quad \text{(transverse tensile)} \\ \sigma_x &= \frac{S}{mn} \quad \text{(planar shear)} \end{aligned} \quad . \tag{12.42}$$

Here we are disregarding the sign of the shear stress, S. Figure 12.14 shows the failure stress with changing fiber orientation, θ. Note the failure mode changes from longitudinal tension to planar shear to transverse tension, as shown by the dashed lines. The agreement with experiment is poor, particularly around $\theta = \pi/4$. This indicates that at intermediate angles, interactions between failure modes do occur.

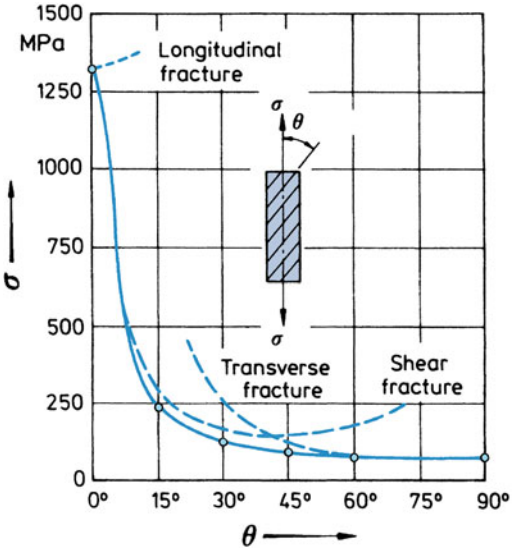

Fig. 12.14 Variation of strength with fiber orientation for boron/epoxy. Quadratic interaction criterion (solid curve) shows better agreement with experimental data than the maximum stress criterion (dashed curve) [After Pipes and Cole (1973)]

12.5.2 Maximum Strain Criterion

This criterion is analogous to the maximum stress criterion. Failure occurs when any one of the strain components is equal to or greater than its corresponding allowable strain. Thus,

$$\begin{aligned} &\varepsilon_1 \geq e_1^T \quad \varepsilon_1 \leq -e_1^C \\ &\varepsilon_2 \geq e_2^T \quad \varepsilon_2 \leq -e_2^C \\ &\varepsilon_6 \geq e_6 \quad \varepsilon_6 \geq e_6 \end{aligned}, \tag{12.43}$$

where e_1^T is the ultimate tensile strain in the fiber direction, e_1^C is the ultimate compressive strain in the fiber direction, e_2^T is the ultimate tensile strain in the transverse direction, e_2^C is the ultimate compressive strain in the transverse direction, and e_6 is the ultimate planar shear strain. This criterion is also not very satisfactory for the same reason as the maximum stress criterion, namely, absence of any interaction of failure modes.

12.5.3 Maximum Work (or the Tsai–Hill) Criterion

This criterion, originally proposed by Hill, is based on a modification of the distortion energy criterion for ductile metals. Hill's modification worked for anisotropic, ductile metals such as metals that have undergone rolling, etc. The Tsai–Hill criterion adopted Hill's modification to orthotropic fiber reinforced composites. According to the Tsai–Hill criterion, failure of an orthotropic lamina will occur under a general two-dimensional stress state when the following expression holds:

$$\frac{\sigma_1^2}{X_1^2} - \frac{\sigma_1\sigma_2}{X_1^2} + \frac{\sigma_2^2}{X_2^2} + \frac{\sigma_6^2}{S^2} \leq 1, \tag{12.44}$$

where X_1, X_2, and S are the longitudinal tensile failure strength, the transverse tensile failure strength, and the inplane shear failure strength, respectively. If compressive stresses are involved, then the corresponding compressive failure strengths should be used.

Consider again a uniaxial stress σ_x applied to an orthotropic lamina. Then, following Eq. (12.41a), we can write

$$\begin{aligned} \sigma_1 &= \sigma_x m^2 \\ \sigma_2 &= \sigma_x n^2 \\ \sigma_6 &= -\sigma_x mn, \end{aligned} \tag{12.45}$$

where $m = \cos\theta$ and $n = \sin\theta$. Substituting these values in Eq. (12.44), we have

$$\frac{m^4}{X_1^2} + \frac{n^4}{X_2^2} + m^2n^2\left(\frac{1}{S^2} - \frac{1}{X_1^2}\right) < \frac{1}{\sigma_x^2} = \frac{1}{\sigma_\theta^2}. \tag{12.46}$$

This expression gives us the off-axis strength of composite lamina as function of fiber orientation. We can use this to verify the validity of the criterion. This criterion does take into account the interaction between the failure modes. However, it does not make any direct distinction between tensile and compressive stresses.

12.5.4 Quadratic Interaction Criterion

As the name indicates, this criterion takes into account the stress interactions. Tsai and Wu (1971) proposed this modification of the Hill theory for a lamina by adding some additional terms. Tsai and Hahn (1980) provide a good account of this criterion. According to this theory, the failure surface in stress space can be described by a function of the form

$$f(\sigma) = F_i\sigma_i + F_{ij}\sigma_i\sigma_j = 1 \quad i,j = 1,2,6, \tag{12.47}$$

where F_i and F_{ij} are the strength parameters. For the case of plane stress, i,j = 1,2,6. We can expand Eq. (12.48) as follows:

$$\begin{aligned} &F_1\sigma_1 + F_2\sigma_2 + F_6\sigma_6 + F_{11}\sigma_1^2 + F_{22}\sigma_2^2 + F_{66}\sigma_6^2 + 2F_{12}\sigma_1\sigma_2 \\ &\quad + 2F_{16}\sigma_1\sigma_6 + 2F_{26}\sigma_2\sigma_6 = 1. \end{aligned} \tag{12.48}$$

For the orthotropic lamina, sign reversal for normal stresses, whether tensile or compressive, is important. The linear stress terms provide for this difference. For the shear stress component, the sign reversal should be immaterial. Thus, terms containing the first degree shear stress must vanish. These terms are $F_{16}\sigma_1\sigma_6$, $F_{26}\sigma_2\sigma_6$, and $F_6\sigma_6$. The stress components in general are not zero. Therefore, for these three terms to vanish, we must have

$$F_{16} = F_{26} = F_6 = 0.$$

Equation (12.49) is now simplified to

$$F_1\sigma_1 + F_2\sigma_2 + F_{11}\sigma_1^2 + F_{22}\sigma_2^2 + F_{66}\sigma_6^2 + 2F_{12}\sigma_1\sigma_2 = 1. \tag{12.49}$$

There are six strength parameters in Eq. (12.49). We can measure five of these by the following simple tests.

12.5.4.1 Longitudinal (Tensile and Compressive) Tests

If $\sigma_1 = X_1^T$, then $F_{11} = \left(X_1^T\right)^2 + F_1X_1^T = 1$.

If $\sigma_1 = -X_1^C$, then $F_{11} = \left(X_1^C\right)^2 + F_1X_1^C = 1$.

From these two expressions, we get

$$F_{11} = \frac{1}{X_1^TX_1^C}, \tag{12.50}$$

and

$$F_1 = \frac{1}{X_1^T} - \frac{1}{X_1^C}. \tag{12.51}$$

12.5.4.2 Transverse (Tensile and Compressive) Tests

If X_2^T and X_2^C are the transverse tensile and compressive strengths, respectively, then proceeding as earlier, we get

$$F_{22} = \frac{1}{X_2^T X_2^C}, \tag{12.52}$$

and

$$F_2 = \frac{1}{X_2^T} - \frac{1}{X_2^C}. \tag{12.53}$$

12.5.4.3 Longitudinal Shear Test

If S is the shear strength, we have

$$F_{66} = \frac{1}{S^2}. \tag{12.54}$$

Thus, we can express all the failure constants except F_{12} in terms of the ultimate intrinsic strength properties. F_{12} is the only remaining parameter and it must be evaluated by means of a biaxial test, which can be quite complicated to do. Many workers (Hoffman 1967; Cowin 1979) have proposed variations of the Tsai–Wu criterion involving F_{12} explicitly in terms of uniaxial strengths. Tsai and Hahn (1980) suggest that, in the absence of other data, we should use $F_{12} = -0.5\sqrt{F_{11}F_{22}}$. Fig. 12.13 shows the variation of strength with orientation assuming $F_{12} = 0$ for the boron/epoxy system (Pipes and Cole 1973). The intrinsic properties of this boron fiber/epoxy system used to obtain the curve in Fig. 12.13 are as follows:

$$X_1^T = 27.3\,MPa \quad X_2^T = 1.3\,MPa \quad S = 1.4\,MPa$$
$$X_1^C = 52.4\,MPa \quad X_2^C = 6.5\,MPa$$

Note the excellent agreement between the computed curve using the quadratic interaction criterion and the experimental values. The agreement with the maximum stress criterion (dashed curve) is poor.

12.5.4.4 Comparison of Failure Theories

Important attributes of the four main failure theories, namely, maximum stress, maximum strain, maximum work, and quadratic interaction are compared in Table 12.1. The applicability of a given theory depends on material properties and the failure modes (Daniel and Ishai 1994). As expected, the maximum stress and maximum strain criteria are generally valid with brittle materials. They do require three subcriteria but are conceptually quite simple and experimental determination of parameters is also quite simple and straightforward. The two interactive theories,

Table 12.1 Comparison of failure theories [After Daniel) and Ishai (1994)]

Criterion	Physical basis	Computational aspects	Experimental characterization
Maximum stress	Tensile behavior of brittle material, no stress interaction	Inconvenient	Simple
Maximum strain	Tensile behavior of brittle material, no stress interaction	Inconvenient	Simple
Maximum work	Valid for ductile anisotropic materials, curve fitting for heterogenous brittle composites	Can be programmed, different functions required for tensile and compressive strengths	Biaxial testing needed
Quadratic interaction	Mathematically consistent, reliable curve fitting	Simple, comprehensive	Complicated, numerous parameters needed

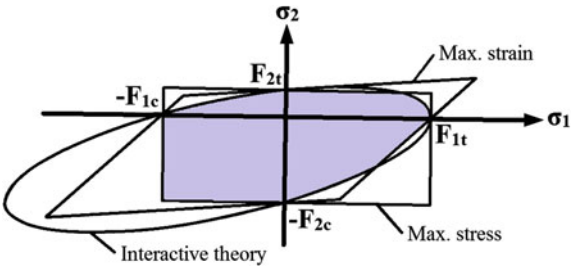

Fig. 12.15 Failure envelopes due to different failure criteria. The shaded past indicates the conservative failure region [After Daniel and Ishai (1994)]

maximum work and quadratic interaction, are more suitable for computational purposes. In particular, the quadratic interaction criterion is quite general and comprehensive. Both require more complicated experimental characterization. According to Daniel and Ishai) (1994), when material behavior and failure modes are not known and when a conservative approach is required, all four criteria should be evaluated and use should be made of the most conservative envelope in each quadrant. Figure 12.15 shows the four criteria in two-dimensional stress space. The shaded part of the envelopes conforms to this conservative approach.

Problems

12.1. For a ceramic fiber with $\mu = 12\%$, show that $\beta \simeq 10$. Show also that if the fiber length is changed by an order of magnitude, the corresponding drop in the average strength is about 20%.

12.2. In a series of tests on boron fibers, it was found that $\mu = 10\%$. Compute the ratio $\bar{\sigma}_B/\bar{\sigma}$, where $\bar{\sigma}_B$ is the average strength of the fiber bundle and $\bar{\sigma}$ is the average strength of fibers tested individually.

12.3. Estimate the work of fiber pullout in a 40% carbon fiber/epoxy composite. Given $\sigma_{\text{fu}} = 0.2\ GPa$, $d = 8\ \mu m$, and $\tau_i = 2\ MPa$.

12.4. How would you go about testing a single fine diameter fiber (recall that carbon fiber has a diameter of about 7 μm)? Do discuss the effect of variability in diameter of the fiber along its length in computing the strength of the fiber.

References

K. Anand, V. Gupta, D. Dartford, Acta Metall. Mater. **42**, 797 (1994)
R.J. Arsenault, R.M. Fisher, Scripta Met. **17**, 67 (1983)
B. Budiansky, N. Fleck, J. Mech. Phys. Solids **41**, 183 (1993)
K.K. Chawla, Metallography **6**, 155 (1973a)
K.K. Chawla, Philos. Mag. **28**, 401 (1973b)
K.K. Chawla, *Ceramic Matrix Composites*, 2nd edn. (Kluwer, Boston, 2003)
K.K. Chawla, M. Metzger, J. Mater. Sci. **7**, 34 (1972)
K.K. Chawla, J. Singh, J.M. Rigsbee, Metallography **19**, 119 (1986)
B.D. Coleman, J. Mech. Phys. Solids **7**, 60 (1958)
G.A. Cooper, J. Mater. Sci. **5**, 645 (1970)
G.A. Cooper, A. Kelly, J. Mech. Phys. Solids **15**, 279 (1967)
A.H. Cottrell, Proc. R. Soc. **282A**, 2 (1964)
S.C. Cowin, J. Appl. Mech. **46**, 832 (1979)
I.M. Daniel, O. Ishai, *Engineering Mechanics of Composite Materials* (Oxford University Press, New York, 1994), p. 126
H.E. Daniels, Proc. R. Soc. **A183**, 405 (1945)
H.E. Dève, Acta Mater. **45**, 5041 (1997)
L.I. Ebert, J.D. Gadd, *Fiber Composite Materials* (ASM, Metals Park, OH, 1965), p. 89
V. Gupta, K. Anand, M. Kryska, Acta Metall. Mater. **42**, 781 (1994)
J. Grape, V. Gupta, Acta Metall. Mater. **43**, 2657 (1995a)
J. Grape, V. Gupta, J. Compos. Mater. **29**, 1850 (1995b)
D.K. Hale, A. Kelly, Ann. Rev. Mater. Sci. **2**, 405 (1972)
N.L. Hancox, J. Mater. Sci. **10**, 234 (1975)
O. Hoffman, J. Compos. Mater. **1**, 200 (1967)
A. Kelly, Proc. R. Soc. London **A319**, 95 (1970)
A. Kelly, *The Properties of Fibre Composites* (IPS Science & Technology Press, Guildford, Surrey, U.K., 1971), p. 5
A. Kelly, H. Lilholt, Philos. Mag. **20**, 311 (1969)
S. Kyriakides, R. Arseculeratne, E.J. Perry, K.M. Liechti, Int. J. Solids Struct. **32**, 689 (1995)
J.R. Lager, R.R. June, J. Compos. Mater. **3**, 48 (1969)

S. Narayanan, L.S. Schadler, Compos. Sci. Technol. **59**, 2201 (1999)
J.O. Outwater, M.C. Murphy (1969), in *Proceedings of the 24th SPI/RP Conference, Paper 11-6* (Society of Plastics Industry, New York, 1969)
M.R. Piggott, in *Developments in Reinforced Plastics*, vol. 4 (Elsevier Applied Science Publishers, London, 1984), p. 131
M.R. Piggott, B. Harris, J. Mater. Sci. **15**, 2523 (1980)
R.B. Pipes, B.W. Cole, J. Compos. Mater. **7**, 246 (1973)
B.W. Rosen, *Fiber Composite Materials* (American Society for Metals, Metals Park, OH, 1965a), p. 58
B.W. Rosen, *Fiber Composite Materials* (American Society for Metals, Metals Park, OH, 1965b), p. 37
B.W. Rosen, *Mechanics of Composite Materials: Recent Advances* (Pergamon Press, Oxford, 1983), p. 105
R.E. Rowlands, *Failure Mechanics of Composites*, vol. 3 of the Series (Handbook of Composites, North-Holland, Amsterdam, 1985), p. 71
H. Saghizadeh, C.K.H. Dharan, *American Society of Mechanical Engineering*. Paper #85WA/Mats-15, Presented at the Winter Annual Meeting, Miami Beach, FL, (1985)
C.R. Schultheisz, A.M. Waas, Prog. Aerospace Sci. **32**, 1 (1996)
S.W. Tsai, H.T. Hahn, *Introduction to Composite Materials* (Technomic, Westport, CT, 1980)
S.W. Tsai, E.M. Wu, J. Compos. Mater. **5**, 58 (1971)
M. Vogelsang, R.J. Arsenault, R.M. Fisher, Met. Trans. A **17A**, 379 (1986)
A.M. Waas, C.R. Schultheisz, Prog. Aerospace Sci. **32**, 43 (1996)
C. Zweben, B.W. Rosen, J. Mech. Phys. Solids **18**, 189 (1970)

Chapter 13
Fatigue and Creep

In Chap. 12, we described the monotonic behavior of a composite under ambient temperature conditions of loading. There are many applications of composites where cyclic fatigue and high temperature (i.e., creep) conditions prevail. Accordingly, in this chapter, we go further in complexity and describe the fatigue and creep behavior of composites. *Fatigue* is the phenomenon of mechanical property degradation leading to failure of a material or a component under cyclic loading. The operative word in this definition is *cyclic*. This definition thus excludes the so called phenomenon of static fatigue, which is sometimes used to describe stress corrosion cracking in glasses and ceramics in the presence of moisture. *Creep* refers to time-dependent deformation in a material, which becomes important at relatively high temperatures ($T > 0.4\ T_m$, where T_m is the melting point in kelvin). We first describe fatigue and then creep of composites.

13.1 Fatigue

Degradation of mechanical properties of a material or a component under cyclic loading is called fatigue. Understanding the fatigue behavior of composites of all kinds is of vital importance, because without such an understanding it would be virtually impossible to gain acceptance of the design engineers. Many high volume applications of composite materials involve cyclic loading situations, e.g., components used in automobile, truck, and mass transit. It would be a fair admission that this understanding of the fatigue behavior of composites has lagged that of other aspects such as the elastic stiffness or strength. The major difficulty in this regard is that the application of conventional approaches to fatigue of composites, for example, the stress versus cycles (S–N) curves or the application of linear elastic fracture mechanics (LEFM), is not straightforward. The main reasons for this are the inherent heterogeneity and anisotropic nature of the composites. These characteristics result in damage mechanisms in composites being very different from

K. K. Chawla, *Composite Materials*,
https://doi.org/10.1007/978-3-030-28983-6_13

those encountered in conventional, homogeneous, or monolithic materials. The fracture behavior of composites is characterized by a multiplicity of damage modes, such as matrix crazing (in a polymeric matrix), matrix cracking (in a brittle matrix), matrix plasticity (in a ductile matrix), fiber fracture, interfacial debonding and delamination, void growth, and multidirectional cracking, and these modes appear rather early in the fatigue life of composites. The early onset of these different fracture modes leads to progressive loss of stiffness during fatigue of a composite, which is very different from the fatigue behavior of monolithic materials. The different types of damage zones formed in a conventional, isotropic material (e.g., a metal, or ceramic, or polymer) and a fiber reinforced composite, which is an anisotropic material, are shown schematically in Figs. 13.1 and 13.2, respectively. In the case of the isotropic material, a single crack propagates in a direction perpendicular to the cyclic loading axis (mode I loading). In the fiber reinforced composite, on the other hand, a variety of subcritical damage mechanisms lead to a highly diffuse damage zone. Despite these limitations, conventional approaches have been used and are therefore described here briefly before we describe some more innovative approaches to the problem of fatigue in composites.

Let us first define some useful parameters for our discussion of the fatigue phenomenon; see Fig. 13.3:

$$\begin{gathered}\text{cyclic stress range, } \Delta\sigma = \sigma_{\max} - \sigma_{\min} \\ \text{cyclic stress amplitude, } \sigma_a = (\sigma_{\max} - \sigma_{\min})/2 \\ \text{mean stress, } \sigma_m = (\sigma_{\max} + \sigma_{\min})/2 \\ \text{stress ratio, } R = \sigma_{\min}/\sigma_{\max}.\end{gathered}$$

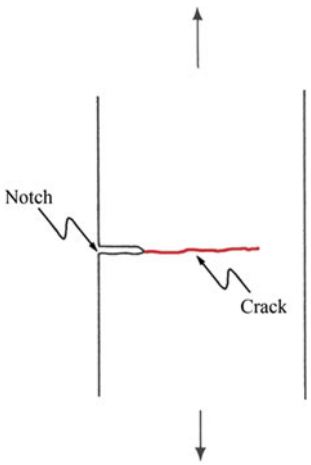

Fig. 13.1 Damage zone in a conventional, homogeneous, monolithic material (isotropic)

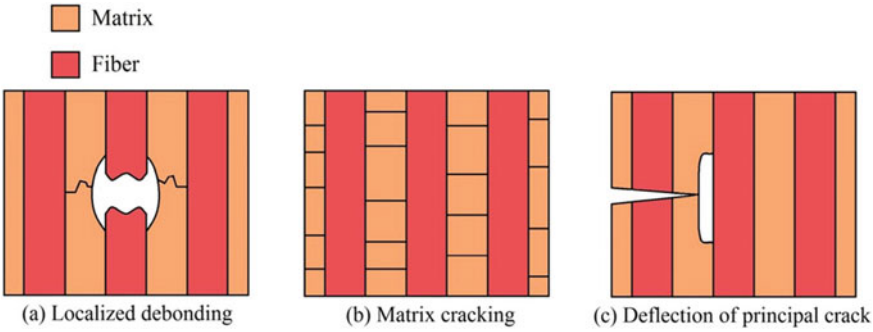

Fig. 13.2 Diffuse damage zone in a fiber reinforced composite (anisotropic): **a** fiber break and local debonding; **b** matrix cracking; **c** deflection of the principal crack along a weak fiber/matrix interface

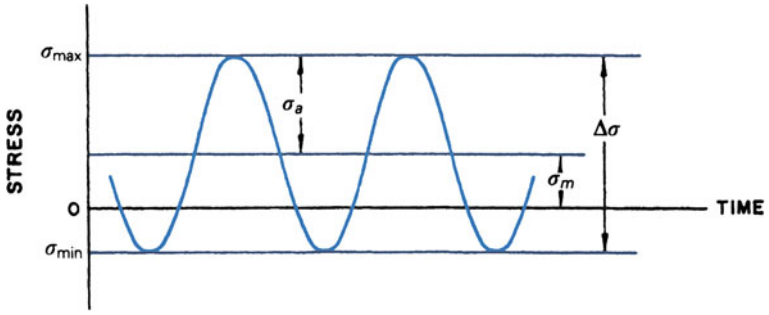

Fig. 13.3 Some useful parameters for fatigue

13.1.1 S–N Curves

We saw in Chap. 10 that in a unidirectionally reinforced fiber composite, elastic modulus and strength improve in the direction of reinforcement. This also has its consequences in the fatigue behavior. S–N curves are commonly used with monolithic materials, especially metals and, to some extent, with polymers. It involves determination of the so-called S–N curves, where S (or σ_a) is the stress amplitude and N is the number of cycles to failure. In general, for ferrous metals, one obtains a fatigue limit or endurance limit. For stress levels below this endurance limit, theoretically, the material can be cycled infinitely. In cases where such an endurance limit does not exist, one can arbitrarily define a cutoff value, a certain number of cycles, say 10^6. Incorporation of fibers generally improves the fatigue resistance of any fiber reinforced composite in the fiber direction. Not surprisingly, therefore, composites containing fibers, aligned along the stress axis and in large volume fractions, do show high monotonic strength values that are translated into high fatigue strength values. Quite frequently, a rule-of-thumb approach in

conventional materials is to increase the monotonic strength, which concomitantly results in an increase in its cyclic strength. This rule-of-thumb assumes that the ratio fatigue strength/tensile strength is about constant. It should also be noted that the maximum efficiency in terms of stiffness and strength gains in fiber reinforced composites occurs when the fibers are continuous, uniaxially aligned and the properties are measured parallel to the fiber direction. As we go off-angle, the strength and stiffness drop sharply. Also, at off angles, the role of the matrix becomes more important in the deformation and failure processes. One major drawback of this S–N approach to fatigue behavior of a material is that no distinction can be made between the crack initiation phase and the crack propagation phase.

The variety of operating mechanisms and the inadequacy of the S–N curve approach have been documented by many researchers. Owen et al. (1967, 1969), for example, studied the fatigue behavior of chopped strand mat glass/polyester composite and observed the following sequence of events in the fatigue failure process: (1) debonding, generally at fibers oriented transverse to the stress axis, (2) cracking in the matrix, and (3) final separation or fracture. The debonding and cracking phenomena set in quite early in the fatigue life. Lavengood and Gulbransen (1969) investigated the importance of fiber aspect ratio and the role of matrix in the fatigue performance of composites. They studied the effect of cyclic loading on short boron fibers (50–55% volume fraction) in an epoxy matrix. They used a low frequency (3 *Hz*) to minimize the hysteretic heating effects and measured the number of cycles required to produce a 20% decrease in the composite elastic modulus, i.e., this was their arbitrary definition of fatigue life. The fatigue life increased with aspect ratio up to about 200, beyond which there was little effect. In all cases, the failure consisted of a combination of interfacial fracture and brittle failure of matrix at 45° to the fiber axis. Incorporation of fibers certainly improves the fatigue resistance of the fiber reinforced polymeric matrix composites in the fiber direction. Not surprisingly, therefore, composites containing these fibers, aligned along the stress axis and in large volume fractions, will show high monotonic strength values, which are translated into high fatigue strength values. S–N curves of unreinforced polysulfone (PSF) and composites with a PSF matrix and different amounts of short fibers (glass and carbon) are shown in Fig. 13.4a. These results were obtained from tests done at room temperature, cycling frequency between 5 and 20 Hz, and at $R = 0.1$ (Mandell et al. 1983). The S–N curves move up with increasing fiber volume fraction. Izuka et al. (1986) studied the fatigue behavior of two different types of carbon fibers (T800 and T300 carbon fiber) in an epoxy matrix. Both had 60% fiber volume fraction (V_f) but T800 carbon fiber has a maximum strength of 4.5 *GPa* and a Young's modulus of 230 *GPa* while T300 carbon fiber has 3.5 *GPa* and 210 *GPa*, respectively. As expected, the higher monotonic strength of T800 carbon fiber resulted in a superior S–N curve for the composite.

The polymeric matrices, however, show a viscoelastic behavior and are, generally, poor conductors of heat. Owing to the viscoelastic nature of the polymer matrix, there will be a phase lag between the stress and the strain, i.e., the strain lags

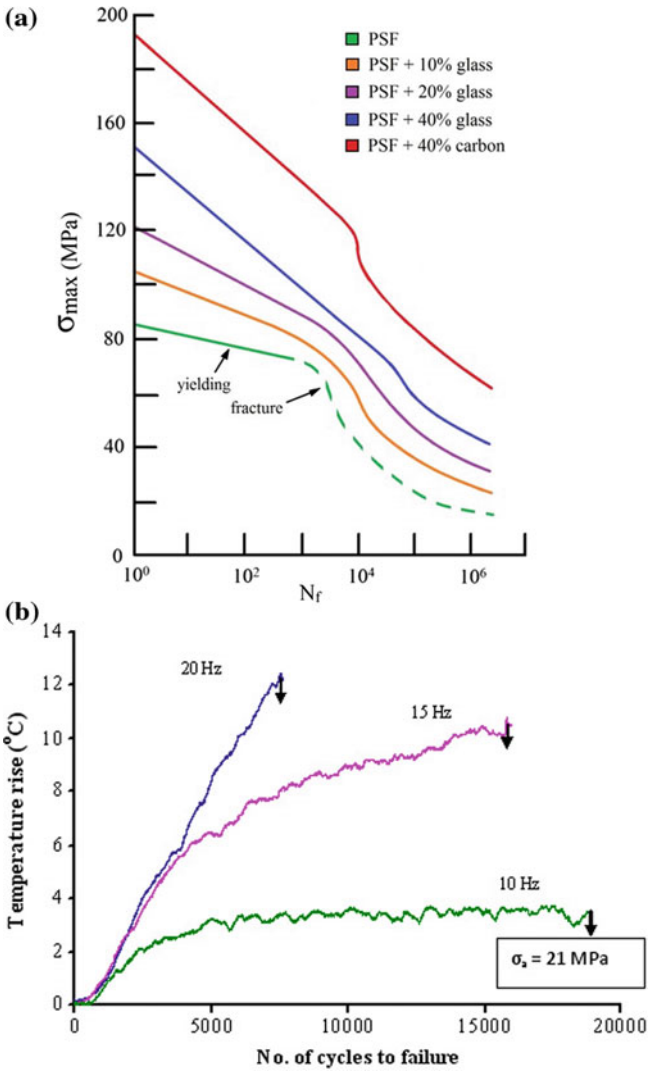

Fig. 13.4 **a** S–N curves of unreinforced polysulfone (PSF) and composites with a PSF matrix and different amounts of short fibers (glass and carbon). [After Mandell et al. (1983).] The S–N curves move up with increasing fiber volume fraction. **b** Hysteretic temperature rise under fatigue for glass fiber/polypropylene composites (Goel et al. 2009). At a given stress amplitude, temperature rises more quickly at higher frequency and leads to premature failure of the composite

the stress or vice versa, and energy is stored in the material in the form of heat in each cycle. This is called hysteretic heating. Because of the low thermal conductivity of the polymeric matrix, the heat generated is not dissipated quickly. This can cause a temperature difference between the interior and the surface of a PMC, and

the fatigue behavior of PMCs becomes even more complex due to such internal heating. The internal heating phenomenon, of course, depends on the cycling frequency. For a given stress level, this temperature difference increases with increasing frequency. Figure 13.4b shows this for glass fiber/polypropylene composites (Goel et al. 2009). At a given stress amplitude, temperature rises more quickly at higher frequency and leads to premature failure of the composite.

Typically, the carbon fibers are much more effective in improving the fatigue behavior of a given polymeric matrix than glass fibers. The reasons for this are the high stiffness and high thermal conductivity of carbon fibers vis à vis glass fibers. The higher thermal conductivity of carbon fibers will contribute to lower hysteretic heating of the matrix at a given frequency.

Examples of S–N curves for fiber reinforced MMCs are shown in Fig. 13.5a, which shows the S–N curves in tension–tension for unidirectionally reinforced boron (40% v/o)/A16061, alumina (50% v/o)/Al, and alumina (50% v/o)/Mg composites (Champion et al. 1978). The cyclic stress is normalized with respect to the monotonic ultimate tensile stress. Note the rather flat S–N curves in all the cases and the fact that the unidirectional composites show better fatigue properties than the matrix when loaded parallel to the fibers. For example, at 10^7 cycles, the fatigue-to-tensile strength ratio of the composite is about 0.77, almost double that of the unreinforced matrix. S–N curves for silicon carbide particle reinforced aluminum matrix composites are shown in Fig. 13.5b. Increase in volume fraction of SiC_p results in an increase in fatigue life (Chawla et al. 1998a, b).

Gouda et al. (1981) observed crack initiation early in the fatigue life at defects in boron fibers in unidirectionally reinforced B/Al composites. These cracks then grew along the fiber/matrix interface and accounted for a major portion of the fatigue life, as would be the case in a composite with a high fiber-to-matrix strength ratio. In composites with low fiber-to-matrix strength ratios, crack propagation may take up a major portion of fatigue life, but the crack would be expected to grow across the fibers and a poor fatigue resistance will result. This simply confirms the observation that in unidirectional composites the fatigue resistance will be maximum along the fiber direction and the greatest efficiency will be achieved if the fibers have uniform properties, as much as possible defect-free, and much stronger than the matrix. Similar results have been obtained by other researchers. For example, McGuire and Harris (1974) studied the fatigue behavior of tungsten fiber reinforced aluminum—4% copper alloy under tension–compression cycling ($R = \sigma_{min}/\sigma_{max} = -1$). They found that increasing the fiber volume fraction from 0 to 24% resulted in increased fatigue resistance. This was a direct result of increased monotonic strength of the composite as a function of the fiber volume fraction. The reader should note that due to the highly anisotropic nature of the fiber reinforced composites in general, the fatigue strength of any off-axis fibrous composite will be expected to decrease with increasing angle between the fiber axis and the stress axis. This has been confirmed by studies involving S–N behavior of alumina fiber reinforced magnesium composites (Hack et al. 1987; Page et al. 1987) It was found that the S–N behavior followed the tensile behavior. Increased fiber volume fractions resulted in enhanced fatigue lifetime in the axial direction but little or no improvement was

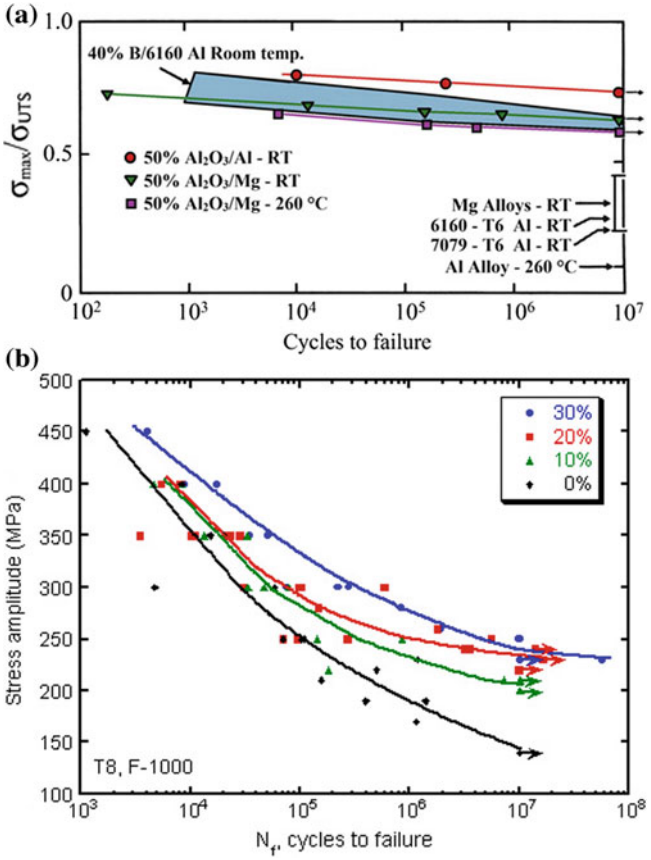

Fig. 13.5 **a** S–N curves for MMCs in tension–tension for unidirectionally reinforced boron fiber (40% v/o)/A16061, alumina fiber (50% v/o)/Al, and alumina fiber (50% v/o)/Mg composites. [After Champion et al. (1978).] **b** S–N curves for silicon carbide particle reinforced aluminum matrix composites [Courtesy of N. Chawla]

observed in the off-axis directions. Fatigue crack initiation and propagation occurred primarily through the magnesium matrix. Thus, alloy additions to increase the strength of the matrix and fiber/matrix interface were tried. The alloy additions did improve the off-axis properties but decreased the axial properties. The reason for this was that while the alloy additions resulted in the matrix and interface strengthening, they decreased the fiber strength. A similar effect of fiber orientation on fatigue properties occurs in PMCs. As an example, Goel et al. (2009) observed better fatigue performance in the longitudinal direction than in the transverse direction in glass fiber/polypropylene composites.

13.1.2 Fatigue Crack Propagation

Fatigue crack propagation tests are generally conducted in an electrohydraulic closed-loop testing machine on notched samples. The results are presented as log *da/dN* (crack growth per cycle) versus log ΔK (cyclic stress intensity factor). Crack growth rate, *da/dN*, is related to the cyclic stress intensity factor range, ΔK, according to the power law relationship formulated by Paris and Erdogan (1963):

$$da/dN = A(\Delta K)^m, \tag{13.1}$$

where A and m are constants that depend on the material and test conditions. The applied cyclic stress intensity range is given by

$$\Delta K = Y\Delta\sigma\sqrt{\pi a},$$

where Y is a geometric factor, $\Delta\sigma$ is the cyclic stress range, and a is the crack length. The major problem in this kind of test is to make sure that there is one and only one dominant crack that is propagating. This is called the *self-similar* crack growth, i.e., the crack propagates in the same plane and direction as the initial crack. Fatigue crack propagation studies, under conditions of self-similar crack propagation, have been made on metallic sheet laminates (McCartney et al. 1967; Taylor and Ryder 1976; Pfeiffer and Alic 1978; Chawla and Liaw 1979; Godefroid and Chawla 1988) and unidirectionally aligned fiber reinforced MMCs (Saff et al. 1988). For the crack arrest geometry, if the interface is weak, then the crack on reaching the interface bifurcates and changes its direction and thus the failure of the composite is delayed. The improved fatigue crack propagation resistance in crack divider geometry has been attributed either to interfacial separation, which relieves the triaxial state of stress, or to an interfacial holding back of crack in the faster crack-propagating component by the slower crack-propagating component. Generally, a relationship of the form of Eq. (13.1) describes the fatigue crack propagation behavior.

In general, the fibers provide a crack-impeding effect but the nature of the fiber (morphology, rigidity, and fracture strain), the fiber/interface, and/or any reaction zone phases that might form at the interface can have great influence.

Fatigue crack propagation studies have also been done on aligned eutectic or in situ composites. Because many of these in situ composites are meant for high temperature applications such as in turbines, their fatigue behavior has been studied at temperatures ranging from room temperature to 1100 °*C*. The consensus is that the mechanical behavior of in situ composites, static and cyclic strengths, is superior to that of the conventional cast superalloys (Stoloff 1987).

It should be emphasized that only fatigue crack propagation rate data obtained under conditions of self-similar propagation can be used for comparative purposes. In a composite consisting of plies with different fiber orientation, in general, the self-similar mode of crack propagation will not be obtained.

13.1.2.1 Fatigue of Composites Under Compression

Fiber reinforced composites generally show lower fatigue resistance in compression than in tension. This may be due to the cooperative buckling of adjacent fibers and the accompanying matrix shear. In monotonic compression of unidirectionally reinforced fiber composites, a fiber kinking mechanism leads to failure. The failure in this case initiates at a weak spot, e.g., at a point where the fiber/matrix bonding is weak. This initial failure will, in turn, destabilize the neighboring fibers, causing more kink failure. Eventually, various kink failure sites can coalesce and lead to transverse tensile loading of the composite and longitudinal splitting. Pruitt and Suresh (1992) showed that in addition to kink band formation, in unidirectional carbon fiber/epoxy composites under cyclic compression, a single mode I crack could start and grow perpendicular to the fiber axis. This compression fatigue phenomenon is thought to be macroscopically similar to that observed in metals, polymers, and ceramics. The origin of a mode I crack ahead of a stress concentration is the presence of residual tensile stresses, which can result from a variety of permanent damage modes involving matrix, fiber, interface, etc.

One can also introduce defects to simulate a delamination in fiber reinforced laminated composites and then study its propagation under conditions of fatigue. Such defects may be introduced in a laminate by one of the following means:

1. Insert circular inserts of different diameters at different interfaces,
2. Insert a hole in the laminate, and
3. Produce defects in a laminate by controlled, low velocity impacts.

Delamination growth under cyclic compression fatigue in a 38-ply T300 carbon/5208 epoxy composite laminate was studied by O'Brien (1984). The maximum strain decreased with cycling. The impacted laminates suffered the most severe degradation on compressive cycling while the laminates with a single implanted delamination suffered the least damage.

13.1.2.2 Fatigue Behavior of CMCs

We describe the fatigue behavior of CMCs under a separate subheading because of some important discoveries in this field. Conventional wisdom had it that cyclic fatigue was unimportant as far as ceramics were concerned. However, in actuality, the subject of cyclic fatigue in ceramics and ceramic matrix composites *is* an important one. Engineers and researchers began to appreciate the importance of cyclic fatigue in ceramics and ceramic matrix composites only in the 1970s. The fracture resistance of CMCs under cyclic conditions needs to be evaluated for design in a variety of potential structural applications. For example, it is not unusual to have a design requirement for a ceramic component in an automotive gas turbine to withstand more than 30,000 cycles of fatigue (low-cycle fatigue) (Helms and Haley 1989). In the case of carbon fiber reinforced glass composites, no significant

loss of strength was observed on cyclic loading (Phillips 1983). However, the density and penetration of matrix cracks was more under cyclic loading than under static loading conditions. Also, under static loading, this CMC showed higher work of fracture than under cyclic loading. Prewo et al. (1986) studied the tensile fatigue behavior of Nicalon-type silicon carbide fiber reinforced lithium aluminosilicate (LAS) glass–ceramic composite. They used two different types of LAS as the matrix material: one showed a linear tensile stress–strain curve to failure (LAS I) while the other showed a markedly nonlinear behavior due to extensive matrix cracking prior to ultimate failure (LAS II). It was observed that the level of tensile stress at which the inelastic behavior (proportional limit) of the composite began had an important bearing on the fatigue behavior of the CMC. The residual tensile strength and elastic modulus of the LAS I composite after fatigue was the same as that of as-fabricated composite. In the LAS II composite, cycling below the proportional limit produced the same result. However, on cycling to stress levels higher than the proportional limit, a second linear stress–strain region having a modulus less than the initial modulus was observed. Presumably, this change in behavior was due to matrix microcracking at stresses above the proportional limit.

As we pointed out above it was generally thought that the phenomenon of cyclic fatigue was unimportant in ceramics. Work by Suresh and coworkers (Suresh et al. 1988, 1991; Han and Suresh 1989) on fatigue crack growth in a variety of brittle solids in compression, tension, and tension–compression fatigue shows that mechanical fatigue effects, i.e., due to cyclic loading, do occur at room temperature in brittle solids as well. A variety of mechanisms such as microcracking, dislocation plasticity, stress- or strain-induced phase transformations, interfacial slip, and creep cavitation can promote an inelastic constitutive response in brittle solids of all kinds under compressive cycling. Particularly, in CMCs, the mechanisms of crack tip deformation differ significantly under static and cyclic loading. They demonstrated that under pulsating compression (i.e., compression–compression fatigue) nucleation and growth of stable fatigue cracks occurred even at room temperature. They showed conclusively that cyclic compressive loading caused mode I fatigue crack growth in SiC whisker reinforced Si_3N_4 matrix composites. They also observed whisker pullout and breakage after fatigue cycling. Such behavior is generally not observed under monotonic loading. This mode I fatigue crack growth under far field cyclic compression occurs because a zone of residual tensile stress is generated at the crack tip during the unloading part of the cycle. Wang et al. (1991) investigated the behavior of a [0/90] carbon fiber reinforced silicon carbide composite under cyclic loading. They studied tension–tension cyclic loading of smooth and notched samples and compression–compression loading. Damage in pulsating tension consisted of cumulative microcracking and spalling. In this regard, it worth pointing out that investigation of cyclic behavior of polycrystalline continuous alumina fiber showed a definite cyclic fatigue effect, i.e., cyclic fatigue of alumina fibers showed more damage than static fatigue (Chawla et al. 2005)

An important problem in high-temperature behavior of polycrystalline ceramics is the presence of glassy phases at intergranular boundaries. Sintering and other processing aids can form glassy phases at the boundaries, which can result in rather

conspicuous subcritical crack growth. Such subcritical crack growth can become very important in ceramic matrix composites because fibers such as silicon carbide can undergo oxidation. Han and Suresh (1989) examined the tensile cyclic fatigue crack growth in a silicon carbide whisker (33 *vol %*)/alumina composite at 1400 °*C*. The composite showed subcritical fatigue crack growth at stress intensity values far below the fracture toughness. The fatigue behavior was characterized by the cyclic stress intensity factor, stress ratio, and frequency. They examined the crack tip region by optical and transmission electron microscopy and found that the nucleation and growth of flaws at the interface was the main damage mechanism. Diffuse microcracking in the wake of the crack and crack deflection/branching were observed. An increase in the test temperature (or the cyclic stress intensity or a reduction in the loading rate) can cause a rather significant increase in the size of the damage zone at the crack tip. Han and Suresh observed oxidation of silicon carbide whiskers to a silica-type glassy phase in the crack tip region at 1400 °*C*, in air. The alumina matrix can react with the main oxidation product, viz., SiO_2, to form aluminosilicates, SiC-rich or stoichiometric mullite, and the like. Viscous flow of glass can result in interfacial debonding, followed by the nucleation, growth, and coalescence of cavities. The important thing to note is that there is a difference in deformation and failure mechanisms under static and cyclic loadings, even in CMCs.

In a manner analogous to PMCs, there can be a hysteretic heating in CMCs under cyclic loading conditions due to interfacial friction (Holmes 1991). Sørensen and Holmes (1995) observed that a lubricating layer might be beneficial in improving fatigue life of CMCs. A thicker coating, which would be expected to provide greater protection to the fiber against abrasion damage, resulted in less frictional heating because of less wear of the fibers during fatigue of a chemical vapor infiltrated (CVI) Nicalon/C/SiC composite (Chawla et al. 1997, 1998a, b). The composite with a thinner coating exhibited much higher frictional heating. At higher frequencies, more heating was observed since the energy dissipated per unit time also increased. Substantial damage in terms of loss of stiffness was observed in fatigue of Nicalon/C/SiC, with most of the damage occurring during the first cycle. At a constant stress, the level of damage was not significantly dependent on frequency. At a given frequency, however, higher stresses induced more damage in both the composites. In the case of the fiber in the form of a plain-weave fabric, a recovery in modulus of these woven composites was observed due to stretching and alignment of the fabric during fatigue, creating a stiffer reinforcing architecture.

The laminate stacking sequence can affect the high-frequency fatigue behavior of CMCs. In SCS-6 fiber/Si_3N_4 composites, frictional heating in angle-ply laminates [±45] was substantially higher than that in cross-ply laminates [0/90] (Chawla 1997). Because the angle ply had a lower stiffness, matrix microcracking in this composite was more predominant. Temperature rise in the CMCs correlated very well with stiffness loss as a function of fatigue cycles (see Sect. 13.1.3).

13.1.2.3 Fatigue of Particle and Whisker Reinforced Composite

Ceramic particle reinforced metal matrix composites, such as silicon carbide or alumina particle reinforced aluminum alloy composites can have improved fatigue properties vis à vis unreinforced aluminum alloys, which can make these composites useful in applications where aluminum alloys would not be considered (Allison and Jones 1993). Such systems have been studied by some researchers (Chawla et al. 1998a, b; Crowe and Hassen 1982; Williams and Fine 1985, 1987; Logsdon and Liaw 1986; Shang et al. 1988; Davidson 1989; Kumai et al. 1990; Bonnen et al. 1990; Christman and Suresh 1988a, b; Hruby et al. 2014). In general, in terms of S–N curve behavior, the composite shows an improved fatigue behavior vis à vis the reinforced alloy. Such an improvement in stress-controlled cyclic loading or high cyclic fatigue is attributed to the higher stiffness of the composite. However, the fatigue behavior of the composite, evaluated in terms of strain amplitude versus cycles or low-cycle fatigue, was inferior to that of the unreinforced alloy (Bonnen et al. 1990). This was attributed to the generally lower ductility of the composite compared to unreinforced alloy.

Particle or short fibers can provide easy crack initiation sites. The detailed behavior can vary depending on the volume fraction of the reinforcement, shape, size, and most importantly on the reinforcement/matrix bond strength. For example, Williams and Fine (1987) observed fatigue crack initiation at the poles of SiC whiskers in 2124 aluminum. They also observed arrest of short cracks at the whisker/Al interfaces. Frequently in aluminum matrix composites, especially those made by casting, there are particles, called constituent particles in aluminum literature, other than SiC, such as $CuAl_2$, $(Fe,Mn)_3$ $SiAl_{12}$, and $Cu_2Mg_5Si_6Al_5$ (Kumai and Knott 1991). During liquid metal processing of particle reinforced MMCs, there occurs the phenomenon of particle pushing ahead of the solidification front (Rohatgi et al. 1994). This results in SiC particles and the constituent particles decorating the cell boundaries in the aluminum alloy matrix, which can affect the fatigue behavior.

Some possible interactions between the ceramic particle reinforcement and the crack tip in the matrix are shown schematically in Fig. 13.6. When the ceramic particles are large, they can be loaded to the point of fracture and the fatigue crack runs through the particles. When we have fine particles, the crack goes around the particles. Figure 13.7 shows schematic representations of crack growth versus cyclic intensity factor for a monolithic alloy and a particulate composite. Levin et al. (1989) observed superior resistance to fatigue crack growth in 15 *vol %* SiC/Al 6061 composite vis à vis Al 6061 alloy, which was attributed to a slower crack growth rate in the composite due to crack deflection caused by the SiC particles. Computer simulation of crack growth behavior in particle reinforced MMCs starting with actual microstructures rather than simplified models has become quite important. Ceramic particle shape, size distribution, spatial distribution, etc., are very important during deformation of these materials, particularly during crack growth.

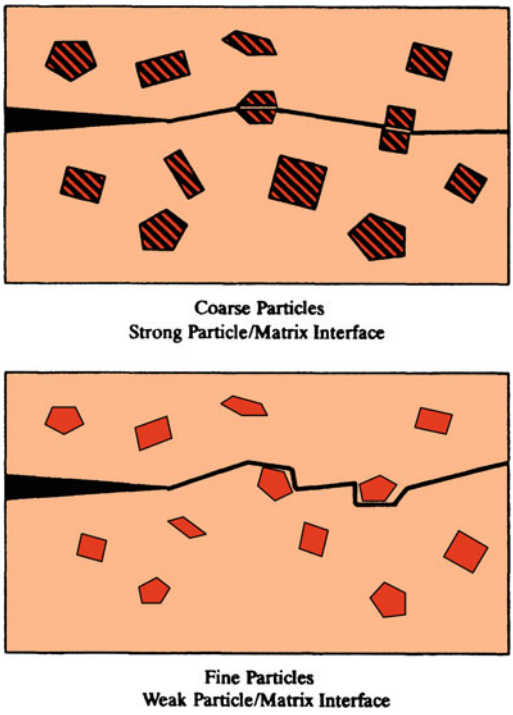

Fig. 13.6 Some possible reinforcement and crack tip interactions

It would appear that choosing the optimum particle size and volume fractions, together with a clean matrix alloy, will result in a composite with improved fatigue characteristics. Shang et al. (1988) examined the effect of particle size on fatigue crack propagation as a function of cyclic stress intensity in a silicon carbide particle reinforced aluminum. They observed that for fine particle size, the threshold stress intensity, ΔK_{th}, for the composite was less than that for the unreinforced alloy, i.e., initial fatigue crack growth resistance of the composite was less than that of the unreinforced alloy. For coarse particles, the threshold intensity values were about

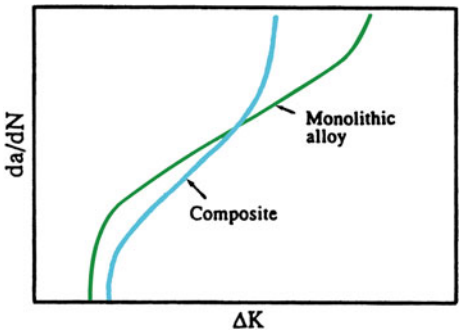

Fig. 13.7 Schematic representation of crack growth versus cyclic intensity factor for a monolithic alloy and a particulate MMC [after Kumai et al. (1990)]

the same for the two, while at very high values of the cyclic stress intensity, the fatigue crack growth of the composite was less than that of the unreinforced alloy.

We digress at this point and say a few words about X-ray Computed Tomography (XCT), which is a relatively new technique. XCT is a very useful nondestructive technique for visualizing internal features in a material. It allows us to obtain three-dimensional images (four-dimensional if we add time) in a nondestructive manner. XCT involves directing X-rays at a material at different directions and measuring the X-ray attenuation as a function X-ray energy, and density and composition of the material. Special algorithm is used to reconstruct the X-ray attenuation distribution in the volume of material under investigation. Essentially, the setup consists of a source, a rotation stage, and a detector, as shown in Fig. 13.8. The specimen is mounted on the rotating stage, placed in between the source and the detector. X-ray source can be a lab-scale system or a synchrotron-based source.

The detector consists of a camera and a scintillator. The scintillator converts the X-rays into visible light which is captured by a CCD (charge coupled device) or CMOS (complementary metal oxide semiconductor) cameras. Small values of angular rotation increment lead to higher number of projections, which result in a higher accuracy of 3D reconstruction of the projections. A typical image set consists of $\sim$1000–1500 projections.

Advanced facilities rely on synchrotron radiation (X-rays produced by bending moving electrons by means of strong magnets) while lab-scale facilities make use of braking-radiation (i.e., X-rays produced by deceleration of electrons, Bremsstrahlung in German) derived X-rays (Singh and Chawla 2018). The lab-scale facility provides X-rays that are polychromatic, cone-beam shape, and are less brilliant than X-rays produced by synchrotron. Synchrotron radiation provides a highly brilliant, monochromatic, parallel beam. The higher brilliance results in reduced scan time and less image artifacts.

Most studies use optical imaging of cracking at the sample surface and of fracture surfaces. X-ray microtomography would appear to be an ideal technique for

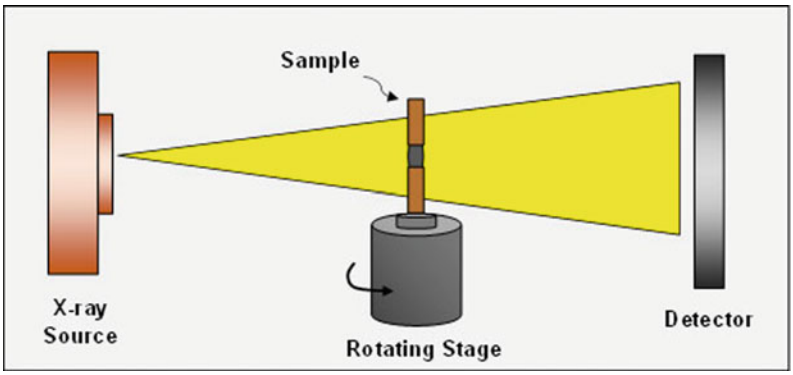

Fig. 13.8 X-ray micro-computed tomography (XCT) setup consisting of X-ray source, sample mounted on a rotating stage, and a detector to capture the projection [Courtesy of Singh and Chawla 2018]

such an analysis because it allows in situ verification through the thickness in a nondestructive manner. Hruby et al. (2014) studied the fatigue crack propagation in behavior of SiC particle reinforced aluminum 2080 (3.6% Cu, 1.9% Mg, 0.25% Zr). The composite had 20 vol.% SiC particles (average particle size of 25 μm). In particular, these authors studied the effect of R-ratio on fatigue crack proposition on SiC particle reinforced aluminum alloy composites: whether the SiC particles cracked ahead of the main crack, or whether the fatigue crack grew through the originally intact SiC particles. At low R-ratio, crack deflects around SiC particles. At high R-ratio, the main finding of this work, Hruby et al. (2014), involving X-ray tomography was that fatigue crack growth in particle reinforced MMCs takes place by:

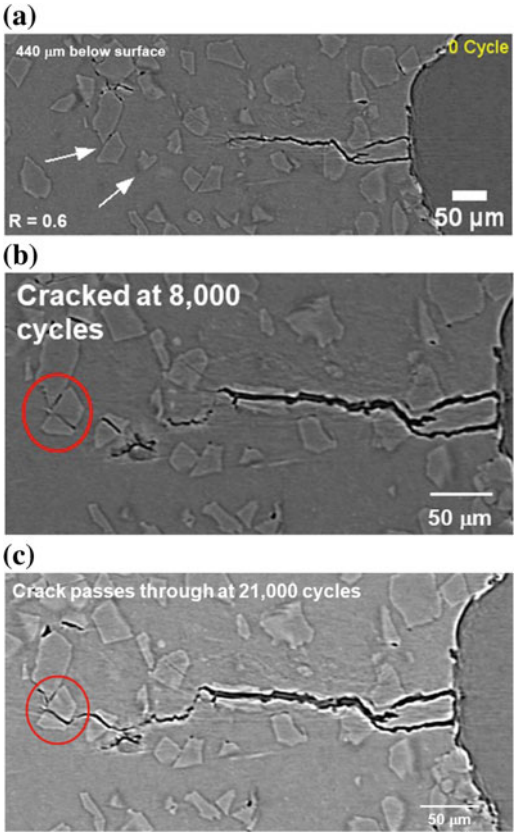

Fig. 13.9 A series of pictures of fatigue crack propagation in SiC/Al2080 alloy at R = 0.6 by X-ray microcomputer tomography. **a** The initial condition. **b** The situation at 8000 cycles **c** SiC particles crack ahead of fatigue crack, at 21,000 cycles [Courtesy of N. Chawla]

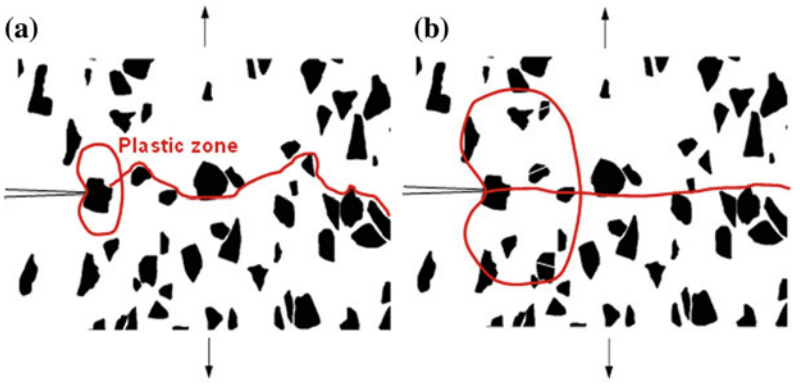

Fig. 13.10 At low K_{max}, ΔK the interaction zone at the crack tip is small, crack path is torturous while at high K_{max}, ΔK the interaction zone at the crack tip is large, crack path is more or less planar [Courtesy of N. Chawla]

- Crack deflection at lower R-ratios.
- Particle fracture ahead of the crack tip at higher R-ratios.

SiC particles crack ahead of the fatigue crack, followed by fatigue crack propagation through cracked particles at 21,000 cycles. All these pictures are from the interior of the sample. Figure 13.9a shows a series of pictures at R = 0.6. The situation at 7000 cycles is shown in Fig. 13.9b while the situation at 8000 cycles is shown in Fig. 13.9c. SiC particles crack ahead of the fatigue crack, followed by fatigue crack propagation through cracked particles at 21,000 cycles. It is worth repeating that all these pictures are from the interior of the sample. For R = 0.1, the crack deflected around the SiC particles. The situation is summarized schematically in Fig. 13.10. At low K_{max}, ΔK the interaction zone at the crack tip is small, crack path is torturous while at high K_{max}, ΔK the interaction zone at the crack tip is large, crack path is more or less planar.

13.1.3 Damage Mechanics of Fatigue

It was mentioned earlier that the complexities in composites lead to the presence of many modes of damage, such as matrix cracking, fiber fracture, delamination, debonding, void growth, and multidirectional cracking. These modes appear rather early in the fatigue life of composites, i.e., these subcritical damage accumulation mechanisms come into play rather early in the fatigue life—well before the fatigue limit, as determined in an S–N test, and a highly diffused damage zone is formed. One manifestation of such damage is the stiffness loss as a function of cycling. In general, one would expect the scatter in fatigue data of composites to be much greater than that in fatigue of monolithic, homogeneous materials. Again, this is

because of the existence of a variety of damage mechanisms in composites, to wit, random distribution of matrix microcracks, fiber/matrix interface debonding, and fiber breaks, etc. With continued cycling, an accumulation of damage occurs. This accumulated damage results in a reduction of the overall stiffness of the composite laminate. Measurement of stiffness loss as a function of cycling has been shown to be quite a useful technique for assessing the fatigue damage in composites. Information useful to designers can be obtained from such curves. In MMCs, the fatigue behavior of boron fiber and silicon carbide fiber reinforced aluminum and titanium alloy matrix composite laminates with different stacking sequences has been examined using the stiffness loss measurement technique (Dvorak and Johnson 1980; Johnson 1988; Johnson and Wallis 1986). It was observed that on cycling below the fatigue limit but above a distinct stress range, ΔS_{SD}, the plastic deformation and cracking (internal damage) in the matrix led to a reduced modulus. Figure 13.11 shows the response of a boron fiber/aluminum matrix composite subjected to a constant cyclic stress range (225 *MPa*) with varying values of $S_{\max}$, the maximum stress. The modulus drop occurred only when $S_{\max}$ was shifted upward. Johnson (1988) proposed a model that envisioned that the specimen reached a saturation damage state (SDS) during constant-amplitude fatigue testing. Gomez and Wawner (1988) also observed stiffness loss on subjecting silicon carbide fiber/aluminum composites to tension–tension fatigue ($R = 0.1$) at 10 *Hz*. Periodically, the cycling was stopped and the elastic modulus was measured. Figure 13.12 shows a typical modulus loss curve for unidirectional silicon carbide fiber/aluminum composites. Modulus at N cycles, E_N, normalized with respect to the original modulus, E_0, is plotted against the log (number of cycles, N). These authors used a special type of silicon carbide fiber, called the SCS-8 silicon carbide fiber, which is a silicon carbide fiber with a modified surface to give a strong bond between the fiber and the aluminum matrix. The SCS coating broke off at high cycles and the fracture surface showed the coating clinging to the matrix. Another example of stiffness loss as a function of number of cycles is for Nicalon fiber/borosilicate glass–ceramic matrix composites (Ramakrishnan and Jayaraman 1993). In CMCs, the matrix can have a lower strain-to-failure than the fibers. In such a case, the matrix starts cracking first. Thereafter, we have two possible routes. In the case of a weak interface, we observe fiber/matrix debonding followed by fiber pullout, etc. In the case of a strong interface, matrix cracking leads to failure and a brittle failure of the composite. Karandikar and Chou (1992) used the approach of stiffness loss as a function of stress cycles with unidirectionally reinforced Nicalon fiber/calcium aluminosilicate (CAS) composites and obtained correlations between crack density and stiffness reduction.

Let us focus our attention on the fatigue behavior of fiber reinforced *laminated composites* that are made by consolidating prepregs. Figure 13.10a shows schematically a comparison of damage accumulation as a function of fatigue cycles in a laminated composite made by appropriately stacking differently oriented plies and a monolithic, homogeneous material under constant stress amplitude fatigue (Hahn and Lorenzo 1984). We plot damage ratio against cycle ratio. The damage ratio is the current damage normalized with respect to the damage at final failure.

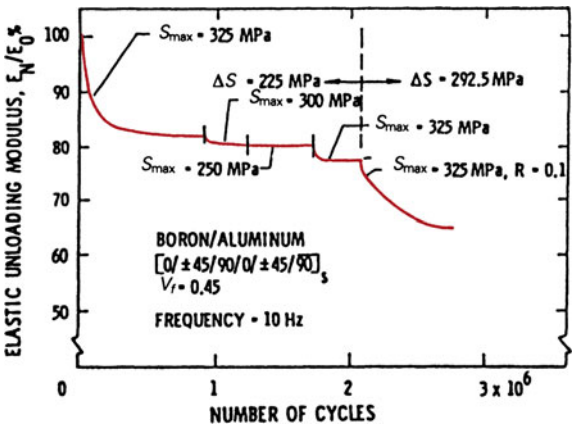

Fig. 13.11 Response of a boron fiber/aluminum matrix composite subjected to a constant cyclic stress range (225 *MPa*) with varying values of S_{max}, the maximum stress [after Johnson (1988)]

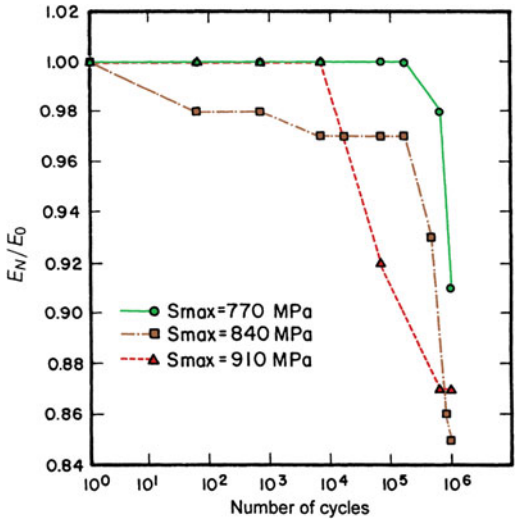

Fig. 13.12 Typical modulus loss curve for unidirectional silicon carbide/aluminum composites. E_N is the modulus after N cycles and E_0 is the modulus in the uncycled state. [After Gomez and Wawner (1988).]

The cycle ratio, similarly, is the number of cycles at a given instant divided by the number of cycles to failure. In a conventional, homogeneous material, the term *damage* simply represents the crack length, and not surprisingly it increases monotonically with cycling. In the case of a laminate, we do not have a simple and unambiguous manifestation of damage, such as a crack length. Instead, damage is

diffused and involves a variety of cracks, so damage, in principle, would mean the crack density. Note that, unlike in homogeneous materials, the damage (i.e., crack density) in laminates accelerates at first and then decelerates with cycling. This distinctive behavior is very important. Such a multiplicity of fracture modes is common to all composites. As an example, Fig. 13.12 shows the fracture surface of B(W)/A1 6061 composite made by diffusion bonding. Note the ductile fracture in aluminum, brittle fracture in boron, fiber pullout (see the missing fiber in top left hand corner), and sheet delamination.

As was pointed out earlier, the fiber reinforced laminates can sustain a variety of subcritical damage (crazing and cracking of matrix, fiber/matrix decohesion, fiber fracture and pullout, ply cracking, delamination, and so on). For example, the cracking of a ply will result in a relaxation of stress in that ply, and with continued cycling, no further cracking occurs in that ply. Ply cracking generally involves cracking in the matrix and along the fiber/matrix interface but rarely any fiber fracture. Other damage accumulating mechanisms include the growth of existing cracks into interfaces leading to ply delamination. The subcritical damage can accumulate rather rapidly on cycling.

The various types of subcritical damage mentioned above result in a reduction of the load-carrying capacity of the composite, which in turn manifests itself as a reduction in stiffness and strength of the composite. Many researchers have experimentally related the stiffness changes in the laminated composites to the accumulated damage under fatigue (Hahn and Kim 1976; Highsmith and Reifsnider 1982; Talreja 1985; Ogin et al. 1985; Johnson 1988). Work with polymer- and metal matrix composites shows that this change in stiffness values is a good indicator of the extent of damage in these composites. Figure 13.14 depicts

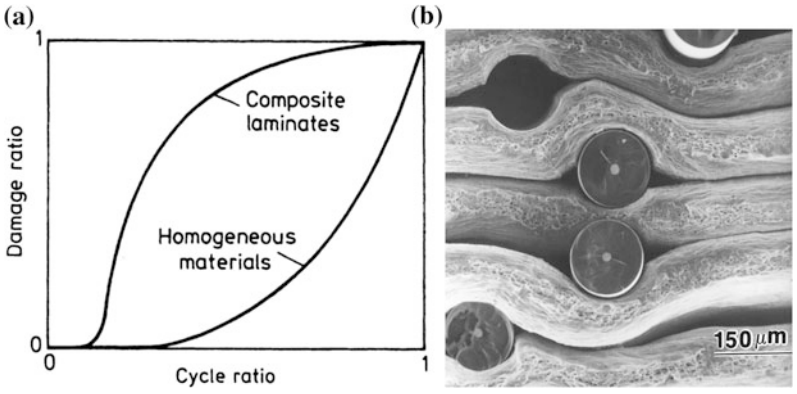

Fig. 13.13 **a** Comparison of damage accumulation as a function of fatigue cycles in a laminated composite (made by appropriately stacking differently oriented plies) and a monolithic, homogeneous material under constant stress amplitude fatigue. [After Hahn and Lorenzo (1984).] **b** Fracture surface of B(W)/A1 6061 composite made by diffusion bonding. Note the different modes of damage: ductile fracture in aluminum, brittle fracture in boron, fiber pullout (see the missing fiber in top-left-hand corner), and sheet delamination

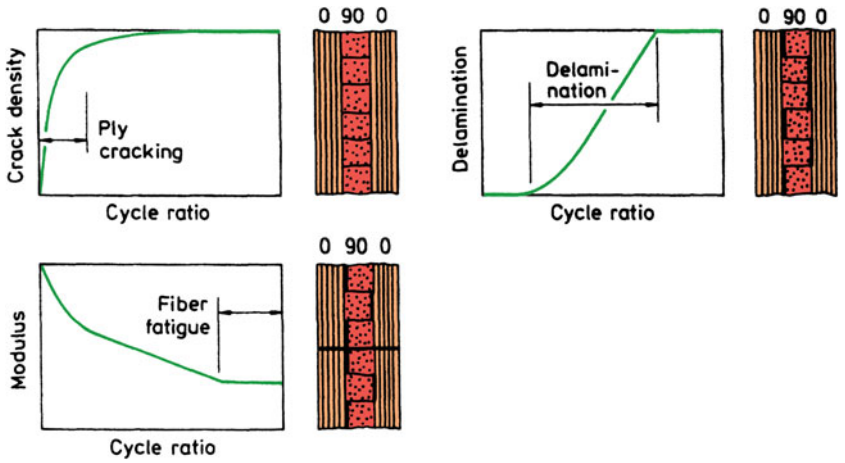

Fig. 13.14 Schematic of changes in crack density, delamination, and modulus in a composite laminate under fatigue [after Hahn and Lorenzo (1984)]

schematically the changes in crack density, delamination, and modulus in a composite laminate under fatigue (Hahn and Lorenzo 1984). Reifsnider et al. (1981) modeled the fatigue development in laminate composites as occurring in two stages. In the first stage, homogeneous, noninteractive cracks appear in individual plies. In the second stage, the damage gets localized in zones of increasing crack interaction. The transition from stage one to stage two occurs at what has been called the *characteristic damage state* (CDS), which consists of a well-defined crack pattern characterizing saturation of the noninteractive cracking. Talreja (1985) used this model to determine the probability distribution of the number of cycles required to attain the CDS.

It can safely be said that the change in stiffness values is a good indicator of the damage in composites. An actual stiffness reduction curve for a $[0°/90°]_s$ glass fiber reinforced laminated composite is shown in Fig. 13.15 (Ogin et al. 1985). Under

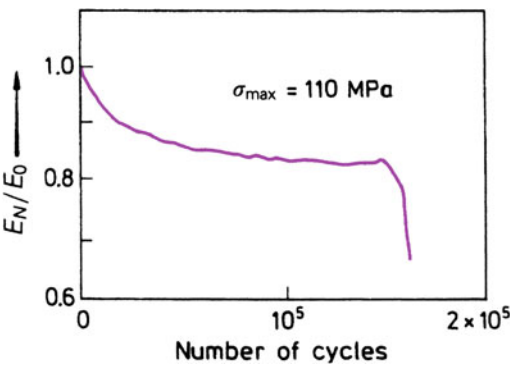

Fig. 13.15 Stiffness reduction curve for a $[0°/90°]_s$ glass fiber reinforced laminated composite [after Ogin et al. (1985)]

cyclic loading of a laminated composite, a variety of damage accumulation mechanisms can start at stress levels below those needed under monotonic conditions. Because of the presence of this multiplicity of failure modes in a fibrous composite, it rarely fails in a simple manner as does a monolithic material. Following Beaumont (1989), we define the failure of the composite when a critical level of damage is reached or exceeded. Let D be the damage parameter that increases as a function of number of cycles, N. Then, dD/dN will be the damage growth rate. We can write for the damage growth rate

$$dD/dN = f(\Delta\sigma, R, D), \tag{13.2}$$

where $\Delta\sigma$ is the cyclic stress range, R is the stress ratio, and D is the current value of damage. Let N_f be the number of cycles to failure, i.e., the fatigue life corresponding to a critical level of damage. Then integrating Eq. (13.2) between limits of initial damage, D_i, and final damage, D_f, we can write for the number of cycles to failure as

$$N_f = \int_{Di}^{Df} dD/f(\Delta\sigma, R, D). \tag{13.3}$$

The main problem is that the function f is not known. One measure of damage is the instantaneous load-bearing capacity or the stiffness, E. We can write

$$E = E_0 g(D), \tag{13.4}$$

where E_0 is the stiffness of the undamaged material and $g(D)$ is a function of damage, D.

Rewriting Eq. (13.4) as $E/E_0 = g(D)$ and differentiating, we get

$$(1/E_0)dE/dN = dg(D)/dN. \tag{13.5}$$

Also,

$$D = g^{-1}(E/E_0),$$

where g^{-1} is the inverse of g. This allows us to rewrite Eq. (13.5) as

$$(1/E_0)dE/dN = g'\left[g^{-1}(E/E_0)\right]f(\Delta\sigma, R, D).$$

The function $g(D)$ can be obtained experimentally by obtaining data in terms of E/E_0 versus N. We can then evaluate the function f as:

$$f(\Delta\sigma, R, D) = \left(1/g'\left[g^{-1}(E/E_0)\right]\right)(1/E_0)dE/dN.$$

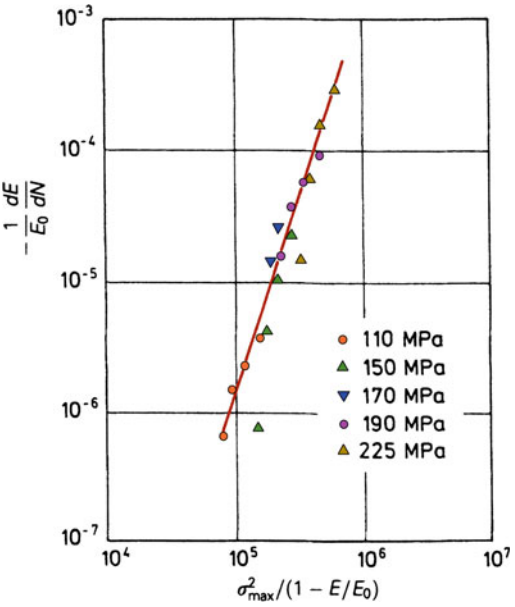

Fig. 13.16 Modulus reduction rate versus a parameter involving the peak stress [after Ogin et al. (1985)]

We can evaluate the right hand side of this expression for a range of $\Delta\sigma$, maintaining constant E/E_0, R, etc. If $2S$ is the average crack spacing, then crack density or damage = $1/2S$. The following relationship was found experimentally for crack growth as a function of cycles, da/dN (Ogin 1985):

$$da/dN \propto \left(\sigma^2_{\max} 2S\right)^n.$$

Total crack length a is proportional to damage or crack density, D, i.e.,

$$dD/dN \propto \left(\sigma^2_{\max}/D\right)^n.$$

Modulus of the damaged material E is given by

$$E = E_0(1 - cD), \tag{13.6}$$

where c is a material constant.

For a given value of E/E_0, we can write the modulus or stiffness reduction rate as

$$(-1/E_0)\, dE/dN = A\left[\sigma^2_{\max}/E_0^2(1 - E/E_0)\right]^n, \tag{13.7}$$

where A and n are constants. The left hand side of this expression can be determined experimentally. Note that both sides are dimensionless quantities. The modulus reduction rate $(-1/E_0)\, dE/dN$, at a given value of E/E_0, is the tangent to the curve shown in Fig. 13.15. This rate of Young's modulus reduction was well described

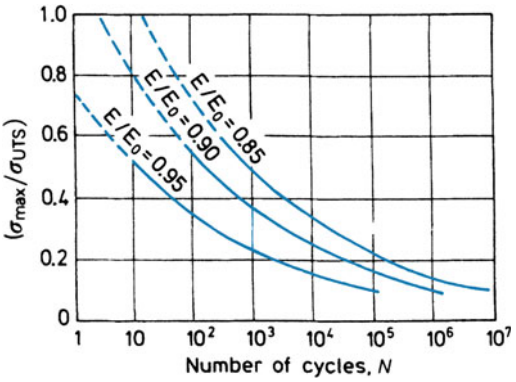

Fig. 13.17 Number of cycles required to attain a given stiffness reduction after cycling at different fractions of the ultimate tensile strength σ_{UTS} [after Ogin et al. (1985)]

over the range of peak fatigue stress between 110 and 225 *MPa* for the glass fiber/epoxy composite by Eq. (13.7); see Fig. 13.16. We can integrate Eq. (13.7) to obtain a diagram relating stiffness reduction to number of cycles for different stress levels, as shown in Fig. 13.17. Such a diagram can be a very useful design aid: It gives us the number of cycles it will take, when the composite is cycled at a certain fraction of the monotonic ultimate strength, to attain a specific amount of stiffness reduction (i.e., a specific amount of damage that the component or the structure can withstand).

13.1.4 Thermal Fatigue

There exists a very fundamental physical incompatibility between the reinforcement (be that fiber, whisker, or particle) and the matrix, to wit, the difference in their thermal expansion (or contraction) coefficients. This problem of thermal expansion mismatch between the components of a composite is a very important one. Thermal stresses arise in composite materials due to the generally large differences in the thermal expansion coefficients (α) of the fiber and the matrix. It should be emphasized that thermal stresses in composites cannot be alleviated by slow cooling or some kind of annealing treatment, techniques that might work in conventional material. The reason for this is that the thermal mismatch will be there even if the temperature change is uniform throughout the volume of the composite. Thermal stresses can be introduced in composites during cooling from high temperature of fabrication, annealing, or curing temperatures or during any temperature excursions (inadvertent or by design) during service. Turbine blades, for example, are very much susceptible to thermal fatigue. The magnitude of thermal stresses in composites is proportional to $\Delta\alpha\Delta T$, where $\Delta\alpha$ is the difference in the expansion coefficients of the two components and ΔT is the amplitude of the thermal cycle (see Chap. 10).

In PMCs and MMCs, the matrix generally has a much higher coefficient of thermal expansion than the fiber. In CMCs, the thermal coefficients of the components may not be that much different but the ceramic materials have very low

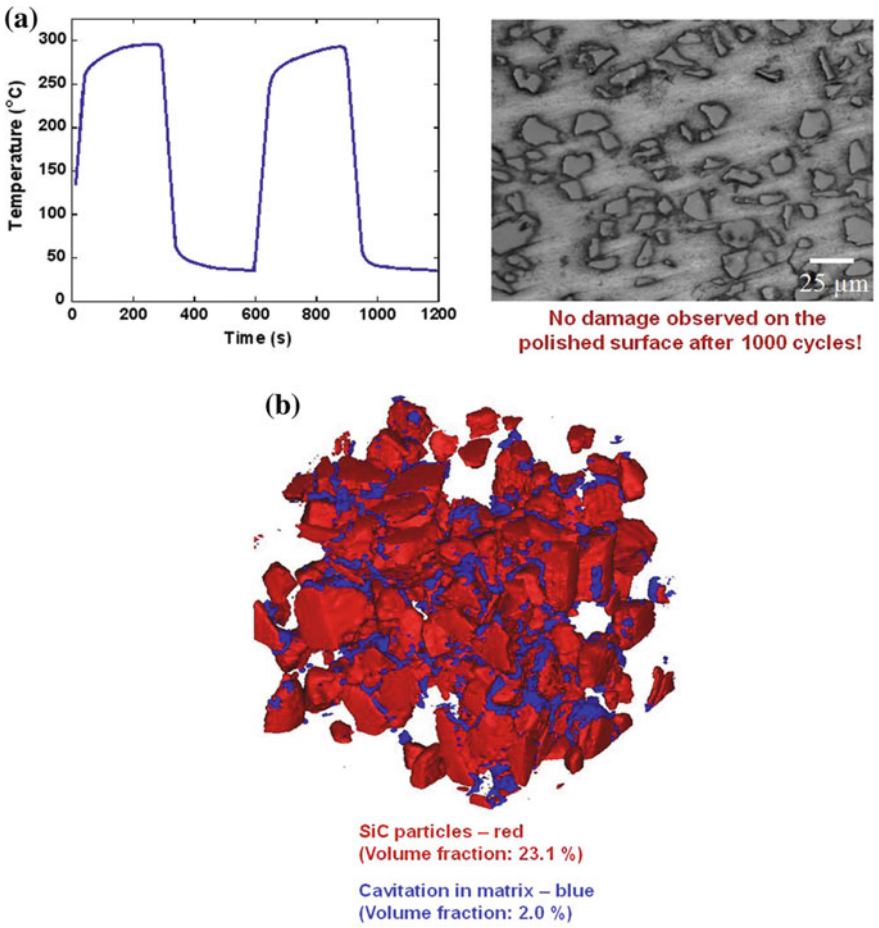

Fig. 13.18 **a** Thermal cycle and the surface of SiC_p/Al composite after thermal cycling. No damage is visible on the surface. **b** Same sample examined by X-ray tomography shows damage in the interior. Blue color shows cavitation, about 2% by volume. The SiC particles are about 25–30 μm in diameter and 20% by vol. [Courtesy of N.C. Chapman and N. Chawla, Arizona State University]

strain-to-failure values, i.e., very low ductility. In general, the matrix has a much higher coefficient of thermal expansion than the fiber. Rather large internal stresses can result when fiber reinforced composites are heated or cooled through a temperature range. When this happens in a repeated manner, we have the phenomenon of *thermal fatigue*, because the cyclic stress is thermal in origin. Thermal fatigue can cause cracking in the brittle polymeric matrix or plastic deformation in a ductile metallic matrix (Chawla 1973a, b, 1975a, b). Cavitation in the matrix and fiber/matrix debonding are other forms of damage observed due to thermal fatigue in composites (Chawla 1973a, b, 1975b; Lee and Chawla 1987; Lee et al. 1988). Xu

et al. (1995) studied the damage evolution as a function of thermal cycles in terms of three metal matrix systems: Al_2O_{3f}/Mg alloy, B_4C_p/6061A1 alloy, and SiC_p/8090A1 alloy. The samples were thermally cycled between room temperature (22 °*C*) and 300 °*C*. The incidence of void formation at the fiber/matrix interface increased with the number of cycles. They observed that loss in stiffness and density could be used as damage parameters. The damage in density and elastic modulus caused by thermal cycling was more severe in the fiber reinforced composite than in the particle reinforced composites.

There has been some work involving the use of X-ray tomography to characterize the internal damage in the form of cavitation in particle reinforced MMCs. This is a very impressive tool, although it must be recognized that such equipment is not a common item, i.e., one has to go to some large scale facility, but it would appear that the effort is worth it. Figure 13.18a show the surface of SiC_p/Al composite after thermal cycling. No damage is visible. However, when examined by X-ray tomography, we observe the damage in the interior of the same sample; see Fig. 13.18b.

In view of the fact that CMCs are likely to find major applications at high temperatures, it is of interest to study their behavior under conditions of isothermal exposure as well as under conditions of thermal cycling. Wetherhold and Zawada (1991) studied the behavior of ceramic-grade Nicalon fiber in an aluminosilicate glass matrix under isothermal and thermal cycling conditions. At 650–700 °*C*, isothermally exposed and thermally cycled samples showed rapid oxidation and loss in strength. Oxidation behavior overshadowed any thermal cycling effect for these test conditions. The embrittlement was attributed to oxygen infiltration from the surface, which destroyed the weak carbon-rich interface in this composite. At 800 °*C*, however, less embrittlement was observed and the fiber toughening effect remained. This decreased embrittlement at higher temperatures was attributed to smoothening of the sample surface by glass flow and slow oxygen infiltration. Boccaccini et al. (1997) studied the cyclic thermal shock behavior of Nicalon fiber reinforced glass matrix composites. The thermal mismatch between the fiber and the matrix in this system was almost nil. A decrease in Young's modulus and a simultaneous increase in internal friction as a function of thermal cycles were observed. The magnitude of internal friction was more sensitive to microstructural damage than Young's modulus. An interesting finding of theirs involved the phenomenon of crack healing when the glass matrix composite was cycled to a temperature above the glass transition temperature of the matrix where the glass flowed and caused crack healing.

It is possible to obtain a measure of the internal stresses generated on subjecting a composite to thermal cycling. Kwei and Chawla (1992) used a computer-controlled servohydraulic thermal fatigue system to perform tests on an alumina fiber/Al–Li alloy composite. Thermal fatigue testing in this case involved subjecting the sample to thermal cycling while its gage length of the sample was kept constant. This constraint resulted in a stress on the sample, which was measured. Such a test provides the stress required to keep the specimen gage length constant as a function of thermal cycles, i.e., a measure of internal stresses generated.

In general, one can reduce the damage in the matrix by choosing a matrix material that has a high yield strength and a large strain-to-failure (i.e., ductility). The eventual fiber/matrix debonding can only be avoided by choosing the components such that the difference in the thermal expansion characteristics of the fiber and the matrix is low.

13.2 Creep

Creep is defined as the time dependent deformation in a material. It becomes important at relatively high temperatures, especially at temperatures greater than 0.4–0.5 T_H, where T_H is the homologous temperature equal to T/T_m, T is the temperature of interest in kelvin, and T_m is the melting point of the material in kelvin. The phenomenon of creep can cause small deformations under a sustained load over a long period of time. In a variety of situations or equipment (e.g., a pressure vessel or a rotating component), such slow deformations can lead to dimensional problems or even failure. Creep sets a limit on the maximum application temperature. In general, this limit increases with the melting point of a material. Without going into the theoretical and modeling details, suffice it to say that the basic governing equation of creep can be written in the following form:

$$\dot{\varepsilon} = A(\sigma/G)^n \exp(-\Delta Q/kT),$$

where $\dot{\varepsilon}$ is the creep strain rate, σ is the applied stress, n is an exponent, G is the shear modulus, ΔQ is the activation energy for creep, k is the Boltzmann's constant, and T is the temperature in kelvin. The stress exponent, n, typically varies between 3 and 7 in the dislocation climb regime and between 1 and 2 when diffusional mechanisms are operating. Pure dislocation creep, grain boundary sliding, vacancy motion in grains and in the grain boundaries, and dislocation can cause creep. The applied stress, grain size, porosity, and impurity content are important variables.

In polymers and PMCs such as Kevlar 49 aramid fiber/epoxy, one can observe creep even at room temperature (Ericksen 1976). At a given temperature, cross-linked thermosets show less creep than thermoplastics. Creep in polymers is the same as defined above, viz., we apply a constant stress and observe the strain as a function of time. There is a related phenomenon called *stress relaxation*, which is also important in polymers. In stress relaxation, we impose a constant strain on the specimen and observe the drop in stress as a function of time. If we substitute a polymeric fiber such as aramid with a more creep-resistant fiber—say alumina, SiC, or even glass—we can make the composite more creep-resistant.

In very simple terms, creep in a PMC or MMC is likely to be dominated by the creep behavior of the matrix. As the matrix deforms in creep, the applied load is transferred to the load-bearing component, viz., fiber. Eventually, the fibers will carry all the load. McLean (1983, 1985) showed that for a composite containing a matrix that follows a power-law creep ($\dot{\varepsilon} = A\sigma^n$), the creep rate in the composite is given by:

$$\dot{\varepsilon}_c = \frac{A\sigma^n \left[1 - \frac{\dot{\varepsilon}}{\dot{\varepsilon}_\infty}\right]^n}{\left[1 + \frac{V_f E_f}{V_m E_m}\right] V_m^n},$$

where $\dot{\varepsilon}_\infty = \left(\sigma_c / L_f E_f\right)$ is the asymptotic creep strain.

A creep curve, strain versus time, for a 25% V_f silicon carbide whisker/2124 aluminum alloy matrix is shown in Figure 13.19 (Lilholt and Taya 1987). The primary, secondary or steady state, and tertiary stages are indicated. The steady-state creep rate as a function of applied stress for the unreinforced silver matrix and tungsten fiber/silver matrix composite at 600 °C are shown in Fig. 13.20 (Kelly and Tyson 1966). The minimum creep rate as a function of the applied stress for Saffil short fiber reinforced aluminum alloys and unreinforced aluminum alloys is shown in Fig. 13.21 (Dlouhy et al. 1993). Note that the creep rate for the composite is lower than that of the control alloy, but the stress exponent or slope of the composite is much higher than that of the unreinforced alloy (Figs. 13.19 and 13.21).

The anomalously high values of the stress exponent, n, and activation energy, Q, have been explained by using the concept of a threshold stress (Webster 1982; Nieh 1984, Nardone and Strife 1987). Nardone and Strife (1987) used the concept of a threshold stress σ_R, for creep deformation in composites. This theory was originally used to explain the high values for Q and n in dispersion strengthened alloys (Davies et al. 1973; Parker and Wilshire 1975; Nardone and Tien 1986, Kerr and Chawla 2004). By introducing the threshold stress, the general steady state creep rate is modified to:

$$\dot{\varepsilon}_{ss} = A\left(\frac{\sigma - \sigma_R}{E}\right)^n \exp\left(\frac{-Q}{RT}\right),$$

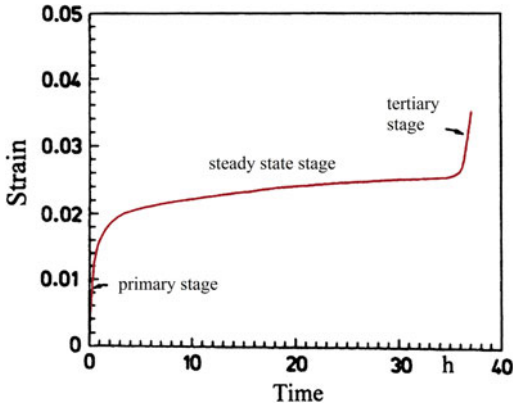

Fig. 13.19 A creep curve, strain versus time, for a 25% V_f silicon carbide whisker/2124 aluminum alloy matrix [after Lilholt and Taya (1987)]

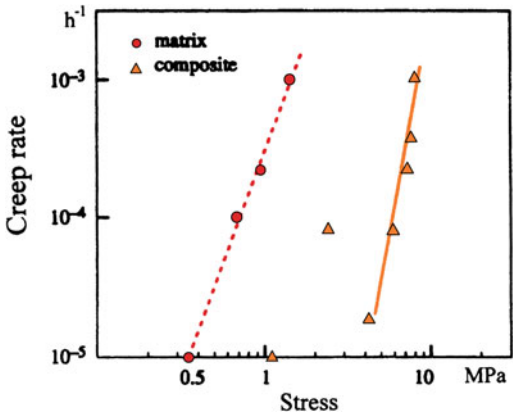

Fig. 13.20 The steady-state creep rate as a function of applied stress for the unreinforced silver matrix and tungsten fiber/silver matrix composite at 600 °*C* [after Kelly and Tyson (1966)]

where A is a constant, E is the elastic modulus of the composite, and Q is the activation energy. The threshold stress in the discontinuously reinforced composite system can be attributed to a variety of sources (Dunand and Derby 1993; Pandey et al. 1992): (1) Orowan bowing between particles, (2) back stress associated with dislocation climb, (3) attractive force between dislocations and particles, resulting from relaxation of the strain field of dislocations at the particle/matrix interface (Artz and Wilkinson 1986).

A threshold stress approach cannot always be used to explain the higher stress exponents observed in MMCs, when compared to the unreinforced alloy. Load transfer to the reinforcement, despite the lower aspect ratios of particles and whiskers, is significant, as the applied load is carried by the high stiffness reinforcement. With increasing load transfer to the reinforcement, the resolved shear stress on dislocations in the matrix may be lowered significantly below that required for Orowan bowing. Dragone and Nix (1992) studied the creep behavior of Al_2O_3 short fiber reinforced Al-5% Mg alloy between 200 and 400 °*C*. They also observed anomalously high values of stress exponent (n $\sim$ 12–15) in the composites, while

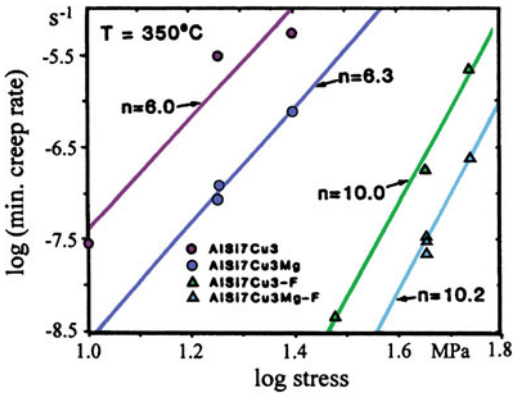

Fig. 13.21 The minimum creep rate as a function of the applied stress for Saffil short fiber reinforced aluminum alloys and unreinforced aluminum alloys. Note that the creep rate for the composite is lower than that of the control alloy, but the stress exponent or slope of the composite is much higher than that of the unreinforced alloy [after Dlouhy et al. 1993]

the unreinforced alloy exhibited much lower, typical values (n $\sim$ 3. The measured activation energy (225 *kJ/mol*) for the composites was also anomalously high. A threshold stress analysis showed that the contribution from Orowan bowing was very small. Using a model consisting of randomly oriented short fibers in the Al alloy matrix, and considering the progressive damage to the fibers during creep, they were able to predict the experimentally observed high values of stress exponent and activation energy. Dragone and Nix (1992) also noted that the arrangement of fibers had a significant effect on the degree of matrix constraint. A decrease in effective stress (increase in matrix constraint) was observed with increasing volume fraction, fiber aspect ratio, and degree of overlap between fibers. The normal and shear stresses at the fiber/matrix interface were also quite large, indicating that void growth or debonding might take place during the creep process.

In some cases, creep behavior of MMCs shows a close correlation between the properties of the matrix and those of the composite (Kelly and Tyson 1966; Kelly and Street 1972a, b; Dragone et al. 1991). In other cases, this is not observed. Creep experiments on an aluminum matrix containing ceramic particles or short fibers show a very high value of stress exponent, $n \sim 20$ and an activation energy for creep, $Q \sim$ 225–400 *kJ/mol*. This is in contrast to the activation energy for self-diffusion in aluminum matrix, $Q \sim 150$ *kJ/mol* (Nieh 1984; Nardone and Strife 1987; Morimoto et al. 1988; Pandey et al. 1992; Dragone and Nix 1992; Dlouhy et al. 1993, Eggler and Dlouhy 1994). Various models have been proposed to rationalize these discrepancies. For a review of these models, the reader is referred to a review article by Dunand and Derby (1993).

In CMCs too, the incorporation of fibers or whiskers can result in improved creep resistance. The creep rate, in four-point bending, of silicon carbide whisker (20 v/o) reinforced alumina was significantly reduced compared to that of the unreinforced alumina (Lin and Becher 1990). For the creep tests done at 1200 and 1300 °*C*, the stress exponent, n in the expression $\dot{\varepsilon} = A(\sigma)^n$, was 2 for the composite, not much different from the value of 2.3 for the unreinforced alumina, indicating that the creep rate controlling process was similar in these two materials at these two temperatures. This improvement was attributed to a retardation of grain boundary sliding by SiC whiskers present at the grain boundaries. The creep curve at 1400 °*C* for the composites showed a marked change in the n value at a stress level of about 125 *MPa* indicating a change in the rate controlling process. A stress exponent value of about 2 is generally thought to be due to grain boundary sliding. The higher stress exponent and the higher creep rate at 1400 °*C* were attributed by the authors to extensive cavitation. There are, however, some differences in the creep behavior of CMCs vis à vis MMCs. Wiederhorn and Hockey (1991) have analyzed the creep behavior of CMCs, both particle and whisker reinforced. In two-phase ceramics, creep rate in tension was faster than in compression for identical stress and temperature conditions. At first sight, this might appear to be due to the ease of cavitation and microcracking during tension rather than in compression because tensile stresses assist cavitation while compressive stresses tend to close the cavities and microcracks. This is not so because Wiederhorn et al.

(1988) observed the asymmetry in creep behavior in CMCs even under conditions where cavitation was absent.

Although continuous ceramic fibers can lead to substantial toughening of ceramics at room temperature, most of these fibers are not sufficiently creep resistant. In fact, creep rates of many fibers are much higher than those of the corresponding monolithic ceramics (Lin and Becher 1990; Routbort et al. 1990; Bender et al. 1991; Pysher et al. 1989). In the case of creep of ceramic matrix composites, one needs to consider the intrinsic creep resistance of the fiber, matrix, and interface region. Oxide fibers are fine grained and generally contain some glassy phase. Nonoxide fibers are also fine grained, multiphasic (with some glassy phase) and susceptible to oxidation (Bender et al. 1991). Nonoxide fiber/nonoxide matrix composites, such as SiC/SiC and SiC/Si_3N_4, generally show good low-temperature strength, but their poor oxidation resistance is a major limitation. Mah et al. (1984) observed that the strength of Nicalon-type SiC fiber was very sensitive to temperature above 1200 °*C* and its environment. Nonoxide fiber/oxide matrix composites or oxide fiber/nonoxide matrix composites, such as carbon/glass, SiC/glass, SiC/alumina, and Al_2O_3/SiC, generally do not possess high oxidation resistance because the permeability constant for the diffusion of oxygen is high, resulting in rapid oxygen permeation through the oxide matrix. Prewo et al. (1986) found that the glass matrix did not prevent the degradation of carbon fiber caused by oxidation. Holmes (1991) observed the formation of a complex glass layer (SiO_2-Y_2O_3-MgO) on the surface of hot pressed SCS-6/Si_3N_4 subjected to creep. The glass layer forms by oxidation of silicon nitride and sintering aids. He also observed that the extent of fiber pullout decreased as the applied stress increased in a creep test. Rather pronounced separation along the fiber/matrix interface was observed after low stress (70 *MPa*) creep.

Creep behavior of laminated ceramic composites has also been studied. The steady state creep rate of monolithic silicon nitride matrix, [0] and [0/90] cross-plied SCS-6/Si_3N_4 composites as a function of applied stress at 1200 °*C* showed that the creep resistance of the composite was superior to that of the monolithic silicon nitride, while the creep resistance of the unidirectional composite was superior to that of the cross-plied composite because the fibers in the 90° direction contribute less to creep resistance than the fibers in the 0° direction (Yang and Chen 1992).

From the preceding discussion of high temperature behavior of nonoxide composites (even when one component is a nonoxide), it would appear that in situations where stability in air at high temperatures is a prime objective, oxide fiber/oxide matrix composites should be most promising because of their inherent stability in air. Some such systems have been investigated (Chawla et al. 1996a, b). Among the oxide fibers, alumina-based and mullite fibers are the most widely used, while glass, glass–ceramics, alumina, and mullite are the most widely used oxide matrices. One can have two categories of oxide/oxide composites: oxide matrix reinforced with uncoated oxide fibers and oxide matrix reinforced with coated oxide fibers. In the first category of oxide/oxide composites, strength and modulus of the composite are generally better than the unreinforced oxide. The toughness characteristics of these composites are not substantially changed because of the strong

chemical bonding at the fiber/matrix interface. Interface tailoring via fiber coating (the second category) is employed extensively in order to achieve the desired properties of the composites.

13.3 Closure

Let us summarize the important points of this chapter. In general, the fatigue resistance of a given material can be enhanced by reinforcing it with continuous fibers or by bonding two different metals judiciously selected to give the desired characteristics. Not unexpectedly, the improvement is greatest when the fibers are aligned parallel to the stress direction. While conventional approaches such as stress versus cycles (S–N) curves or fatigue crack propagation tests under conditions of self-similar crack propagation can be useful for comparative purposes and for obtaining information on the operative failure mechanisms, they do not provide information useful to designers. Fatigue crack propagation under mixed-mode cracking conditions should be analyzed analytically and experimentally. Novel approaches such as that epitomized by the measurement of stiffness reduction of the composite as a function of cycles seem to be quite promising. Because many applications of composites do involve temperature changes, it is important that thermal fatigue characteristics of these composites be evaluated in addition to their mechanical fatigue characteristics.

In regard to creep behavior of composites, introduction of creep resistant reinforcement, especially creep resistant fibers in a matrix that undergoes substantial creep, can result in a composite that is more creep resistant than the unreinforced matrix. Experimental observations show that the stress exponent for the composite in the creep rate versus stress curve is frequently much higher than that for the unreinforced alloy.

Problems

13.1. List some of the possible fatigue crack initiating sites in particle, short fiber, and continuous fiber reinforced composites.

13.2. What factors do you think will be important in the environmental effects on the fatigue behavior of fiber reinforced composites?

13.3. Acoustic emission can be used to monitor damage in carbon fiber/epoxy during fatigue. Under steady loading conditions, the damage is controlled by fiber failure, and one can describe the acoustic emission by

$$\frac{dN}{dt} = \frac{A}{(t+T)^n},$$

where N is the total number of emissions, t is the time, T is a time constant, and A is constant under steady loading conditions. Taking $n = 1$, show that

log t is a linear function of the accumulated counts. (Hint: see M. Fuwa, B. Harris, and A.R. Bunsell, J. *App. Phys*., 8 (1975) 1460.)

13.4. Discuss the effects of frequency of cycling in regard to hysteretic heating in PMCs and CMCs.

13.5. Discuss the fatigue behavior of an aramid fiber reinforced PMC subjected to fatigue at negative and positive stress ratio (R).

13.6. Which one will have a better creep resistance in air: an oxide/oxide composite or a nonoxide/nonoxide system? Explain your answer.

13.7. Diffusional creep involving mass transport becomes important at low stresses and high temperatures. Discuss the importance of reinforcement/matrix interface in creep of a composite under these conditions.

13.8. Assume that the creep of fiber and matrix can be described by a power law and that a well bonded interface exists. Assume also that the strain rate of the composite is given by the volume weighted average of the strain rates of the fiber and matrix. Derive an expression for the strength of such a composite.

13.9. In some composites, residual thermal stress distribution obtained at room temperature on cooling from the high processing temperature results in compressive radial gripping at the interface. Discuss the effect of high temperatures on creep in such a composite.

References

J.E. Allison, J.W. Jones, *Fundamentals of Metal Matrix Composites*, ed. by S. Suresh, A. Mortensen, A. Needleman (Butterworth-Heinemann, Boston, 1993), p. 269

E. Artz, D.S. Wilkinson, Acta Metall. **34**, 1893 (1986)

P.W.R. Beaumont, *Design with Advanced Composite Materials*, ed. by L.N. Phillips (Springer, Berlin, 1989), p. 303

B.A. Bender, J.S. Wallace, D.J. Schrodt, J. Mater. Sci. **12**, 970 (1991)

A.R. Boccaccini, D.H. Pearce, J. Janezak, W. Beier, C.B. Ponton, Mater. Sci. Technol. **13**, 852 (1997)

J.J. Bonnen, C.P. You, J.E. Allison, J.W. Jones, in *Proceedings of the International Conference on Fatigue*, p. 887

A.R. Champion, W.H. Krueger, H.S. Hartman, A.K. Dhingra, in *Proceedings of the 1978 International Conference on Composite Materials (ICCM/2)* (TMS-AIME, New York, 1978), p. 883

K.K. Chawla, Metallography **6**, 155 (1973a)

K.K. Chawla, Philos. Mag. **28**, 401 (1973b)

K.K. Chawla, Fibre Sci. Technol. **8**, 49 (1975)

K.K. Chawla, Grain boundaries in engineering materials, in *Proceedings of the 4th Bolton Landing Conference* (Claitor's Publishing Division, Baton Rouge, 1975b), p. 435

N. Chawla, Metall. Mater. Trans. **28A**, 2423 (1997)

K.K. Chawla, P.K. Liaw, J. Mater. Sci. **14**, 2143 (1979)

K.K. Chawla, H. Schneider, Z.R. Xu, M. Schmücker, in *High Temperature Materials: Design & Processing Considerations, Engineering Foundation Conference*, Davos, Switzerland, 19–24 May 1996 (TMS, Warrendale, 1996), p. 235

N. Chawla, J.W. Holmes, R.A. Lowden, Scr. Mater. **35**, 1411 (1996)

N. Chawla, C. Andres, J.W. Jones, J.E. Allison, Metall. Mater. Trans. **29**, 2843 (1998a)
N. Chawla, Y.K. Tur, J.W. Holmes, J.R. Barber, A. Szweda, J. Am. Ceram. Soc. **81**, 1221 (1998b)
N. Chawla, M. Kerr, K.K. Chawla, J. Am. Ceram. Soc. **88**, 101 (2005)
T. Christman, S. Suresh, Acta Metall. **36**, 1691 (1988a)
T. Christman, S. Suresh, Mater. Sci. Eng. **102A**, 211 (1988b)
C.R. Crowe, D.F. Hasson, in *Proceedings of the 6th International Conference on the Strength of Metals and Alloys* (Pergamon, Oxford, 1982), p. 859
D.L. Davidson, Eng. Fract. Mech. **33**, 965 (1989)
P.W. Davies, G. Nelmes, K.R. Williams, B. Wilshire, Metal. Sci. J. **7**, 87 (1973)
A. Dlouhy, N. Merk, G. Eggeler, Acta Met. Mater. **41**, 3245 (1993)
T.L. Dragone, W.D. Nix, Acta. Metall. Mater. **40**, 2781 (1992)
T.L. Dragone, J.J. Schlautmann, W.D. Nix, Metall. Trans. **22A**, 1029 (1991)
D.C. Dunand, B. Derby, *Fundamentals of Metal Matrix Composites*, ed. by S. Suresh, A. Mortensen, A. Needleman (Butterworth-Heinemann, Boston, 1993), p. 191
G.J. Dvorak, W.S. Johnson, Int. J. Fract. **16**, 585 (1980)
G. Eggeler, A. Dlouhy, *High Performance Composites: Commonalty of Phenomena*, ed. by K.K. Chawla, P.K. Liaw, S.G. Fishman (TMS, Warrendale, 1994), p. 477
R.H. Eriksen, Composites **7**, 189 (1976)
L.B. Godefroid, K.K. Chawla, *3rd Latin American Colloquium on Fatigue and Fracture of Materials*, Rio de Janeiro, Brazil (1988)
A. Goel, K.K. Chawla, U.K. Vaidya, N. Chawla, M. Koopman, Mater. Charact. **60**, 537 (2009)
J.P. Gomez, F.W. Wawner, Personal communication (1988)
M. Gouda, K.M. Prewo, A.J. McEvily, *Fatigue of Fibrous Composite Materials* (ASTM STP 723, American Society of Testing and Materials, Philadelphia, 1981), p. 101
J.E. Hack, R.A. Page, G.R. Leverant, Metall. Trans. A **15A**, 1389 (1987)
H.T. Hahn, R.Y. Kim, J. Compos. Mater. **10**, 156 (1976)
H.T. Hahn, L. Lorenzo, *Advances in Fracture Research, ICF6*, vol. 1 (Pergamon Press, Oxford, 1984), p. 549
L.X. Han, S. Suresh, J. Am. Ceram. Soc. **72**, 1233 (1989)
H.E. Helms, P.J. Haley, *Ceramic Materials and Components for Engines*, ed. by V.J. Tennery (American Ceramic Society, Westerville, 1989), p. 1347
A.L. Highsmith, K.L. Reifsnider, *Damage in Composite Materials* (ASTM STP 775, American Society for Testing and Materials, Philadelphia, 1982), p. 103
J.W. Holmes, J. Mater. Sci. **26**, 1808 (1991)
P. Hruby, S.S. Singh, J.J. Williams, X. Xiao, F. De Carlo, N. Chawla, Int. J. Fatigue **68**, 136 (2014)
Y. Izuka, T. Norita, T. Nishimura, K. Fujisawa, Carbon Fibers (Noyes Publications, Park Ridge, 1986), p. 14
W.S. Johnson, Mechanical and physical behavior of metallic and ceramic composites, in *9th Risø International Symposium on Metallurgy and Materials Science*, Risø National Laboratory, Roskilde, Denmark (1988), p. 403
W.S. Johnson, R.R. Wallis, in *Composite Materials: Fatigue and Fracture*, ASTM STP 907, ASTM, Philadelphia (1986), p. 161
P.G. Karandikar, T.-W. Chou, Ceram. Eng. Sci. Proc. **13**, 882 (1992)
A. Kelly, W.R. Tyson, J. Mech. Phys. Solids **14**, 177 (1966)
A. Kelly, K.N. Street, Proc. R Soc. Lond. A **328**, 267 (1972a)
A. Kelly, K.N. Street, Proc. R Soc. Lond. A **328**, 283 (1972b)
M. Kerr, N. Chawla, Acta Mater. **52**, 4527 (2004)
S. Kumai, J.F. Knott, Mater. Sci. Eng. **A146**, 317 (1991)
S. Kumai, J.E. King, J.F. Knott, Fatigue Fract. Eng. Mater. Struct. **13**, 511 (1990)
L.K. Kwei, K.K. Chawla, J. Mater. Sci. **27**, 1101 (1992)
R.E. Lavengood, L.E. Gulbransen, Polym. Eng. Sci. **9**, 365 (1969)
C.S. Lee, K.K. Chawla, in *Proceedings of the Industry-University Advanced Materials Conference* (TMS-AIME, Warrendale, PA, 1987), p. 289

C.S. Lee, K.K. Chawla, J.M. Rigsbee, M. Pfeifer, *Cast Reinforced Metal Composites*. (ASM International, Metals Park 1988), p. 301
M. Levin, B. Karlsson, J. Wasén, *Fundamental Relationships Between Microstructures and Mechanical Properties of Metal Matrix Composites* (TMS, Warrendale, 1989), p. 421
H. Lilholt, M. Taya, in *Proceedings of ICCM/6* (Elsevier, Amsterdam, 1987), pp. 2.234–2.244
H.-T. Lin, P.F. Becher, J. Am. Ceram. Soc. **73**, 1378 (1990)
W.A. Logsdon, P.K. Liaw, Eng. Fract. Mech. **24**, 737 (1986)
T. Mah, N.L. Hecht, D.E. McCullum, J.R. Hoenigman, H.M. Kim, A.P. Katz, H.A. Lipsitt, J. Mater. Sci. **19**, 1191 (1984)
J.F. Mandell, F.J. Mcgarry, D.D. Huang, C.G. Li, Polym. Compos. **4**, 32 (1983)
R.F. McCartney, R.C. Richard, P.S. Trozzo, Trans. ASM **60**, 384 (1967)
M.A. McGuire, B. Harris, J. Phys. D Appl. Phys. **7**, 1788 (1974)
M. McLean, *Directionally Solidified Materials for High Temperature Service* (The Metals Society, London, 1983)
M. McLean, in *Proceedings of 5th International Conference on Composite Materials (ICCM/V)* (TMS-AIME, Warrendale, 1985), p. 639
T. Morimoto, T. Yamaoka, H. Lilholt, M. Taya, J. Eng. Mater. Tech. Trans. ASME **110**, 70 (1988)
V.C. Nardone, J.K. Tien, Scr. Mater. **20**, 797 (1986)
V.C. Nardone, J.R. Strife, Metall. Trans. **18A**, 109 (1987)
T.G. Nieh, Metall. Trans. **15A**, 139 (1984)
T.K. O'Brien, Interlaminar fracture of composites, NASA TM-85768 (1984)
T.K. O'Brien, K.L. Reifsnider, J. Compos. Mater. **15**, 55 (1981)
S.L. Ogin, P.A. Smith, P.W.R. Beaumont, Compos. Sci. Tech. **22**, 23 (1985)
M.J. Owens, R. Dukes, J. Strain. Anal. **2**, 272 (1967)
M.J. Owens, T.R. Smith, R. Dukes, Plast. Polym. **37**, 227 (1969)
R.A. Page, J.E. Hack, R. Sherman, G.R. Leverant, Met. Trans. A **15A**, 1397 (1987)
A.B. Pandey, R.S. Mishra, Y.R. Mahajan, Acta Metall. Mater. **40**, 2045 (1992)
P.C. Paris, F. Erdogan, J. Basic Eng. Trans. ASME **85**, 528 (1963)
J.D. Parker, B. Wilshire, Metal Sci J **9**, 248 (1975)
N.J. Pfeiffer, J.A. Alic, J. Eng. Mater. Tech. **100**, 32 (1978)
D.C. Phillips, *Handbook of Composites*, vol. 4 (North-Holland, Amsterdam, 1983), p. 472
K.M. Prewo, J.J. Brennan, G.K. Layden, Am. Ceram. Soc. Bull. **65**, 305 (1986)
L. Pruitt, S. Suresh, J. Mater. Sci. Lett. 1356 (1992)
D.J. Pysher, K.C. Goretta, R.S. Hodder Jr., R.E. Tressler, J. Am. Ceram. Soc. **72**, 284 (1989)
V. Ramakrishnan, N. Jayaraman, J. Mater. Sci. **28**, 5580 (1993)
K.L. Reifsnider, E.G. Henneke, W.W. Stinchcomb, J.C. Duke, *Mechanics of Composite Materials* (Pergamon Press, New York, 1981), p. 399
P.K. Rohatgi, R. Asthana, S.N. Tewari, C.S. Narendranath, High Performance Composites: Commonalty of Phenomena, ed. by K.K.Chawla, P.K. Liaw, S.G. Fishman (TMS, Warrendale, 1994), p. 93
J.L. Routbort, K.C. Goretta, A. Dominguez-Rodriguez, A.R. de Arrellano-Lopez, J. Hard. Mater. **1**, 221 (1990)
C.R. Saff, D.M. Harmon, W.S. Johnson, J. Met. **40**, 58 (1988)
J.K. Shang, W. Yu, R.O. Ritchie, Mater. Sci. Eng. A **102**, 181 (1988)
S. Singh, N. Chawla, *Handbook of Mechanics and Materials* (2018)
B.F. Sørensen, J.W. Holmes, Scr. Met. et Mater. **32**, 1393 (1995)
N.S. Stoloff, *Advances in Composite Materials* (Applied Science Publications, London, 1987), p. 247
S. Suresh, J. Hard Mater. **2**, 29 (1991)
S. Suresh, L.X. Han, J.J. Petrovic, J. Am. Ceram. Soc. **71**, cl58–c161 (1988)
R. Talreja, *Fatigue of Composite Materials* (Technical University of Denmark, Lyngby, 1985a)
L.G. Taylor, D.A. Ryder, Composites **1**, 27 (1976)
Z. Wang, C. Laird, Z. Hashin, B.W. Rosen, C.F. Yen, J. Mater. Sci. **26**, 5335 (1991)
D. Webster, Metall. Mater. Trans. **13A**, 1511 (1982)

R.C. Wetherhold, L.P. Zawada, Fractography of glasses and ceramics, in *Ceramic Transactions* ed. by V.D. Frechete, J.R. Varner, vol. 17 (American Ceramic Society, Westerville, 1991), p. 391
S.M. Wiederhorn, B.J. Hockey, Ceram Int **17**, 243 (1991)
S.M. Wiederhorn, W. Liu, D.F. Carroll, T.-J. Chuang, J. Am. Ceram. Soc. **12**, 602 (1988)
D.R. Williams, M.E. Fine, in *Proceedings of the Fifth International Conference on Composite Materials (ICCM/V)* (TMS-AIME, Warrendale, 1985), p. 639
D.R. Williams, M.E. Fine, in *Proceedings of the 6th International Conference on Composite Materials (ICCM/VI)*, vol 2 (Elsevier Applied Science, London, 1987), p. 113
Z.R. Xu, K.K. Chawla, A. Wolfenden, A. Neuman, G.M. Liggett, N. Chawla, Mater. Sci. Eng. A **A203**, 75 (1995)
J.-M. Yang, S.T. Chen, Adv. Compos. Lett. **1**, 27 (1992)

Suggested Reading

J. Lamon, Creep of ceramic matrix composites, Int. Mater. Rev. **65** (2020)
R. Talreja, *Fatigue of Composite Materials* (Technical University of Denmark, Lyngby, 1985b)
R. Talreja (ed.), *Damage Mechanics of Composite Materials* (Elsevier, Amsterdam, 1994)

Chapter 14
Designing with Composites

Understanding how to design with composites, especially fiber reinforced composites, is very important because composite materials do not represent just another new class of materials. Although there have been, over the years, ongoing efforts by researchers to improve the properties of different materials such as new alloys, composite materials, especially fiber reinforced composites, represent a rather radical departure. Schier and Juergens (1983) analyzed the design impact of composites on fighter aircraft. The authors echoed the sentiments of many researchers and engineers in making the following statement: "Composites have introduced an extraordinary fluidity to design engineering, in effect forcing the designer-analyst to create a different material for each application…" A single component made of a laminated composite can have areas of distinctively different mechanical properties. For example, the wing-skin of an F/A-18 airplane is made up of 134 plies. Each ply has a specific fiber orientation and geometric shape. Computer graphics allow us to define each ply "in place" as well as its relationship to other plies. The reader can easily appreciate that storage and transmission of such engineering data via computer makes for easy communication between design engineers and manufacturing engineers. In this chapter, we discuss some of the salient points in regard to this important subject of designing with composites.

14.1 General Philosophy

We will make a few general philosophical points about designing with composites before going into the specifics. The basic philosophy behind the composite materials is that, in principle, one can tailor-make a material for any desired function. Thus, one should start with a function, not a material. A suitable composite material, say to meet some mechanical and/or thermal loading conditions, can then be made. An important corollary that follows is that one must exploit the anisotropy that is invariably present in fiber reinforced composites. Before discussing some

K. K. Chawla, *Composite Materials*,
https://doi.org/10.1007/978-3-030-28983-6_14

specific design procedures, we review some of the advantages and fundamental characteristics of fiber reinforced composites that make them so different from conventional monolithic materials.

14.2 Advantages of Composites in Structural Design

The main advantages of using composites in structural design are as follows.

14.2.1 Flexibility

- Ply lay-up allows for variations in the local detail design.
- Ply orientation can be varied to carry combinations of axial and shear loads.

14.2.2 Simplicity

- Large one-piece structures can be made with attendant reductions in the number of components.
- Selective reinforcement can be used.

14.2.3 Efficiency

- High specific properties, i.e., enhanced properties on a per-unit-weight basis.
- Savings in materials and energy.

14.2.4 Longevity

- Generally, properly designed composites show better fatigue and creep behavior than their monolithic counterparts.

14.3 Some Fundamental Characteristics of Fiber Reinforced Composites

Composite materials come with some fundamental characteristics that are quite different from conventional materials. This is especially true of fiber reinforced composites. Among these important characteristics are the following:

- *Heterogeneity*: Composite materials, by definition, are heterogenous. There is a large area of interface and the in situ properties of the components are different from those determined in isolation.
- *Anisotropy*: Composites in general, and fiber reinforced composites in particular, are anisotropic. For example, as we saw in Chap. 10, the modulus and strength are very sensitive functions of fiber orientation.
- *Coupling Phenomena*: Coupling between different loading modes, such as tension–shear, is not observed in conventional isotropic materials. We saw in Chap. 11 that in fiber reinforced composites such coupling phenomena can be very important. These coupling phenomena make designing with composites more complex, as we shall see in Sect. 14.4.
- *Fracture Behavior*: Monolithic, conventional isotropic materials show what is called a *self-similar crack propagation*. This means that the damage mode involves the propagation of a single dominant crack; one can then measure the damage in terms of the crack length. In composites, one has a multiplicity of fracture modes. A fiber reinforced composite, especially in the laminated form, can sustain a variety of subcritical damage (cracking of matrix, fiber/matrix decohesion, fiber fracture, ply cracking, delamination). For example, in a [0/90] laminate, the 90° ply is likely to be weaker than the 0° ply, so it will crack first. Such cracking of a ply, will result in a relaxation of stress in that ply, and with continued loading, no further cracking occurs in that ply. Ply cracking could involve cracking in the matrix or along the fiber/matrix interface. Other damage accumulating mechanisms include the growth of existing cracks into interfaces leading to ply delamination.

14.4 Design Procedures with Composites

It is worth reemphasizing that composite materials, particularly fiber reinforced composite materials, are not just another kind of new material. When designing with composites, one must take into account their special characteristics delineated in the preceding section. First, composite materials are inherently heterogeneous at a microstructural level, consisting as they do of two components that have different elastic moduli, different strengths, different thermal expansion coefficients, and so on. We saw in the micromechanical analysis (Chap. 10) that the structural and physical properties of composites are functions of (a) component characteristics,

(b) geometric arrangement of one component in the other, and (c) interface characteristics. Even after selecting the two basic components, one can obtain a range of properties by manipulating the items (b) and (c). Second, the conventional monolithic materials are generally quite isotropic; that is, their properties do not show any marked preference for any particular direction, whereas fiber reinforced composites are highly anisotropic because of their fibrous nature. The analysis and design of composites should take into account this strong directionality of properties, or, rather, this anisotropy of fiber reinforced composites must be exploited to the fullest advantage by the designer. The reader is referred to some figures in previous chapters: Fig. 11.4 shows the marked influence of fiber orientation on the different elastic moduli of a composite. In a similar manner, Fig. 12.14 shows the acute dependence of the composite strength on fiber orientation. Figure 10.7 shows the marked influence of fiber orientation on the coefficient of thermal expansion of a fiber reinforced composite.

In laminated composites, the ply stacking sequence can affect the properties of a composite. Recall Fig. 8.5, which showed tensile creep strain at ambient temperature as a function of time for two different stacking sequences (Sturgeon 1978). At a given stress level, the laminate with carbon fibers at ±45° showed more creep strain than one containing plies at 0°/90°/±45°. The reason for this was that in the ±45° sequence, the epoxy matrix had creep strain contributions from (a) tension in the loading direction, (b) shear in the ±45° directions, and (c) rotation of the plies in a scissor-like action. As we saw in Chap. 11, the 0° and 90° plies do not contribute to the scissor-like rotation due to the absence of tension–shear coupling in these specially orthotropic laminate. Thus, the addition of 0° and 90° plies reduced the matrix shear deformation. Thus, for creep resistance, the 0°/90°/±45° sequence is to be preferred over the ±45° sequence.

For conventional materials, the designer needs only to consult a handbook or manual to obtain one unambiguous value of, say, modulus or any other property. For fiber reinforced composite laminates, however, the designer has to consult what are called *performance charts* or *carpet plots* representing a particular property of a given composite system. Such plots, sometimes also referred to as *parametric plots*, are made for fiber reinforced plies at 0°, ±45°, and 90°. Figure 14.1 shows such plots for Young's modulus and the tensile strength, both in the longitudinal direction, for a 65% V_f carbon fiber/epoxy composite having a 0°/±45°/90° ply sequence (Kliger 1979). A conventional material, say aluminum, would be represented by just one point on such graphs. The important and distinctive point is that, depending on the components, their relative amounts, and the ply stacking sequence, we can obtain a range of properties in fiber reinforced composite laminates. In other words, one can tailor-make a composite material as per the final objective. Figure 14.1 provides a good example of the versatility and flexibility of laminates. Say our material specifications require, for an application, a material that is stronger in the x direction ($\sigma_x = 500\ MPa$) and a stiffness in the y direction equal to that of aluminum ($E = 70\ GPa$). We can then pick a material combination that gives us a composite with these characteristics. Using Fig. 14.1a, b, we can choose the following ply distribution:

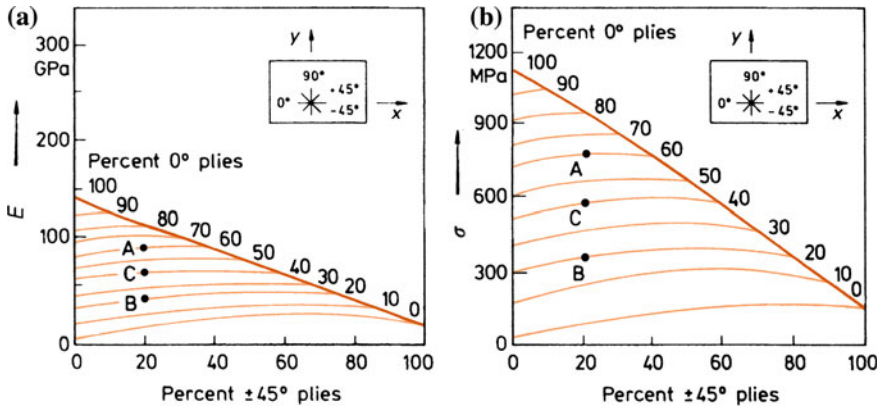

Fig. 14.1 Carpet plots for 65% V_f carbon/epoxy with a 0°/±45°/90° stacking sequence: **a** Young's modulus, **b** tensile strength (from Kliger 1979, used with permission)

60% at 0°,
20% at 90°, and
20% at ±45°.

Point A has a $\sigma_x = 725$ *MPa* and an $E_x = 90$ *GPa*. If we interchange the x and y coordinates and the amounts of the 0° and 90° plies, we get point B, which corresponds to a $\sigma_y = 340$ *MPa* and an $E_y = 40$ *GPa*. Thus, σ_x is now higher than required and E_y is too low. We now take some material from 0° and move it to 90°. Consider the following ply distribution:

40% at 0°,
40% at 90°, and
20% at ±45°.

This is represented by point C, having $\sigma_x = 580$ *MPa* and $E_y = 70$ *GPa*. Reversing the x and y coordinates again gives point C with $\sigma_x = 580$ *MPa* and $E_y = 70$ *GPa*. Point C then meets our initial specifications.

Stacking sequences other than [0°/±45°/90°] can also satisfy one's requirements. A [0°/±30°/±60°/90°] arrangement gives quasi-isotropic properties in the plane. Carpet plots, however, work for three-ply combinations and the sequence [0°/±45°/90°] has some other advantages as described later. It should be pointed out that carpet plots for strengths in compression and shear, shear modulus, and thermal expansion coefficients can also be made. It is instructive to compare the expansion behavior of monolithic and fiber reinforced composites. Figure 14.2 compares the thermal expansion coefficients of some metals and composites as a function of fiber orientation (Fujimoto and Noton 1973). It should be recalled that cubic materials are isotropic in thermal properties, even in single crystal form. Noncubic monolithic materials in a polycrystalline form, with randomly distributed grains, will also be practically isotropic in thermal properties. Thus, titanium, steel,

and aluminum are each represented by a single point on this figure. Not unexpectedly, fiber reinforced composites such as boron/epoxy and carbon/epoxy show highly anisotropic thermal expansion behavior. Both aramid and carbon fibers have negative expansion coefficients parallel to the fiber axis. One can exploit such anisotropy quite usefully to make components that show well-controlled expansion characteristics. Although aerospace applications of composite materials get much attention, one should appreciate the fact that composites, in one form or another, have been in use in the electrical and electronic industry for quite a long time. These applications range from cables to printed circuit boards. There are many applications of composites in the electronic packaging industry (Seraphim et al. 1986). An interesting example is that of the leadless chip carrier (LCC) that allows electronic designers to pack more electrical connections into less space than is possible with conventional flat packs or dual inline packages, which involve E glass/epoxy resin laminates. Glass/epoxy laminate, however, is not very suitable for LCC as a substrate because it expands and contracts much more than the alumina chip carrier (the coefficient of expansion, α, of E glass/epoxy can vary in the range of 14–17 $\times$ 10^{-6} K^{-1}, while that of alumina is $\sim 8 \times 10^{-6}$ K^{-1}). Aramid fiber (40–50 *v/o*)/epoxy composite provides the desired matching expansion characteristics with those of the alumina chip carrier. Thus, the thermal fatigue problem associated with the E glass/epoxy composites and the ceramic chip carrier is avoided. It should be pointed out that, in general, thermal expansion of particulate composites, assuming an isotropic distribution of particles in the matrix, will be more or less isotropic.

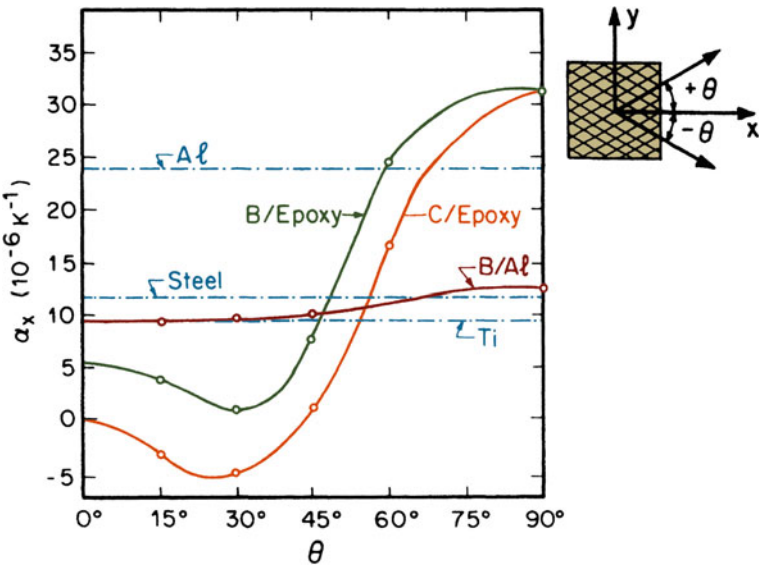

Fig. 14.2 Variation of thermal expansion coefficients with orientation θ (from Fujimoto and Noton 1973, used with permission)

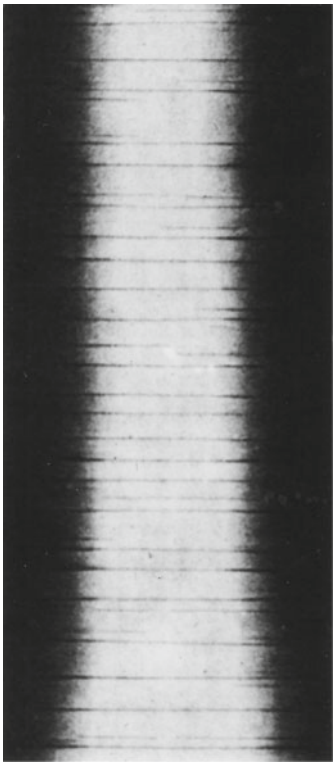

Fig. 14.3 Delaminations, as observed by contrast enhanced X-ray radiography in a $[0°/\pm45°/90°]_s$ carbon/epoxy laminate upon fatigue testing [from Bergmann 1985, used with permission]

We saw in Chap. 11 that laminated composites show coupling phenomena: tension–shear, tension–bending, and bending–twisting. We also saw in Chap. 10 that certain special ply sequences can simplify the analyses. Thus, using a balanced arrangement (for every $+\theta$ ply there is a $-\theta$ ply in the laminate), we can eliminate shear coupling. In such an arrangement, the shear distortion of one layer is compensated by an equal and opposite shear distortion of the other layer. Yet another simplifying arrangement consists of stacking the plies in a symmetric manner with respect to the laminate midplane. Such a symmetric laminate gives $[B_{ij}]$ identically zero and thus eliminates stretching–bending and bending–torsion coupling. The phenomenon of edge effects, described in Sect. 11.7, should also be taken into account while arriving at a ply stacking sequence. Because of the edge effects, individual layers of different fiber orientation deform differently under tensile stress giving rise to out-of-plane tensile, compressive, shear and/or bending stresses in the neighborhood of the free edges. An arrangement that gives rise to compressive stresses in the thickness direction in the vicinity of the edges is to be preferred over one that gives rise to tensile stresses. Tensile stresses in the thickness direction near a free edge would tend to cause undesirable delamination in the composite. As an example, we show in Fig. 14.3 delaminations as observed by contrast enhanced X-ray radiography, in a $[0°/\pm45°/90°]_s$ carbon/epoxy laminate upon fatigue testing

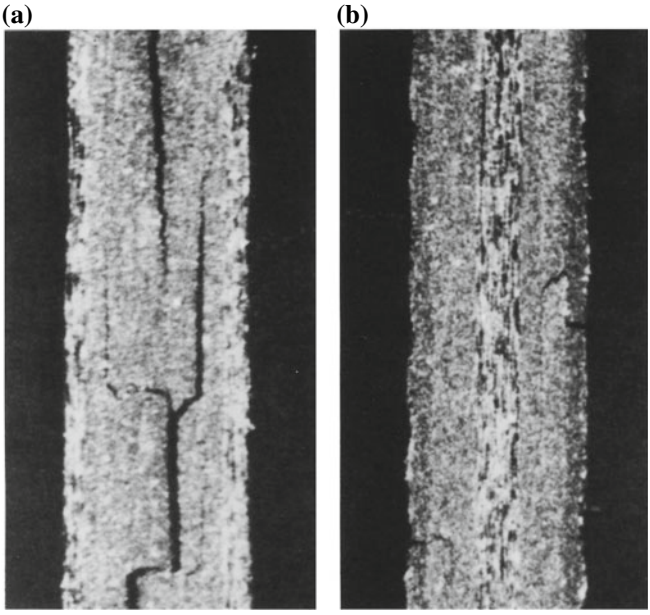

Fig. 14.4 Comparison of crack patterns at the free edges of a carbon/epoxy laminate: **a** $[0°/\pm45°/90°]_s$ and **b** $[90°/\pm45°/0°]_s$. Note the greater severity of edge delaminations in **a** than in **b** [from Bergmann 1985, used with permission]

(Bergmann 1985). The delaminations proceed from both sides toward the specimen center. Mere stacking choice of the plies can make a big difference. This is shown in Fig. 14.4. The laminate with the sequence $[90°/\pm45°/0°]_s$ showed relatively less damage than the laminate with the sequence $[0°/\pm45°/90°]_s$. Figure 14.4 compares the crack patterns at the free edges of $[0°/\pm45°/90°]_s$ and $[90°/\pm45°/0°]_s$ laminates shortly before failure. Note the greater degree of delaminations in $[0°/\pm45°/90°]_s$ than in $[90°/\pm45°/0°]_s$. The reason for this different behavior of these laminates, identical in all respects except the stacking sequence, is due to the difference in the state of stress near the free edges. Finite element calculations showed (Bergmann 1985) that in the $[0°/\pm45°/90°]_s$ sequence, there were large interlaminar tensile stresses in the thickness direction while in the $[90°/\pm45°/0°]_s$ sequence, there were mostly compressive interlaminar stresses.

A little reflection will convince the reader that computer simulations involving complex finite element analyses can be used extensively in the design and analyses of laminated fiber composites. In view of the rather tedious matrix calculations involved, this should not be surprising at all. Computer codes can be very cost-effective in the analysis and design of fiber composite structures. Most codes specify, among other things, the interply layers, laminate failure stresses, laminate requirements at critical locations in the composite, etc. Many such codes are available commercially. An example of commercially available computer code is

the FiberSIM suite of software tools that converts a CAD (computer-aided design) system into a composite design and manufacturing environment. Among its features are:

- Composite engineering environment: This allows engineers to work in their CAD environment with objects such as plies, cores, and tool surfaces. Forms and menus are used to enter and manage the geometry and other data required to define a composite part.
- Flat pattern/producibility: This module alerts the engineer to manufacturing problems such as wrinkling, bridging, and material width limitations. It also generates net flat patterns for woven and unidirectional complex curvature plies.
- Laminate properties: Exact fiber orientations are obtained for use in generating properties of a laminated composite.

14.5 Hybrid Composite Systems

An extra degree of flexibility in fiber composites can be obtained by making what are called *hybrid composites*, wherein one uses more than one type of fiber; see Fig. 14.5. Cost-performance effectiveness can be increased by judiciously using different reinforcement types and selectively placing them to get the highest strength in highly stressed locations and directions. For example, in a hybrid composite laminate, the cost can be minimized by reducing the carbon fiber content, while the performance is maximized by "optimal placement and orientation of the fiber." Figure 14.6 shows the increases in specific flexural modulus (curve *A*) and specific tensile modulus (curve *B*) with weight % of carbon fiber in a hybrid composite (Riggs 1985). Figure 14.7 shows the changes in flexural fatigue behavior as we go from 100% unidirectional carbon fibers in polyester (curve *A*) to unidirectional carbon faces over chopped glass core (curve *B*) to 100% chopped glass in polyester resin (curve *C*) (Riggs 1985); keeping the fiber volume fraction constant.

An extension of this concept is the so called fiber metal laminates such as GLARE, an acronym for glassfiber/epoxy and aluminum laminates. GLARE consists of alternating layers of aluminum sheets and glass fiber reinforced epoxy composite. Such composites are used in the fuselage of the superjumbo aircraft of Airbus A380. They show high strength, excellent fatigue, and fracture resistance,

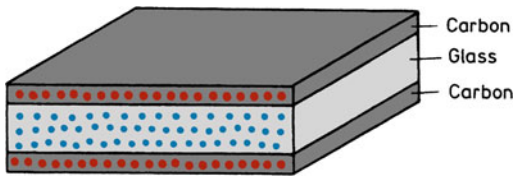

Fig. 14.5 Schematic of a hybrid laminate composite containing carbon and glass fibers

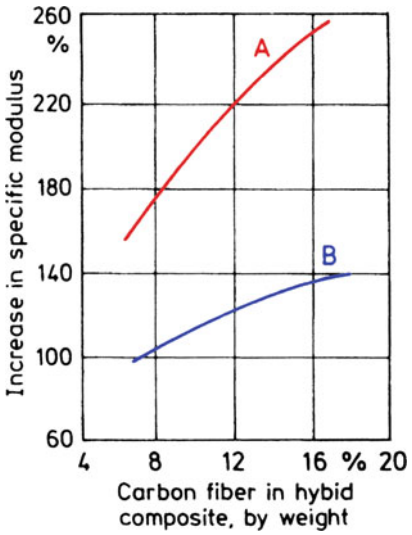

Fig. 14.6 Change in specific flexural modulus and specific tensile modulus with weight % carbon fibers [from Riggs 1985, reprinted by permission]. *A* = specific flexural modulus; *B* = specific tensile modulus

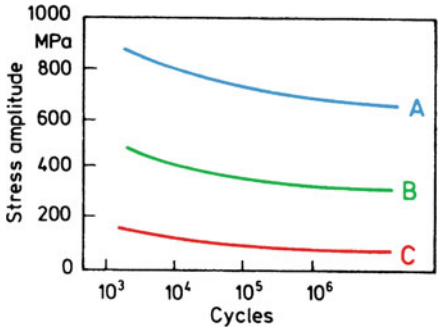

Fig. 14.7 Flexural fatigue behavior of 100% carbon fiber composite (curve *A*), carbon fiber facings with chopped glass fiber core (curve *B*), and 100% chopped glass fiber composite (curve *C*) [from Riggs 1985, reprinted by permission]

combined with the advantages of metal construction such as formability, machinability, toughness, and impact resistance. We discuss this in Chap. 15.

Problems

14.1. Following are the data for a 60% V_f, unidirectionally reinforced, carbon fiber/epoxy composite:

$$\begin{aligned}\text{Longitudinal tensile strength} &= 1200\,MPa\\ \text{Longitudinal compressive strength} &= 1000\,MPa\\ \text{Transverse tensile strength} &= 50\,MPa\\ \text{Transverse compressive strength} &= 250\,MPa.\end{aligned}$$

Calculate F_{11}, F_{22}, F_{66}, F_1, F_2, and F_{12}^*. Take $F_{12}^* = -0.5$. Compute the focal points plot the failure envelope for this composite.

14.2. For a carbon/epoxy composite, the strength parameters are as follows:

$$F_{11}(GPa)^{-2} = 0.45$$
$$F_{22}(GPa)^{-2} = 101$$
$$F_{12}(GPa)^{-2} = -3.4$$
$$F_{66}(GPa)^{-2} = 215$$
$$F_1(GPa)^{-1} = 0$$
$$F_2(GPa)^{-1} = 21.$$

Compute the off-axis uniaxial strengths of this composite for different θ and obtain a plot of σ_x versus θ.

References

H. Bergmann, *Carbon Fibres and Their Composites* (Springer, Berlin, 1985), p. 184

W.T. Fujimoto, B.R. Noton, in *Proceedings of the 6th St. Louis Symposium on Composite Material Engineering and Design* (American Society for Metals, Metals Park, OH, 1973), p. 335

H.S. Kliger, Mach. Des. **51**, 150 (1979)

J.P. Riggs, *Encyclopedia of Polymer Science and Engineering*, vol. 2, 2nd edn (Wiley, New York, 1985), p. 640

J.F. Schier, R.J. Juergens. Astronaut. Aeronaut. **44**, (1983)

D.P. Seraphim, D.E. Barr, W.T. Chen, G.P. Schmitt, *Advanced Thermoset Composites* (Van Nostrand Reinhold, New York, 1986), p. 110

J.B. Sturgeon, Creep of engineering materials. J. Strain Anal. Monogr. 175 (1978)

Suggested Reading

C.C. Chamis (ed.), *Structural Design and Analysis, Parts I and II* (Academic Press, New York, 1974)

I.M. Daniel, O. Ishai, *Engineering Mechanics of Composite Materials*, 2nd edn. (Oxford University Press, New York, 2005)

G. Lubin (ed.), *Handbook of Composites* (Van Nostrand Reinhold, New York, 1982)

S.R. Swanson, *Introduction to Design and Analysis with Advanced Composite Materials* (Prentice Hall, Upper Saddle River, NJ, 1997)

Chapter 15
Nonconventional Composites

We devote this chapter to some nonconventional composites. Nonconventional composites include nanocomposites (polymer, metal, and ceramic matrix), self-healing composites, self-reinforced composites, biocomposites, and laminates made of bidimensional layers. Important as these topics are, we provide below a brief description of these topics.

15.1 Nanocomposites

Nanocomposites are composites that have one component that has at least one dimension in the *nm* range (i.e., equal or less than 100 *nm*); generally, it will be the reinforcement phase which may take the form of nanotubes, nanofibers, or nanoparticles. Although nanocomposites can have a polymeric, metallic, or ceramic matrix, a polymer matrix is more common (Barrera 2000; Barrera et al. 2005; Shofner et al. 2003, 2006). Metal matrix nanocomposites can have excellent strength and wear (see, for example, Fukuda et al. 2011). However, we need to devise processing techniques to make these materials in bulk, in a cost-effective manner, with no voids or other defects.

15.1.1 Polymer Clay Nanocomposites

A special type of nanocomposite, called nanoclay composites, has made good progress into commercial production. Polymer matrix reinforced with nanoclay particles have become commercially viable (Ajayan et al. 2003; Koo 2006; Lee et al. 2005; Okada and Usuki 2006; Paul and Robeson 2008). Most of the clay additives are in the form of platelets that have been organically treated. They are commonly called nanoclays because the thickness of the clay additives is in the

K. K. Chawla, *Composite Materials*,
https://doi.org/10.1007/978-3-030-28983-6_15

nanometer range. Chemically, these clays are layered magnesium aluminum silicates. Their dimensions are as follows: thickness of about 1 *nm* and length or width in the range of 70–150 *nm*, which would give an aspect ratio of over 100. Surface modification of the clays makes it possible to disperse them in thermoplastic materials. These nanoclay particles can enhance the modulus (function of amount of particles added) while lowering the coefficient of thermal expansion.

The work in this area was pioneered by Toyota researchers in 1990 when they first used clay/nylon 6 composites for timing belt covers. Some of the earliest commercial successes can be credited to Toyota, GM, and Ford. Major automakers have started making use of nanocomposites in their autos. General Motors Corp., in particular, in 2001, used a thermoplastic olefin (TPO) step-assist for the 2002 GMC Astro/Safari van that was enhanced with a clay nanomaterial. GM also used clay nanocomposites in the Chevrolet Impala. These products are made of thermoplastic polyolefin–clay nanocomposite. The nanocomposites are lighter, stiffer, and cost-effective compared to the conventional polymeric materials. The cost-effectiveness part is important because automobile industry is loath to use anything that is not cost-effective, the exception being sports cars. In addition, the crash requirement in autos is very important. This characteristic has to do with the energy absorbed in the impact, which in the case of autos depends more on strain than on stress.

In regard to nanoclay composites, mention should be made of Southern Clay Products Co. Cloisite® and Nanofil® are commercially available clay additives from this company that are used in automotive clay nanocomposites. These are organically modified, nanometer scale, layered magnesium aluminum silicate platelets. The key issue in nanoclay/polymer composites is that of polymer/clay compatibility at the interface. This requires that, in most cases, one must impart an organophilic character to the clay. This is commonly accomplished by adding amino acids, organic ammonium salts, or tetra organic phosphonium solution. The surface modification of platelets with an organic graft allows dispersion and miscibility with the thermoplastic matrix materials. The additives serve to reinforce thermoplastics resulting in somewhat higher stiffness and lower coefficient of thermal expansion. The additives also improve gas barrier properties of thermoplastics. The surface char formation and flame retardance of thermoplastic systems have also been improved by incorporating the nanoclay particles into the structure. In the case of hydrophilic polymers and silicate layers, pretreatment is not necessary. Most polymers are hydrophobic and are not compatible with hydrophilic clays. In such cases, a treatment that results in exfoliation of the clays is needed. By exfoliation, we mean peeling of clay flakes or platelets from one another and dispersion into the polymer matrix. There is some confusion about such terminology in the literature. Let us define these terms. By intercalation, we mean some of the organic polymer is inserted between the flakes of the clay, which would increase the interlayer spacing but individual flakes stay together. In an exfoliated structure, the layers of the clay are well separated and the individual layers are distributed throughout the organic matrix. A third alternative is dispersion of complete clays within the polymer matrix; this is akin to use of the clay as conventional filler. Figure 15.1 shows

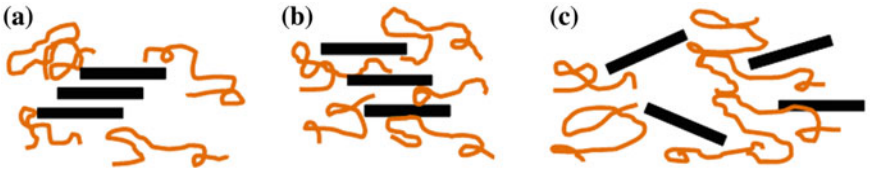

Fig. 15.1 Three different morphologies of platelets (black) dispersed in a polymeric matrix: **a** immiscible, **b** intercalated, and **c** miscible. Note the increased spacing between sheets in (**b**)

schematically three different morphologies: immiscible, intercalated, and miscible platelets. The treatment or process of exfoliation can result in nanoclay sheets with aspect ratios between 100 and 1000.

It should be pointed out that, in general, the nanoclays improve the strength and stability of the resin, i.e., they are more functional than conventional "fillers" such as talc or mica used in sheet molding processes. Also, the use of nanoclays results in enhanced aesthetics such as surface quality, color appearance, and enhanced scratch resistance. However, generally, the amount of nanoparticles used is very small, 2–3% by weight.

The key to clay/polymer composites is polymer/clay compatibility at the interface. This requires that, in most cases, one must impart an organophilic character to the clay. In the case of hydrophilic polymers and silicate layers, pretreatment is not necessary. Most polymers, however, are hydrophobic and are not compatible with hydrophilic clays. Following methods can be used to make the clays compatible with polymers.

Solution induced intercalation: In this method, one solubilizes polymer in an organic solvent and the clay is dispersed in the solution, following which either the solvent is evaporated or the polymer precipitated. The clay dispersion is not very good; the process is expensive because of the high cost of the solvents required, and health and safety issues.

In situ polymerization: In this method, the clay layers are dispersed in the matrix by polymerization. The silicate layers are mixed with the monomer together with the polymerization initiator and/or the catalyst.

Melt processing: In this case, the silicates layers are dispersed into the polymer melt. The silicates need to be surface treated through the organo-modification prior to introducing in the polymer melt.

15.2 Self-Healing Composites

Self-healing or self-repairing of materials is a very interesting concept. The concept is quite general inasmuch as it is applicable to monolithic materials as well, not just composites. For an overview of this field, the reader is referred to van der Zwaag (2007). The concept of self-healing is taken from the field of medicine. The basic

premise is that, in a self-healing system, when damage occurs, the system realizes that something is wrong. Then, without human intervention, the self-healing system makes the necessary adjustments and return to normal operation. The process has been called an autonomic healing process (White et al. 2001). The term autonomic, again borrowed from medicine, refers to automatic functioning of a system. The self-healing process mimics the spontaneous healing processes observed in living systems when they are damaged. In a living system, damage (for example, formation of a bruise) triggers an autonomic healing process, i.e., when an organism is damaged, there is a natural healing response. Researchers have applied this concept to synthetic material design and have developed self-healing materials. The basic idea is to incorporate a healing agent in the material of interest, which will come into action when damage in the form of a crack appears. It is easy to appreciate the appeal of this concept in composites by recalling that increasing amounts of PMCs are being used in civilian infrastructure (bridges, decks, columns, etc.).

The idea of autonomic healing in a composite work is shown schematically in Fig. 15.2. The healing or repair agent (a kind of crosslinking polymer) encapsulated in a hollow microsphere (or a hollow fiber) can be embedded in the matrix. The polymer matrix has a catalyst distributed in it that serves to polymerize the healing agent. Damage in the form of a crack is shown in Fig. 15.2a. When the crack propagates and breaks the microsphere, the healing agent is released through capillary action. Polymerization occurs when the healing agent encounters the catalyst and the crack faces are closed by bonding as shown in Fig. 15.2c. A self-healing PMC can be made by using a microencapsulated healing agent and a solid chemical catalyst, both dispersed within the polymer matrix phase. Healing or closure of a crack will occur when the crack propagates through the microcapsules releasing the healing agent onto the crack plane. The healing agent, under the action of chemical catalyst, initiates polymerization and bonding of the crack faces. Kessler et al. (2003) used this approach in a carbon fiber/epoxy composite. The self-healing composite system consisted of a healing agent, microcapsule shell, chemical catalyst, epoxy matrix, and carbon fiber. They used the monomer, dicyclopentadiene (DCPD) as the healing agent, which possesses low viscosity and excellent shelf life when stabilized with 100–200 *ppm p-tert*-butylcatechol. The healing agent was encapsulated in poly ureaformaldehyde by in situ polymerization (White et al. 2001) to yield the self-healing PMC.

Self-healing was demonstrated on width-tapered double cantilever beam fracture specimens in which a midplane delamination was introduced, which was allowed to heal. Specifically, healing at room temperature yielded as much as 45% recovery of undamaged value of interlaminar fracture toughness, while healing at 80 $^{\circ}C$ increased the recovery to over 80% (Kessler et al. 2003). An extension of this concept was reported by Kirkby et al. (2007). They embedded shape memory alloy (SMA) wires in the composite and observed improvements in performance, which were attributed to three effects:

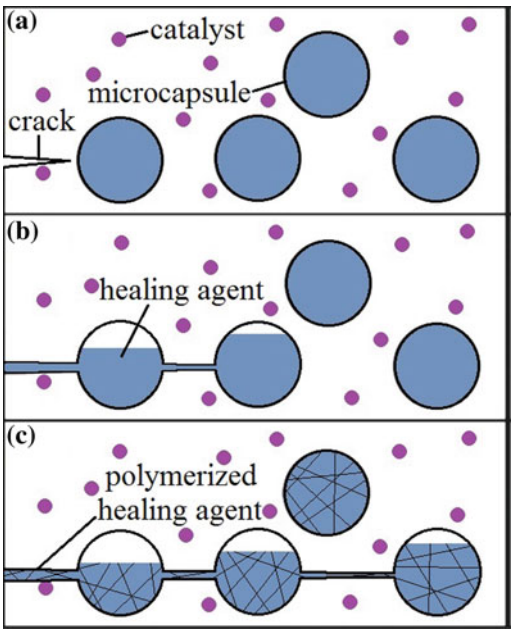

Fig. 15.2 The concept of autonomic healing in a composite. The healing agent is encapsulated in hollow microspheres. **a** Damage in the form of a crack. The matrix has catalyst in it and microcapsules containing the healing agent. **b** When the crack breaks the microsphere, the healing agent is released. **c** Polymerization occurs and the crack faces are closed

(i) crack closure, which reduces the crack volume and the amount of healing agent required,
(ii) heating of the healing agent during polymerization, which improved the crosslinking, and
(iii) mechanical registration of the two crack faces, which resulted in a reduced crack volume on closure.

15.3 Self-reinforced Composites

A class of polymer matrix composites, called self-reinforced or single polymer composites (SPC) has chemically the same reinforcement and matrix. Commonly, polypropylene is reinforced with glass fibers to increase its strength and stiffness. This, however, reduces the recyclability of polypropylene, one of the hallmarks of thermoplastics such as polypropylene. It also causes problems in achieving an acceptable surface finish. Enter the concept of self-reinforcement, i.e., use aligned polypropylene to reinforce polypropylene, such a material will have an intermediate stiffness, good impact performance, a "class A" surface finish, and it is fully recyclable (Capiati and Porter 1975; Matabola et al. 2009). By aligned polypropylene, one means polypropylene fiber wherein the molecular orientation of chains has been introduced, e.g., by hot drawing.

The main driving force for this is the fact that they are easily recyclable and thus bring in economic and environmental benefits. The mechanical properties of these self-reinforced composites are slightly less than, but comparable to, the conventional fiber reinforced composites. The main difficulty in processing them is the rather small difference in the melting point of the fiber and the matrix. The processing window is generally very short, 1–2 °*C*; however, the sheets can be post formed over a range of 20 °*C* because the remelted skins of the tapes have a lower softening temperature. As we saw in Chap. 2, drawing of thermoplastics can result in some chain alignment, which in turn can lead to an increase in modulus. Polypropylene (PP) fibers in a polypropylene matrix, called self-reinforced polypropylene are available commercially: Curv® and Moldable Fabric Technology (MFT) are self-reinforced 100% PP composites that contain PP fibers in a PP matrix. The process of making such self-reinforced composites is to heat and compact highly oriented, small diameter fibers under suitable time, temperature, and pressure conditions to form a composite wherein a substantial proportion of the original molecular orientation of fibers is retained. Generally, in practice, this means that some 10–20% of the original fiber gets melted and loses the superior mechanical characteristics but serves to produce matrix. Figure 15.3 shows the microstructure of such a composite. The material properties are enhanced through molecular orientation, resulting in *self-reinforcement*.

The tapes are woven into fabric to provide ease of handling and balance. This material offers excellent impact resistance, lightweight, and high stiffness compared to non-drawn PP. Curv® is used in automotive exterior (bumpers, body panels,

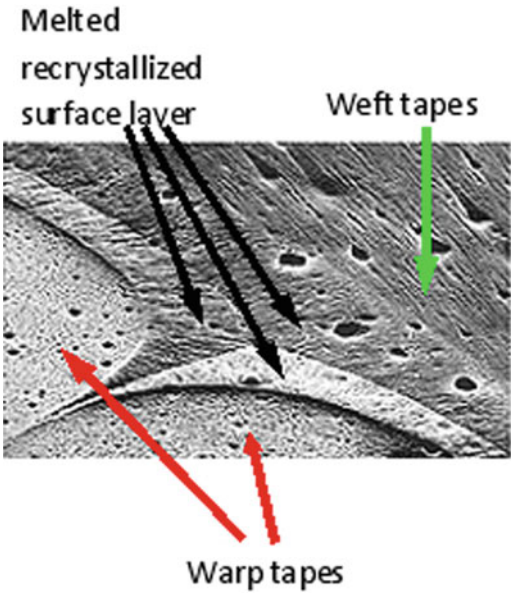

Fig. 15.3 Microstructure of a self-reinforced composite (PP fabric in a PP matrix)

underbody shields, wheel arch liners), interior (load floors, pillar trims, and door and head liners), audio products, sporting and travel goods as well as for ballistic protection.

15.4 Biocomposites

Biocomposites can be defined as composites that have at least one component that is derived from biological or natural sources. There is a growing interest in these composites (see, for example, Fuqua and Ulven 2008; Mohanty et al. 2005; Sui et al. 2009; Wool and Sun 2005). The main attributes of biocomposites that are driving the effort in this area are the following:

- Biodegradable,
- Renewable,
- Cheap, and
- Natural resource.

Biocomposites, based on these attributes, are environmentally friendly. However, the ultimate test for their success in the commercial arena will depend on whether they meet the application requirements. Among the problem areas in their widescale acceptance are the following:

- High moisture absorption,
- Poor wettability of fibers by polymeric resins leading to poor interfacial bonding, and
- High viscosity of bioresins that makes processing more difficult.

There are many examples of composites found in nature. Shells (abalone and mussel) are good examples of how living organisms synthesize layered composites that show high strength and high toughness. Layers of calcium carbonate ($CaCO_3$, orthorhombic crystal structure) and an organic adhesive are stacked in a brick and mortar type structure. The mortar gluing together the bricks of calcium carbonate is a thin film of proteins and polysaccharides. This biocomposite consists of about 95% inorganic mineral and 5% organic polymer, with electrostatic forces acting at the interface. The organic glue is strong enough to hold layers of calcium carbonate together, but weak enough to allow the layers to slide and thus absorb the energy of an impact or to deflect an oncoming crack instead of letting it propagate in a catastrophic manner through the brittle calcium carbonate. Such ingenius and natural materials science and engineering work done by nature is the source of inspiration in the field of biomimetics. Some work related to synthetic laminates is described in the next section.

15.5 Laminates

Laminates are multilayered composite materials. We discussed fiber reinforced laminates made by appropriately stacking fiber reinforced plies. The laminates we are discussing in this section are, in general, made by putting together sheets, except for a variety called fiber metal laminates (see below). Some of these laminates have been in commercial use for a long time while others are potential candidates for a variety of applications because of their superior properties: high strength (ambient and high temperature), fatigue resistance, wear resistance, and biocompatibility.

Examples of laminated structural materials can be found in nature and in historical manmade objects. The unique structure of laminates found in nature offers the desired functional properties. Examples include bones, tooth, shells of mussels, etc. For example, abalone shell consists of protein layers separating the mesolayers. Among historic examples, we should mention metallic laminates made of steel that have been used to make Samurai swords. The famous iron pillar of Delhi consists of laminae of wrought iron. Other mundane examples include copper/aluminum and copper/stainless laminates for use in kitchen utensils. Researchers have explored multilayered composites consisting of metal/metal and metal/ceramic laminates. Extensive work on ultrahigh carbon steel (UHCS) laminates, which have

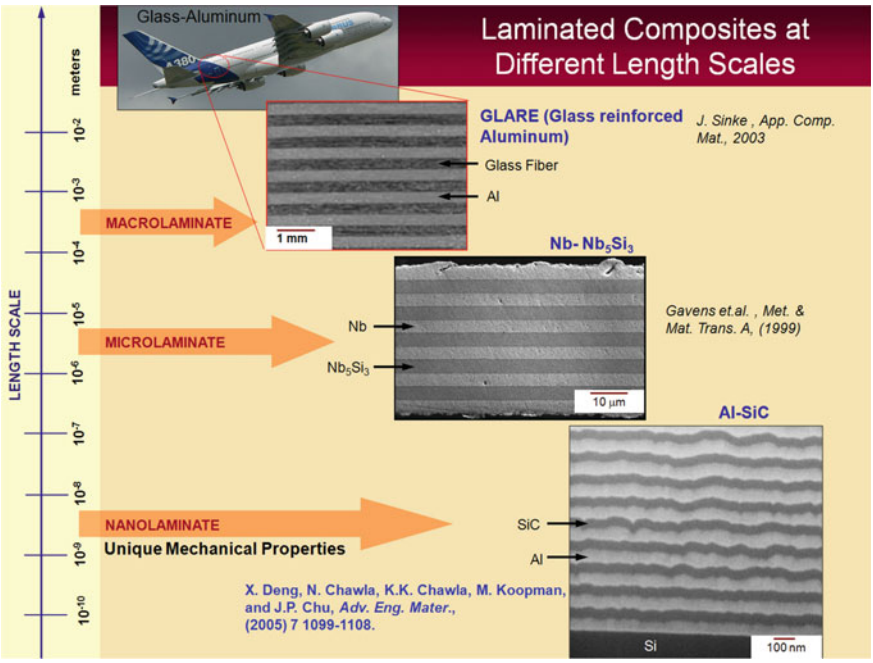

Fig. 15.4 A general view of the structure of laminates at different length scales

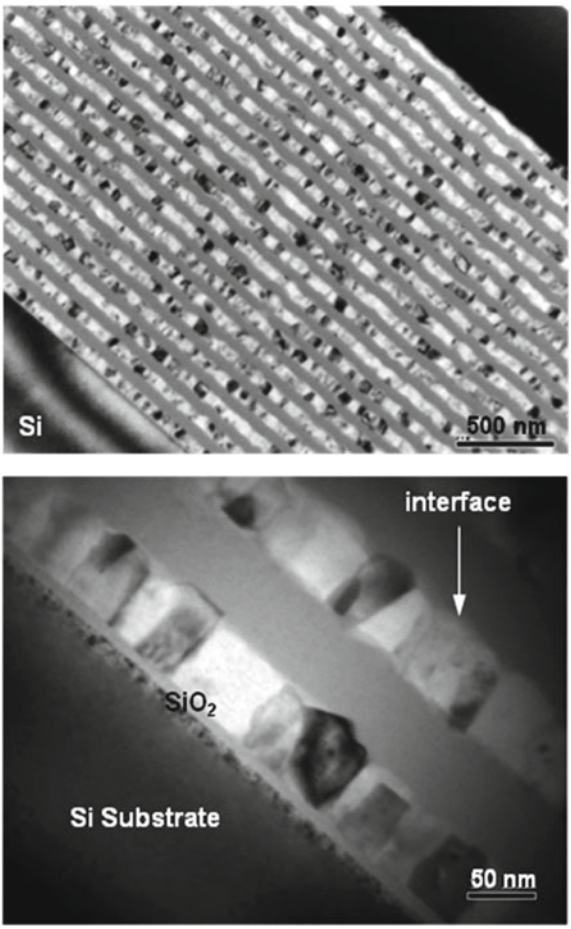

Fig. 15.5 Microstructure of SiC/Al nanolaminate. Note the well-bonded interface and absence of any reaction product at the interface

compositions very similar to ancient Damascus or Wootz steels, showed excellent impact properties (Verhoeven et al. 1998; Lesuer et al. 1996).

A general view of the structure of laminates at different length scales is provided in Fig. 15.4 (Deng et al. 2005; Woerden et al. 2003; Gavens et al. 1999). Here we wish to highlight the microstructure of the multilayered Al/SiC composites made by DC/RF magnetron sputtering. Figure 15.5a shows the nanolaminate as observed in SEM while Fig. 15.5b shows the interface in this system as observed in a transmission electron microscope (TEM); no reaction product is observed at the interface between Al and SiC. The elastic and plastic behavior of the multilayered materials, as investigated by nanoindentation showed a high degree of flexibility of brittle SiC layers, see Fig. 15.6, before and after indentation. Cracking under indentation

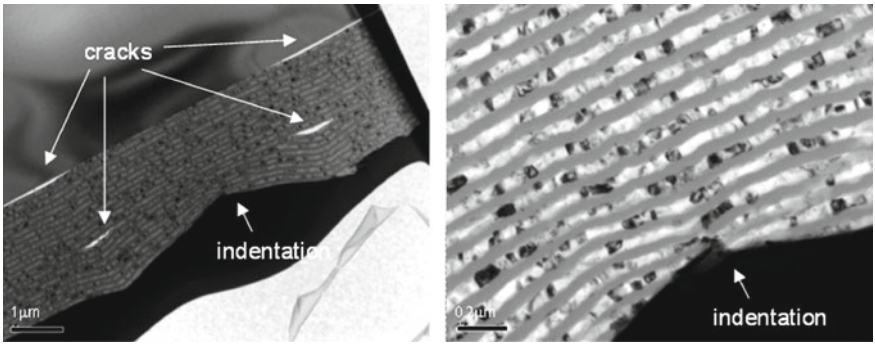

Fig. 15.6 Deformation of SiC/Al nanolaminate in a nanoindenter. Note the well-bonded interface and the extreme flexibility of SiC, an inherently brittle material

started at a depth of 1000 *nm* in SiC layers. This occurred at sites where kinks formed in SiC, which appeared to occur at sites of shear localization.

15.5.1 Ceramic laminates

Multilayered ceramic capacitors (MLCCs) represent a commercially very important and successful ceramic/metal laminate system. Barium titanate ($BaTiO_3$) is a ferroelectric material with a high dielectric constant. MLCCs are laminates made of alternate layers of $BaTiO_3$ dielectric and inner electrodes of Pd or Pt–Ag or Ni. The inner electrodes are exposed at the opposite sides of the laminate. They are widely used in electronics industry. These capacitors, manufactured by alternately layering electrodes and thin dielectric, are small, efficient, reliable, and cost-effective; they are used in virtually every electronic circuit.

Laminated glass is an example of glass/polymer laminate that is widely used but not appreciated as a sheet laminate composite, which is what it really is. One of the flat glass products (about 25% total flat glass production is consumed by automobile industry in the US) that amounts to over $500 million market. U.S. and many other countries require by law that automobile windshields be made of laminated glass. The glass composition is mostly SiO_2 with some $Na_2O + CaO + K_2O + MgO + Al_2O_3$. The laminate is made of two sheets of tempered glass (each 0.75 *mm* thick) bonded by a layer (2.5 *mm*) of tough plastic (PVB—polyvinyl butaryl) in an autoclave. PVB/glass has good adhesion. PVB is transparent and can be tinted to protect against UV radiation. The finished laminated glass is virtually indistinguishable from ordinary glass, because the PVB is invisible and covered on both sides by the glass. The main advantage is that if the glass laminate gets broken, the glass shards stick to the plastic interlayer rather than cleanly breaking apart and do a lot more damage. The minor disadvantage is that the PVB laminated glass has less strength than ordinary glass of the same size and thickness.

15.5.2 Hybrid composites

A hybrid composite material, erroneously named fiber metal laminate (FML), has been developed. It consists of a metal sheet (~ 0.3 *mm* thick) which can be aluminum, steel, titanium, magnesium, etc., and a polymer matrix composite (PMC) prepreg, which consists of fiber reinforced polymer, see Fig. 15.7. The composite consists of alternate layers of PMC and metal sheet. In principle, the fiber can be continuous or not; it can be glass, aramid, or carbon, and the resin matrix can be any polymer but is commonly epoxy. The nomenclature scheme goes as follows:

- GLARE: GLAss fiber REinforced,
- ARALL: ARamid fiber reinforced ALuminum Laminates,
- CARE: CArbon fiber REinforced, and
- TIGR: TItanium/GRaphite–epoxy laminates.

Common aircraft fuselage material is an aluminum alloy. In the Airbus A380 jumbo aircraft, the panels for the upper fuselage section of the aircraft are made of GLARE which consists of laminates made of alternate layers of glass fiber/epoxy (a PMC) and aluminum sheet. Such hybrid composites combine advantages of metals and PMCs, to wit:

- Excellent fatigue and impact properties,
- High strength and stiffness,
- Flame resistance,
- Easily machined or formed, and
- Mechanical fastening capability.

There is some interesting history with the use of GLARE in aircraft. Earlier, fuselage construction with ARALL was tried. It was observed that under loading conditions encountered in an aircraft fuselage, the aramid fibers around a fatigue

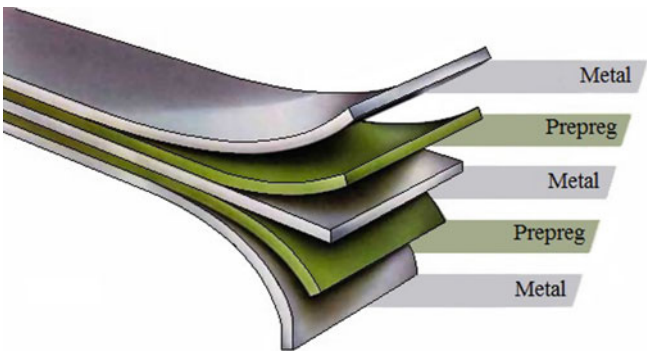

Fig. 15.7 A fiber metal laminate (FML) made of a metal sheet and a polymer matrix composite (PMC) prepreg which consists of a fiber reinforced polymer composite

crack would break. Once the fiber was broken, the crack in the fiber would grow and lead to delamination, which would place a compressive stress on the aramid fibers, causing buckling. Low compressive stress of aramid fibers is well known (see Chap. 2; Chawla 2016). It was observed that aramid fibers would break under rather low compressive loads. It also became evident that ARALL was also sensitive to strength reductions caused by any holes that might be drilled in it. Such holes are unavoidable in a large structure such as a fuselage; they would lead to premature fatigue cracks to develop. Although the use of ARALL was not suitable for fuselage construction, the weight savings by using this material were very attractive. Earlier, ARALL was used in the C-17 military transport plane. Because of heavy weight problems toward the rear of the plane, the large aluminum cargo door was replaced with ARALL.

This was followed by replacing aramid with glass fibers in the new FML called GLARE, which has superior blunt notch strength and the ability to handle greater compressive stresses than ARALL. GLARE is also more resistant to impact than ARALL, and for this reason, the first commercial application of GLARE was in the cargo floor of Boeing's 777 where the excellent impact properties of GLARE were put to use. The next stage of use of GLARE was in the form of panels for the fuselage of Airbus's A380 aircraft. At first the manufactured flat panels lacked the cost-effectiveness necessary for the material to break ahead of conventional aluminum structures despite the excellent mechanical properties. The cost of manufacture of GLARE composites was roughly 7–10 times that of aluminum per kilogram and the next step was to lower the cost of manufacturing (Vlot 2001). The dimensions of metal sheet with the required 0.3–0.4 *mm* thickness were limited to a width of 1.65 *m*. For the aluminum/S2-glass fiber in epoxy system, failure occurred primarily at the metal/adhesive interface. The thicker specimens debonded faster than thinner ones. Hence, the need for very thin aluminum sheet to increase the fatigue resistance of GLARE. The manufacture of flat panels of GLARE in an autoclave, although expensive, was an important step in GLARE production. The main source of fatigue resistance in GLARE is the intact bridging fibers in the wake of the crack; they restrain the crack opening. Figure 15.8 shows the slow fatigue crack growth characteristics of GLARE compared to those of monolithic aluminum alloy.

Yet another type of *hybrid composite is a* composite containing more than one type of fiber. We described this in Chap. 13. Such composites, by using two or more type of fibers, extend the idea of tailor making a composite material to meet specific property requirements. Partial replacement of expensive fibers by cheaper but adequate fiber types is another attractive feature of hybrid composites. Additionally, there is the possibility of obtaining a synergistic effect in the fatigue behavior of hybrid composites. Phillips observed enhanced fatigue strength in a carbon–glass hybrid system. Such synergistic results are by no means universal. For example, in the case of the flexural fatigue strength versus the number of cycles for 100% unidirectional carbon fiber/polyester, 100% chopped glass fiber/polyester, and unidirectional carbon fiber faces over chopped glass core, the hybrid composite curve was intermediate between the 100% carbon and 100% glass curves.

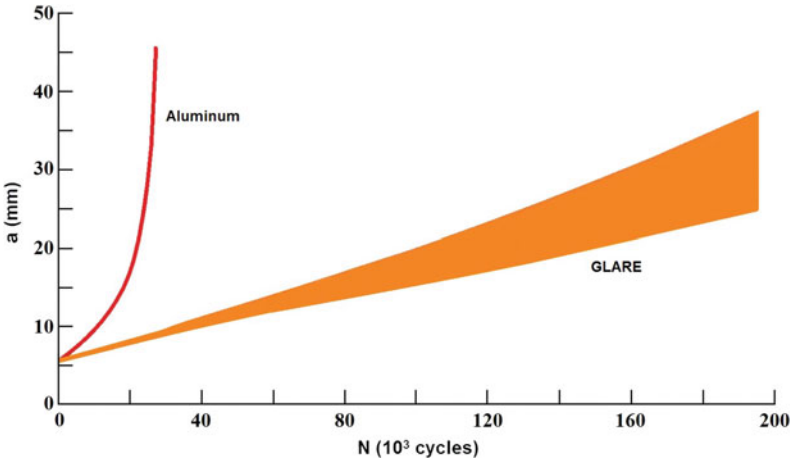

Fig. 15.8 Fatigue crack growth in GLARE composites compared to that in monolithic aluminum alloy

Another version of hybrid laminated MMCs is a family of layered composites consisting of metallic outer skins with a viscoelastic core material (for example, polyethylene, nylon, polypropylene, paper, or cork). Such composites will be useful where sound and vibration damping are required. The viscoelastic layer provides a high loss factor, i.e., a high capacity to convert vibrational energy to heat.

Although such composites are commonly made of metal and thermoset matrix PMCs containing continuous fibers, this concept of hybrid composites has been extended to thermoplastics and discontinuous fibers (Abdullah and Cantwell 2006; Kulkarni et al. 2007).

References

M.R. Abdullah, W.J. Cantwell. **66**, 1682 (2006)
P.M. Ajayan, L.S. Schadler, P.V. Braun, *Nanocomposite Science and Technology* (Wiley-VCH, Weinheim, 2003), pp. 122–138
E.V. Barrera, J Mater **52**, 38 (2000)
E.V. Barrera, M.L. Shofner, E.L. Corral, *Carbon Nanotubes: Science and Applications* (CRC Press, Boca Raton, FL, 2005)
N.J. Capiati, R.S. Porter, J. Mater. Sci. **10**, 1671 (1975)
K.K. Chawla, *Fibrous Materials*, 2nd edn. (Cambridge University Press, Cambridge, 2016)
X. Deng, N. Chawla, K. Chawla, M. Koopman, J.P. Chu, Adv. Eng. Mater. **7**, 1099 (2005)
H. Fukuda, K. Kondoh, J. Umeda, B. Fugetsu, Compos. Sci. Technol. **71**, 705 (2011)
M.A. Fuqua, C.A. Ulven, J. Biobased Mater. Bioenergy **2**, 258 (2008)
A.J. Gavens, D. Van Heerden, T.P. Weihs, T. Foecke, Metall. Mater. Trans. A **30**, 2959 (1999)
E. Kirkby, V. Michaud, J.-A. Månson, J. Rule, N. Sottos, S. White. in *Proceedings of the First International Conference on Self Healing Materials* (Springer, Noordwijk aan Zee, The Netherlands, 2007)

M.R. Kessler, N.R. Sottos, S.R. White. Compos. A **34**, 743 (2003)
J.H. Koo, *Polymer Nanocomposites* (McGraw-Hill, New York, 2006), pp. 95–122
R.R. Kulkarni, K.K. Chawla, U.K. Vaidya, M.C. Koopman. in *Proceedings of the International SAMPE Symposium*, vol. 52 (Baltimore, MD, 2007), p. 10
H. Lee, P.D. Fasulo, W.R. Rodgers, D.R. Paul, Polymer **46**, 11673 (2005)
D.R. Lesuer, C.K. Syn, O.D. Sherby, J. Wadsworth, J.J. Lewandowski, W.H. Hunt, Int. Mater. Rev. **41**, 169 (1996)
K.P. Matabola, A.R. De Vries, F.S. Moolman, A.S. Luyt, J. Mater. Sci. **44**, 6213 (2009)
A.K. Mohanty, M. Misra, L.T. Drzal (eds.), *Natural Fibers, Biopolymers, and Biocomposites* (CRC Press, Boca Raton, FL, 2005a)
A. Okada, A. Usuki, Macromol. Mater. Eng. **291**, 1440 (2006)
D.R. Paul, L.M. Robeson, Polymer **49**, 3187 (2008)
M.L. Shofner, V.N. Khabashesku, E.V. Barrera, Chem. Mater. **18**, 906 (2006)
M.L. Shofner, F.J. Rodriguez-Macias, R. Vaidyanathan, E.V. Barrera, Compos. A Appl. Sci. Manuf. **34**, 1207 (2003)
G. Sui, M.A. Fuqua, C.A. Ulven, W.H. Zhong, Biores. Technol. **100**, 1246 (2009)
J.D. Verhoeven, A.H. Pendray, W.E. Dauksch, JOM **50**(9), 58 (1998)
S.R. White, N.R. Sottos, P.H. Geubelle, J.S. Moore, M.R. Kessler, S.R. Sriram, E.N. Brown, S. Viswanathan, Nature **409**, 794 (2001)
H.J.M. Woerden, J. Sinke, P.A. Hooimeijer. Appl. Compos. Mater. **10**, 307 (2003)
R. Wool, X.S. Sun, *Bio-Based Polymers and Composites* (Elsevier Academic Press, Burlington, MA, 2005)
S. van der Zwaag (ed). Self Healing Materials (Springer, Dordrecht, The Netherlands, 2007)

Suggested Reading

S.R. Bakshi, D. Lahiri, A. Agarwal, Int. Mater. Rev. **55**, 41 (2010)
T.C. Mauldin, M.R. Kessler. Int. Mater. Rev. **55**, 317 (2010)
A.K. Mohanty, M. Misra, L.T. Drzal (eds.), *Natural Fibers, Biopolymers, and Biocomposites* (CRC Press, Boca Raton, FL, 2005b)
A. Vlot, J.W. Gunnick, *Fibre Metal Laminates: An Introduction* (Kluwer Academic Publishers, Dordrecht, The Netherlands, 2001)
L.B. Vogelesang, J. Schijve, R. Fredell. in *Case Studies in Manufacturing with Advanced Materials*, vol. 2, ed. by A. Demaid, J.H.W. de Wit (Elsevier, Amsterdam, 1995), pp. 253–271
S. van der Zwaag (ed.), *Self Healing Materials* (Springer, Dordrecht, The Netherlands, 2007b)

Chapter 16
Repair and Recycling of Composites

Repair and recycling of composites are very important topics. This is particularly true with increasing use of composite materials in the civilian aerospace industry. When there is damage to a composite component, we try to repair it until we reach the point of what is *termed* the end-of-life of the component. At that point, we simply replace the component. The replacement is followed by efforts to recover and reuse the components that were used to make the composite. In particular, the efforts involve recovery of expensive fibers such as carbon fibers with the least amount of damage. Although we mentioned the end-of-life concept, it should be pointed out there is some waste material that results during the processing of composite components such as an aircraft fuselage or wind turbine blade; which must be recycled.

Repair of composites has to do with alleviating the damage done to a composite part during service. Damage to a composite in service can occur because of fatigue, wear, impact, environment, lightning strike, etc. The first thing that we should appreciate is that the damage mechanisms in composites are different from those observed in conventional materials. When the damage level reaches a level such that the operation is impaired, then one must decide whether to replace or repair the part.

One of the major sources of damage in a fiber reinforced laminated aircraft composite structure (think of Boeing 787 or Airbus 350 aircraft) is the impact damage, which may occur during ground handling (e.g., tool drops, service vehicle collisions), take-off, landing, and in-flight due to impact by a foreign object (foreign object damage or FOD). Other sources of damage include erosion, abrasion, manufacturing defects, excess heat exposure, and fluid infiltration. All these can lead to a drop in strength. Note the damage due to impact may be visible on the external surfaces or it may be a nonvisual, internal damage in the form of ply delaminations, matrix cracking, and fiber fracture. Nondestructive evaluation techniques can be used to assess the degree of damage and repair requirements.

K. K. Chawla, *Composite Materials*,
https://doi.org/10.1007/978-3-030-28983-6_16

16.1 Repair Techniques

We describe some common repair techniques for composites.

16.1.1 Cosmetic Repair

Just as the name indicates this is only for appearance sake. It is nothing but a superficial, nonstructural filler (or resin injection) that serves to keep the fluids out until a more permanent repair can be done. Clearly, such a repair will not provide much strength. Such a cosmetic repair might be fine for nonstructural locations in an application.

16.1.2 Bolted and Bonded Repairs

Bolted repairs for composite structures are similar to those for metallic structures. However, there are some differences between the bolted repairs for composites and metals:

(a) Different tools are used for drilling fastener holes in composites than the ones used for metallic structures.
(b) Special care is needed in drilling holes in laminated composites to prevent splintering on the backside of the hole. A support on the backside will be of help.
(c) Polymer matrix composite has a brittle epoxy as a common matrix material. Thus, fasteners that expand to fill the hole (e.g., driven rivets) would not be appropriate.
(d) Sharing of loads in different fasteners in composites is not uniform because composite materials do not undergo plastic yielding like metals.

In general, bonded repairs are commonly used for thin (3–4 *mm*) laminates while bolted repairs are used for thick laminates.

In a bonded repair, adhesive bonding of the parent and repair patch is used. The strength of the bond is a function of the type of repair patch, surface treatment, adhesive type, curing conditions, etc. Curing temperature can be an issue if the repair patch requires curing at 175 $^{\circ}C$ or higher, which is likely to lead to residual thermal stresses due to thermal mismatch, resulting in damage.

16.1.3 Bonded Repair

The damage needs to be assessed in a nondestructive manner, followed by accurate machining of the damaged region. Machining of composite structures is especially critical in view of the inherent heterogeneity of fiber reinforced composites. After identifying and assessing the extent of the damage, the damaged region needs to be accurately machined to remove material and edges tapered for implementing bonded scarf repairs.

There are some important factors that should be taken into account about patch repair. For example, one should match the strength and stiffness of the patch to that of the parent structure. This, however, is not always possible. The repair operating temperature should not exceed the maximum operating temperature of the resin. Obviously, in the case of any adhesive joint, it would be preferable to have the joint failure to occur in the adherends. The most common joint types used in the aircraft industry are the following: double lap, single lap, scarf, and stepped lap, all of which have different characteristics and capabilities. Single lap joints have the lowest strength joint capability due to the eccentricity of the load path, which can induce bending of the adherends and a significant increase in peel stresses causing premature failure. Double lap joints have lower peel stresses due to the reduction of the load path eccentricity and thus have a higher strain capacity compared to single lap joints. Scarf joints, with virtually no eccentricity of the load and minimal peel stresses, are the most efficient joints for the following reasons: They are very effective in restoring the original strength of the composite structure, and they preserve the aerodynamic smoothness of the structure. Nevertheless, scarf joints require the removal of large amounts of undamaged material to preserve a shallow scarf angle, which may cause further damage to the parent laminate and thereby compromise its structural integrity.

Figure 16.1 shows a damaged region of a laminated PMC. In order to repair the damage, first we remove the material around the damaged region and then apply a repair patch. The two main patch repair techniques, scarf and lap, are shown in Fig. 16.1. In the scarf technique, the repair material is inserted into the laminate in place of the material removed because of damage, see Fig. 16.1. In the lap

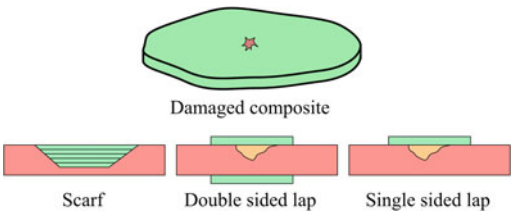

Fig. 16.1 Two main patch repair techniques: scarf and lap. In the scarf technique, the repair material is inserted into the laminate in place of the material removed because of damage. In the lap technique, the repair material is applied either on one side (single sided lap) or on both sides (double sided lap)

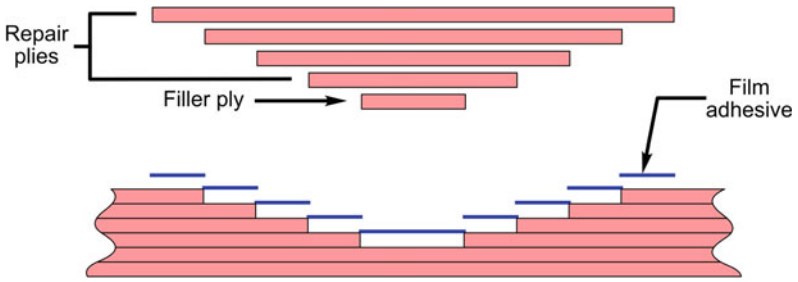

Fig. 16.2 Schematic of a scarf joint between the prepared repair area and the repair patch

technique, the repair material is applied either on one side (single sided lap) or on both sides (double sided lap) as shown in Fig. 16.1.

Sometimes, a doubler, which is a localized area of extra layers of reinforced composite, is used. The objective is to provide stiffness or strength to the damaged part. The doublers can be mechanically fastened or adhesively bonded at the damaged area. Doublers are used for structural repairs in primary loaded parts of a structure. It should be recognized that repairs using doublers may not be aerodynamically smooth, and may cause "signature" problems where low observability by radar is required. They also leave the original damage in place and transfer load around the damaged region.

Figure 16.2 shows a detailed schematic of a scarf joint between the prepared repair area and the repair patch. The repair patch is made very precisely by replacing each ply of the damaged composite laminate. The repair patch should fit exactly the area to be replaced. A final cosmetic or sanding layer allows a smooth and/or cosmetic surface. In a bonded repair, adhesive bonding between the parent laminate and repair material is of paramount importance. The bond strength will depend on the surface preparation, type of adhesive, curing conditions and joint design (stepped or plane scarf, scarf angle, etc.) (Katnam et al. 2013). The objective is to insure that load gets transferred between the two adherends (the patch and the parent composite) properly. The design of joint should enhance shear stress state and reduce peel stresses. Finite element analysis is resorted to analyze and predict the design strength.

16.1.4 Pre-cured Composite Patch

Pre-cured carbon fiber reinforced epoxy composite patch can be bonded to the outside of the damaged area and a chemical heat pack is applied to cure the resin. This technique is used to cure the resin at a relatively low temperature in about an hour and the pre-cured patch is meant to be applied when the aircraft is at the gate. It works for light damage and restores sufficient strength to enable the aircraft to be cleared for flight until a proper repair can be done.

16.2 Recycling of Composites

Eventually, however, there comes a point when the useful life of a component made of a composite material, be that an aircraft part or a fishing rod, comes to an end. At that stage, we need to make use of strategies/techniques that allow us to recycle or reclaim the components that constituted the composite component. Service or use is the main reason that a material or a component loses its restorable value. With increasing use of composites in different walks of life: aerospace, energy, transportation, civil infrastructure, and recreation, it behooves us to tackle the problem of recycling of composites seriously. Figure 16.3 shows schematically the change in value of the constituents of a PMC as a function of life cycle (Manson 1994).

It should be pointed out that many recycling procedures result in a material that is suitable for use in applications less demanding than the original application because of a considerably reduced intrinsic value of the material after each step.

Recyclability of self reinforced thermoplastic composites such as polypropylene fiber in polypropylene matrix is quite straightforward because both the components are thermoplastic. At the end of life, the component made of such a composite can simply be remelted and regranulated. The granules can then be reprocessed. Most PMCs have crosslinked thermosets as matrix materials, which means recycling of these composites is not straightforward. Frequently, one has to be satisfied with the reclamation of the costly fibrous component.

There are, however, certain items that cause restoring the value in case of PMCs difficult. Paint removal of a polymer or composite can frequently be a cause of poor recycling. In thermosetting materials, the crosslinking phenomenon makes recycling very difficult. Continuous fiber reinforced composites pose a great difficulty in recycling; especially the recovery of continuous fibers.

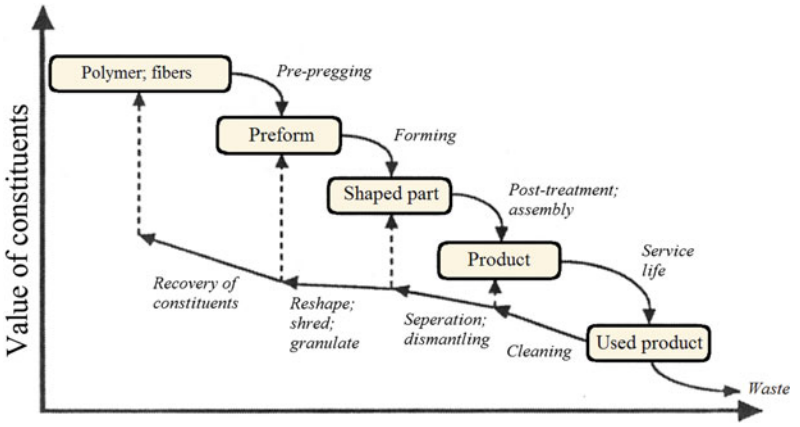

Fig. 16.3 A schematic of the change in value of the constituents of a PMC as a function of life cycle [Manson 1994]

We describe below some important recycling technique, first for PMCs then MMCs such as particle reinforced aluminum composites and tungsten carbide/cobalt composites.

16.2.1 Mechanical Recycling

This involves, just as the name says, mechanical grinding the composite component at the end of its life or even the composite scrap from the shop floor. Strictly speaking, grinding is the term used for the step that follows crushing or shredding. After the grinding step, one can separate the recyclates into different sizes. Sieving can be used to separate the recyclates into resin-rich and reinforcement-rich categories. Commonly, the reinforcements are the particles or short fibers used in sheet molding or bulk molding compounds. One can separate the recyclates by the fiber length as well.

The grinding step is followed by the use of the comminuted product as a filler or reinforcement in a new composite, generally meant for less-demanding applications than the virgin material (Pickering 2006). There is the option of using a variety of thermal techniques that breakdown the composite scrap. Recall that sheet molding compound (SMC) is a polymer matrix composite containing particles/short fibers (see Chap. 5). Such a material can easily be ground into a fine powder and reused as a filler. Such a technique would not work with continuous fiber reinforced thermoset matrix PMCs. As we know, thermosets are the most common matrix materials in PMCs, and they are not amenable to recycling in a manner similar to metals and thermoplastics. Thus, it becomes important to recover the expensive fibers without contamination and damage for reuse.

16.2.2 Thermal Techniques for Recycling

Thermal techniques include pyrolysis, fluidized bed pyrolysis and pyrolysis assisted with microwaves. These techniques allow the recovery of fibers. The resin matrix is volatilized into lower weight molecules. Volatilization of the resin matrix results in gases such as carbon dioxide, hydrogen and methane, and an oil fraction, but also char on the fibers. These processes work between 450 and 700 $^{\circ}C$ depending on the type of matrix resin. The lower temperatures are likely to be used for unsaturated polyester resins, while higher temperatures are likely to be used for epoxies or thermoplastics. Sometimes the term *tertiary recycling* (i.e., recovery of the monomer) is used.

The main limitation of simple thermal recycling approach of pyrolysis is that the resulting fibers are a jumbled mass of short fibers, whereas the desired form is that of long continuous fibers. What should be recognized is that while short, jumbled form of fibers may not be suitable for high-performance components; there are

less-demanding applications such as sporting goods or even automotive components where they can be profitably used.

Fluidized bed process is a more advanced version of pyrolysis technique of recycling. Fluidized bed reactors are commonly used in chemical processing industries. The main feature of a fluidized bed reactor is a bed of solid particles (commonly silica sand) that is supported by an up flow of gas. A high conversion rate coupled with a large throughput is the key feature of a fluidized bed reactor. Specifically, the process used at the University of Nottingham in UK involves shredding of the used composite to 6–22 *mm,* followed by feeding it into the fluidized bed reactor where it is volatilized, decomposing the polymer matrix and separating the fibers. The silica particles in the fluidized bed retain all the contaminants. At the same time, the temperatures used in the fluidized bed reactor are low enough to keep the fibers undamaged.

The fluidized bed process allows a rapid heating of the materials, and the fibers are separated from the matrix by attrition of the matrix. Some oxygen is required to minimize char formation; the char would otherwise contaminate the fibers. In some cases, there is some reduction in the strength of recovered fibers compared to the virgin fibers. The amount of strength reduction depends on the temperature used in the process (Oliveux et al. 2015).

16.2.3 Microwave Assisted Pyrolysis

Techniques involving microwave assisted pyrolysis can be used to recover fibers from the composite. It is done in an inert atmosphere, and the polymer matrix is converted into gases and oil. Microwaves carry energy, but the main advantage of using microwaves is that the material is heated in its core and the heat transfer is very fast, enabling energy savings (Oliveux et al. 2015).

16.2.4 Solvolysis

Solvolysis is a chemical treatment that involves the use of a solvent to degrade the resin. This technique can involve a wide range of solvents, temperature, pressure, and catalysts. The main advantage of solvolysis compared to pyrolysis is a lower temperature required to degrade the polymer matrix.

Frequently a supercritical fluid is used (Pinero-Hernanz et al. 2008). A supercritical fluid is simultaneously above its critical temperature and pressure. In the supercritical state, it has a high diffusivity and solubility, which allows it to decompose and oxidize. Alcohols (e.g., methanol, ethanol) may be used to recycled glass fiber reinforced unsaturated polyester composites. Ethanol and methanol did not work well when treating epoxy matrix composites. However, propanol has

shown much better performance, which was attributed to its favorable oleophilic behavior.

As an example of the work involving propanol, we cite the work of Yan et al. (2016) on carbon fiber/epoxy composites. They evaluated the effects of degradation temperature, reaction time, and additive on the efficiency of the recovery of carbon fibers from the epoxy matrix by supercritical 1-propanol. Their results indicated that the rate of decomposition of the epoxy matrix increased, but the mechanical properties of the recycled fibers decreased slightly with temperature. The decomposition rate of the epoxy resin and tensile strength of the recycled carbon fibers decreased with reaction time. An addition of 1 *wt%* of KOH to 1-propanol improved the recovery efficiency significantly. An increase in the KOH concentration above 1 *wt%* did not increase the decomposition rate and the mechanical properties of the recycled fibers became worse. There were slight changes in the surface chemistry of the recycled carbon fibers and their contact angle with epoxy resin. Supercritical 1-propanol would appear to be quite promising for recycling of carbon fiber/epoxy composites.

It would appear that the tertiary approach to recycle PMCs is quite viable. This involves chemical degradation of thermosetting polymeric matrix and recovering the reinforcement fiber for reuse. In this process, thermosetting polymer is broken down into a low molecular weight hydrocarbon mixture. This is accomplished by application of heat, pressure, and catalyst in a suitable reaction vessel containing a liquid heat transfer fluid (Allred and Gosau 2016). Recovered items may include not just fibers, but also some nanomaterials, whiskers, and fillers. The process is thought to be quick and scalable to handle large quantities (thousands of tons) of composite scrap. Both cured and uncured scrap sources can be readily processed. The overall recycling process involves collection and size reduction of scrap, processing in a reaction vessel, separation of heat transfer fluid, catalyst, and hydrocarbons from reinforcements, purifying recovered solids, separation of hydrocarbons, surface chemical treatment of solids, production of nonwoven mat, and packaging of solids and hydrocarbons for reuse. It is thus possible to recover monomers from the resin and to avoid the formation of char residues. Depending on the nature of the resin, more or less high temperatures and pressures are necessary to degrade the resin.

16.3 Recycling of Aluminum Matrix Composites

Particle reinforced metal matrix composites such as SiC_p/Al or Al_2O_{3p}/Al are more cost-effective than continuous fiber reinforced MMCs. There are two main reasons for this: the high cost of continuous fibers and the cost of processing the composites thereof. Also, secondary fabrication (extrusion, forging, rolling, etc.) is very difficult with continuous fiber reinforced composites MMCs.

Recycling of MMCs at the end of their life will make them economically more viable. The ultimate objective is always to obtain a part or component that performs

a function in a cost-effective manner. We describe recycling of two types of particulate MMCs: silicon carbide or alumina reinforced aluminum and tungsten carbide/cobalt composites (commonly referred to as cemented carbides).

One of the problems of recycling of composites made of alumina or silicon carbide particles in an aluminum matrix is that a mass of unreinforced aluminum is visually indistinguishable from a mass of reinforced aluminum. Of course, there is the density difference between aluminum and particle (SiC or Al_2O_3) reinforced aluminum composite, which can be exploited for separation purposes.

There are two important aspects in the recycling MMCs (Schuster et al. 1993; Lloyd 1994; Nishida 2001):

1. Recycling of MMCs as MMCs, i.e., without separating the reinforcement from the matrix. This can be quite economical where it is possible to use. However, one should be mindful of certain steps in such reuse of MMCs. It should not involve excessive use of treatments involving thermal excursions or lengthy thermal exposures because they can cause adverse chemical interactions at the interface. Some aluminum metal matrix composites can be recycled and reused, especially if the Si content is sufficient to retard formation of aluminum carbide, which is highly deleterious to mechanical properties. Addition of virgin metal to the reinforced material to obtain a composite with a desired particle volume fraction may be required.
2. Recovery or reclamation of the original components. This involves separating the components by using fluxing materials. Fluxes are materials that remove impurities in the form of slag in extractive metallurgy. For example, limestone is commonly used as a flux in smelting iron ores. Other common fluxes are silica, dolomite, lime, borax, and fluorite.

A fluxing material should have a lower surface energy with the ceramic reinforcement than with the metal matrix. This approach is similar to tertiary recycling of PMCs (see above), i.e., one attempts to recover the original components. There are two ways to do this: mechanical or chemical. Various mechanical methods of separating the metal and ceramic particles, such as crushing, shredding, and gravity separation, can be used. Chemical techniques are the ones that involve the use of fluxing materials. These fluxing materials should have lower surface energies with the ceramic reinforcement than with the metal matrix. Al can be reclaimed from scrap by melting at 700 °C, and by adding salt and bubbling argon through the melt to form froth that concentrates alumina and SiC particles dewetted by the salt. Figure 16.4 shows this process of chemical separation via fluxing. Using combined argon and salt fluxes, silicon carbide particles can be removed from the melt and 85–90% of the aluminum can be reclaimed (Lloyd 1994).

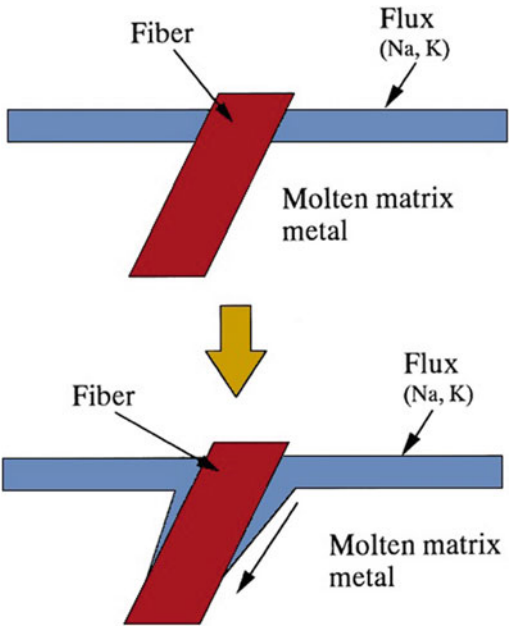

Fig. 16.4 Chemical action of fluxing materials to separate the metal matrix from fiber or particle [after Nishida 2001]

16.4 Recycling of Tungsten Carbide/Cobalt Composites

Particulate composites consisting of WC particles in a cobalt matrix have been around for much longer time. Techniques for their recycling and/or recovery of valuable tungsten have been in use in the industry for quite some time. Although, it must be admitted that the viability of recycling depends on the market price of tungsten.

16.4.1 Direct-Reuse Recycling Methods

The simplest method of direct-reuse recycling is to grind the WC/Co scrap to produce a usable component.

Use is made of differential contraction between tungsten carbide and cobalt when subjected to a temperature change combined with impact to obtain a coarse powder. The cold stream process uses embrittlement and impact breaking to reduce the cemented carbide scrap to a coarse powder. As originally developed, the cold stream process used blasts of air to impact the scrap particles against a surface with sufficient energy as to cause fracture.

16.4.2 Chemical Recovery Methods

The scrap can be chlorinated or oxidized, followed by alkali or acid leaching. Tungsten, a valuable commodity, is recovered as ammonium para tungstate or as tungstic acid.

The leaching process uses a high temperature heat treatment (1800 °*C*) followed by a rapid quench; this results in a material that can be comminuted to the state of presintered powder through conventional comminution methods. The effects of grain growth, induced thermal stress and phase transformation combined with the rapid quench, create a laminar structure with extremely brittle layers.

16.4.2.1 Zinc recycling process

This process is also called the "PRZ", an abbreviation for "process of recycling with zinc" and is very commonly used for recycling of WC/Co composites or cemented carbides. This process is also referred to as the Bernard process in the U.S. In this process, the scrap material is packed into graphite crucibles together with zinc and placed in a furnace. The furnace is evacuated, filled with argon, and heated to a temperature between 750 and 960 °*C*, exact temperature depending on the furnace type, nature of the scrap, etc. This treatment of WC/Co with molten zinc at these temperatures results in zinc and cobalt forming a liquid alloy. The zinc is removed by distillation, and what is left is a mixture of WC and Co, in which the bond between the two has been broken. This product is then broken down mechanically to a particle size similar to that of the grain size of the original cemented carbide microstructure. The zinc vapors are recovered by condensation in a cooler zone of the furnace.

16.4.2.2 Acid leaching process

One can recover a variety of metals, tungsten, vanadium, chromium, and molybdenum from the carbide scrap by treatment with an alkali metal hydroxide in the presence of oxygen, generally at an elevated temperature and pressure for a period of time sufficient to form a water-soluble alkali metal hydroxide. The different metals are then recovered from the water-soluble alkali metal salt by chemical means. This material is digested in an acidic solution that selectively dissolves the cobalt but not the tungsten. Cobalt hydroxide and oxychloride are precipitated by raising the pH to between 6 and 10. The tungsten and cobalt compounds are separated from the slurry and redissolved in an aqueous solution with a pH greater than 11. The product is spray-dried and carburized as necessary.

Hydrothermal techniques have also been investigated; in these techniques, the cobalt matrix is extracted by using hydrochloric acid at 110 °*C*, and subsequently

pulverized by ball milling. Acid leaching has been tried successfully, but is known to have a negative environmental impact.

Problems

1. Describe some of the experimental techniques to measure the characteristics of recovered fibers after chemical recovery of PMCs.
2. Bolted external patches are more suitable for thick laminates. Why?
3. Honeycomb structures are commonly used in aircrafts. Discuss the applicability of bolted repairs in honeycomb structures.
4. Adhesives are generally thermosets. Discuss the problems in using such adhesives for patch repair in thermoplastic laminates.
5. Mention was made in the text of the importance of nondestructive techniques to assess the damage in the composites. Describe some of these techniques, especially the technique of shearography.
6. In the text, we described two types of bonded patch configurations: stepped and scarf. Make a schematic sketch of shear stress distribution along the bondline in the adhesive in the two cases.
7. What are the sources of void formation in the film adhesives used for repair work?
8. Discuss the surface preparation techniques for bonded repairs.
9. Windmills represent a significant part of green energy effort. However, this effort will remain incomplete without the ability to recycle the turbine blades. Discuss the recyclability of wind turbine blades. Specifically, point out the main problems that should be overcome and indicate possible solutions.

References

R.E. Allred, J.M. Gosau. in *Proceedings of Composites and Advanced Materials Expo (CAMX)* (Anaheim, CA, 2016)

K.B. Katnam, L.F.M. da Silva, T.M. Young, Prog. Aerosp. Sci. **61**, 26 (2013)

D.J. Lloyd, Int. Mater. Rev. **39**, 1 (1994)

J.A. Manson, in *High Performance Composite: Commonalty of Phenomena*, ed. by K.K. Chawla, P.K. Liaw, S.G. Fishman (The Minerals, Metals & Materials Society, Warrendale, PA., 1994), p. 1

Y. Nishida, Adv. Eng. Mater. **3**, 315 (2001)

G. Oliveux, O.D. Luke, G.A. Leeke, Prog. Mater. Sci. **72**, 61 (2015)

S.J. Pickering, Compos. A. Appl. Sci. Manuf. **37**, 1206 (2006)

R. Pinero-Hernanz, J. Garcia-Serna, C. Dodds, J. Hyde, M. Poliakoff, M.J. Cocero, S. Kingman, S. Pickering, E. Lester, J. Supercrit. Fluids **46**, 83 (2008)

D.M. Schuster, M.D. Skibo, R.S. Bruski, J. Miner. Metals Mater. Soc. **45**(5), 26 (1993)

H. Yan, C. Lu, D. Jing, C. Chang, N. Liu, X. Hou. New Carbon Mater. **31**, 46 (2016)

Appendix A: Matrices

Definition

A *matrix* is an array of numbers subject to certain operations. For example,

$$\begin{bmatrix} 3 & 2 & 9 & 7 \\ 0 & -63 & 49 & 5 \\ 1 & 5 & 4 & 8 \end{bmatrix} \qquad 3 \text{ rows}, 4 \text{ columns}$$

$$\begin{bmatrix} a_{11} & a_{12} & \cdots & a_{1n} \\ a_{21} & a_{22} & \cdots & a_{2n} \\ \vdots & \vdots & \cdots & \vdots \\ a_{m1} & a_{m2} & \cdots & a_{mn} \end{bmatrix} \qquad m \text{ rows}, \ n \text{ columns}$$

.

The a_{ij} are called the *elements* of the matrix.

Notation

$$A = [A] = (a_{ij}) = \left[a_{ij}\right]_{m,n}.$$

K. K. Chawla, *Composite Materials*,
https://doi.org/10.1007/978-3-030-28983-6

Null Matrix

In a *null matrix*, all the elements are zero, that is,

$$[N] = [0].$$

Any matrix multiplied by a null matrix results in a null matrix. Thus,

$$[A][N] = [N].$$

Square Matrix

The number of rows, called the *order* of the matrix, is equal to the number of columns. For example,

$$[A] = \begin{bmatrix} a_{11} & a_{12} \\ a_{21} & a_{22} \end{bmatrix}$$

is a square matrix of order 2.

Determinant

Associated with every square matrix $[A]$, there is a numerical value called its *determinant*, $|A|$.

$$[A] = a_{ij}\big(\text{cof}\, a_{ij}\big),$$

where $\text{cof}\, a_{ij} = (-1)^{i+j}|M_{ij}|$. cof a_{ij} is the *cofactor* of a_{ij} and M_{ij} is the *minor* of a_{ij}, obtained by eliminating the row and the column of a_{ij}.

Consider the matrix

$$[A] = \begin{bmatrix} a_{11} & a_{12} \\ a_{21} & a_{22} \end{bmatrix}.$$

Determinant $[A] = \begin{vmatrix} a_{11} & a_{12} \\ a_{21} & a_{22} \end{vmatrix}$

$$\begin{aligned}
\operatorname{cof} a_{11} &= (-1)^2 |M_{11}| = M_{11} = a_{22} \\
\operatorname{cof} a_{12} &= (-1)^3 |M_{12}| = -M_{12} = -a_{21} \\
\operatorname{cof} a_{21} &= (-1)^3 [M_{21}] = -M_{21} = -a_{12} \\
\operatorname{cof} a_{22} &= (-1)^4 |M_{22}| = M_{22} = a_{11} \\
|A| &= \sum_{i=1}^{n} a_{ij} \left(\operatorname{cof} a_{ij}\right) = a_{11}a_{22} + a_{12}(-a_{21}) \\
&= a_{11}a_{22} - a_{12}a_{21}.
\end{aligned}$$

Another example is

$$[A] = \begin{bmatrix} 1 & 2 & -1 \\ 3 & 4 & 0 \\ 0 & 3 & 2 \end{bmatrix}$$

$$\operatorname{cof} a_{11} = M_{11} = \begin{vmatrix} 4 & 0 \\ 3 & 2 \end{vmatrix} = 8 - 0 = 8$$

$$\operatorname{cof} a_{12} = -M_{12} = \begin{vmatrix} 3 & 0 \\ 0 & 2 \end{vmatrix} = -6 + 0 = -6$$

$$\operatorname{cof} a_{13} = M_{13} = \begin{vmatrix} 3 & 4 \\ 0 & 3 \end{vmatrix} = 9 - 0 = 9$$

$$|A| = 1 \times 8 + 2 \times (-6) - 1 \times 9 = 8 - 12 - 9 = -13.$$

Diagonal Matrix

A square matrix whose nondiagonal elements are zero is called a *diagonal matrix*.

$$a_{ij} = 0 \quad \text{for } i \neq j$$

For example,

$$\begin{bmatrix} 3 & 0 & 0 \\ 0 & 2 & 0 \\ 0 & 0 & 1 \end{bmatrix}.$$

Identity Matrix

A diagonal matrix whose elements are unity is called an *identity matrix*.

$$[I] = \begin{bmatrix} 1 & 0 & 0 \\ 0 & 1 & 0 \\ 0 & 0 & 1 \end{bmatrix}$$

$$[I][A] = [A]$$

Column or Row Matrix

All the elements in a column or row matrix are arranged in the form of a column or row. For example,

$$\text{column matrix} \quad \begin{bmatrix} a_1 \\ a_2 \\ \vdots \\ a_n \end{bmatrix}$$

$$\text{row matrix} \quad [\, b_1 \quad b_2 \quad \cdots \quad b_n \,].$$

Transpose Matrix

The substitution of columns by rows of the original matrix produces a *transpose matrix*. The transpose of a row matrix is a column matrix and vice versa. For example,

$$[A] = \begin{bmatrix} 0 & -5 & 1 \\ 8 & 4 & 2 \end{bmatrix} \qquad [A]^T = \begin{bmatrix} 0 & 8 \\ -5 & 4 \\ 1 & 2 \end{bmatrix}$$

$$[a] = [\, 2 \quad 3 \quad -7 \,] \qquad [a]^T = \begin{bmatrix} 2 \\ 3 \\ -7 \end{bmatrix}$$

$$[AB]^T = [B]^T [A]^T$$

Symmetric Matrix

A square matrix is *symmetric* if it is equal to its transpose, that is,

$$A^T = A$$

$$a_{ij} = a_{ij} \quad \text{for all } i \text{ and } j.$$

Antisymmetric or Skew-Symmetric Matrix

$$A^T = -A$$

$$a_{ij} = -a_{ji} \text{ for all } i \text{ and } j.$$

For $i = j$, $a_{ii} = -a_{ii}$, that is, the diagonal elements of a skew-symmetric matrix are zero.

Singular Matrix

A square matrix whose determinant is zero is called a *singular matrix*.

Inverse Matrix

$[A]^{-1}$ is the inverse matrix of $[A]$ such that

$$[A][A]^{-1} = [I] = [A]^{-1}[A]$$

$$[A]^{-1} = \tfrac{1}{[A]}[\text{cof } A]^T.$$

We now give some examples of inverse matrix determination.

Example 1

$$A = \begin{bmatrix} a_{11} & a_{12} \\ a_{21} & a_{22} \end{bmatrix}$$

$$[A]^{-1} = \begin{bmatrix} a_{22} & -a_{12} \\ -a_{21} & a_{11} \end{bmatrix} \frac{1}{a_{11}a_{22} - a_{12}a_{21}}.$$

Example 2

$$A = \begin{bmatrix} a_{11} & 0 & \cdots & 0 \\ 0 & a_{22} & \cdots & 0 \\ \vdots & \vdots & \cdots & \vdots \\ 0 & 0 & \ldots & a_{nn} \end{bmatrix}$$

$$A^{-1} = \begin{bmatrix} 1/a_{11} & 0 & \cdots & 0 \\ 0 & 1/a_{22} & \cdots & 0 \\ \vdots & \vdots & \cdots & \\ 0 & 0 & \ldots & 1/a_{nn} \end{bmatrix}.$$

Example 3

$$A = \begin{bmatrix} \cos\theta & -\sin\theta \\ \sin\theta & \cos\theta \end{bmatrix}$$

$$|A| = \cos^2\theta + \sin^2\theta = 1$$

$$A^{-1} = \begin{bmatrix} \cos\theta & \sin\theta \\ -\sin\theta & \cos\theta \end{bmatrix}.$$

Example 4

$$T = \begin{bmatrix} m^2 & n^2 & 2mn \\ n^2 & m^2 & -2mn \\ -mn & mn & m^2 - n^2 \end{bmatrix} \quad \begin{matrix} m = \cos\theta \\ n = \sin\theta \end{matrix}.$$

There is a very important matrix called the *transformation matrix*:

$$|A| = 1$$

$$T^{-1} = \begin{bmatrix} m^2 & n^2 & -2mn \\ n^2 & m^2 & 2mn \\ mn & -mn & m^2 - n^2 \end{bmatrix}.$$

Note that T^{-1} is obtained by replacing θ by $-\theta$ in T.

Some Basic Matrix Operations

The equality [A] = [B] is valid if and only if $a_{ij} = b_{ij}$.

Addition and Subtraction

To perform the operations of addition or subtraction, the matrices must be *compatible*, that is, they must have the same dimension:

$$[A] + [B] + [C] = [D]$$

$$a_{ij} + b_{ij} + c_{ij} = d_{ij}.$$

Similarly,

$$[E] = [A] - [B]$$

$$e_{ij} = a_{ij} - b_{ij}.$$

Multiplication

To perform the operation of multiplication, the number of columns of one matrix must be equal to the number of rows of the other matrix:

$$[A]_{m\times n}[B]_{n\times r} = [C]_{m\times r}$$

$$c_{ij} = \sum_{k=1}^{n} a_{ik}b_{kj}$$

$$\begin{bmatrix} 3 & 5 \\ 9 & 8 \end{bmatrix}\begin{bmatrix} 1 & 0 \\ 4 & 3 \end{bmatrix} = \begin{bmatrix} 3\times 1+5\times 4 & 3\times 0+5\times 3 \\ 9\times 1+8\times 4 & 9\times 0+8\times 3 \end{bmatrix} = \begin{bmatrix} 23 & 15 \\ 41 & 24 \end{bmatrix}.$$

Matrix multiplication is associative and distributive but not commutative. Thus,

$$[AB][C] = [A][BC]$$

$$[A][B + C] = [A][B] + [A][C]$$

$$[A][B] \neq [B][A].$$

The order of the matrix is very important in matrix multiplication.

Appendix B: Fiber Packing in Unidirectional Composites

Geometrical Considerations

Consider a composite containing uniaxially aligned fibers. Assume for the sake of simplicity that the fibers have the same cross sectional form and area. Then for any uniaxial arrangement of fibers, we can relate the fiber volume fraction V_f, the fiber radius r, and the center-to-center spacing of fibers R as

$$V_f = \alpha\left(\frac{r}{R}\right)^2,$$

where α is a constant that depends on the geometry of the arrangement of fibers.

Let S be the surface-to-surface distance between the fibers. The fiber radius is r. Then,

$$S = R - 2r = \sqrt{\frac{\alpha}{V_f}}\mathrm{r} - 2\mathrm{r} = \mathrm{r}\left(\sqrt{\frac{\alpha}{V_f}} - 2\right).$$

Hexagonal array

The area of the equilateral triangle in Fig. B.1 is $A_\Delta = \sqrt{3}/4\ R^2$.

Each triangle contains area of half a circle = $0.5A_o = 0.5\ \pi\ r^2$.

Thus,

$$\begin{aligned} V_f &= 0.5A_o/A_\Delta = 0.5\pi r^2/\left(\sqrt{3/4}\right)R^2 = 2/\sqrt{3}\pi(r/R)^2 \\ \alpha_{hex} &= 2\sqrt{3}\pi. \end{aligned} \tag{B.1}$$

K. K. Chawla, *Composite Materials*,
https://doi.org/10.1007/978-3-030-28983-6

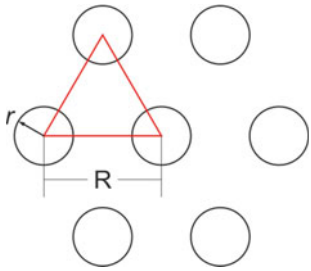

Fig. B.1 A hexagonal array of fibers

Square array

The area of the right triangle in Fig. B.2 is $A_\Delta = 0.5\ R^2$.
Each triangle contains area of half a circle = $0.5A_o = 0.5\ \pi\ r^2$.
Thus,

$$V_f = 0.5A_o/A_\Delta = 0.5\,\pi\,r^2/0.5R^2 = \pi(r/R)^2$$
$$\alpha_{sq} = \pi. \tag{B.2}$$

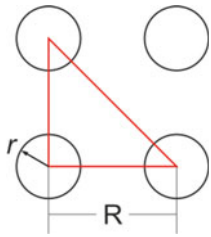

Fig. B.2 A square array of fibers

General case

The area of the isosceles triangle Fig. B.3 is $A_\Delta = 1/2\ R^2 \sin\gamma$.
Each triangle contains area of half a circle = $0.5A_o = 0.5\ \pi\ r^2$.
Thus,

$$V_f = 0.5A_o/A_\Delta = 0.5\,\pi\,r^2/0.5\,R^2 \sin\gamma = \pi \sin\gamma(r/R)^2$$
$$\alpha_{gen} = \pi \sin\gamma. \tag{B.3}$$

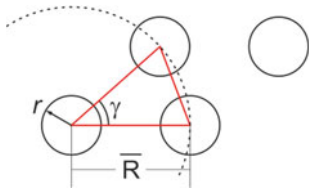

Fig. B.3 A general array of fibers

Check:

For $\gamma = 60°$, 1/sin 60° = 1.155 = $2\sqrt{3}$, and for $\gamma = 90°$, 1/sin 90° = 1.

The square and hexagonal cases are special cases of a more general, "rectangular" approach. In unidirectionally reinforced composites, the fibers may be arranged in layers, but not necessarily in a square or hexagonal array. Let us call the average distance to the next inline neighbor $\bar{R}$ and determine the angle to the next layer. In the general (rectangular) case, α will depend on the angle γ. Question: what angles are possible and how does V_f change with the angle? We leave this in the exercises for the reader to do.

If $S = 2r$, then $\bar{R} = 4r$. If the next layer touches, the base of the isosceles triangle is $2r$ and the corresponding angle γ = 2 a sin 1/4 = 28.9°.

Plausibility check:

In the hexagonal arrangement, $S = 0$ and $R = 2r$. Thus, γ = 2 a sin ¼ = 60°.

Fiber distances $S = 2r$ and $S = 0$

$$\text{For } S = 2r, V_f = \alpha/16, \tag{B.4}$$

$$\text{For } S = 0,\ V_{f,\max} = \alpha/4 \tag{B.5}$$

Arrangement	α	$\alpha/16$	$V_{f,\max} = \alpha/4$
Hexagonal	$2\sqrt{3} = 3.628$	0.227	0.907
Square	$\pi = 3.142$	0.196	0.785

Exercises

1. For $S = 2r$, make a plot of $\alpha/16$ versus the angle in the range 28.9° to 90°.
2. In the rectangular arrangement, the densest fiber packing is achieved when the layers touch (α = 28.9°). Keep this angle constant and move the fibers closer together (lim V_f as S $\rightarrow$ 0). Use the ratio r/R, which is 0.25 at $S = 2r$ and 0.5 at $S = 0$, make a plot of V_f versus r/R.
3. We can also check the transition from square to hexagonal by making a plot of V_f vs. angle γ for $S = 0$, in the range of 60° to 90°.

Note: I wish to express my gratitude to Prof. O. Weichold for discussions and providing the figures for this appendix.

Appendix C: Some Important Units and Conversion Factors

Stress (or Pressure)

1 $dyn = 10^5$ newton (N)
1 $N\ m^{-2} = 10\ dyn\ cm^{-2} = 1$ pascal (Pa)
1 $bar = 10^5\ N\ m^{-2} = 10^5\ Pa$
1 hectobar = 100 bars = $10^8\ cm^{-2}$
1 kilobar = $10^8\ N\ m^{-2} = 10^9\ dyn\ cm^{-2}$
1 $mm\ Hg = 1\ torr = 133.322\ Pa = 133.322\ N\ m^{-2}$
1 $kgf\ mm^{-2} = 9806.65\ kN\ m^{-2} = 9806.65\ kPa = 100$ atmospheres
1 $kgf\ cm^{-2} = 98.0665\ kPa = 1$ atmosphere
1 $lb\ in^{-2} = 6.89476\ kN\ m^{-2} = 6.89476\ kPa$
1 $kgf\ cm^{-2} = 14.2233\ lb\ in^{-2}$
$10^6\ psi = 10^6\ lb\ in^{-2} = 6.89476\ GN\ m^{-2} = 6.89476\ GPa$
1 $GPa = 145{,}000\ psi$.

Density

1 $g\ cm^{-3} = 62.4280\ lb\ ft^{-3} = 0.0361\ lb\ in^{-3}$
1 $lb\ in^{-3} = 27.68\ g\ cm^{-3}$
1 $g\ cm^{-3} = 10^3\ kg\ m^{-3}$.

K. K. Chawla, *Composite Materials*,
https://doi.org/10.1007/978-3-030-28983-6

Viscosity

1 $poise = 0.1\ Pa\ s = 0.1\ Nm^{-2}\ s$
1 $GN\ m^{-2}\ s = 10^{10}\ poise$.

Energy

1 $erg\ cm^{-2} = 1\ mJ\ m^{-2} = 10^{-3}\ J\ m^{-2}$
$10^{8}\ erg\ cm^{-2} = 47.68\ ft\ lb\ in^{-2} = 572.16\ psi\ in$.

Fracture Toughness

1 $psi\ in^{1/2} = 1\ lbf\ in^{-3/2} = 1.11\ kN\ m^{-3/2} = 1.11\ kPa\ m^{-1/2}$
1 $ksi\ in^{1/2} = 1.11\ MPa\ m^{-1/2}$
1 $MPa\ m^{-1/2} = 0.90\ ksi\ in^{1/2}$
1 $kgf\ mm^{-2}\ mm^{1/2} = 3.16 \times 10^{4}\ N\ m^{-2}\ m^{1/2}$.

Appendix D: Some Important Concepts of Statistics

The following figures provide clarification/amplification of some statistical concepts used in Chap. 12 (Figs. D.1, D.2, D.3).

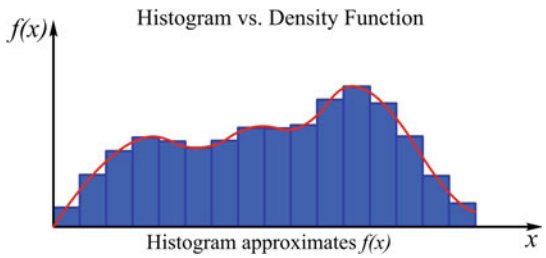

Fig. D.1 Plot of histogram vs. density function

K. K. Chawla, *Composite Materials*,
https://doi.org/10.1007/978-3-030-28983-6

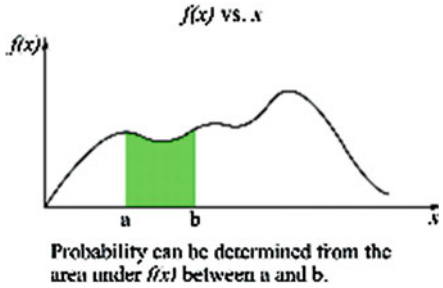

Fig. D.2 Plot of density function vs. x

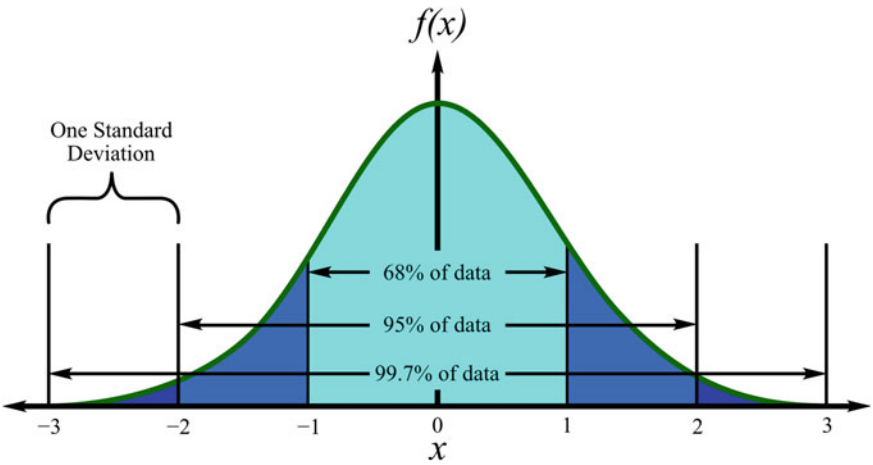

Fig. D.3 Density function vs. x showing normal distribution

Plot of $f(x)$ versus x showing a normal distribution.

Author Index

K. K. Chawla, *Composite Materials*,
https://doi.org/10.1007/978-3-030-28983-6

Subject Index

K. K. Chawla, *Composite Materials*,
https://doi.org/10.1007/978-3-030-28983-6